The Design, Synthesis, and Evaluation of Nitroreductase Triggered Sensors and Theranostics

A thesis submitted to Maynooth University in fulfilment of the requirements for the degree of

Doctor of Philosophy

By

Conor Geraghty, B.Sc.

Department of Chemistry,

Maynooth University,

Maynooth,

Co. Kildare, Ireland.

February 2024

Research Supervisor: Dr. Robert Elmes

Head of Department: Prof. Denise Rooney

Mam and Dad, Thank You for Everything.

Table of Contents

Declaration

I declare the work presented in this thesis was carried out in accordance with the regulations of Maynooth University. The work is original, except where indicated by reference, and has not been submitted before, in whole or in part, to this or any other university for any other degree.

Signed:  Date: 14/02/2024

Conor Geraghty, B.Sc. (Hons)

Acknowledgements

The PhD has been a journey like no other, full of ups and downs. It's been the biggest challenge I have faced so far and after what has been a whirlwind of 4 years it feels a bit surreal that I'm now finally finished. Throughout the 4 years I've been so lucky to have an amazing support system around me, all of whom have helped me reach the end goal and without doubt added to my experience as a PhD student. I'd like to take this opportunity to thank all of you who have been part of my journey it wouldn't have been half the experience without you all.

Firstly, I would like to thank my supervisor Dr. Robert Elmes. Thank you for all your support and guidance. You've always been there for support throughout, be it with my lab projects, thesis writing, or even when the chips were down from failing experiments, you'd lift the mood with your optimism. Thank you for noticing my potential and ability back when I was a final year undergraduate and for taking me on as a PhD student. Working under you has been a pleasure.

I would also like to extent my thanks to all the admin, technical staff, and academic staff within the department who have helped progress my research along the way be it using equipment, requiring glassware, demonstrating, or sending off samples for analysis. I'd like to give a special thanks to Ria for keeping me in check with health and safety and for going the extra mile to ensure that we had everything we needed in the synthesis lab. A big thanks to Noel also, there is literally nothing that man can't fix.

To all the Elmes group, thank you for all the craic shared over the last 4 years. Wynner, we started together, and we finished together, thank you for your great friendship throughout the entirety of the process. From the late nights out to the late nights correcting lab reports we shared a lot of laughs and memories. When things got highly stressful, we could share the experience and make light of it all of which kept the ball moving. Faz, thank you for all the laughs and making me feel like a young lad again when you joined. All the craic we had really did help those long days of gruelling chemistry pass. Keep up the lifting and you might lift more than me one day. Luke M, thank you for showing me the ropes at the beginning, you were some man for all the goss and keeping us all up to date with any drama. Ste, thanks for all the laughs and shared synthesis agony, continue to have faith in the dendrimer as you say somebody has got to do it. Luke B, thanks for all the Guinness shared, the food reviews, and for all the help with the biology. To the rest of the group Xuanyang, Emily, and Jordan thanks for your friendship and best of luck

with the rest of the PhD. I'd like to thank former group members also, Lokesh for his mentorship, Ales, Hua, and Oisin.

Thank you to all PhD students past and present Steely, Harlei, Amanda, Michelle, Kyle, Eoin, Colm, Caytlin, Darren, Sinead, Adam, Keela, Andreaa, Athira, Joe, Keelan, and anyone else who I have forgotten. Thanks for all the coffee, lunch breaks and pints along the way. Best of luck to all of you who are finishing up soon you'll be grand!

To the lads I've grown up with in Maynooth, who know me too well, and whom I've known for too long. Thank you for the mad weekends, holidays, and for all the nights out in The Roost over the last 8 years. A special thanks to Paddy, Ham, and Joe for all the weekends spent golfing which were a much-needed escape from the lab, always winning made it thoroughly enjoyable.

To my girlfriend Laura, my love and best friend, thank you so much for everything that you've done for me over the last two years. You've been my rock supporting me through some very tough times throughout this journey. Your endless support, kindness, and huge amounts of patience required to put up with my madness has helped push me to the finish line. You always managed to put a smile back on my face and lift my mood when it was much needed. I'm so grateful to have you in my life and I can't wait to see what life brings us now that I'm finished.

Last and certainly not least I would like to thank my Family. Sinead, thanks for being a such a supportive sister throughout this process the chats and laughs we'd have after a day's work would always be a mood lifter, I'm lucky to have a sister who is also a great friend.

Mam and Dad, words can't describe how thankful I am for everything that you've done for me. For all the support you've provided me mentally and emotionally, and all the support financially. I will be forever grateful, none of this would've been possible without you. You always gave me the push I needed to excel academically from all the evenings spent doing homework as a child to financially supporting me throughout my studies. We all knew that taking on the PhD was going to be a more difficult and different path than most and it for sure wasn't the easiest at times, but with all the love and support you provided me I battled through it all and made it out the other side. You raised me to be strong, resilient, and to always take the bull by the horns. Thank you so much Mam and Dad.

I would like to thank all those who are no longer with us today and have been supporting me from the above. I would also like to thank God for giving me the strength and fortitude to weather the storm and who continues to lead me throughout life.

I would like to take this opportunity to thank myself. The last 4 years have been enjoyable and rewarding but they also pushed me to new limits serving me a great deal of stress and anxiety. I hold myself proud for never quitting when the going was tough and to have the willpower and resilience to stick it out right until the end. There's no success without failure that much is for sure.

"Our greatest weakness lies in giving up. The most certain way to succeed is always to try just one more time." - Thomas Edison

"Study hard what interests you the most in the most undisciplined, irreverent and original manner possible." – Richard Feynman

Abstract

Poorly developed vasculature results in low intracellular O_2 regions within tumour tissues. Such areas of hypoxia are under intense reductive stress due to the lack of O_2 and lead to the upregulation of oxidoreductase enzymes such as nitroreductases (NTRs). NTRs are a particularly valuable marker for reductive stress being capable of reducing nitroaromatics to corresponding amino derivatives, a feature that has been exploited in the design of hypoxia sensitive fluorescent imaging agents. To date, 1,8-naphthalimide fluorophores have attracted considerable attention owing to their exceptional fluorescence characteristics, making them ideal candidates for the design of NTR responsive fluorescent probes. Given their synthetic versatility, which allows for the consequential modulation of fluorescence, coupled with their inherent sensitivity and selectivity, 1,8-naphthalimide fluorophores are considered highly applicable for monitoring NTR activity in hypoxic environments.

This thesis entitled 'The Design, Synthesis, and Evaluation of Nitroreductase Triggered Sensors and Theranostics' is divided into 6 chapters and begins with Chapter 1, an introductory chapter which provides a literature review regarding the background and current research in the field of cancer, hypoxia, fluorescent sensors, and NTR based 1,8-naphthalimide fluorescent sensors. This chapter also outlines the aims and the objectives of the research carried out within this thesis.

Chapter 2 details the synthesis and luminescence response of 3 novel Ru(II) polypyridyl complexes, a moiety not yet exploited for NTR sensing. It was proposed that the MLCT emission of these compounds could be quenched by nitroaromatic moieties allowing for an OFF-ON luminescence response in the presence of NTR. These complexes exhibited luminescence Turn-ON responses towards NTR, with one compound in particular displaying a significant OFF-ON response coupled with sensitivity and selectivity towards NTR. This compound was further investigated with regards to its DNA binding ability as well as its potential as an imaging agent for NTR *in cellulo.*

Chapter 3 introduces four novel self immolative dendrimers designed to elicit a blue to green ratiometric fluorescent response in the presence of NTR. The synthesis of these dendrimers through the use of carbamate bond formation allows for the modulation of either fluorophore or prodrug. The fluorescent response of each probe was evaluated first by using a reducing agent and then by NTR under physiological conditions. One compound in particular established remarkable change in fluorescence as well as

exceptional selectivity towards NTR, showcasing the utility of such a design as a self immolative theranostic approach for NTR sensing.

Chapter 4 presents two novel fluorescence sensors for NTR described as quaternarised phenanthroline-naphthalimide conjugates. By quaternarization of the phenanthroline moiety, a compound with water solubility and potential DNA binding ability is achieved through its cationic nature, without the requirement of a heavy metal. Both compounds were observed to be responsive towards NTR with one of the compounds displaying both exceptional sensitivity towards varying concentrations of NTR and selectivity towards NTR in comparison to other biologically relevant species.

Chapter 5 consists of a thesis summary that outlines the key findings and future work for each chapter. Subsequently, Chapter 6 includes the general experimental procedures as well as the synthesis and characterisation of all compounds. Literature references are also provided, followed by the Appendix which consists of the spectroscopic data that validates the work described in the main text.

Abbreviations

TME	Tumour microenvironment
HIF	Hypoxia inducible factor
DNA	Deoxyribonucleic acid
O_2	Oxygen
S_o	Ground state
S_1	Singlet excited state
Na^+	Sodium
K^+	Potassium
Mg^+	Magnesium
Ca^{2+}	Calcium
Zn^{2+}	Zinc
F^-	Fluoride
Cl^-	Chloride
MeCN	Acetonitrile
PET	Photoinduced electron transfer
ROS	Reactive oxygen species
H_2O_2	Hydrogen peroxide
$ONOO^-$	Peroxynitrite
FRET	Fluorescence resonance energy transfer
Cys	Cysteine
Hcy	Homocysteine
GSH	Glutathione
H_2S	Hydrogen sulfide
DNBS	2,4-dinitrobenzenesulfonyl

PBS	Phosphate-buffered saline
Ru(II)	Ruthenium (II)
Phen	1,10 - Phenanthroline
Bpy	2,2’ – Bipyridine
Dppz	Dipyridophenazine
ICT	Internal-charge transfer
NTR	Nitroreductase
NADH	Nicotinamide adenine dinucleotide
HAPs	Hypoxia-activated prodrugs
UV	Ultraviolet
HClO	Hypochlorous acid
Φ	Quantum yield
nm	Nanometre
LOD	Limit of detection
ATP	Adenosine triphosphate
MLCT	Metal to ligand charge transfer
DMSO	Dimethyl sulfoxide
DMF	Dimethylformamide
NIR	Near infrared
NEt_3	Triethylamine
NMR	Nuclear magnetic resonance
IR	Infrared spectroscopy
HRMS	High resolution mass spectrometry
COSY	Correlated Spectroscopy
HSQC	Heteronuclear single quantum coherence

HMBC	Heteronuclear Multiple Bond Correlation
MHz	Megahertz
EtOH	Ethanol
H_2O	Water
HCl	Hydrochloric acid
AcOH	Acetic acid
K_2CO_3	Potassium carbonate
CO_2	Carbon dioxide
H_2	Hydrogen gas
Pd/C	Palladium on carbon
N_2H_4	Hydrazine
$SnCl_2$	Tin chloride
Vis	Visible
FMN	Flavin mononucleotide
NaCl	Salt
BSA	Bovine serum albumin
LCMS	Liquid chromatography mass spectroscopy
stDNA	Salmon testes deoxyribonucleic acid
P/D	Phosphate to Dye ratio
DAPI	4’,6-diamino-2-phenylindole
STED	Stimulated emission depletion microscopy
d-LSCM	Diffraction limited confocal scanning microscopy
E. coli	Escherichia coli
S.aureus	Staphylococcus aureus
λ	Lambda

CPT	Camptothecin
DCM	Dichloromethane
THF	Tetrahydrofuran
MeOH	Methanol
DMSO-d_6	Deuterated dimethyl sulfoxide
$CDCl_3$	Deuterated chloroform
$Na_2S_2O_4$	Sodium dithtionite
Rt	Retention time
Eq	Equivalents
ESI	Electrospray ionisation
Et2O	Diethyl ether
EtOAc	Ethyl acetate
EtOH	Ethanol
$CHCl_3$	Chloroform
ATR	Attenuated total reflectance
m/z	Mass to charge ratio
NaOAC	Sodium acetate
NH_4PF_6	Ammonium Hexafluorophosphate
$MgSO_4$	Magnesium sulphate
SiO_2	Silicon dioxide
RBF	Round bottom flask
ppm	Parts per millions
W	Watt
g	Gram
mg	Milligram

min	Minutes
mL	Millilitre
µg	Microgram
NEt_3	Triethylamine
V	Volt
rt	Room temperature
TLC	Thin Layer Chromatography
µL	Microlitre
µM	Micromolar
mM	Millimolar
hr	Hour
min	Minutes
RT	Room temperature

Chapter 1

Introduction

1. Introduction

1.1 Cancer

Cancer defined by the World Health Organisation 'is a generic term for a large group of diseases that can affect any part of the body.'[1] A key characteristic of cancer is metastasis which is the rapid division of abnormal cells which can invade and spread amongst other parts of the body and to other organs. It is these metastases that are responsible for the large number of fatalities caused by cancer worldwide. In 2020 cancer accounted for 10 million deaths worldwide.[1] In Ireland, cancer is the second most frequent cause of mortality. Between the years of 2011-2013, a total of 8,700 deaths were as a result of cancer.[2]

The characteristics of cancer are best described by the 'Hallmarks of Cancer' published by Douglas Hanahan and Robert A. Weinberg.[3-5] The concept being that it was possible to unify all cancer cells at the cellular phenotype level with a set of shared commonalities. Proposing that a shared set of underlying cellular parameters could be used to distinguish phenotypes of a wide range of human tumours. Developing upon the original six hallmarks of cancer there are now eight hallmarks seen in Figure 1.1. In addition to these eight hallmarks genome instability and tumour-promoting inflammation were included as enabling characteristics.[4]

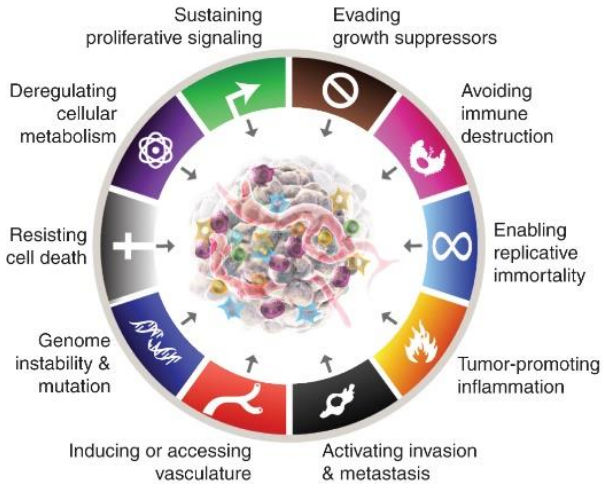

Figure 1.1: *The eight hallmarks of cancer, including genome instability and tumour-promoting inflammation as enabling characteristics. Adapted with permission form Cancer Discov. 2022;12(1):31-46.*

Whilst changes in gene expression, protein function, and mitogenic signalling all contribute to these phenotypes.[4] There are many genetic and phenotypic variations amongst tumours known as intertumor and intratumor heterogeneity. Subclones of the tumour that can be spatially separated, or coexisting are genetically diverse and can result in dynamic changes as the disease undergoes progression. Genomic instability is largely responsible for the genetic diversity within tumours which results in diverse cell populations. Different mechanisms of instability can occur throughout tumour development resulting in distinct genomic characteristics that impact tumour evolution and patient outcomes.[6]

Current methods of treatment for cancer rely on traditional practices such as surgery, radiotherapy, and chemotherapy. There are also newer methodologies of treatment for example hormone therapy, stem cell therapy, immunotherapy, and targeted chemotherapeutics.[7] Whilst there has been vast amounts of research carried out in these areas there is growing interest in therapeutic strategies targeting the tumour microenvironment (TME).[8] In recent years research has shown that genetic mutation is not solely responsible for the development of cancer and that the TME owes to the complexity of the disease.[9] Within the TME resides cells that are genetically more stable in comparison to cancer cells, suggesting a significant therapeutic advantage by avoiding drug resistance caused by genomic instability in cancer cells.[10]

The TME is a dynamic and complex multicellular environment in which a tumour grows. It consists of a variety of immune cells and encompasses the extracellular matrix along with the various excreted molecules. The TME also includes the vascular network of blood and lymphatic vessels, facilitating communication among its diverse cellular components as well as heterogeneous cancer cells.[11]

The TME has its own set of hallmarks with two in particular posing as promising targets for cancer therapy, the immune microenvironment and the hypoxic niche.[8, 12, 13] It is suggested that the hypoxic niche extends throughout the entire TME as there is a constant state of hypoxia in malignant and stromal cancer cells as well as the surrounding microenvironment.[8, 12]

1.2 Hypoxia

Tumour hypoxia was initially proposed by Thomlinson et al. in 1955 from examining the tumour tissue of patients diagnosed with lung cancer.[14] Since then, over the last six decades of clinical and experimental research it has been demonstrated that hypoxia is a prevalent characteristic in 90% of solid tumours.[14, 15]

Oxygen (O_2) plays a critical role in both cell metabolism and various physiological processes. Upon its binding to haemoglobin, it is transported through the bloodstream towards capillaries and then enters tissue cells through the process of diffusion.[16] As cancer cells sustain proliferative growth outwards from a blood vessel, the oxygen demand surpasses that of oxygen supply due to dysregulated angiogenesis, resulting in hypoxic areas within the tumour (Figure 1.2).[17] Tissue that are located at 100-200 µm from an adequate blood vessel are deemed to be undergoing hypoxia, a widespread condition in solid tumours.[18-21] Hypoxia can be described as acute or chronic. Acute hypoxia can arise from transient opening and closing of blood vessels from within the tumour. Whereas chronic hypoxia is the term given to cells in the TME with reduced oxygen diffusion because of their distance from the blood vessel.[22]

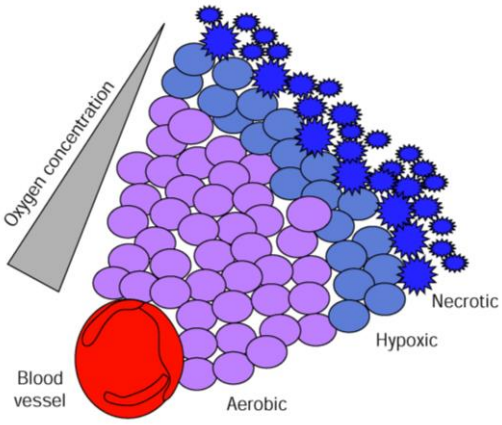

Figure 1.2: *Hypoxic cells at a distance from the blood vessel with depleted oxygen concentration. Adapted from The Lancet Oncology Volume 1, Issue 1, September 2000, Pages 25-29.*

Cells within these hypoxic areas contribute to the malignant alteration of tumours through hypoxia inducible factors (HIFs) which are regulated by a multitude of signalling pathways.[23-26] These comprise of α (HIF-1α, HIF-2α, and HIF-3α) and β (HIF-1β)

subunits. HIF-2α and HIF-3α are expressed in certain tissues whereas HIF-1α is widely expressed amongst body tissues.[27, 28] Under normoxic conditions, HIF-1α is degraded as a consequence of hydroxylation by the oxygen-dependent proline hydroxylase (PHD) family and interaction with von Hippel-Lindau tumour suppressor protein followed by subsequent ubiquitination.[29, 30] Conversely, under hypoxic conditions PHD activity is inhibited due to the low concentrations of oxygen < 10%, allowing for the dimerization of HIF-1α with HIF-1β forming a heterodimer that can translocate into the nucleus and bind to the hypoxia response element in target gene promotors thus reducing the cells oxygen consumption (Figure 1.3).[31-33] HIF regulates cancer cell growth by regulating genes related to glycolysis, angiogenesis, and apoptosis/stress response.[34]

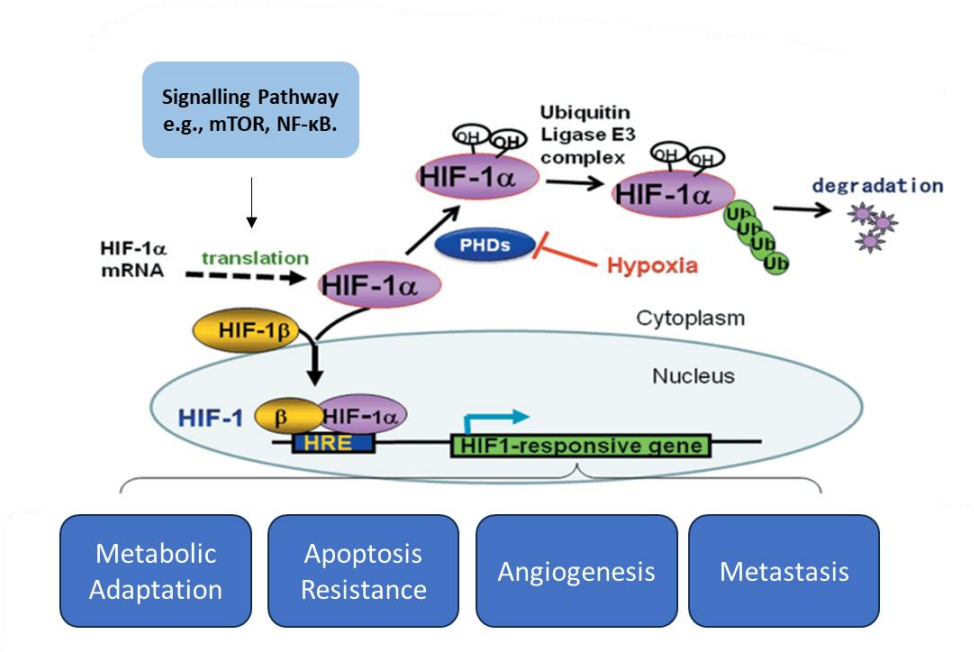

Figure 1.3: *Regulation of HIF-1 in the presence of PHDs. Under normoxic conditions HIF-1α undergoes degradation whereas under hypoxic conditions dimerization occurs between HIF-1α with HIF-1β allowing for the expression of HIF-1 responsive genes. Adapted from Cancer Science, Volume 100, Issue8, August 2009, Pages 1366-1373.*

HIF results in the production of glucose transporters (GLUTs) and the activation of aerobic glycolysis. GLUTs and aerobic glycolysis are important to generate adenosine triphosphate (ATP) in an oxygen deficient environment contributed by the Warburg effect.[35, 36] HIF-mediated upregulation of angiogenic factors, such as vascular endothelial growth factor (VEGF) and erythropoietin (EPO), stimulates angiogenesis the formation

of new blood vessels improving oxygen delivery to hypoxic tissues. This also promotes endothelial cell proliferation and migration.[37-39] Key mediators of hypoxia HIF-1α and HIF-2α are pivotal in cancer progression and therapy resistance as it induces changes in TME stromal cells, including immune cells.[40] HIF can also inhibit apoptosis promoting cell survival through expression of inhibitor of apoptosis protein 2, and regulation of tumour suppressor protein p53.[41, 42]

Cancer cells under hypoxia have an increased expression of drug resistant genes that promote the efflux of chemotherapeutic drugs and as a result lower the intracellular drug concentration for example through multidrug resistance-associated protein 1 (MRP1) expressions induced by HIF-1α.[43-45] Furthermore, hypoxic tumour cells are also resistant towards radiation therapy due to the low O_2 partial pressure (<10 mmHg). At 1 mmHg, cancer cells display three times greater resistance to radiation compared to normoxic cells.[46, 47] This radio resistance arises from the role of oxygen in the radiochemical process to induce DNA damage. Oxygen facilitates the generation of DNA strand breaks through free radicals such as hydroxyl radicals produced by ionizing radiation. In clinical trials it has been shown that double strand breaks of DNA to be 2 to 3-fold under hypoxic conditions with activation of additional DNA repair pathways.[15, 47, 48]

Given that hypoxia is present to varying degrees in solid tumours and is associated with treatment resistance and patient prognosis, it is deemed to be an appealing target for refining therapies while also serving as a predictive and prognostic biomarker for treatment.[42, 49-51]

1.2.1 Methods of Measuring Hypoxia

Given the clinical importance of hypoxia in cancer progression there is an increasing need of methods for assessing tumour hypoxia of which can be either invasive or non-invasive.[52]

Direct methods of measurement have been of major clinical importance for hypoxia most notably the direct partial pressure of oxygen (pO_2) measurement via oxygen electrode. The polarographic electrode is an invasive and direct technique used to measure tissue oxygen concentration by employing the electrochemical reduction of oxygen molecules. This method has been viewed as the gold standard. The method depends on accessible lesions in which the electrode can be inserted whereby oxygen is measured from several points per needle.[53-56] There are however many disadvantages to oxygen electrodes

regarding their application in clinical practice. Due to the electrode being highly invasive it is difficult to repeat measurements and requires skilled technical staff. It is also difficult to generate 3D oxygen maps due to limiting spatial resolution. Halogenated anaesthetics and difficulty in differentiating between necrotic and hypoxic tissue can also give rise to differentiating oxygen measurements.[54]

Immunolabelling of endogenous and exogenous markers is another method used to identify hypoxic cells and is achieved through immunohistochemical (IHC) or immunofluorescent (IF) imaging techniques. This is achieved through immunolabelling HIF-1α and HIF-2α or using exogenous probes such as pimonidazole forming hypoxic adducts which can be detected through antibodies specific to the probe via IHC or IF. Whilst this technique is useful there is the invasive disadvantage of requiring a biopsy making deeper tumour tissue difficult to access. Furthermore, the sample size required for biopsy is small which may not represent the entirety of the tumour.[52, 57, 58]

Magnetic resonance imaging (MRI) is a non-invasive method of evaluating hypoxia allowing for 3D images of tumours. Blood-oxygen-level dependent (BOLD) functional MRI measures the magnetic distortions caused by the paramagnetic character of deoxygenated haemoglobin and Tumour Oxygenation Level-Dependent (TOLD) MRI measures O_2 concentration of the tumour tissue. Electron Paramagnetic Resonance Imaging (EPRI) is similar to TOLD MRI in the sense that it also measures O_2 concentration via a spin probe.[59-61]

To date there has been more selective techniques developed based on the exploitation of the bioreductive environment characteristic of the hypoxic tumour microenvironment which includes that of ^{19}F NMR, positron emission tomography (PET), single-photon emission computed tomography (SPECT), and fluorescence imaging. All of which exploit the use of a recognition moiety capable of undergoing reduction in a reducing environment.[62-66]

1.2.2 Fluorescence as a Technique for Measuring Hypoxia

Fluorescence is a useful approach to monitor hypoxia. It is the phenomenon by which a fluorophore absorbs photons at a specific wavelength resulting in an excitation of the fluorophore to a singlet excited state (S_1). A photon is then emitted upon relaxation of the fluorophore to its ground state (S_o) with accordance to Kasha's rule stating that fluorescence occurs from the lowest S_1 excited state. This is best described by a simple

Jablonski diagram in Figure 1.4. Fluorescence is widely applicable as a method of measurement as changes in wavelength of emission, quantum yield, and fluorescence lifetimes are all measurable outputs.[67, 68]

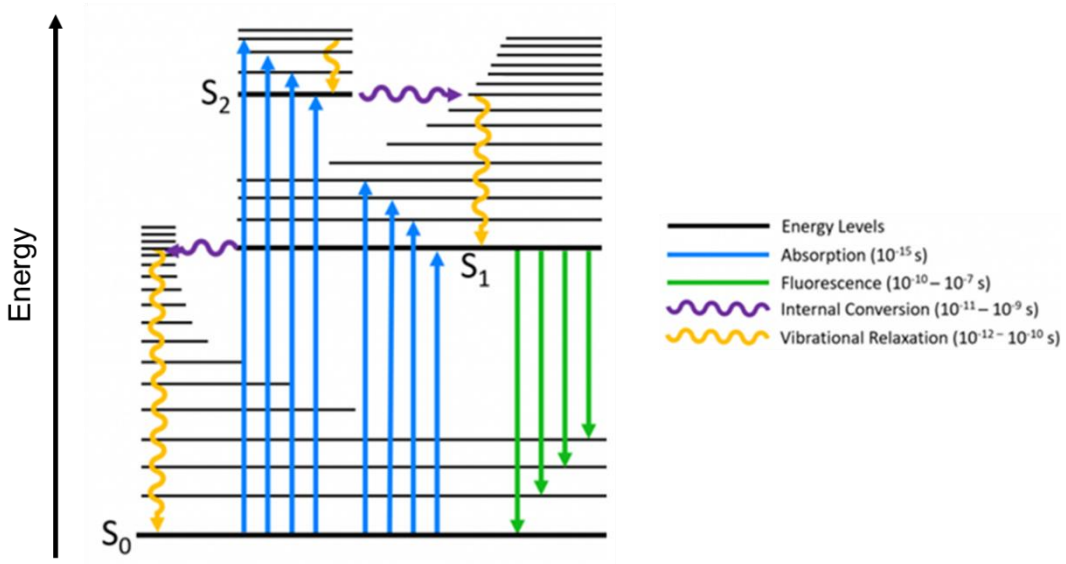

Figure 1.4: *The Jablonski diagram shows the absorption of a blue photon of light resulting in excitation to S_2 excited state, followed by vibrational relaxation and internal conversion to the lowest lying S_1 excited state resulting in the emission of a green photon.*[69]

An alternative method for real-time hypoxia monitoring involves the introduction of vectors designed to express fluorescent proteins specifically under hypoxic conditions. The concept is to incorporate a human response element that results in the production of a green fluorescent protein by the HIF-complex.[70] This approach has been well utilized in showing the development of a hypoxic core in colorectal carcinoma cell line HCT116 spheroids. It's also been used to establish the metabolic phenotypes of hypoxic cells.[71, 72] This approach has also been applied *in vivo*. Wang and coworkers successfully established an MDA-MB-231 an epithelial like cell line in which a DNA construct (GFP-5HRE-ODD-mCherry) was introduced, this allowed for the constant expression of GFP while only allowing for the expression of mCherry (a red fluorescent protein) under hypoxic conditions. By applying intravital imaging techniques, real-time monitoring of individual hypoxic cells within an orthotopic tumour situated in a living mouse model could be visualised.[73]

In lieu of introducing a DNA construct to induce the synthesis of a fluorescent protein in response to hypoxia, some research groups are exploring the utilization of bioreductive activators of fluorescence. These activators are designed to trigger fluorescence in the presence of specific substrates and can be termed fluorescent chemosensors. The design of these chemosensors is incredibly versatile. Activators can consist of anions, cations, small molecules, or biomolecules. While Fluorescence can be activated by a variety of fluorophores with varying photophysical properties as previously mentioned.[74, 75]

Fluorescence-based imaging techniques heavily rely on small molecule-based dyes due to their compact size, facile chemical modification, consistent reproducibility, and compatibility with biological systems. Among the prominently developed organic fluorescent dyes are rhodamine, coumarin, fluorescein, anthocyanins, naphthalimide, BODIPY, and quinoline. These dyes have found widespread use in applications like ion sensing, enzyme analysis, and cellular imaging within scientific research.[76]

Desirable characteristics such as minimal invasiveness, heightened sensitivity, precise spatial and temporal resolution, real-time capabilities, and in situ detection, fluorescence has emerged as a predominant approach for cellular and molecular imaging. Its focus extends to unveiling the localization and identification of intracellular molecules.

Fluorescent signals have been widely utilized for analysing various biological processes both *in vitro* and *in vivo*. Methods like confocal microscopy offer detailed views with precise high spatial and temporal resolutions. This allows for sensitive sensing of specific enzymes within cells, offering insights into their functions and significance in biological activities. Additionally, the concept of fluorescent probes that become active ('turn on') under certain conditions has brought unmatched levels of sensitivity and specificity. This has sparked a growing fascination with fluorescent imaging agents that are activated through reduction processes.[66] However, to further understand this concept, and place the overall thesis within context, the following section will detail an overview of the concept of fluorescent chemosensors.

1.3 Fluorescent Chemosensors

Fluorescent chemosensors are compounds that consist of a binding site, a fluorophore, and a mechanism for communication between these components seen in Figure 1.5.

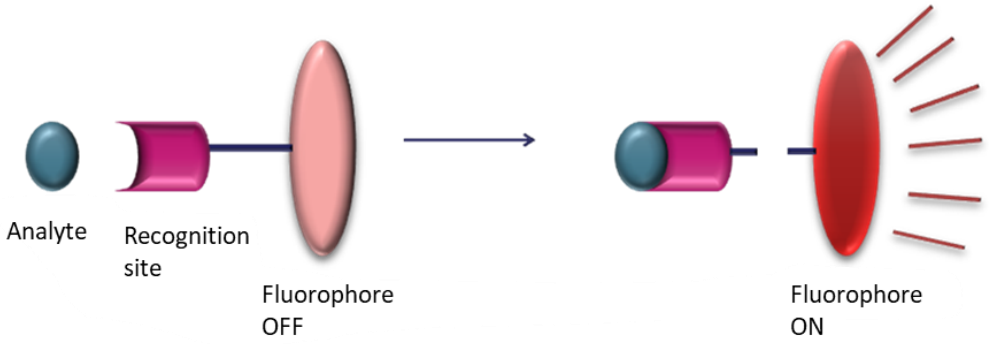

Figure 1.5: *A general schematic of the workings of a chemosensor upon binding of an analyte with the recognition site.*

The origins of fluorescent chemosensors trace back to 1867 when F. Goppelsröder introduced the first example, which involved a highly fluorescent morin chelate for detecting aluminum ions (Al^{3+}). In subsequent decades thanks to the groundbreaking work of de Silva and Czarnik, there has been a rapid and expansive growth in the development of fluorescent chemosensors.[77, 78] This progress was also accompanied by advancements in microscopic imaging technologies. A variety of chemosensors have been designed for the sensing of a wide range of biologically significant analytes, including cations, anions, small neutral molecules, and biomolecules such as proteins and DNA. Initially, these chemosensors primarily targeted metal ions due to the easier selectivity of their binding in water compared to anions or neutral species.[74]

1.3.1 Fluorescence Chemosensors for Cations and Anions

One example of such sensors is compound **1.1** (Figure 1.6) a commercially available sensor capable of measuring potassium (K^+) in whole blood or serum. As potassium binds to the cryptand PET quenching is interrupted and increasing emission at 540 nm is observed with increasing concentration of KCl. Furthermore, this sensor was selective for potassium amongst other cations of clinical relevance such as calcium and sodium.[79]

There have also been sensors developed for other cations such as magnesium (Mg^{2+}). Farruggia *et al.* synthesised two diaza-18-crown-6 hydroxyquinoline derivatives **1.2** (Figure 1.6) both of which showed significant fluorescence enhancement upon binding with Mg^{2+} as PPT and PET are both hindered. Both chemosensors displayed exceptional sensitivity and selectivity towards Mg^{2+} with no fluorescence output observed for other divalent cations such as Ca^{2+}. Both chemosensors were also applicable to live cell imaging of Mg^{2+} in live cells.[80]

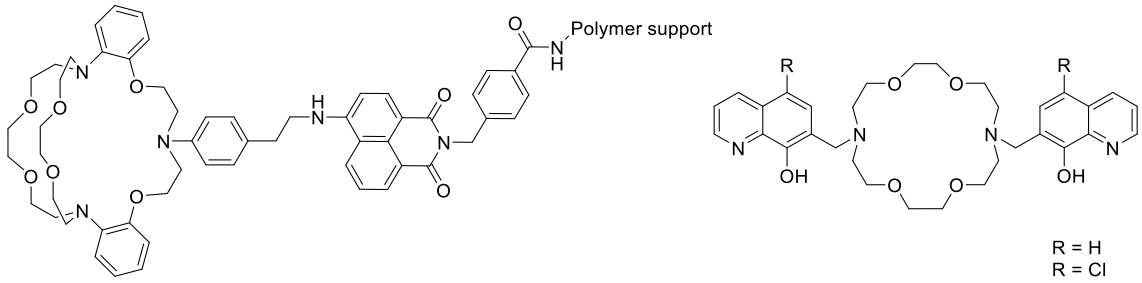

1.1 **1.2**

Figure 1.6: *Compound **1.1** and Compound **1.2**.*

There has also been chemosensors developed for d-block metal cations such as zinc (Zn^{2+}) owing to its abundance in the human body and its involvement in programmed cell death and neurological disease.[81] The Lippard group developed a far-red emitting probe **1.3** (Figure 1.7) for the detection of zinc. The sensor exhibits a reversible and broad dynamic range response when exposed to exogenously introduced Zn^{2+} within the lysosomes of HeLa cells, endogenous Zn^{2+} within insulin granules of MIN6 cells, and zinc-abundant mossy fiber boutons within hippocampal tissue extracted from mice.[82]

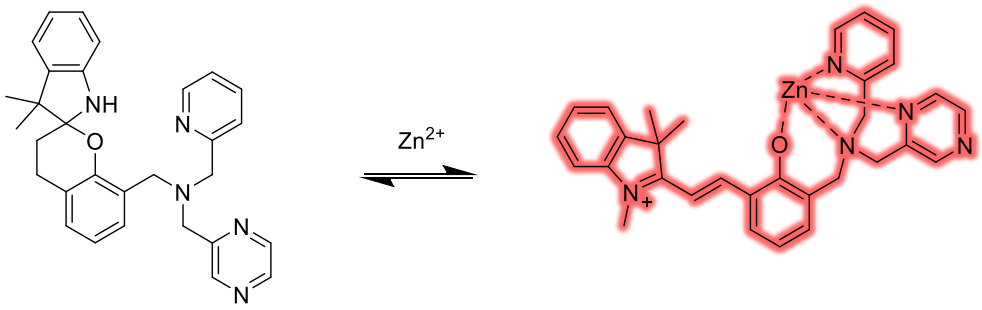

1.3

Figure 1.7: *Compound **1.3** upon binding to Zn^{2+}.*

The advancement of chemosensors with selectivity for anions historically lagged behind their cation counterparts due to the hydration properties of anions. This transformation has been catalysed by the importance of anions in both biological and industrial processes,

coupled with the imperative to devise innovative techniques for detecting anionic contaminants in the environment. Over the past several decades, there has been a proliferation of fluorescent chemosensors designed for the precise identification of anions, employing mechanisms rooted in host-guest interactions or chemical reactions.[83]

An example of an anion chemosensor is **1.4** by Amendola *et al.* which is composed of a pyrene moiety serving as the fluorophore and a urea binding group. **1.4** exhibits a noteworthy and distinctive fluorescence response pattern described as "on–off–on" upon interaction with fluoride ions (F^-), as seen in Figure 1.8. In its initial state within acetonitrile (MeCN), **1.4** emits fluorescence with typical pyrene characteristics, peaking at 394 nm. However, upon the introduction of F^- ions, the fluorescence is switched off. This can be attributed to an electron transfer process within the excited complex and the subsequent transformation of this complex into a less emissive excited tautomeric state. However, with the continued addition of F^- ions, the fluorescence reactivates, with a yellow emission, while a novel emission band cantered at 500 nm emerges. This emission can be ascribed to a charge-transfer mechanism facilitated by the deprotonation of the receptor induced by F^- ions.[84]

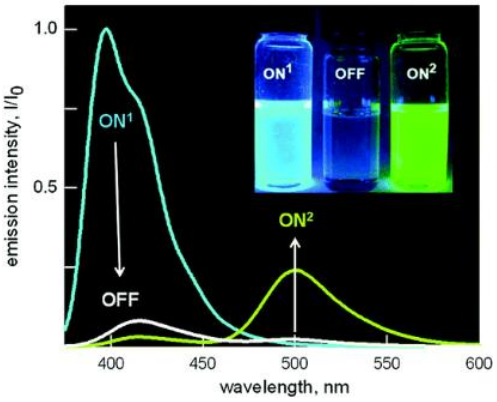

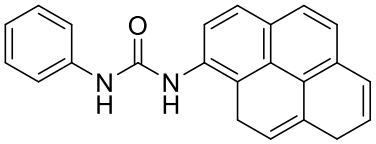

1.4

Figure 1.8: *The emission spectra changes of compound **1.4** upon increasing addition of F^-.*

1.3.2 Fluorescence Chemosensors for Small Molecules

Whilst cation/anion binding through previous examples of host guest interaction can result in changes in fluorescence, similar changes can also be observed through reactions with anions or small molecules. These can include both neutral and anionic molecules of both reactive oxygen species (ROS), reactive nitrogen species (RNS), and reactive sulfur species (RSS). Hydrogen peroxide (H_2O_2) is a ROS species known to be associated with Alzheimer's disease and reactive with boronate based fluorescent probes. B. C. Dickinson *et al.* synthesized five fluorescent probes **1.5**, **1.6**, **1.7**, **1.8**, and **1.9**, all consisting of aryl boronic ester moieties (Figure 1.9), all of which were responsive and selective towards H_2O_2 in aqueous solution amongst other biologically relevant ROS such as hypochlorous acid (HClO), nitric oxide (NO), superoxide (O_2^{-}) , tert-butyl hydroperoxide (*t*BuOOH), and hydroxyl radical ($OH^{\cdot}$) resulting in fluorescence intensity enchancements.

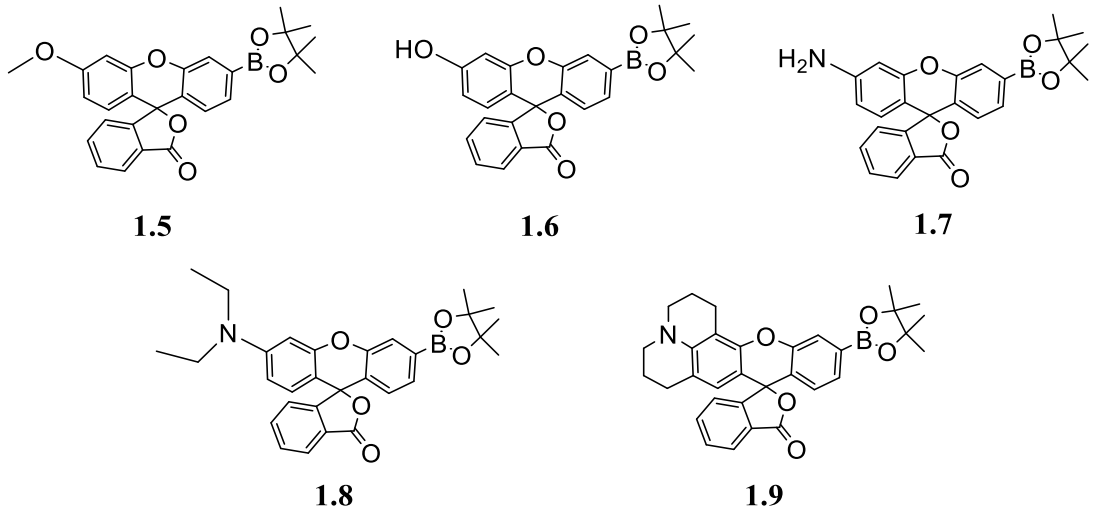

Figure 1.9: *Removal of the boronic ester constituent for each probe by reaction with H_2O_2 results in restoration of fluorescent intensity of the methoxyfluorescein (**1.5**), fluorescein (**1.6**) or rhodol derivatives, aminophenol (**1.7**), diethylaminophenol (**1.8**), and julolidine (**1.9**).*

In live A431 cells under oxidative stress and incubated with **1.5**, **1.8**, and **1.9** an increase in intracellular fluorescence was observed, the same probes also displayed fluorescence intensity increases in RAW264.7 macrophages under induced H_2O_2 production.[85]

Peroxynitrite ($ONOO^{-}$) an anionic reactive nitrogen species is a strong oxidant in both physiological and pathological processes. The Qian research group developed a mitochondria-specific fluorescent chemosensor **1.10** which relies on Fluorescence Resonance Energy Transfer (FRET) for the ratiometric detection of $ONOO^{-}$, as illustrated in Figure 1.10. This chemosensor **1.10** is composed of two cyanine dyes, Cy3 and Cy5,

strategically designed to exploit the distinct reactivity of these dyes towards $ONOO^-$. When excited at 530 nm, the chemosensor exhibits fluorescence emission at 660 nm due to the efficient FRET process from Cy3 to Cy5. However, a remarkable transformation occurs upon the introduction of $ONOO^-$ into the system. An increase in fluorescence intensity at 560 nm accompanied by a concomitant decrease at 660 nm. This phenomenon can be attributed to the selective oxidation of the Cy5 component within **1.10** by $ONOO^-$. Furthermore, the authors demonstrated the chemosensor's potential in semi-quantitative analysis of cellular $ONOO^-$ levels.[86]

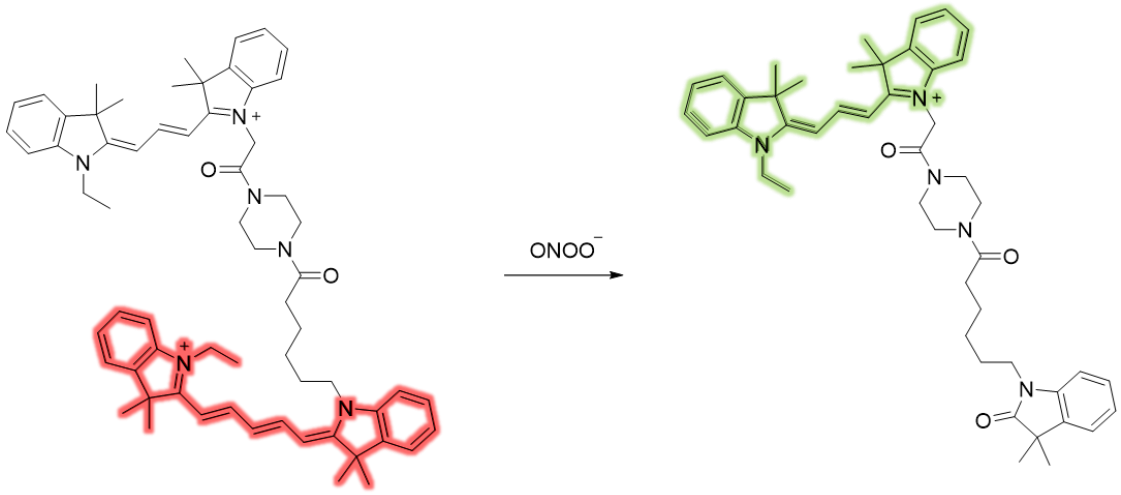

1.10

Figure 1.10: *Reaction of Compound **1.10** consisting of two cyanine dyes Cy3 (green) and Cy5 (red) with $ONOO^-$.*

Cysteine (Cys), homocysteine (Hcy), glutathione (GSH) and hydrogen sulfide (H_2S) play critical roles in a variety of biological processes. A subgroup of chemosensors designed for the detection of thiols consist of a 2,4-dinitrobenzenesulfonyl (DNBS) moiety known to quench the fluorescence of the given fluorophore. In a recent development, a novel fluorescent probe based on the BODIPY scaffold **1.11** (Figure 1.11), has been reported for the specific detection of thiols. Upon exposure to Cysteine (Cys) or Glutathione (GSH) in a phosphate-buffered saline (PBS) solution for a brief period of 10 minutes, an astonishing 20- to 25-fold increase in fluorescence at 570 nm was observed as the DNBS moiety is removed forming sulfur dioxide in the process. To validate its practical applicability, this probe was successfully employed for cellular imaging using monkey renal fibroblast COS-7 cell lines.[87]

An interesting approach was taken by Ji and co-workers with Probe **1.12** in Figure 1.11 which represents a cleverly designed complex, featuring a DNBS moiety linked to a

Ru(II) poly(1,10-phenanthroline) complex as its luminophore. The red emission from the metal to ligand transfer of the ruthenium complex is quenched by the DNBS moiety as a result of a dark singlet excited state. Upon the introduction of 20 μM Cys the amino derivate of the compound is formed as DNBS is removed and an extraordinary 90-fold amplification in phosphorescent emission at 600 nm is observed. What's particularly interesting is the probe's remarkable selectivity for Cys, exceeding other amino acids by more than 40-fold. This high degree of specificity underscores the probe's utility as a precision tool for thiol detection within complex chemical environments. Moreover, to validate its applicability, fluorescence imaging of NCI-H446 cells was successfully carried out.[88]

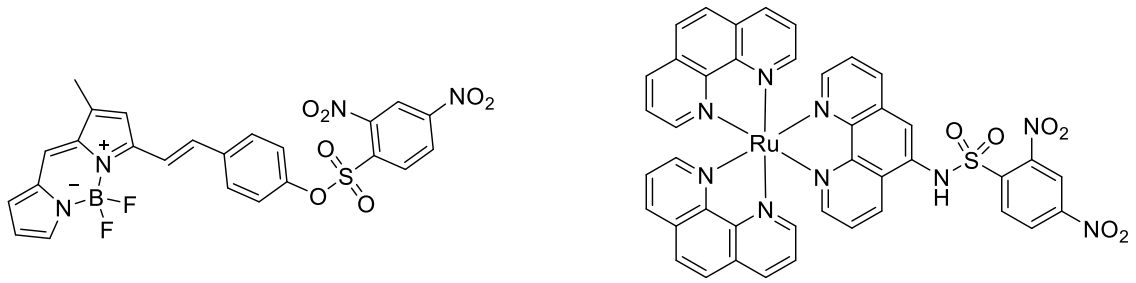

1.11 **1.12**

Figure 1.11: *Structure of compounds **1.11** and **1.12**.*

The above examples aim to highlight the structural diversity and potential use of chemosensors targeting small molecule analytes to a wide variety of diagnostic applications. However, a vast array of chemosensors have also been developed to measure the activity of large biomolecules such as enzymes. The primary aim may be to understand certain biochemical pathways. Or in other instances the objective is to distinguish between qualitative disparities that arise in an anatomical region such as a tumour, this is achieved through corelating the specific anatomical region to the activity level of an enzyme of interest. This often necessitates an enzyme activated fluorescent chemosensor; a synthetic substrate that produces a measurable output upon undergoing an enzyme-catalysed reaction.[89]

1.3.3 Enzyme Activated Fluorescent Chemosensors

The design and synthesis of small molecules that exhibit changes in fluorescence output due to a reaction or interaction with an enzyme have garnered substantial research interest recently due to their versatile applicability spanning across a wide variety of enzymes.[74, 77, 90] There are many advantages to these kind of fluorescent sensors as previously mentioned such as high sensitivity and selectivity, synthetic versatility and feasibility, tuneable emission characteristics, and high spatiotemporal resolutions. These sensors not only serve as a diagnostic tool but also as indispensable tools for elucidating the involvement of various analytes in disease and thus contributing to the biological understanding of such analytes.

Enzyme activated fluorescent chemosensors aim to function within densely populated cellular milieu and so there are often challenges when these probes are applied to biological imaging applications where important factors have to be taken into consideration such as the cytotoxicity of the probe, probe stability, uptake and localisation, modes of activation, and enzyme rates.[91]

Various methodologies have been employed so far to achieve desired fluorescent modulations.[92-95] In Figure 1.12, the three predominant strategies commonly employed in this context are shown using a 1,8-naphthalimide fluorophore as an example. Firstly, we have the enzymatic cleavage of a blocking group, resulting in the liberation of an active fluorophore.[96-98] Secondly, enzymatic transformations can be harnessed to convert these blocking groups into alternative substituents.[99-101] Lastly, enzymatic processes can facilitate the release of fluorescent quenchers.[102-104] Further elaboration on the comprehensive spectrum of modulations will be provided in subsequent sections of this chapter.

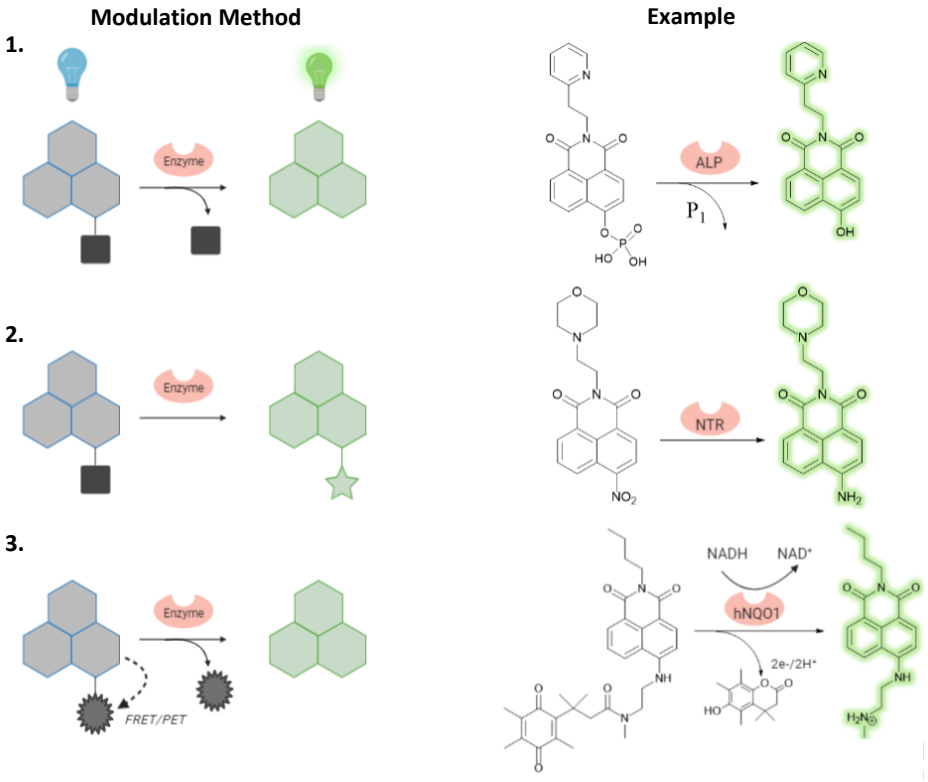

Figure 1.12: *Illustrative depiction of the structural frameworks utilized in crafting enzyme-responsive 1,8-naphthalimide fluorogenic probes, with examples of differing enzymes capable of reacting with a given blocking group/fluorescent quencher* ***(1)*** *Cleavage of a blocking group via alkaline phosphatase (ALP) to release an active fluorophore,*[105] ***(2)*** *transformation of blocking group by NTR from nitro to amino derivatives,*[106] ***(3)*** *Release of a fluorescent quencher by DT-diaphorase upon reduction of the quinone moiety.*[107]

Enzyme activated fluorescent chemosensors take advantage of several photophysical mechanisms aimed at eliciting alterations in fluorescence. Numerous techniques have been harnessed for the precise modulation of fluorescence emission. These encompass Förster Resonance Energy Transfer (FRET), Photoinduced Electron Transfer (PET), Internal-charge Transfer (ICT), Through-bond Energy Transfer (TBET), Excited-state Intramolecular Proton Transfer (ESIPT), Aggregation-induced Emission (AIE), Restriction of Intramolecular Motion (RIM), and Monomer–excimer based ratiometric sensing, among others.[108, 109]

In the context of enzyme activated chemosensor design, an equally significant aspect to consider is the choice of fluorophore scaffold. In considering an ideal fluorophore, one must take into account the physicochemical attributes, including the excitation and

emission properties,[95, 110] photostability,[111] solvatofluorochromism,[112] and membrane permeability.[113] As previously shown, several fluorophore options exist for the design and synthesis of chemosensors such as coumarins, rhodamines, BODIPY's, fluorescein, cyanines, and 1,8-naphthalimides. All of which have been applied in the detection of an extensive array of enzymatic analytes.[93, 94, 114, 115]

With such a vast scope of enzymes that can be targeted such as oxidoreductases, transferases, hydrolases, lyases, isomerases, and ligases there is already a large library of such chemosensors reported in literature.[91] All of which have differing substrate/recognition units and fluorophores. Take oxidoreductases for example, within this class resides the nitroreductase enzyme, which has the ability to reduce nitroaromatic components. Probe **1.13** (Figure 1.13) is an example of a coumarin based probe for NTR which is an OFF-ON probe displaying a 5-fold increase in fluorescence intensity at 455 nm in the presence of NTR upon reduction of the nitrobenzyl moiety.[116] A similar design with a different substrate unit and fluorophore can also be seen in the case of probe **1.14** (Figure 1.13), here a nitroimidazole moiety is used and the fluorophore of choice is a resorufin derivative capable of a much longer wavelength of emission at 705 nm upon reduction of the nitroimidazole moiety.[117]

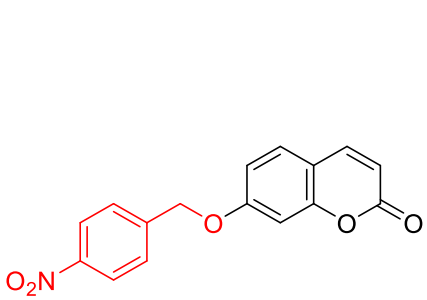

1.13

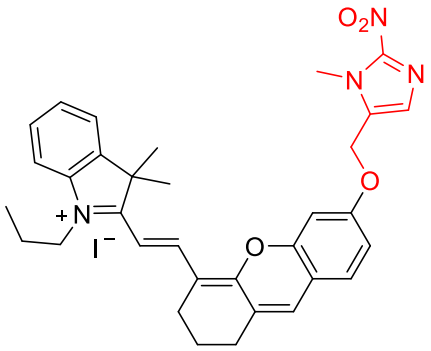

1.14

Figure 1.13: *Compounds **1.13** and **1.14**.*

The idea of varying either the substrate unit or the fluorophore is consistent for all enzymes previously mentioned and can also be seen in transferases. If we take acyltransferases for example, we can see in Probe **1.15** and **1.16** (Figure 1.14) that the glutamyl amide moiety is present in both compounds but both differ in terms of fluorophore. With probe **1.15** releasing an indocyanine and probe **1.16** releasing a silarhodamine in the presence of γ-glutamyltransferase.[118, 119]

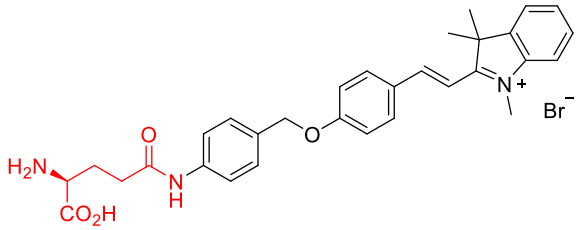

1.15

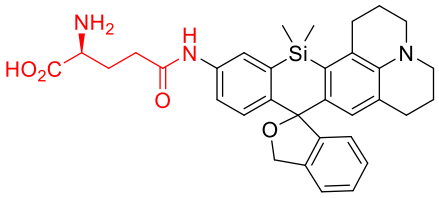

1.16

Figure 1.14: *Compounds **1.15** and **1.16**.*

Furthermore, this concept can also be applied to hydrolases such as glycosidases, these probes incorporate a monosaccharide as an enzyme activatable unit in this case β-D-galactopyranoside. When **1.17** (Figure 1.15) reacts with β-galactosidase the β-glycosidic bond is broken, and fluorescence is turned on at 720 nm as the cyanine fluorophore is released. The same reaction is also observed for **1.18** (Figure 1.15) except in this case there is the release of a BODIPY fluorophore resulting in a change of fluorescence from 575 nm to 730 nm.[120, 121]

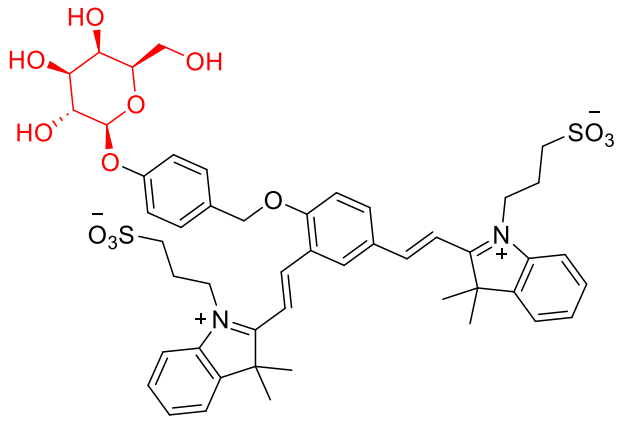

1.17

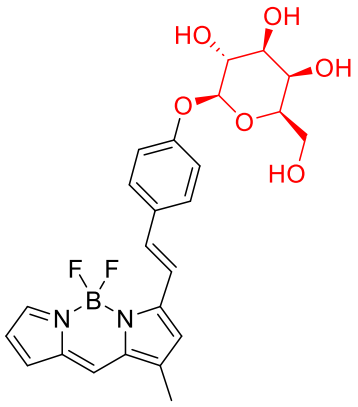

1.18

Figure 1.15: *Compounds **1.17** and **1.18**.*

With such variability and versatility in terms of the design and synthesis of enzyme activated fluorescent chemosensors they have become an appealing target to target hypoxic regions under reductive cell stress.

1.4 Targeting Hypoxia

The basis of forming selective imaging agents for hypoxia is based on utilising a motif capable of undergoing reduction only under hypoxic conditions. A strategy that has been applied in developing both hypoxia-activated prodrugs and fluorescent probes for tumour hypoxia.[122]

Selectively targeting the hypoxic environment is achieved through exploiting oxidoreductase enzymes which are upregulated under reductive stress. Reductive stress can be seen as the opposite of oxidative stress. While oxidative stress disrupts redox homeostasis by promoting an abundance of oxidants O_2^- and H_2O_2 relative to antioxidants (superoxide dismutases, catalase, glutathione peroxidases, and thioredoxins), reductive stress results from an increase in the concentration of reducing agents such as reduced nicotinamide adenine dinucleotide (NADH). Consequently, an excessive accumulation of reducing equivalents, in comparison to oxidizing species, dysregulates redox homeostasis and contributes to reductive stress.[123, 124]

As previously mentioned, HIF can contribute to the Warburg effect resulting in a switch from oxidative phosphorylation to glycolysis.[35, 36] This shift leads to an enhanced generation of NADH as a biproduct, a pivotal electron donor in the cell. The outcome is an imbalance of the NAD+ and NADH equilibrium.[122] It is also known that this imbalance can occur in the mitochondria where oxidative phosphorylation is slowed down due to a lack of oxygen under hypoxic conditions. NADH-producing reactions in the tricarboxylic acid cycle are inhibited thus diminishing the efficiency with which the malate-aspartate shuttle can transport the NADH generated during glycolysis into the interior of the mitochondrial matrix, ultimately contributing to the buildup of NADH that contributes to the environment of reductive stress.[125] Under these reducing environmental conditions, there is also an upregulation of various oxidoreductase. Examples of such enzymes include nitroreductases (NTRs), azoreductases, cytochrome p450 reductase, and xanthine oxidase.[126, 127]

Hypoxic regions within tumours can be considered regions that are under intensive reductive stress with great amounts of oxidoreductase enzymes present. Reductive stress can therefore be deemed useful as a biomarker for hypoxia and for developing motifs specific to tumour hypoxia.

1.4.1 Hypoxia Activated Prodrugs

Hypoxia-activated prodrugs (HAPs) operate based on bioreductive activation. Bioreduction is carried out by oxidoreductase enzymes in hypoxic cells resulting in cytotoxic species also known as the active drug.[128]

The main classes of bioreductive prodrugs are nitroaromatics, quinones, aromatic N-oxides, Aliphatic N-oxides, and transition metal complexes. The conversion of the prodrug from an inactive species to an active species occurs via a two-step process. For most HAPs such as nitroaromatics, quinones, and benzotriazine di-oxides. The first step involves the formation of an oxygen-sensitive intermediate, which is carried out by a one-electron reduction via a flavin-dependent oxidoreductase enzyme. The second step occurs when oxygen pressure is low (less than 5-10 mmHg in hypoxic regions) resulting in further reduction and the formation of the active species. If oxygen pressure is that of normal tissue in between 20-80 mmHg the intermediate is re-oxidized back to its inactive form (Figure 1.16).[17, 128]

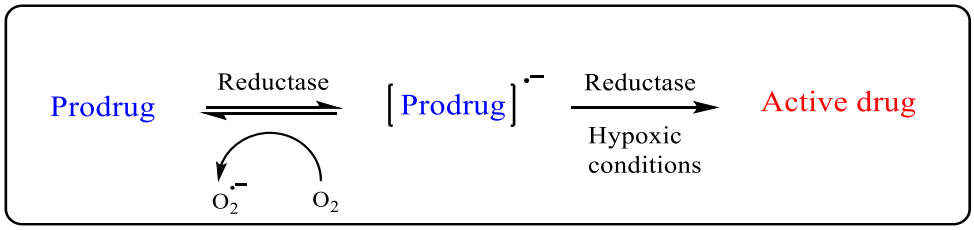

Figure 1.16: *Schematic of the bioreductive activation mechanism for hypoxia-activated prodrugs*.

In recent years HAPs research has been successful in its approval in clinical trials. Five compounds in particular managed to reach phase III of clinical trials TH-302 (**1.19**), porfiromycin (**1.20**), EO9 (**1.21**), tirapazamine (**1.22**), and nimorazole (**1.23**) and are yet to attain regulatory approval (Figure 1.17).[122]

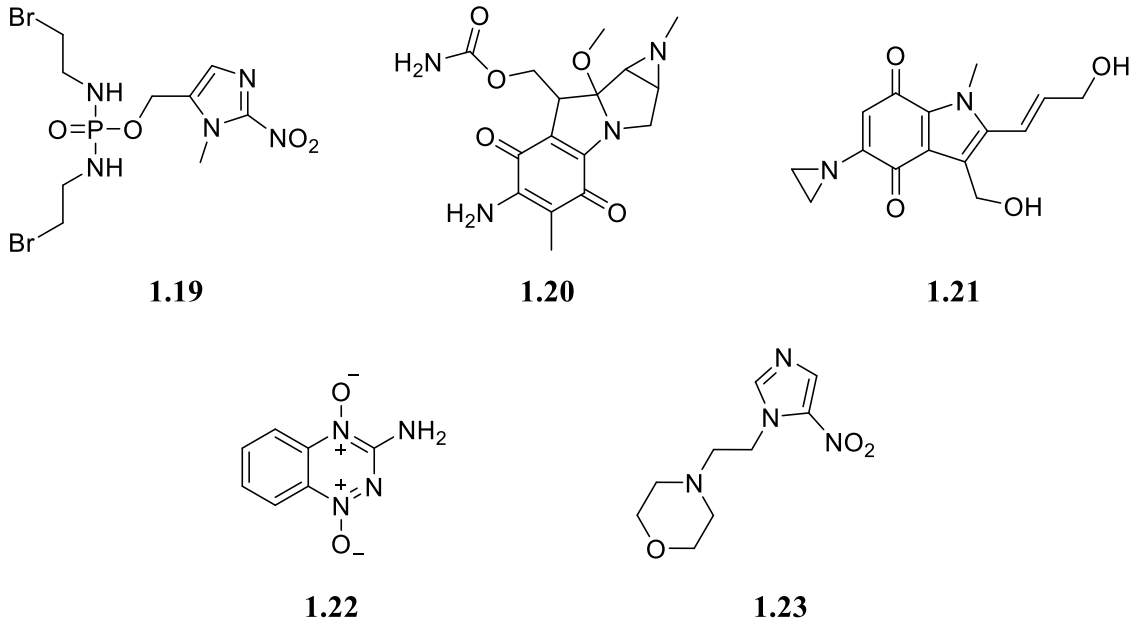

1.19 **1.20** **1.21**

1.22 **1.23**

Figure 1.17: *Structure of HAP's that have reached Phase III of clinical trials.*

Amongst these compounds TH-302 (**1.19**) is of interest, as it takes advantage of a 2-nitroimidazole moiety. Since the discovery of Varghese *et al.* in 1976 that 2-nitroimidazoles are capable of forming adducts with cellular nucleophiles in hypoxic cells. There has been great effort put into the design of 2-nitroimidazoles based HAPs and imaging agents. The reason being, they have high electron affinity and selective hypoxic toxicity that is dependent on a bioreductive mechanism resulting in reactive intermediates having the capability to bind to macromolecules in the cell such as proteins (Figure 1.18).[129-132]

TH-302 (**1.19**) is a good example that proves the efficiency and effectiveness of 2-nitroimidazole based prodrugs. The 2-nitroimidazole moiety of TH-302 undergoes a bioreductive activation mechanism under hypoxic conditions which releases the active drug, a DNA cross linking agent (bromo-isophosphoramide mustard) via reduction of nitro group to an amine followed by fragmentation (Figure 1.18). The cross-linking agent can interfere with transcription and translation of DNA leading to tumour cell death. It was also reported that TH-302 contributed to the downregulation of HIF-1α. TH-302 showed great promise as a hypoxic selective drug reaching phase III clinical trials.[122, 133]

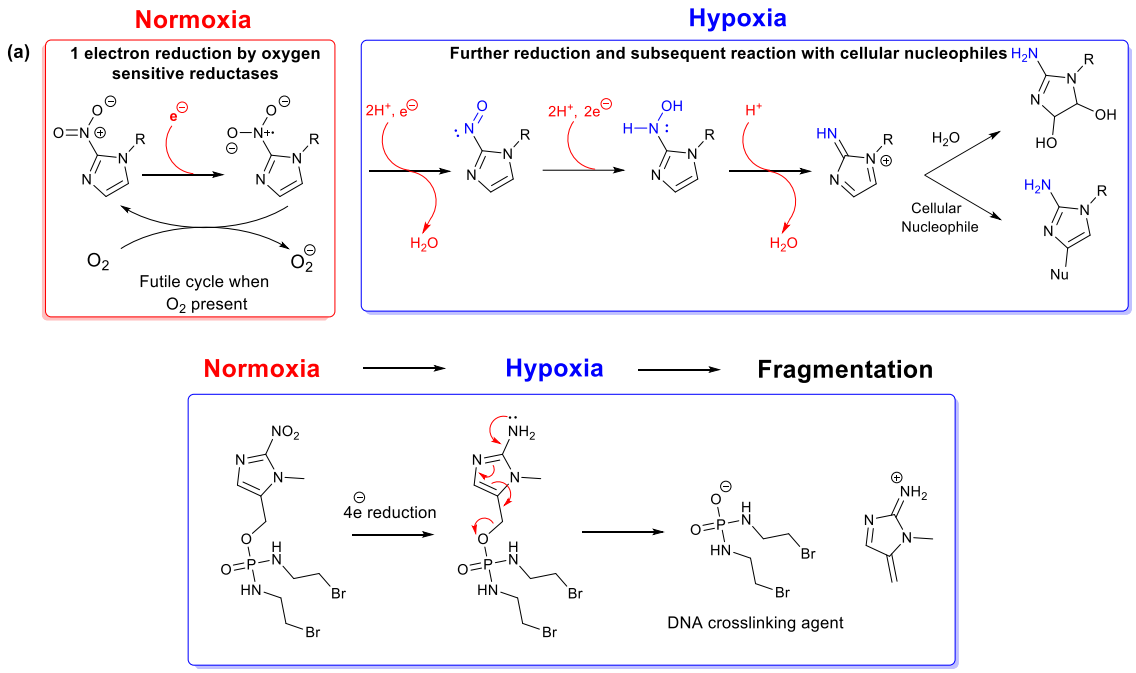

Figure 1.18: *(a) Schematic showing the reduction of 2-nitroimidazole motif under both normoxic and hypoxic conditions. Under normoxic conditions there is a 1 electron reduction to a reactive nitro radical which can be back oxidized to the nitro compound, however under hypoxia follows further reduction to the nitroso, hydroxylamine and amine derivative. (b) A schematic that shows the fragmentation of TH-302 under hypoxia.*

Whilst HAPs consisting of a 2-nitroimidazole moiety are capable of undergoing reduction under hypoxic conditions it's is also important to recognise the role of the oxidoreductase enzymes in this process. Nitroreductase is an enzyme that reduces a nitro group to its corresponding amine. Understanding the substrate units that nitroreductase can reduce can enhance the knowledge on the design of HAPs. More interestingly, it can lead to the development of nitroreductase responsive fluorescent probes capable of eliciting a measurable fluorescence response in hypoxic cells or tissue.

To date, 1,8-naphthalimide fluorophores have garnered substantial interest due to their remarkable fluorescence properties, which deem them suitable candidates for the design of nitroreductase responsive fluorescent probes. Their inherent sensitivity and selectivity coupled with their synthetic versatility and consequential modulation of fluorescence, considers these probes widely applicable for monitoring nitroreductase activity in hypoxic environments.[90]

1.5 The 1,8-Naphthalimide Fluorophore

Firstly documented by Middleton and his colleagues in 1986[134], the 1,8-naphthalimide core has many advantageous characteristics that stand out amongst other fluorophores, these include a large Stokes shift, resistance to photobleaching, and a brightness comparable to other fluorophores that possess high quantum yields.[135] The photophysical characteristics of the naphthalimide fluorophore are largely affected by the electronic properties of its substituents. For instance, taking the 4-position on the 1,8-naphthalimide core and incorporating a nitro functional group results in a broad absorption peak with λ_{max} of approximately 360 nm with limited fluorescence observed on the fluorescence emission spectra.

This can be attributed to the blocking of ICT caused by the electronegativity of the oxygen atoms, hindering the conjugation throughout the 1,8-naphthalimide core from the donor nitrogen of the nitro substituent. In contrast, if the nitro substituent was to be replaced with an amine a "push–pull" ICT excited-state would be observed as electrons from the nitrogen donor can be pushed into the 1,8-naphthalimde core, this red shifts both absorption and emission bands to 450 and 550 nm, respectively (Figure 1.19) and increases the fluorescent quantum yield substantially.[136] In more recent studies, there has been substantial research focus on 4-hydroxy-1,8-naphthalimide. This compound exhibits UV absorption peaks at approximately 380 nm and emits light at around 550 nm or 450 nm in aqueous solutions. Furthermore, in DMSO, its quantum yields observed we comparable to that of the 4-amino-1,8-naphthalimides.[137]

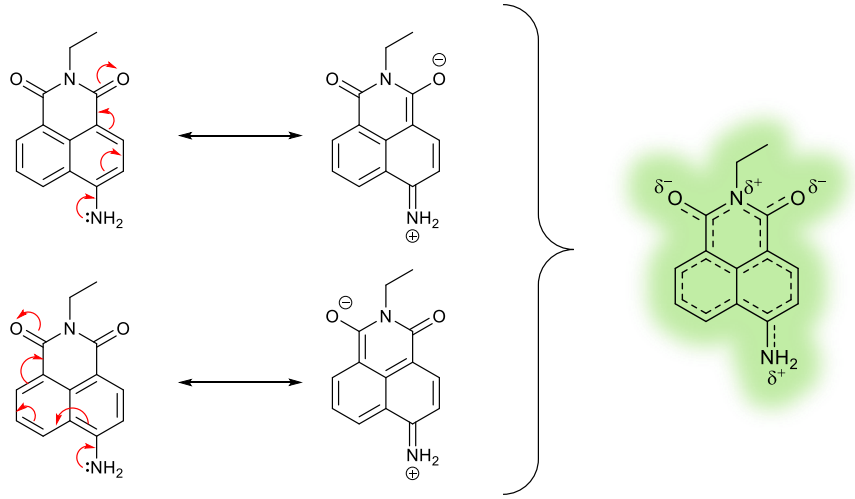

Figure 1.19: *Schematic depicting the ICT that occurs withing the 4-amino-1,8-naphthalimide fluorophore throughout the push pull excited state.*

The characteristics possessed by the 1,8-naphthalimide are qualities that are essential for their application in biological contexts, including assay development and confocal microscopy. Particularly noteworthy is the ability to fine-tune the ICT excited state. For instance, by introducing an electron-withdrawing carbamate or ester group at the 4-position a blue emission (with a peak around 450 nm) can be observed through spectroscopy or through confocal microscopy. However, upon conversion to an electron-donating amino functional group the emissive properties are significantly altered, resulting in green emission (with a peak around 550 nm). Additionally, the ether- and esterification of 4-hydroxy-1,8-naphthalimide also induces a shift toward shorter wavelengths in the emission maxima, offering further advantages in the design of fluorescent probes. The influence of electron donating and withdrawing substituents on the ICT, can alter the photophysical characteristics of the 1,8-naphthalimide core. [138, 139]

1.5.1 1,8-Naphthalimide Chemosensors for Cations and Anions

The 1,8-naphthalimide fluorophore has shown significant success as a chemosensor for the detection of various analytes, including: cation recognition[140], anion recognition[136] and small molecules.[141] Compound **1.24** and **1.25** in Figure 1.20 are examples of 1,8-naphthalimide cation sensors. **1.24** shows enhancement in the fluorescence emission intensity at 416 nm upon binding Zn(II) within the cyclam moiety, and displayed significant selectivity towards Zn(II) in the presence of biologically relevant divalent metals.[142] Compound **1.25** was capable of sensing Cu(II). As a result of Cu(II) binding deprotonation of the secondary amines of the naphthalimide moiety was observed through a yellow to pink colorimetric response as well as a green to red fluorescence response.[143]

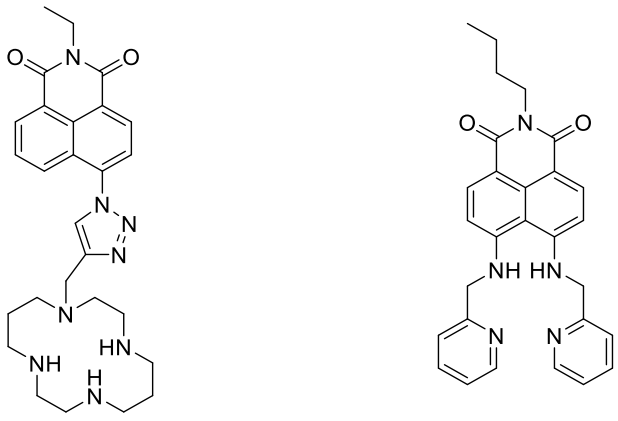

1.24 **1.25**

Figure 1.20: *Structure of compounds **1.24** and **1.25**.*

Many anion sensing based 1,8-naphthalimides make use of a urea or a thiourea moiety to achieve anion binding as seen in Figure 1.21. Compounds **1.26** and **1.27** were shown to bind F^- ions in DMSO observed by its decreasing emission intensity observed at 530 nm. Whereas, only minor decreases in the emission intensity was observed for other anions such as Acetate (AcO^-). It was proposed that the initial binding of F^- to the thiourea followed be deprotonation establishes an electron rich receptor capable of enhanced PET quenching.[144] Compound **1.28** consists of two naphthalimides linked together via a urea. Increasing the number equivalents of F^- in DMSO results in a two-step deprotonation of the urea moiety resulting in a decrease of the absorption band at 400 nm, an increase followed by subsequent decrease at 540 nm, and an increase at 600 nm. It was noted that AcO^- and dihydrogen phosphate ($H_2PO_4^-$) only result in deprotonation of one NH of the urea. Establishing that the two-step deprotonation was unique to F^-.[145]

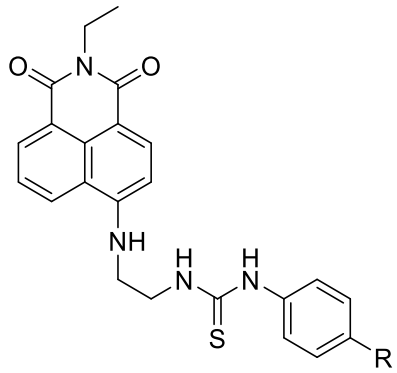

1.26, R = H
1.27, R = CF_3

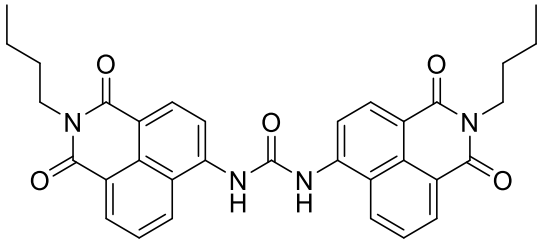

1.28

Figure 1.21: *Structure of compounds **1.26**, **1.27**, and **1.28**.*

1.5.2 1,8-Naphthalimide Chemosensors for Small Molecules

1,8-naphthalimides targeted to sense small molecules are designed with a moiety that the small molecule can either interact or react with. In Figure 1.22 Compound **1.29** for example can detect HClO, prior to the addition of HClO the ICT of **1.29** was hindered resulting in weak fluorescence. However, upon increasing concentrations of HClO the dimethythiocarbamate is oxidised and removed resulting in a green fluorescence enhancement at 550 nm. Furthermore, due to the presence of the phenylsulfonamide compound **1.29** was capable of imaging HClO present in the golgi of HeLa cells.[146] Compound **1.30** (Figure 1.22) displayed significant fluorescence intensity enhancement upon the removal of the aryl boronic ester moiety in the presence of H_2O_2. Compound

1.30 proved selective for H_2O_2 in comparison to other ROS species and was capable of imaging lysosomes via red emission in both HeLa cells and in RAW 264.7 cells.[147]

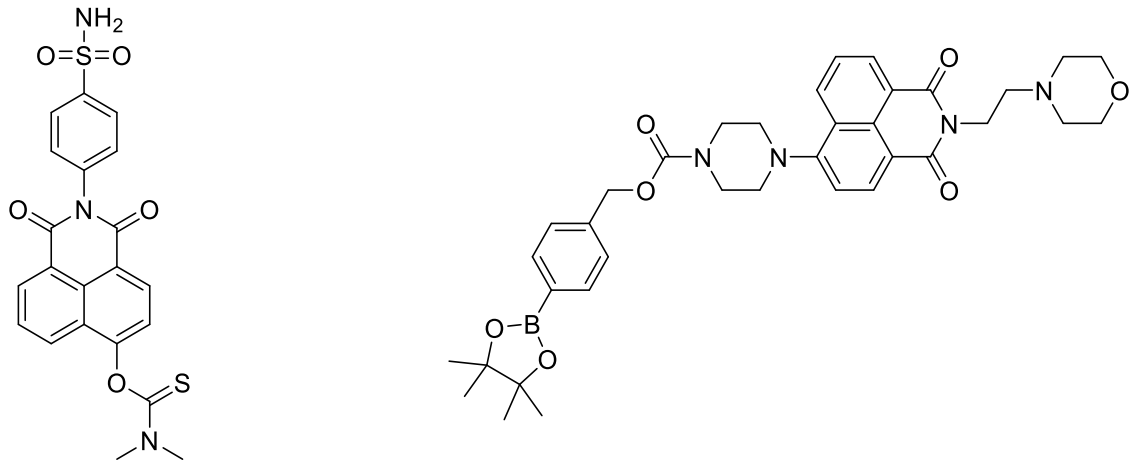

1.29 **1.30**

Figure 1.22: *Structure of compounds **1.29** and **1.30**.*

More interestingly, there has been an increasing interest for enzyme activated chemsosensors which make use of the 1,8-naphthalimide core. The next section will provide a summary of the recent advancements in the development of 1,8-napthalimide based enzyme activated fluorescent chemosensors for the flavin associated oxidoreductase enzyme nitroreductase, known to be upregulated under hypoxic conditions. Examples will include the differing designs and substrate moieties for nitroreductase as well as the different responses that can be elicited upon activation of the substrate be it 'turn on' or 'ratiometric' response.[90]

1.6 1,8-Naphthalimide Based Fluorescent Chemosensors for Nitroreductase

Nitroreductases (NTRs) are flavin-associated oxidoreductase enzymes. Categorised into two primary subgroups; Type I NTRs are oxygen insensitive and exhibit the capability to undergo reduction in the presence of O_2, while type II NTRs are oxygen sensitive and therefore only function in an oxygen poor environment.[148] NTR is a homodimeric globular protein consisting of two subunits, each composed of a core domain comprising four beta strands surrounded by alpha helices, as well as an excursion domain (Figure 1.23). The placement of the two FMN cofactors is approximately 27 Å apart, in contact with both subunits, and strategically positioned near the hydrophobic base of a cavity encircled by positively charged groups. The isoalloxazine portion of the FMN cofactor is oriented with its *re* face directed towards the proposed substrate-binding site. Whereby, reduction of nitroaromatic moieties can take place via a ping-pong bi-bi mechanism.[149-151]

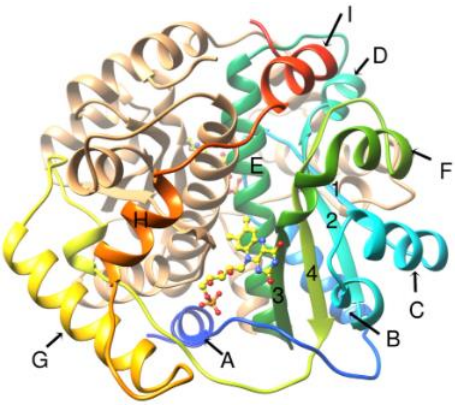

Figure 1.23: *Ribbon diagram of NfsA (Escherichia coli nitroreductase). One subunit is in light brown and the other subunit is in differing colours. The alpha helices are labelled A–I, and the beta strands are labelled 1–4. FMN is displayed as a ball and stick structure.*[149]

Due to the relevance of hypoxia in various diseases, type II NTRs, in recent years have been considered as a noteworthy biomarker for hypoxic tumour formation as previously mentioned. NTR's can reduce a nitro functionality to the corresponding nitroso or amino derivatives (Figure 1.24) and so numerous NTR based sensors have been developed that leverage this property in both prodrug strategies as seen with HAP's and fluorometric techniques for detecting tumour hypoxia.[17, 65]

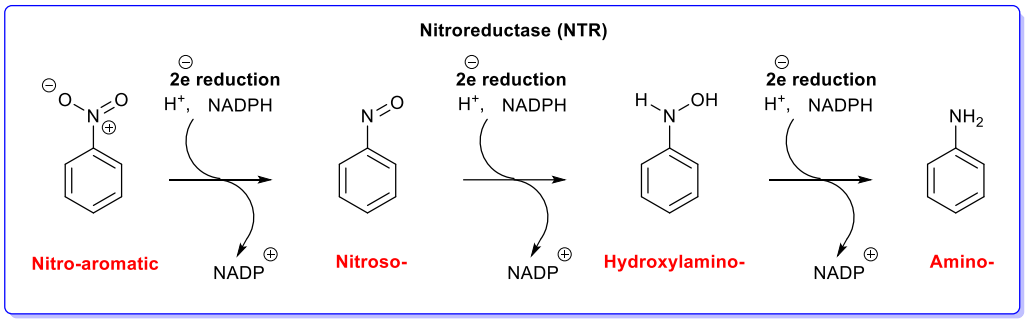

Figure 1.24: *Schematic representing the 2-electron reduction of a nitroaromatics in the presence of NTR and NADPH involving a series of consecutive electron transfer events necessary for the full reduction to the amino group.*

With such boastful photophysical characteristics established by the 1,8-naphthalimide fluorophore and the capability to modulate the fluorescence through substituent changes at the 4-position influencing the sensitive ICT, naphthalimides can be deemed highly suitable to NTR sensing.

Qian and co-workers have developed several fluorescent probes designed for hypoxia detection, utilising 1,8-naphthalimides as seen in Figure 1.25. By linking the naphthalimide to 2-nitroimidazole they synthesised structures **1.31** and **1.32**, it was observed in various lung cancer and ovarian cancer cell lines 95D cells, V79 Chinese hamster, and CHO that these compounds exhibited a substantial increase in fluorescence intensity in hypoxic conditions. Notably, **1.32** under hypoxic conditions had an emission profile 20 times greater in comparison to the normoxic conditions in V79 cells.[152]

Qian and co-workers also developed probes **1.33** and **1.34,** with probe **1.33** demonstrating a significant difference in fluorescence between cells in normoxic and hypoxic conditions.[153] They also investigated a series of naphthalimide *N*-oxides (compounds **1.35** – **1.39**) and assessed their ability to bind to DNA, as well as their potential as fluorescent probes for hypoxia. Although not considered to be targeted by NTR and more likely reduced by cytochrome P450 reductases these compounds proved capable of distinguishing between cells in hypoxic and normoxic environments.

In their findings, compound **1.35** stood out as particularly effective marker for hypoxia, showing a 17-fold increase in fluorescence when incubated for 4.5 hours in V79 Chinese

hamster cells under hypoxic conditions. This enhanced response was attributed to the reduction of the N-oxide to a tertiary amine and the conversion of the nitro group to a primary amine.[154]

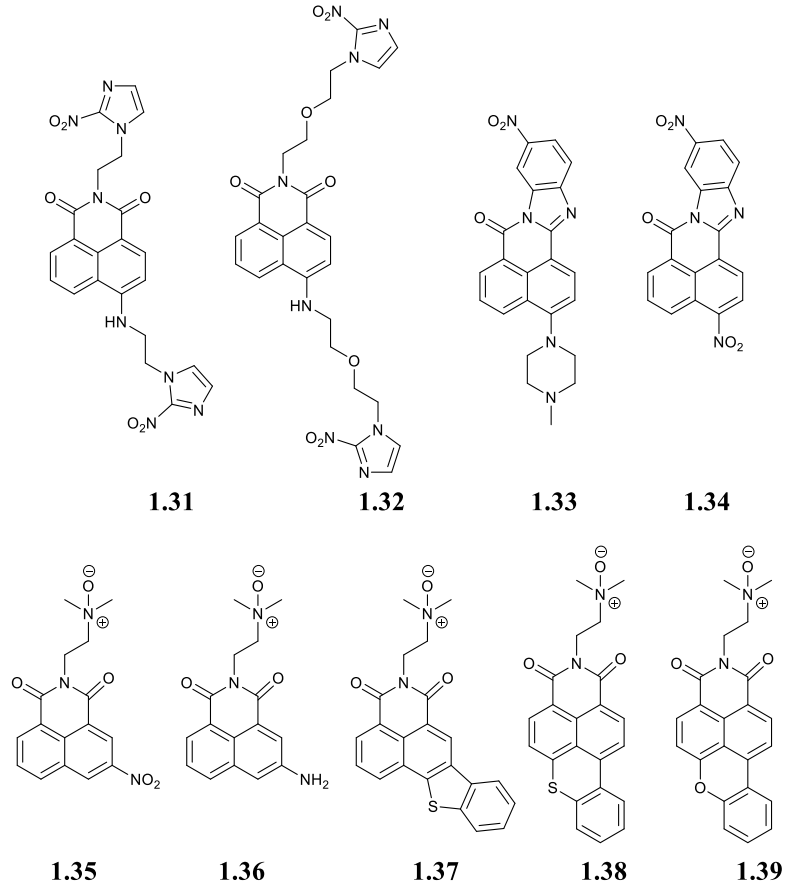

Figure 1.25: *compounds **1.31–1.39**.*

Cui *et al.* developed a ratiometric probe for hypoxia using the 1,8-naphthalimide, one of the earlier examples in literature. Compound **1.40** in Figure 1.26 was a highly selective sensor with the design entailing a p-nitrobenzyl group that was linked to the 4-amino position through a carbamate linkage. The sensor was activated by NTR in the presence of NADH resulting in a change from blue to green fluorescence. This shift in emission from 475 nm to 550 nm occurred due to the release of the 4-amino-1,8-naphthalimide fluorophore through a 1,6-elimination process, accompanied by the loss of CO_2 and aza-quinone-methide. **1.40** was non cytotoxic and effective in detecting hypoxia in A549 cells through its ratiometric blue to green response.[155]

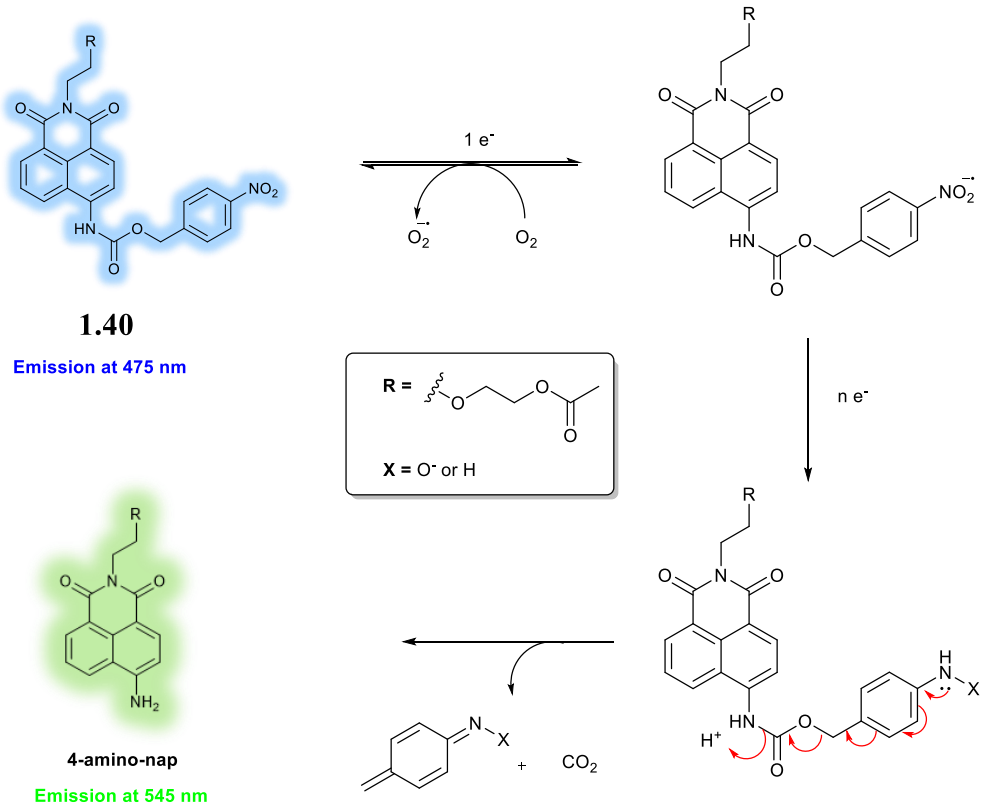

Figure 1.26: *Schematic showing the reduction of **1.40** involving a 1,6-elimination with subsequent release of CO2 and aza-quinone-methide.*

Ma and colleagues developed a naphthalimide-based probe, compound **1.41** in Figure 1.27, which was capable of establishing an off to on fluorescence response in the presence of NTR. This probe consisted of a morpholine unit linked to a 4-nitro-1,8-naphthalimide, and prior to treatment with NTR, it displayed very low fluorescence (Φf = 0.002 at 543 nm). However, upon exposure to NTR, a substantial increase in fluorescence (Φf = 0.13) was observed due to the reduction of the nitro group to the corresponding amino derivative. This change in fluorescence was directly proportional to the concentration of NTR, with a detection limit of 2.2 ng mL−1. Additionally, the application of **1.41** did not significantly affect the viability of A549 cells, even at concentrations as high as 2 mM. **1.41** could be seen to specifically target lysosomes within living cells, as confirmed through co-localization studies with a known commercial lysosomal tracker called DND-99 (Figure 1.27). Moreover, it could simultaneously provide imaging of the hypoxic status of A549 cells by visualizing lysosomal NTR activity under hypoxic conditions.[106]

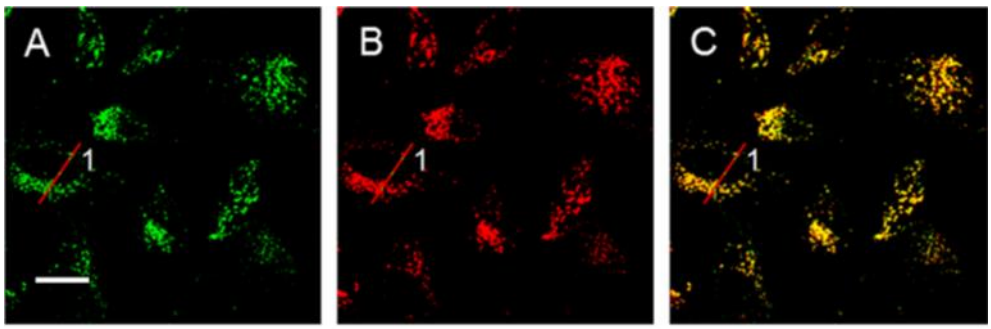

1.41

Figure 1.27: *Colocalization experiment of DND-99 (100 nM) and probe **1.41** (2 mM) in hypoxic A549 cells. (A) Emission from Lyso-NTR. (B) Emission from DND-99. (C) Merged image of images A and B. The scale bar used in the images was set at 20 mm for reference.*

Compound **1.42** designed and synthesised by He *et al.* was introduced as a ratiometric fluorescent probe designed with a dual function to detect both NTR activity and acidity a key factor in a cancer environment simultaneously. This innovative probe harnessed the concept of weak ICT caused by the carbamate moiety within its structure and efficient PET quenching resulting from the nitro-group attached to a 1,8-naphthalimide via a carbamate linkage as well as the morpholine moiety itself (Figure 1.28). It was observed that **1.42** exhibited significant quenching of fluorescence in a neutral aqueous solution ($\Phi = 0.02$).

However, weak blue fluorescence ($\Phi = 0.11$) was observed in an acidic environment where the morpholine group underwent protonation. The subsequent addition of NTR triggered the reduction of the 4-nitrobenzyl moiety, resulting in the release of a highly emissive product with a large quantum yield ($\Phi = 0.78$). Importantly, no noticeable fluorescence response without both analytical inputs of NTR and acidity (Figure 1.28). **1.42** demonstrated high sensitivity at pH 5, with a low detection limit of 0.92 μg mL^{-1}. Confocal fluorescence microscopy imaging of lung carcinoma A549 cells confirmed its effectiveness in detecting both acidity and NTR *in cellulo*, deeming **1.42** suitable for tumour imaging.[156]

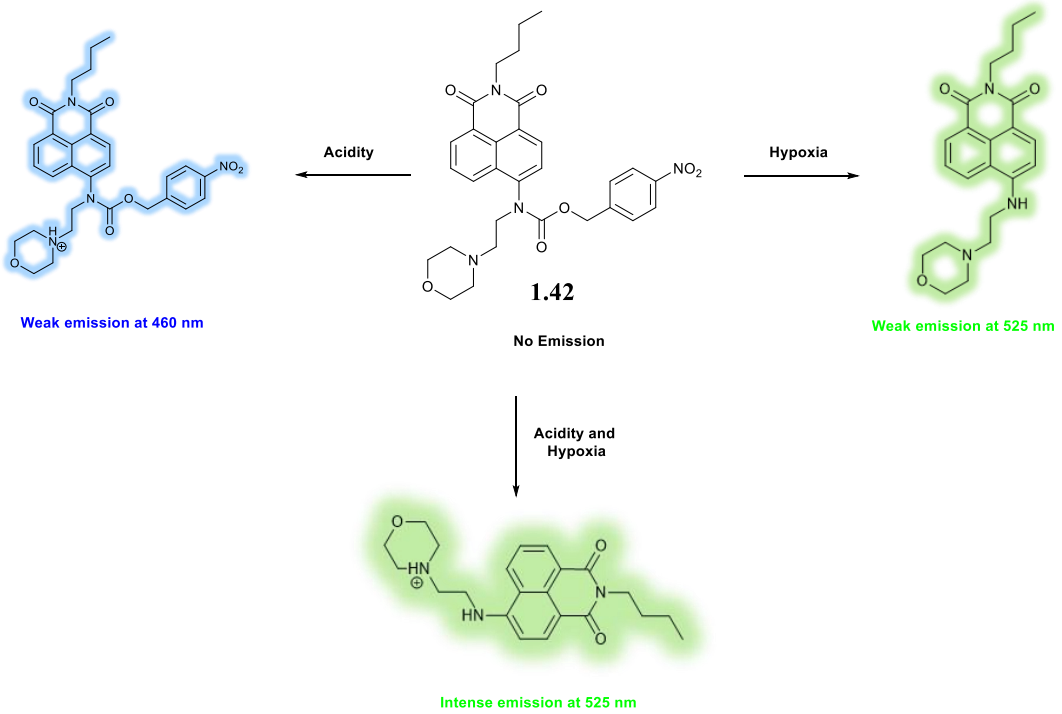

Figure 1.28: *schematic showing the Proposed detection mechanisms of probe **1.42**.*

Similarly, Fang *et al.* have also synthesised a naphthalimide fluorophore based on a dual function in Figure 1.29. They utilized a hybrid like structure consisting of 1,8-naphthalimide and rhodamine compound **1.43**, which incorporates recognition sites for both ATP and NTR. This innovative design allowed them to effectively demonstrate distinct fluorometric responses to ATP and NTR individually but also a combination of ATP and NTR.[157]

Initially, **1.43** exhibited weak fluorescence due to quenching caused by the spirocyclic rhodamine structure and the nitro group within the 1,8-naphthalimide. Upon introducing NTR, the nitro substituent is reduced and an enhancement in fluorescence intensity was observed at 520 nm, due to the subsequent formation of the 4-amino-1,8-naphthalimide moiety and its highly emissive profile. Similarly, the introduction of ATP led to an enhancement in fluorescence intensity at 580 nm, as ATP causes the spirocyclic structure of rhodamine to open. In both cases, there is a linear relationship established between both concentration and fluorescence of the respective analyte, which allows for the calculation of a 0.12 μg mL^{-1} LOD for NTR and 0.05 mM LOD for ATP.

Through confocal fluorescence microscopy, it was observed that by varying the wavelengths of excitation of **1.43** the presence of ATP and NTR could be determined.

Upon incubating **1.43** with HeLa cells, it was noticed that ATP levels within cells are significantly influenced by the concentration of O_2. More interestingly, it was observed NTR activity increased with decreasing O_2 content from 20% to 1%. Alternatively, ATP concentration decreased with decreasing O_2 content (Figure 1.29).

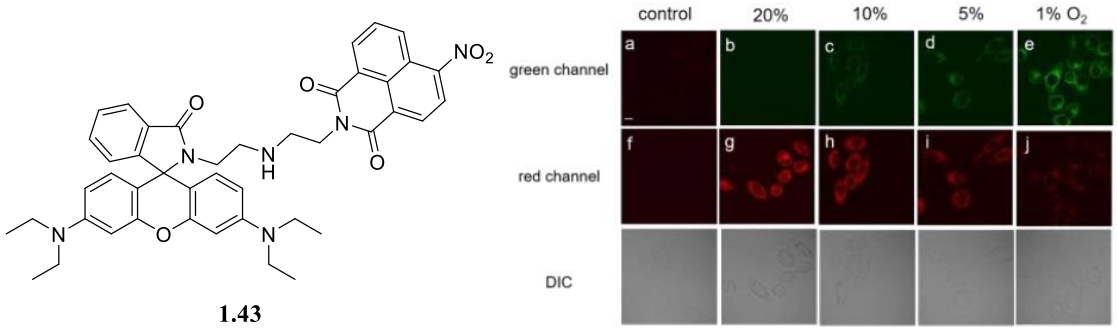

Figure 1.29: *The structure of probe **1.43** and confocal fluorescence images of HeLa cells exposed to compound **1.43** under different O_2 concentrations (20%, 10%, 5%, and 1%). Two separate channels were utilized for detection: a green channel (λ_{ex} = 405 nm) and a red channel (λ_{ex} = 559 nm).*

Liu and co-workers demonstrated the effectiveness of naphthalimide-based probes for detecting NTR. They synthesised compound **1.44** a turn on probe for the sensing of NTR in both bacterial and mammalian cells (Figure 1.30). Structurally, **1.44** consists of a 4-hydroxy-1,8-naphthalimide ether linked to a 4-nitrobenzyl group. Upon exposure to NTR in the presence of NADH, **1.44** elicited a fluorescence response, with a significant enhancement in fluorescence intensity at 489 nm. The detection sensitivity of the probe was significant, with an LOD of 3.4 ng mL^{-1}. Through confocal microscopy, the researchers demonstrated that the probe could penetrate *E. coli* and *S. aureus* cells, where an increase in blue emission intensity was observed upon interacting with intracellular NTR. The same turn on in blue emission response was also observed in breast and liver cancer cell lines MCF-7 and HepG-2 with no cytotoxicity observed.[158]

Compound **1.45** in Figure 1.30 reported by Wei and colleagues made use of a carbonate linker, to modulate the fluorescence of the 1,8-naphthalimide fluorophore. A green fluorescence at 550 nm was observed upon **1.45** reacting with NTR and NADH. Once again, the fluorescence a linear relationship was established between **1.45** and NTR

within the concentration range of 0.1–0.3 μg mL^{-1}. **1.45** was also effective in the imaging hypoxic malignant glioma U87 cells.[159]

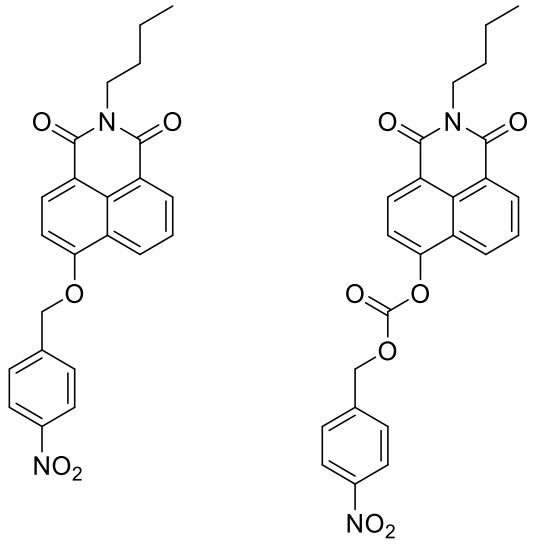

1.44 **1.45**

Figure 1.30: *Compounds **1.44** and **1.45**.*

Lin and colleagues developed compound **1.46**, featuring a 4-nitro-1,8-naphthalimide core with a methylsulphonamide group designed to target the endoplasmic reticulum (Figure 1.31). **1.46** sought to take advantage of NTR's ability to reduce the 4-nitro functionality to its 4-amino derivative, leading to the activation of naphthalimide's ICT, resulting in a green fluorescence turn on response. This probe proved to be highly sensitive, with an LOD at 36 ng mL^{-1}. Furthermore it demonstrated selectivity and biocompatibility amongst other biologically relevant analytes, and established remarkable photostability allowing for both one-photon and two-photon excitation.[160]

The researchers further proved the capability of **1.46** to image NTR in HeLa cells. In normoxic conditions, the cells exhibited no fluorescent signal. However, under hypoxic conditions, a significant fluorescence signal became evident. Furthermore, co-localization studies, carried out in with ER-Tracker Red, revealed a substantial degree of overlap as indicated by Pearson's colocalization coefficient of 0.90, suggesting that the spatial distribution of both signals was consistent with each other. **1.46** was shown to be successful as an imaging agent as it was further applied to visualize the activity of endogenous NTR through two-photon fluorescence excitation in mouse tumour.

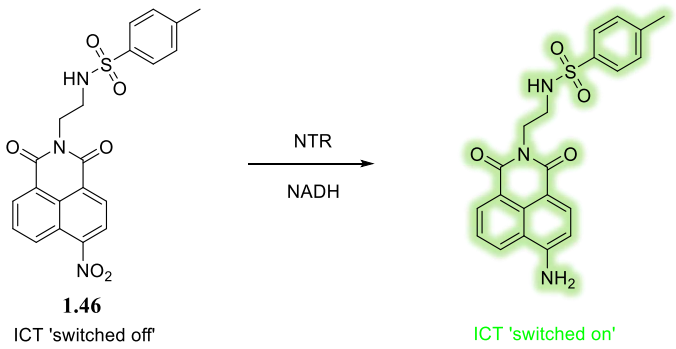

Figure 1.31: *Compound **1.46** and the proposed mechanism upon reduction by NTR.*

The Elmes group synthesised two compounds **1.47** and **1.48** in Figure 1.32 both of which being examples of 2-nitroimidazole-1,8-naphthalimide conjugates. Like prior examples, these probes make use of the reduction-fragmentation mechanism carried out by NTR, resulting in a ratiometric fluorescent response perceptible to the naked eye (Figure 1.32).

Notably, the 2-nitroimidazole component demonstrates significantly higher sensitivity to NTR when compared to its 4-nitrobenzyl counterpart reaching a plateau in fluorescence intensity over the course of 30 minutes for concentrations ranging from 0.02–5 μg mL^{-1} NTR, a linear response was also observed within this range. **1.47** could detect reductive stress in HeLa cells using both flow cytometry and confocal microscopy methods methods, as well as maintaining a high level of biocompatibility and causing minimal cytotoxic effects.[99]

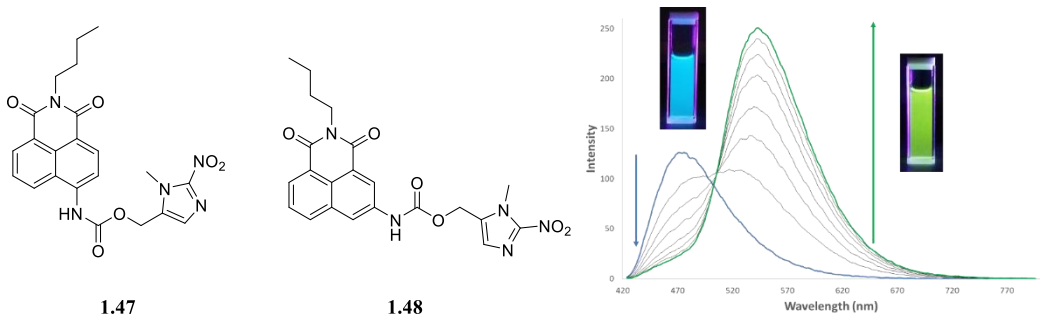

Figure 1.32: *Compounds **1.47** and **1.48** and the ratiometric change in fluorescence observed for **1.47** (10 μM) (λ_{ex} = 345 nm) upon addition of NTR (1 μg mL^{-1}) over 10 minutes. Within the graph is an inset representing the Naked eye changes seen under UV light.*

A series of 1,8-naphthalimides designed for biological imaging purposes with a focus on hypoxia-responsive properties were designed by Jolliffe, New, and co-workers. They developed various methods to diversify the range of available structures. While the 3 or 4- position of 1,8-naphthalimides are typically modified, or the imide, recent efforts have enabled the introduction of substitutions at the 6-position as well. This innovative approach enhances the versatility of the fluorophore scaffold, enabling the creation of molecules that incorporate a sensing group, a targeting group, and an ICT donor to optimize their photophysical characteristics.

Utilizing this methodology, initially involves the synthesis of a crucial intermediate **1.49**, followed by functionalisation at the imide position with aspartic acid to afford **1.50**, and subsequent Suzuki coupling, the researchers successfully syntehsised **1.51** as a hypoxia sensor. This compound was effectively applied for imaging hypoxic and necrotic regions within DLD-1 tumor cell spheroids (Figure 1.33).[161-163]

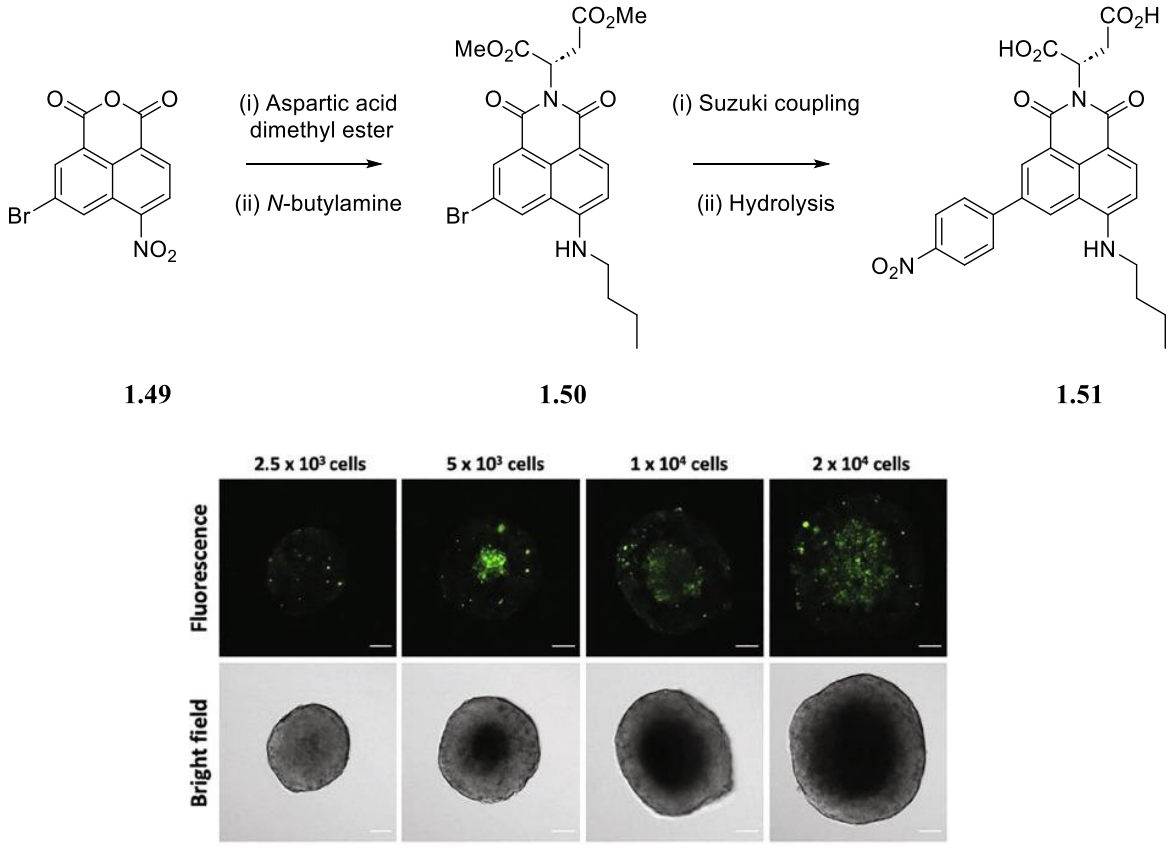

Figure 1.33: *Synthesis of compound **1.51** showing intermediates **1.49** and **1.50** (Top). Confocal microscopy images of **1.51** in DLD-1 spheroids (Bottom).*

In a recent study by Tang and their research team, they have introduced a ratiometric fluorescent probe compound **1.52** consisting of a water-soluble conjugated polymer combined with a p-nitrobenzene-modified 1,8-naphthalimide, (Figure 1.34). The fluorescence of **1.52** is quenched due to two mechanisms: PET taking place between the naphthalimide and the nitrobenzene group and FRET occurring between the polymer and the naphthalimide, and photoinduced electron transfer This quenching results in an exceptionally low background signal.[164] However, when the nitro group is reduced by NTR, FRET is turned on, and the PET process is interrupted. This leads to a fluorescence enhancement at 526 nm, allowing for the detection of NTR at a LOD of 19.7 ng mL^{-1}. Importantly, **1.52** showed low cytoxicity selectivity, and high selectivity deeming in useful for imaging of intracellular NTR in A549 tumour cells undergoing hypoxia.

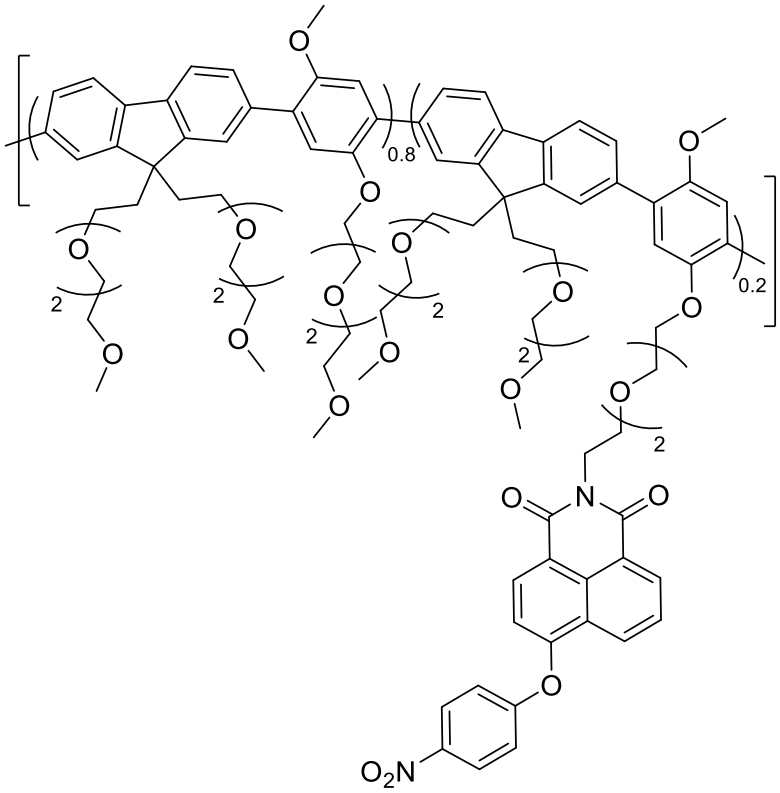

1.52

Figure 1.34: *Structure of compound **1.52**.*

The above sections have given a background to the field of hypoxia as a biomarker for tumours, chemosensors in general, and chemosensors developed for the detection of nitroreductase utilising the 1,8 – naphthalimide fluorophore. It is clear from the literature that a vast amount of work has been conducted in exploiting chemosensors for the

detection of various biological analytes. More interesting is the application of 1,8-naphthalimides for the detection of hypoxia and NTR. Given the versatility that exists within the 1,8-naphthalimide in terms of what can be substituted at the imide site, or the 4-position leaves an open scope of designs to be sought after to contribute to the library of chemosensors for hypoxia. This thesis will aim to expand the knowledge of 1,8-naphthalimides as chemosensors for hypoxia and seeks to develop chemosensors of greater variety. The following section will consist of the aims of this thesis and provide a summary of the work discussed in each chapter.

1.7 Aims

Chemosensors for hypoxia taking advantage of a 1,8-naphthalimide motif has been in constant growth and development in recent years. With hypoxia and the upregulation of NTR acting as a promising biomarker for malignant tumours there has been an ever-increasing interest in the design of selective 1,8-naphthalimide NTR activated fluorescent chemosensors. The aim of this research is to expand on the current knowledge based around 1,8-naphthalimide fluorophores but also to develop new motifs for NTR sensing.

The first objective was to synthesise a Ru(II) polypyridyl complex capable of sensing NTR (Chapter 2). While several probes have been reported recently there remains a lack of examples that display photophysical characteristics in the red or NIR regions. Ru(II) polypyridyl complexes display many of the desired characteristics for an NTR chemosensor including red emission, long luminescence lifetimes, large stoke shift and water solubility, but have not been exploited in this capacity to date. We sought to design three novel Ru(II) poly(1,10-phenanthroline) complexes to act as substrates for NTR and give rise to a 'switch on' of the Ru(II) metal-to-ligand-charge-transfer (MLCT) based emission.

The second objective was to develop a family of NTR sensitive self immolative dendrimers utilising 1,8-naphthalimide fluorophores (Chapter 3). While there have been chemosensors and theranostics for NTR cited in literature, to the best of our knowledge there has been no attempt to develop a self immolative dendrimer for NTR utilising 1,8-naphthalimide moieties as fluorophores or a theranostic consisting of a 1,8-naphthalimide fluorphore and a prodrug. The ability of these dendrimers to immolate in the presence of NTR was investigated through a detailed photophysical evaluation.

The third objective was to investigate the utility of quaternarised naphtalimide-phenathroline conjugates for NTR (Chapter 4). The interest here resided in the fact that by quaternarising the phenathroline moiety, a compound with water solubility is achieved through its cationic nature without the requirement of a heavy metal. Solubility is an issue faced for many small organic chemosensors generally requiring DMSO as a co-solvent. The response of these quaternarised naphtalimide-phenathroline conjugates were evaluated towards NTR.

Chapter 2

Ruthenium (II) Polypyridyl Complexes: A Novel Moiety for NTR Sensing

2. Ruthenium (II) Polypyridyl Complexes: A Novel Moiety for NTR Sensing

2.1 Introduction

As mentioned in Chapter 1 there has been a vast array of fluorescent chemosensors developed for the detection of cations, anions, small molecules, and large biomolecules such as enzymes. Amongst these the 1,8-naphthalimide has been exploited in the application of fluorescent chemosensors for NTR a flavin associated oxidoreductase enzyme upregulated in the hypoxic tumour microenvironment. Several probes have been reported recently for NTR, however, there remains a lack of examples that display photophysical characteristics in the red or NIR regions.

Ru(II) polypyridyl complexes display many of the desired characteristics of an appropriate fluorophore including red emission, long luminescence lifetimes, large stoke shift and water solubility, but have not yet been exploited for the sensing of NTR to date. Indeed, there has been considerable use of Ru(II) polypyridyl complexes as sensors in the realm of cation and ion sensing.[165] More interesting is their 'Turn – On' luminescent response in the presence of small molecules or large biomolecules, resulting from the ^{3}MLCT excited state which can be described by the simplified Jablonski diagram in Figure 2.1.[166]

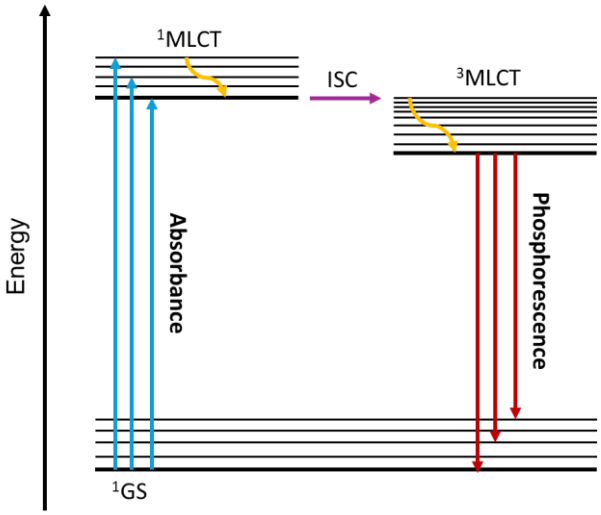

Figure 2.1: *A simplified Jablonski diagram showing the excitation of the ^{1}MLCT at approximately 450 nm, vibrational relaxation (yellow arrow), followed by intersystem crossing (ISC) (purple arrow) to the lowest spin forbidden ^{3}MLCT which results in phosphorescence emission at approximately 600nm upon relaxation to the ^{1}GS (singlet ground state).*[167]

A diverse array of Ru(II) complexes has been conjugated with peptides and biomolecules to facilitate targeted delivery. These complexes primarily focus on enhancing cellular uptake rather than modulating luminescence.[168] In order to develop a Ru(II) polypyridyl complex capable of modulating fluorescence there is a requirement for a PET quenching moiety. This involves modifying one of the ligands of the complex with an electron acceptor capable of inducing a dark excited state. In this state, rather than acquiring fluorescence through relaxation from S_1 to S_0, the relaxation is non-radiative (Chapter 1 – Figure 1.4).[88] This is seen to be the case with the vast majority of Ru(II) polypyridyl complexes developed for biomolecule sensing.

If we consider thiols and hypochlorous acid (HClO) we gain insight to these PET quenching moieties. In the case of thiols and HClO we can see a repetitive pattern of utilising dinitro phenyl moiety to quench the red emission arising from the ^{3}MLCT of Ru(II) polypyridyl complexes, this can be seen for complexes **2.1**, **2.2**, and **2.3** (Figure 2.2). Complex **2.1** when oxidised by HClO results in 190-fold increase in luminescence intensity as the Ru(II) carboxybipyridine complex is formed and was successful in sensing HClO exogenously when incubated with HeLa cells. Complex **2.2** and **2.3** can detect and image thiols whereby the dinitro phenyl group is cleaved by thiophenol in the case of **2.2**, and Cys in the case of **2.3** resulting in a turn on in luminescence intensity at approximately 600 nm, complex **2.3** was capable of imaging NCI-H446 cells via red luminescence.[88, 169, 170]

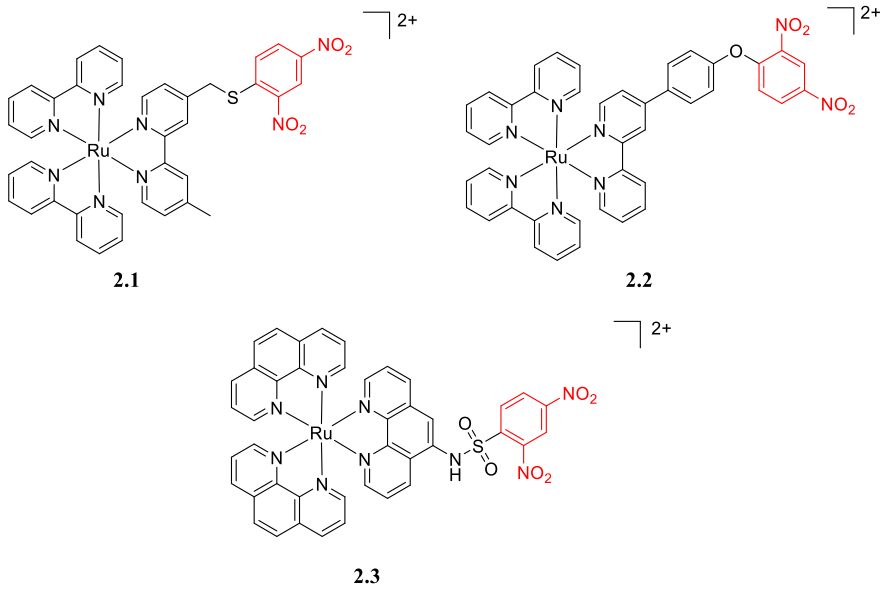

Figure 2.2: *Complexes **2.1**, **2.2**, and **2.3** highlighted in red is the dinitro phenyl group consistent amongst all compounds to quench the luminescence from the ^{3}MLCT excited state.*

Another example of this turn-on in luminescence has been observed by the interaction of Ru(II) polypyridyl complexes with DNA. Since Barton and coworkers established the light switch behaviour of $[Ru(bpy)_2dppz]^{2+}$ in 1990 there has been an extensive amount of research conducted on this concept, the complex being quenched in water and switching on upon intercalating DNA.[171-173] Researchers have since explored the utilization of Ru(II) complexes that incorporate intercalating groups or attached organic chromophores for the purpose of DNA interaction. These modified structures offer the potential for specific DNA targeting, improved photophysical characteristics, and the ability to induce DNA cleavage.[174-176]

Compound **2.4** (Figure 2.3) is an example of a Ru(II) complex that consists of a dppz ligand which can elicit a light switch effect towards mitochondrial DNA. Increments were observed in both hyperchromicity at 450 nm and luminescence intensity at approximately 610 nm with increasing concentration of calf thymus DNA. Furthermore, because of the mitochondrial penetrating peptide, compound **2.4** establishes uptake and localisation to mtDNA in HeLa cells observed through confocal microscopy. Compound **2.4** was also deemed to be applicable as a theranostic due to its capability to both image and trigger photoinduced cell death upon irradiation at 470 nm.[177] Compound **2.5** (Figure 2.3) is a Bi-chromophoric ruthenium polypyridyl complex which showed significant quenching of the MLCT emission arising from the Ru(II) complex. In a PBS solution compound **2.5** has a significantly low quantum yield of < 0.001. The addition of stDNA resulted in 27% hypochromism and an 11-fold increase in luminescence enhancement, showing the effectiveness of the 4-nitronaphthalimide moiety to contribute to a light switch effect.[175]

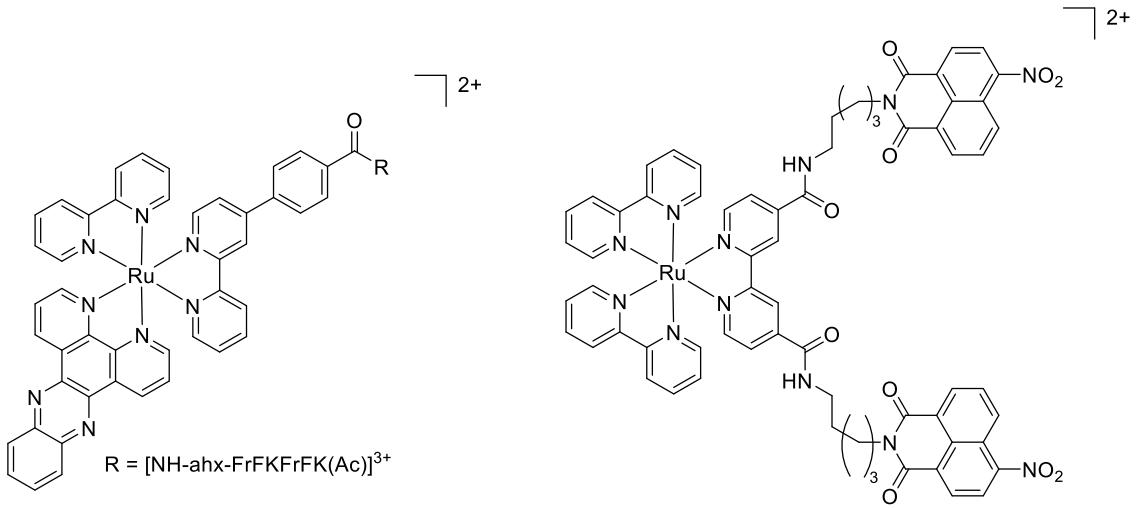

2.4 **2.5**

Figure 2.3: *Structure of Compounds **2.4** and **2.5**.*

$Ru(bpy)_3$-4-nitro- and -4-amino-1,8-naphthalimide conjugates **2.6** and **2.7** (Figure 2.4) were developed by Gunnlaugsson and co-workers. Notably, **2.6** had weak emission at 625 nm upon excitation at 450 nm into the MLCT absorption band (Φ_{MLCT} = 0.001). Whereas **2.7** had a much stronger emission profile Φ_{MLCT} = 0.018 in PBS 7.4 solution. Both complexes were shown to interact with DNA with significant changes in both the absorption and emission spectra, with **2.7** showing an approximately 2.6-fold increase in luminescence enhancement upon increasing concentrations of st-DNA in comparison to minor enhancements observed for **2.6**. Furthermore, **2.7** was superior in its ability to photocleave pBR322 DNA in comparison to **2.6** deeming it useful as a photosensitiser.[176] It is suggested that the triplet excited states of both the MLCT and the naphthalimide are in equilibrium with recorded intersystem crossing from the ^{1}MLCT to the triplet excited state of the naphthalimide moiety.[178] As the triplet excited state of the naphthalimide can undergo non radiative decay thus giving off no luminescence it is proposed that this is what may quench the luminescence arising from the ^{3}MLCT excited state for compound **2.6**. However, in the case of compound **2.7** the likelihood is that the triplet excited state of the naphthalimide sits higher in energy than the ^{3}MLCT and so there is a greater extend of intersystem crossing to that of the ^{3}MLCT that results in phosphorescence upon relaxation to its ground state.

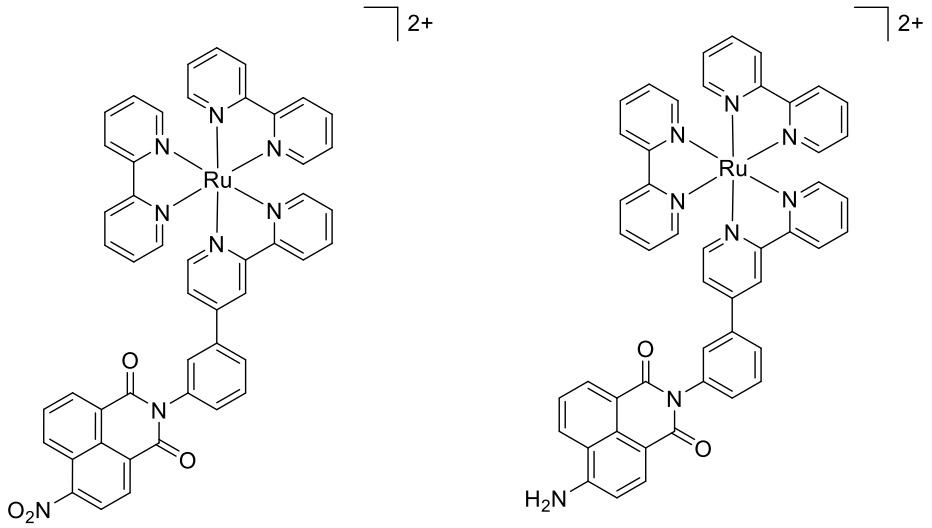

2.6 **2.7**

Figure 2.4: *Complex **2.6** and **2.7**.*

To our knowledge there has been no 'turn on' sensors developed for NTR that utilise ruthenium as a luminophore. However there has been some approaches made towards hypoxia sensing these include complexes **2.8**, **2.9**, and **2.10** (Figure 2.5). Complex **2.8** is

a dual emissive probe consisting of a Ru(II) chromophore that exhibits oxygen-sensitive phosphorescence and a coumarin unit which is unaffected by changes in oxygen levels and emits a constant fluorescence signal.[179] **2.8** was capable of eliciting strong phosphorescent signals in hypoxic A549 cells whilst weaker signals were observed in aerobic cells where oxygen could quench the Ru(II) chromophore. Complex **2.9** shows three reversible two-photon luminescent probes, utilizing the redox shift of the quinone/hydroquinone pair to selectively detect hypoxia.[180] Initially, **2.9** show no luminescence due to anthraquinone quenching after photoexcitation. However, under hypoxic conditions, reductases reduce these probes, leading to the formation of two-photon luminescent Ru(II) hydro-anthraquinone complexes and a substantial increase in luminescence intensity. These probes have proven effective for visualizing internal hypoxia in 3D tumour spheroids and monitoring hypoxia-reoxygenation cycles in living zebrafish. Complex **2.10** the nitroimidazole–ruthenium conjugate selectively accumulated in hypoxic A549 cells compared to normoxic cells.[181] Its luminescence properties were highly responsive to its environment, with binding to human serum albumin leading to an enhancement in luminescence intensity and lifetime, while binding to calf thymus DNA resulted in reduced emission and a shorter luminescence lifetime. Unfortunately, complex **2.10** exhibited high cytotoxicity to cells, making it unsuitable for use as an imaging agent.

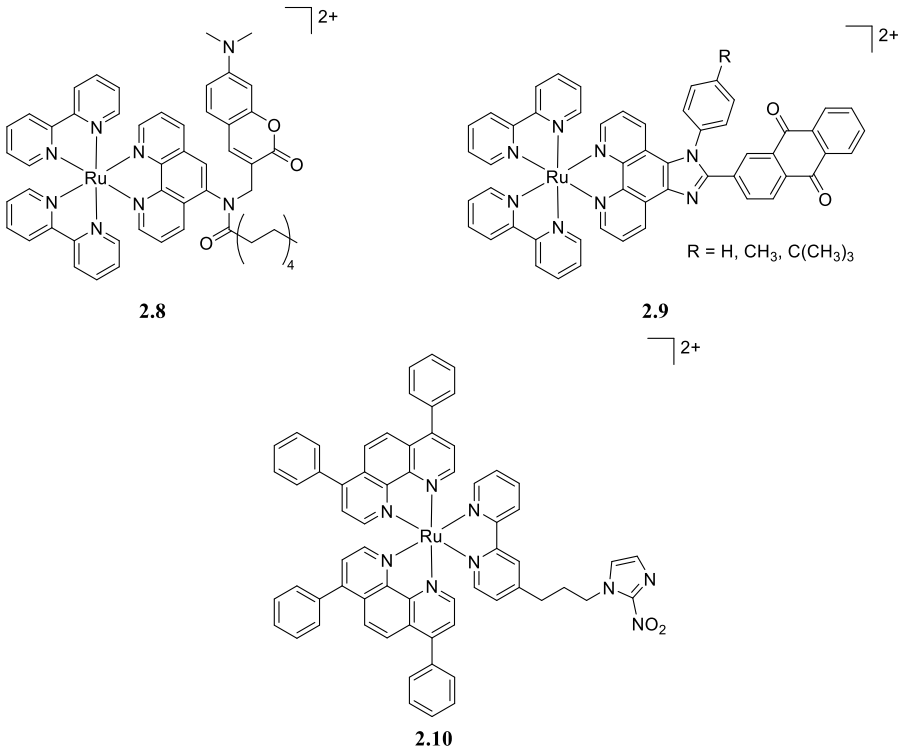

Figure 2.5: *Complexes **2.8**, **2.9**, and **2.10**.*

2.2 Chapter Objectives

The objective of this chapter is to synthesise three novel Ru(II) poly(1,10-phenanthroline) complexes that act as substrates for NTR and give rise to a 'switch on' of the Ru(II) ^{3}MLCT based emission. The complexes are based off two main design principles, for compound **2.11** and **2.12** (Figure 2.6) there is a carbamate linker between that of the Ru(II) and the nitroreductase substrate, and for Compound **2.13** there is a direct conjugation between the 4-nitro-1,8-naphthalimide and the phenanthroline bound to the Ru(II) centre.

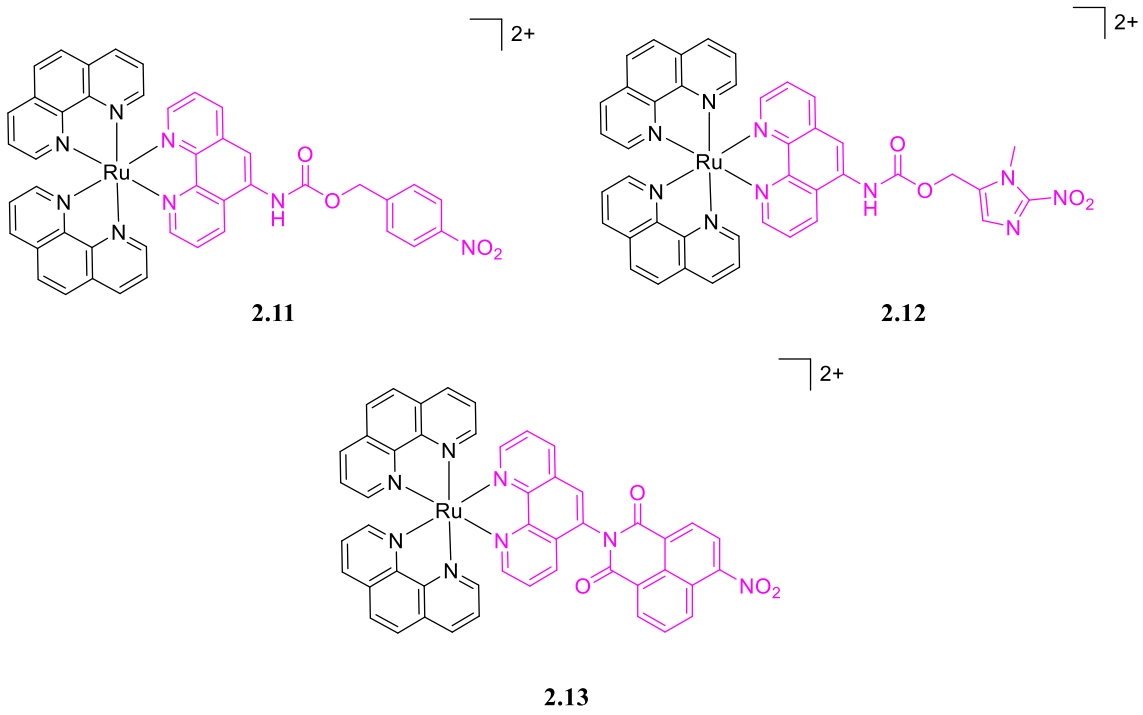

Figure 2.6: *Target structures **2.11**, **2.12**, and **2.13** for Chapter 2.*

In the case of complexes **2.11** and **2.12** there is a carbamate linkage between that of the 1,10-phenanthroline-5-amine and the 4-nitrobenzyl or the 2-nitroimidazole moiety respectively. Both moieties are well established substrates for NTR and are capable of inducing PET quenching on the appending fluorophore.[75] The 4-nitrobenzyl moiety as seen in **2.1** is the most popular substrate for NTR amongst literature due to its commercial availability. However, the 2-nitroimidazole has gathered recent attention owing to its rapid reduction and selectivity towards NTR and hypoxic tumour cell lines.[99, 117] Upon reduction of **2.11** or **2.12** in the presence of NTR and the co-factor NADH it is expected that the complex will be reduced to the corresponding amino derivative and undergo self-immolation to result in the release of an amino Ru(II) luminophore eliciting the OFF-ON turn on in luminescence response as seen in Figure 2.7.

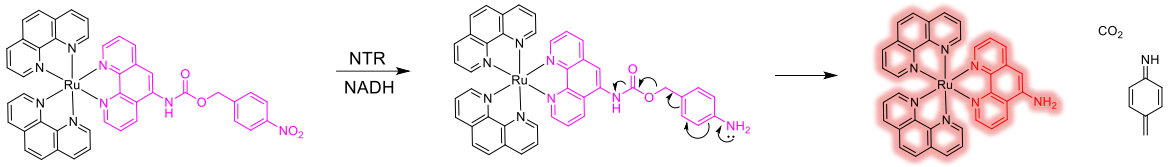

Figure 2.7: *Schematic showing the OFF-ON turn on in luminescence as a result of the self-immolation that results upon NTR and NADH in reducing* ***2.11*** *to the corresponding amino derivative.*

Compound **2.13** is expected to display the same OFF-ON turn on in luminescence through the direction reduction of the 4-nitro-1,8-naphthalimide moiety to the corresponding amino derivative as seen in Figure 2.8. It is intended that 4-nitro-1,8-naphthalimide moiety will act as a PET quencher until it is reduced in the presence of NTR and NADH. As shown in the introduction of this chapter, Gunnlaugsson and co-workers have shown that 4-nitro-naphthalimides are efficient quenchers of Ru(II) MLCT emission while 4-amino-naphthalimide conjugates display significantly higher emission quantum yields. We expect that modulating this structural change may lead to a measurable fluorescence response.

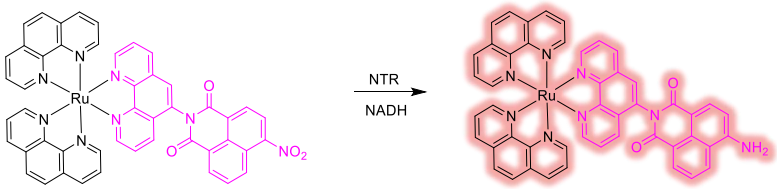

Figure 2.8: *Schematic showing the OFF-ON turn on in luminescence as a result of the direct reduction carried out by NTR and NADH in reducing* ***2.13*** *to the corresponding amino derivative.*

Overall, this chapter will outline the work synthesis and evaluation of these Ru(II) probes for NTR as well as some preliminary results on their use in biological models.

2.3 Synthesis and Characterisation of 2.11, 2.12, 2.13, and 2.29

2.3.1 Synthesis of Compound 2.11

The synthesis of novel ligand compound **2.14** was firstly synthesised prior to complexation to Dichlorobis(1,10-phenathroline)ruthenium(II) as seen in Scheme **2.1**.

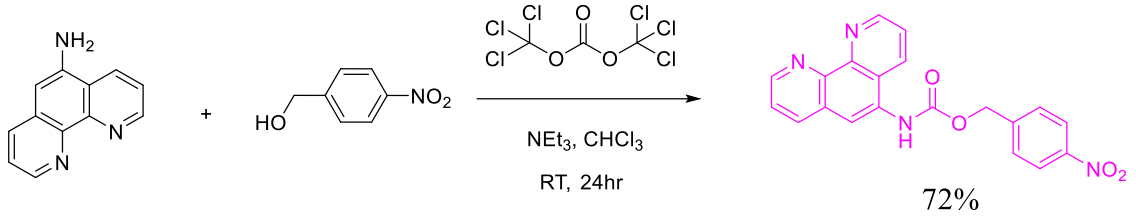

2.15 **2.14**

Scheme 2.1: *Reaction scheme for compound **2.14**.*

The initial step involved the reduction of commercially available 5-nitro-1,10-phenanthroline to its corresponding amino derivative **2.15** using reducing conditions 10% Pd/C and N_2H_4 refluxed in EtOH to yield a solid in 85% yield. Compound **2.15** was then subjected to a reaction with triphosgene and NEt_3 to result in a proposed carbamoyl chloride intermediate, which was then further reacted with 4-nitrobenzyl alcohol in a one pot reaction to form the carbamate linkage between the 4-nitrobenzyl moiety and **2.15** to afford **2.14** in a 72% yield. The main impurities present consist of **2.15**, excess 4-nitrobenzyl alcohol and the isocyanate derivative of **2.15** which were solubilised by the MeCN during the precipitation process. The ligand was fully characterised using ^{1}H NMR, ^{13}C NMR, IR and HRMS analysis. ^{1}H NMR peaks were assigned using ^{1}H-^{1}H COSY analysis. The ^{1}H NMR spectrum (500 MHz, DMSO-d_6) of **2.14** can be seen in Figure 2.9.

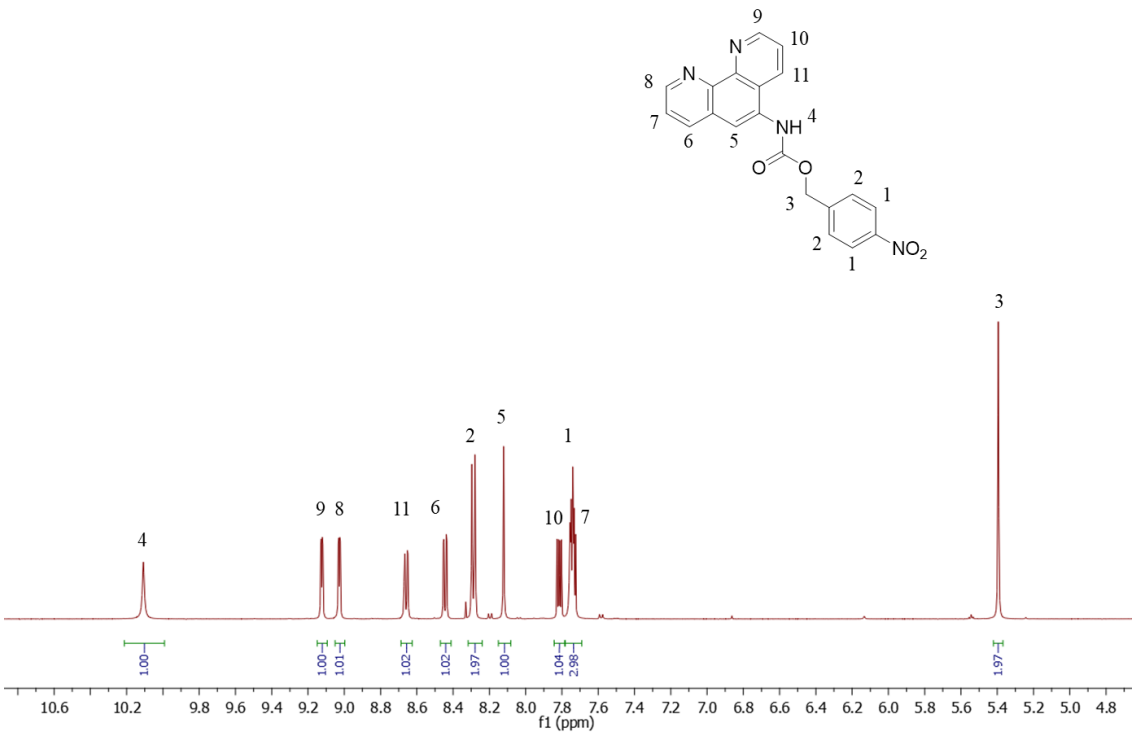

Figure 2.9: *^{1}H NMR of compound **2.14** in DMSO-d_6.*

As shown in Figure 2.9 the sharp singlet of the carbamate NH is shifted downfield to 10.11 ppm as a result of the strong electron withdrawing properties of the carbamate moiety as well as the electron deficient phenanthroline moiety. The CH_2 protons can also be seen to appear as a singlet at 5.39 ppm upon formation of the carbamate where previously these protons would've shown as a doublet on the 4-nitrobenzyl alcohol. The singlet of the phenanthroline portion at 8.12 ppm also shifted downfield due to the enhanced electron withdrawing properties of the neighbouring carbamate linkage. Characteristic doublets for the 4-nitrobenzyl group can also be seen at 8.29 ppm and as a multiplet at 7.73 ppm.

Compound **2.14** was then complexed to **2.16** Dichlorobis(1,10-phenathroline)ruthenium(II) which was synthesised as previously reported,[182, 183] to give Compound **2.11** following Scheme 2.2.

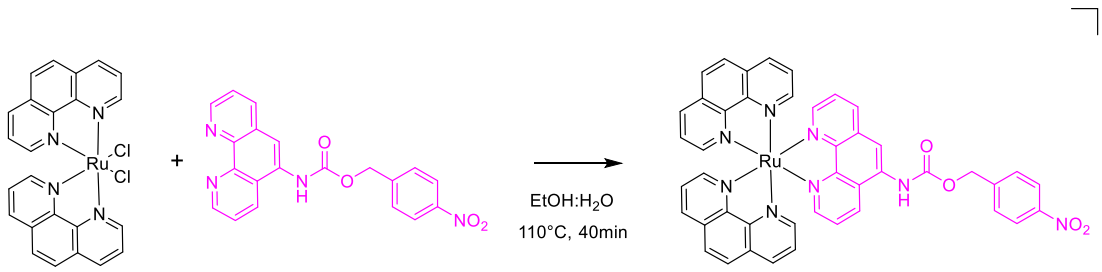

2.16 **2.14** **2.11**

Scheme 2.2: *Reaction scheme for compound **2.11**.*

2.16 and **2.14** were reacted in a 1:1 EtOH:H_2O using microwave chemistry to rapidly increase the complexation of ligand **2.14** in comparison to traditional reflux. Microwave chemistry relies on the efficient heating of substances through microwave dielectric heating. This process depends on a material's capacity to absorb microwave energy and convert it into heat, primarily through dipolar polarization and ionic conduction. When materials are irradiated with microwaves, dipoles or ions align with the electric field, causing energy loss as heat due to molecular friction and dielectric loss. This rapid and direct energy transfer leads to high localized temperatures, activating a significant portion of reacting species, reducing reaction times, and enhancing overall yield and reproducibility compared to traditional conductive heating methods.[184] The literature suggests such complexations can take 18-24 hours through traditional reflux. However, utilising microwave enhanced chemistry allows for the reaction to occur over much shorter time periods of 45 – 60 minutes.

Ammonium hexafluorophosphate was added to form the water insoluble ammonium hexafluorophosphate salt that could then be isolated via centrifugation and purified by column chromatography to give **2.11** in 42% yield. The chloride salt of the complex was re-formed by dissolution in methanol followed by stirring with Amberlite IRA-400 ion exchange resin. Compound **2.11** was fully characterised using ^{1}H NMR, ^{13}C NMR, IR and HRMS analysis. ^{1}H NMR peaks were assigned using ^{1}H-^{1}H COSY, HSQC and HMBC analysis. The ^{1}H NMR spectrum (500 MHz, DMSO-d_6) of **2.11** can be seen in Figure 2.10.

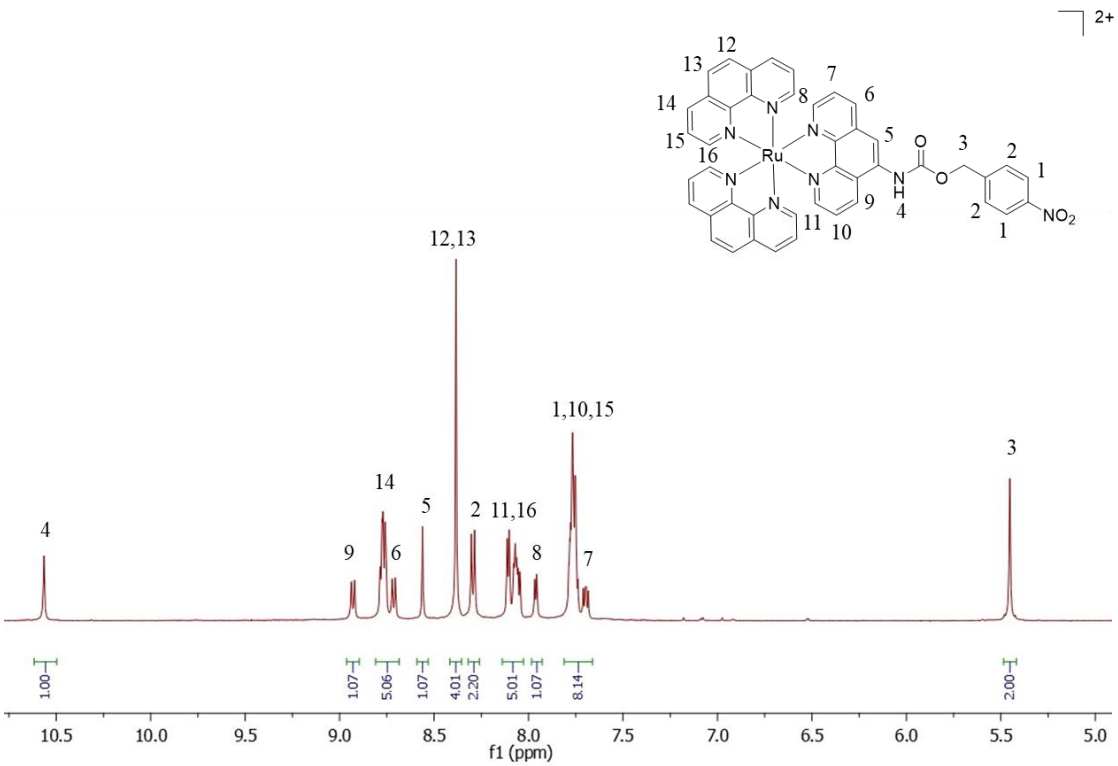

Figure 2.10: *^{1}H NMR of compound **2.11** in DMSO-d_6.*

It can be seen from Figure 2.10 that **2.14** has been successfully complexed to the Ru(II) metal centre to result in **2.11**, as all peaks are clearly visible associated with the modified ligand. Furthermore, peaks labelled 8 and 11 can be seen to have shifted upfield which is to be expected because of the electron density shielding provided upon complexation. Peaks labelled 6 and 9 do not result in a similar upfield shift due to the distance of these protons from the metal centre.

As compound **2.11** is a doubly charged species it can also be characterised by its half the mass (M) represented by M/2. Looking at the HRMS (Figure 2.11) it can be seen that there is strong ionisation at 418.0724 corresponding the M^{2+} ion and at 835.1358 corresponding to the M^{+} ion.

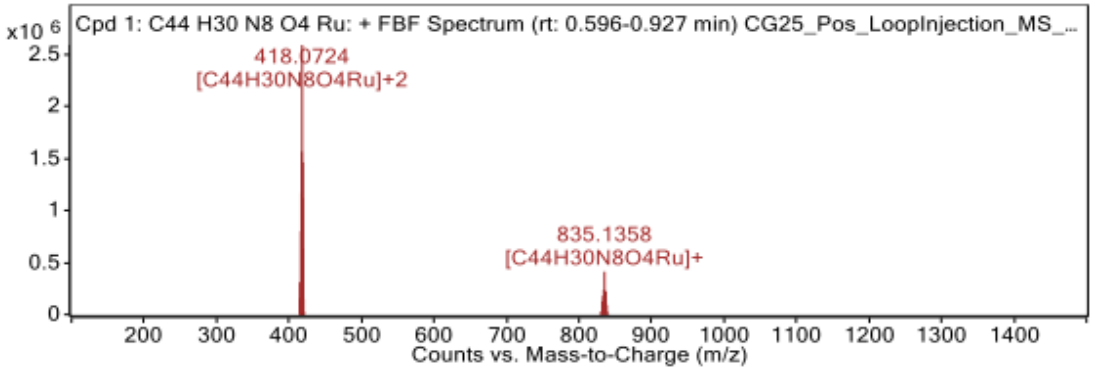

Figure 2.11: *HRMS of compound **2.11**.*

2.3.2 Synthesis of Compound 2.12

Compound **2.12** was synthesised following scheme 2.3 which required the initial synthesis of **2.17** and **2.18**. This alternative synthetic route was followed due to the instability of the ligand highlighted purple within structure **2.12** where the carbamate of the ligand was cleaved upon complexation to **2.16** under the same microwave conditions as previously stated to form compound **2.11**.

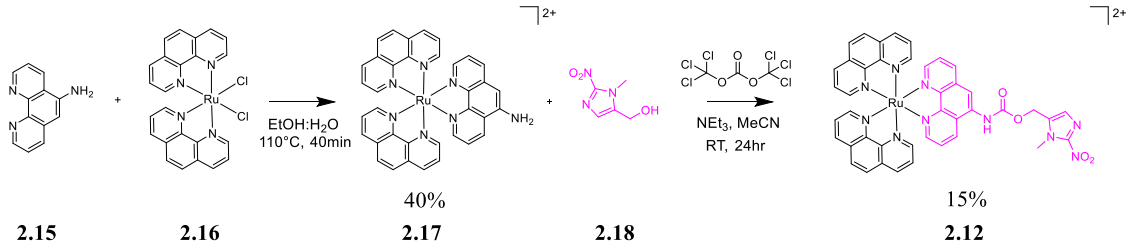

Scheme 2.3: *Reaction scheme for compound **2.12**.*

2.17 was synthesised through the complexation of **2.15** to **2.16** in a 1:1 EtOH:H_2O in the microwave as described above and provided the desired complex in 40% yield after column chromatography. As previously, Compound **2.17** was fully characterised using ^{1}H NMR, ^{13}C NMR, and IR analysis. ^{1}H NMR peaks were assigned using ^{1}H-^{1}H COSY, HSQC and HMBC analysis. The ^{1}H NMR spectrum (500 MHz, DMSO-d_6) of **2.17** can be seen in Figure 2.12.

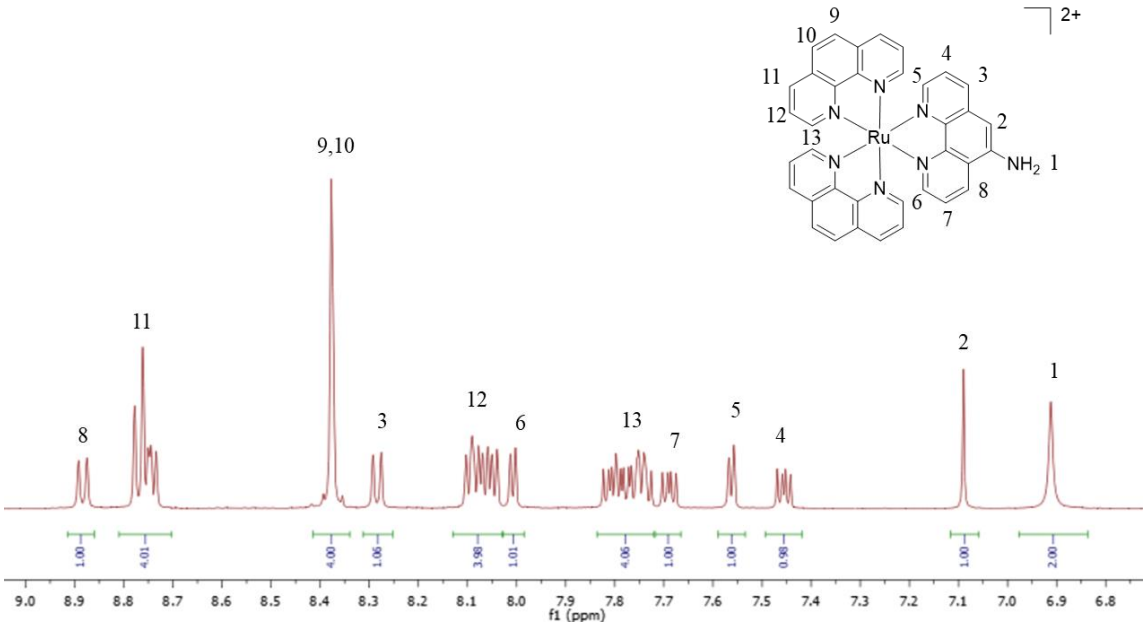

Figure 2.12: *^{1}H NMR of compound **2.17** in DMSO-d_6.*

From the ^{1}H NMR of **2.17** in Figure 2.12 key characteristic peaks of the coordinated ligand **2.15** can be seen. The broad singlet at 6.91 ppm integrating for 2H is representative

of the NH_2 and the singlet at 7.09 ppm is representative of the of the singlet on the modified ligand. Peaks of the ancillary ligands can be observed from the multiplet at 8.75 ppm integrating for 4H and the intense singlet at 8.38 ppm integrating for 4H.

2.18 was synthesised through a 6-step synthetic pathway as seen in scheme **2.4** which was adapted and adjusted from literature.[185]

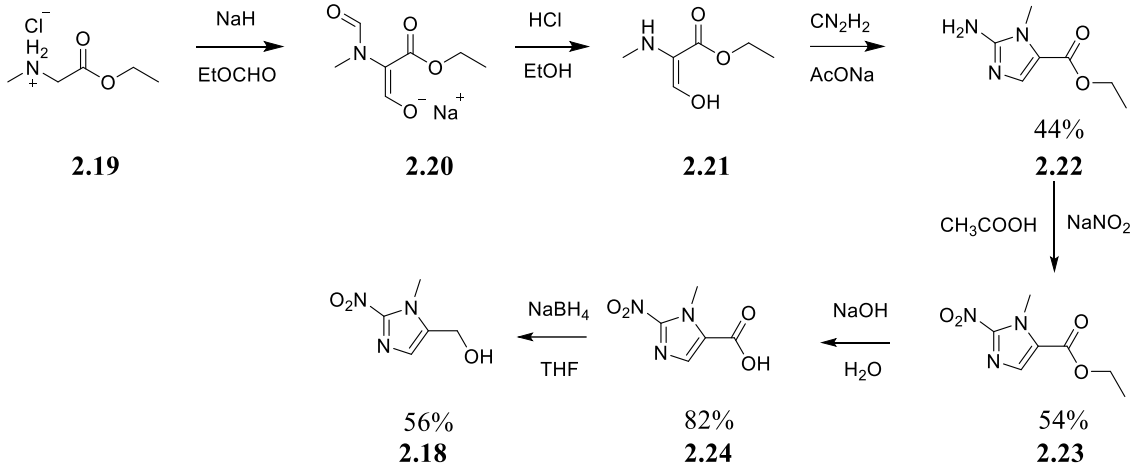

Scheme 2.4: *Reaction scheme for the synthesis of Compound **2.18**.*

2.19 was reacted with Sodium hydride in a solution of ethyl formate to initially form the neutral form of **2.19** and to form the enolate **2.19** as the reactive species with ethyl formate. This resulted in the formation of the N-formyl moiety and the formylation of the α-carbon to afford **2.20** as a solid. Ethanol and HCl were then added to the solid and further refluxed to afford alcohol **2.21** with the removal of the N-formyl group. The white precipitate formed was filtered out of the solution (the N-formylated product) and the filtrate was concentrated and diluted with 10% AcOH and adjusted to pH 3. Cyanamide was added to the reaction mixture and refluxed resulting in the imidazole formation of **2.22**. K_2CO_3 was added to the and the precipitate **2.22** was collected to yield the product in 44% yield.

A Sandmeyer reaction was used to go from the amino derivative **2.22** to the nitro derivative **2.23**. **2.22** was dissolved in glacial acetic acid and treated with sodium nitrite. **2.23** was extracted from the reaction mixture and worked up to remove the acid. Solvent was removed *in vacuo* to yield an oil that was purified by column chromatography to afford the product in 54% yield.

Hydrolysis of **2.23** to **2.24** was carried out in a 1 N aqueous solution of NaOH. The carboxylic acid moiety of 11 was exploited for precipitation by using concentrated HCl

which resulted in the formation of white precipitate. The organic compound was extracted concentrated to afford a solid in 82 % yield.

The final step to form **2.18** was a reduction from the carboxylic acid to the alcohol. **2.24** was reacted with isobutyl chloroformate with use of NEt_3 as a base. This allows for the formation of a carbonate. Sodium borohydride was then added followed by the addition of water this process hydrolysed the carbonate moiety releasing CO_2 gas affording **2.18** as the alcohol. The aqueous layer was separated from organic layer and the solvent was removed *in vacuo* to afford a solid in 56 % yield. **2.18** was characterised using ^{1}H NMR, ^{13}C NMR, and IR. ^{1}H NMR peaks were assigned using ^{1}H-^{1}H COSY in Figure 2.13.

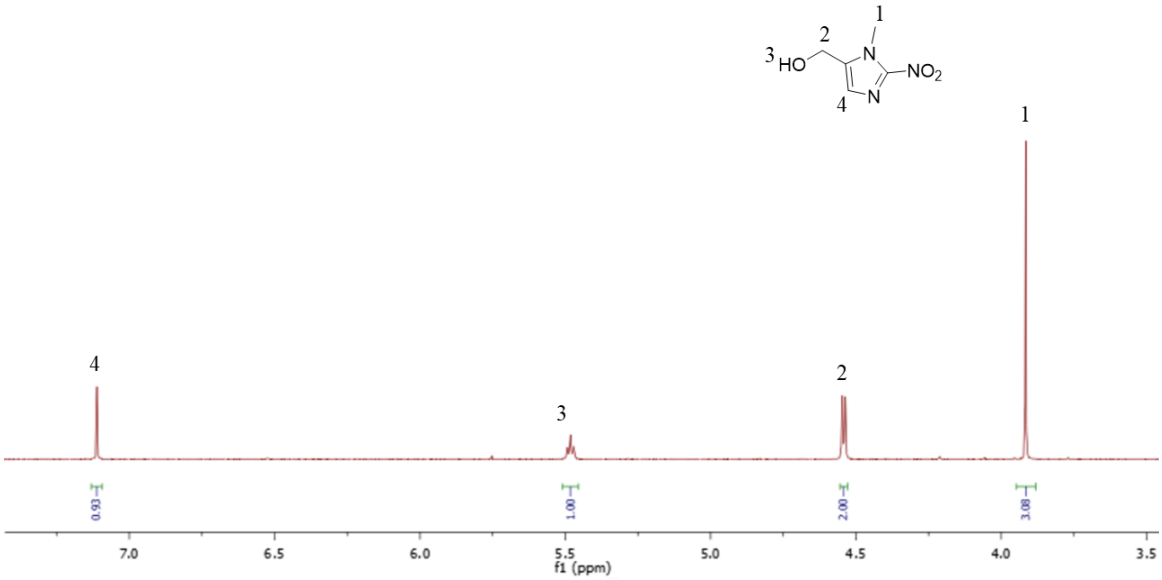

Figure 2.13: *^{1}H NMR of compound **2.18** in DMSO-d_6.*

From Figure 2.13 the methyl substituent is observed as a singlet integrating for 3H at 3.92 ppm. The singlet integrating for 1H at 7.11 ppm is the heterocyclic proton of the imidazole moiety. Whereas the peaks at 5.48 ppm and 4.54 ppm are representative of the hydroxymethyl substituent as observed through the correlations seen in the ^{1}H-^{1}H COSY in Figure 2.14.

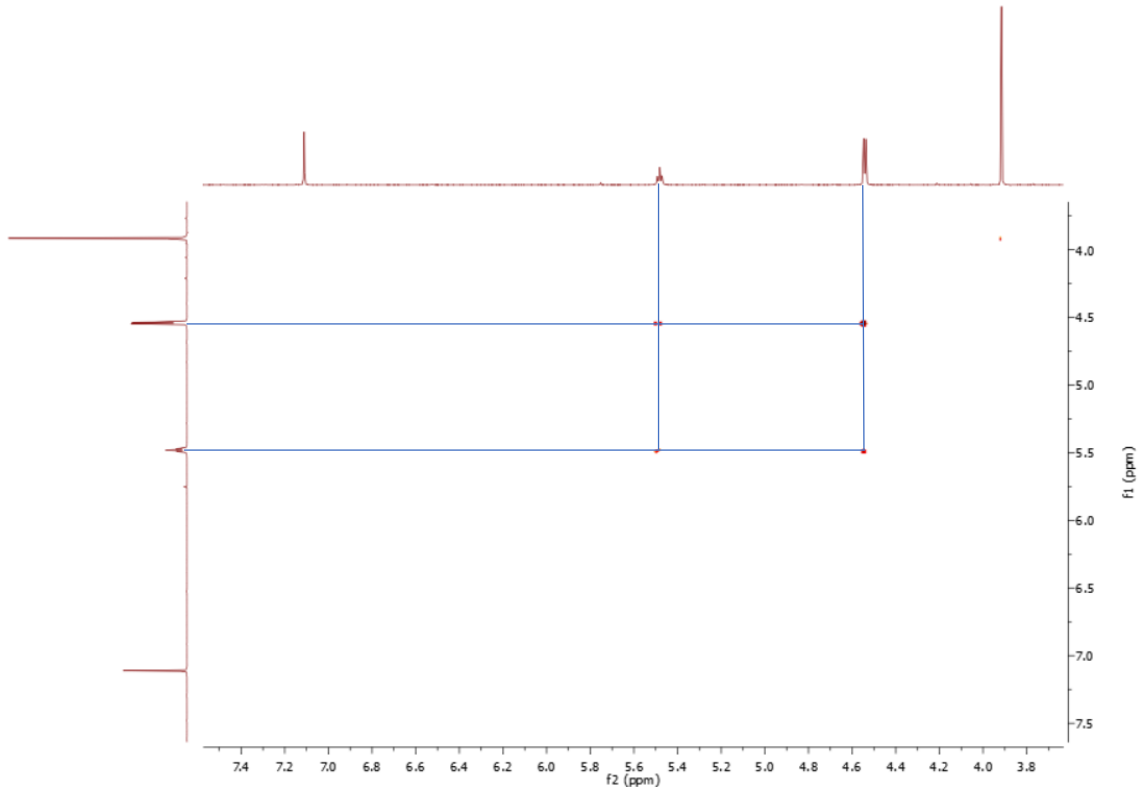

Figure 2.14: *^{1}H-^{1}H COSY of compound **2.18** in DMSO-d_6.. Correlations shown by blue lines.*

The carbamate linkage was then formed between **2.17** and **2.18**. This was done with the use of triphosgene and NEt_3 as the base which resulted in the formation of 2.12 which was then isolated following previous methods of column chromatography in 15% yield. Compound **2.12** was fully characterised using ^{1}H NMR, ^{13}C NMR, and IR analysis. The ^{1}H NMR spectrum (500 MHz, DMSO-d_6) of 5 can be seen in Figure 2.15. Key characteristic peaks for the novel imidazole moiety can be observed. The peak at 4.00 ppm integrating for 3 H represents the N-methyl substituent of the imidazole and the peak at 7.36 ppm integrating for 1 H represents the aromatic proton of the imidazole ring. Furthermore, evidence of carbamate formation is observed through the singlet at 5.43 ppm integrating for 2 H and the singlet at 10.50 ppm integrating for 1 H representative of the NH. Peaks residing within 7.25 ppm and 9.00 ppm are all characteristic of the coordinated phenanthroline ligands.

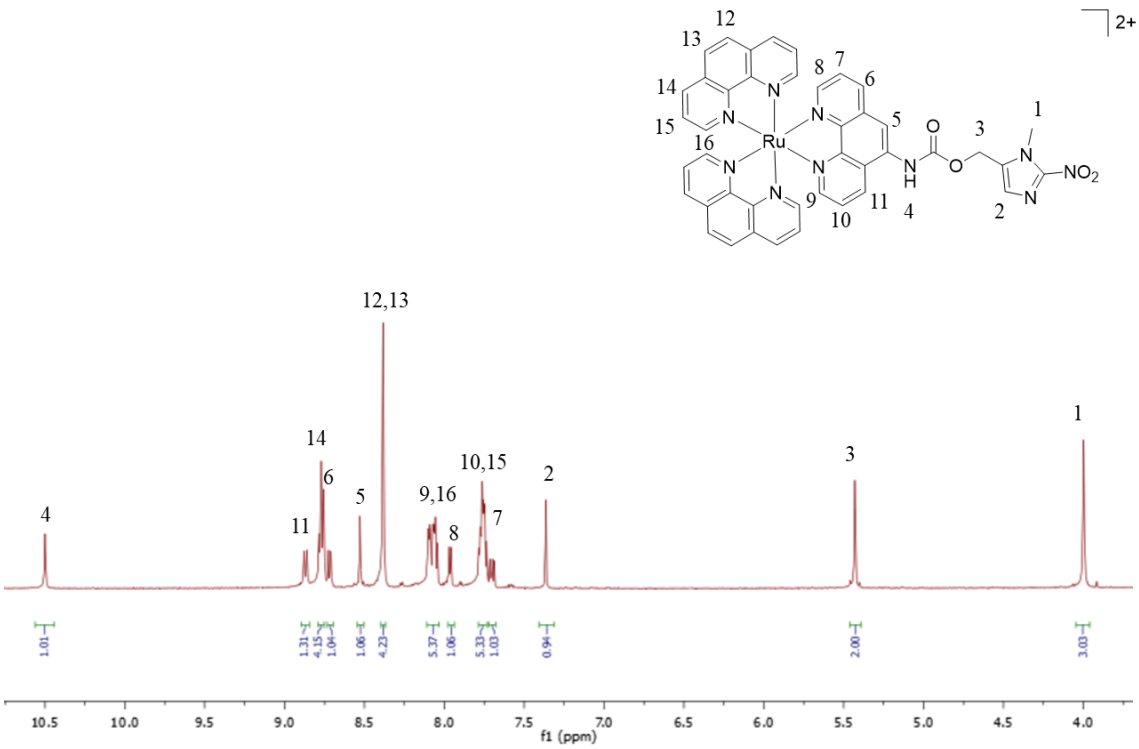

Figure 2.15: *^{1}H NMR of compound **2.12** in DMSO-d_6.*

More evidence of the formation of **2.12** can be seen in the HRMS data provided in Figure 2.16. Where strong ionisation at 420.0710 corresponds to the M^{2+} ion and at 985.1032 corresponds to $[M + PF_6]^+$.

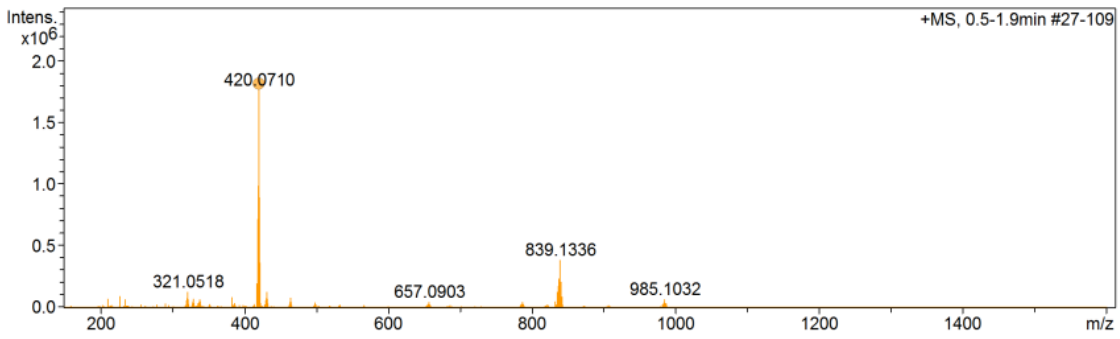

Figure 2.16: *HRMS of Compound **2.12**.*

2.3.3 Synthesis of Compound 2.13

The synthesis of compound **2.13** firstly involved the condensation **2.15** and 4-nitro-1,8-naphthalic anhydride as seen in Scheme 2.5. The amine of **2.15** underwent condensation into the anhydride moiety of the 4-nitro-1,8-naphthalic anhydride in neat AcOH to result in compound **2.25**. **2.25** precipitated out of the AcOH as the reaction cooled back to room temperature and was isolated through filtration in 75 % yield.

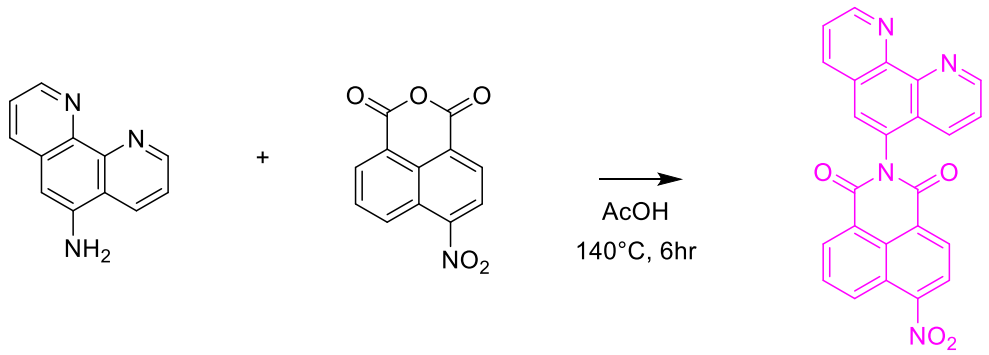

2.15 **2.25**

Scheme 2.5: *Reaction scheme for compound **2.25**.*

Compound **2.25** was fully characterised using ^{1}H NMR, ^{13}C NMR. ^{1}H NMR peaks were assigned using ^{1}H-^{1}H COSY. The ^{1}H NMR spectrum (500 MHz, DMSO-d_6) of **2.25** can be seen in Figure 2.17. Where distinctive peaks of the phenanthroline moiety are seen such as the singlet at 8.23 ppm integrating for 1 H and the doublet of doublets observed at 9.21 ppm and 9.16 ppm both integrating for 1 H. Characteristic doublet of doublets integrating for 1 H that appears almost like a triplet was observed for the naphthalimide moiety at 8.17 ppm.

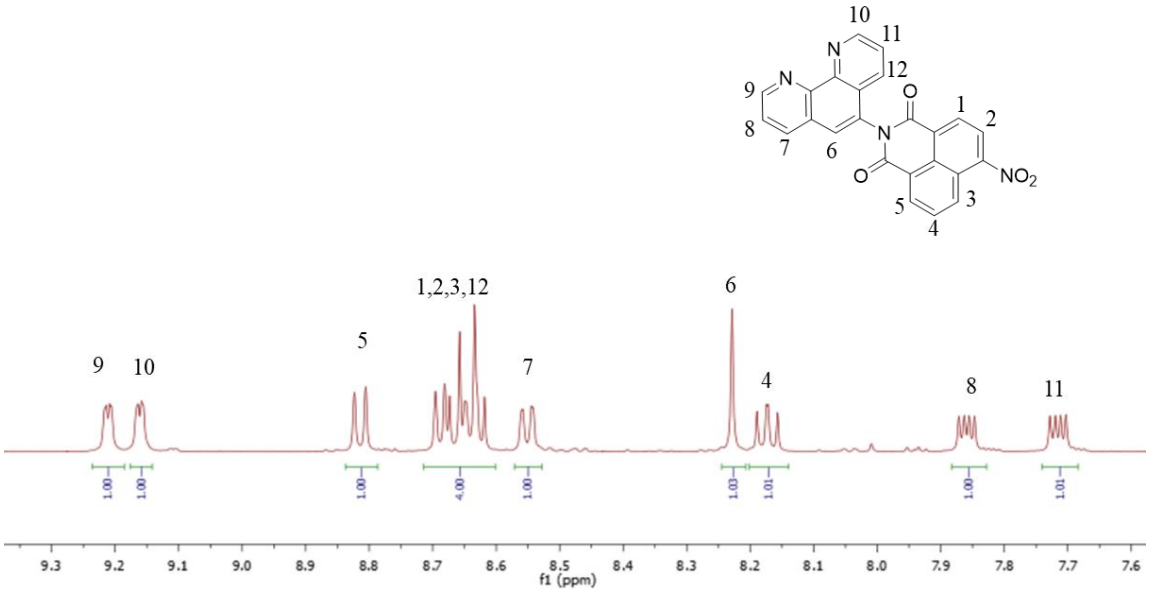

Figure 2.17: *^{1}H NMR of compound **2.25** in DMSO-d_6.*

Compound **2.25** was then complexed onto **2.16** to give compound **2.13** as seen in Scheme 2.6.

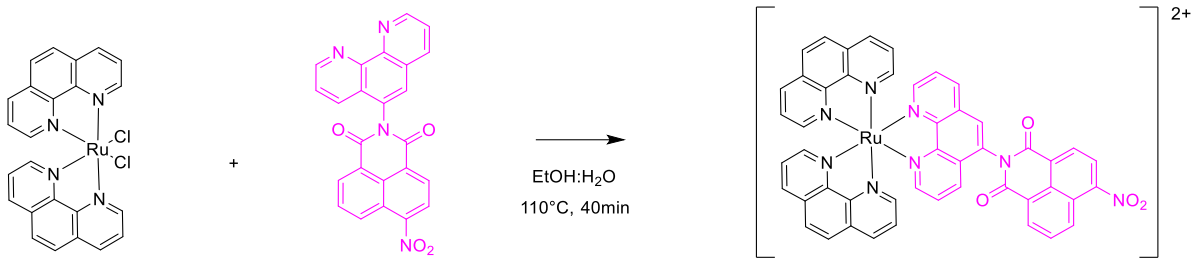

61%

2.16 **2.25** **2.13**

Scheme 2.6: *Reaction scheme for compound **2.13**.*

Again using a 1:1 EtOH:H_2O solution with the application of microwave chemistry **2.25** was complexed onto **2.16**. The reaction mixture was then filtered and ammonium hexafluorophosphate was added to the filtrate to form an orange precipitate. However, in this instance Compound **2.13** was purified through recrystallisation using a diethyl ether diffusion to yield a red crystalline solid in 61% yield. **2.13** was fully characterised using ^{1}H NMR, ^{13}C NMR, and IR analysis. The ^{1}H NMR spectrum (500 MHz, DMSO-d_6) of **2.13** can be seen in Figure 2.18 and was assigned using ^{1}H-^{1}H COSY, HSQC, and HMBC. From Figure 2.18 we can distinguish some peaks which are representative of the coordinated ligand 14.

Peaks at 8.69 ppm and 8.56 ppm are representative the protons labelled 1 and 2 of the 4-nitro-1,8-naphthalimide moiety. Whilst the doublet of doublet at 8.96 ppm integrating for 1H is representative either of protons labelled 7/12 of the phenanthroline moiety of the conjugate ligand. Furthermore, ancillary ligand protons labelled 16 and 17 are represented by a multiplet integrating for 4H at 8.41 ppm.

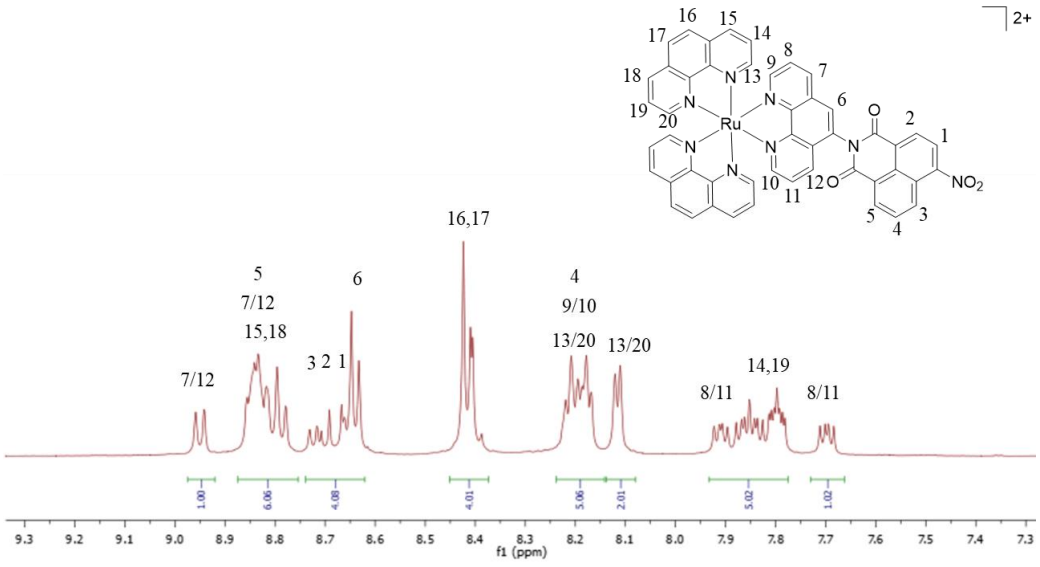

Figure 2.18: *^{1}H NMR of compound **2.13** in DMSO-d_6.*

From the ^{13}C NMR in Figure 2.19 two signature carbonyl carbon peaks downfield at 162.9 ppm and 163.7 ppm of the 4-nitro-1,8-naphthalimide moiety were observed, again confirming the presence of the complexed ligand.

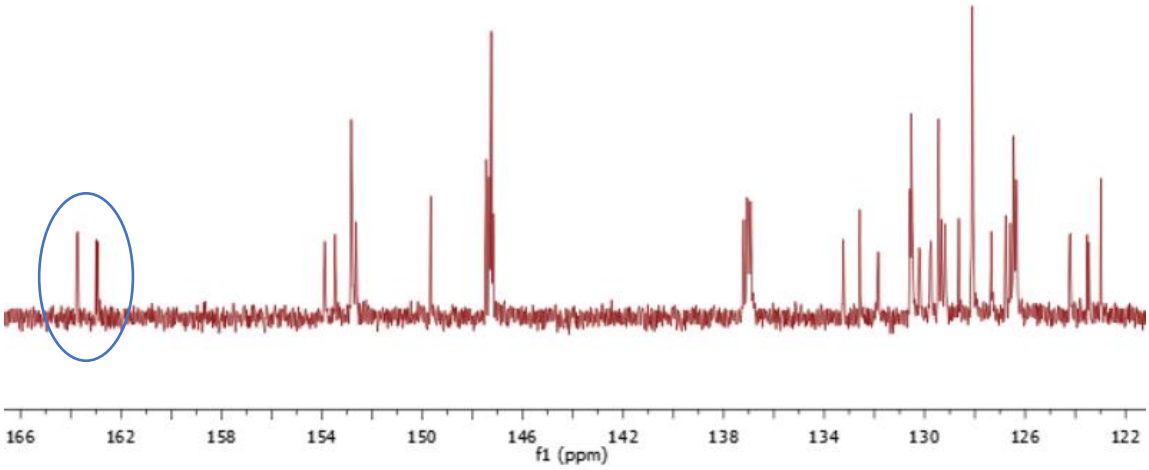

Figure 2.19: *^{13}C NMR of compound **2.13**. Carbonyl carbon peaks circled in blue in DMSO-d_6.*

Further confirmation of the successful synthesis of **2.13** can be seen using HRMS data (Figure 2.20). Where strong ionisation at 441.0647 corresponding to the M^{2+} ion is observed for **2.13**.

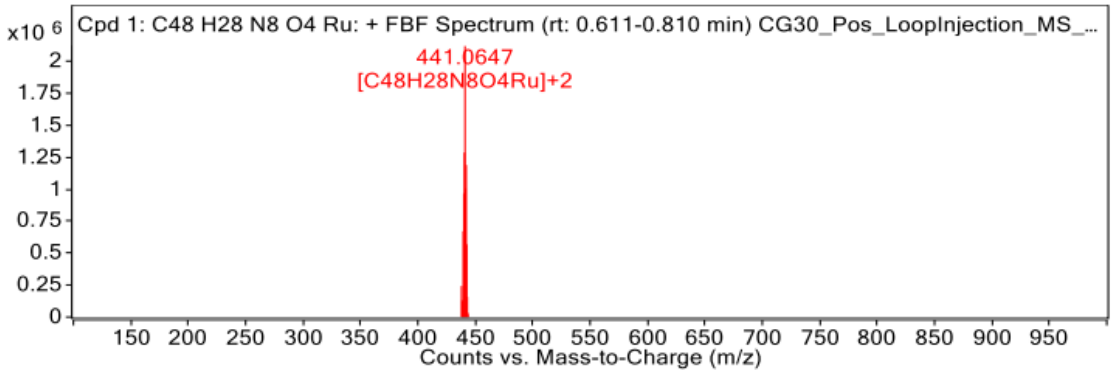

Figure 2.20: *HRMS of compound **2.13**.*

2.3.4 Synthesis of Compound 2.29

The amino derivative **2.26** of compound **2.13** was also synthesised, this was done by firstly synthesising the amino derivative of compound **2.25**. Unfortunately, direct reduction of compound **2.25** utilising a variety of reduction conditions such as Pd/C and H_2 / N_2H_4, and $SnCl_2$ and HCl did not result in quantitative conversion of **2.25** and instead

provided a mixture of both the hydroxylamine and amine derivatives observed through LCMS. The same results were also obtained by direct reduction of compound **2.13**. An alternative synthetic pathway was therefore followed as seen in Scheme 2.7.

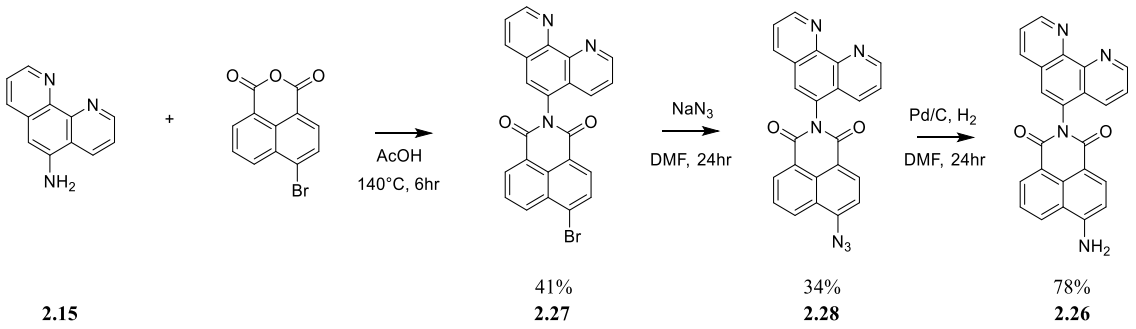

Scheme 2.7: *Reaction scheme for compound **2.26**.*

The first step required the condensation of the amine on **2.15** into the anhydride site of the 4-bromo-1,8-naphthalic anhydride. This was carried out in acetic acid in a pressure tube. **2.27** was isolated as a precipitate from room temperature AcOH in 41% yield. NaN_3 was then used to go from **2.27** to the corresponding azide derivative **2.28** which was precipitated out of DMF by the addition of water in 34% yield. **2.28** was reduced to the amino derivative **2.26** through standard reducing conditions using Pd/C and H_2 to yield the final product as a yellow solid in 78% yield.

Compound **2.26** was fully characterised using ^{1}H NMR, ^{13}C NMR and IR. The ^{1}H NMR spectrum (500 MHz, DMSO-d_6) of **2.26** can be seen in Figure 2.21 and was assigned using ^{1}H-^{1}H COSY.

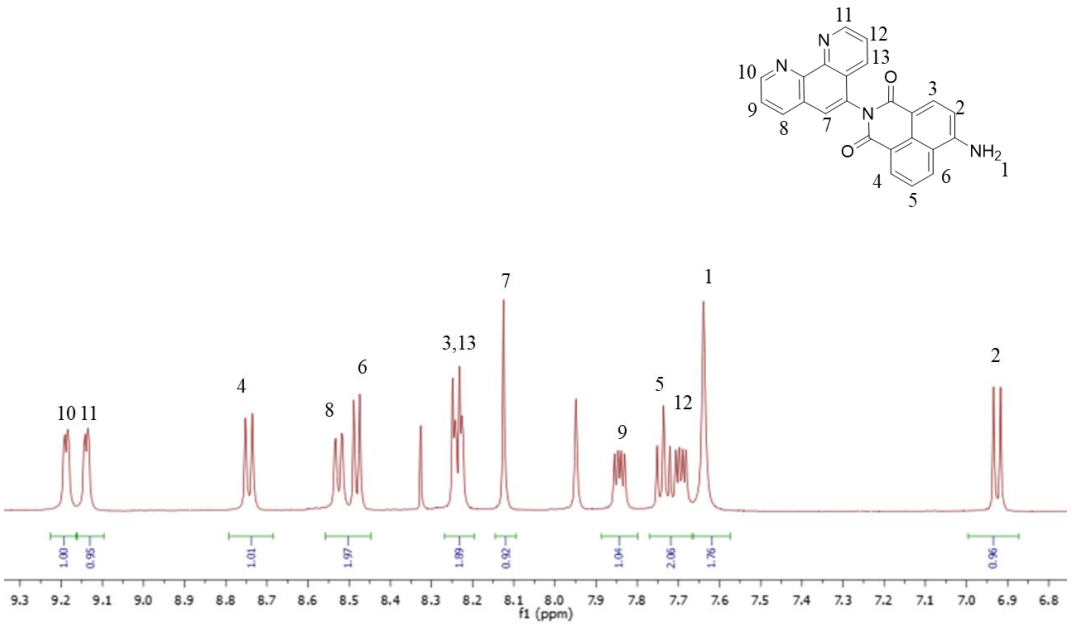

Figure 2.21: *^{1}H NMR of compound **2.26** in DMSO-d_6.*

Key signals in Figure 2.21 indicate successful synthesis of **2.26**. The distinctive peak at 7.64 ppm integrating for 2 H represents the aromatic amine of the naphthalimide moiety. Characteristic doublets both integrating for 1 H at 6.93 ppm and 8.25 ppm are also associated with the naphthalimide moiety. Peaks corresponding to the phenanthroline moiety are the doublet of doublets integrating for 1 H at 9.14 ppm and 9.18 ppm. The characteristic singlet of the phenanthroline portion is also observed at 8.12 ppm integrating for 1 H.

2.26 was then complexed onto **2.16** as seen in Scheme 2.8 following the same microwave chemistry conditions as previously described to result in compound **2.29** in 44% yield.

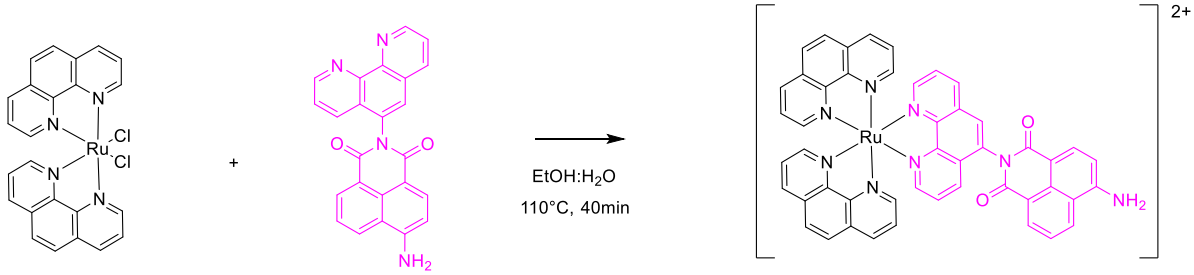

2.16 **2.26** 44% **2.29**

Scheme 2.8: *Reaction scheme for compound **2.29**.*

Compound **2.29** was fully characterised using ^{1}H NMR, ^{13}C NMR, IR. The ^{1}H NMR can be seen in Figure 2.22 and was assigned using ^{1}H-^{1}H COSY, HSQC, and HMBC. Characteristic doublet of doublet of the naphthalimide moiety can be observed at 7.86 ppm and 7.75 ppm two peaks corresponding to the same proton label number 5 are observed as a result of atropoisomerism. Furthermore, evidence of the amine of the naphthalimide is observed as a broad singlet at 7.69 ppm, and proton labelled 2 was seen to upfield shift to 6.95 ppm when compared to corresponding proton labelled 1 at 8.65 ppm of compound **2.13** in previous Figure 2.18. This shows how the electronics on the naphthalimide moiety change upon reduction from the nitro to the amine derivative.

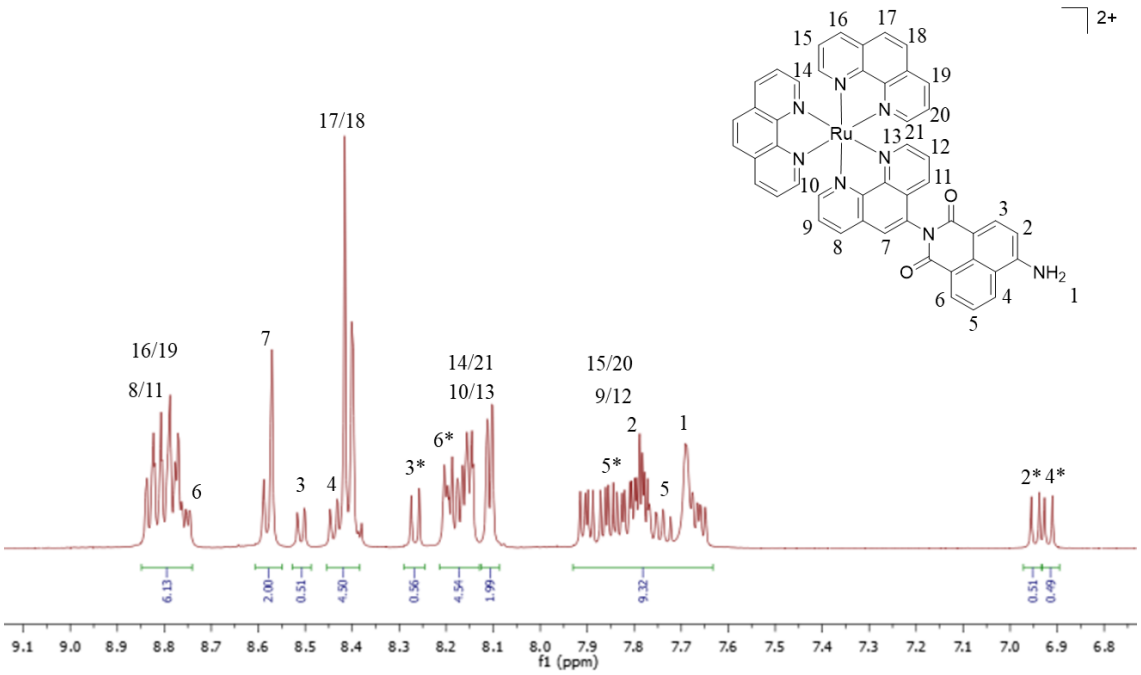

Figure 2.22: *^{1}H NMR of compound **2.29** in DMSO-d_6.*

Further confirmation of the successful synthesis of **2.29** can be seen using HRMS data in Figure 2.23. Where strong ionisation at 426.0774 corresponding to M/2 of the M^{2+} ion is observed for **2.29** and at 852.1529 corresponding to the M^{+} ion.

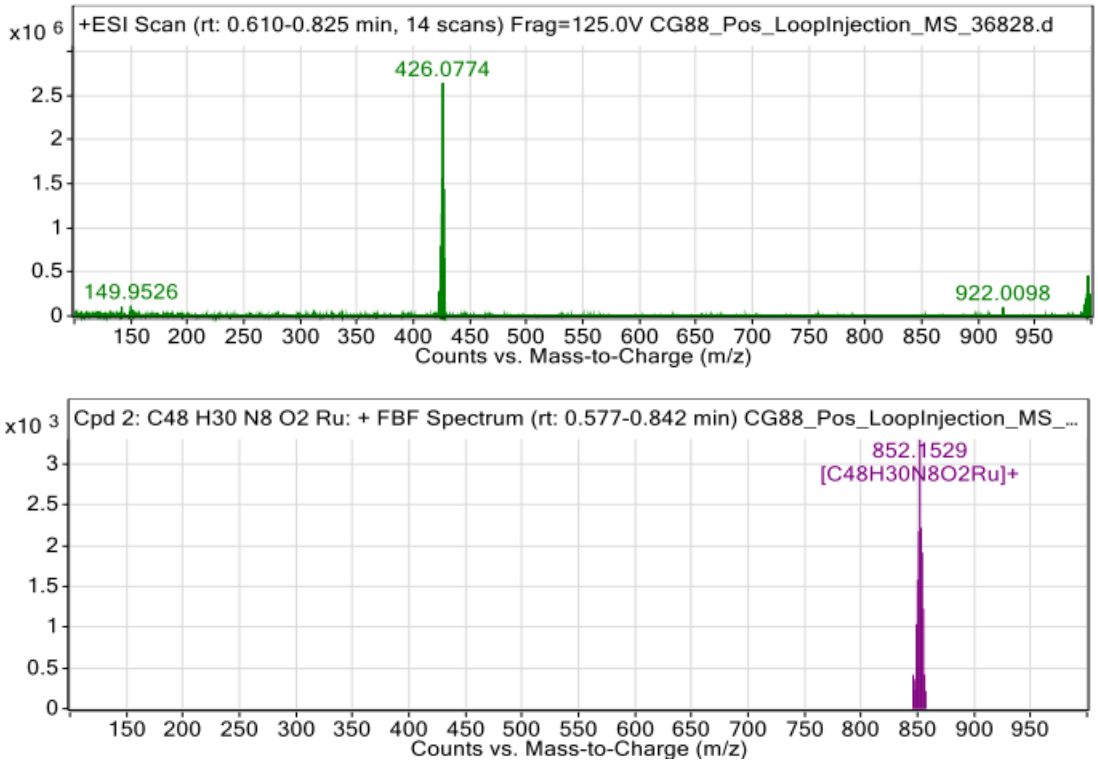

Figure 2.23: *HRMS of compound **2.29**.*

Having successfully synthesised compounds **2.11**, **2.12**, **2.13**, **2.17**, and **2.29** it was necessary to investigate the absorption and emission characteristics of each compound to determine their applicability as OFF-ON luminescent sensors towards NTR. It is necessary to compare those compounds with a nitroaromatic moiety to the corresponding amino derivatives to determine differences in both luminescence intensity and quantum yield. This gives an indicator as to how efficient the nitroaromatic moiety is at quenching MLCT emission.

2.4 Photophysical Characterisation of 2.11, 2.12, 2.13, 2.17, and 2.29

With compounds 2.11, 2.12, 2.13, 2.17, and 2.29 successfully synthesised Figure 2.24a, the next objective was to evaluate their photophysical properties, sensitivity, and selectivity towards NTR.

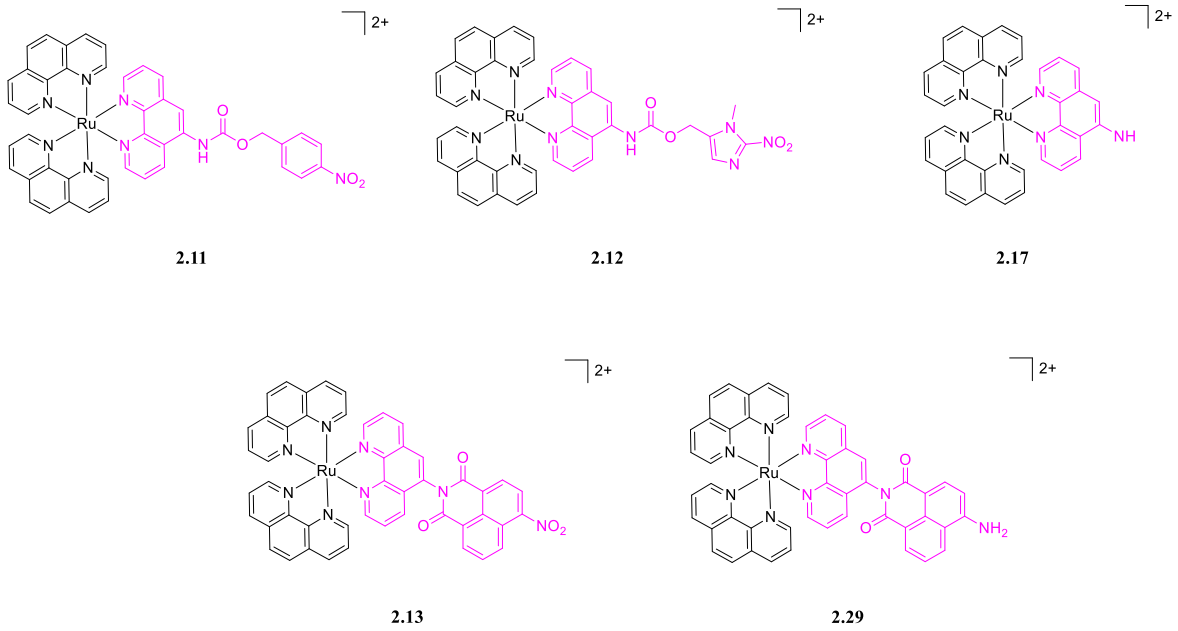

Figure 2.24a: *Structures of compounds 2.11, 2.12, 2.13, 2.17, and 2.29.*

2.4.1 Absorption and Emission Spectra of 2.11, 2.12, and 2.17.

The absorption spectra of compound **2.11**, **2.12**, and **2.17** was recorded at pH 7.4 in 10 mM phosphate buffer. In general, the chloride salt of the compound was dissolved as a concentrated solution 3 mM in DMSO to allow for complete dissolution. Solutions for analysis were then made by dilution of the stock in 10 mM PBS. At no stage did the total conc. of DMSO go above 1%.

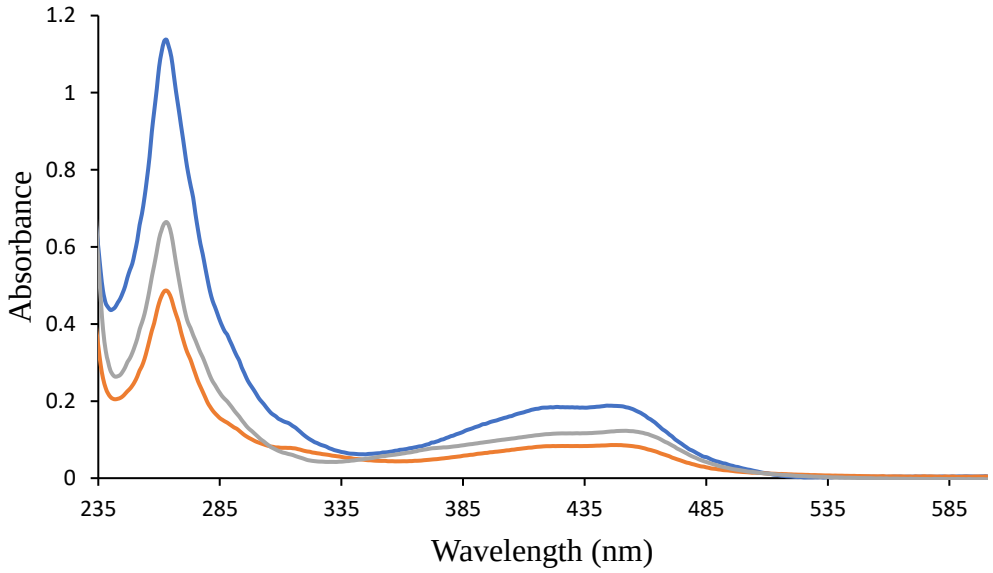

Figure 2.24b: *The UV/Vis spectra of compound (10μM)* ***2.11*** *(blue),****2.12*** *(orange), and* ***2.17*** *(grey) in 10 mM phosphate buffer at pH 7.4.*

The UV/vis spectra in Figure 2.24b shows similarities between compound **2.11**, **2.12**, and **2.17**. Compound **2.11** had a λ_{max} 263 nm and 444 nm. The broad band at 263 nm was characteristic of π-π* intra-ligand transitions of the ancillary phenanthroline ligands as well as the π-π* intra ligand transition of ligand **2.14**. The broad band centred at 444 nm can be assigned to the MLCT transitions within the Ru(ll) polypyridyl centre.[88] Compound **2.12** shows similar characteristics as seen for compound **2.11** with a λ_{max} 263 nm characteristic of π-π* intra-ligand transitions and a broad band at 446 nm representative of MLCT transitions. Similarly with compound **2.17** the λ_{max} 263 nm was observed and an MLCT absorption band at 452 nm.

Upon excitation into the MLCT band at 450 nm of compound **2.11** emission spectra Figure 2.25 is obtained.

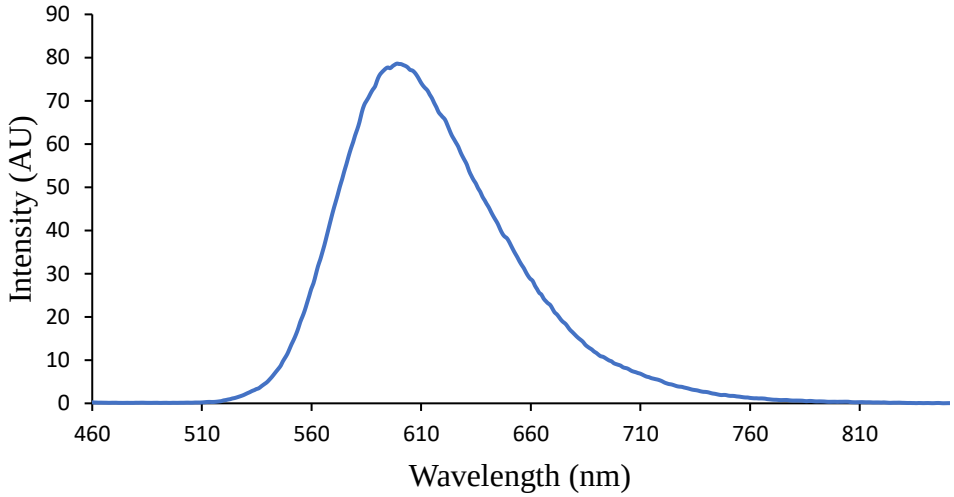

Figure 2.25: *The emission spectra of compound **2.11** (10 μM) in 10 mM phosphate buffer at pH 7.4. λ_{ex} = 450 nm. Ex slit width: 5 nm and Em slit width: 5 nm.*

The emission spectrum in Figure 2.25 shows that upon excitation at 450 nm luminescent emission is observed at 599 nm for compound **2.11** which is characteristic of Ru(II) polypyridyl complexes.[88, 168]

Upon excitation into the MLCT band of compound **2.12** at 450 nm emission spectra Figure 2.26 is obtained.

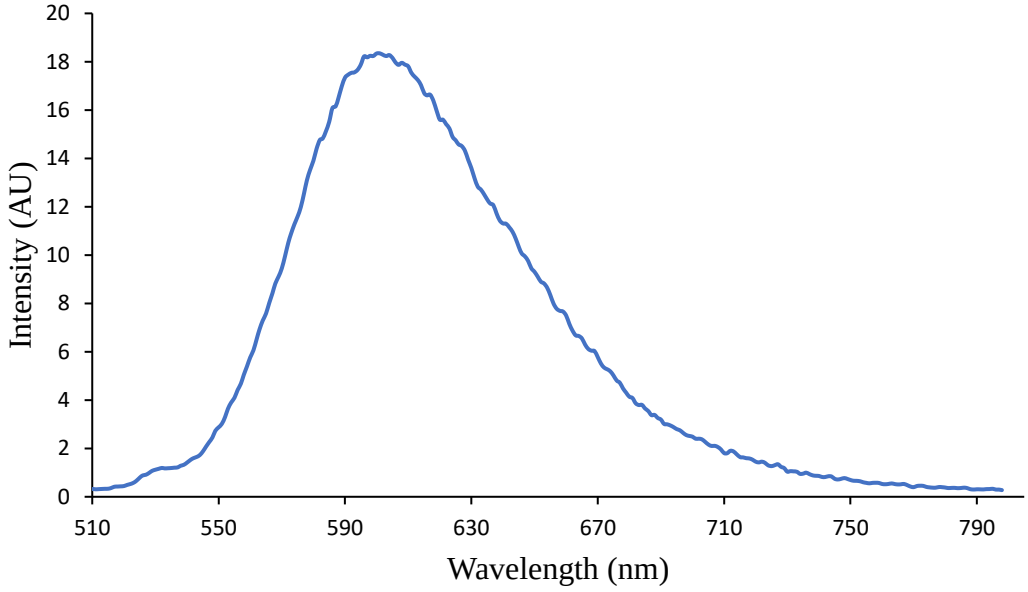

Figure 2.26: *The emission spectrum of compound **1.12** (10 μM) in 10 mM phosphate buffer at pH 7.4. λ_{ex} = 450 nm. Ex slit width: 5 nm and Em slit width: 5 nm.*

The emission spectra in Figure 2.26 shows that upon excitation at 450 nm luminescent emission is observed at 601 nm which was again consistent with the MLCT emission observed for Ru(II) polypyridyl complexes. As compound **2.17** was the immolated complex of compound **2.11** and **2.12** it was of interest to compare the photophysical characteristics of **2.17** to these parent compounds to establish if there could be a significant turn-on in the luminescence intensity of the complexes in the presence of NTR and known co-factor NADH.

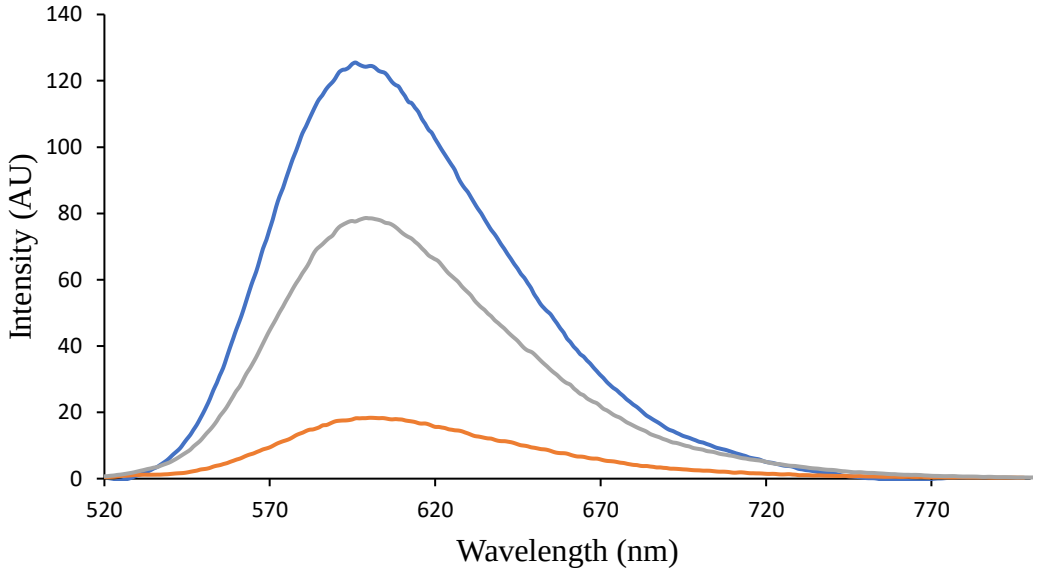

Figure 2.27: *The emission spectra of compound (10 μM)* ***2.11****,* ***2.12****, and* ***2.17*** *in 10 mM phosphate buffer at pH 7.4 showing the varying degrees of luminescence intensity for each compound. Compound* ***2.11*** *(grey), Compound* ***2.12*** *(orange), Compound* ***2.17*** *(blue).* λ_{ex} *= 450 nm. Ex slit width: 5 nm and Em slit width: 5 nm.*

The emission spectra in Figure 2.27 showed that upon excitation at 450 nm luminescent emission is approximately 600nm for all Ru(II) polypyridyl complexes. It can be seen that the luminescence intensity was greatest for compound **2.17** with emission λ_{max} of 596 nm and a quantum yield of Φ_{MLCT} = 0.032 (the quantum yield of each complex was determined in an aerated PBS solution utilising $[Ru(bpy)_3]^{2+}$ as a reference compound where n = 1. An error between 8-10% is normal for the reference method). This was expected as the luminophore **2.17** is predicted to be released and turn on luminescence upon reaction with NTR and NADH. Compounds **2.11** and **2.12** are less luminescent than compound **2.17** which was expected due to the expected dark singlet excited state that is predicted to be introduced as a consequence of the nitroaromatic moieties present in both of these compounds capable of PET quenching.[88, 117, 169]

Compound **2.11** had a quantum yield of $\Phi_{MLCT} = 0.02$ and compound **2.12** had a quantum yield of $\Phi_{MLCT} = 0.011$. The 2-nitroimidazole moiety of compound **2.12** poses to be a greater electron sink to quench the luminescence when carbamate linked to compound **2.17** as there is an observed 6.9-fold difference in the luminescence intensity between that of compound **2.12** and **2.17**. Comparatively compound **2.11** quenches luminescence to a lesser extent than that observed for compound **2.12** with a 1.6-fold difference in the luminescence intensity between that of compound **2.11** and **2.17**. The 2-nitroimidazole moiety is likely a better PET quencher than the 4-nitrobenzyl moiety. This can be determined from the reduction potentials recorded for both substrates in literature. The 2-nitroimidazole has a reduction potential of -0.39 V whereas the 4-nitrobenzyl moiety has a reduction potential of -0.49 V.[117] As the 2-nitroimidazole moiety has a more positive reduction potential it may have a greater affinity for the electrons arising from the PET quenching process.[117]

2.4.2 Absorption and Emission Spectra of 2.13 and 2.29.

The absorption spectrum of compound **2.13** was recorded at pH 7.4 in 10 mM phosphate buffer (Figure 2.28).

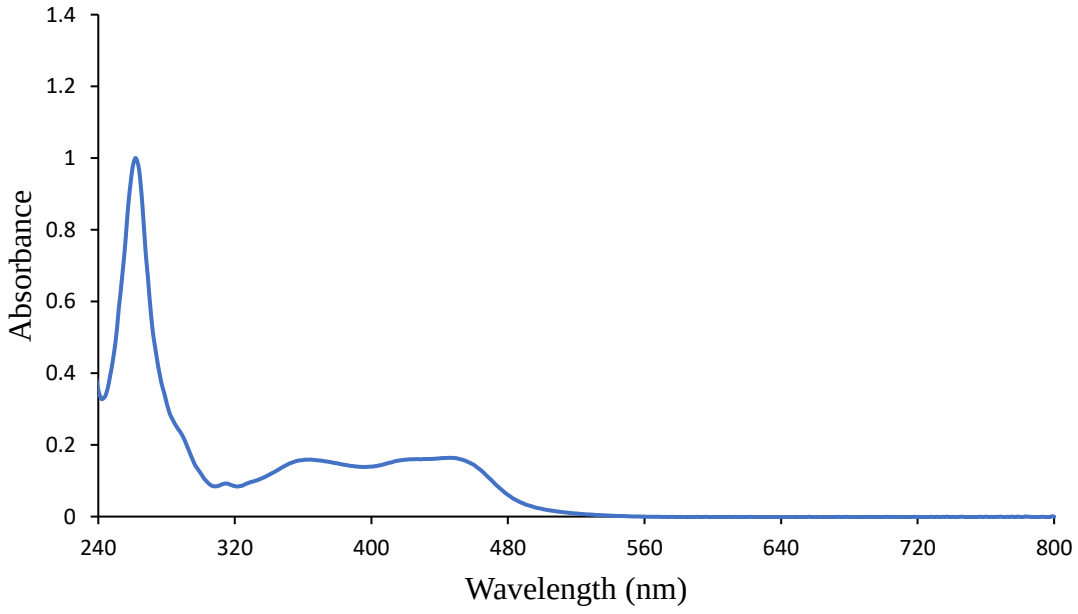

Figure 2.28: *The UV/Vis spectrum of compound **2.13** (10 μM) in 10 mM phosphate buffer at pH 7.4.*

Examination of the UV/vis spectrum of compound **2.13** shows bands characteristic of both the Ru(II) polypyridyl and 4-nitro-l,8-naphthalimide chromophores, The band

centred at 262 nm was attributed mainly to π-π* intraligand transitions, the band at 364 nm to the 4-nitro-1,8-naphthalimide π-π* transitions, and the band centred at 445 nm to the MLCT transitions of the Ru(II) polypyridyl centre.[176]

When the UV/Vis spectrum of compound **2.13** was compared to that of compound **2.29** the key difference is the disappearance of the band centred at 364 nm as compound **2.29** is the amine derivative of the compound and so there will be a bathochromic shift to approximately 450 nm as this is the expected absorption of amine functionalised naphthalimides.[186] For compound **2.29** we again see a band centred at 262 nm which is mainly to π-π* intraligand transitions, and a band at 448 nm which is attributed to the MLCT transitions of the Ru(II) polypyridyl centre seen in Figure 2.29.

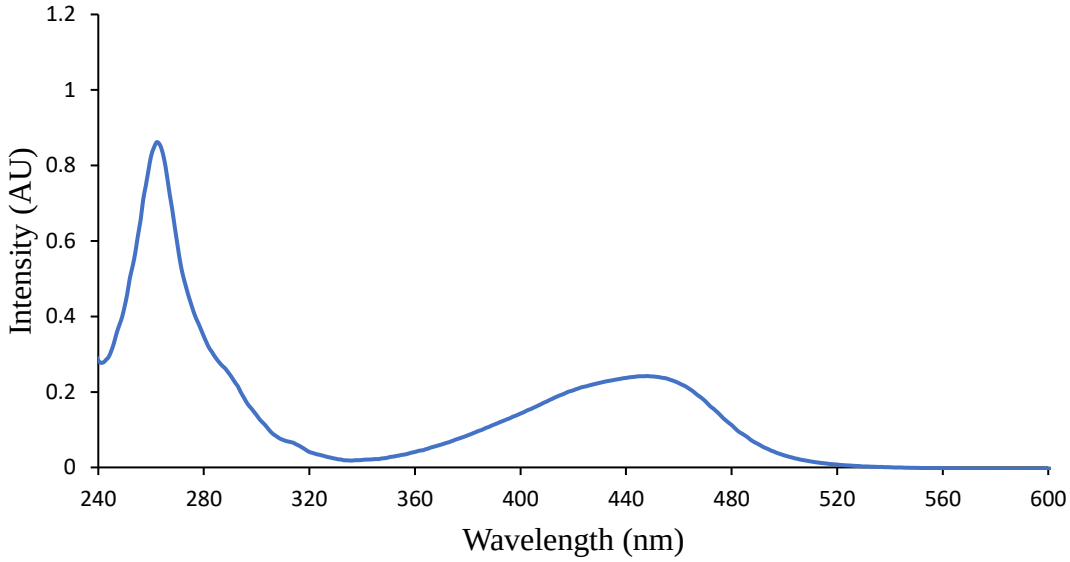

Figure 2.29: *The UV/Vis spectrum of compound **2.29** (10 μM) in 10 mM phosphate buffer at pH 7.4.*

In Figure 2.30 by overlaying the emission spectra of compound **2.13** and compound **2.29** in 10 mM phosphate buffer at pH 7.4 we gain insight as to how intensely these compounds can give off luminescence at approximately 605 nm when excited at MLCT absorption wavelength 445 nm.

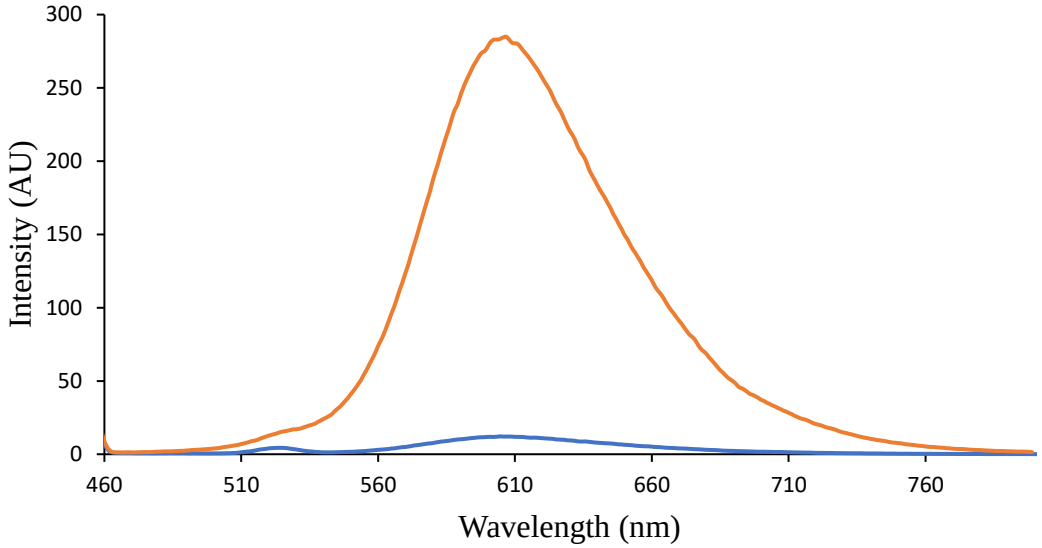

Figure 2.30: *The emission spectra of compound (10 μM)* ***2.13*** *(blue) and* ***2.29*** *(orange) in 10 mM phosphate buffer at pH 7.4.* λ_{ex} *= 445 nm. Ex slit width: 10 nm and Em slit width: 10 nm.*

From Figure 2.30 it was clear that there is a significant difference in the luminescent intensity between compound **2.13** and compound **2.29**, with the luminescent intensity of compound **2.29** being 23.3-fold greater with Φ_{MLCT} = 0.005 than that of compound **2.13** with Φ_{MLCT} = 0.0005. This was similar to what was observed by Gunnlaugsson and co-workers.[176] Following literature precedent there is strong communication between that of the naphthlaimide moiety and the Ru(II) polypyridyl centre. It is suggested that the triplet excited states of both the MLCT and the naphthalimide are in equilibrium with recorded intersystem crossing from the ^{1}MLCT to the triplet excited state of the naphthalimide moiety.[178] As the triplet excited state of the naphthalimide can undergo non radiative decay thus giving off no luminescence it is proposed that this is what may quench the luminescence arising from the ^{3}MLCT excited state. However, in the case of the amino derivative compound **2.29** the likelihood is that the triplet excited state of the naphthalimide sits higher in energy than the ^{3}MLCT and so there is a greater extend of intersystem crossing to that of the ^{3}MLCT that results in phosphorescence upon relaxation to its ground state.

Given the difference in the quantum yields and luminescence intensity of compounds **2.11** and **2.12** in comparison to compound **2.17**, and compound **2.13** in comparison to compound **2.29**, compounds **2.11**, **2.12**, and **2.13** were subject to treatment with NTR and NADH to determine if the expected turn on luminescent response could be achieved upon reduction of these nitro compounds to their corresponding amino derivatives.

2.5 Luminescence Response of 2.11, 2.12, and 2.13 Towards NTR

Firstly, the luminescent response of all 3 compounds was determined to establish if the probes are NTR sensitive. This was done by incubating each of the compounds with NTR (oxygen sensitive NTR expressed by *E. coli*) and its cofactor NADH. NTR works via a ping-pong bi-bi mechanism, this mechanism involves the subsequential binding and release of substrates and products as well as the transfer of electrons from a cofactor to the substrate.[151] Firstly, NADH is recruited by the enzyme in which it reduces the flavin mononucleotide (FMN) substituent with the release of NAD^+, this then allows for the substrate moiety of the fluorophore/luminophore to be recruited and reduced to the released nitroso derivative (scheme 2.9). This 2 e^- reduction is repeated to result in the amino derivative which will result in a turn-on in luminescence.[187]

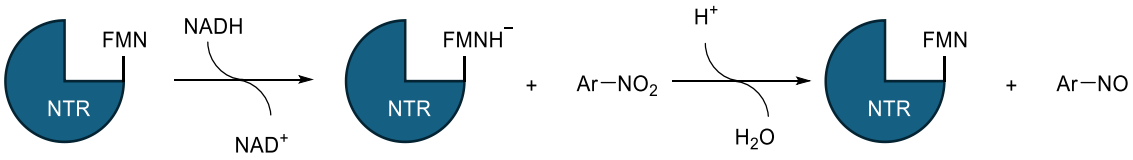

Scheme 2.9: *Proposed mechanism of the NTR reduction of a nitroaromatic moiety.*

The emission spectrums were measured at pH 7.4 in 10 mM PBS with <1% DMSO as co-solvent in the presence of NADH (500 µM) at 25 °C.

2.5.1 Compound 2.11 Treated with NTR.

In Figure 2.31 compound **2.11 (**10 µM) was treated with NTR (5 µg mL^{-1}) in the presence of the co factor NADH (500 µM) over 60 minutes. The luminescence intensity increased over the course of 1 hour as a result of the reduction of the 4-nitrobenzyl moiety and subsequent self-immolation to give compound **2.17**. This resulted in a 1.6-fold increase in the luminescence enhancement at 600 nm. However, as previously mentioned sufficient quenching of the ^{3}MLCT emission was poor in the case of compound **2.11** so a lesser turn on response was expected.

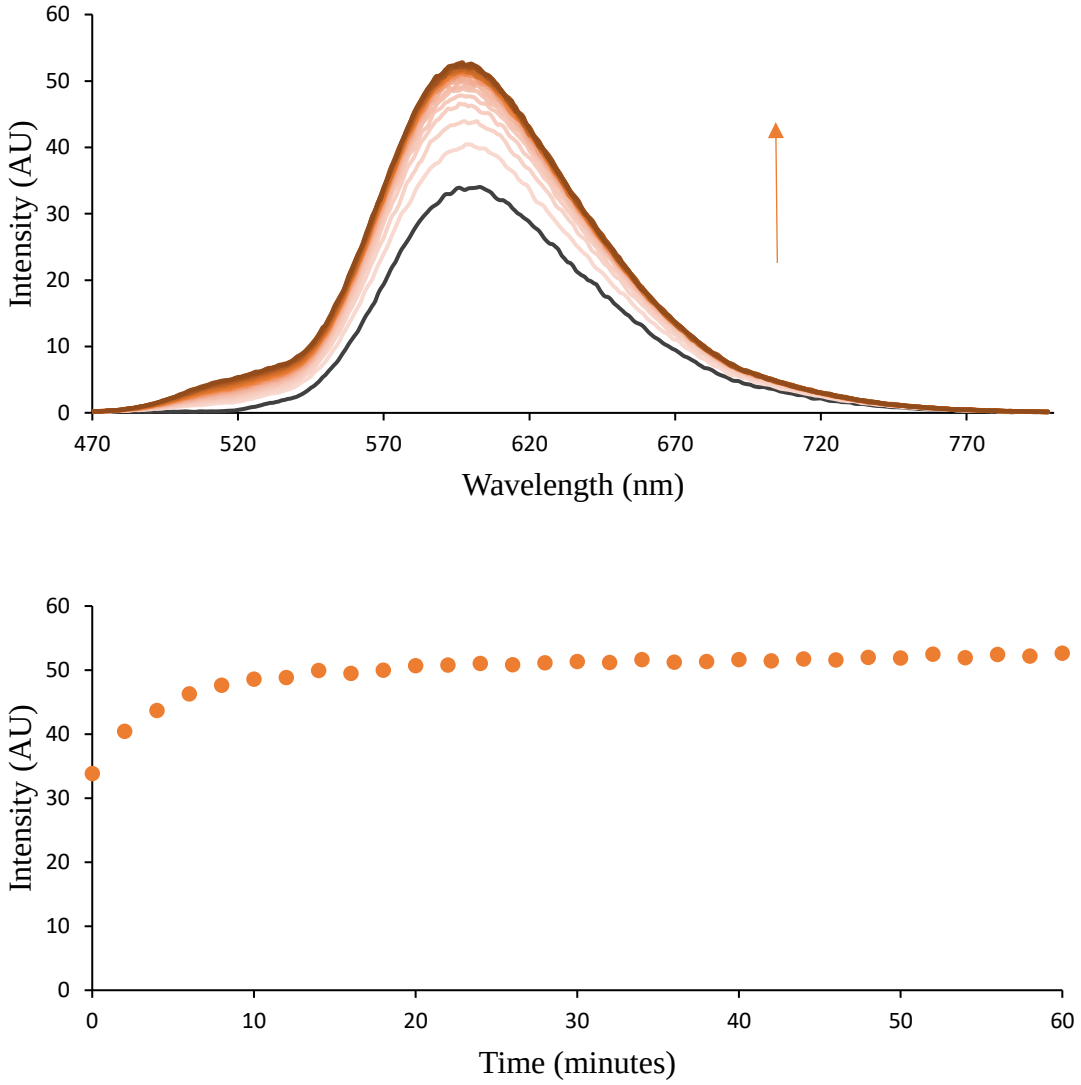

Figure 2.31: *(Top) Changes in the emission spectrum of compound* ***2.11*** *(10 µM) at various time points (0 - 60mins) after addition of NTR (5 µg mL^{-1}), NADH (500 µM) in 10 mM phosphate buffer at pH 7.4. The black line is representative of compound* ***2.11*** *+ 500 µM NADH. (Bottom) Shows changes in the luminescence intensity as a function of time from (0 - 60 minutes) at λ_{em} = 605 nm after addition of NTR. λ_{ex} = 450 nm. Ex slit width: 5 nm and Em slit width: 5 nm. n = 1.*

2.5.2 Compound 2.12 Treated with NTR.

In Figure 2.32, Compound **2.12** (10 µM) was treated with NTR (5 µg mL^{-1}) in the presence of the co factor NADH (500 µM). In this case there was a greater increase in the luminescence intensity of **2.12** in the presence of NTR likely due to the 2-nitroimidazole moiety acting as a greater electron sink as previously mentioned. A 4.1-fold increase in luminescence intensity was observed at 605 nm. While there was a greater luminescence

enhancement in the presence of NTR in comparison to compound **2.11** the probe was still to some extent luminescent in the absence of NTR.

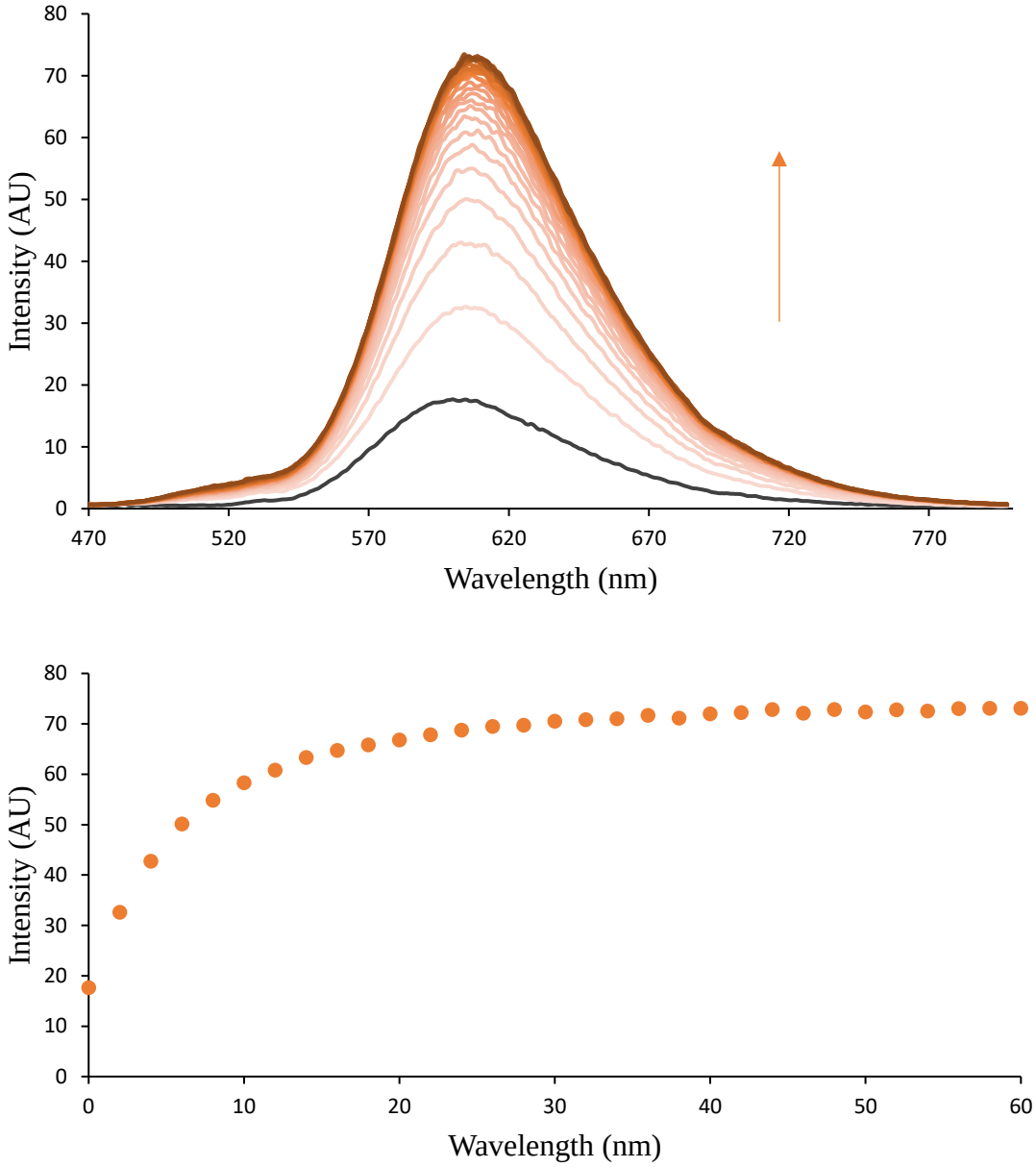

Figure 2.32: *(Top) Changes in the emission spectrum of compound* ***2.12*** *(10 µM) at various time points (0 - 60mins) after addition of NTR (5 µg mL^{-1}) NADH (500 µM) in 10 mM phosphate buffer at pH 7.4. The black line is representative of compound* ***2.12*** *+ 500 µM NADH. (Bottom) Shows changes in the luminescence intensity as a function of time from (0 - 60 minutes) at λ_{em} = 605 nm after addition of NTR. λ_{ex} = 450 nm. Ex slit width: 5 nm and Em slit width: 5 nm. n = 1.*

2.5.3 Compound 2.13 Treated with NTR.

Compound **2.13** (10 µM) showed an exceptional turn-on in luminescence intensity seen in Figure 2.33 when treated with NTR (5 µg mL^{-1}) which resulted in a significant 13.8-fold increase in luminescence enhancement. There is a significant deal of quenching established by the 4-nitro-1,8-naphthalimide moiety which was turned on when reduced to its corresponding amino derivative compound **2.29** in the presence of NTR. The expected naked eye turn on response can be observed in the insert of Figure 2.33.

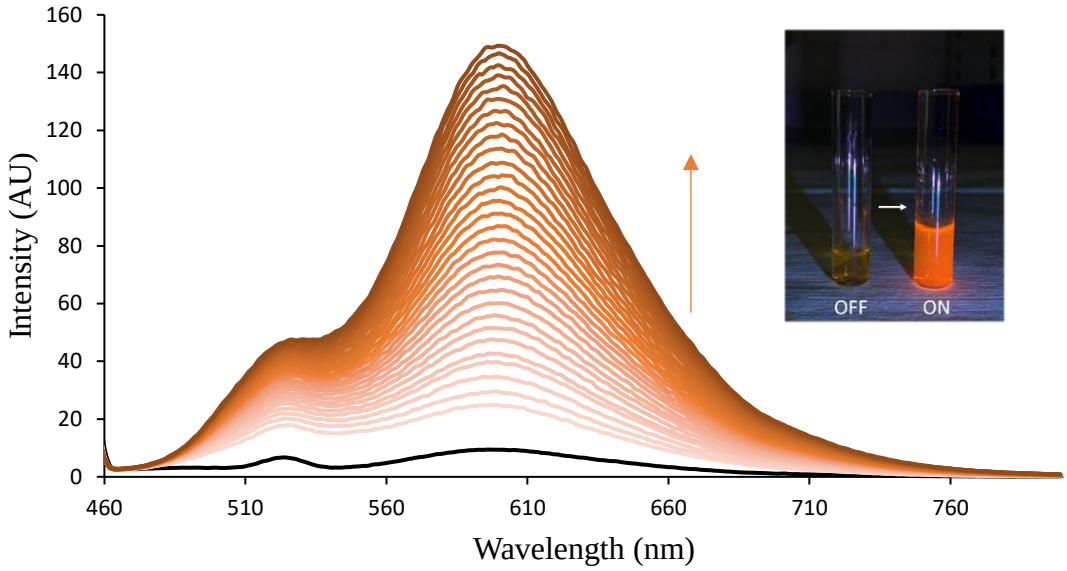

Figure 2.33: *(Top) Changes in the emission spectrum of compound **2.13** (10 µM) at various time points (0 - 60mins) after addition of NTR (5 µg mL^{-1}), NADH (500 µM) in 10 mM phosphate buffer at pH 7.4. The black line is representative of compound 3 + 500 µM NADH. (Insert) Compound **2.13** (1:1 DMSO:PBS) (left) sodium dithionite (right) showing the expected naked eye response under reducing conditions (5 mM $Na_2S_2O_4$). λ_{ex} = 445 nm. Ex slit width: 10 nm and Em slit width: 10 nm. n = 1.*

What was interesting was the absence of a plateau for compound **2.13** over the course of 60 minutes. Compound **2.11** and **2.12** displayed a plateau of luminescence at approximately 30 minutes which was not the observed with compound **2.13**. However, at 30 minutes compound **2.13** had already established a much greater fold of luminescence enhancement of 9.3-fold, and 15.9-fold after 60 minutes as seen in Figure 2.34. In comparison to compound **2.13**, compound **2.11** was poorly responsive towards NTR due to the inability of the 4-nitrobenzyl moiety to fully quench the MLCT emission prior to reaction, deeming it unsuitable as an OFF-ON NTR luminescent sensor. The same can be said for compound **2.12** even though there was significantly greater quenching the probe

is still not completely switched OFF nor does it achieve a fold increase in luminescence intensity superior to that of compound **2.13**. Given the significance of the OFF-ON response of compound **2.13** towards NTR and its continuous increase in luminescent intensity over time, it was of interest to carry out time dependent studies towards different concentrations of NTR.

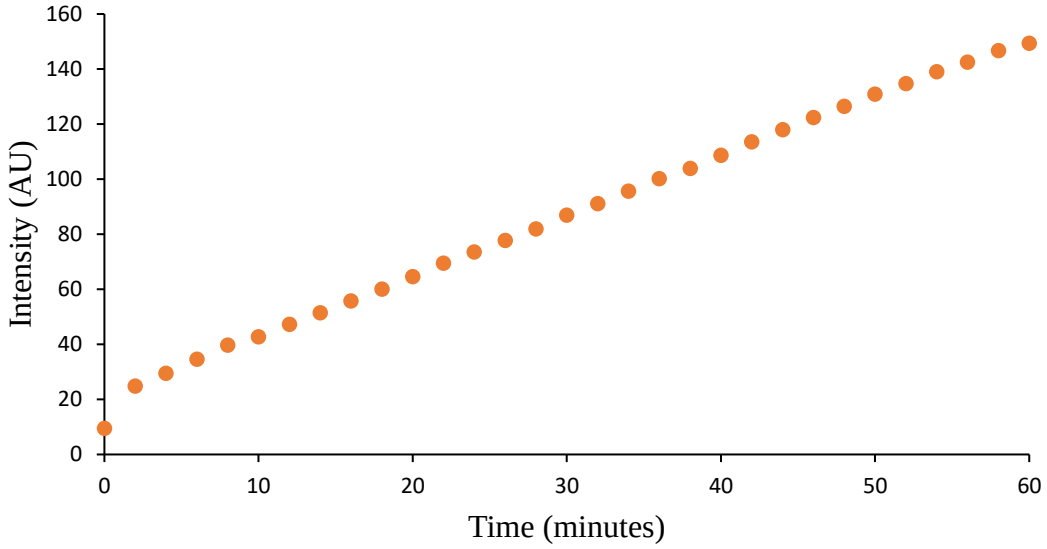

Figure 2.34: *Changes in the luminescence intensity for compound **2.13** (10 μM) as a function of time from (0 - 60 minutes) at 600 nm after addition of NTR (5μg mL^{-1}), NADH (500 μM) in 10 mM phosphate buffer at pH 7.4. λ_{ex} = 445 nm. Ex slit width: 10 nm and Em slit width: 10 nm. n = 1.*

2.6 Sensitivity of 2.13 Towards NTR

Considering the above results our efforts were focused on determining the utility of compound **2.13** as both a sensitive and selective probe for NTR. To evaluate compound **2.13** sensitivity towards NTR we analysed the turn on response towards varying concentrations of NTR.

It is only over long time periods do we observe a plateau in the luminescence intensity of compound **2.13**. In Figure 2.35 a plateau is observed for lower concentrations of NTR as low as 0.02 μg mL^{-1}. This is a significant result comparable to the LOD of previously cited naphthalimide based NTR probes in literature.[157, 160] However, at higher concentrations much longer time periods are required to reach a plateau in intensity.

Nevertheless, it can be said that compound **2.13** over the course of 660 minutes displays sensitivity towards NTR as these plateaus can be seen to increase with increasing concentrations of NTR.

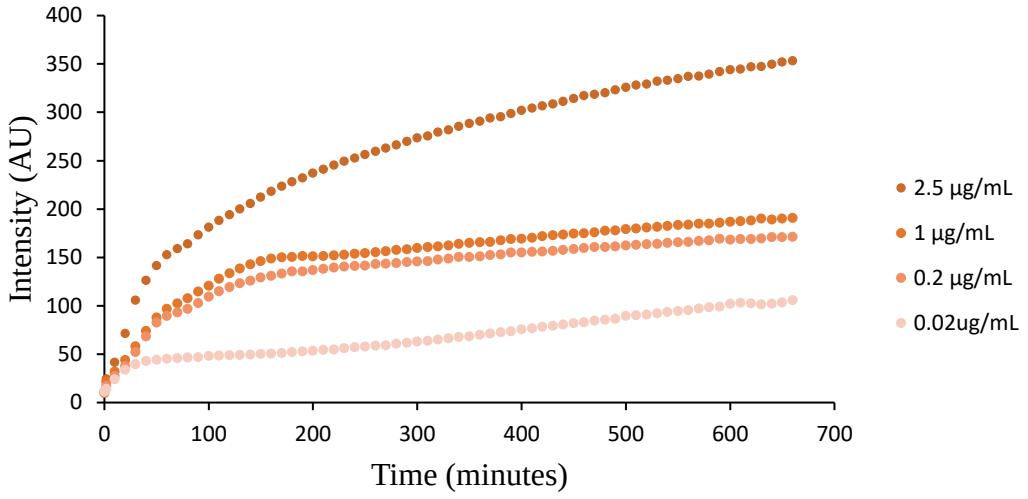

Figure 2.35: *Compound **2.13** treated with varying concentrations of NTR (0.02 µg mL^{-1}-2.5 µg mL^{-1}) and NADH (500 µM) in 10 mM phosphate buffer at pH 7.4. over the course of 660 minutes at 600 nm. λ_{ex}= 445 nm. Ex slit width: 10 nm and Em slit width: 10 nm. n = 1*

Furthermore, looking at 300-minute time points where there was generally a large discrepancy in term of luminescence intensity of compound **2.13** when treated with varying concentrations of NTR. In Figure 2.36, it can be seen that as the concentration increased from 0.02 µg mL^{-1} - 5 µg mL^{-1} there was an increase in luminescence intensity at 600 nm for compound **2.13**.

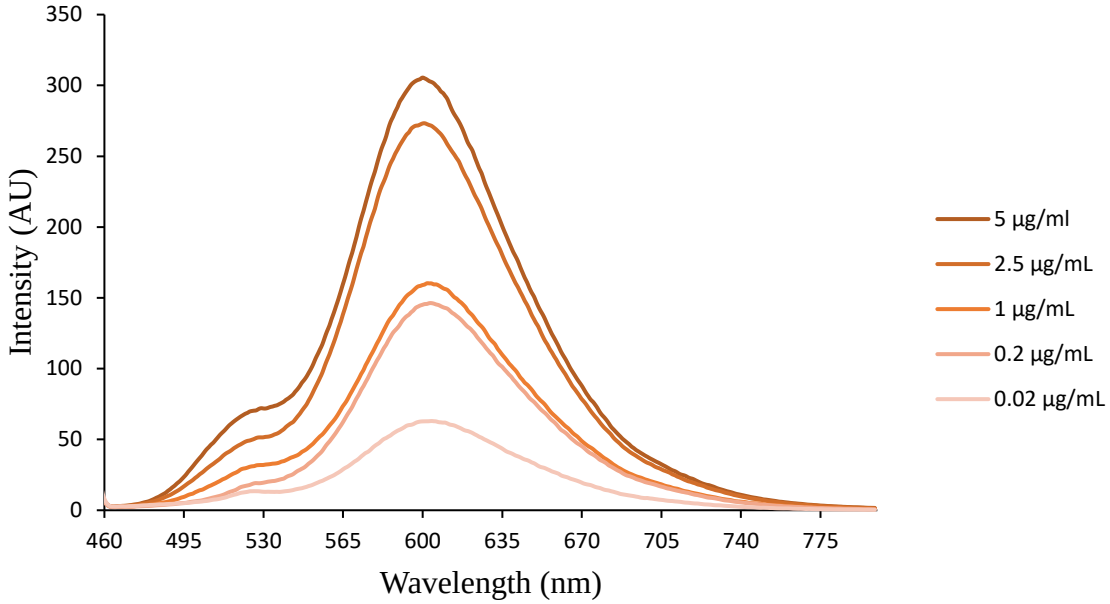

Figure 2.36: *300-minute time stamps of compound **2.13** (10 µM) treated with varying concentrations of NTR (0.02 µg mL^{-1} - 5 µg mL^{-1}) and NADH (500 µM) in 10 mM phosphate buffer at pH 7.4. λ_{ex} = 445 nm. Ex slit width: 10 nm and Em slit width: 10 nm. n = 1.*

These longer time periods required to reach the plateau in luminescence intensity are not entirely unusual for compounds that rely on the direct reduction of the 4-nitro substituent of the 4-nitro-1,8-naphthalimide.[160, 162] This could be due to the lack of hydrophobic interactions and key hydrogen bonding interactions with surrounding amino acid residues by the Ru(II) moiety required to fix **2.13** within the hydrophobic interspace of NTR, consequently resulting in a poorer fit in the active site of the enzyme.[117] However, substantial hydrophobic interactions, π-π stacking and hydrogen bonding with the oxygens of the nitro substituent should be established by the interactions of the 4-nitro-1,8-naphthalimide moiety within the binding pocket, this may suggest that the 4-nitro-1,8-naphthalimide may have a lower reduction potential and is consequently less readily reduced by NTR in comparison to that of known substrates that are highly reactive such as the 2-nitroimidazole moiety seen in compound **2.12**.[162, 188]

2.7 The Selectivity of 2.13 Towards NTR

To first determine that compound **2.13** was indeed selective for NTR and that the luminescent response is a product of the reduction from **2.13** to **2.29**, dicoumarol was added to a solution of NTR and NADH thus inhibiting NTR through the inhibition of the FMN active site through π-overlap.[189]

In Figure 2.37 NTR (2.5 μg mL^{-1}) and NADH (500 μM) were treated with varying concentrations of dicoumarol (0 – 100 μM) prior to the addition of compound **2.13 (**10 μM). When looking at the bar chart it was noted that upon introducing 1 eq of dicoumarol to 1 eq of compound **2.13** there was a 2-fold reduction in the luminescence intensity in comparison to when no dicoumarol was added prior to the introduction of compound **2.13**. Furthermore, 10 eq of dicoumarol to 1 eq of compound **2.13** quenched almost all the expected luminescent emission of compound **2.13** by 21.5-fold.

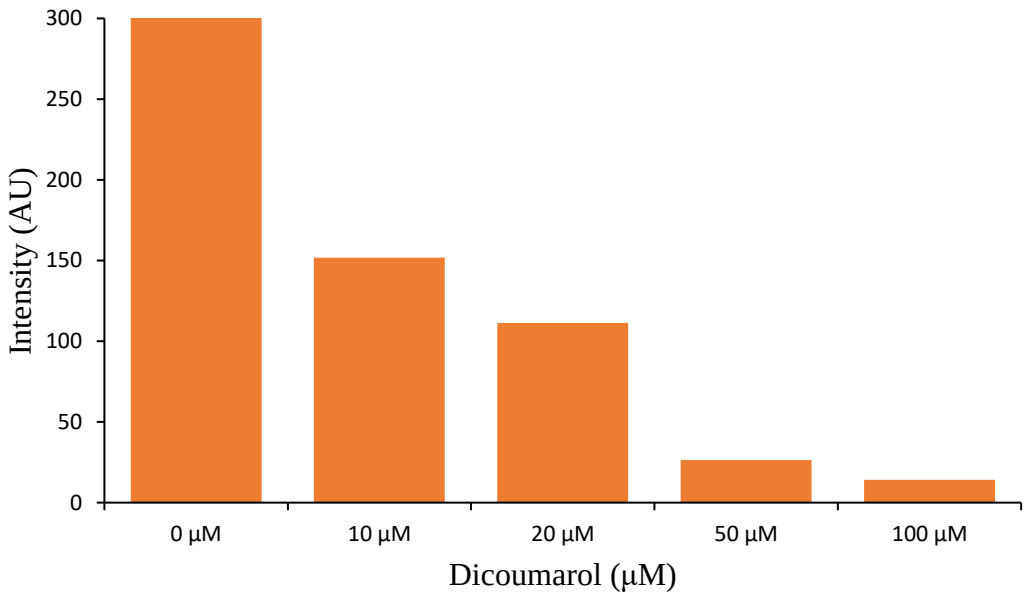

Figure 2.37: *Varying concentrations of dicoumarol (0 – 100 μM) in the presence of compound* ***2.13*** *(10μM), NTR (2.5 μg mL^{-1}), 500 μM NADH in 10 mM phosphate buffer at pH 7.4 over 300 minutes. λ_{em} = 600 nm. λ_{ex} = 445 nm. Ex slit width: 10 nm and Em slit width: 10 nm. n = 1.*

To further examine the reaction selectivity of compound **2.13** for NTR various potential biological interfering species were examined in Figure 2.38 these included salt NaCl, amino acids such as cysteine and homocysteine, reactive oxygen species H_2O_2, ascorbic acid (vitamin C), glucose, BSA and PBS. Cytochrome C a small soluble electron carrier hemeprotein located in the inner mitochrondrial membrane was included due to its ability

to carry out electron transfer. DT-diaphorase another oxidoreductase enzyme known to be upregulated under hypoxic conditions involved in the reduction of quinone moieties to hydroxyquinones was also included as part of the study. Compound **2.13** (10 µM) and NADH (500 µM) were present with each species to determine if they could reduce compound **2.13** and result in a similar Turn-ON in luminescence that was achieved by NTR.

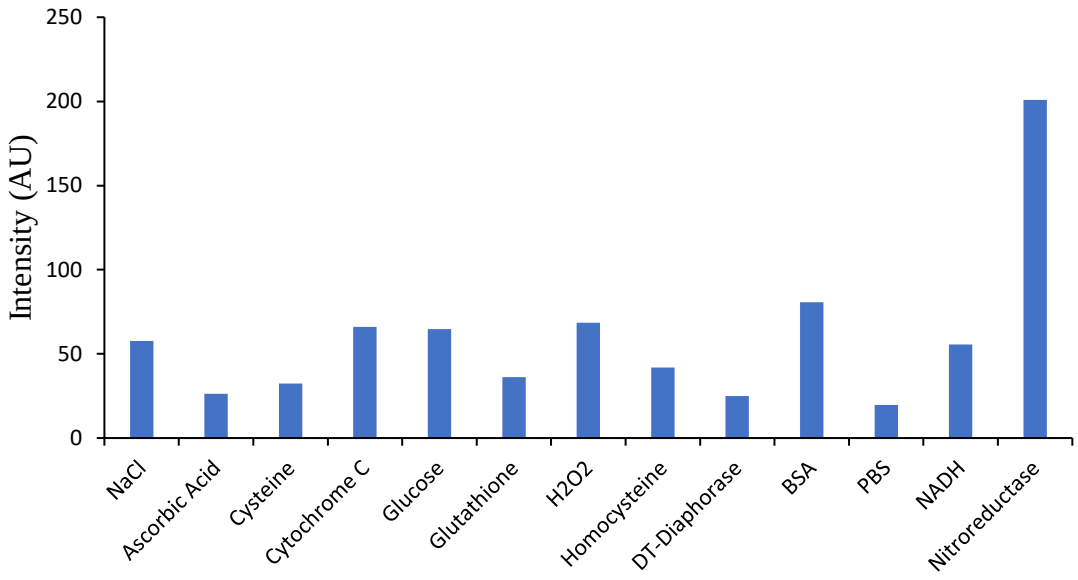

Figure 2.38: *Selectivity study of compound **2.13** (10 µM) and NADH (500 µM) in 10 mM phosphate buffer at pH 7.4 over 300 minutes reacted with different species: NaCl (50 mM), Ascorbic acid (1 mM), cysteine (1 m), cytochrome C (1 µg mL^{-1}), glucose (1 mM), glutathione (1 mM), H_2O_2 (1 mM), homocysteine (1 mM), DT-diaphorase (1 µg mL^{-1}), BSA (10 µg mL^{-1}), PBS (blank NADH absent), NADH (500 µM), Nitroreductase (1 µg mL^{-1}). λ_{em} = 600 nm. λ_{ex} = 445 nm. Ex slit width: 10 nm and Em slit width: 10 nm. n = 1*

It can be noted from Figure 2.38 that compound **2.13** was indeed selective for NTR as the greatest luminescent enhancement was elicited from compound **2.13** in the presence of NTR (1 µg mL^{-1}) and NADH (500 µM). Whilst NADH is a co-factor for NTR it could also be considered a mild reducing agent by itself which could potentially have given rise to the observed minor enhancements in luminescence observed for some of the samples that exhibited similar luminescence intensity to that of the NADH sample. In the case of BSA with a slighter greater luminescence intensity than the NADH sample, this could be attributed to the binding and subsequent shielding of **2.13** from water by hydrophobic regions within the protein structure, the same could be said for cytochrome C.[190] Interestingly, DT-diaphorase another flavoenzyme involved in the 2-electron reduction of

quinones to their corresponding hydroquinones in the presence of NADH did not elicit any significant luminescence response.[90]

2.8 LCMS Study of 2.13 Towards NTR

The increases in luminescence intensity from compound **2.13** is suggested to arise from the reduction of the nitro substituent to an amine by NTR and co factor NADH to give compound **2.29**. Whilst this can be assumed to be occuring through the use of emission spectra as previosuly referred to, we can also take advantage of the LCMS to show that through mass changes and changes in the UV trace at 254 nm that indeed compound **2.13** is reduced to compound **2.29**. In Figure 2.39 an LCMS trace of compound **2.13** is provided. Compound **2.13** was then treated with NTR and NADH for 1 hour and another LCMS is provided.

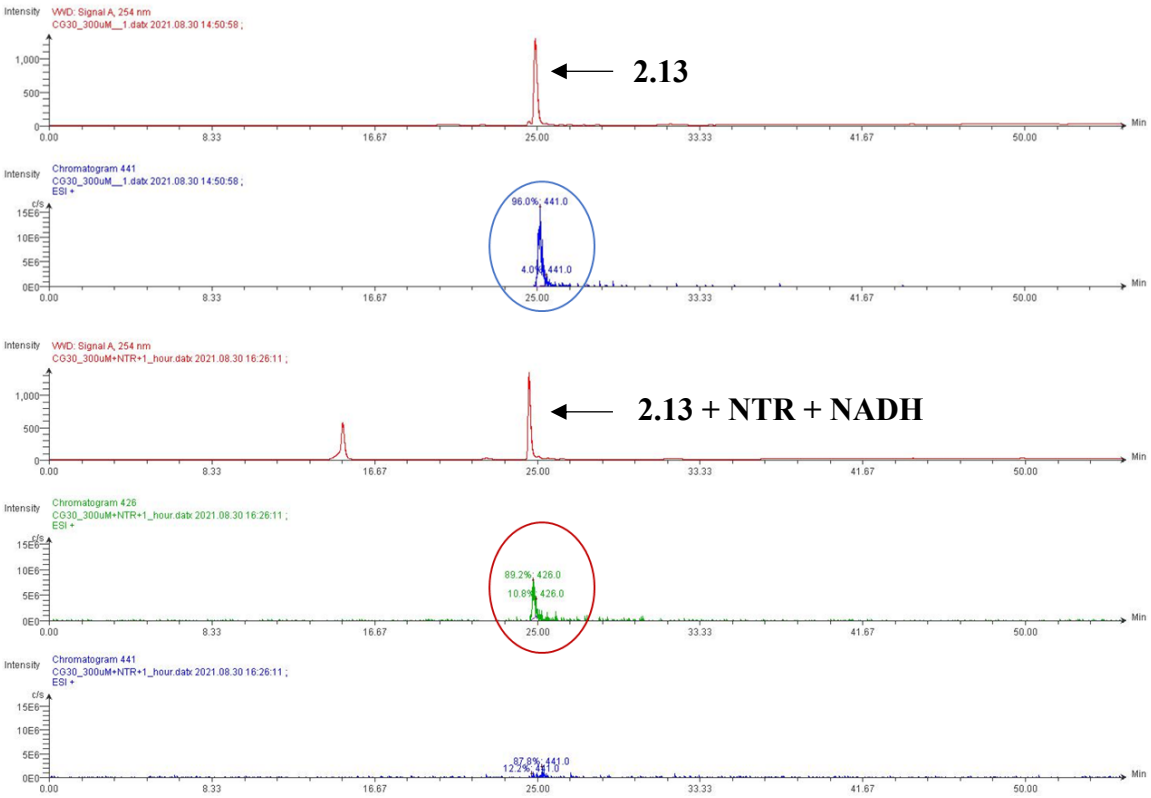

Figure 2.39: *(Top) LCMS trace of compound **2.13** circled in blue is the corresponding M/2. Bottom is the LCMS trace of compound **2.13** after 1 hour treatment with NTR (15 μg mL^{-1}) and NADH (250 μM), circled in red is the corresponding M/2.*

It can be seen in Figure 2.39 that the peak at Rt = 24.90 minutes showed strong ionisation at 441 corresponding to M/2 of the M^{2+} ion for **2.13**. After reaction of compound **2.13** with NTR (15 µg mL^{-1}) and excess NADH (500 µM) there was evident ionisation at 426 corresponding to M/2 of the M^{2+} ion for compound **2.29** under the peak at Rt = 24.56 minutes. It was also observed that there was minimal ionisation at 441 corresponding to M/2 of the M^{2+} ion for **2.13** after 1 hour treatment with NTR and excess NADH. It was noted that the Rt values of **2.13** and **2.29** only slightly differ whereas clear changes in the ionisation were observed after reaction of compound **2.13** with NTR and excess NADH.

Compound **2.13** displays novel responsiveness and selectivity towards NTR. Given the literature precedent, the focus of Ru(II) complexes as DNA sensors has been well established as discussed in the introduction of this chapter. Light switch behaviour was established by compound **2.4** with observed luminescence enhancements upon increasing the concentration of calf thymus DNA. Furthermore, **2.7** showed a 2.6-fold increase in luminescence enhancement upon increasing concentrations of st-DNA. It was therefore of interest to investigate the interactions of compound **2.13** and **2.29** with DNA.

2.9 UV/Vis DNA Titrations of 2.13 and 2.29

The interaction of Compound **2.13** and **2.29** with double stranded DNA was firstly examined using UV/Vis absorption spectroscopy. The titrations were carried out by addition of small aliquots of stDNA to a 10 mM phosphate buffer solution pH 7.4 of each complex. Changes in the ^{3}MLCT band were monitored for each complex. Upon the titration of **2.13** and **2.29** with stDNA significant changes were observed in their absorption spectra. In Figure 2.40 there was a 19 % hypochromism at 361 nm, with only 6% hypochromism experienced by the MLCT band at 446 nm for compound **2.13**.

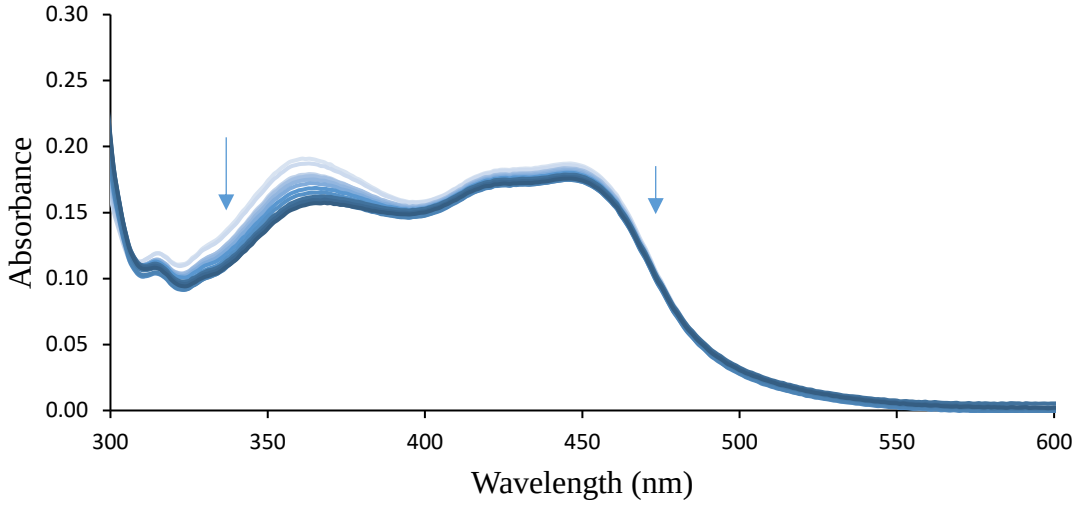

Figure 2.40: *The changes in the UV/Visible absorption spectrum of compound **2.13** (10 μM) with increasing additions of stDNA (0-211.2 μM) in 10 mM phosphate buffer pH 7.4.*

The UV/Vis absorption spectrum of Compound **2.29** in Figure 2.41 had a greater degree of hypochromicity observed at 447nm than that observed for compound **2.13**, with 18 % hypochromism of the MLCT band at 447 nm.

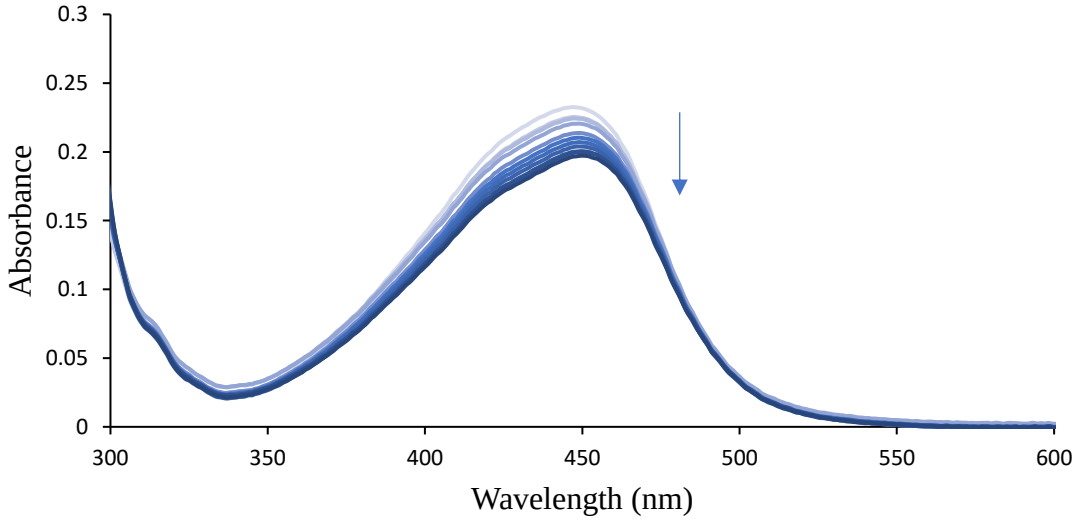

Figure 2.41: *The changes in the UV/Visible absorption spectrum of compound **2.29** (10 μM) with increasing additions of stDNA (0-211.2 μM) in 10 mM phosphate buffer pH 7.4.*

The distinct reductions in absorption observed in the spectra of both complexes strongly indicates interactions taking place with DNA. For compound **2.13**, the significant 19% decrease in absorption in the π–π* bands suggests that the 4-nitro-1,8-naphthalimide moiety is likely intercalating between the stacked bases, which was the anticipated

behaviour of such a planar structure interacting with DNA.[191] Additionally, alterations in the MLCT region affirm the binding of the Ru(II) metal centre to DNA. In the instances of compound **2.29**, where the MLCT and the 4-amino-1,8-naphthalimide bands overlap, it's challenging to conclude about the individual hypochromism changes. Nevertheless, the notable 18 % decline in absorbance coupled with a slight shift toward longer wavelengths are indicators of intercalation and tight binding of the metal center to DNA.[176]

2.10 Luminescence Enhancement of 2.13 with DNA

Referring to the introduction of this chapter, Ru(II) polypyridyl naphthalimide conjugates show luminescent enhancements in the presence of DNA.[176] It was therefore of interest to determine if compound **2.13** could elicit a dual response that upon reduction of compound by NTR in the presence of NADH and reaching a plateau of luminescence intensity, by then introducing DNA, could this result in a further increase in the luminescent intensity of compound **2.13** (Figure 2.42).

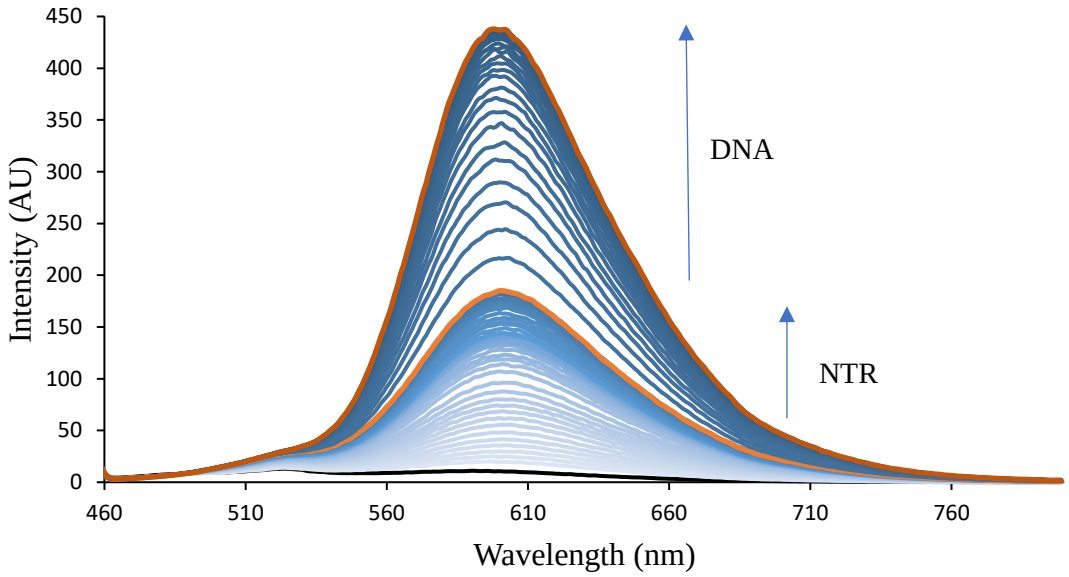

Figure 2.42: *compound **2.13** (10 µM) treated with NTR (1 µg mL^{-1}) and NADH (500 µM) for 240 minutes followed by the addition of increasing concentrations of stDNA (11.06 µM – 276.5 µM) in 10 mM phosphate buffer pH 7.4. λ_{ex} = 445 nm. Ex slit width: 10 nm and Em slit width: 10 nm. n = 1.*

From Figure 2.42 it is observed that there was a 17.3-fold increase in the luminescence intensity of compound **2.13** after treatment with NTR (1 µg mL^{-1}) for 240 minutes with a significant further increase in the luminescence intensity upon the addition of stDNA (11.06 µM – 276.5 µM) establishing an overall 41.2-fold increase in luminescence intensity. This enhancement was indicative of a binding interaction of compound **2.13** with stDNA. It is suggested that the 4-amino-1,8-naphthalimide moiety binds tightly to DNA and places the Ru(II) centre in the DNA groves whereby it is shielded from the aqueous environment and oxygen molecules which can cause quenching of Ru(II) polypyridyl complexes.[175] This luminescent enhancement was similarly observed for compound **2.29** when treated with stDNA (0 µM - 281.6 µM) as seen in Figure 2.43, where there was an established 3- fold increase in the luminescence intensity indicating that it was likely that the amino derivative is responsible for the additional enhancement observed.

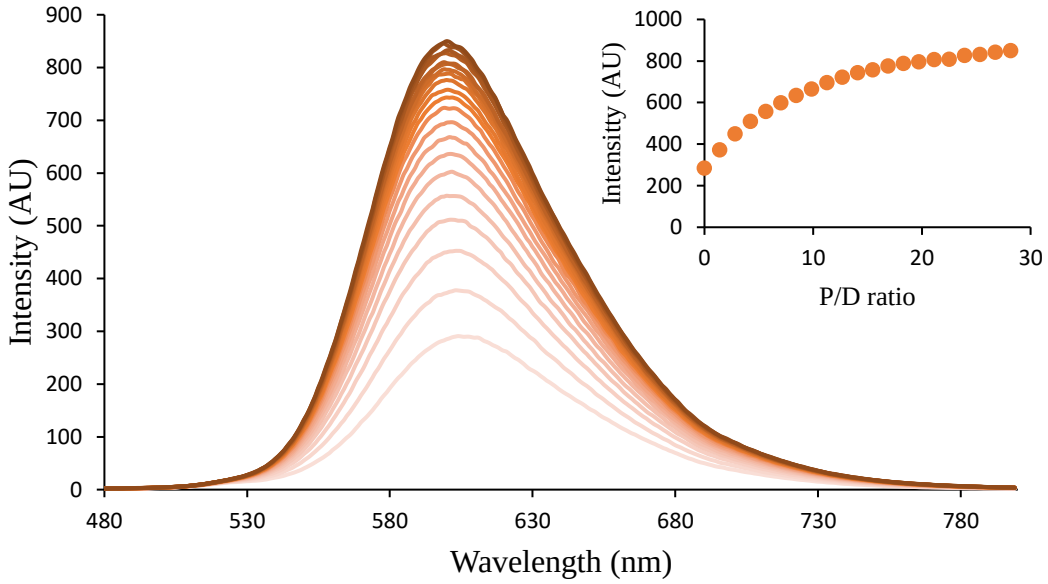

Figure 2.43: *Treatment of compound **2.29** (10 µM) with increasing concentrations of stDNA (0 µM - 281.6 µM) in 10 mM phosphate buffer pH 7.4. λ_{ex} = 445 nm. Ex slit width: 10 nm and Em slit width: 10 nm. n = 1.*

Furthermore, there is negligible increase in the luminescence intensity of compound **2.13** when treated with stDNA prior to the addition of NTR in Figure 2.44

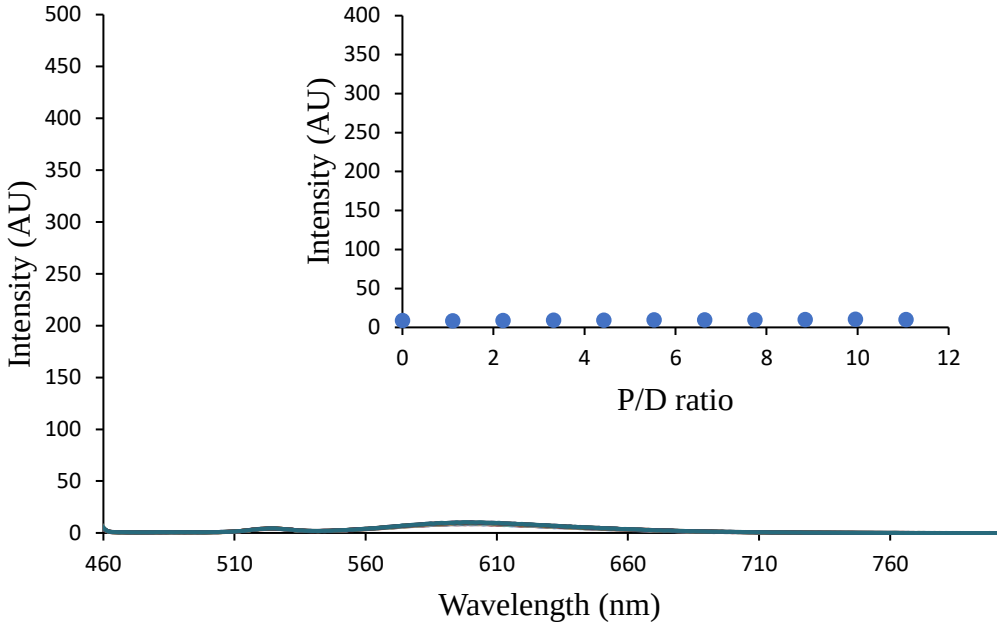

Figure 2.44: *Treatment of compound **2.13** (10 μM) with increasing concentrations of stDNA (0 – 110.6 μM) in 10 mM phosphate buffer pH 7.4. λ_{ex} = 445 nm. Insert shows changes in luminescence intensity with increasing P/D ratio, λ_{em} = 600 nm. Ex slit width: 10 nm and Em slit width: 10 nm. n = 1.*

Interestingly, it was observed that if NTR (1 µg mL^{-1}) was introduced that we again see a significant Turn-on in luminescence of 36.7-fold increase in luminescence intensity (Figure 2.45) much greater than if compound **2.13** was just treated with NTR and NADH.

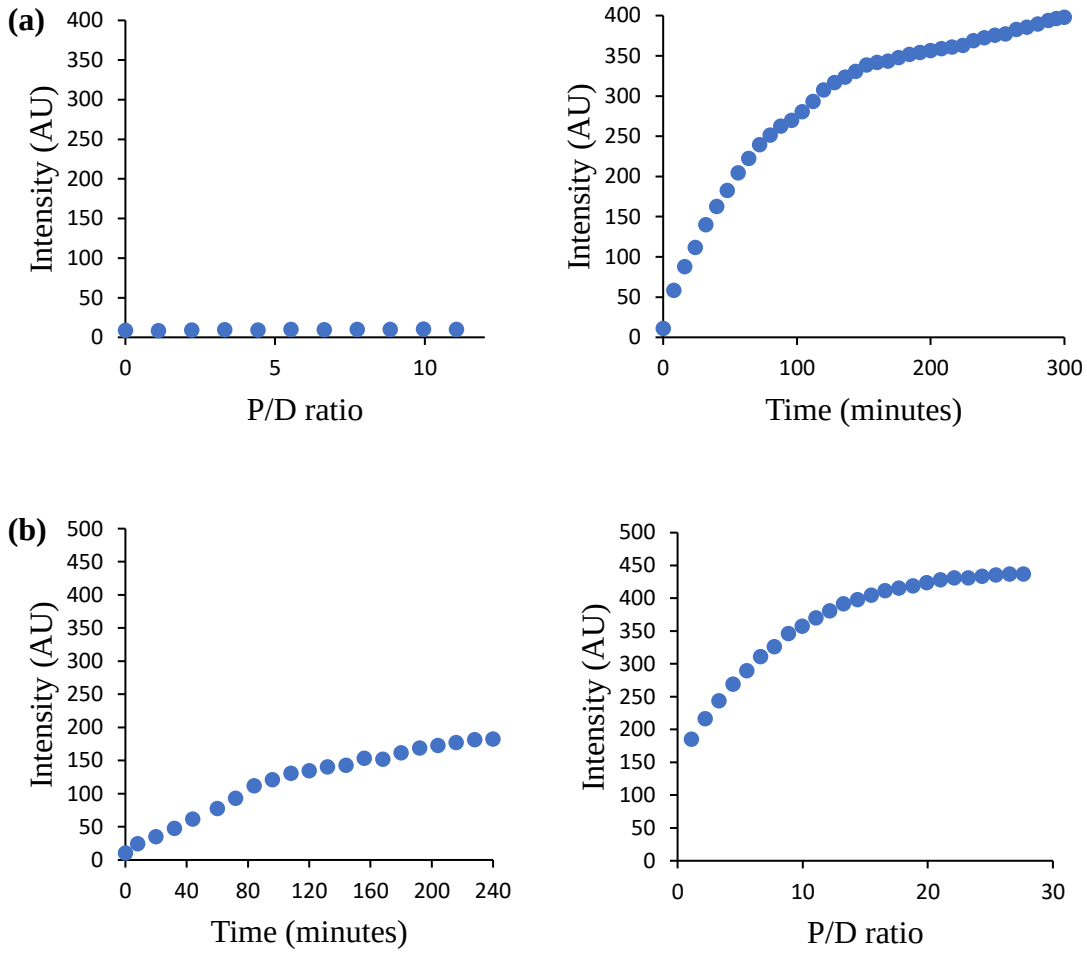

Figure 2.45: *(a) Treatment of compound* ***2.13*** *(10 µM) with increasing P/D ratio of stDNA (0 – 110.6 µM) (left). Addition of NTR (1 µg mL^{-1}) and NADH (500 µM) (right). (b) Treatment of compound* ***2.13*** *(10 µM) with NTR (1 µg mL^{-1}) and NADH (500 µM) (left). Increasing P/D ratio of stDNA (0 – 276.5 µM) after compound* ***2.13*** *has been treated with NTR (right). λ_{em} = 600 nm. Ex slit width: 10 nm and Em slit width: 10 nm. n = 1.*

Given the successful Turn-On responses observed by compound **2.13** towards both NTR and DNA it was of interest to carry out biological imaging using a cancer cell line to determine the utility of compound **2.13** to monitor NTR and DNA *in cellulo*. Firstly, to be considered a viable imaging agent **2.13** must be non-cytotoxic and so the cytotoxicity of compound **2.13** was determined.

2.11 Cytotoxicity of 2.13

Cytotoxicity was assessed on the glioma cell line T98G a cancer cell line derived from a human glioblastoma multiforma tumor (Figure 2.46) and a non-cancerous cell line dermal fibroblasts (Figure 2.47) by The Grillon group in the centre national de la researche scientifique (CNRS), Orleans, France. Cells were plated in 96-well plates and incubated in either a standard normoxic incubator or a hypoxia workstation (1% O_2). Cells were then treated for 24h with compound **2.13** at various concentration (in triplicate) in the culture medium containing 0.5% DMSO. Cytotoxicity was determined using the Alamar Blue Cell Viability Reagent. Fluorescence was measured using the CLARIOstar Microplate Reader (Ex 545 +/- 20, Em 600 +/- 40). Results were expressed as the percentage of cell viability compared to the control (0.5% DMSO in the medium).

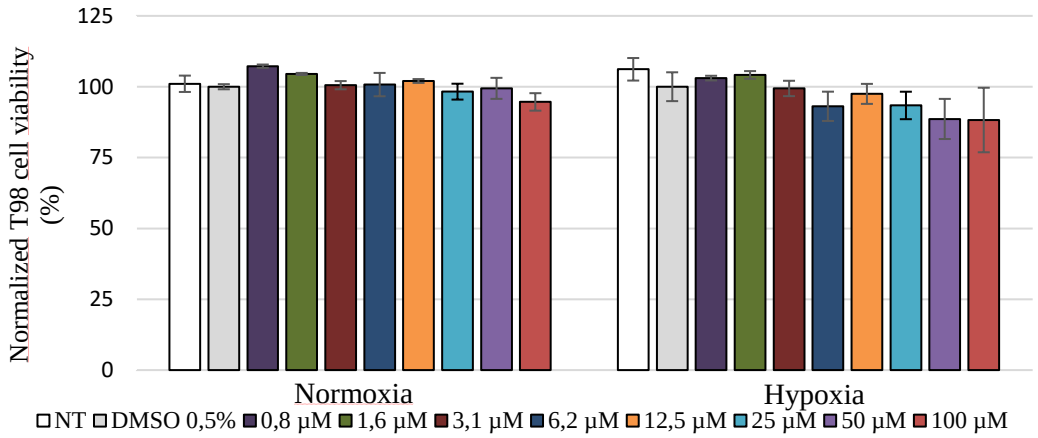

Figure 2.46: *Cell viability of glioma cell line T98G incubated with varying concentrations of compound **2.13** under normoxia and hypoxia. n = 3.*

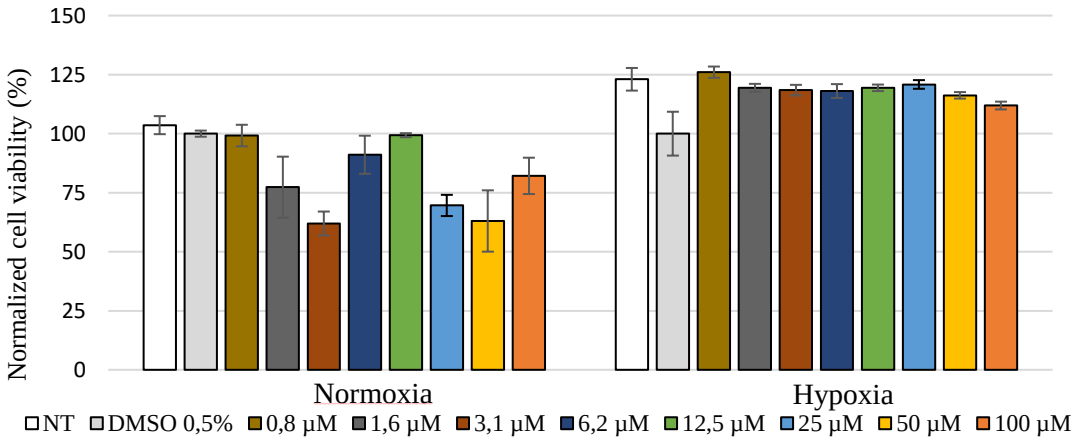

Figure 2.47: *Cell viability of dermal fibroblasts incubated with varying concentrations of compound **2.13** under normoxia and hypoxia. n = 3.*

Across the glioma cell line T98G and dermal fibroblasts compound **2.13** establishes minimal cell cytotoxicity over a concentration range of 0.8 µM – 100 µM deeming it useful as an imaging agent. Under normoxic conditions in the dermal fibroblast cell line compound **2.13** establishes some variability in cell viability however the cells remain quite viable above 75% at 100 µM suggesting low toxicity.

Cytotoxicity was also assessed on the glioma cell line T98G for compound **2.11** (Figure 2.48) and compound **2.12** (Figure 2.49). Over the concentration range of 0.8 µM – 100 µM minimal cell cytotoxicity was observed. The same was observed for dermal fibroblasts (see appendix).

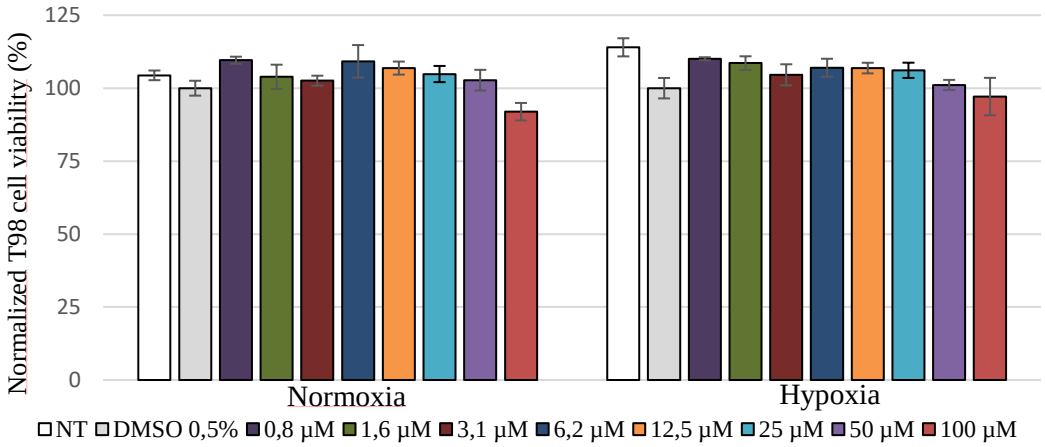

Figure 2.48: *Cell viability of glioma cell line T98G incubated with varying concentrations of compound **2.11** under normoxia and hypoxia. n = 3.*

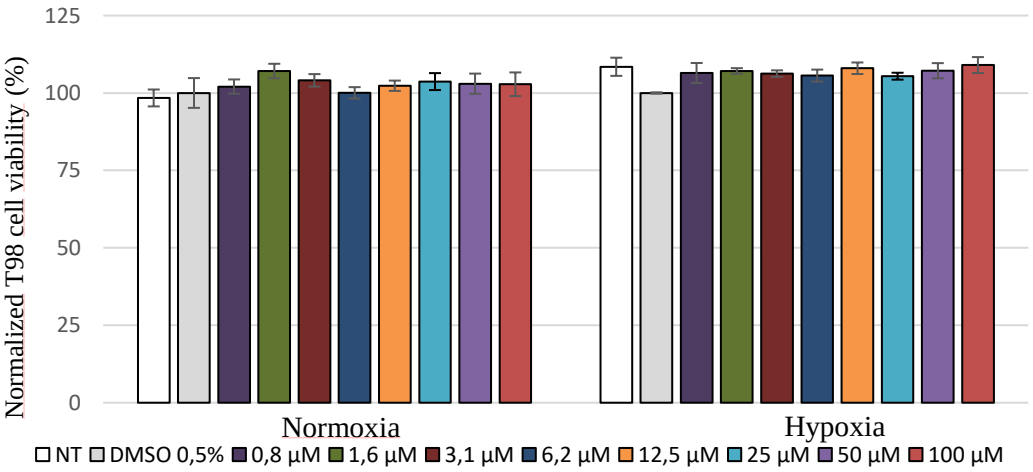

Figure 2.49: *Cell viability of glioma cell line T98G incubated with varying concentrations of compound **2.12** under normoxia and hypoxia. n = 3.*

2.12 Confocal Microscopy of 2.29

Compound **2.29** was first applied to HeLa cells to determine if luminescence of any kind could be observed within the cells through the use of confocal microscopy. It was seen in Figure 2.50 that compound **2.29** was up taken by HeLa cells and displayed luminescence in the cytosol. More interestingly, through the use of DAPI nuclear staining we can see localisation of compound **2.29** within the nucleus with what appears to be greater luminescence intensity, this coincides with what was observed experimentally for compound **2.29**.

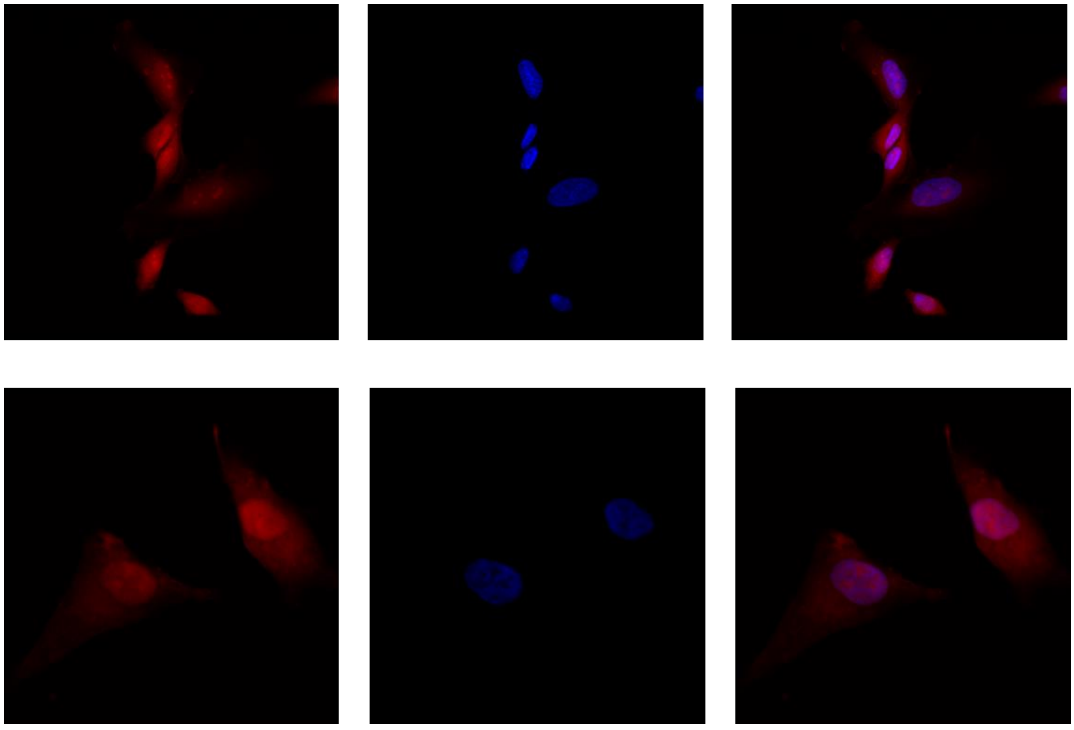

Figure 2.50: *Confocal microscopy images of Compound **2.29** in HeLa cells. The images on the left show luminescent HeLa cells through the red filter. The images in the middle show DAPI staining of the nucleus. The images on the right show luminescence from **2.29** in the nucleus of the HeLa cells. λ_{ex} = 488nm laser for compound **2.29**. λ_{ex} = 405nm laser for DAPI. λ_{em} = 585-685nm for compound 18. λ_{em} = 416-452nm for DAPI.*

Optimisation of compound **2.13** HeLa cell work is still required. Two methods were used, **2.13** was incubated with HeLa cells to allow for uptake of the complex and then transferred to a hypoxia chamber or incubated with glutathione ethyl ester (to mimic a state of hypoxia by decreasing the oxygen level).[192] Sufficient incubation time periods up to 42 hours were provided for both methods which were then mounted in glycerol/PBS mix, sealed and imaged immediately. There was no increased signal observed in comparison to **2.13** under normoxic conditions which raised uncertainty if **2.13** was up taken by cells.

2.13 Confocal Microscopy of 2.13

To display the turn on response *in cellulo* bacteria strain *staphylococcus aureus* can be used as bacteria are known to express NTR.[158] In Figure **2.51** through the application of stimulated emission depletion microscopy (STED) analysis it was observed that when compound **2.13** was added to *S. aureus* there was a desired red luminescent turn on response achieved within the bacteria due to the reduction of the nitro substituent on compound **2.13** to the corresponding amine derivative **2.29** by NTR. To determine that NTR was responsible for the observed switch on in luminescence the bacteria were pretreated with dicoumarol an NTR inhibitor (previously discussed in this chapter) followed by the addition of compound **2.13**. It was observed that no turn-on luminescence response was achieved because of the inability of NTR to carry out the reduction of compound **2.13**. As a control compound **2.29** was incubated with S. aureus in the presence and absence of dicoumarol where it was seen that the red luminescence was present in both images as expected as the amine derivative is always switched on.

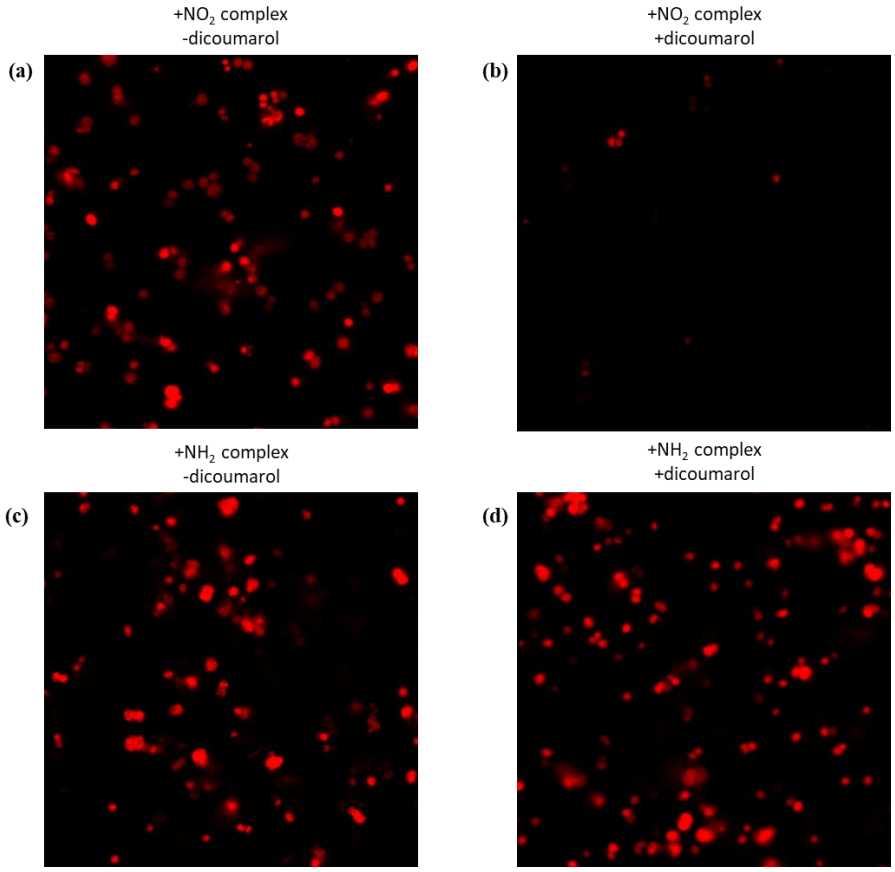

Figure 2.51: *Confocal microscopy of (a) S. aureus incubated with compound **2.13**. (b) S. aureus incubated with compound **2.13** in the presence of dicoumarol. (c) S. aureus incubated with compound **2.29**. (d) S. aureus incubated with compound **2.29** in the presence of dicoumarol. Excitation laser $\lambda_{455\ nm}$, depletion laser $\lambda_{775\ nm}$, 30% power.*

2.14 Conclusions and Future Work

In conclusion, we synthesised 3 novel Ru(II) polypyridyl complexes for the sensing of NTR. The complexes were based off two main design principles, for compound **2.11** and **2.12** there was a carbamate linker between that of the Ru(II) and the nitroreductase substrate. In the case of compound **2.11** we successfully carbamate linked a commercially available 4-nitrobenzyl moiety to the Ru(II) centre and for compound **2.12** we successfully carbamate linked a 2-nitroimidazole moiety to the Ru(II) centre. The successful synthesis of compound **2.13** resulted from the direct conjugation between the 4-nitro-1,8-naphthalimide and the phenanthroline bound to the Ru(II) centre. Novel structures were characterised by NMR, HRMS, and IR spectroscopy.

To determine the utility of compounds **2.11**, **2.12**, and **2.13** as luminescent probes for NTR the UV/Vis and emission spectra were recorded for each compound to distinguish any differences in the quenching of the MLCT emission established by each compound in comparison to their amino derivatives. Compounds **2.11** – **2.13** were then reacted with NTR in the presence of the enzyme cofactor NADH to determine any turn-on response in luminescent intensity. The greatest turn-on in luminescent enhancement was recorded for compound **2.13** with a 15.9-fold enhancement in the luminescence intensity after treatment with NTR (5 μg mL^{-1}) for 60 minutes at 600 nm. The order of greatest turn-on in luminescence intensity follows compound **2.13** > **2.12** > **2.11**.

Compound **2.13** was sensitive to varying concentrations of NTR ranging from 0.02 μg mL^{-1} to 5 μg mL^{-1} Compound **2.13** also displayed excellent selectivity towards NTR as the turn-on response significantly diminished with increasing concentration of dicoumarol. Compound **2.13** was also shown to be selective for NTR in comparison to other biologically relevant species. Through the use of the LCMS the reduction of the nitro substituent to the amine was shown, which proved that the reduction mechanism carried out by NTR was indeed responsible for the observable turn-on response.

It was further confirmed that compound **2.13** was capable of binding stDNA through potential intercalation and the electrostatic attraction of Ru(II) metal centre as noted by the hypochromism seen in the UV/Vis DNA titrations for both compound **2.13** and **2.29**. This interaction was taken advantage of to achieve an enhanced luminescent response. When compound **2.13** was treated with NTR (1 μg mL^{-1}) for 240 minutes a 17.3-fold increase in luminescent intensity was observed however upon the addition of stDNA (11.06 μM – 276.5 μM) this fold increase was seen to increase to 41.2-fold.

In terms of cytotoxicity glioma cell line T98G and dermal fibroblasts were viable over the concentration range of 0.8 μM – 100 μM with minimal cell cytotoxicity for **2.11** – **2.13**. Moreover, this deemed **2.13** useful as an imaging agent as it was shown to be non-cytotoxic. Compound **2.29** was applied to HeLa cells and showed that the nucleus of the cells appeared to have a greater luminescence intensity than the cytosol which was expected. However, due to the difficulty faced regarding the luminescence turn-on of **2.13** under hypoxic conditions and potential issues faced with the uptake of **2.13**, no HeLa cell results were obtained. Alternatively, *S. aureus* was used to achieve the turn on response of **2.13** *in cellulo*. Compound **2.13** was selectively turned on by NTR in *S. aureus* deeming it useful as an imaging agent for NTR in bacteria.

Future work will be to carry out the sensitivity and selectivity photophysical studies for NTR sensing in triplicate and further investigate the binding affinity towards stDNA. Additionally, the DNA photosensitising ability of compound **2.29** towards pBR322 DNA will be examined to determine if the reduced amino derivative acts as a superior photosensitiser than that of compound **2.13**. Further consideration will also be given regarding uptake of compound **2.13** into a cancer cell line under hypoxic conditions to achieve a desired turn-on response. Given the success of a turn on response in a hypoxic tumour cell line it would also be of interest to determine if upon reduction that different lifetimes could be observed for different regions or organelles within hypoxic cells by the amino derivative compound **2.29**, further enhancing the selectivity of the probe. Other future studies to be considered could be the treatment of multicellular tumour spheroids with compound **2.13** as these can mimic hypoxic and normoxic niches within tumours.

Chapter 3

Self Immolative Dendrimers: A Novel Theranostic for NTR Sensing

3. Self immolative dendrimers: A Novel Theranostic for NTR Sensing

3.1 Introduction

In recent years self immolative dendrimers have emerged as a revolutionary platform for applications in fluorescence imaging. Since being reported by Shabat, de Groot, and McGrath in the early 2000's there has been significant progress in the development of the dendritic design towards theranostics.[193-196] The self immolative theranostic design follows that of a fluorescent prodrug concept whereby an adapter unit links a trigger moiety, which is activatable by an analyte or enzyme, to a fluorophore and a chemotherapy drug. Upon reaction of the trigger moiety with by an analyte there is subsequent self-immolation resulting in the emission of fluorescent signals and the release of an active chemotherapy drug. The research aims to achieve targeted delivery of chemotherapy agents, enable real-time monitoring of tumour locations, and assess drug release kinetics, all while mitigating the adverse impact of chemotherapy drugs on healthy tissues.

The renowned work of Shabat and co-workers established the use of these dendrimers for drug delivery, reporter delivery, and theranostics.[197-199]

Early work showed the ability of compound **3.1** (Figure 3.1) to incorporate two differing prodrugs camptothecin (CPT) and doxorubicin (DOX), and a catalytic antibody 38C2 as the trigger moiety. Bioactivation of a heterodimeric prodrug immolating both CPT and DOX resulted in a significant and noteworthy enhancement in toxicity of the human Molt-3 leukemia cell line.[197]

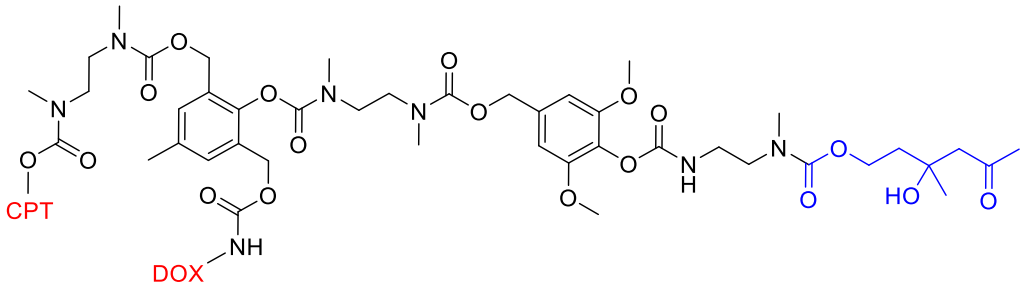

3.1

Figure 3.1: *Structure of compound **3.1**.*

Similarly, compound **3.2** (Figure 3.2) utilises two differing reporter groups 6-aminoquinoline and 4-nitrophenol, due to their carbamate linkages to the adapter unit the signals of these reporters are switched off. However, upon the introduction of bacterial enzyme penicillin-G–amidase and cleavage of the phenylacetamide trigger moiety the 6-

aminoquinoline can be detected by fluorescence emission at 460 nm and 4-nitrophenol gives off a visible yellow colour. The PEG5000 group para to the trigger improves the solubility of the dendrimer.[198]

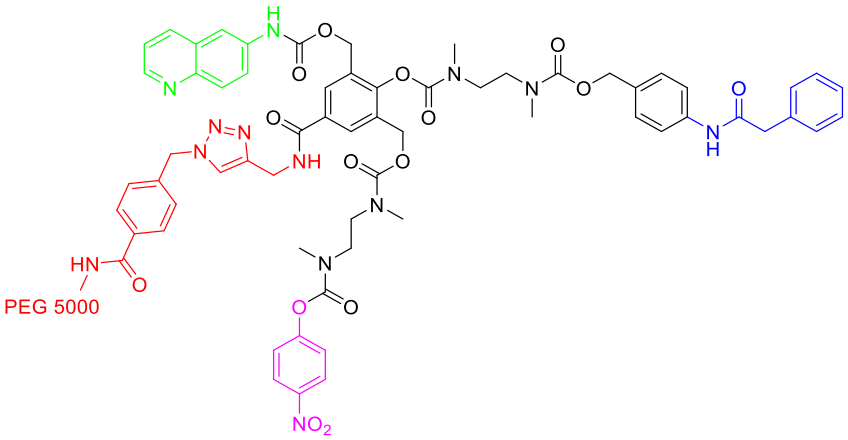

3.2

Figure 3.2: *Structure of compound **3.2**.*

Compound **3.3** (Figure 3.3) is an example of a theranostic capable of real-time in vivo monitoring of drug release. It takes advantage of a latent fluorogenic linker QCy7 which is masked by a phenylboronic ester and linked to CPT. In the presence of H_2O_2 the phenylboronic ester moiety is removed and the resulting phenolate undergoes 1,4-elimnation followed by decarboxylation to release QCy7 as the active fluorophore and CPT. This release is monitored by a large turn on response at 720 nm. Compound **3.3** showed exceptional correlation between emitted NIR fluorescence with drug release and *in vitro* toxicity. The activation of the compound **3.3** was successfully within murine models, revealing specific localisation within tumour sites following systemic administration.

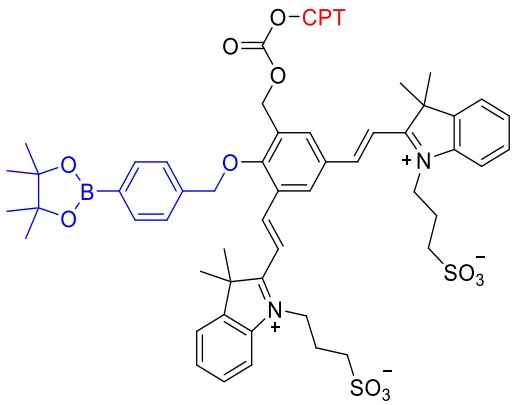

3.3

Figure 3.3: *Structure of compound **3.3**.*

To date there has been little exploitation of NTR using theranostics. The majority of such theranostics recently developed have a focus on some photo therapy aspect avoiding the use of an adapter unit capable of undergoing self-immolation. This can be seen for compound **3.4** and compound **3.5** (Figure 3.4). Compound **3.4** has a very weak NIR signal at 1046 nm and low photoacoustic and photothermal signals. However, upon increasing NTR concentration up to 5 μg mL^{-1} a fluorescence increase is observed accompanied by increases in both photoacoustic and photothermal signals. This increase in temperature was also observed *in vivo* in mice when irradiated with a 980 nm NIR laser.[200] Compound **3.5** a fluorescein derivative shows increasing fluorescence intensity upon the addition of NTR at 635 nm and displayed photodynamic therapy efficiency under hypoxic conditions in HeLa cells. HeLa tumour growth in mice was also completely inhibited when intratumorally injected with compound 22 and irradiated with 590 nm LED.[201]

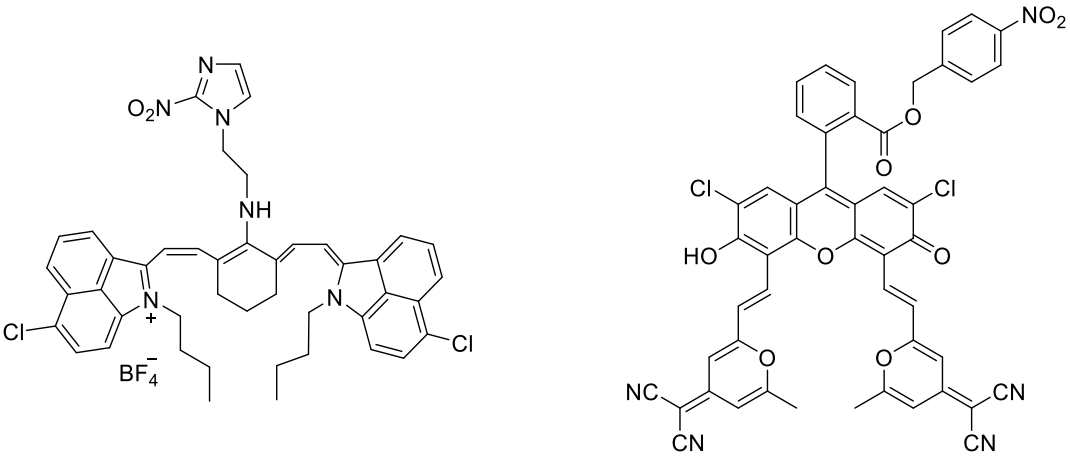

3.4 **3.5**

Figure 3.4: *Structures of compound **3.4** and **3.5**.*

Given the unique properties of self-immolative dendrimers, a class of multifunctional molecules, it can be said that these types of theranostics allow for a vast amount of versatility in terms of delivering diagnostic and therapeutic units. More interesting is how this can be applied selectively to tumour microenvironments rich with NTR by incorporating a nitroaromatic substrate as the tigger moiety. However, despite the great potential of self-immolative dendrimers in this context, their utilisation as theranostics for NTR has not yet been fully exploited, leaving a significant gap in the literature yet to be explored.

3.2 Chapter Objectives

The objective of this chapter is to synthesise 4 novel NTR responsive dendrimers based on the previously mentioned dendritic design. The two designs are simply portrayed by Figure 3.5 whereby an adapter unit links 3 moieties together, in this case a trigger, reporter/fluorophore, and a drug.

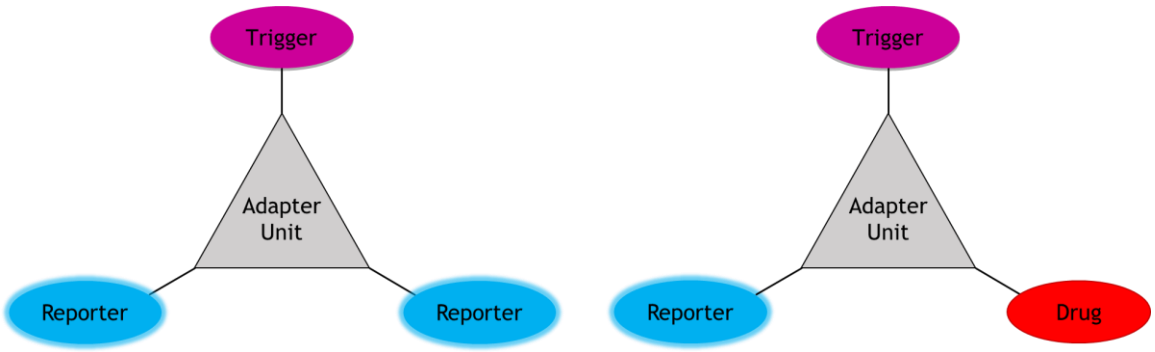

Figure 3.5: *Basic design of NTR responsive dendrimers.*

The expected release mechanism for this design is seen in Figure 3.6. Upon reduction of the nitroaromatic trigger to the amine derivative there is removal of the trigger moiety and formation of a phenol intermediate. This intermediate undergoes a self immolative 1,4-elimination cascade to result in a quinone methide intermediate and the release of the reporter resulting in a change of fluorescence from blue to green emission. The methide is quenched by water to restore aromaticity of the ring resulting in subsequent 1,4-elimination to release from what was a prodrug to now the active drug. The methide is quenched once again to afford 2,6-bis-hydroxymethyl-p-cresol.

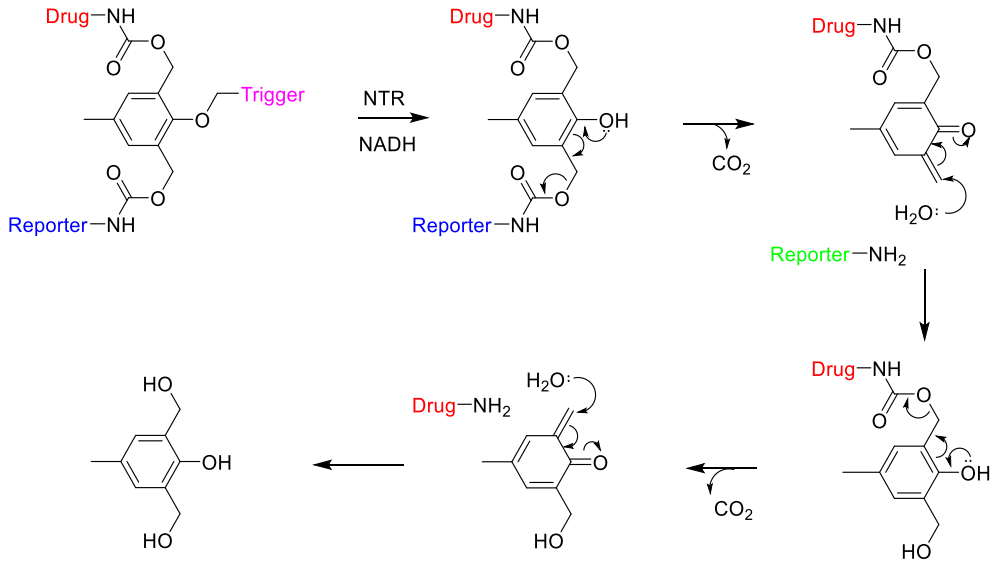

Figure 3.6: *The reduction and self-immolation of an NTR responsive dendrimer.*

With this design and release mechanism principle in mind we set out to synthesise compound **3.6**, **3.7**, **3.8**, and **3.9**. Compound **3.6** and **3.7** in Figure **3.7** consists of a 4-nitrobenzyl trigger moiety ether linked to the adapter unit and two 4-amino-1,8-naphthalimides carbamate linked to the adapter unit. As the naphthalimide moieties are bound to the adapter unit via carbamate their fluorescence is modulated as referred to in Chapter 1 and therefore are expected to result in a red shift in emission wavelength upon reduction of the 4-nitrobenzyl trigger by NTR and NADH, resulting in the self-immolation of the naphthalimide moieties causing a blue to green change in the emission wavelength.

Given the potential insolubility issues that could be faced with compound **3.6** due to the presence of the n-butyl moieties of the naphthalimide fluorophores it was of interest to incorporate an acetylated ethylene glycol moiety on the imide of the naphthalimide as this would be expected to improve the solubility of compound **3.7** in aqueous solution.

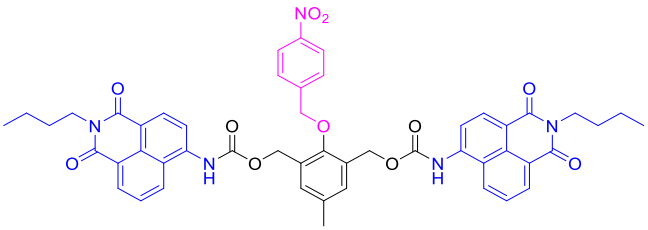

3.6

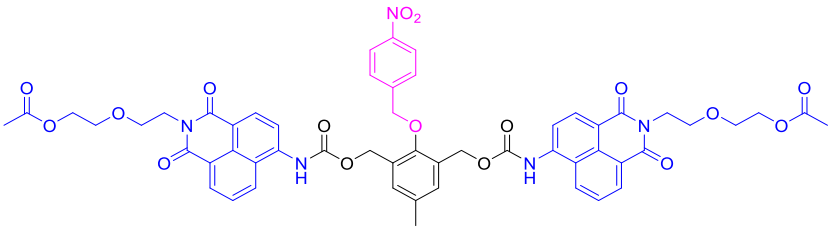

3.7

Figure 3.7: *Structures of compounds **3.6** and **3.7**. 4-nitrobenzyl trigger moiety (purple). Naphthalimide moieties (blue).*

Compounds **3.8** and **3.9** in Figure 3.8 take into account the theranostic approach whereby **3.8** consists of a 4-nitrobenzyl trigger moiety ether linked to the adapter unit, a 4-amino-1,8-naphthalimide carbamate linked to the adapter unit, and amonafide carbamate linked to the adapter unit. Amonafide is a topoisomerase II inhibitor and can also act as a DNA intercalator, by inhibiting topoisomerase II there is subsequent DNA cleavage as a result of the suppression of DNA re-ligation ultimately leading to cell death. While amonafide displayed a significant amount of efficacy during phase II clinical trials for breast cancer,

its progression halted at phase III trials due to dose-dependent bone marrow toxicity. In literature precedent prodrug strategies through the use of carbamate functionalities at the 3-amine position of amonafide have been exploited.[202, 203] Compound **3.9** follows a similar design to that of compound **3.8** but rather uses sulfisoxazole as the therapeutic moiety. Sulfisoxazole is known to possess antibiotic activity against both gram-positive and gram-negative bacteria. This along with the expression of NTR in bacteria allows for the monitoring of the release of sulfisoxazole in bacteria due to the change in fluorescence expected to be observed from the naphtalimide moiety.[204-206] Furthermore, varying the drug moiety establishes the synthetic versatility amongst these dendrimers.

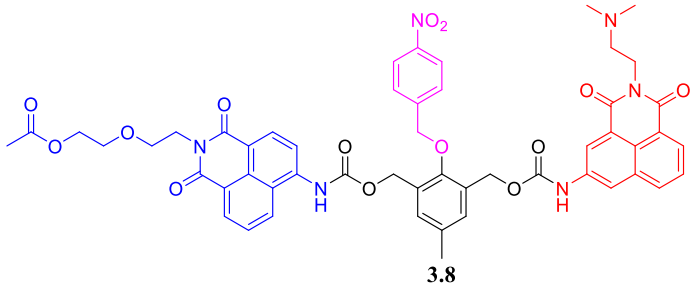

3.8

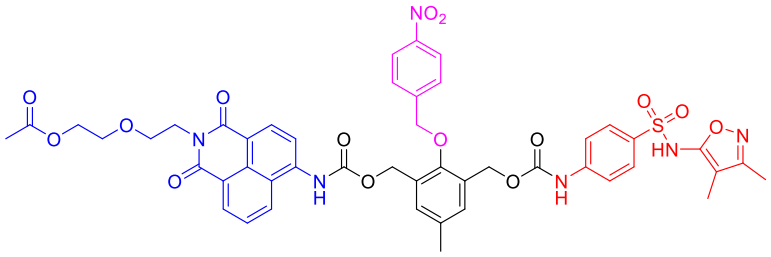

3.9

Figure 3.8: *Structures of compounds **3.8** and **3.9**. 4-nitrobenzyl trigger moiety (purple). Naphthalimide moieties (blue). Therapeutic moieties (red).*

The proposed synthetic pathway for the aforementioned dendrimers can be seen in Figure 3.9 and 3.10. The aim of the synthesis was to generate the carbamoyl chloride derivates of the aromatic amines in question be it a fluorophore or drug through the use of triphosgene. The carbamoyl chloride derivatives can then be further reacted with the hydroxymethyl substituent of the adapter unit (ether linked to the enzyme substrate highlighted in purple) to form a carbamate linkage between either the fluorophore or drug moiety.

In Figure 3.9 to attain two fluorophores on each side of the adapter unit the carbamoyl chloride derivative of the fluorophore in question is added in excess to the adapter unit.

In Figure 3.10, the formation of carbamate linkages between the adapter unit and both the fluorophore and the drug necessitates the initial synthesis of an intermediate compound. This intermediate consists of a single fluorophore carbamate linked to the adapter unit. This can then be followed up by forming the carbamoyl chloride of the drug and carbamate linking it to the free hydroxymethyl substituent on the intermediate to form a suspected prodrug moiety.

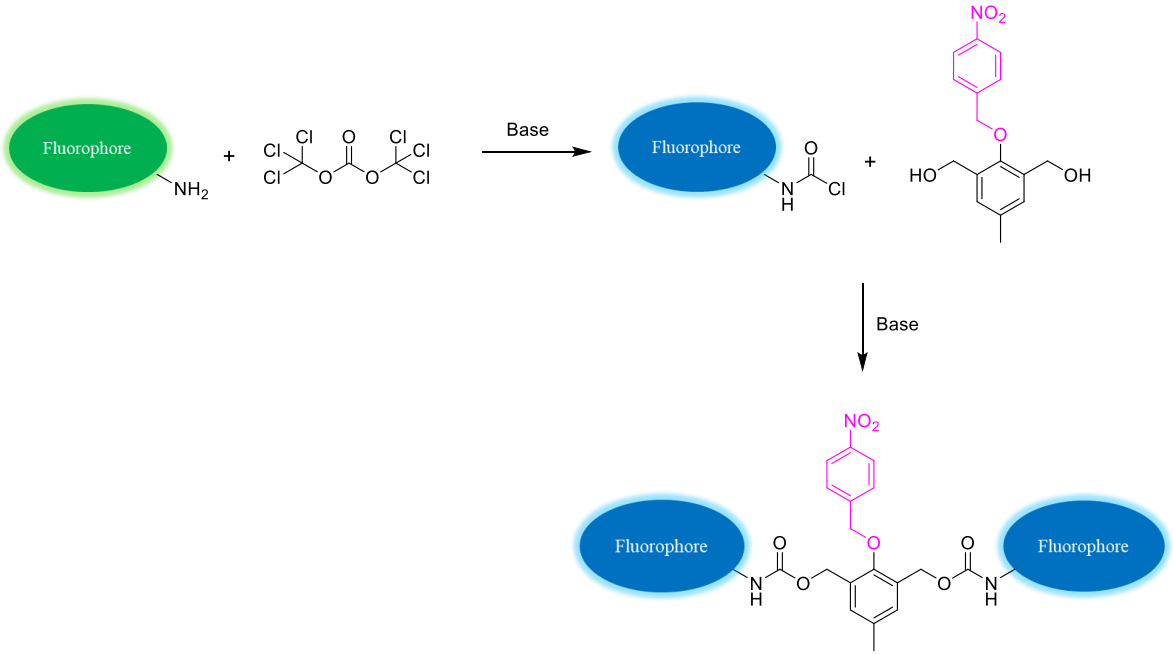

Figure 3.9: *The proposed synthetic pathway of compounds **3.6** and **3.7**.*

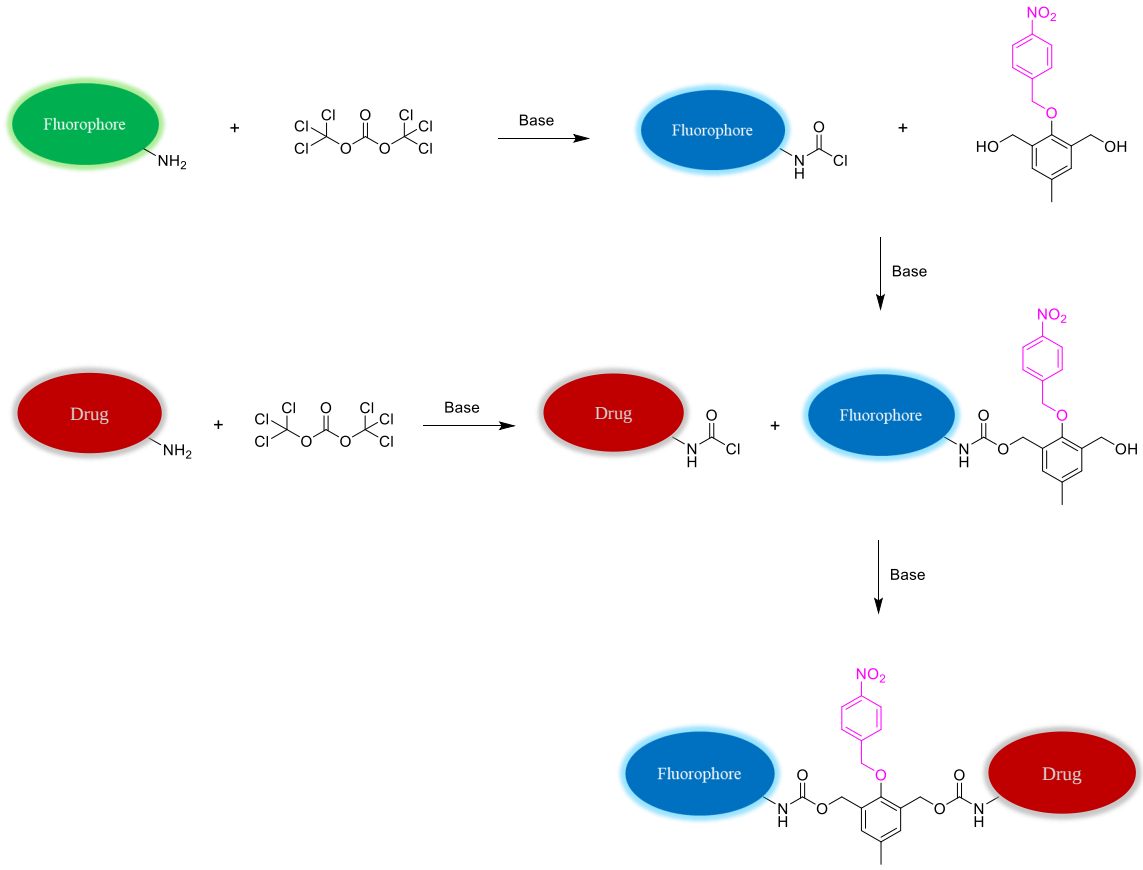

Figure 3.10: *The proposed synthetic pathway of compounds **3.8** and **3.9**.*

3.3 Synthesis and Characterisation 3.6, 3.7, 3.8, and 3.9

3.3.1 Synthesis of 3.10, 3.11 and 3.12

The synthesis of **3.10**, **3.11**, and **3.12** were firstly required for the synthesis of **3.6** and **3.7**. Scheme 3.1 shows the synthesis of **3.10**.

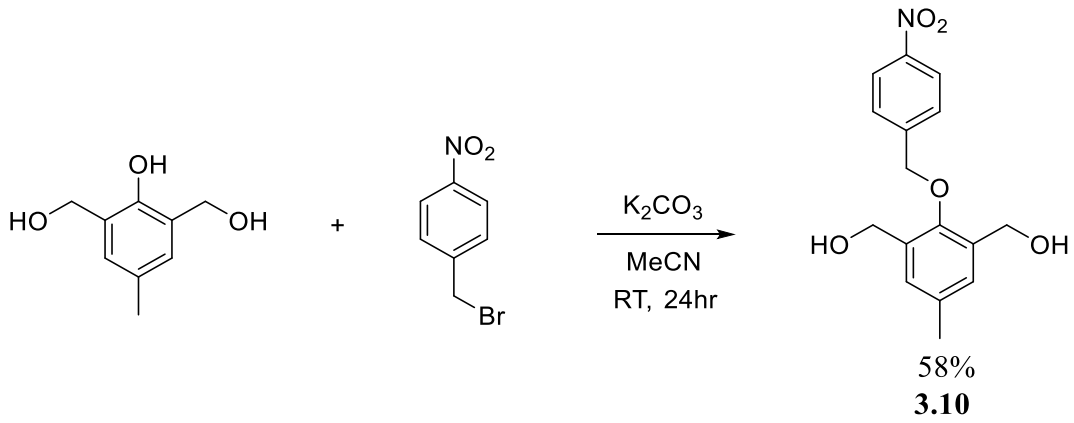

Scheme 3.1: *Synthesis of compound **3.10**.*

Compound **3.10** was synthesised via Williamson ether synthesis through the reaction of 2,6-bis-hydroxymethyl-p-cresol with 4-nitrobenzyl bromide in the presence of potassium

carbonate as the base. This resulted in **3.10** in a 58 % yield possessing an ether linkage between the 4-nitrobenzyl and the cresol unit. **3.10** was fully characterised using ^{1}H NMR, ^{13}C NMR, and IR. ^{1}H NMR peaks were assigned using ^{1}H-^{1}H COSY analysis. The ^{1}H NMR spectrum (500 MHz, DMSO-d_6) of **3.10** can be seen in Figure 3.11.

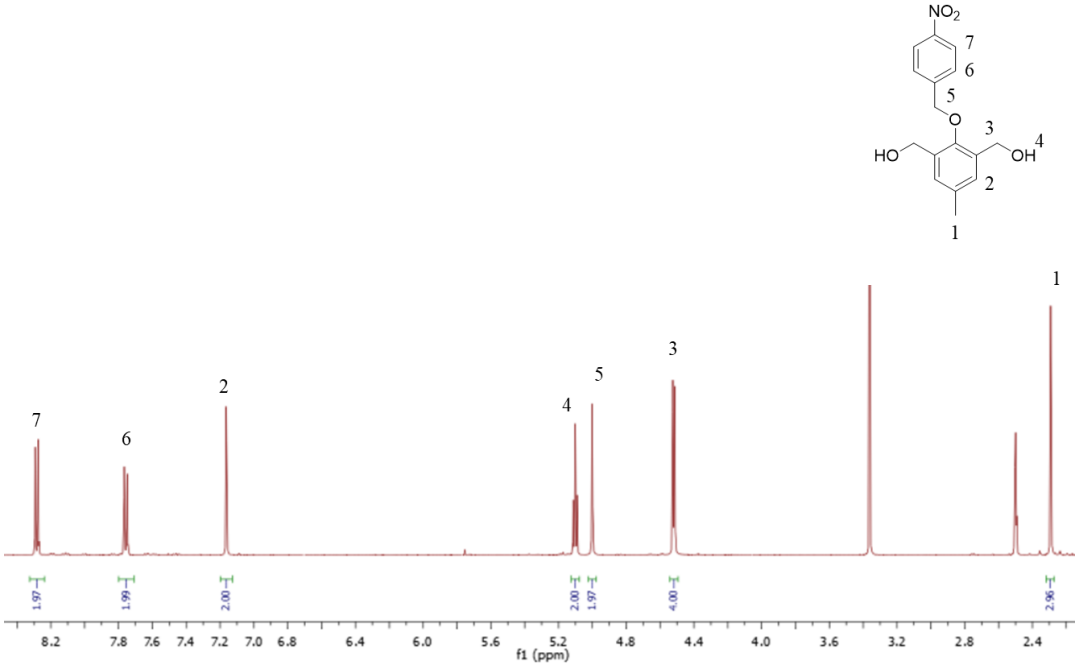

Figure 3.11: *^{1}H NMR of compound **3.10** in DMSO-d_6.*

The ^{1}H NMR spectrum (500 MHz, DMSO-d_6) in Figure 3.11 displays key characteristic peaks for compound **3.10**. The doublets observed at 8.27 ppm and 7.75 ppm both integrating for 2H are representative of the aromatic protons of the 4-nitrobenzyl moiety. The peak at 5.00 ppm integrating for 2H indicates the presence of the ether linkage. It was also seen that the clearly resolved triplet at 5.10 ppm integrates for 2H characteristic of the hydroxyl moieties of the adapter unit.

Compound **3.11** was synthesised following Scheme 3.2, which involved a condensation of n-butyl amine into the anhydride site of the 4-nitro-1,8-naphthalic anhydride to result in **3.13** in 66 % yield. This intermediate was then reduced to the corresponding amino derivative in the presence of Pd/C and H_2 to afford compound **3.11** in 91 % yield.

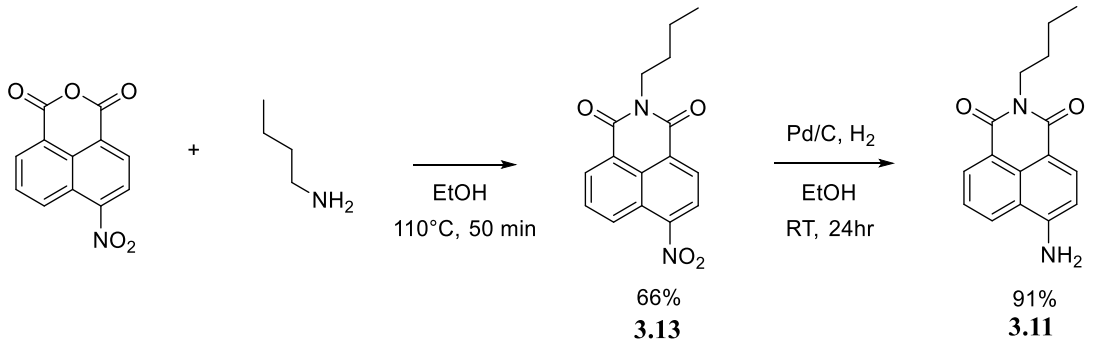

Scheme 3.2: *Synthesis of compound **3.11**.*

Compound **3.11** agreed with literature ^{1}H NMR and can be seen in Figure 3.12.

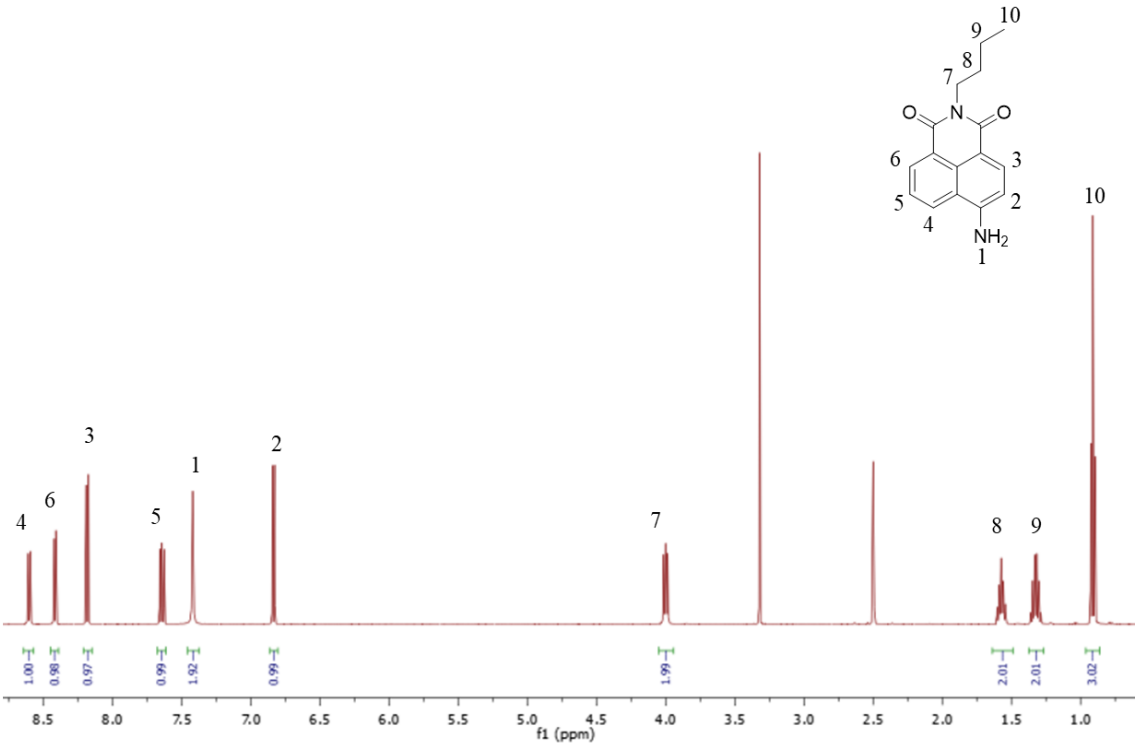

Figure 3.12: *^{1}H NMR of compound **3.11** in DMSO-d$_6$.*

From the ^{1}H NMR in Figure 3.12 the NH_2 protons appear as a singlet integrating for 2H at 7.42 ppm and signature doublets of the naphtalimide moiety are observed at 6.83 ppm and 8.17 ppm both integrating for 1H. Furthermore, we can see n-butyl moiety peaks at 4.00 ppm, 1.56 ppm, 1.32 ppm, and 0.91 ppm all integrating for the correct number of protons.

Compound **3.12** was synthesised following scheme 3.3. Given the potential insolubility issues that could be faced with compound **3.6** due to the presence of the n-butyl moieties of the naphthalimide fluorophores it was of interest to determine if by incorporating a acetylated ethylene glycol moiety could this improve the solubility of compound **3.7** as it

is cited that self immolative dendrimers usually incorporate a PEG like moiety to enhance their solubility and functionalities of this kind have shown to enhance the water solubility of naphthalimides.[155, 198, 207]

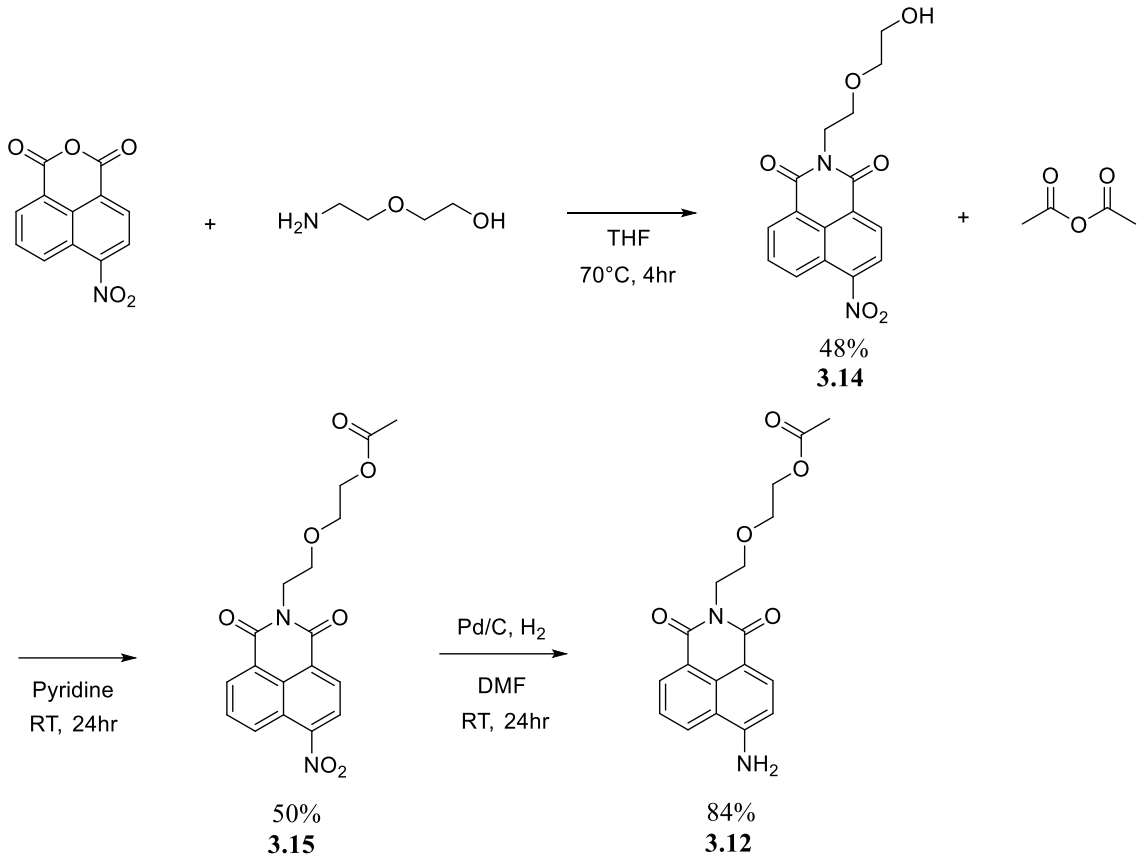

Scheme 3.3: *Synthesis of compound 3.12.*

The synthesis of **3.12** first required the condensation between 4-nitro-1,8-naphthalic anhydride and 2-(2-aminoethoxy) ethanol to afford compound **3.14** in 48 % yield. Compound **3.14** was then acetylated in the presence of acetic anhydride and pyridine to result in **3.15** in 50 % yield, this was done in order to protect the aliphatic alcohol which would be reactive with future steps in the synthesis. Compound **3.15** was then reduced to compound **3.12** in the presence of Pd/C and H_2 to result in the amino derivative and desired compound **3.12** in 84 % yield. Compound **3.12** was fully characterised using ^{1}H NMR, ^{13}C NMR, IR, and HRMS. ^{1}H NMR peaks were assigned using ^{1}H-^{1}H COSY analysis. The ^{1}H NMR spectrum (500 MHz, DMSO-d_6) of **3.12** can be seen in Figure 3.13.

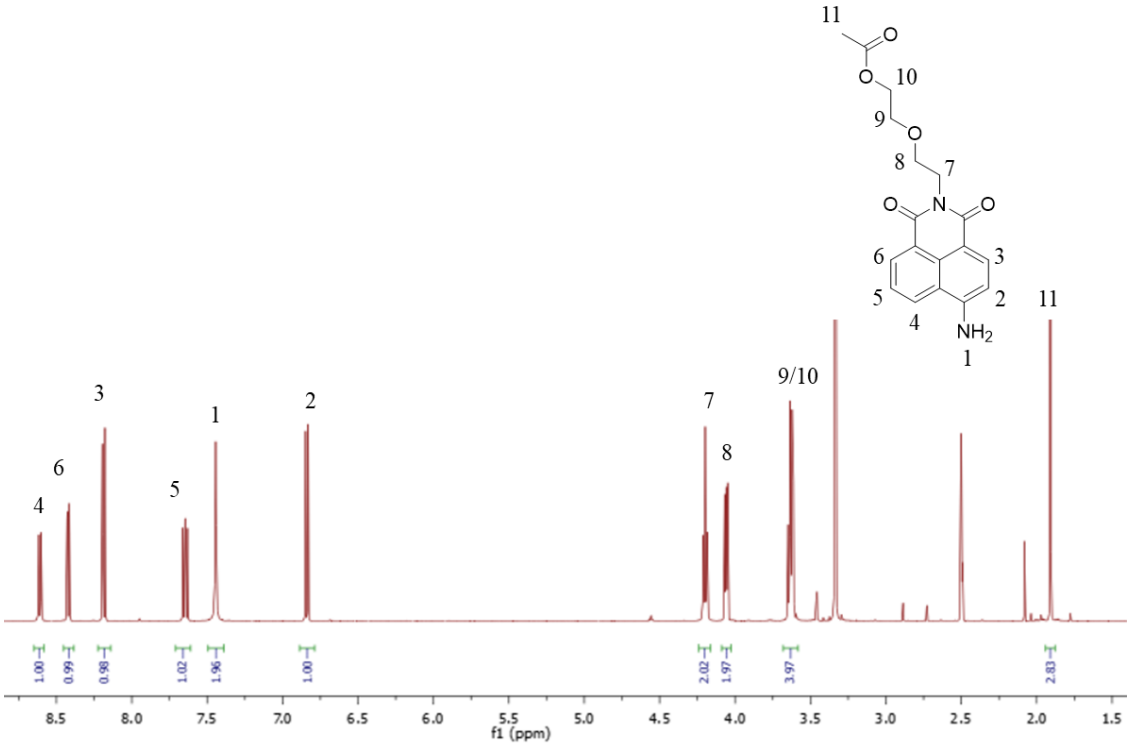

Figure 3.13: *^{1}H NMR of compound **3.12** in DMSO-d_6.*

From Figure 3.13 key characteristic signals of the naphthalimide are observed such as the doublets both integrating for 1H at 6.83 ppm and 8.18 ppm, and the singlet at 7.44 ppm integrating for 2H representative of the aromatic NH_2. Furthermore, we can also see the peaks representative of the acetylated ethylene glycol moiety as the CH_3 protons of the acetyl group appear as a singlet integrating for 3H at 1.91 ppm as well as the expected signals along the chain of the acetylated ethylene glycol all integrating for 2H at 4.20 ppm, 4.06 ppm, and 3.62 ppm.

3.3.2 Synthesis of 3.6 and 3.7.

The synthesis of **3.6** and **3.7** were carried out following scheme 3.4.

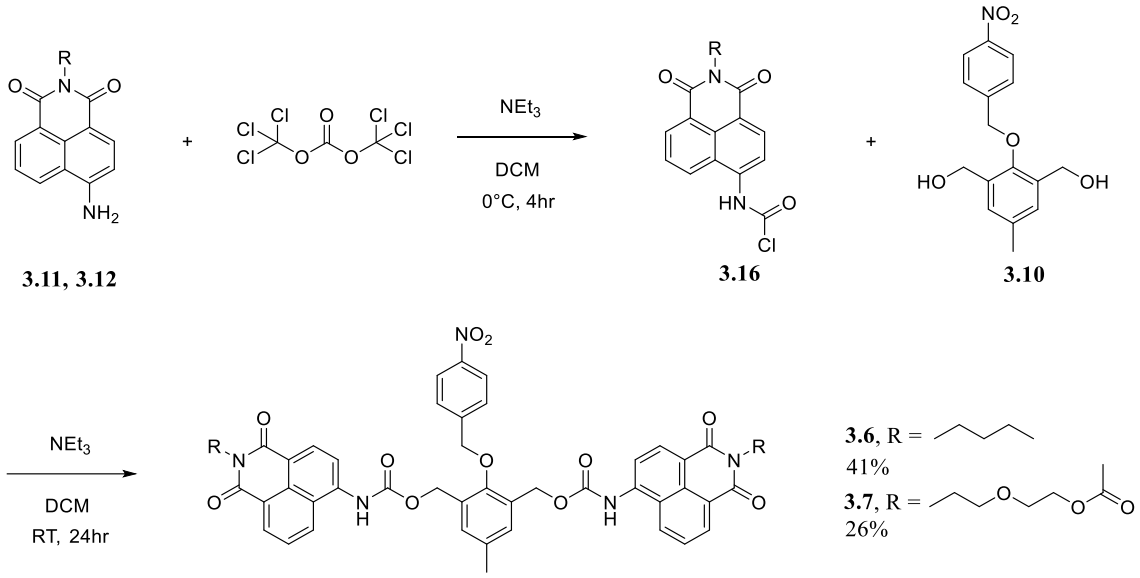

Scheme 3.4: *The synthesis of compound **3.6** and **3.7** represented by the varying R group.*

The same synthetic pathway was used to synthesise both compound **3.6** and compound **3.7**. Compounds **3.11** and **3.12** were reacted with triphosgene in the presence of NEt_3 as a base. This allowed for the formation of a highly reactive intermediate species compound **3.16**, the carbamoyl chloride derivative of either **3.11** or **3.12**. Following a one pot reaction compound **3.10** was then introduced in a manner so that there were at least 3 equivalents of the carbamoyl chloride in excess of **3.10** this favoured the carbamate formation on both hydroxymethyl substituents of 28 rather than just mono carbamate formation. The method of isolation of **3.6** and **3.7** differed in the sense that **3.6** was isolated in a 41 % yield through precipitation of the target compound by simply adding methanol to the crude mixture of compounds. Whereby, compound **3.7** required the use of column chromatography which resulted in a 26 % yield.

Compounds **3.6** and **3.7** were fully characterised using ^{1}H NMR, ^{13}C NMR, IR, and HRMS. ^{1}H NMR peaks were assigned using ^{1}H-^{1}H COSY, HSQC, and HMBC analysis. The ^{1}H NMR spectrum (500 MHz, DMSO-d_6) of **3.6** can be seen in Figure 3.14 and the ^{1}H NMR spectrum (500 MHz, $CDCl_3$) of **3.7** can be seen in Figure 3.16.

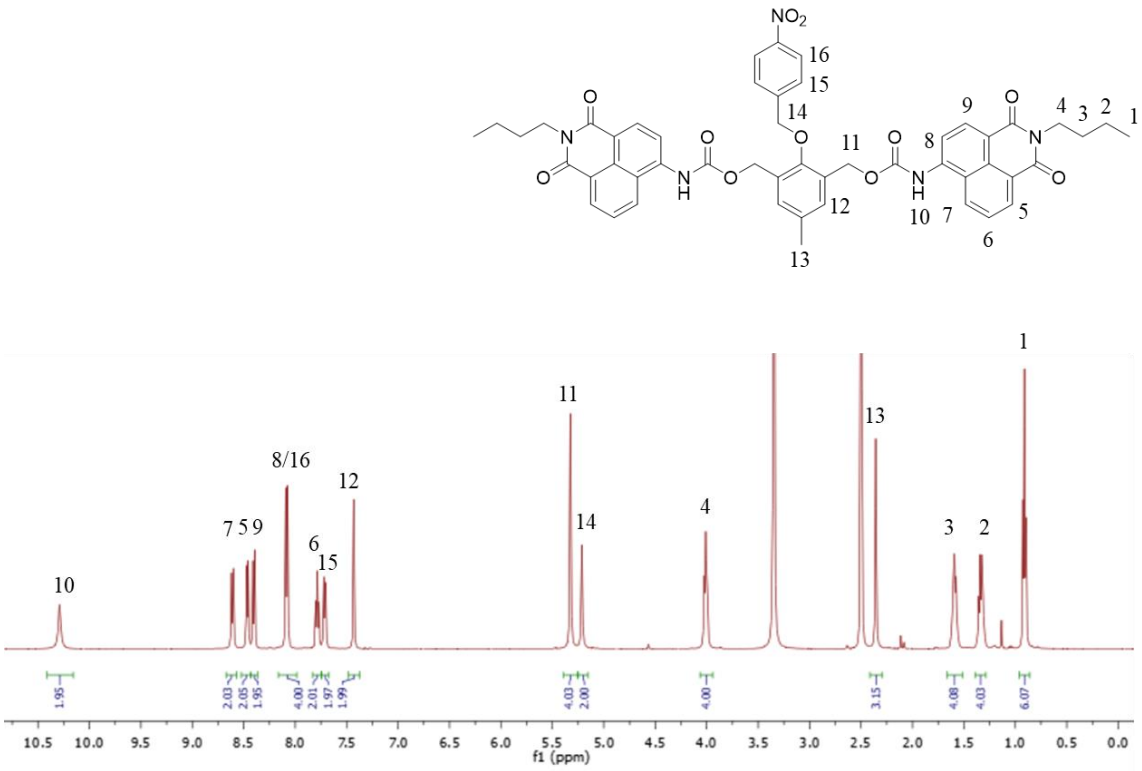

Figure 3.14: *^{1}H NMR of compound **3.6** in DMSO-d_6.*

From Figure 3.14 there was clear evidence of the synthesis of the target compound **3.6**. The broad singlet at 10.29 ppm integrating for 2H was indicative of the NH protons as a result of carbamate bond formation with the aromatic NH_2 moiety of compound **3.11**. Moreover, the appearance of the intense singlet at 5.32 ppm integrating for 4H shows that disubstitution of **3.11** onto compound **3.10**, as disubstitution results in a compound with a centre of symmetry meaning this peak represents both CH_2's on the hydroxymethyl substituents of compound **3.10**. If disubstitution had not occurred a doublet integrating for 2H would be expected to be observed in the 4.50 – 5.50 ppm region of the ^{1}H NMR spectrum. Furthermore, confirmation of compound **3.6** was observed through HRMS. The HRMS in Figure 3.15 showed ionisation at 892.3189 corresponding to $[M + H]^+$ of compound **3.6**.

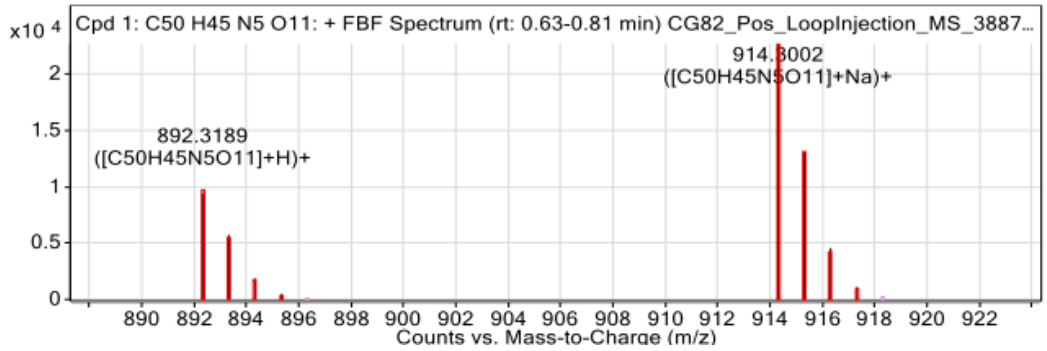

Figure 3.15: *HRMS of compound **3.6**.*

The same can be said for Figure 3.16. Compound **3.7** again possesses a centre of symmetry and evidence of target compound formation can be assigned. The broad singlet at 7.54 ppm integrating for 2H was indicative of the NH protons as a result of carbamate bond formation with the aromatic NH_2 moieties of compound **3.12**. Moreover, the appearance of the intense singlet at 5.37 ppm integrating for 4H shows that disubstitution of **3.12** onto compound **3.10**.

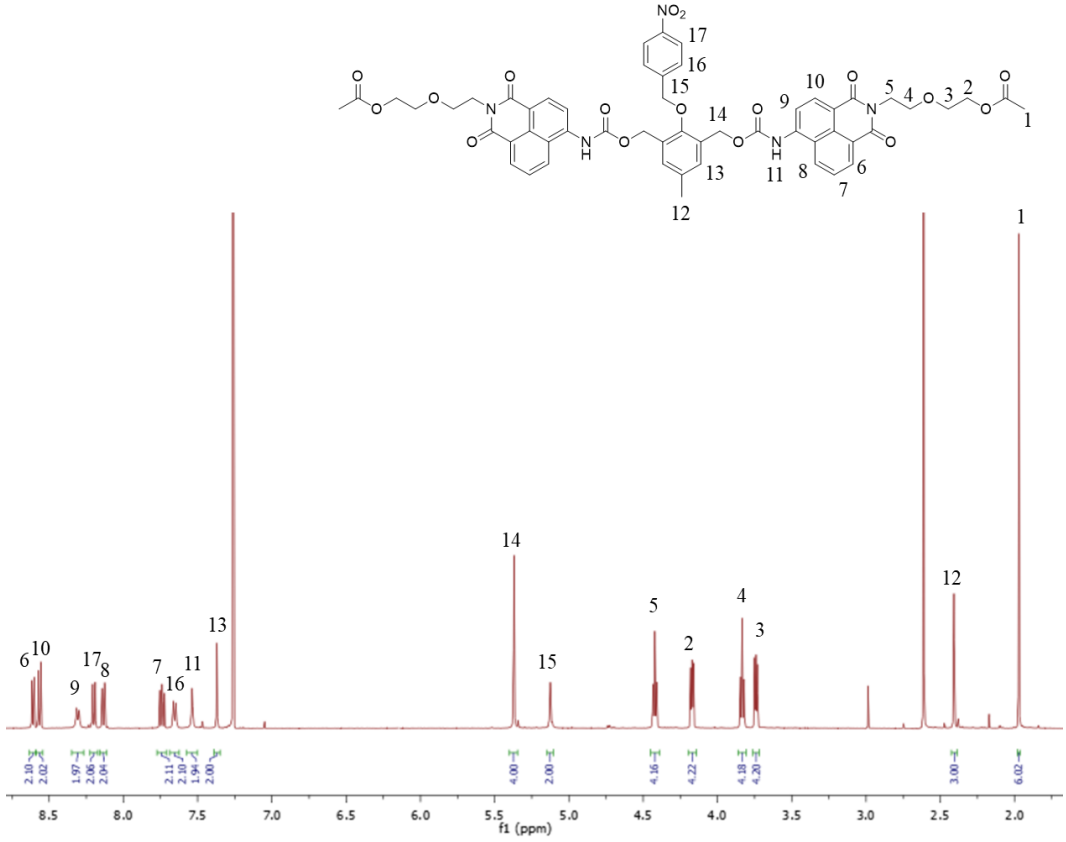

Figure 3.16: *^{1}H NMR of compound **3.7** in $CDCl_3$.*

Further confirmation of compound **3.7** can be observed from the HRMS in Figure 3.17. Figure 3.17 showed ionisation at 1062.3019 corresponding to $[M + Na]^+$ of compound **3.7**.

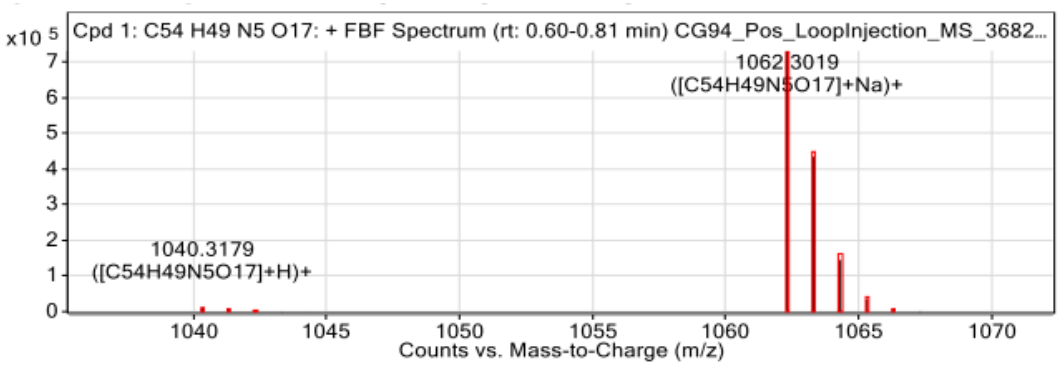

Figure 3.17: *HRMS of compound **3.7**.*

3.3.3 Synthesis of 3.8 and 3.9.

The synthesis of **3.8** and **3.9** required intermediate product compound **3.17**, compound **3.18** (amonafide) and compound **3.19** (sulfisoxazole). Compounds **3.17** and **3.18** were synthesised whereas **3.19** was purchased commercially. Compound **3.17** was initially required as an intermediate product and consisted of compound **3.12** mono carbamate linked to compound **3.10**. Scheme 3.5 shows the reaction scheme for the synthesis of compound **3.17**. The reaction follows similar steps and conditions as seen for compounds **3.6** and **3.7**. However, in this case to attain mono substitution of the fluorophore moiety an excess equivalent of compound **3.10** was added to the carbamoyl chloride intermediate compound **3.20** which was formed in the one pot reaction. This was achieved by adding compound **3.10** dropwise at 0°C to afford compound **3.17** in a 59 % yield.

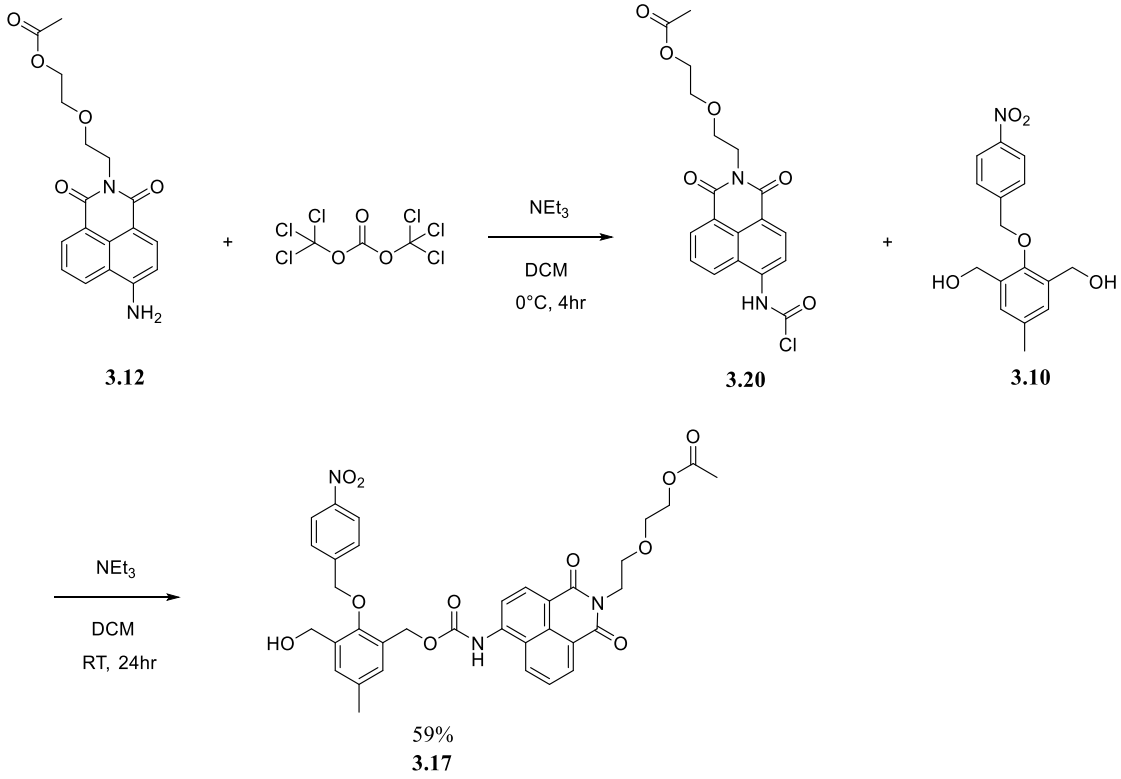

Scheme 3.5: *Synthesis of compound **3.17**.*

Compound **3.17** was fully characterised using ^{1}H NMR, ^{13}C NMR, IR, and HRMS. ^{1}H NMR peaks were assigned using ^{1}H-^{1}H COSY, HSQC, and HMBC analysis.

In Figure **3.18** a ^{1}H-^{1}H COSY spectra of compound **3.17** can be seen where the correlations are observed for neighbouring protons of the naphthalimide moiety (blue lines), the 4-nitrobenzyl moiety (red lines), the acetylated ethylene glycol moiety (green lines), and the coupling between the CH_2 and the OH on the hydroxymethyl substituent (yellow lines)

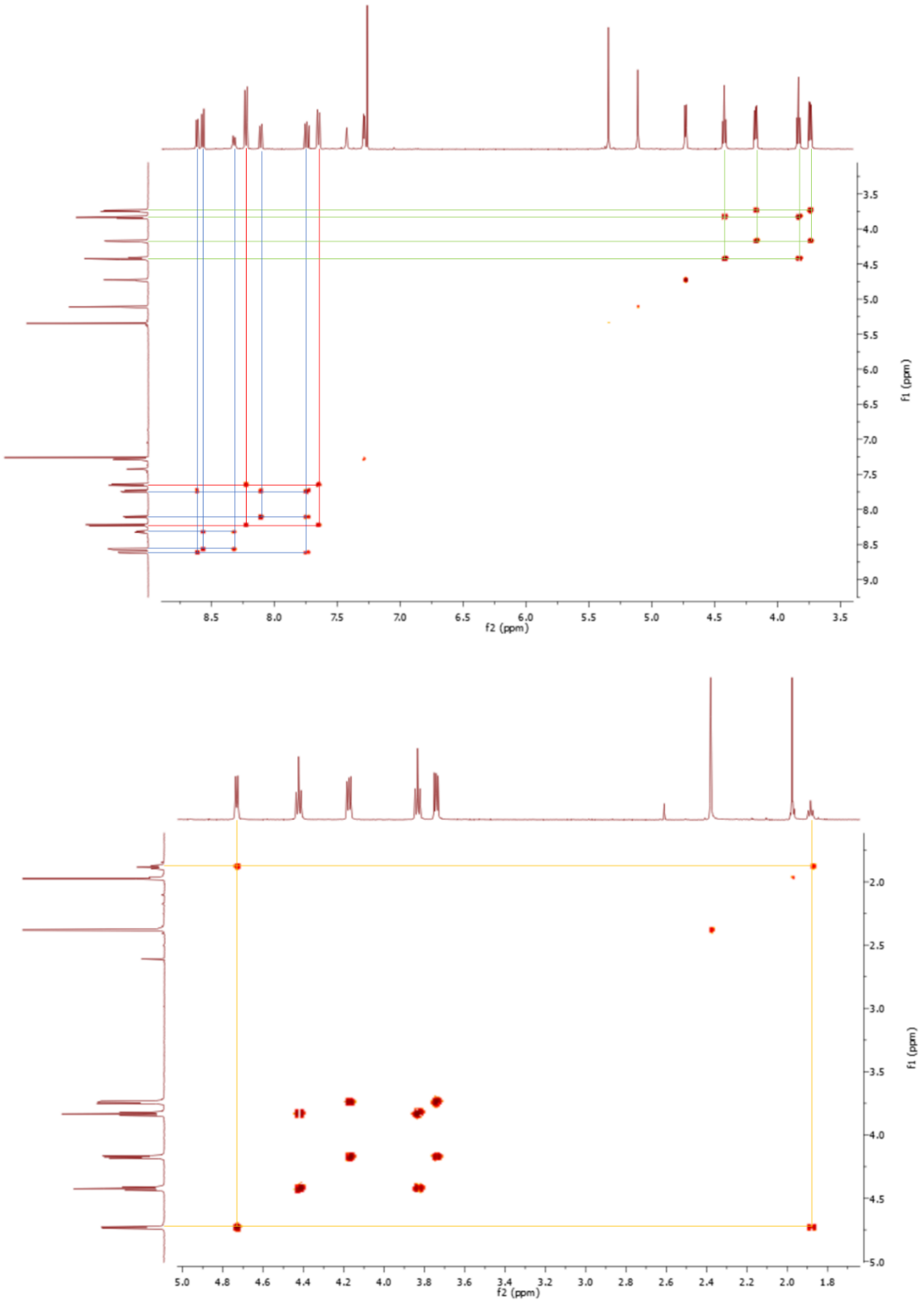

Figure 3.18: *^{1}H-^{1}H COSY spectra of compound **3.17** in $CDCl_3$.*

The ^{1}H NMR spectrum (500 MHz, $CDCl_3$) of **3.17** can be seen in Figure 3.19. From the ^{1}H NMR of compound **3.17** it can be seen that the characteristic NH signal of the carbamate at 7.42 ppm integrating for 1H was indicative of mono substation of compound **3.17**. Furthermore, downfield shift of the CH_2 protons on the hydroxyl methyl substituent

of compound **3.10** was observed as a result of the deshielding effect established by the formation of the carbamate moiety at 5.34 ppm integrating for 2H. The free hydroxymethyl substituent of compound **3.17** can be confirmed as the doublet at 4.73 ppm integrating for 2H is the expected splitting that would be observed due to the neighbouring OH.

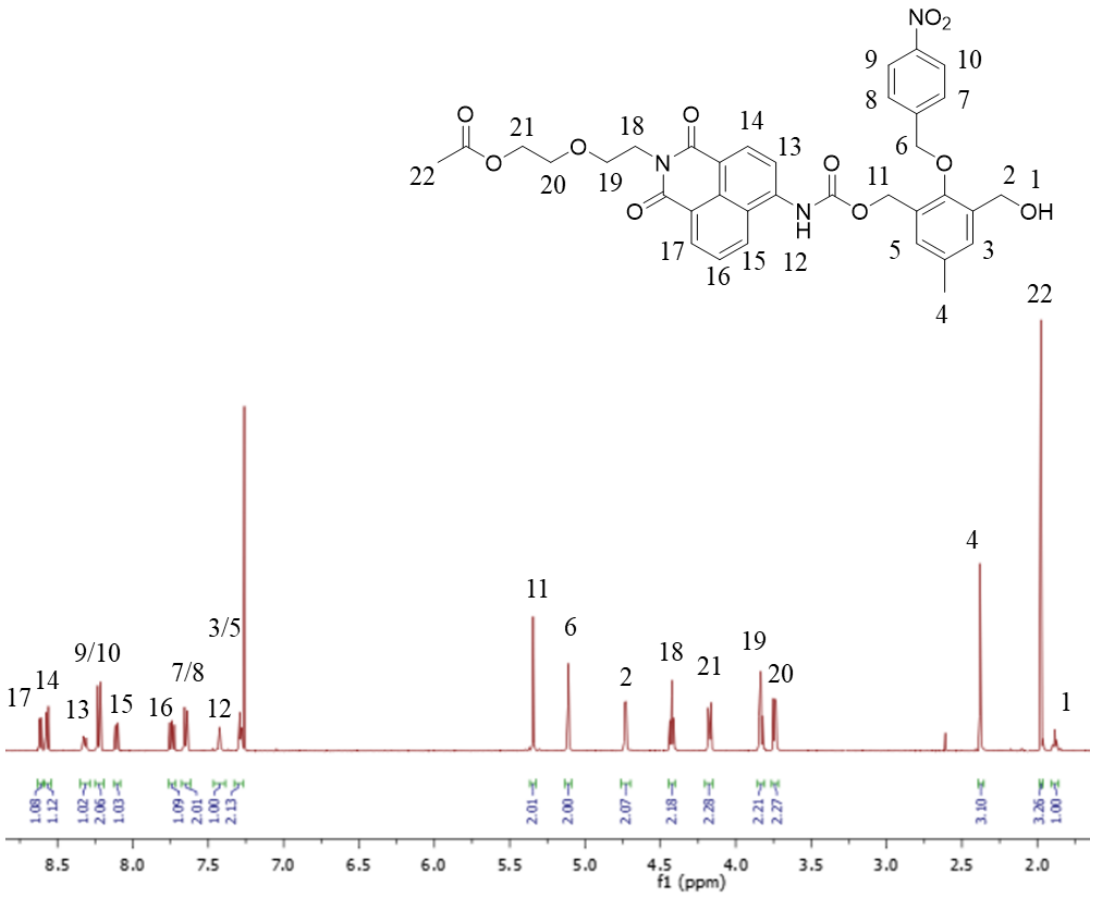

Figure 3.19: *^{1}H NMR of compound **3.17** in $CDCl_3$.*

To further confirm the synthesis of compound **3.17**, the HRMS in Figure 2.20 showed ionisation at 624.2008 corresponding to $[M + Na]^+$

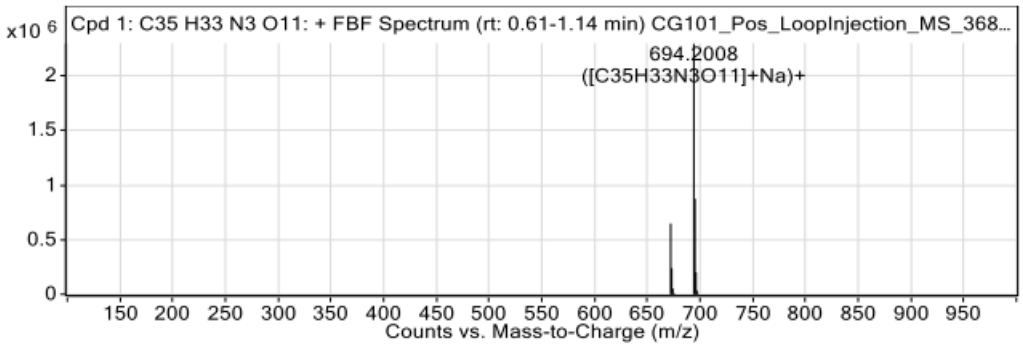

Figure 3.20: *HRMS of compound **3.17**.*

Compound **3.18** required for further reaction with compound 35 was synthesised following Scheme 3.6.

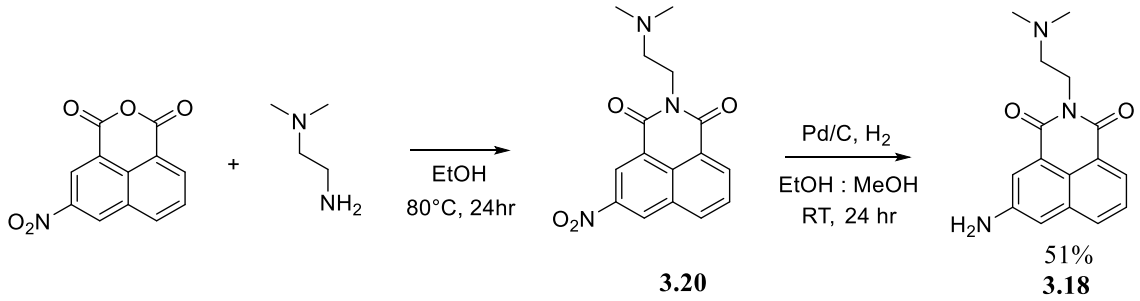

Scheme 3.6: *The synthesis of compound **3.18**.*

To synthesise compound **3.18**, 3-nitro-1,8-naphthalic anhydride and *N*,*N*-dimethylethylenediamine undergo a condensation reaction to result in compound **3.20** which was then reduced to its corresponding amino derivative following reducing conditions of Pd/C and H_2 to afford compound **3.18** in 51 % yield. Compound **3.18** was fully characterised using ^{1}H NMR, ^{13}C NMR, IR, and HRMS. ^{1}H NMR peaks were assigned using H-H COSY, HSQC, and HMBC analysis. The ^{1}H NMR spectrum (500 MHz, DMSO-d_6) of **3.18** can be seen in Figure 3.21 and agrees with literature spectra of the same compound.

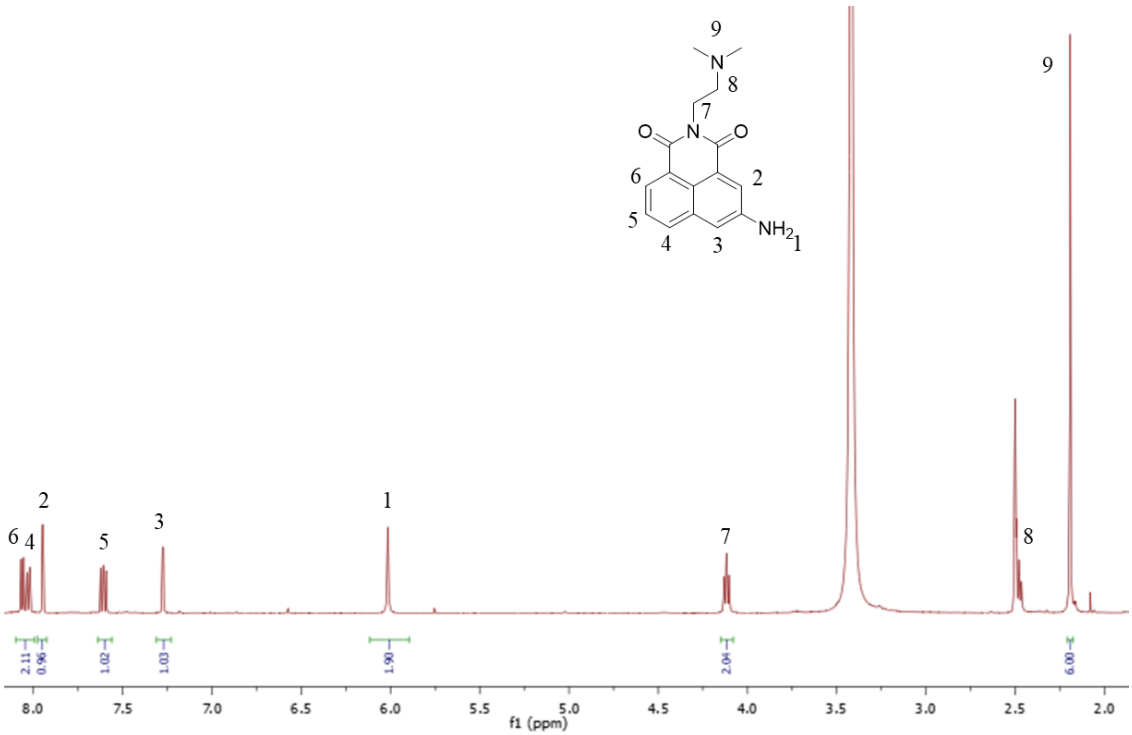

Figure 3.21: *^{1}H NMR of compound **3.18** in DMSO-d_6.*

From Figure 3.21 we can assign key peaks of compound **3.18**. The peak at 6.01 ppm integrating for 2H corresponds to the NH_2 substituent, while characteristic triplet at 7.61 ppm integrating for 1H is representative of the naphthalene moiety. The dimethyl amine substituent can be seen to be represented at 2.19 ppm as a singlet integrating for 6H.

Compounds **3.8** and **3.9** were synthesised following scheme 3.7. The same synthetic pathway and conditions were followed for each compound with the only variable being the change in solvent. In both cases compound **3.18** or **3.19** were reacted with triphosgene to form a carbamoyl chloride intermediate which was then reacted with compound **3.17** in a one pot reaction to result in compound **3.8** or compound **3.9** which were then purified via column chromatography to result in relatively low yields of the target compounds, 4 % yield and 3 % yield respectively.

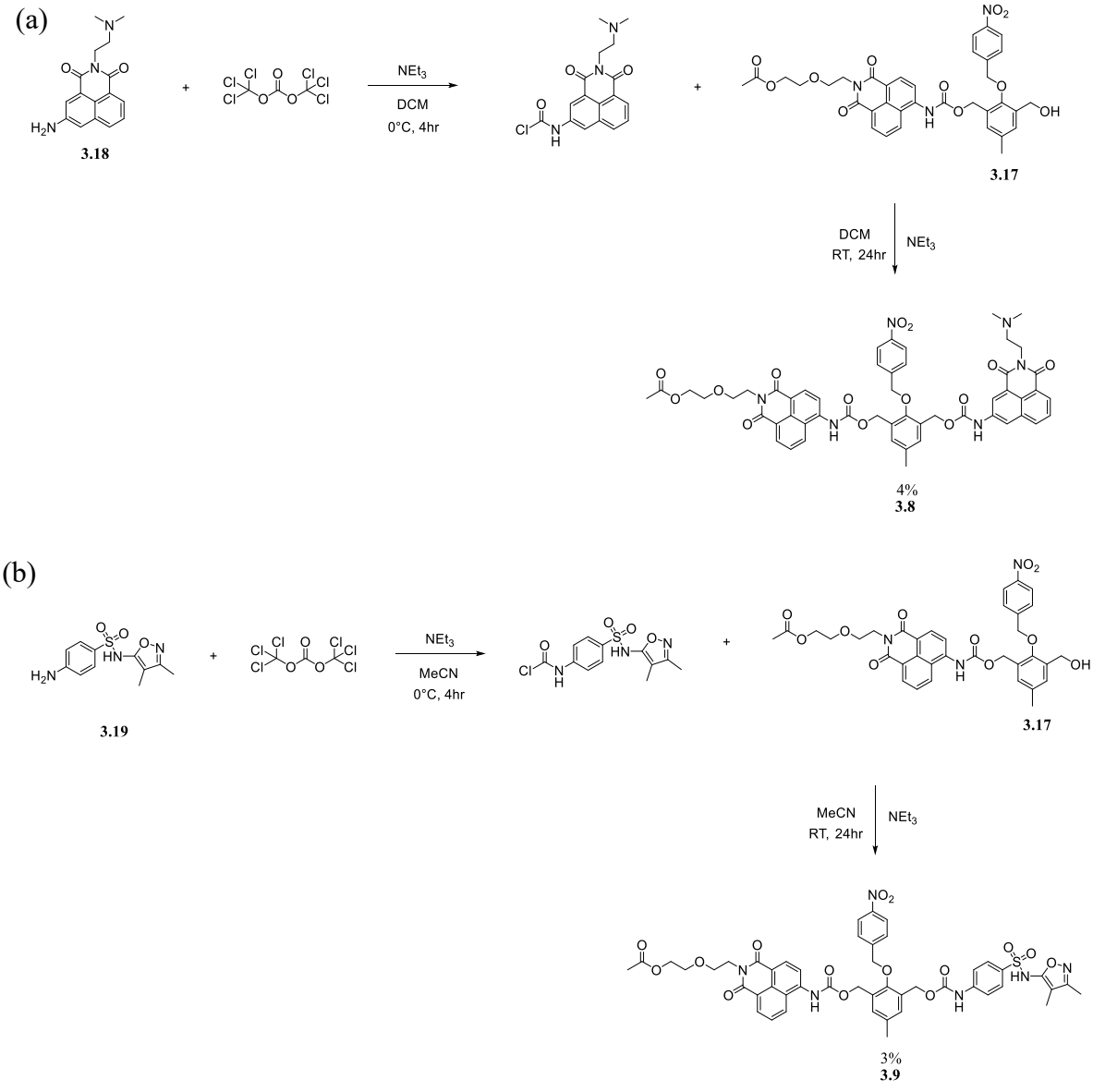

Scheme 3.7: *The synthesis of compounds **3.8** (a) and **3.9** (b).*

Attempts to increase the percentage yields of **3.8** and **3.9** were carried out with no success and were monitored using TLC. The use of nucleophilic base DMAP in place of NEt_3 upon addition of compound **3.17** to the reaction mixture did not result in the formation of

3.8 or **3.9**. Furthermore, given the potential for isocyante formation rather than carbamoyl chloride formation upon reaction of **3.18** or **3.19** with triphosgene a catalyst known as dibutyltin dilaurate was added to the reaction mixture upon the addition of compound **3.17**. Dibutyltin dilaurate increases the reactivity of **3.17** towards the isocyante derivates of **3.18** and **3.19** however no product formation was observed through TLC analysis. The reaction mixture was also refluxed at this point in the reaction to overcome any kinetic barriers but again no product formation was observed.

Attempts to synthesise a reactive intermediate avoiding the use of triphosgene were also carried out whereby a p-nitrophenyl leaving group was reacted with the amine of **3.19**. Whilst the synthesis of this compound was successful, no reaction was observed between this derivative and compound **3.17**. Whilst Scheme **3.7** was very low yielding possibly due to the poor solubility of amonafide upon hydrochloride salt formation, it was the only pathway that could yield the desired target compounds **3.8** and **3.9** to obtain proof of principle data.

Compound **3.8** was fully characterised using ^{1}H NMR, ^{13}C NMR, IR, and HRMS. ^{1}H NMR peaks were assigned using ^{1}H-^{1}H COSY, HSQC, and HMBC analysis. The ^{1}H NMR spectrum (500 MHz, $CDCl_3$) of 26 can be seen in Figure 3.22.

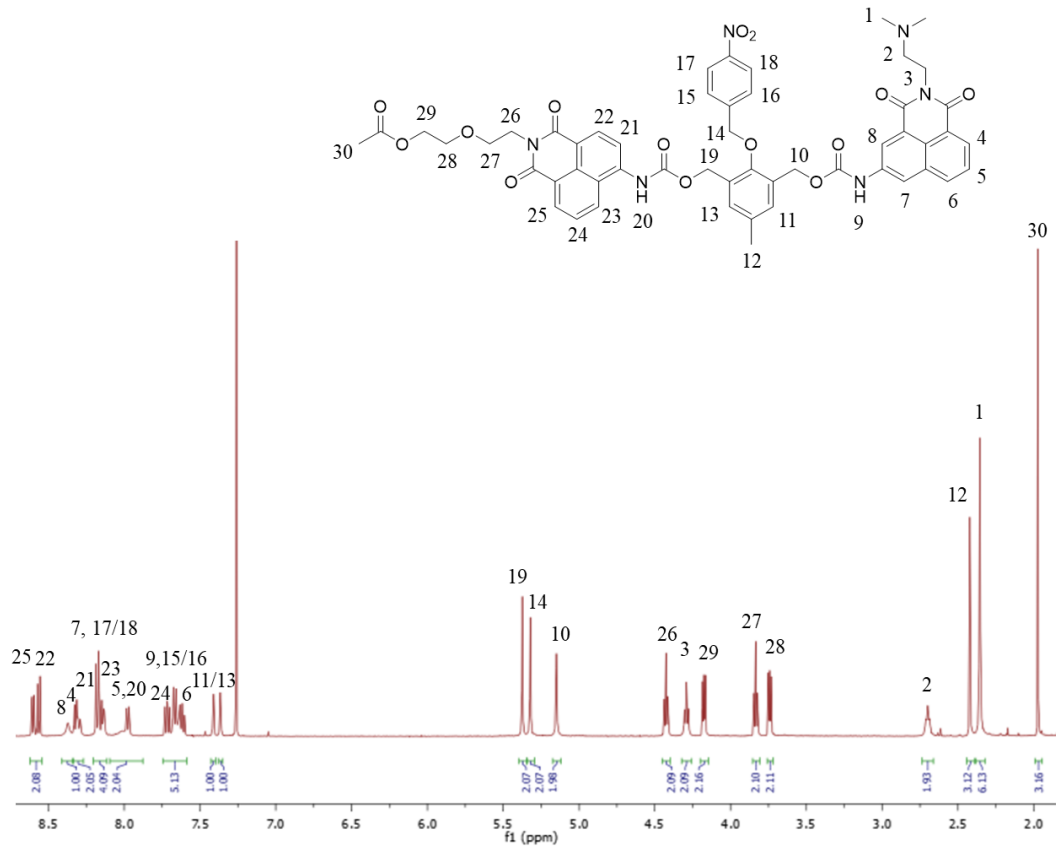

Figure 3.22: *^{1}H NMR of compound **3.8** in $CDCl_3$.*

From Figure 3.22 the addition of compound **3.18** via carbamate was clearly noted by the singlet at 5.15 ppm integrating for 2H which is the CH_2 of the hydroxymethyl substituent of compound **3.17**. Previously this would've appeared as a doublet due to the coupling observed with the free neighbouring OH. The dimethyl amine substituent can also be seen at 2.36 ppm integrating for 6H a characteristic peak indicating that of the amonafide moiety of compound **3.8**. Further confirmation of compound **3.8** was observed through HRMS and LCMS. The HRMS in Figure 3.23 showed ionisation at 981.3307 corresponding to $[M + H]^+$ of compound **3.8**.

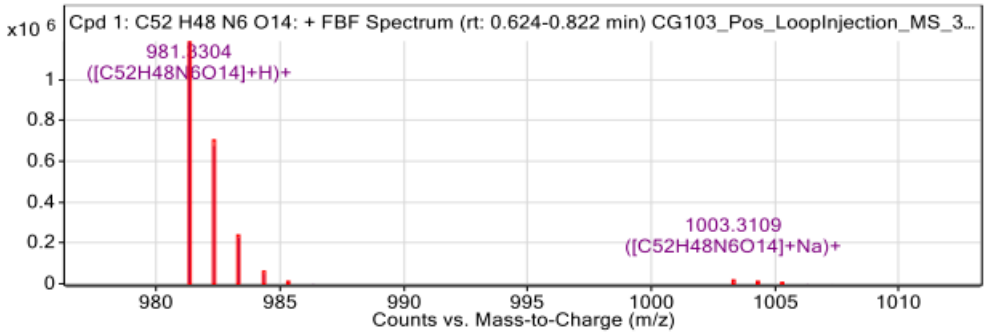

Figure 3.23: *HRMS of compound **3.8**.*

The LCMS in Figure 3.24 showed one peak at Rt = 31.03 minutes on the UV chromatogram with corresponding ionisation under the UV peak to that of $[M + H]^+$ of compound **3.8** at 981.

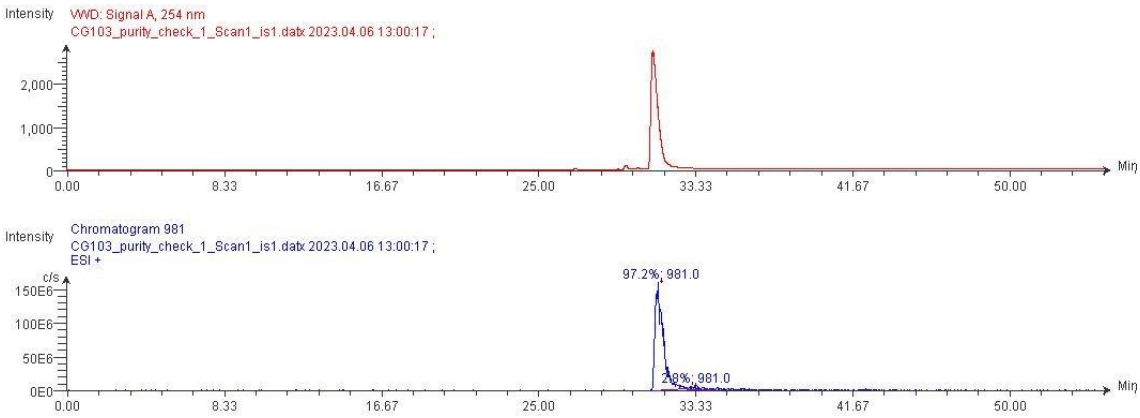

Figure 3.24: *LCMS of compound **3.8**.*

The synthesis of compound **3.9** was also confirmed using ^{1}H NMR, ^{13}C NMR, IR, and HRMS. ^{1}H NMR peaks were assigned using ^{1}H-^{1}H COSY, HSQC, and HMBC analysis. The ^{1}H NMR spectrum (500 MHz, $CDCl_3$) of **3.9** can be seen in Figure 3.25.

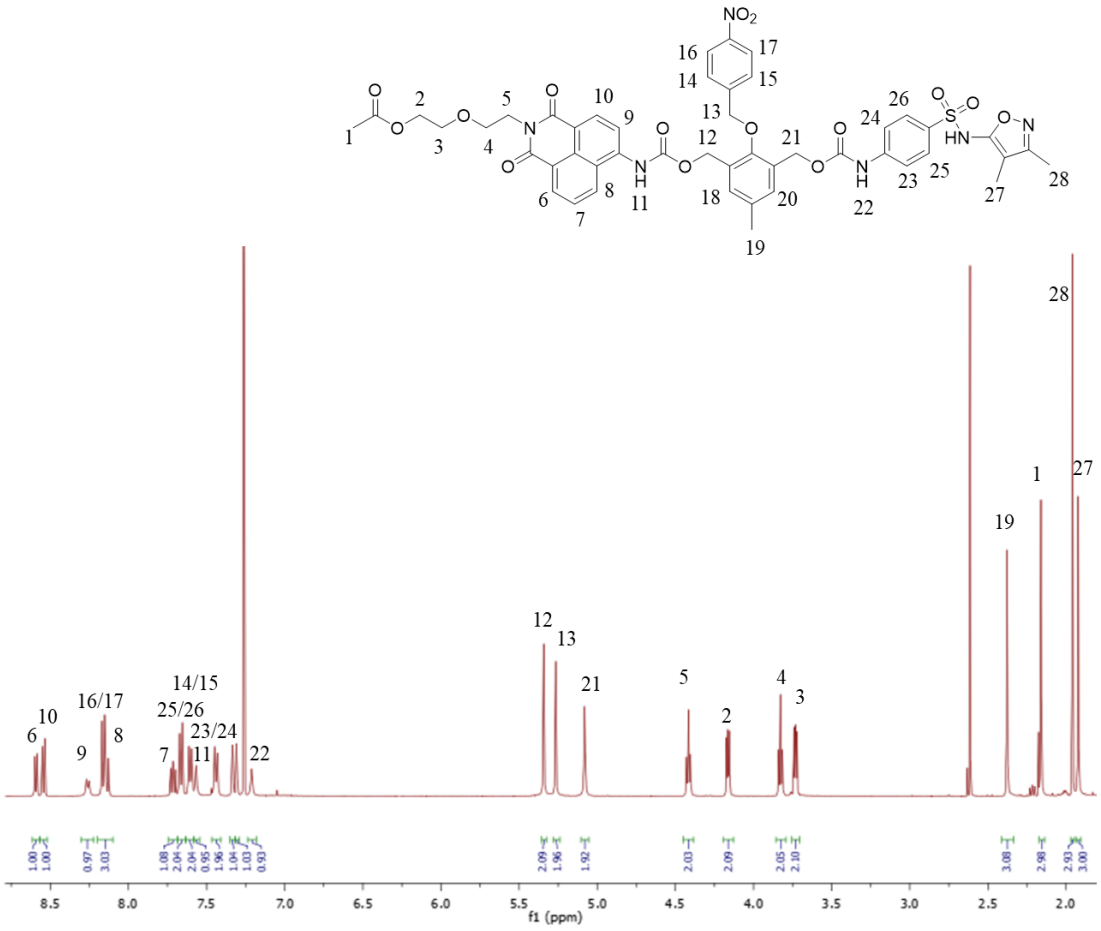

Figure 3.25: *^{1}H NMR of compound **3.9** in $CDCl_3$.*

As previously mentioned in the case of compound **3.8**. From Figure 3.25 we can determine the carbamate formation to form **3.9** between compound **3.17** and **3.19** as the previously observed doublet is now a singlet integrating for 2H at 5.08 ppm. Signals corresponding to the **3.19** can also be observed at 7.43 ppm integrating for 2H representing aromatic protons of the benzenesulfonamide moiety, as well as the two methyl substituents of the oxazole moiety appearing as singlets at 1.96 ppm and 1.92 ppm both integrating for 3H. Again, with the use of HRMS and LCMS we can further confirm the synthesis of compound **3.9**. The HRMS in Figure 3.26 showed ionisation at 965.2651 corresponding to $[M + H]^+$ of compound **3.9**.

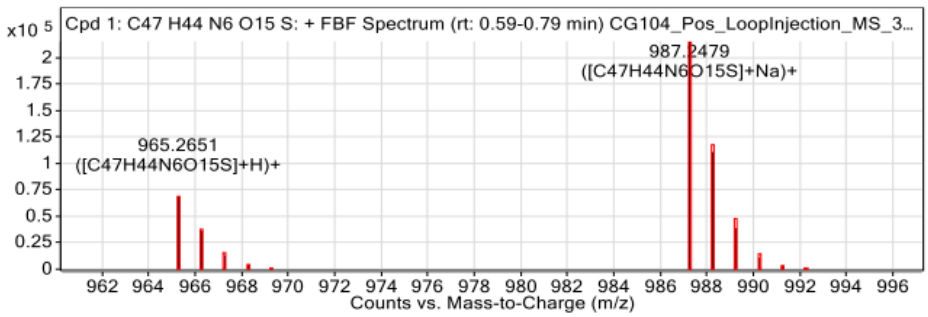

Figure 3.26: *HRMS of compound **3.9**.*

The LCMS in Figure 3.27 showed one peak at Rt = 39.67 minutes on the UV chromatogram with corresponding ionisation under the UV peak to that of M + H compound **3.9** at 965.

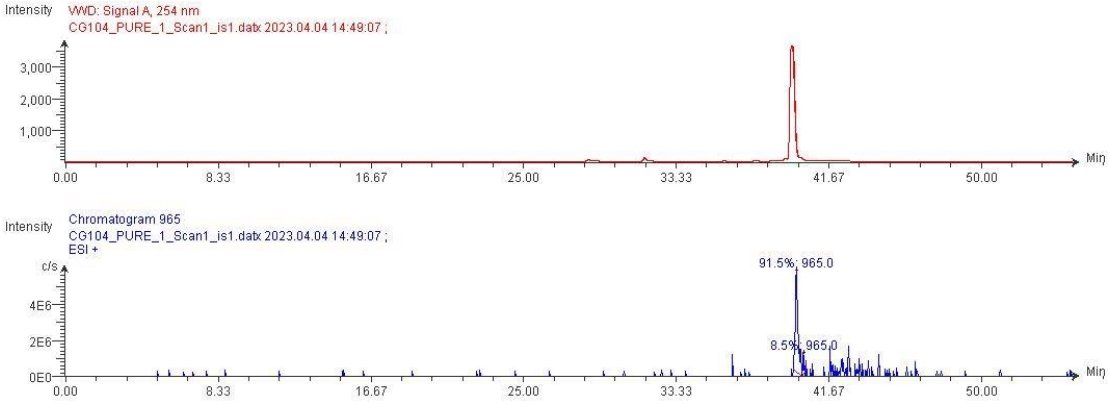

Figure 3.27: *LCMS of compound **3.9**.*

3.4 Photophysical Characterisation of 3.6, 3.7, 3.8, 3.9, and 3.21

With compounds **3.6** – **3.9**, and **3.21** successfully synthesised, the next objective was to evaluate their photophysical properties. In order to fully understand their ability to immolate and their sensitivity to NTR, a series of spectroscopic measurements were carried out to understand their ground and excited state properties.

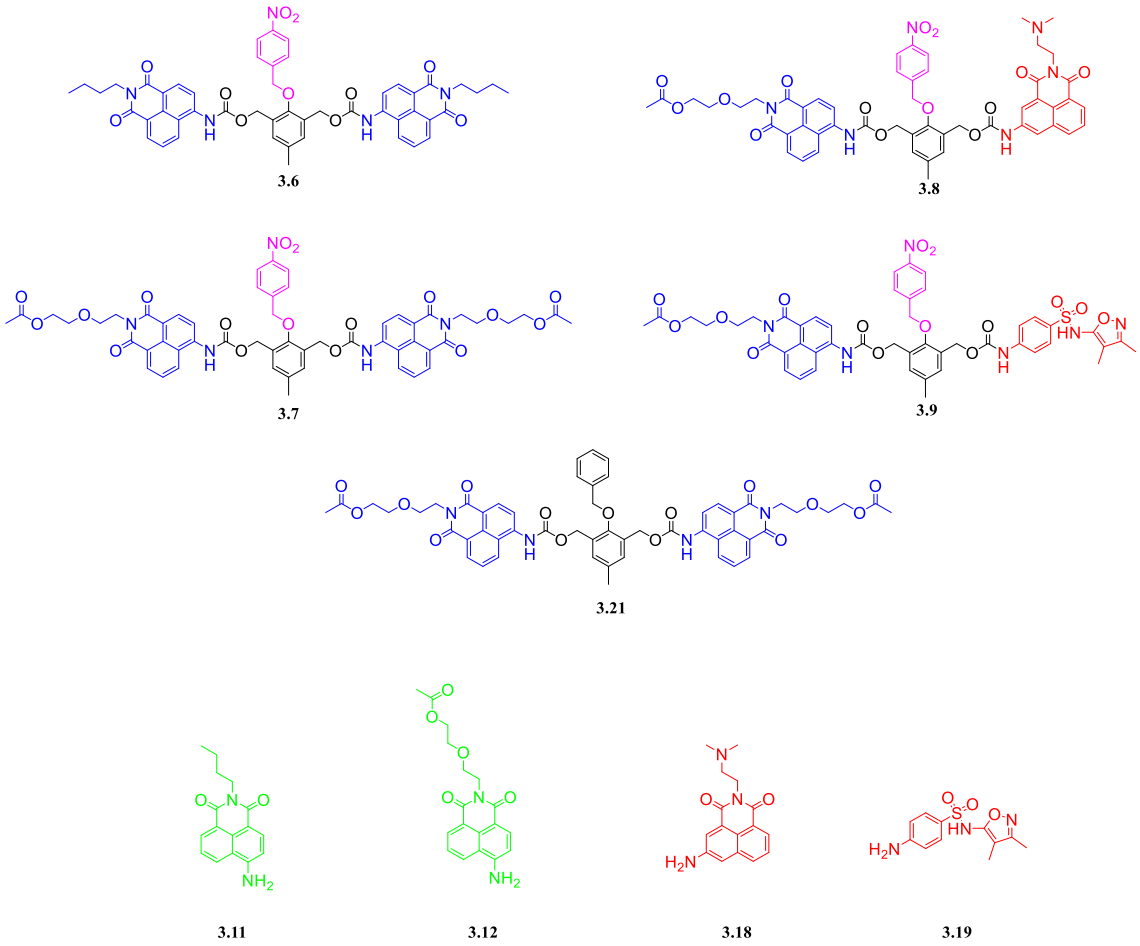

Figure 3.28: *Structures of compounds to be measured.*

3.4.1 Absorption and Emission Spectra of 3.6, 3.7, 3.8, 3.9, and 3.21

The absorption spectra of compounds **3.6, 3.7, 3.8, 3.9, and 3.21** were recorded at pH 7.4 in 10 mM phosphate buffer. In general, the compound was dissolved as a concentrated solution in DMSO (3 mM) to allow for complete dissolution. Solutions for analysis were then made by dilution of the stock in 10 mM PBS. At no stage did the total conc. of DMSO go above 1%.

The UV/vis spectra in Figure 3.29 show similarities between compound **3.6** and **3.7**. Compound **3.6** had a λ_{max} 252 nm and 385 nm. The band at 252 nm is characteristic of π-π* naphthalimide transitions whereas the broad band at 385 nm is a characteristic ICT absorption of carbamate functionalised amino naphthalimides.[99] Similarly compound **3.7** had a λ_{max} 250 nm and 383 nm and control compound **3.21** (synthesised in similar manner to compound **3.6** and **3.7**, refer to Chapter 6) had a λ_{max} of 384 nm. In comparison, compound **3.11** and **3.12** displayed an expected bathochromic shift in the wavelength of absorption observed at 433 nm and 432 nm respectively. The hypsochromic shift in wavelength of compound **3.6** and **3.7** is indicative of carbamate functionalisation attributing to the blocking of ICT of the naphthalimide moieties **3.11** and **3.12** in each structure.

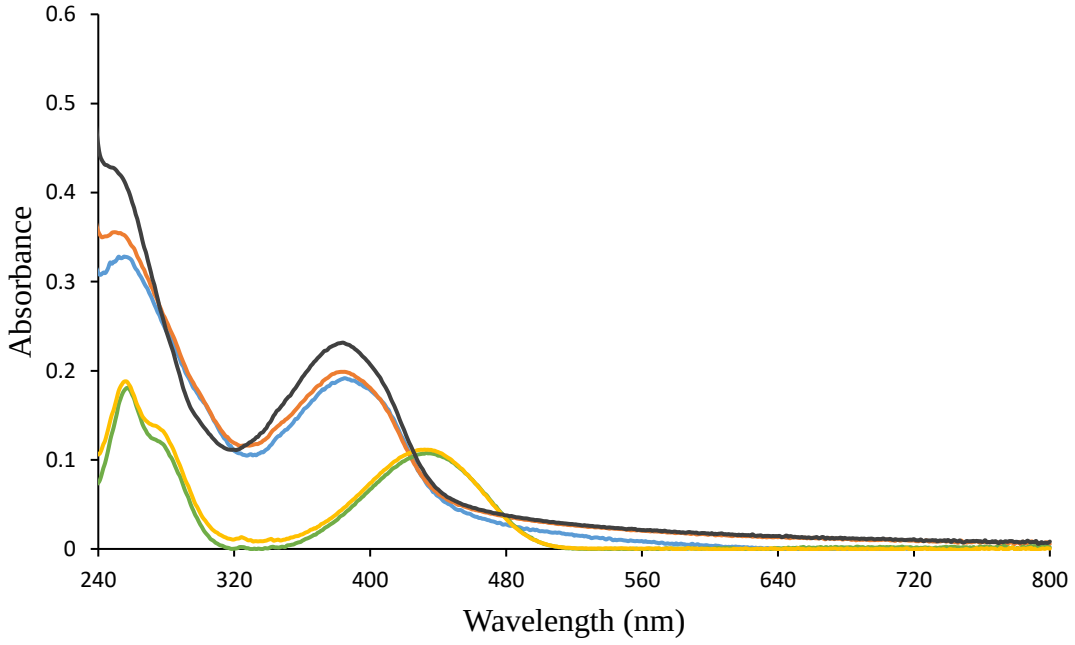

Figure 3.29: *The UV/Vis spectra of compound **3.6** (blue),**3.7** (orange), **3.11** (green), **3.12** (yellow) and control compound **3.21** (black) in 10 mM phosphate buffer at pH 7.4. All compound concentrations are 10 µM.*

The UV/vis spectra in Figure 3.30 shows similarities in the absorption spectra of compound **3.8** and **3.9**. Compound **3.8** had a λ_{max} 253 nm and 383 nm. Likewise, compound **3.9** had a λ_{max} 250 nm and 382 nm. When compared to **3.8** and **3.9** the expected immolated fluorophore compound **3.12** displayed a bathochromic shift in the wavelength of ICT absorption observed at 433 nm. The bathochromic shift was shorter when comparing compound amonafide **3.18** to compound **3.8** with absorption bands established at 346nm and 413 nm and this was likely a consequence of unfavourable delocalisation

of ICT within 3-substituted-1,8-naphthalimides.[99] Moreover no change in absorption was observed for sulfisoxazole **3.19** as it only exhibited π-π* transitions at 251 nm. The hypsochromic shift in wavelength of compound **3.8** and **3.9** is again representative of carbamate functionalisation attributing to the blocking of ICT of both compound **3.12** and **3.18**.

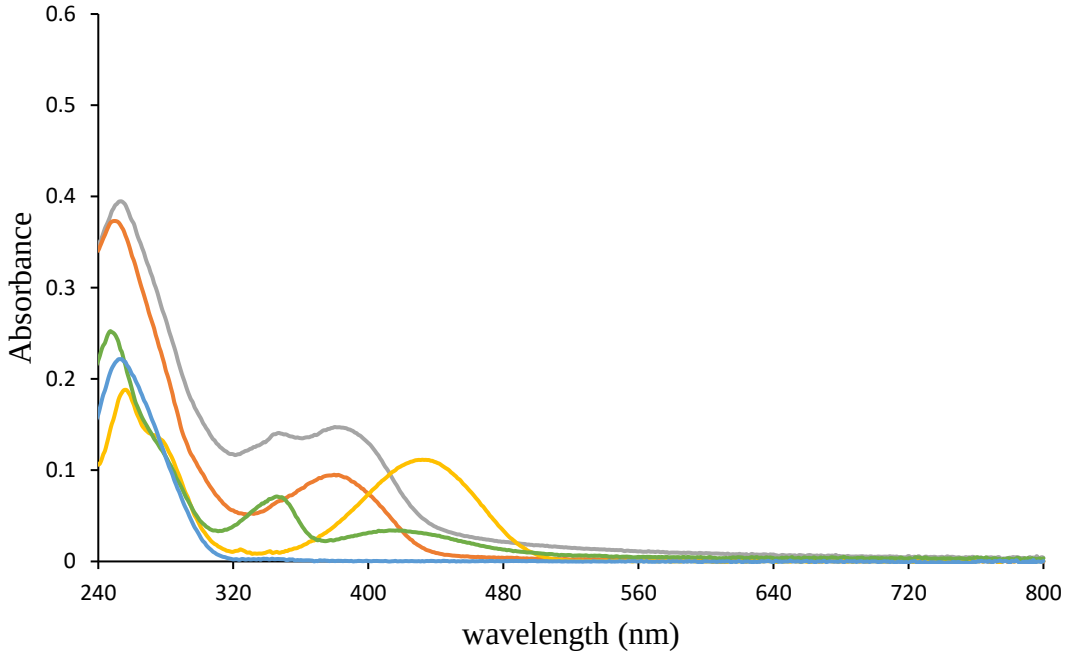

Figure 3.30: *The UV/Vis spectra of compound **3.8** (grey), **3.9** (orange), **3.12** (yellow), **3.18** (green) and **3.19** (blue) in 10 mM phosphate buffer at pH 7.4. All compound concentrations are 10 µM.*

To determine what the expected ratiometric response would be for compounds **3.6**, **3.7**, **3.8**, and **3.9** each compound was excited at 420 nm. This wavelength was chosen as it would excite the ICT absorption band of the carbamate functionalised naphthalimide moieties in all compounds and would also excite the expected immolated fluorophores **3.11** and **3.12** in each case. In Figure 3.31 it was noted that the maximum wavelength of emission for compound **3.6** was 484 nm and for compound **3.11** was 546 nm which would give rise to what would be expected to be a 62 nm red shift in the emission wavelength upon self-immolation of compound **3.6**. Compound **3.7** established a broad emission band centred at 489 nm and for compound **3.12** an emission band centred at 544 nm which would give rise to a predicted 55 nm red shift in the emission wavelength upon self-immolation of compound **3.7**. Compound **3.21** had an emission band centred at 493 nm which differs by 51 nm when compared to compound **3.12**.

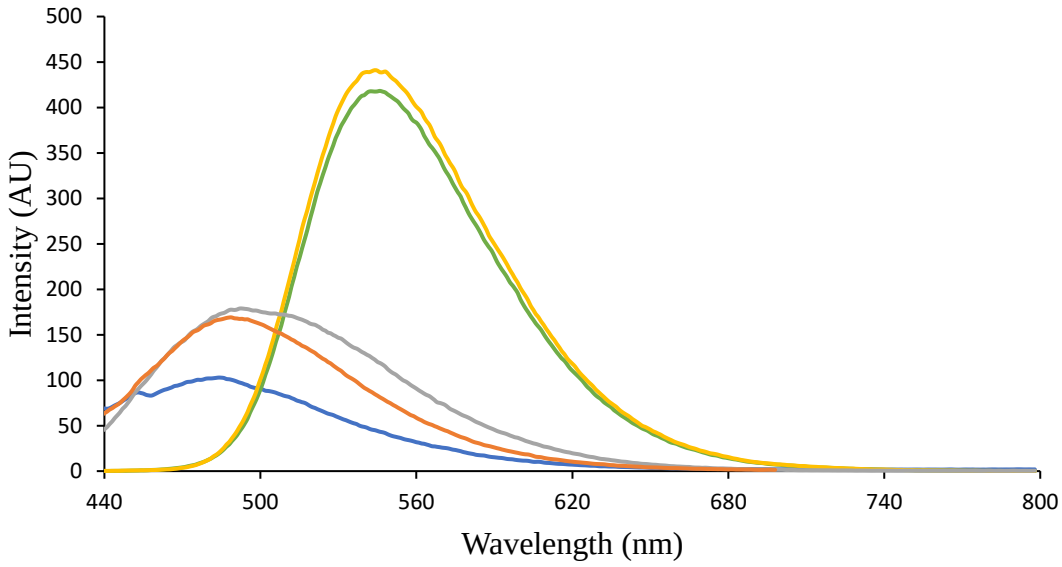

Figure 3.31: *The emission spectra of 10μM of compound **3.6** (blue), **3.7** (orange), **3.11** (green), **3.12** (yellow) and control compound **3.21** (grey) in 10 mM phosphate buffer at pH 7.4. All compound concentrations are 10 μM. λ_{ex} = 420 nm. **3.6**, **3.7**, and **3.21** Ex slit width: 5 nm and Em slit width: 10 nm. **3.11** and **3.12** Ex slit width: 5 nm and Em slit with: 5 nm.*

In Figure 3.32 it can be seen that the maximum wavelength of emission for compound **3.8** was 487 nm and for compound **3.12** was 544 nm which would result in an expected 57 nm red shift in the emission wavelength upon self-immolation of compound **3.8**. Furthermore, the emissions band for compound **3.18** centred at 587 nm which poses an even greater red shift in comparison to compound **3.12** of 100 nm. However, **3.18** is inherently weakly fluorescent due to its poor delocalisation of ICT. Compound **3.9**

produced a broad emission band centred at 492 nm which would give rise to a predicted 52 nm red shift in the emission wavelength upon self-immolation in comparison to compound **3.12**.

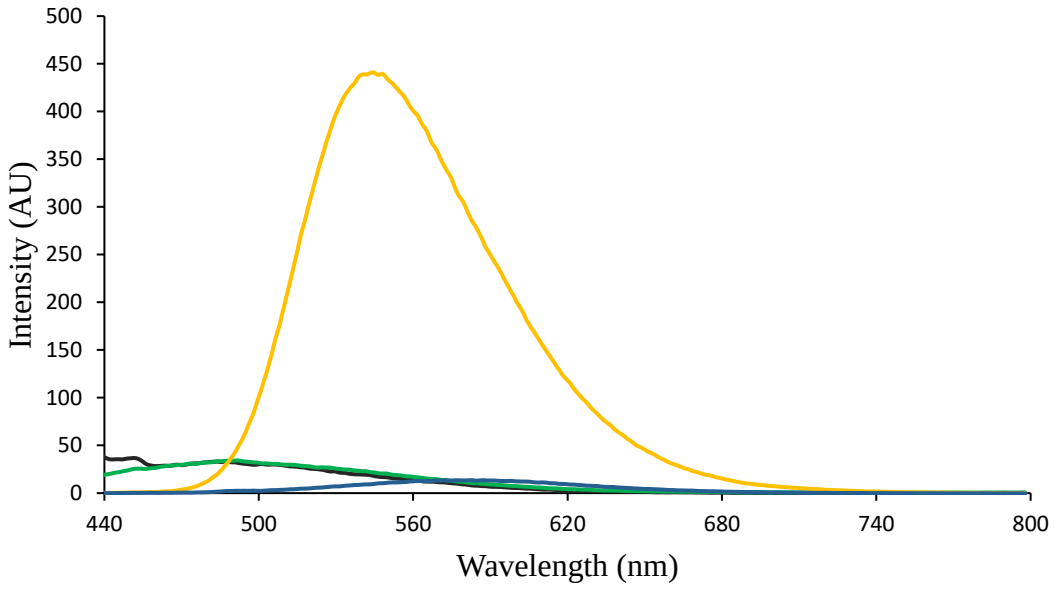

Figure 3.32: *The UV/Vis spectra of compound **3.8** (black), **3.9** (green), **3.12** (yellow), **3.18** (blue) in 10 mM phosphate buffer at pH 7.4. All compound concentrations are 10 µM. λ_{ex} = 420 nm. **3.8** and **3.9** Ex slit width: 5 nm and Em slit width: 10 nm. **3.12** and **3.18** Ex slit width: 5 nm and Em slit with: 5 nm.*

Given the stark differences in both absorption and emission wavelengths of compounds **3.6**, **3.7**, **3.8**, and **3.9** when compared to their relevant fluorophores **3.11** and **3.12**. The next step was to determine could these differences be observed as a ratiometric fluorescence response in the presence of a reducing agent.

3.5 Sodium Dithionite Fluorescence Response of 3.6, 3.7, 3.8, 3.9

To understand if the chemical reduction of the nitro substituent on each compound to the corresponding amino derivative could result in subsequent self-immolation and a ratiometric change in the fluorescent emission wavelength sodium dithionite $Na_2S_2O_4$ was used in place of NTR. This was done in order to investigate all parameters that may affect the self-immolation of the novel set of dendrimers. $Na_2S_2O_4$ can tolerate changes

to solvent and pH whereas an enzyme like NTR would not be suited to such variations, it is also inexpensive in comparison to NTR. Compound **3.7** was used to determine the conditions required for self-immolation due to the fact that it was likely to be the most soluble in an aqueous solution out of the 4 dendrimers, owing to the presence of the two the acetylated ethylene glycol moieties on the head of the 1,8-naphthalimides.

3.5.1 Fluorescence Response of 3.7 to Sodium Dithionite

In general, the compound was dissolved as a concentrated solution in DMSO (3 mM) to allow for complete dissolution. Solutions for analysis were then made by dilution of the stock in either 10 mM PBS or 10 mM Tris HCl buffer. The percentage of DMSO was varied throughout the study.

Initially it was determined if any fluorescence response could be attained upon the addition of $Na_2S_2O_4$ (1mM) towards compound **3.7** (10 µM) where the amount of DMSO present in 10 mM PBS 7.4 was less than 1 %. In Figure 3.33 it can be seen that negligible change in fluorescence was observed other than a decrease in the fluorescence intensity centred at 488 nm. No ratiometric change in fluorescence was observed which initially was thought to be a consequence of initial reduction but slow immolation, previously cited for dendrimers based on a similar adapter unit.[198]

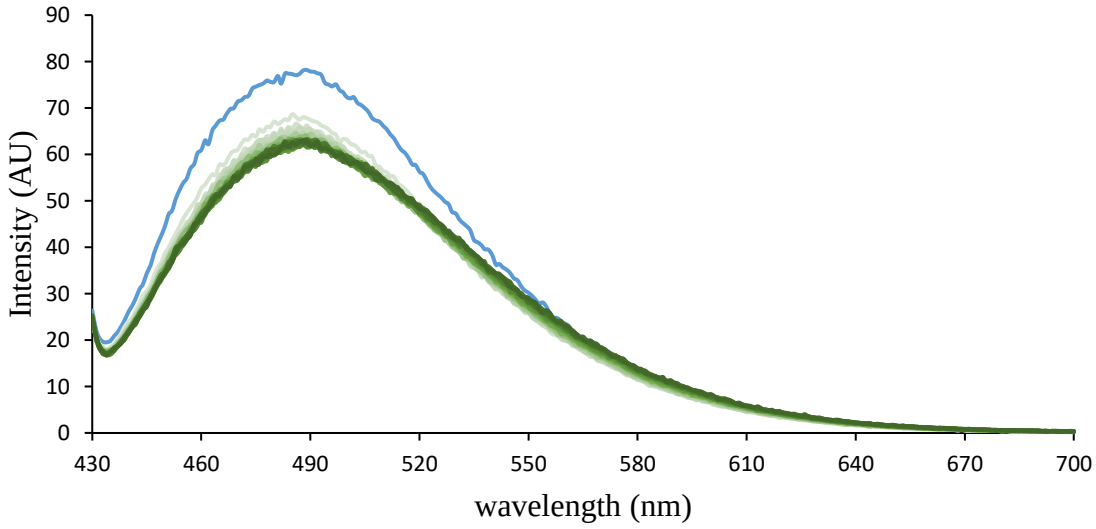

Figure 3.33: *The emission spectra of compound **3.7** (10 µM) (blue) and the addition of $Na_2S_2O_4$ (1mM) (green) in 10 mM phosphate buffer at pH 7.4 over 180 minutes. λ_{ex} = 420 nm. Ex slit width: 5 nm and Em slit with: 5 nm.*

Taking into account that the self-immolation process may not be occurring upon reduction of compound **3.7** to its corresponding amino derivative a change in buffer was taken into consideration to determine if a more basic buffer could increase the rate of self-immolation in the case that either the amine or phenol intermediates formed were somewhat stable (refer to Figure 3.6 in the introduction of this chapter). In the initial stages of the development of self immolative dendrimers bases such as triethylamine were utilised in non-physiological solutions to promote self-immolation likely to deprotonate the phenol intermediate formed.[193] Furthermore, basic solutions consisting of $NaHCO_3$ have also been used in examples where self-immolation of a dendritic unit is required.[208]

In Figure 3.34 a 10mM Tris HCl Buffer solution at pH 8.7 was used and the fluorescence response of compound **3.7** was monitored upon the addition of $Na_2S_2O_4$ (1mM) where the amount of DMSO present in 10 mM Tris HCl Buffer 8.7 was less than 1 %.

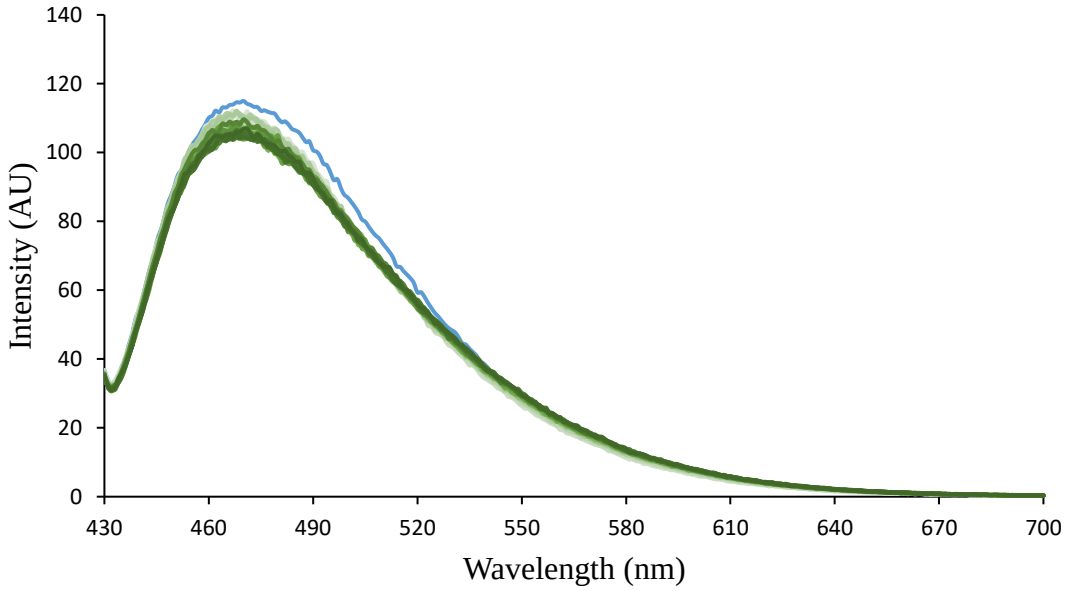

Figure 3.34: *The emission spectra of compound **3.7** (10μM) (blue) and the addition of $Na_2S_2O_4$ (1mM) (green) in 10 mM Tris HCl Buffer 8.7 over 180 minutes. λ_{ex} = 420 nm. Ex slit width: 5 nm and Em slit with: 5 nm.*

As negligible changes in fluorescence were again observed for compound **3.7** in a more basic buffer the solubility of compound **3.7** was brought into question. The percentage of DMSO was varied in order to determine if the compound posed issues of insolubility in the aqueous buffered solutions. In Figure 3.35 the percentage volume of DMSO in 10 mM phosphate buffer at pH 7.4 was increased to 10 % and 20 % where negligible changes were observed similar to when less than 1 % of DMSO was used.

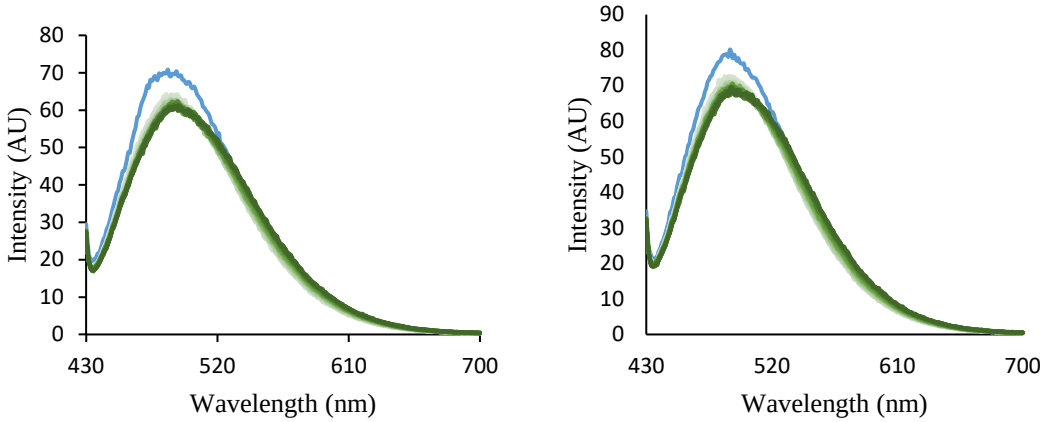

Figure 3.35: *The emission spectra of compound **3.7** (10μM) (blue) and the addition of $Na_2S_2O_4$ (1mM) (green) in 10 mM phosphate buffer at pH 7.4 over 180 minutes. 10 % DMSO (left). 20 % DMSO (right). λ_{ex} = 420 nm. Ex slit width: 5 nm and Em slit with: 5 nm.*

However, upon increasing the volume of DMSO in 10 mM phosphate buffer at pH 7.4 to 50 % significant changes in fluorescence wavelength and fluorescence intensity were observed as seen in Figure 3.36.

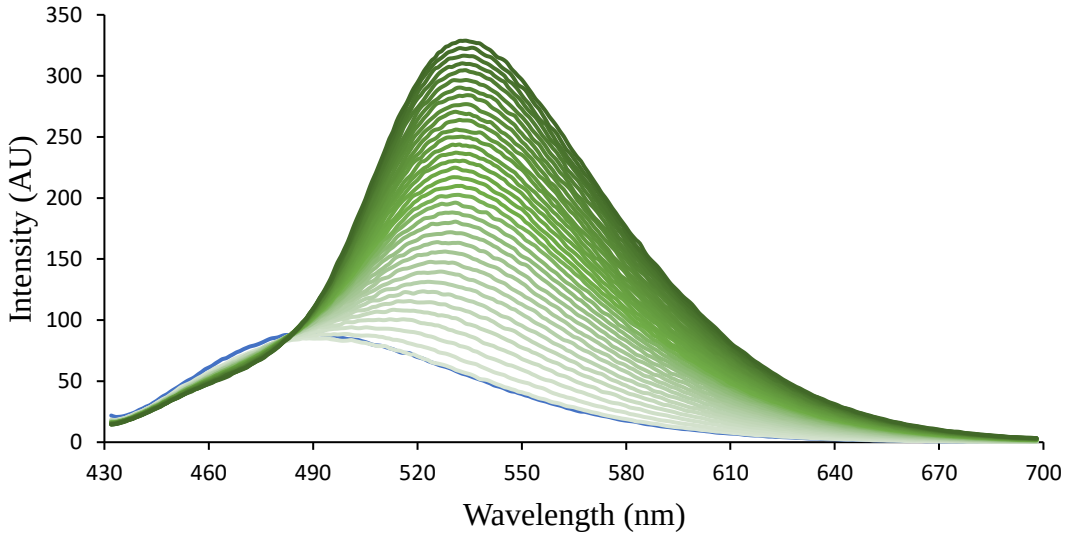

Figure 3.36: *The emission spectra of compound **3.7** (10μM) (blue) and the addition of $Na_2S_2O_4$ (1mM) (green) in 10 mM phosphate buffer at pH 7.4 over 180 minutes. DMSO 50 %. λ_{ex} = 420 nm. Ex slit width: 5 nm and Em slit with: 5 nm.*

From Figure 3.36 it can be seen that compound **3.7** established a significant change in both emission wavelength and fluorescence intensity. Compound **3.7** showed a significant enhancement in the fluorescence intensity at 534 nm by 5.9 - fold and a red shift in the λ_{em} by 43 nm, which was indicative of the release of compound **3.12** from the expected

reduction and self immolative fragmentation of compound **3.7**. Knowing the capability of compound **3.7** to elicit a change in fluorescence upon reaction with $Na_2S_2O_4$ in 10 mM phosphate buffer at pH 7.4 where the volume of DMSO was 50% the same conditions were applied but 10 mM Tris HCl Buffer 8.7 was used in place of PBS (Figure 3.37). The hypothesis was that the more basic pH would increase the rate of immolation and thus the intensity of fluorescence compound **3.12** upon fragmentation. However, this was not observed, whilst there was a significant red shifted change in the λ_{em} wavelength by 43 nm the fluorescence intensity enhancement centred at 528 nm was 2-fold in comparison to the 5.9-fold enhancement observed in PBS 7.4 with 50 % DMSO. This could be due to the more basic media resulting in the deprotonation of the liberated fluorophore compound **3.12**.

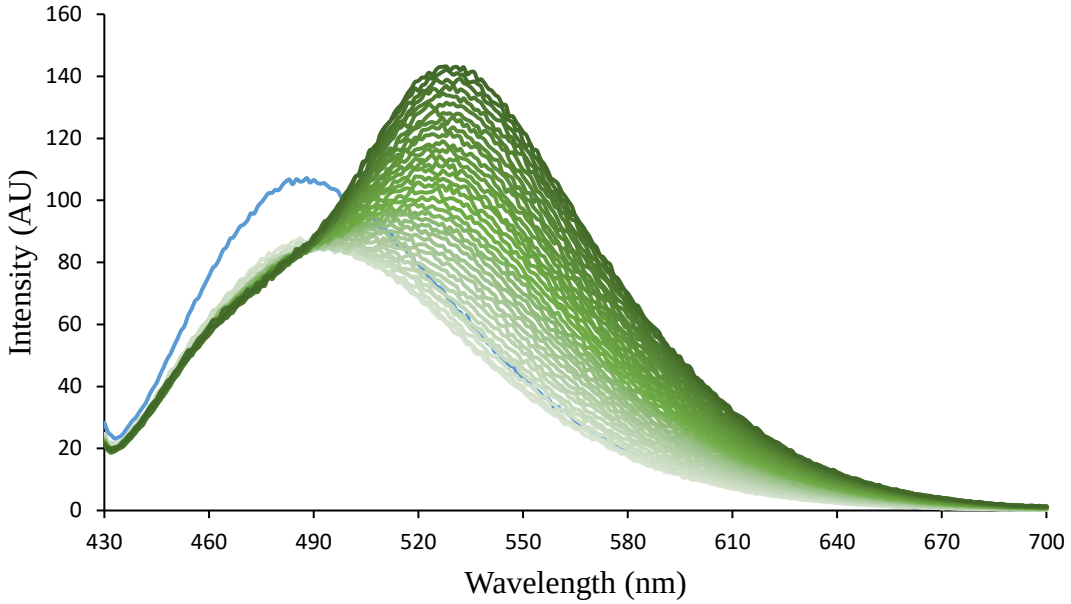

Figure 3.37: *The emission spectra of compound **3.7** (10μM) (blue) and the addition of $Na_2S_2O_4$ (1mM) (green) in Tris HCl Buffer 8.7 over 180 minutes. DMSO 50 %. λ_{ex} = 420 nm. Ex slit width: 5 nm and Em slit with: 5 nm.*

3.5.2 Fluorescence Response of 3.6, 3.8, and 3.9 to Sodium Dithionite

Knowing that a 50 % volume of DMSO in 10 mM phosphate buffer at pH 7.4 elicited the greatest response for compound **3.7** when reacted with $Na_2S_2O_4$ (1 mM), the same conditions were applied to compound **3.6**, **3.8**, and **3.9** to determine if any response could be observed upon the reduction of each compound.

In Figure 3.38 it was observed that no significant changes to the λ_{em} wavelength nor the fluorescence intensity of compound **3.6** occurred. This was likely due to compound **3.6** precipitating out of solution. In comparison to compound **3.7** the head of compound **3.6** consisted of an N-butyl moiety which is lipophilic and would not contribute to the solubility of compound **3.6** in aqueous solution.

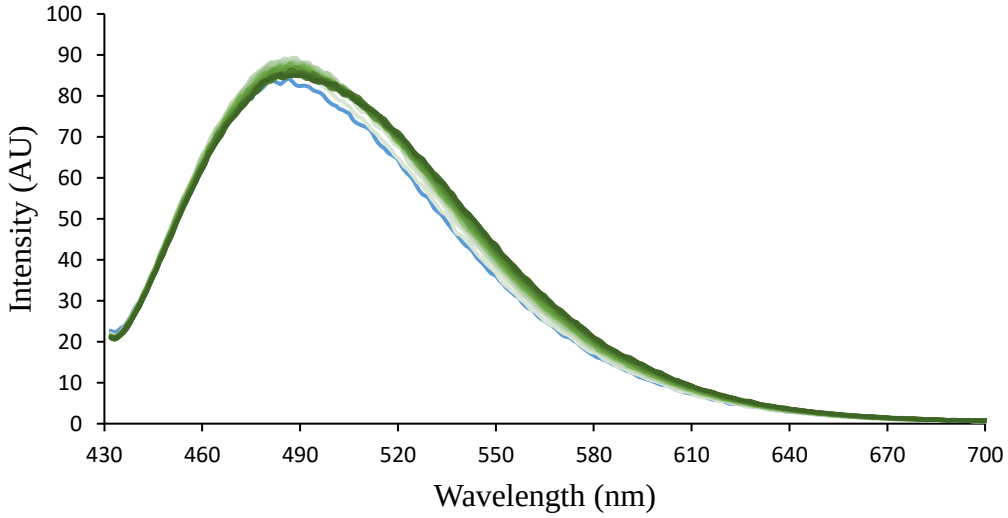

Figure 3.38: *The emission spectra of compound **3.6** (10μM) (blue) and the addition of 1mM $Na_2S_2O_4$ (green) in 10 mM phosphate buffer at pH 7.4 over 180 minutes. DMSO 50 %. λ_{ex} = 420 nm. Ex slit width: 5 nm and Em slit with: 5 nm.*

The two theranostic compounds **3.8** and **3.9** were also evaluated under the same conditions. In Figure 3.39 compound **3.8** showed both a change in λ_{em} wavelength and fluorescence intensity. The λ_{em} was observed to red shift by 48 nm from 484 nm to 532 nm. The fluorescence intensity at 532 nm was also seen to increase by 3.9 - fold. This gave an indication that compound **3.12** was indeed being released upon reduction by $Na_2S_2O_4$.

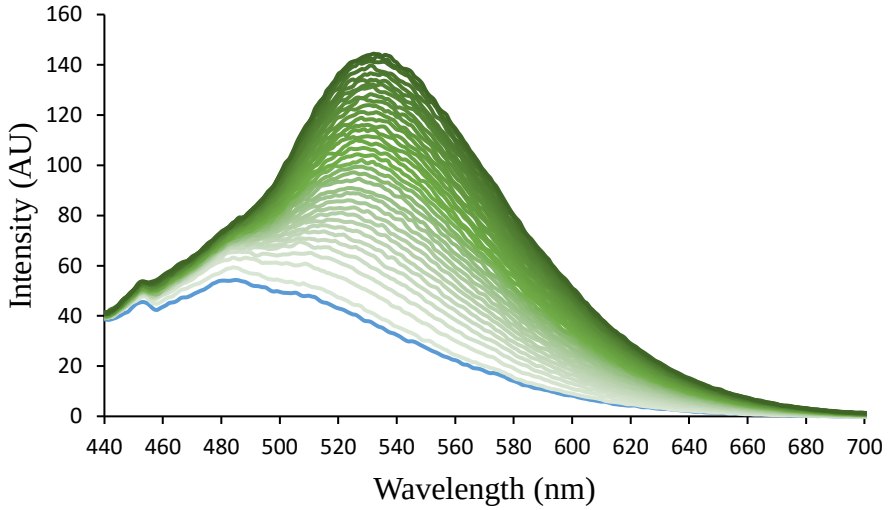

Figure 3.39: *The emission spectra of compound **3.8** (10μM) (blue) and the addition of 1mM $Na_2S_2O_4$ (green) in 10 mM phosphate buffer at pH 7.4 over 180 minutes. DMSO 50 %. λ_{ex} = 420 nm. Ex slit width: 5 nm and Em slit with: 10 nm.*

Compound **3.9** displayed a large 10.9 - fold increase in the fluorescence intensity at 533 nm it also exhibited a 58 nm red shift in the emission wavelength from 475 nm to 533 nm as seen in Figure 3.40. This suggested that the release of compound **3.12** was indeed occurring through the reduction followed by the onset of self immolative fragmentation facilitated by $Na_2S_2O_4$.

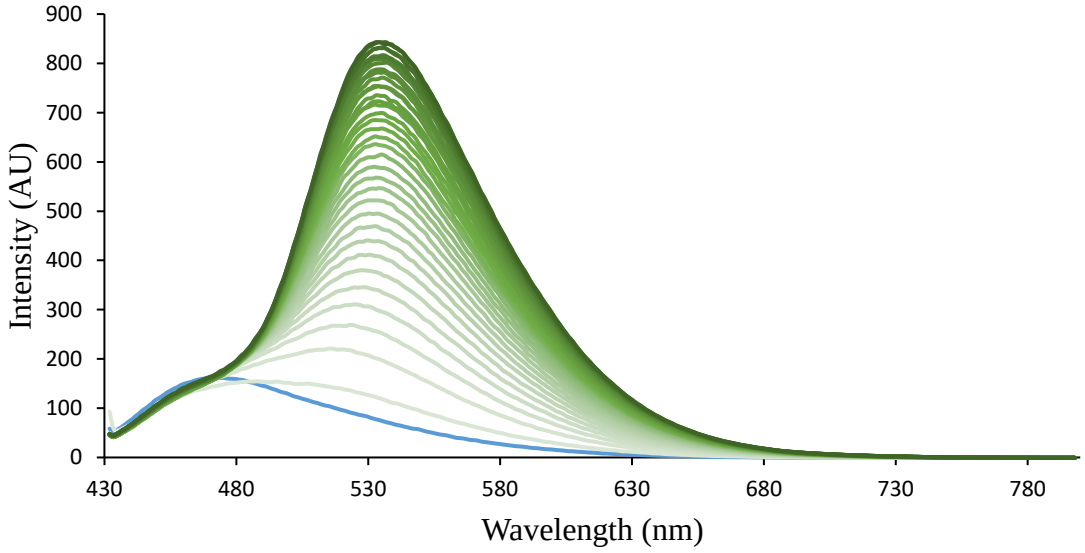

Figure 3.40: *The emission spectra of compound **3.9** (10μM) (blue) and the addition of $Na_2S_2O_4$ (1mM) (green) in 10 mM phosphate buffer at pH 7.4 over 180 minutes. DMSO 50 %. λ_{ex} = 420 nm. Ex slit width: 5 nm and Em slit with: 10 nm.*

Given the fact that there was an increase in the fluorescence intensity observed at approximately 533 nm for compounds **3.7**, **3.8** and, **3.9** was an indicator of the proposed release of compound **3.12**. To be certain that compound **3.12** was released via a reduction event followed by self immolative fragmentation control compound **3.21** was placed under the same conditions. From Figure 3.41 it was observed that no fluorescent enhancement at 533 nm was observed nor was there a change in the emission wavelength which indicated that the reduction by $Na_2S_2O_4$ reducing the 4-nitrobenzyl moiety to a p-aminobenzyl moiety results in self immolative fragmentation of compounds **3.7**, **3.8**, and **3.9** which lead to the release of the fluorophore compound **3.12** and the observed red shifts in wavelengths and fluorescence enhancements at 533 nm.

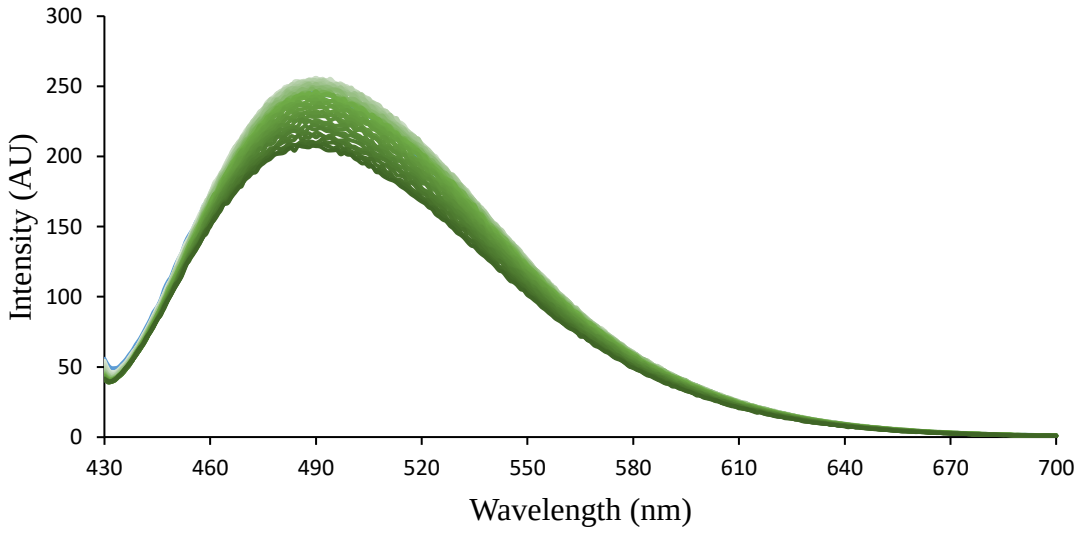

Figure 3.41: *The emission spectra of control compound **3.21** (10μM) (blue) and the addition of $Na_2S_2O_4$ (1mM) (green) in 10 mM phosphate buffer at pH 7.4 over 3 hours. DMSO 50 %. λ_{ex} = 420 nm. Ex slit width: 5 nm and Em slit with: 5 nm.*

3.6 NTR Fluorescence Response of 3.6, 3.7, 3.8, and 3.9.

As reduction and subsequent self-immolation was shown to occur in the presence of $Na_2S_2O_4$ in the case of compounds **3.7**, **3.8**, and **3.9**, it was of interest to determine the applicability of these dendrimers towards the sensing of NTR. As previously mentioned, this is done by incubating each of the compounds with NTR (oxygen sensitive NTR expressed by *E. coli*) and its cofactor NADH. The emission spectrums were measured at pH 7.4 in 10 mM PBS with <1% DMSO as co-solvent in the presence of 500 µM NADH over the course of 24 hours. As solubility has already been shown to be an issue in the case of compound **3.7** we sought to increase the temperature of the following experiments to that of physiological conditions at 36.7 °C.

In the case of Figure 3.42 it was seen that a 26 nm red shift in the emission wavelength was observed for compound **3.6** from 484 nm to 510 nm coupled with a minor enhancement of 1.5-fold in the fluorescence intensity observed at 510 nm. Whilst the red shift is suggestive of the release of fluorophores **3.11** a much greater fold increase in the fluorescence intensity was to be expected as two fluorophores were to be released upon reduction of NTR followed by self immolative fragmentation. The poor response is likely due to the poor solubility of compound **3.6** as noted in the previous section.

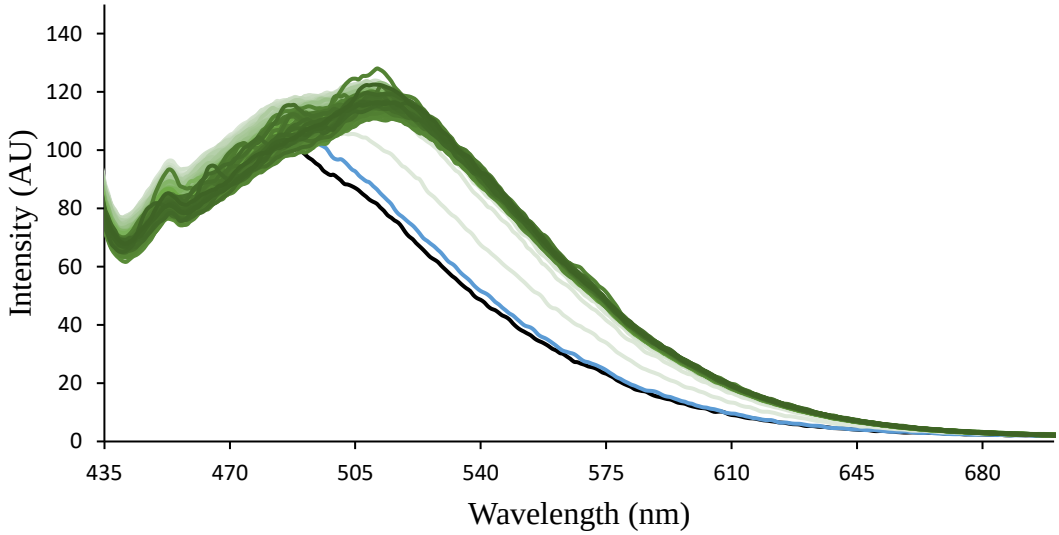

Figure 3.42: *Compound **3.6** (10 µM) in PBS 7.4 (black). Compound **3.6** (10 µM) in PBS 7.4 and NADH (500 µM) (blue). Changes upon the addition of NTR (8 µg mL^{-1}) (green) over 24 hours. λ_{ex} = 420 nm. Ex slit width: 5 nm and Em slit with: 10 nm.*

Compound **3.7** displayed a 32 nm red shift in fluorescence from 507 nm to 539 nm with an initial increase in fluorescence intensity followed by a decrease as it shifted towards

539 nm (Figure 3.43). This was likely due to the insolubility of compound **3.7** as shown in the previous section. Whilst there is some indication that fluorophores **3.12** are released seen by the shift in the λ_{em} wavelength. The absence of an increase in the fluorescence intensity at 539 nm suggests that compound **3.7** lacks solubility and precipitates out of solution.

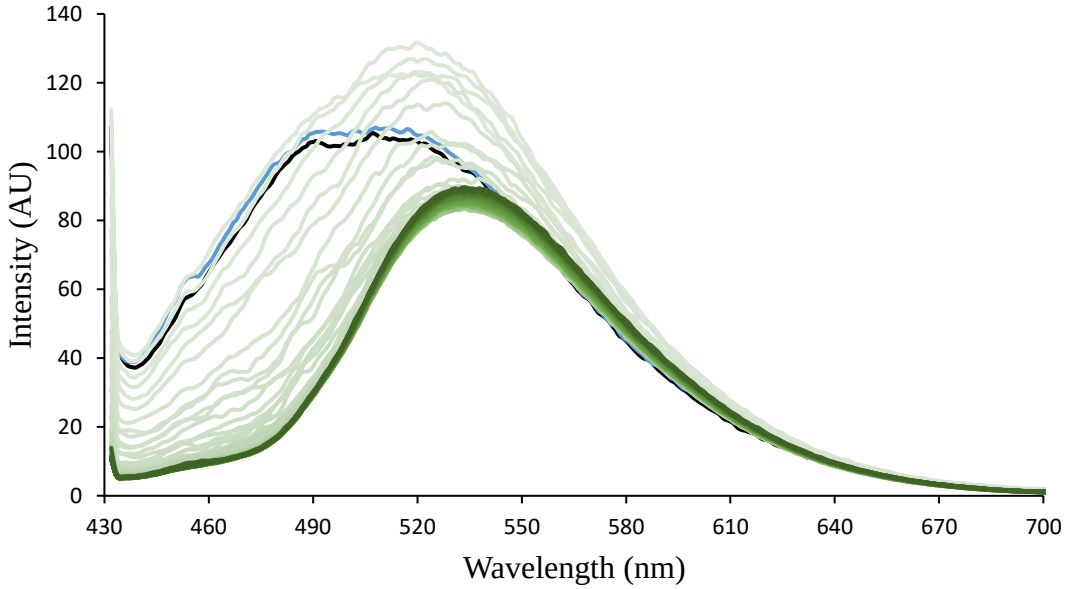

Figure 3.43: *Compound **3.7** (10 µM) in PBS 7.4 (black). Compound **3.7** (10 µM) in PBS 7.4 and NADH (500 µM) (blue). Changes upon the addition of NTR (8 µg mL^{-1}) (green) over 24 hours. λ_{ex} = 420 nm. Ex slit width: 5 nm and Em slit with: 10 nm.*

Compound **3.8** established a ratiometric response towards NTR and NADH seen in Figure 3.44 with a 38 nm red shift in the λ_{em} wavelength from 487 nm to 525 nm. The fluorescence intensity at 487 nm was observed to have decreased by 1.9-fold whilst the fluorescence intensity at 525 nm increased by 2.2-fold. From this it can be suggested that the release of compound **3.12** was occurring upon reduction of compound **3.8** by NTR followed by self immolative fragmentation however the response at 525 nm was not as intense as the response observed in the 50 % DMSO solution with $Na_2S_2O_4$ in Figure 3.39.

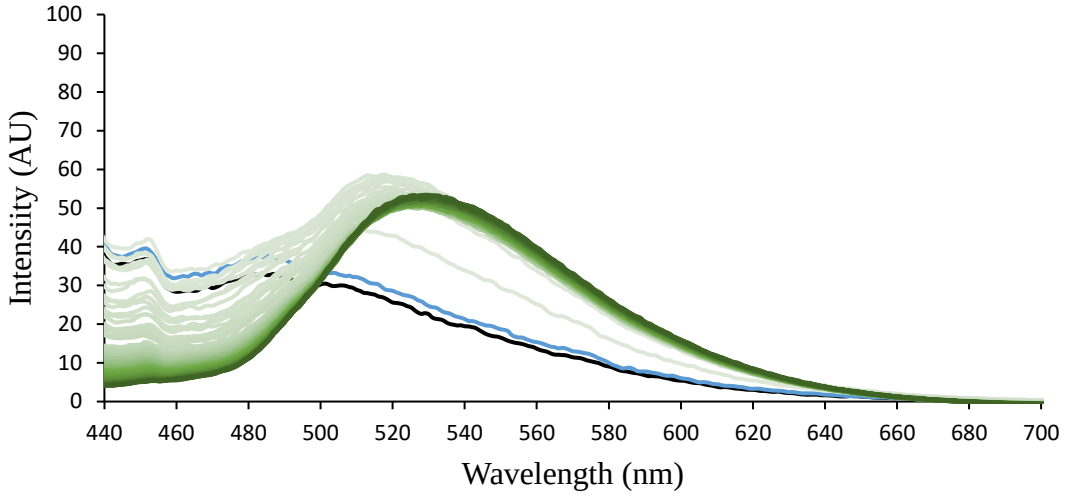

Figure 3.44: *Compound **3.8** (10 µM) in PBS 7.4 (black). Compound **3.8** (10 µM) in PBS 7.4 and 500 µM NADH (blue). Changes upon the addition of NTR (8 µg mL^{-1}) (green) over 24 hours. λ_{ex} = 420 nm. Ex slit width: 5 nm and Em slit with: 10 nm.*

Compound **3.9** elicited the greatest response towards NTR and NADH seen in Figure 3.45. Compound **3.9** had a red shift in the λ_{em} wavelength of 48 nm and resulted in a significant enhancement of 19.2-fold in fluorescence at 540 nm indicative of the release of compound **3.12**.

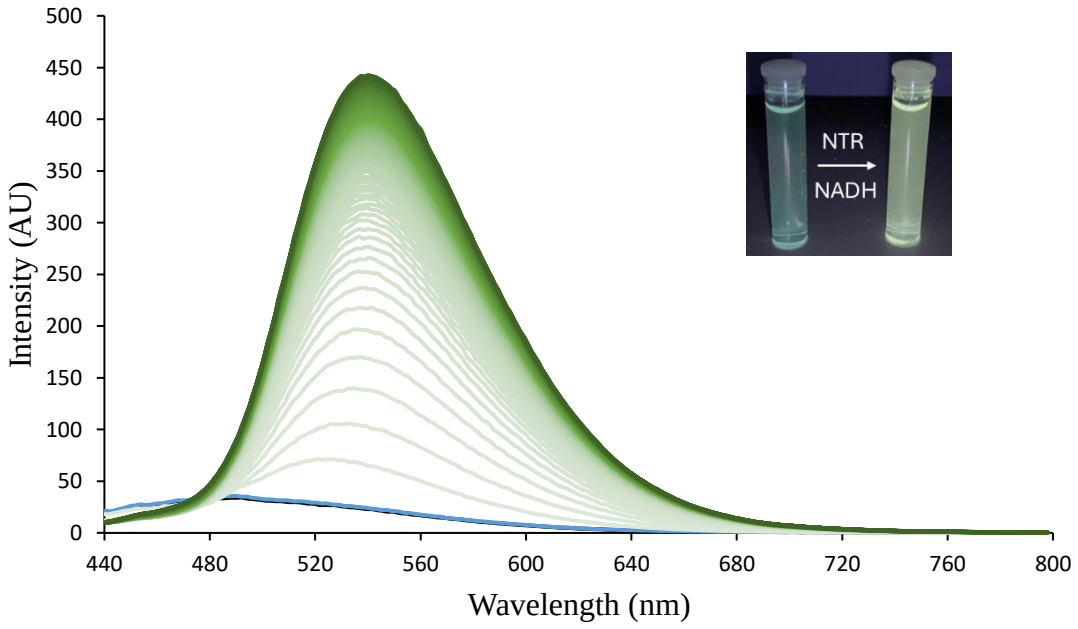

Figure 3.45: *Compound **3.9** (10 µM) in PBS 7.4 (black). Compound **3.9** (10 µM) in PBS 7.4 and NADH (500 µM) (blue). Changes upon the addition of NTR (8 µg mL^{-1}) (green) over 24 hours. λ_{ex} = 420 nm. Insert: Naked eye visual upon the addition of (8 µg mL^{-1} NTR) to compound **3.9** (10 µM) in PBS 7.4 and NADH (500 µM). Ex slit width: 5 nm and Em slit with: 10 nm.*

Compound **3.9** in Figure 3.46 showed a linear increase in fluorescence over 80 minutes and continued to increase as long as 300 minutes where then a plateau in the fluorescence intensity began to form. This fluorescence enhancement was of great noteworthiness as the time required to reach a plateau in fluorescence intensity was much greater than previously cited probes using the same adapter unit in literature as this design avoided the use of 1,2-dimethylethylenediamine spacers (refer to the introduction of this chapter). This can be owed to the fact that the carbamate moieties directly functionalised onto the adapter unit could potentially increase the rate of immolation through their strong electron withdrawing properties. The strong electron withdrawing properties that the imide moiety of the naphthalimide has on the NH on the carbamate, and the *para* positioned sulfonamide has on the NH of the sulfisoxazole **3.19**, is likely to contribute to faster immolation times. This strong withdrawing effect could decrease the pK_a of the phenol intermediate forming the phenolate, which in turn would increase the rate that electrons can cascade through the adapter unit to result in the required 1,4 – elimination.[209, 210] Furthermore, referring to the introduction of this chapter by utilising a 4-nitrobenzyl moiety directly linked to the adapter unit this would lead to an expected increase the rate that the phenol intermediate was formed as no cyclisation was required of a 1,2-dimethylethylenediamine spacer. Ether linkages of this kind have shown rapid release of fluorophores as cited in literature.[116]

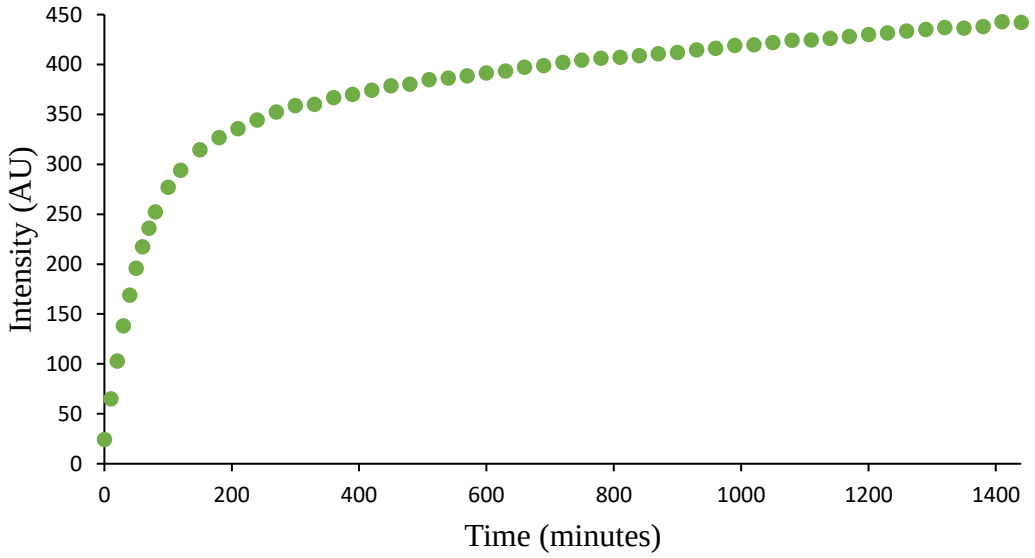

Figure 3.46: *Intensity as a function of time of Compound **3.9** (10 µM) in PBS 7.4 and NADH (500 µM) upon the addition of NTR (8 µg mL^{-1}). λ_{ex} = 420 nm. λ_{em} = 540 nm. Ex slit width: 5 nm and Em slit with: 10 nm. n = 1.*

To validate that the changes in fluorescence observed for compounds **3.6**, **3.7**, **3.8**, and **3.9** were caused by NTR and NADH, a control compound was used. Control compound **3.21** was treated with NTR and NADH under the same conditions as seen in Figure 3.47. A much smaller degree of a 15 nm red shift in the λ_{em} wavelength is observed in control compound **3.21** with a slight 1.3-fold increase observed in the fluorescence intensity at 508 nm.

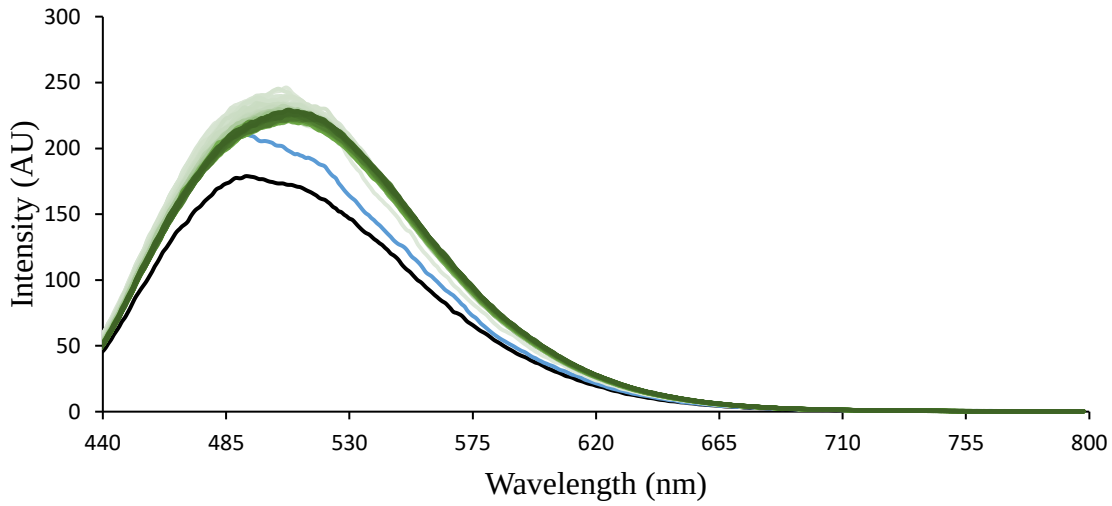

Figure 3.47: *control compound **3.21** (10 μM) in PBS 7.4 (black). 10 μM of control compound **3.21** (10 μM) in PBS 7.4 and NADH (500 μM) (blue). Changes upon the addition of NTR (8 μg mL^{-1}) (green). λ_{ex} = 420 nm. Ex slit width: 5 nm and Em slit with: 10 nm.*

While this result questions the validity of NTR and NADH to react with compound **3.6** and **3.7**, the differences in λ_{em} wavelength observed and changes in the fluorescence intensity in the case of compounds **3.8** and **3.9** differ by a larger degree. Especially in the case of compound **3.9** where a 19.2-fold increase in fluorescence intensity at 540 nm was observed as well as a 48 nm shift in the λ_{em} wavelength which was greater than that of compound **3.6**, **3.7**, **3.8**, and control compound **3.21**.

The naked eye response upon excitation with a UV torch of compounds **3.7**, **3.8**, and **3.9** in Figure 3.48 provided a nice visual as to how compound **3.9** displayed a superior ratiometric fluorescent response in comparison to compounds **3.7** and **3.8**. Compound **3.9** provided a blue to green fluorescence response towards NTR and NADH. Compound **3.7** appeared mildly green fluorescent both before and after treatment with NTR and NADH. Compound **3.8** appeared weakly fluorescent prior to treatment with NTR and NADH with minimal visual changes in fluorescence observed post treatment.

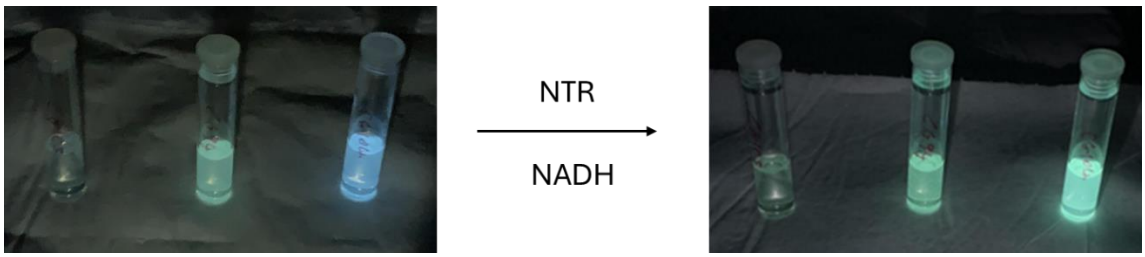

Figure 3.48: *The naked eye response upon excitation with a UV torch of compounds **3.7**, **3.8**, and **3.9**. Left: compounds **3.7** (middle), **3.8** (left), and **3.9** (right) all 40 µM in PBS 7.4. Right: Incubation with NTR (8 µg mL^{-1}) and NADH (500 µM) after 72 hours.*

Considering the above results our efforts were focused on determining the utility of compound **3.9** as a selective probe for NTR.

3.7 Selectivity of 3.9 Towards NTR

To first determine that compound **3.9** is in fact selective for NTR and that the fluorescent response is a consequence of the reduction from **3.9** to its corresponding amine derivative and subsequent self-immolation to release compound **3.12,** dicoumarol can be added to a solution of NTR and NADH thus inhibiting NTR as previously referred to in chapter 2.

In Figure 3.49, NTR (2.5 µg mL^{-1}) and NADH (500 µM) were treated with varying concentrations of dicoumarol prior to the addition of compound **3.9** (10 µM). When looking at the bar chart it was noted that upon introducing 1 eq of dicoumarol to 1 eq of compound **3.9** there was a 1.1 - fold reduction in the fluorescence intensity at 540 nm in comparison to when no dicoumarol was added prior to the introduction of compound **3.9**. Furthermore, 10 eq of dicoumarol to 1 eq of compound **3.9** quenches the fluorescence emission at 540 nm of compound **3.9** by 1.7 - fold.

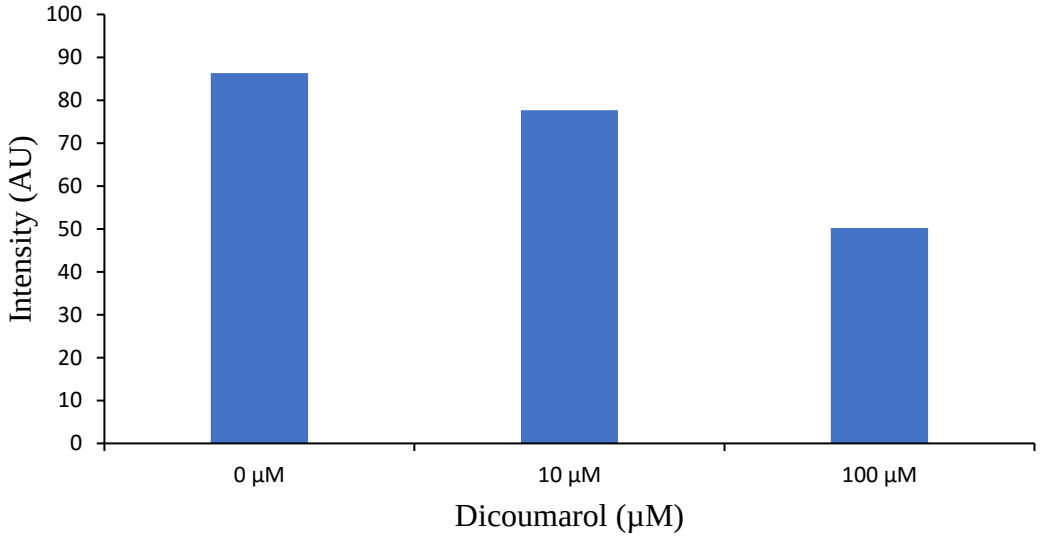

Figure 3.49: *Varying concentrations of dicoumarol in the presence of compound **3.9** (10µM), NTR (2.5 µg mL^{-1}), and NADH (500 µM) over 24 hours. λ_{em} = 540 nm. λ_{ex} = 420 nm. Ex slit width: 5 nm and Em slit with: 10 nm. n = 1.*

To further examine the reaction selectivity of compound **3.9** various potential biological interfering species were examined in Figure 3.50 these include salt NaCl, amino acids such as cysteine and homocysteine, reactive oxygen species H_2O_2, ascorbic acid (vitamin C), glucose, BSA and PBS. Cytochrome C a small soluble electron carrier hemeprotein located in the inner mitochrondrial membrane is included due to its ability to carry out electron transfer. DT-diaphorase another oxidoreductase enzyme known to be upregulated under hypoxic conditions involved in the reduction of quinone moieties to

hydroxyquinones was also included as part of the study. Compound **3.9** (10 µM) and NADH (500 µM) were present with each species to determine if they could reduce compound **3.9** and result in a similar fluorescence response that was achieved by NTR.

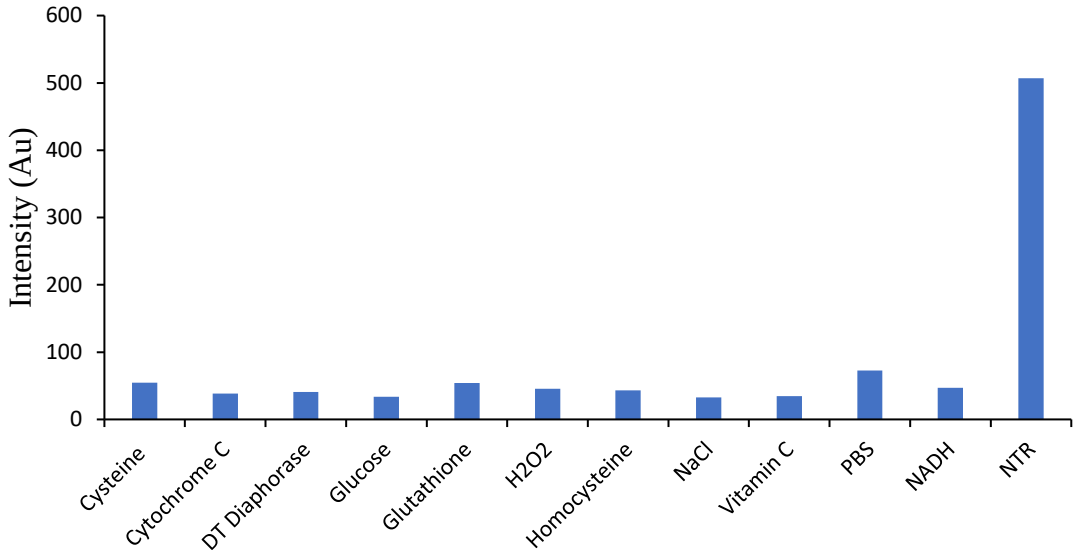

Figure 3.50: *Fluorescent responses of compound **3.9** of (10 µM) and NADH (500 µM) reacted with different kinds of species, NaCl (50 mM), Ascorbic acid (1 mM), cysteine (1 m), cytochrome C (1 µg mL^{-1}), glucose (1 mM), glutathione (1 mM), H_2O_2 (1 mM), homocysteine (1 mM), DT-diaphorase (1 µg mL^{-1}), BSA (10 µg mL^{-1}), PBS (blank NADH absent), NADH (500 µM), Nitroreductase (8 µg mL^{-1}) over 24 hours. λ_{em} = 540 nm. λ_{ex} = 420 nm. Ex slit width: 5 nm and Em slit with: 10 nm. n = 1.*

From Figure 3.49 it can be seen that dicoumarol has an effect on the fluorescence intensity of compound **3.9,** whilst the excess of 100 µM doesn't have the desired inhibition as was achieved for compound **2.13** in chapter 2, the decrease in fluorescence intensity observed would suggest reduction by NTR and NADH was taking place. From Figure **3.50** it can be said that compound **3.9** was indeed selective for NTR as the greatest fluorescence enhancement was elicited from compound **3.9** in the presence of NTR (8 µg mL^{-1}) and NADH (500 µM).

3.8 LCMS Study of 3.9 Towards NTR

The change in fluorescence established by compound **3.9** was suggested to arise from the reduction of the nitro substituent to an amine by NTR and co factor NADH followed by self immolative fragmentation to give compound **3.12** and the release of sulfisoxazole **3.19**. Whilst this can be assumed to be occuring through the use of emission spectra, LCMS can also be used to show that through mass changes and changes in Rt in the UV trace at 254 nm that compound **3.9** results in the release of compound **3.12** and **3.19**. In this study compound **3.9** and compound **3.21** were treated with NTR and NADH for 72 hours to give sufficient time for complete self immolation to occur was provided. In both cases the compound was dissolved in DMSO to give a 3mM concentration and added to 1 mL of PBS solution to result in 50 µM concentration of the compound. The 50 µM of compound was shaken with 8 µg mL^{-1} of NTR and 500 µM NADH for 72 hours and subject to lyophalisation. The components were rediluted with DMSO 250 µL prior to running LCMS samples. This was done in order to obtain peaks of suitable intensity on the UV chromatogram as well as to redisolved any fragments that may have precipitated out of the PBS solution.

In Figure 3.51 a pure trace of compound **3.9** is seen with no treatment of NTR or NADH. One peak can be obsereved in the UV trace at 254nm at an Rt = 39.67 minutes with a corresponding mass of 965 the mass of $[M + H]^+$ for compound **3.9**.

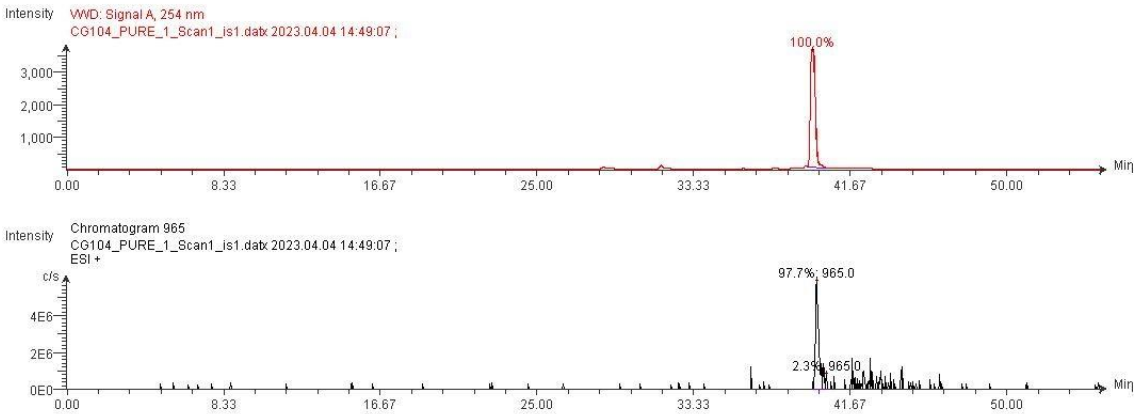

Figure 3.51: *LCMS of compound **3.9**.*

In Figure 3.52 a trace of compound **3.9** was provided after treatment with 8 µg mL^{-1} of NTR and 500 µM NADH for 72 hours.

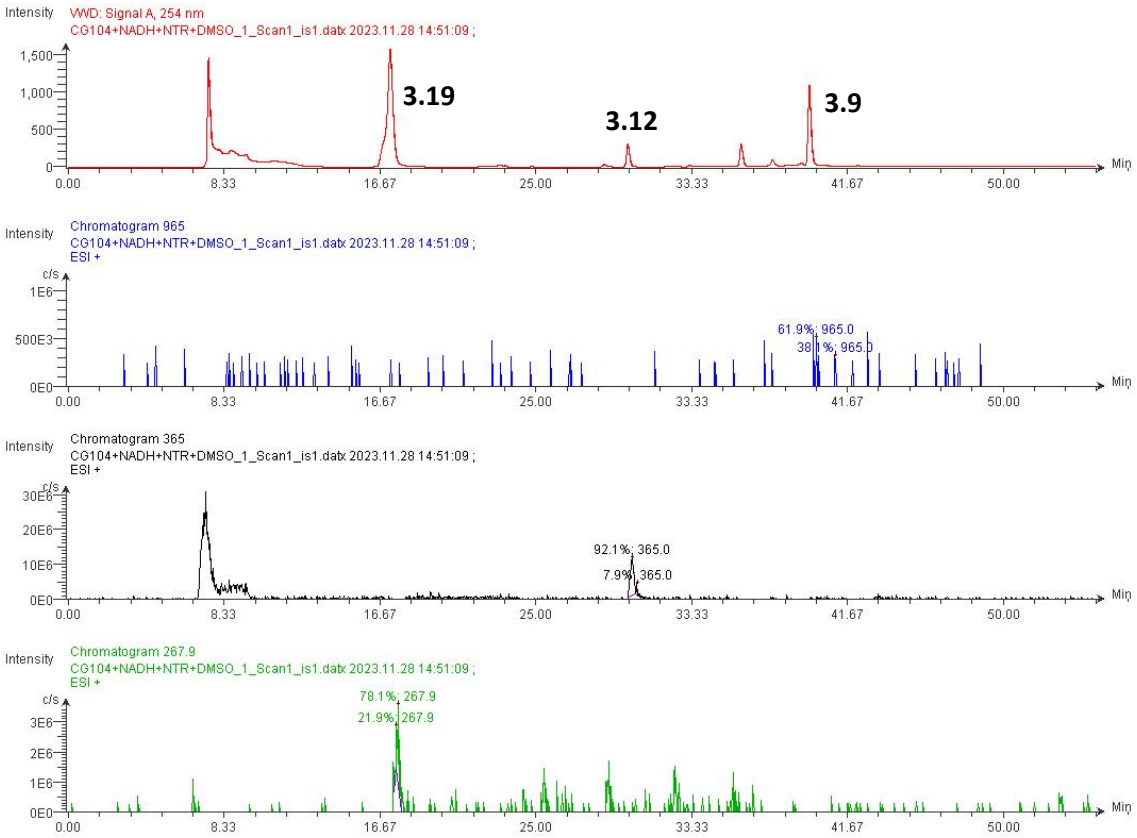

Figure 3.52: *LCMS trace of compound **3.9** after 72-hour treatment with NTR (8 µg mL^{-1}) and NADH (500 µM).*

It can be seen in Figure 3.52 that the peak at Rt = 39.62 minutes shows ionisation at 965 corresponding to the mass of $[M + H]^+$ for compound **3.9**. The peak at Rt = 35.97 minutes was a likely fragment of the self-immolation as no strong ionisation was observed under the peak. At Rt = 29.90 minutes there was ionisation for 365 which corresponds to the mass of $[M + Na]^+$ for compound **3.12**. The peak at Rt = 17.19 minutes shows ionisation for NADH (appendix) and [M + H] of **3.19** at 267.9. Interestingly, there was another peak observed at Rt = 7.47 minutes that corresponds to the mass of compound **3.12** but does not match the ionisation pattern nor the Rt of compound **3.12** (appendix).

In comparison, Figure 3.53, an LCMS trace of control compound **3.21** was treated with NTR and NADH for 72 hours to give sufficient time for complete self-immolation to occur was provided. However, the peaks and masses observed in Figure 3.52 were not observed for compound **3.21** in Figure 3.53. At Rt = 42.07 minutes a mass of 1017 was observed for $[M + Na]^+$ of compound **3.21**. However, no UV peaks at 254 nm were

observed for compound **3.12** except for the peak an Rt = 7.52 minutes as previously explained. The ionisation of **3.19** at 267.9 doesn't appear as strongly under the peak observed at Rt = 17.28 as seen in Figure 3.52.

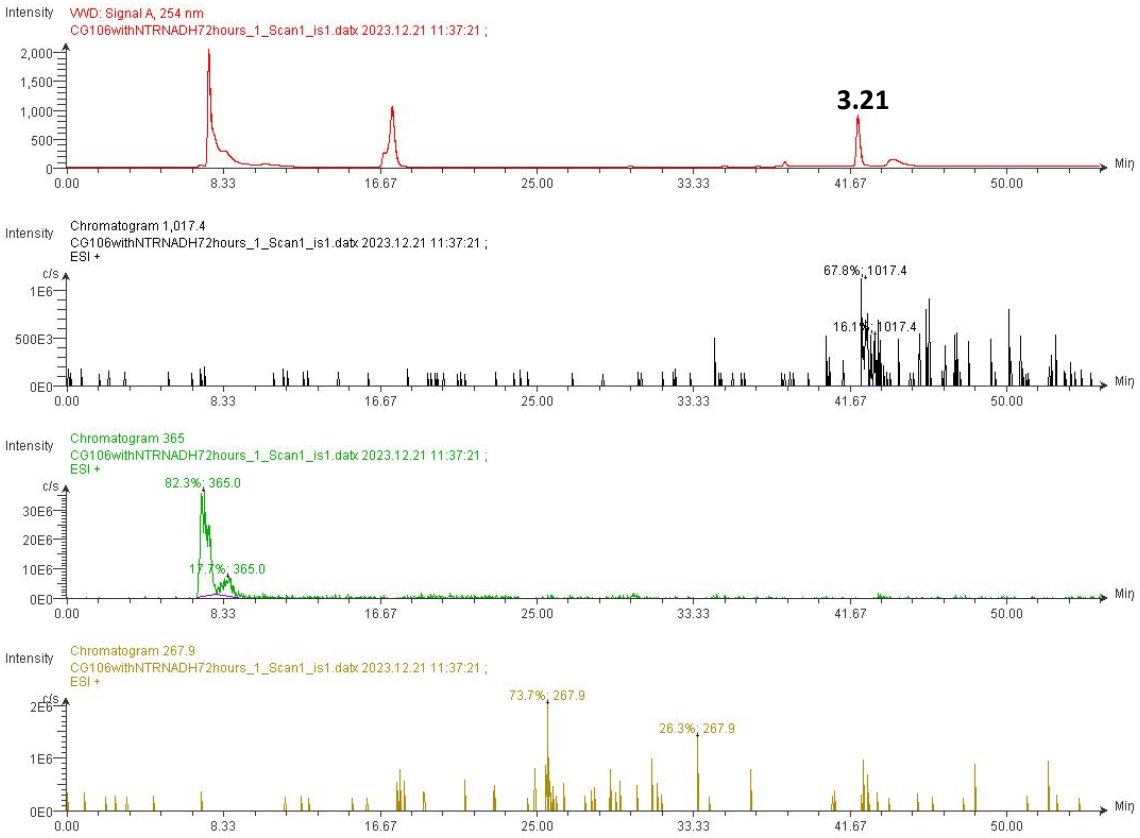

Figure 3.53: *LCMS trace of compound **3.21** after 72 hour treatment with NTR (8 µg mL^{-1}) and NADH (500 µM).*

By comparing both Figure 3.52 and Figure 3.53, it can be confirmed that there was release of compound **3.12** from parent compound **3.9**. There was also some evidence to suggest that the sulfisoxazole **3.19** component was also released due to the ionisation under the peak at Rt = 17.19 minutes for 267.9 in Figure 3.52 not appearing in the chromatogram of compound **3.21** in Figure 3.53.

3.9 Conclusions and Future work

In conclusion, four novel NTR dendrimers **3.6**, **3.7**, **3.8**, and **3.9** were synthesised. All compounds were synthesised in a similar fashion with the use of triphosgene to generate carabamate linkages between the adapter unit and either the fluorophore or drug in use. The success of this synthesis proved the versatility of such a design to modulate the fluorophores or drugs bound to the adapter unit. In the case of **3.6** and **3.7** it was shown that two of the same fluorophores can be added to the same adapter unit such as 4-amino-n-butylnaphthalimides in the case of compound **3.6**, and a more water soluble naphthalimide compound **3.12** in the case of compound **3.7**. More interestingly, for compound **3.8** and **3.9** it was shown that having synthesised intermediate compound **3.17** a wide selection of drugs could be chosen and modulated to their corresponding prodrug through carbamate formation with the adapter unit. amonafide **3.18** and sulfisoxazole **3.19** were chosen as the drug candidates and were carbamate linked to the adapter unit to result in **3.8** and **3.9** respectively.

The desired modulation of the naphthalimide fluorophore was achieved for all compounds **3.6**, **3.7**, **3.8**, and **3.9** in the UV/Vis studies with an expected hypsochromic shift observed in comparison to the expected liberated fluorophore in each case. A blue shift was also observed for all compounds noted by their fluorescence emission spectra. Such changes were expected to be observed upon formation of the carbamate linkage with **3.11** or compound **3.12** due to the quenching of the ICT process.

The sodium dithionite studies showed that solubility in aqueous solution posed a problem for the reduction and immolation in the case of compound **3.7**. However, upon suitable ratio of DMSO:PBS 1:1 a fluorescence response was elicited for compounds **3.7**, **3.8**, and **3.9**. When all compounds were reacted under physiological conditions with NTR with <1% DMSO the greatest response was observed for compound **3.9** towards 8 μg mL^{-1} NTR with a 19.2-fold increase in fluorescence intensity at 540 nm and a 48 nm shift in the λ_{em}. Compound **3.9** also displayed selectivity towards NTR with the turn-on response diminished in the presence of dicoumarol. Compound **3.9** was also shown to be selective for NTR in comparison to other biologically relevant species.

From the fluorescence changes observed for compound **3.9** it was clear that compound **3.12** was released as seen by the significant turn on in fluorescence at 540 nm. To determine that both compound **3.12** and sulfisoxazole **3.19** were released upon the reduction and immolation of compound **3.9** by NTR and NADH, LCMS studies were

carried out whereby compound **3.9** and **3.21** were treated with 8 μg mL^{-1} of NTR and 500 μM NADH for 72 hours. This provided evidence of both compounds **3.12** and **3.19** release. In comparison no release of compound **3.12** by compound **3.21** was observed.

Given the successful fluorescent response of compound **3.9** coupled with the release of sulfisoxazole, future work will be to carry out the sensitivity and selectivity photophysical studies for NTR sensing in triplicate and perform similar studies as seen in chapter 2. Whereby, it would be determined if a blue to green emissive response could be observed through confocal microscopy within *S. aureus* in the presence and absence of dicoumarol. Moreover, the cytotoxicity of compound **3.9** towards bacteria would be determined to understand if bacteria pretreated with dicoumarol are viable as the compound should not be reduced to allow for immolation, in comparison to those bacteria that are not treated with dicoumarol where **3.9** is reduced to release sulfisoxazole. This study would help determine the utility of this dendritic design as a self immolative theranostic for NTR.

As there appeared to be insolubility issues faced with compounds **3.6**, **3.7** and **3.8** with little to no response observed in the presence of NTR and NADH a redesign could be implemented. Whereby, instead of a methyl substituent in the para position of the adapter unit a solubilising moiety could be incorporated as seen in Figure 3.54 which incorporates a PEG moiety to compound **3.8**.[198] If improved solubility results in the desired fluorescence responses the applicability of the theranostic could be assessed towards a cancer cell line under hypoxic conditions.

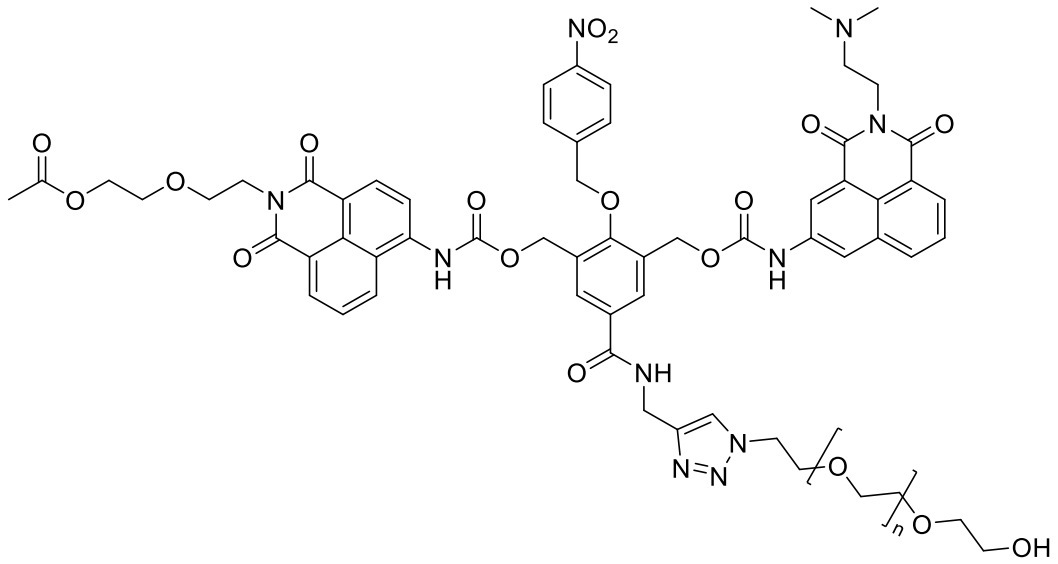

Figure 3.54: *Modification to compound **3.8**.*

Chapter 4

Quaternarised Naphthalimide-Phenanthroline Conjugates as Fluorescent Sensors for NTR

4. Quaternarised Naphthalimide-Phenanthroline Conjugates as Fluorescent Sensors for NTR

4.1 Introduction

As seen in chapter 2, the use of ruthenium polypyridyl complexes have been the focus of intensive research regarding their application as luminophores due to their appealing photophysical properties arising from the ^{3}MLCT excited state, these include luminescence at longer wavelengths and long-lived luminescent lifetimes. Another key characteristic of such complexes is their water solubility with chloride Cl^- counter ions which is a highly advantageous trait for NTR sensing. Nitroaromatic compounds consisting of large degrees of aromaticity often lack solubility in aqueous solution as seen in chapter 3, where generally there is a requirement of DMSO as a co-solvent. In order to overcome this, efforts have been made to introduce solubilising such probes.[164, 211-213]

Quaternarisation of phenanthroline moieties has been exploited in literature as a method to bind DNA without the use of a heavy metals such as Ru(II), but also to achieve water solubility of such ligands that would be rendered insoluble in aqueous solution prior to quaternarisation. Thomas *et al.* showed the ability of quaternarised dppz derivates to bind DNA whilst also establishing water solubility as the nitrate salts seen for compound **4.1** and **4.2** in Figure 4.1.

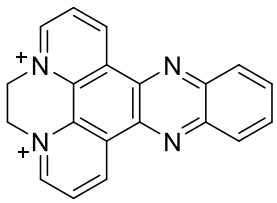

4.1

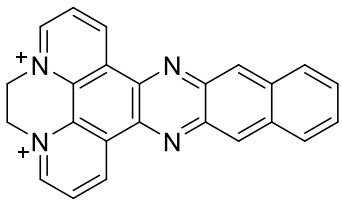

4.2

Figure 4.1: *Structure of compounds **4.1** and **4.2***

Compound **4.1** was shown to have the ability to bind DNA with similar affinity to many metal complexes of dppz with a binding constant of 3.78×10^5 mol^{-1} dm^3, whilst compound **4.2** showed the same capabilities at an order of magnitude greater than that observed for compound **4.1**. Compound **4.2** had a binding constant of 1.33×10^6 mol^{-1} dm^3 and was comparable to $[Ru(phen)_2(dppz)]^{2+}$ in terms of its DNA binding affinity. Interestingly, emission was quenched for both compounds upon binding to DNA. In the case of compound **4.1** emission at approximately 510 nm decreased and was completely quenched upon addition of calf thymus DNA. Whereas, in the case of compound **4.2**

emission is quenched and blue shifted from 637 nm to 625 nm with luminescence still residing as a result of poly(dA).poly(dT) induced enhancement of luminescence due to the poor quenching of ICT by adenine sites in comparison to that of guanine sites.[214, 215]

In terms of naphthalimide conjugates Gunnlaugsson and co-workers synthesised compounds **4.3**, **4.4**, and **4.5** seen in Figure 4.2. In the case of compound **4.3** a hypochromic shift of 25% was noted upon addition of DNA. Compound **4.4**, characterized by a wedged structure, exhibited a comparable alteration of 21%. Notably, compound **4.5** displayed more pronounced hypochromic changes with a substantial 42% reduction in the absorption band centered at 450 nm for the naphthalimide moiety, accompanied by an 11% decrease in the diquaternaristed-centred band at 311 nm. Furthermore, fluorescence emission centred at 530 nm was quenched in order of magnitude of **4.3** > **4.5** > **4.4** upon addition of DNA. Through the use of ethidium bromide displacement assay it was also shown the interaction with **4.5** includes not only intercalation with the 1,8-naphthalimide but also involves a significant extent of groove association facilitated by the wedged arrangement of the diquaternarised moiety.[216]

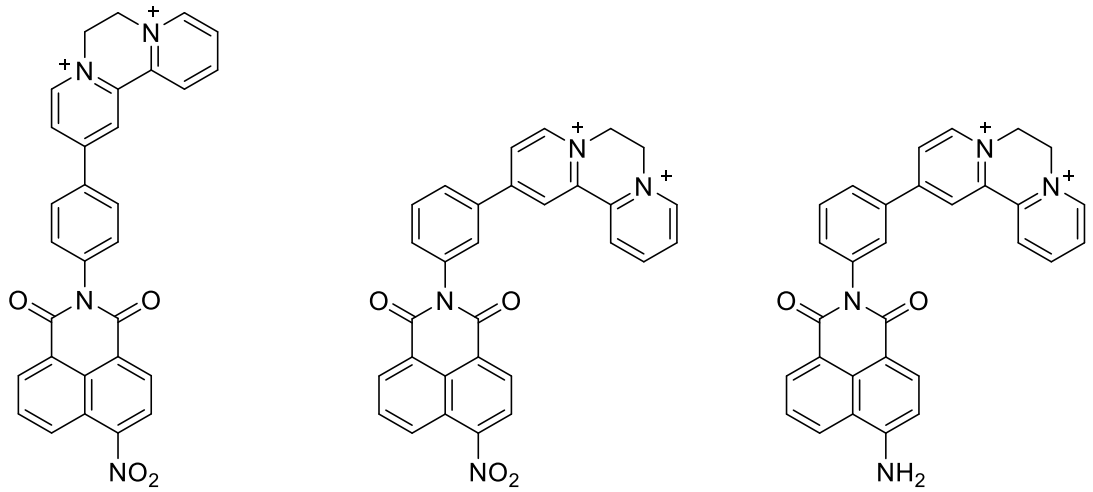

4.3 **4.4** **4.5**

Figure 4.2: *Structures of compounds **4.3**, **4.4**, and **4.5**.*

The applicability of such quaternarised compounds to impose cancer cell death was shown by compound **4.6** in Figure 4.3. Compound **4.6** demonstrated notable DNA affinity with a binding constant of 6.5×10^5 M^{-1}. Its binding occurred through intercalation and was capable of light-mediated cleavage of plasmid DNA through the generation of suggested singlet oxygen. Compound **4.6** also exhibited efficient uptake by diverse malignant cancer cell lines, with subsequent induction of cell death upon photoactivation.[217]

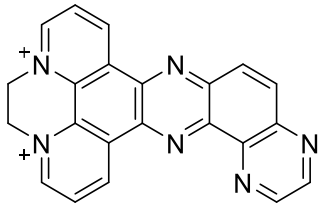

4.6

Figure 4.3: *The structure of compound **4.6**.*

Chapter objectives 4.2

The objective of this chapter was to synthesise compounds **4.7** and **4.8** seen in Figure 4.4 and evaluate their responses towards NTR and NADH.

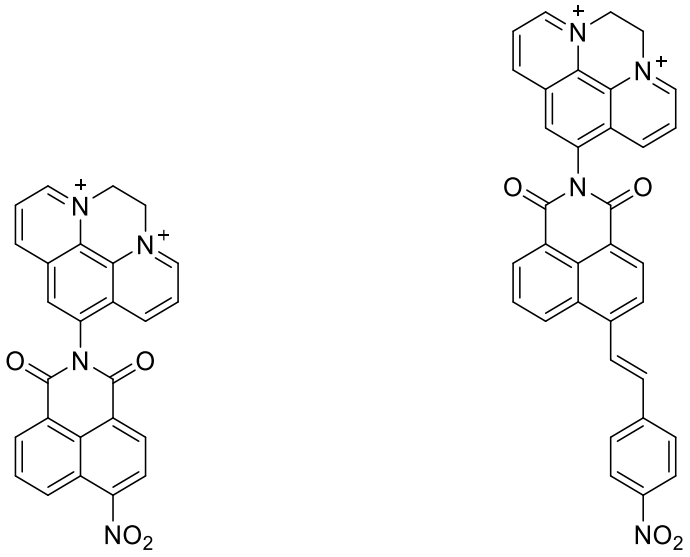

4.7 **4.8**

Figure 4.4: *Structure of compound **4.7** and **4.8**.*

Given the OFF-ON response achieved for compound **2.13** in Chapter 2, which consisted of the naphthalimide-phenanthroline conjugate ligand, it was of interest to synthesise compound **4.7**. It was hypothesized that by quaternizing the ligand itself, it could potentially serve as an OFF-ON fluorescent sensor for NTR, achieving both water solubility of the ligand coupled with potential DNA binding capabilities without the use of the Ru(II) centre. In Figure 4.5 the expected OFF-ON to result in green fluorescence can be seen upon the reduction of compound **4.7** by NTR and NADH to its corresponding amine derivative

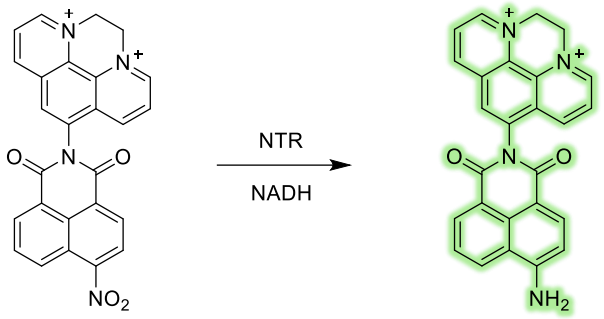

Figure 4.5: *The expected fluorescent response of compound **4.7** in the presence of NTR and NADH.*

Following upon this concept we sought to extend the conjugation of the probe to result in compound **4.8**. In theory the degree of conjugation should result in a greater degree of ICT of the naphthalimide and subsequently red shift the absorption wavelength and emission wavelength of the naphthalimide.[218] In Figure 4.6 the predicted ratiometric fluorescence response from green to orange/red can be seen upon the reduction of compound **4.8** by NTR and NADH.

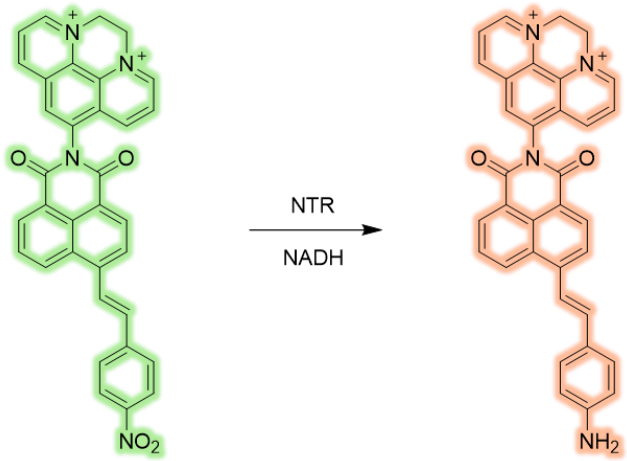

Figure 4.6: *The expected fluorescent response of compound **4.8** in the presence of NTR and NADH.*

4.3 Synthesis and Characterisation of 4.7 and 4.8

4.3.1 Synthesis of 4.7

The synthesis of compound **4.7** firstly involved the condensation of 1,10-phenanthroline-5-amine and 4-nitro-1,8-naphthalic anhydride which can be seen in chapter 2. The amine of the 1,10-phenanthroline-5-amine underwent condensation into the anhydride moiety of the 4-nitro-1,8-naphthalic anhydride in neat AcOH to result in compound **2.25**. **2.25** was then precipitated from AcOH and isolated through filtration in 75 % yield. Compound **2.25** was fully characterised using ^{1}H NMR, ^{13}C NMR, IR, and HRMS. The ^{1}H NMR spectrum (500 MHz, DMSO-d_6) of **2.25** can be seen in the appendix.

Compound **2.25** was refluxed in neat dibromoethane to result in the quaternarisation of the phenanthroline moiety to form compound **4.7** which resulted in a precipitate that was filtered (Scheme 4.1). The filtered solid was washed with water and the filtrate was collected. NH_4PF_6 was added to the filtrate to form a precipitate which was isolated and purified via diethyl ether diffusion to result in the PF_6^- salt of compound **4.7** in a 21 % yield which was then exchanged to the Cl^- salt via amberlite chloride ion exchange resin.

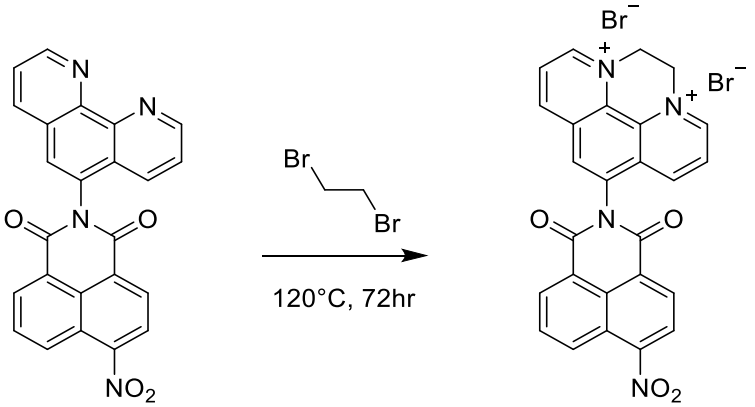

2.25 **4.7**

Scheme 4.1: *Synthesis of compound **4.7**.*

Compound **4.7** was fully characterised using ^{1}H NMR, ^{13}C NMR, H-H COSY, HSQC, HMBC, IR, and HRMS. The ^{1}H NMR spectrum (500 MHz, DMSO-d_6) of **4.7** can be seen in Figure 4.7.

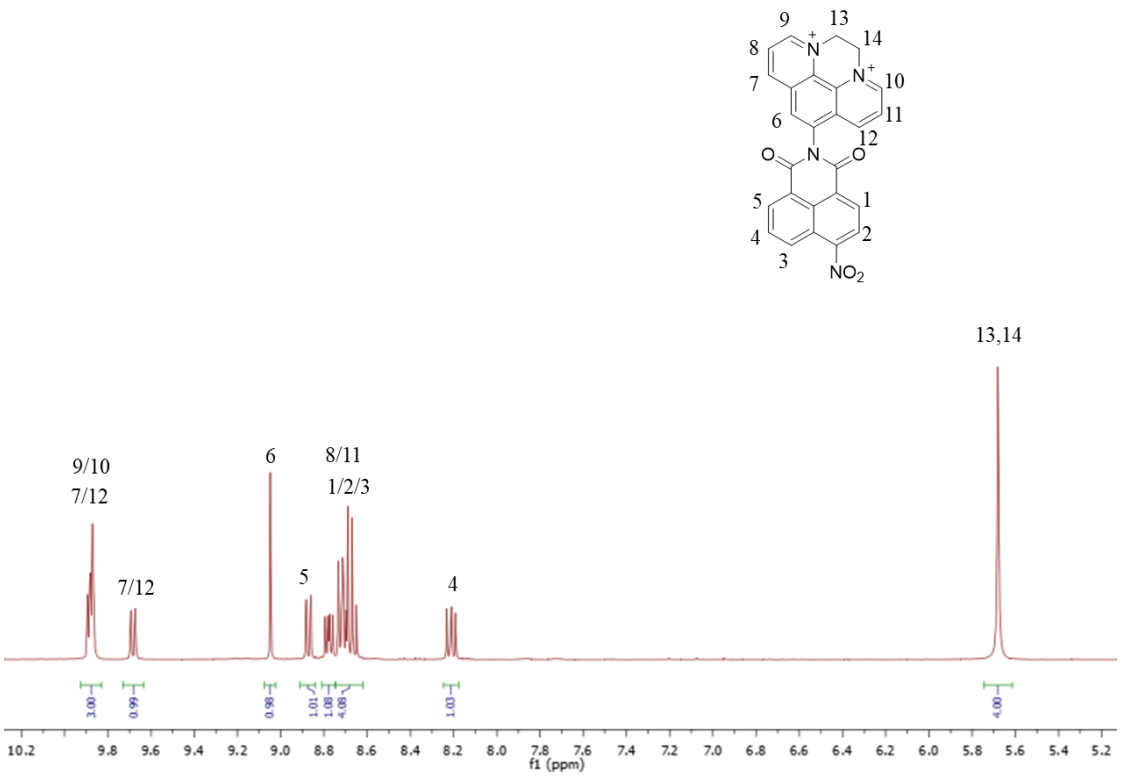

Figure 4.7: *^{1}H NMR of Compound **4.7** in DMSO-d_6.*

From Figure 4.7, the key characteristics of compound **4.7** can be observed with the quaternarisation of the ligand as an ethylene bridge observed as a singlet at 5.68 ppm integrating for 4H. Furthermore, the quaternarisation results in electron deficient quaternary amines which results in significant downfield shifts of the neighbouring protons labelled 9 and 10 to approximately 9.88 ppm. Characteristic triplet of the 4-nitro-naphthalimide moiety can also be observed integrating for 1H at 8.21 ppm.

To further confirm the synthesis of compound **4.7**, HRMS was carried out as seen in Figure 4.8. The HRMS showed ionisation at 448.1166 corresponding to M^+ of compound **4.7**.

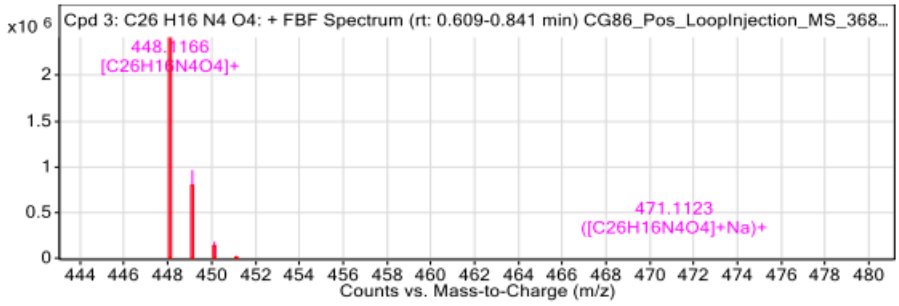

Figure 4.8: *HRMS of compound **4.7**.*

4.3.2 Synthesis of 4.8

The synthesis of compound **4.8** required the synthesis of compound **4.9**, which was synthesised by Wynne, C. via a Heck reaction.[219] Compound **4.9** and 5-amine-1,10-phenanthroline was dissolved in DMF with NEt_3 as a base as well as $Zn(OAc)_2$ as a lewis acid catalyst, and heated to 210°C with the use of microwave chemistry to afford compound **4.10** as a crude mixture seen in Scheme 4.2.

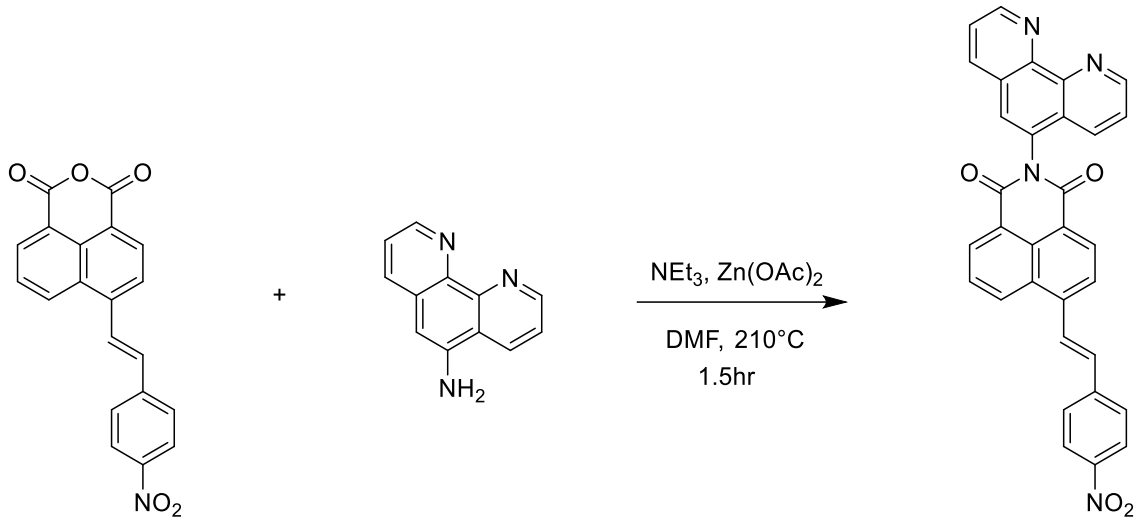

4.9 **4.10**

Scheme 4.2: *Synthesis of compound **4.10**.*

The crude mixture consisting mostly of compound **4.10** was refluxed in neat dibromoethane to afford the quaternarization of the 1,10-phenanthroline moiety to form compound **4.8** which can be seen in Scheme 4.3. A precipitate formed that was filtered and washed with water so that the compound **4.8** was be dissolved in the filtrate. NH_4PF_6 was added to the filtrate to form a precipitate which was isolated and purified via diethyl ether diffusion to result in the PF_6^- salt of compound **4.8** which was exchanged to the Cl^- salt via amberlite chloride ion exchange resin to result in a 11 % yield.

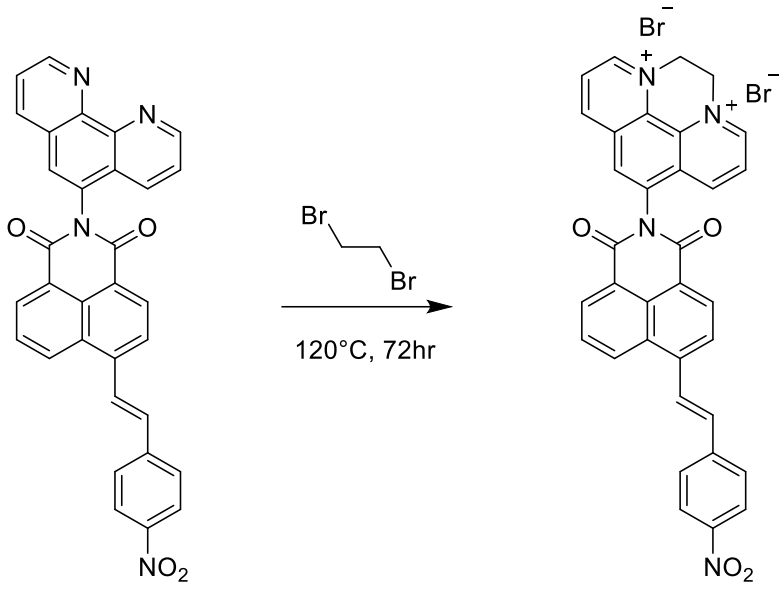

4.10 11% **4.8**

Scheme 4.3: *Synthesis of compound **4.8**.*

Compound **4.8** was fully characterised using ^{1}H NMR, ^{13}C NMR, HSQC, HMBC, IR, and HRMS. The ^{1}H NMR spectrum (500 MHz, DMSO-d$_6$) of **4.8** can be seen in Figure 4.9.

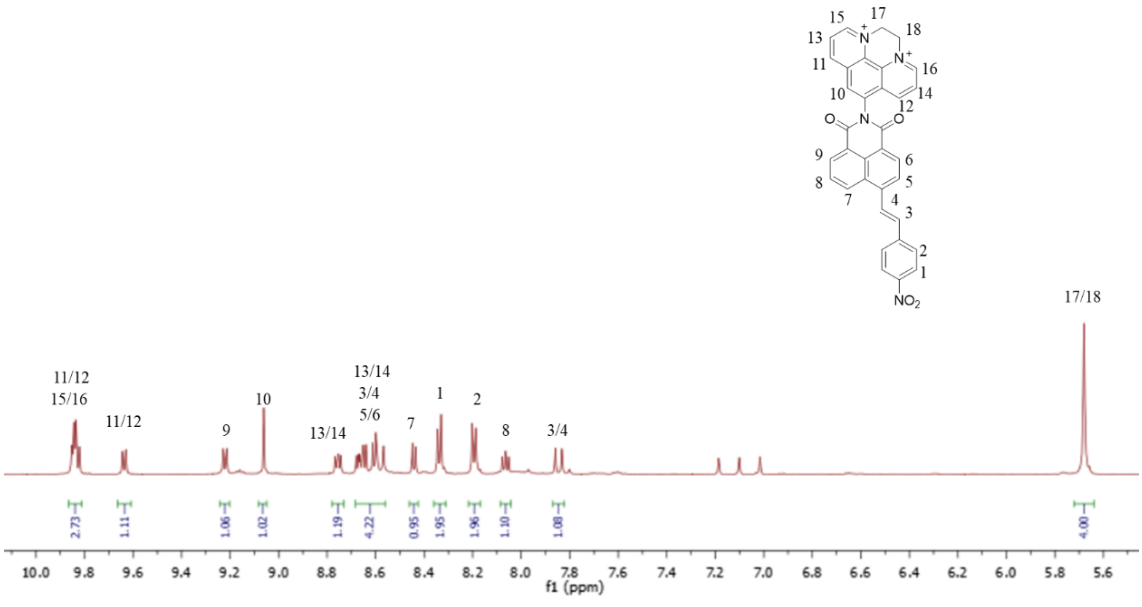

Figure 4.9: *^{1}H NMR of Compound **4.8** in DMSO-d$_6$.*

From Figure 4.9, the key characteristics of compound **4.8** can be observed with the quaternarisation of the ligand as an ethylene bridge observed as a singlet at 5.68 ppm integrating for 4H. Doublets of the 4-nitrobenzene moiety can be seen at 8.34 ppm and 8.19 ppm both integrating for 2H. Clear indication of one of the vinyl protons can be seen

at 7.85 ppm integrating for 1 H as a doublet this is further confirmed by the coupling constant of ***J*** = 16.08 Hz which falls within the range of vinylic trans protons.

To further confirm the synthesis of compound **4.8**, HRMS was carried out as seen in Figure 4.10. The HRMS showed ionisation at 550.1631 corresponding to M^+ of compound **4.8**.

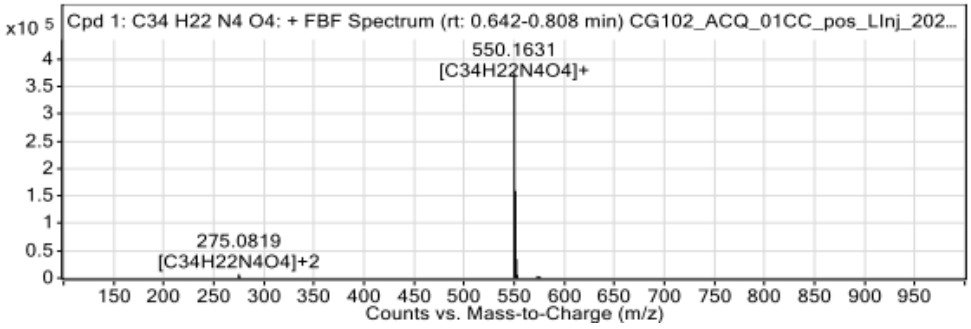

Figure 4.10: *HRMS of compound **4.8**.*

4.4 Photophysical Characterisation of 4.7 and 4.8

With compounds **4.7** and **4.8** successfully synthesised, the next objective was to evaluate their photophysical properties. Spectroscopic measurements were carried out to determine if these compounds had a turn-on fluorescence response in the presence of NTR and NADH.

4.4.1 Absorbance Spectra of 4.7 and 4.8

The absorption spectra of compounds **4.7** and **4.8** were recorded at pH 7.4 in 10 mM phosphate buffer. In general, compound **4.7** was dissolved as a concentrated solution 1.5 mM in PBS to allow for complete dissolution and compound **4.8** was dissolved as a concentrated solution 3 mM in DMSO to allow for complete dissolution. Solutions for analysis were then made by dilution of the stock in 10 mM PBS. At no stage did the total conc. of DMSO go above 1% for compound **4.8**.

The UV/Vis of compound **4.7** can be seen in Figure 4.11. The absorption peak at 357 nm was characteristic of that of the 4-nitro-1,8-naphthalimide moiety, whereas the peak at 301 nm was likely to be representative of the diquaternarised phenanthroline moiety. The

peak that can be seen at 282 nm was the π-π* transitions of either the naphthalimide or phenanthroline moieties.

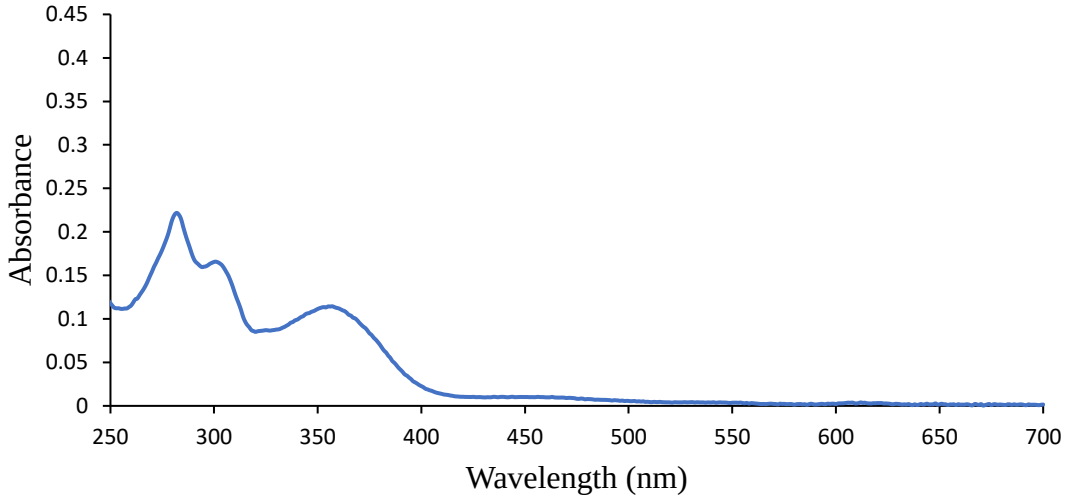

Figure 4.11: *The UV/Vis spectrum of compound **4.7** (10 μM) at pH 7.4 in 10 mM phosphate buffer.*

The UV/Vis spectrum of compound **4.8** can be seen in Figure 4.12. Where in comparison to compound **4.7** in Figure **4.11** it was noted that the naphthalimide absorption band underwent a bathochromic shift to 401 nm. This occurred as a result of the increased degree of conjugation in compound **4.8** resulting in a higher absorption wavelength. Similarly, the peak at 306 nm appeared to be representative of the diquaternarised phenanthroline moiety whilst π-π* transitions of either the naphthalimide or phenanthroline moieties appeared at 285 nm.

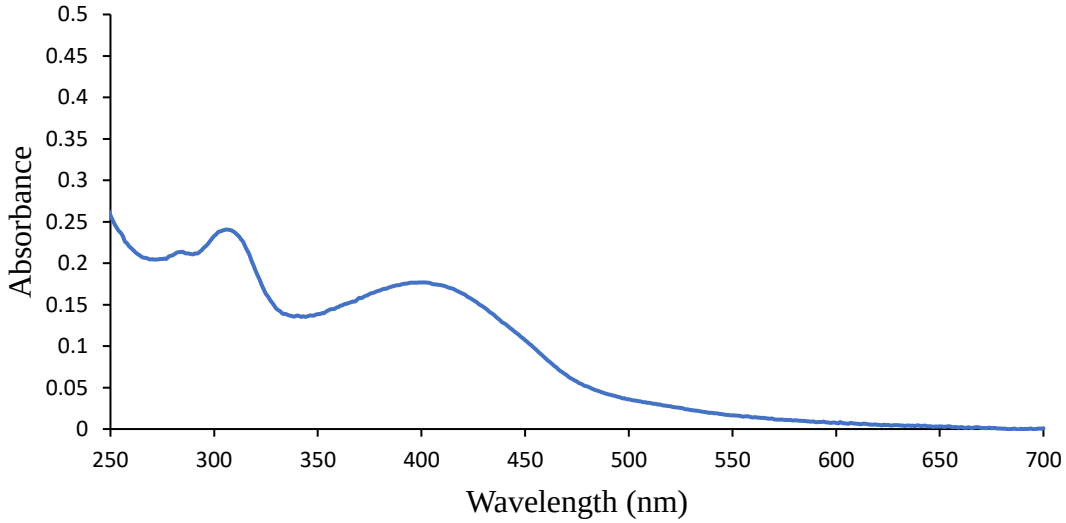

Figure 4.12: *The UV/Vis spectrum of compound **4.8** (10 μM) at pH 7.4 in 10 mM phosphate buffer.*

4.5 Fluorescence Response of 4.7 and 4.8 Towards NTR.

4.5.1 Excitation Spectra of 4.7 and 4.8 Towards NTR.

To determine the wavelength of excitation for compound **4.7** and **4.8** excitation spectra of each compound were obtained. These studies were carried out again at pH 7.4 in 10 mM phosphate buffer.

From Figure 4.13 it was seen that upon the addition of NTR (8 µg mL^{-1}) and NADH 500 µM to compound **4.7** over 30 minutes, the excitation spectra at approximately 455 nm, when measured at emission wavelength 540 nm, showed the greatest enhancements in intensity. Therefore, this wavelength was selected as the excitation wavelength for **4.7**. This was expected to be the wavelength that the amine derivative of **4.7** would be estimated to absorb. This result was anticipated as the wavelength of the amine derivative of 4-amino-1,8-naphthalimides typically absorbs around this wavelength.

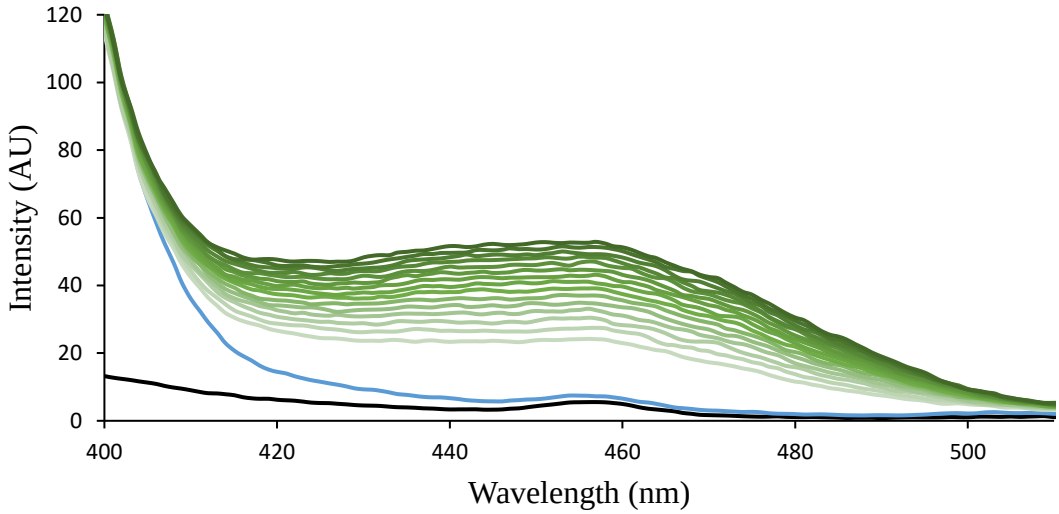

Figure 4.13: *Excitation spectrum of compound **4.7**. Compound **4.7** (10 µM) in PBS (black), Compound **4.7** (10 µM) and NADH (500 µM) (blue). Compound **4.7** changes upon the addition of NTR (8 µg mL^{-1}) and NADH (500 µM) (green) over 30 minutes. λ_{em} = 540 nm*

In Figure 4.14 it was similarly seen that upon the addition of NTR (8 µg mL^{-1}) and NADH 500 µM to compound **4.8** over 30 minutes, the excitation spectra at approximately 450 nm showed the greatest enhancements in intensity which was not expected. Given that the absorbance of compound **4.8** had red shifted in comparison to compound **4.7** in the UV/Vis spectra it was thought that upon reduction of **4.8** to the corresponding amine derivative, the excitation wavelength would be much greater than that of compound **4.7**.

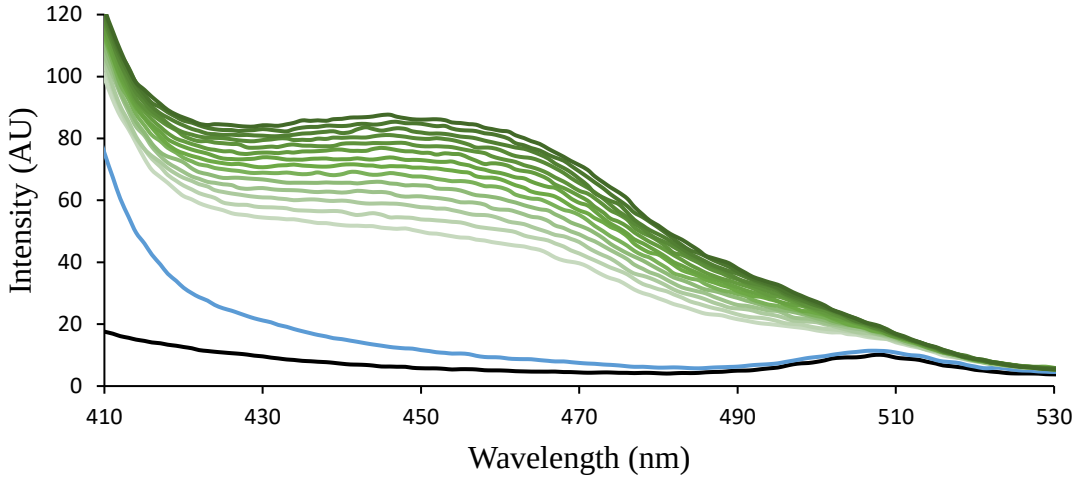

Figure 4.14: *Excitation spectrum of compound **4.8**. Compound **4.8** (10 µM) in PBS (black), Compound **4.8** (10 µM) and NADH (500 µM) (blue). Compound **4.8** changes upon the addition of NTR (8 µg mL^{-1}) and NADH (500 µM) (green) over 30 minutes. λ_{em} = 610 nm.*

Given that the excitation wavelengths of both compounds **4.7** and **4.8** were known the fluorescence response of each was monitored in response to NTR and co-factor NADH.

4.5.2 Emission Spectra of 4.7 and 4.8 Towards NTR.

The emission spectra were measured at pH 7.4 in 10 mM PBS, in the case of compound **4.7** no pre dissolution with DMSO was required. However, for compound **4.8** < 1% DMSO as co-solvent was required. In both cases NTR (4 µg mL^{-1}) and NADH (500 µM) was added to the compound (10 µM) and the emission spectra were recorded over 120 minutes.

In Figure 4.15 it was noted that compound **4.7** established an OFF-ON response with a 12.3-fold increase in fluorescence intensity at 530 nm upon the addition of 4 µg mL^{-1} of NTR.

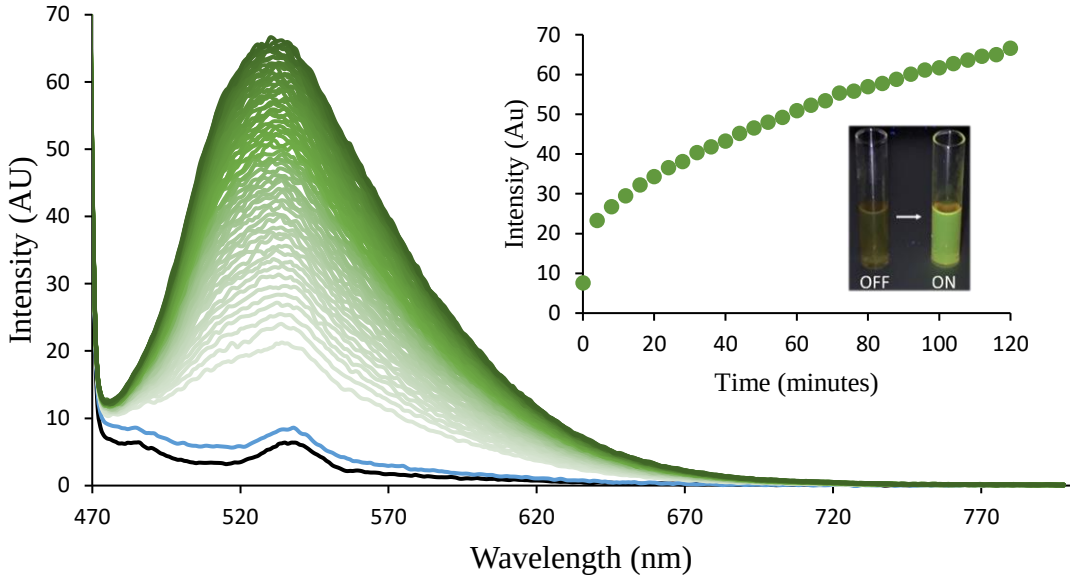

Figure 4.15: *Emission spectrum of compound **4.7**. Compound **4.7** (10 µM) in PBS (black), Compound **4.7** (10 µM) and NADH (500 µM) (blue). Compound **4.7** changes upon the addition of NTR (4 µg mL^{-1}) and NADH (500 µM) (green) over 120 minutes. λ_{em} = 530 nm. λ_{ex}= 455 nm. (Insert) Compound **4.7** (1:4 DMSO: PBS) (left) sodium dithionite (right) showing the expected naked eye response under reducing conditions (5 mM $Na_2S_2O_4$). Ex slit width: 10 nm and Em slit width: 10 nm. n = 1.*

Similarly, in Figure 4.16 an OFF-ON response was also established for compound **4.8** at 529 nm with a fluorescence intensity increase of 4.8-fold.

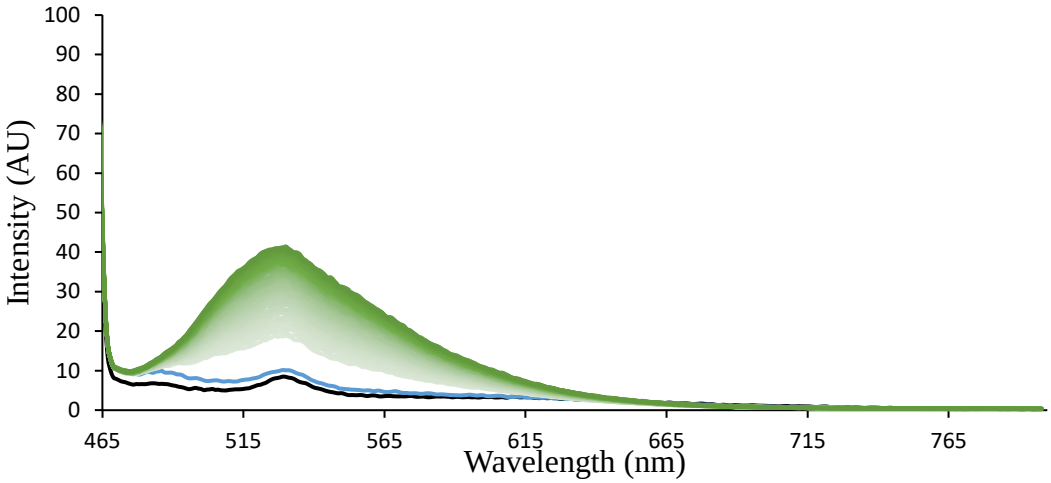

Figure 4.16: *Emission spectrum of compound **4.8**. Compound **4.8** (10 µM) in PBS (black), Compound **4.8** (10 µM) and NADH (500 µM) (blue). Compound **4.8** changes upon the addition of NTR (4 µg mL^{-1}) and NADH (500 µM) (green) over 120 minutes. λ_{ex}= 450 nm. Ex slit width: 10 nm and Em slit width: 10 nm. n = 1.*

As compound **4.7** provided a greater fold increase of 12.3 - fold at 530 nm in comparison to compound **4.8** it was used for further studies to determine its sensitivity and selectivity towards NTR. Unfortunately, the expected red shift in the emission wavelength of compound **4.8** did not occur. This could be in part due to solvatochromism characteristic of naphthalimide fluorophores.[218]

4.6 Sensitivity of Compound 4.7 Towards NTR.

Considering the above results our efforts were focused on determining the utility of compound **4.7** as both a sensitive and selective probe for NTR. To evaluate compounds **4.7** sensitivity towards NTR we analysed the turn on response towards varying concentrations of NTR. From Figure 4.17 it was seen that compound **4.7** was sensitive to increasing concentrations of NTR from 0.5 µg mL^{-1} to 8 µg mL^{-1} over the course of 120 minutes. An 18.8 - fold increase in the fluorescence intensity was observed at 530 nm when compound **4.7** was treated with 8 µg mL^{-1} NTR and even at lower concentrations of 0.5 µg mL^{-1} NTR there was a 3 - fold increase in the fluorescence intensity.

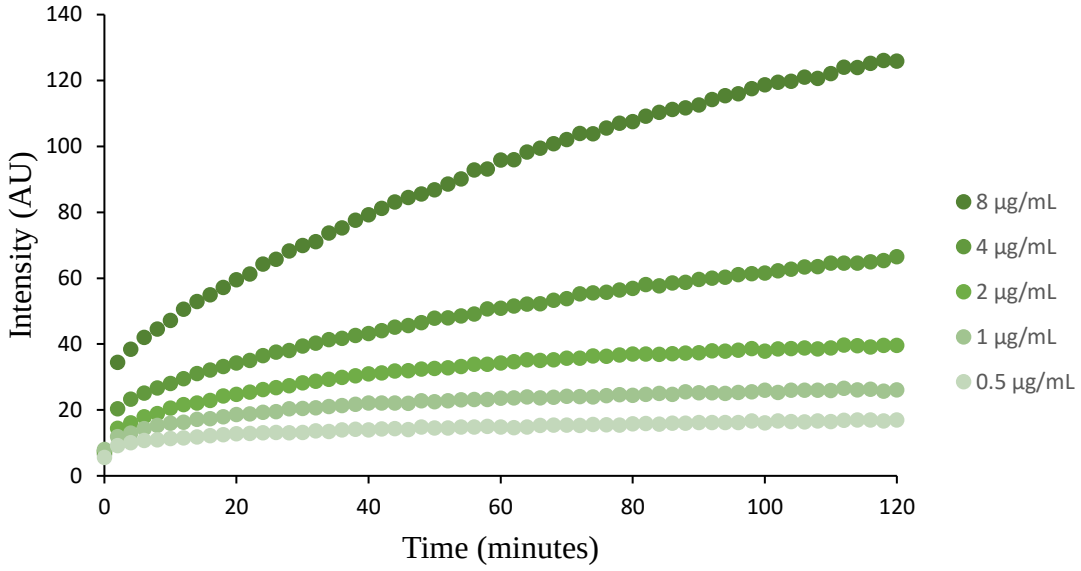

Figure 4.17: *Compound **4.7** treated with varying concentrations of NTR (0.5 µg mL^{-1} to 8 µg mL^{-1}) and NADH (500µM) over the course of 120 minutes. λ_{em} = 530 nm. λ_{ex}= 455 nm. Ex slit width: 10 nm and Em slit width: 10 nm. n = 1.*

Given the sensitivity of compound **4.7** towards NTR the selectivity of the compound was determined to confirm NTR was solely responsible for the OFF-ON response observed.

4.7 Selectivity of Compound 4.7 Towards NTR.

To first determine that compound **4.7** was in fact selective for NTR and that the fluorescent response is a consequence of the reduction of **4.7** to its corresponding amine derivative dicoumarol can be added to a solution of NTR and NADH thus inhibiting NTR as referred to in previous chapters.

In Figure 4.18, NTR (2.5 µg mL^{-1}) and NADH (500 µM) were treated with varying concentrations of dicoumarol prior to the addition of compound **4.7** (10 µM). When looking at the bar chart it was observed that upon introducing 1 eq of dicoumarol to 1 eq of compound **4.7** there was a 1.6-fold reduction in the fluorescence intensity in comparison to when no dicoumarol was added prior to the introduction of compound **4.7**. Furthermore, 10 eq of dicoumarol to 1 eq of compound **4.7** quenches the fluorescence emission of compound 7 by 3.2-fold. The decrease in fluorescence intensity observed from 0 µM to 100µM of dicoumarol would suggest reduction of compound **4.7** by NTR and NADH was indeed taking place.

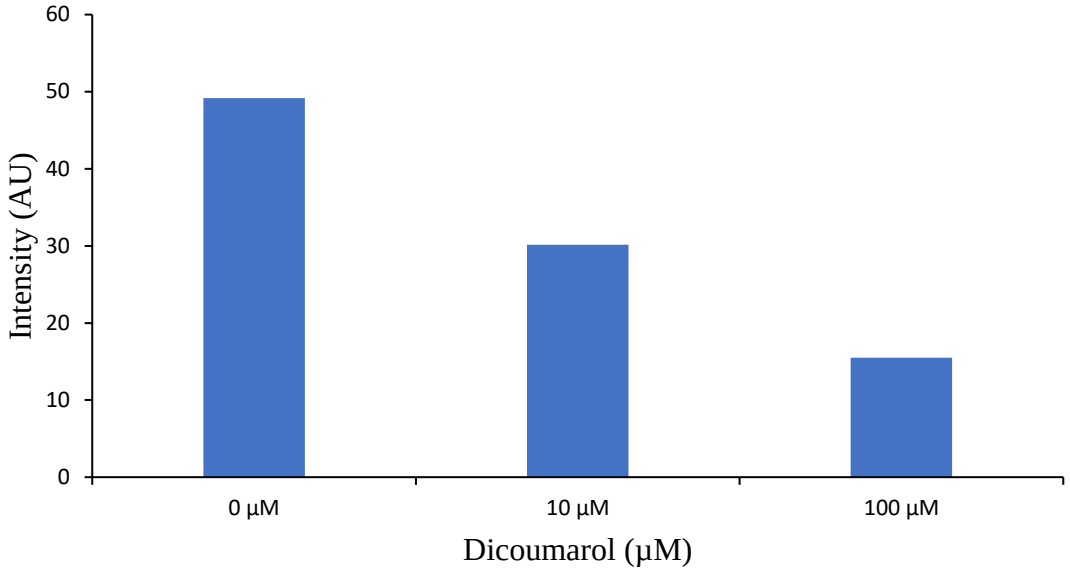

Figure 4.18: *Varying concentrations of dicoumarol in the presence of compound* ***4.7*** *(10µM), NTR (2.5 µg mL^{-1}), and NADH (500 µM). λ_{em} = 530 nm. λ_{ex} = 455 nm. Ex slit width: 10 nm and Em slit width: 10 nm. n = 1.*

Compound **4.7** selectivity was further tested in the presence of various potential biological interfering species which can be seen in Figure 4.19 these include salt NaCl, amino acids such as cysteine and homocysteine, reactive oxygen species H_2O_2, ascorbic acid (vitamin C), glucose, BSA and PBS. Cytochrome C a small soluble electron carrier hemeprotein located in the inner mitochrondrial membrane, and DT-diaphorase another oxidoreductase enzyme known to be upregulated under hypoxia. Compound **4.7** (10 µM) and NADH (500 µM) were present with each species to determine if they could reduce compound **4.7** and result in a similar fluorescence response that was achieved by NTR.

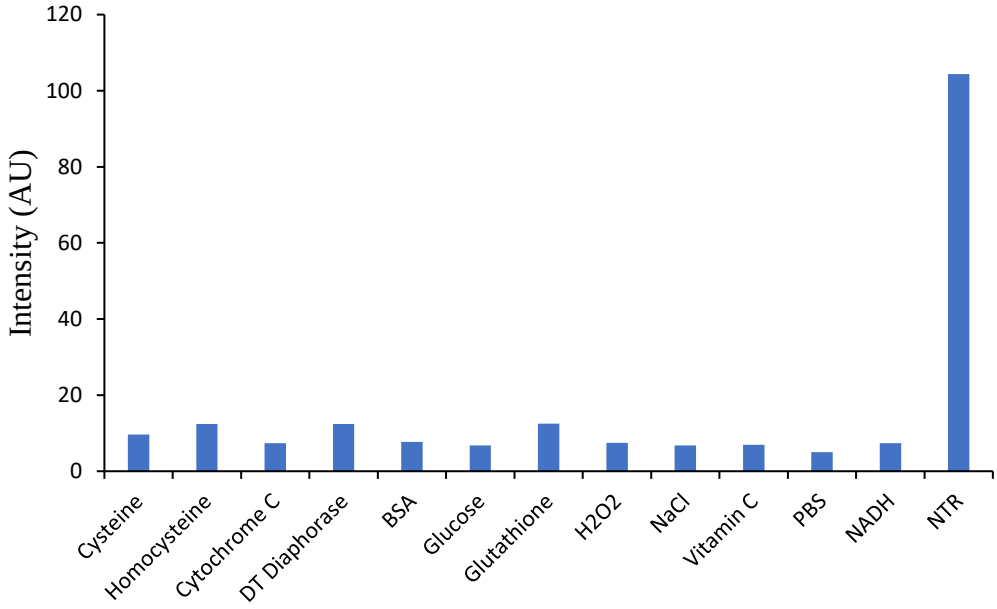

Figure 4.19: *Fluorescent responses compound **4.7** (10 µM) and NADH (500 µM) reacted with different kinds of species, NaCl (50 mM), Ascorbic acid (1 mM), cysteine (1 m), cytochrome C (1 µg mL^{-1}), glucose (1 mM), glutathione (1 mM), H_2O_2 (1 mM), homocysteine (1 mM), DT-diaphorase (1 µg mL^{-1}), BSA (10 µg mL^{-1}), PBS (blank NADH absent), NADH (500 µM), Nitroreductase (8 µg mL^{-1}). λ_{em} = 530 nm. λ_{ex} = 455 nm. Ex slit width: 10 nm and Em slit width: 10 nm. n = 1.*

In Figure 4.19 the greatest fluorescence enhancement was elicited from compound **4.7** in the presence of NTR (8 µg mL^{-1}) and NADH (500 µM). Therefore, it can be said that compound **4.7** was deemed selective for NTR amongst other biologically relevant species. Given the sensitivity and selectivity of compound **4.7** another way to determine that the reduction event in the presence of NTR and NADH was responsible for the observed OFF-ON fluorescence response was to carry out an LCMS study.

4.8 LCMS Study of 4.7 Towards NTR

The increases in fluorescence intensity from compound **4.7** was expected to be as a result of the reduction of the nitro substituent to an amine by NTR and co factor NADH. Whilst this was suggested from the emission spectra the LCMS can also be taken advantage of to show that through mass changes and changes in the UV trace at 254 nm that indeed compound **4.7** was reduced to the corresponding amine. In Figure 4.20 an LCMS trace of compound **4.7** was provided. Compound **4.7** was then treated with NTR and NADH for 5 hours and another LCMS is provided.

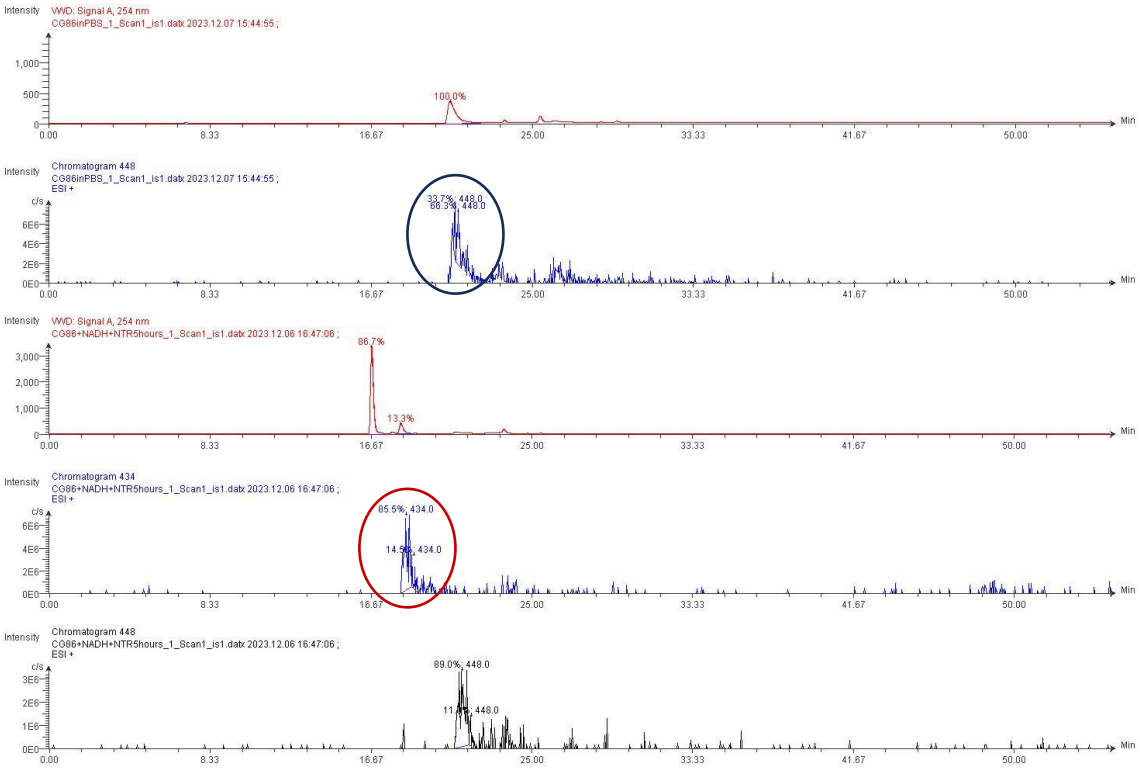

Figure 4.20: *(Top) LCMS trace of compound **4.7** (300 uM) circled in black is the corresponding M^+. Bottom is the LCMS trace of compound **4.7** after 5-hour treatment with NTR (15 µg mL^{-1}) and NADH (1 mM), circled in red is the corresponding M^+.*

From Figure 4.20 the peak at Rt = 20.73 minutes showed strong ionisation at 448 corresponding to M^+ ion for compound **4.7**. After the reaction of compound **4.7** with 15 µg mL^{-1} of NTR and 1 mM NADH there was evident ionisation at 434 corresponding to the M^+ ion of the hydroxylamine derivative of compound **4.7** at Rt = 18.19 minutes. This was an interesting result as there was not complete reduction to the corresponding amine derivative of compound **4.7** which suggests that it was the hydroxylamine that was responsible for the OFF-ON fluorescence responses observed for compound **4.7** seen in scheme 4.4.

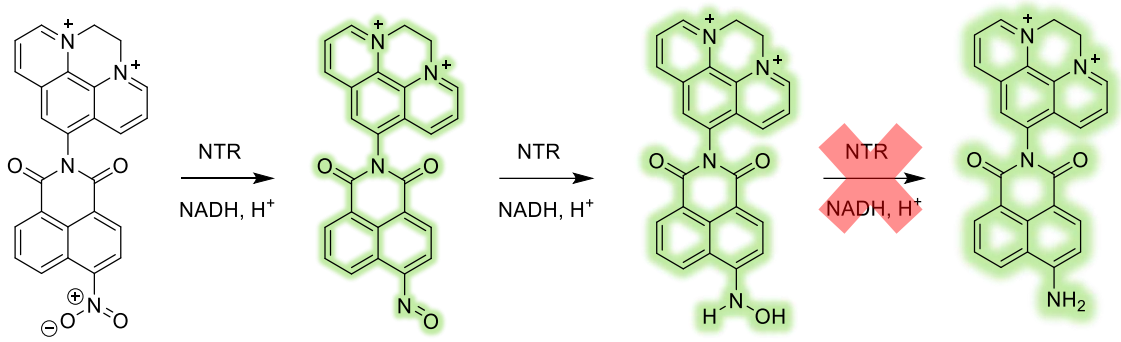

Scheme 4.4: *Reduction of compound **4.7** by NTR and NADH.*

Given the sensitivity and selectivity achieved by compound **4.7** it was of interest to determine if **4.7** was capable of DNA binding as seen for similar quaternarised ligands referred to in the introduction of this chapter.

4.9 Compound 4.7 in The Presence of DNA.

The interaction of Compound **4.7** with double stranded DNA was firstly examined using UV/Vis absorption spectroscopy. The titration was carried out by addition of small aliquots of stDNA to a 10 mM phosphate buffer solution pH 7.4 and changes in the absorption band were monitored in Figure 4.21. It was noted from the absorption spectra that there was a 27% hypochromism at 355 nm for compound **4.7** which was indicative of a decrease in the naphthalimide centred absorption. This suggested that binding of the naphthalimide moiety had occurred. The lack of hypochromism observed at 306 nm may suggested that the majority of the binding takes place by naphthalimide intercalation with DNA whilst the wedged quaternarised phenathroline moiety points away.[216]

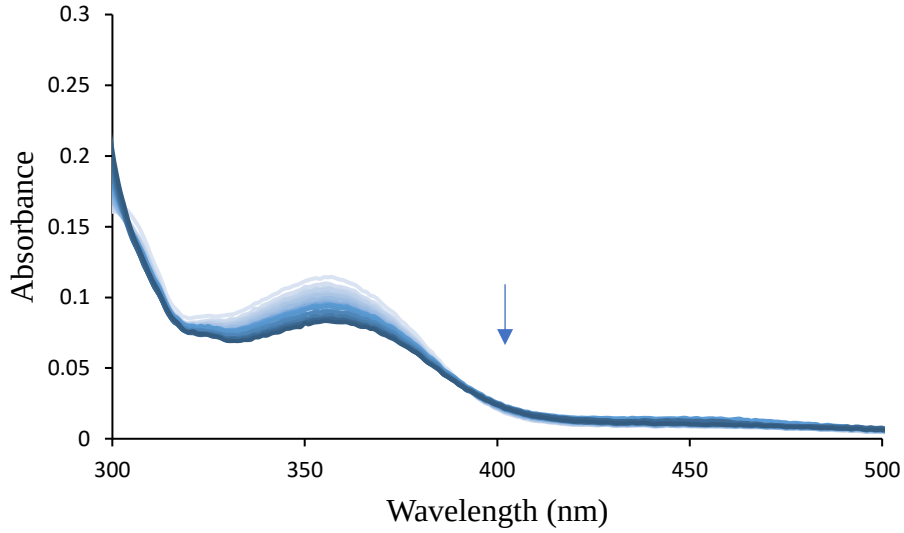

Figure 4.21: *The changes in the UV/Visible absorption spectrum of 10 µM compound 7 with increasing additions of stDNA (0-211.2 µM) in 10 mM phosphate buffer pH 7.4.*

It was then determined if stDNA would have an effect on the fluorescence response of **4.7** upon reaction with NTR and NADH. In Figure 4.22 compound **4.7** was treated with NTR (8 µg mL^{-1}) and NADH (500 µM) over a period of 1200 minutes to ensure that a plateau in the fluorescence intensity at 530 nm was reached. Upon reaching the plateau of fluorescence intensity a stDNA titration was carried out to determine any changes in the fluorescence intensity. After increasing the DNA concentration from 0 – 110.6 µM represented by a P/D ratio (0 – 11.06) it was noted that minimal change was observed in the fluorescence intensity. This was an interesting result and may suggest minimal interaction of the diquaternarised phenanthroline portion with stDNA. Generally, a degree of quenching in this case can be considered an additional indicator of a strong binding interaction. The strong oxidizing properties of the diquaternarised moiety imply that the quenching of emission is likely a result of electron transfer from the DNA bases to the diquat centre. The closer the diquaternarised phenanthroline to the bases the greater this process is enhanced.[216]

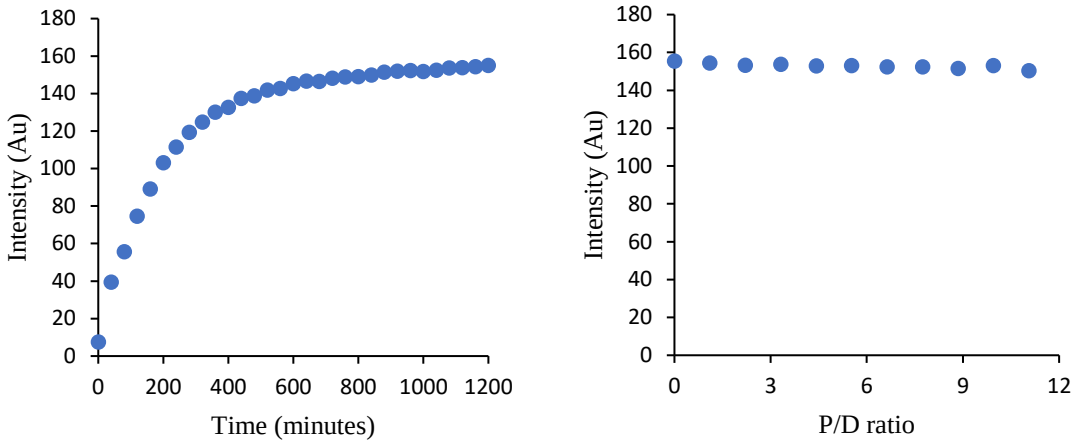

Figure 4.22: *Treatment of compound **4.7** (10 µM) with NTR (8 µg mL^{-1}) and NADH (500 µM) (left). Increasing P/D ratio (0 – 11.06) of stDNA after compound **4.7** has been treated with NTR (right). λ_{em} = 530 nm. λ_{ex} = 455 nm. Excitation slit width: 10 nm and Emission slit width: 10 nm. n = 1.*

4.10 Conclusions and Future Work

In conclusion, two novel fluorescence sensors for NTR compound **4.7** and **4.8** were synthesised. Both of which followed a similar synthetic pathway which involved the use of dibromoethane to quaternarise the phenanthroline portion of the compounds **2.25** and **4.10**.

Firstly, an excitation spectrum of each compound treated with NTR (8 μg mL^{-1}) and NADH was ran to determine the excitation wavelength of the supposed amine derivative of each compound as the amine derivatives of compound **4.7** and **4.8** were not synthesised. Having the excitation wavelengths of compound **4.7** and **4.8**, 455 nm and 450 nm respectively emission spectra of each compound was determined in the presence of NTR (4 μg mL^{-1}) and NADH (500 μM) where it was determined that compound **4.7** elicited a greater response than compound **4.8** at 530 nm.

Compound **4.7** was shown to be water soluble as the Cl^- salt, sensitive towards NTR over a range of concentrations from 0.5 μg mL^{-1} to 8 μg mL^{-1}, and established an 18.8-fold increase in the fluorescence intensity at 530 nm when treated with 8 μg mL^{-1} over 120 minutes. Compound **4.7** also displayed excellent selectivity towards NTR with 10 eq of dicoumarol to 1 eq of compound **4.7** quenching the fluorescence emission of compound **4.7** by 3.2-fold. Furthermore, Compound **4.7** was also shown to be selective for NTR in comparison to other biologically relevant species. The reduction mechanism of NTR on compound **4.7** was shown through LCMS runs whereby it was found that the hydroxylamine derivative of compound **4.7** was responsible for the OFF-ON fluorescence response observed.

To determine if compound **4.7** had any binding interactions with DNA, a DNA titration using stDNA was carried out. A 27% hypochromism at 355 nm for compound **4.7** was observed which was indicative of a decrease in the naphthalimide centred absorption which suggested that the naphthalimide moiety was largely responsible for DNA binding. This was also seen when compound **4.7** was treated with NTR and NADH prior to the treatment of increasing concentrations of stDNA. A lack of strong fluorescence quenching may indicate weak binding from the quaternarised phenanthroline moiety of compound **4.7**.

Future work will be to conduct sensitivity and selectivity photophysical studies for NTR sensing in triplicate. Additionally, the amine derivative of compound **4.7** would be synthesised to determine its photophysical characteristics and to compare its DNA

binding to that of compound **4.7**. It would then be of interest to investigate the DNA photosensitising ability of compound **4.7** with pBR322 DNA and to determine if the amine derivative acts as a superior photosensitiser than that of compound **4.7**. Further consideration will also be given regarding uptake of compound **4.7** into a cancer cell line under hypoxic conditions to achieve a desired turn-on response.

Given the long response times observed for compound **4.7** and given the successful synthesis of the amine derivative of **4.7** it would be of interest to synthesise compound **4.11** (Figure **4.23**) an expected blue to green, fluorescent probe for NTR. It was established in Chapter 2 that the 2-nitroimidazole moiety resulted in a rapid response towards NTR and co-factor NADH. Moreover, the reduction of the 2-nitroimidazole moiety would result in self-immolation to release the amine derivative of compound **4.7** which could potentially have greater fluorescence than the hydroxyl amine derivative formed upon reduction of compound **4.7** as seen in the LCMS studies in this chapter.

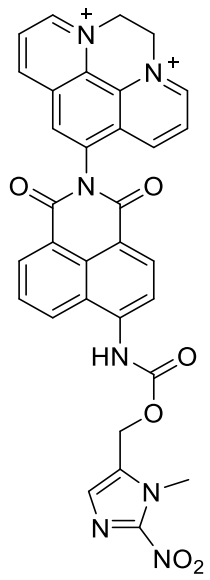

Figure 4.23: *Structure of compound **4.11**.*

Chapter 5

Thesis Summary

5.1 Thesis Summary and Future Work

Chemosensors for hypoxia that take advantage of a 1,8-naphthalimide motif have been in constant growth and development in recent years. Given the association between hypoxia and the upregulation of NTR, which serves as a biomarker for malignant tumors, there has been a growing focus on the development of selective fluorescent chemosensors activated by NTR, particularly those based on 1,8-naphthalimide. The aim of the research described in this thesis was to build upon the existing understanding of 1,8-naphthalimide fluorophores while also exploiting novel motifs for sensing NTR.

Chapter 2 details the synthesis and luminescence response of Ru(II) polypyridyl complexes capable of sensing NTR. Three new Ru(II) polypyridyl complexes were designed and synthesised for NTR sensing. Complexes **2.11** and **2.12** featured a carbamate linker between Ru(II) to nitroreductase substrates, 4-nitrobenzyl and 2-nitroimidazole moieties, respectively. Compound **2.13** resulted from direct conjugation between 4-nitro-1,8-naphthalimide and phenanthroline bound to Ru(II). Characterized by NMR, HRMS, and IR spectroscopy, these complexes exhibited luminescent turn-on responses to NTR. Compound **2.13** elicited the greatest luminescent response of 17.3-fold enhancement at 600 nm. It displayed sensitivity to varying NTR concentrations, excellent selectivity, and DNA binding ability resulting in an enhanced luminescence response of 41.2-fold. Moreover, in cellular studies, compound **2.29**, the amine derivative of compound **2.13** showed potential to image HeLa cells whilst compound **2.13** showed potential as an imaging agent for NTR in bacteria. Future work for compound **2.13** is to consider applications in DNA photosensitizing studies and cancer cell imaging under hypoxic conditions.

In Chapter 3, four novel nitroreductase (NTR) dendrimers (**3.6**, **3.7**, **3.8**, and **3.9**) were successfully synthesized using triphosgene to form carbamate linkages between the adapter unit and either the fluorophore or drug. This design demonstrated versatility in modulating the attached fluorophores or drugs. For compounds **3.6** and **3.7**, two of the same fluorophores **3.11** in the case of **3.6** or **3.12** in the case of **3.7** were linked to the same adapter unit. Compounds **3.8** and **3.9** showcased the ability to choose and modulate various drugs to be appended to the dendrimer upon synthesising **3.17**, either amonafide or sulfisoxazole were carbamate-linked to **3.17**, resulting in the corresponding theranostics **3.8** and **3.9**. UV/Vis and fluorescence studies confirmed the successful modulation of naphthalimide fluorophores **3.11** and **3.12**, exhibiting expected hypsochromic shifts due to the carbamate linkage formation. Sodium dithionite studies

revealed issues faced with solubility which were addressed by optimizing DMSO:PBS ratios, yielding fluorescence responses for compounds **3.7**, **3.8**, and **3.9**. Compound **3.9** exhibited a remarkable 19.2-fold increase in fluorescence intensity at 540 nm and exceptional selectivity towards NTR. Furthermore, LCMS studies confirmed the release of compound **3.12** and sulfisoxazole **3.19** upon reduction and immolation of compound **3.9** by NTR and NADH. Future work involves confocal microscopy studies in bacteria, assessing cytotoxicity, and consideration of a redesign for compounds **3.6**, **3.7**, and **3.8** to improve solubility and to explore potential applications in cancer cell lines under hypoxic conditions.

In chapter 4, two novel fluorescence sensors for NTR, compounds **4.7** and **4.8**, were synthesized following a common synthetic pathway involving dibromoethane to quaternarise the phenanthroline moiety. Compound **4.7** demonstrated superior responsiveness at 530 nm compared to compound **4.8**. Compound **4.7** exhibited sensitivity to NTR across a concentration range (0.5 μg mL^{-1} to 8 μg mL^{-1}), achieving an 18.8-fold increase in fluorescence intensity at 530 nm after 120 minutes. Selectivity towards NTR, as confirmed by dicoumarol quenching, and specificity against other biologically relevant species were also observed. LCMS studies revealed the hydroxylamine derivative of compound **4.7** as the responsible species for the observed fluorescence response. DNA titration studies suggested naphthalimide binding of compound **4.7** with no influence on the fluorescence of compound **4.7** upon reduction by NTR. Future work involves the synthesis of the amine derivative of compound **4.7** for further exploration of DNA interactions and photosensitizing abilities. Future work also involves the synthesis of compound **4.11** as a blue-to-green, fluorescent probe for NTR, as this could lead to rapid response times and enhanced fluorescence intensity.

5.2 Publications

Conor Geraghty, Conor Wynne, Robert B. P. Elmes, 1,8-Naphthalimide based fluorescent sensors for enzymes. *Coordination Chemistry Reviews* 2021, *437*, 213713.

Luke E. Brennan, Lokesh K. Kumawat, Magdalena E. Piatek, Airlie J. Kinross, Daniel A. McNaughton, Luke Marchetti, **Conor Geraghty**, Conor Wynne, Hua Tong, Oisin N. Kavanagh, Finbarr O'Sullivan, Chris S. Hawes, Philip A. Gale, Kevin Kavanagh, and Robert B.P. Elmes, Potent antimicrobial effect induced by disruption of chloride homeostasis, *Chem*, 9, (**2023**), 3138–3158.

Chapter 6

Experimental procedures

6.1 General Procedures and Instrumentation

Reagents were all of commercial quality. Solvents were dried by standard methods – DCM was distilled over CaH_2 and MeCN was dried over 3 Å molecular sieves. Silica gel 60 (230-400 mesh) was used for flash chromatography. Analytical TLC was performed on aluminium sheets coated with a 0.2 mm layer of silica gel 60 F254. LC-MS was performed on an Agilent Technologies 1200 series setup, utilising an Agilent Eclipse XDB-C18 (5µm, 4.6 x 150mm) column at 40°C. A flow rate of 0.2 ml min^{-1} and gradient of 0.1% of formic acid in CH_3CN (solvent A) in 0.1% of formic acid in H_2O (solvent B) was used as mobile phase. Electrospray in positive & negative mode was used for ionisation. Compounds were lyophilised on a Labconco Freezone 1 Dry system. NMR spectra were recorded using a Bruker Ascend 500 spectrometer, operated at 500 MHz for ^{1}H NMR analysis and 126 MHz for ^{13}C analysis, both at 293 K. The residual solvent peak was used as an internal standard for DMSO-d_6 and TMS for $CDCl_3$. Chemical shifts (δ) were reported in ppm. NMR spectra were processed on MestReNova software. *J* values are given in Hz. The NMR spectra assignments were based on ^{1}H NMR, ^{13}C NMR, ^{1}H-^{1}H COSY, HSQC, and HMBC spectra. Multiplicity is given as s = singlet, d = doublet, dd = doublet of doublets, t = triplet, q = quartet, m = multiplet. High resolution mass spectra (HRMS) were recorded by Bath University on an Agilent 6200 series TOF/6500 series Q-TOF instrument with an ESI source. IR spectra were obtained *via* ATR as a solid on a zinc selenide crystal in the region of 4000 – 400 cm^{-1} using a Perkin Elmer Spectrum 100 FT-IR spectrophotometer. Microwave experiments were carried out in a CEM Discovery MW, with an IR sensor for reaction temperature monitoring. UV-visible spectroscopy measurements were made at 25 ºC on a Lambda 365 Perkin Elmer UV-vis spectrophotometer. Fluorescence emission spectra were performed at 25 ºC and 37 ºC on an Agilent Spectrofluorometer equipped with a 450 W xenon lamp for excitation. Quartz cuvettes of 1 cm path length were used for UV/Vis and Fluorescence studies.

6.2 Synthetic Procedures for Chapter 2

1,10-phenanthrolin-5-amine (2.15)

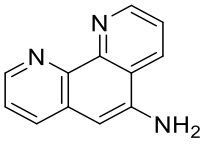

5-nitro-1,10-phenanthroline (1 g, 4.44 mmol) and 10% palladium on carbon (0.1 g) was stirred in EtOH (100 mL) in a round bottom flask. Hydrazine monohydrate (3.23 mL, 66 mmol) was added slowly dropwise at room temperature. The reaction mixture was brought to reflux at 80°C for 18 hours. The reaction mixture was filtered through celite and solvent was removed *in vacuo* to yield a brown solid that was triturated with petroleum ether to afford the product as a brown solid. (0.735 g, 85 % yield). **^{1}H NMR** (500 MHz, DMSO-d_6) δ 9.05 (dd, J = 4.2, 1.6 Hz, 1H), 8.71 – 8.65 (m, 2H), 8.04 (dd, J = 8.2, 1.7 Hz, 1H), 7.73 (dd, J = 8.3, 4.2 Hz, 1H), 7.50 (dd, J = 8.1, 4.2 Hz, 1H), 6.87 (s, 1H), 6.15 (s, 2H). **^{13}C NMR** (126 MHz, DMSO-d_6) δ 149.3, 149.3, 146.2, 144.8, 142.7, 140.5, 132.7, 130.8, 130.6, 123.2, 122.0, 121.8, 101.8. This is in agreement with previously published NMR data in the literature.[220]

4-nitrobenzyl (1,10-phenanthrolin-5-yl)carbamate (2.14)

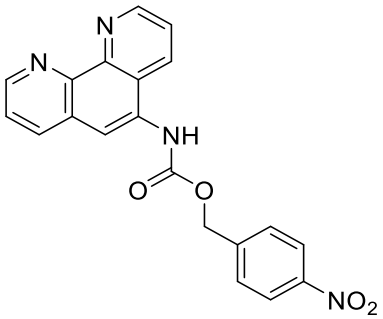

Compound **2.15** (0.1 g, 0.51 mmol) was dissolved in anhydrous $CHCl_3$ (25 mL) in a round bottom flask. Triethylamine (0.4 mL, 2.97 mmol) was added and stirred. This mixture was then added dropwise to a $CHCl_3$ solution of triphosgene (0.23 g, 0.77 mmol) at 0°C in a round bottom flask. After 4 hours the solvent was removed by bubbling nitrogen through the reaction mixture. When dried (4-nitrophenyl)methanol (0.195 g, 1.275 mmol) and triethylamine (0.4 mL, 2.97 mmol) dissolved in $CHCl_3$ (25 mL) was added and the reaction was stirred for 24 hours. The solvent was removed *in vacuo* and MeCN (20 mL) was added to the crude solid. The precipitate formed was collected via centrifugation to afford the product as a pale pink solid. (0.138 g, 72 % yield). **^{1}H NMR** (500 MHz, DMSO-

d$_6$) δ 10.11 (s, 1H), 9.12 (dd, *J* = 4.2, 1.6 Hz, 1H), 9.03 (dd, *J* = 4.3, 1.7 Hz, 1H), 8.66 (dd, *J* = 8.4, 1.5 Hz, 1H), 8.44 (dd, *J* = 8.2, 1.7 Hz, 1H), 8.29 (d, *J* = 8.7 Hz, 2H), 8.12 (s, 1H), 7.81 (dd, *J* = 8.4, 4.2 Hz, 1H), 7.78 – 7.69 (m, 3H), 5.39 (s, 2H). **^{13}C NMR** (126 MHz, DMSO-*d*$_6$) δ 154.50, 149.98, 149.34, 147.13, 145.84, 144.55, 143.69, 135.78, 131.74, 131.56, 128.48, 128.08, 124.56, 123.67, 122.94, 119.21, 64.99. **IR** (ATR): ν_{max} (cm^{-1}) = 3134, 2962, 2904, 1715, 1607, 1543, 1510, 1454, 1409, 1344, 1210, 1156, 1120, 1078, 1043, 1013, 872, 803, 766, 739, 701, 623, 578, 515, 476. **HRMS** (ESI+) *m/z* calcd for $C_{20}H_{14}N_4O_4$ $[M + H]^+$ 375.1049, found 375.1093 (+1.31 ppm).

6-nitro-2-(1,10-phenanthrolin-5-yl)-1H-benzo[de]isoquinoline-1,3(2H)-dione (2.25)

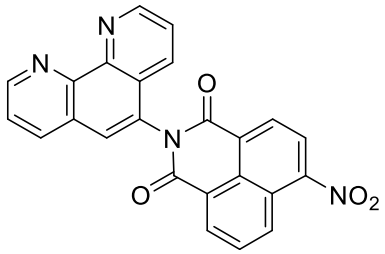

Compound **2.15** (0.459 g, 2.351 mmol) and 4-nitro-1,8-naphthalic anhydride was dissolved in acetic acid (10 mL) in a boiling tube and heated to 140°C for 6 hours. The reaction mixture was poured into of deionised water (150 mL) and a pale brown precipitate was formed. The precipitate was filtered and washed with saturated sodium bicarbonate solution and water to afford a brown solid. (0.747 g, 75 % yield). **^{1}H NMR** (500 MHz, DMSO-*d*$_6$) δ 9.21 (dd, *J* = 4.0, 1.2 Hz, 1H), 9.16 (dd, *J* = 2.9 Hz, 1H), 8.81 (d, *J* = 8.8 Hz, 1H), 8.71 – 8.60 (m, 4H), 8.55 (dd, *J* = 8.1, 1.2 Hz, 1H), 8.23 (s, 1H), 8.17 (dd, *J* = 8.7, 7.5 Hz, 1H), 7.86 (dd, *J* = 8.0, 4.3 Hz, 1H), 7.72 (dd, *J* = 8.3, 4.2 Hz, 1H). **^{13}C NMR** (126 MHz, DMSO-*d*$_6$) δ 163.7, 162.9, 151.0, 150.3, 149.6, 145.9, 145.5, 136.6, 132.2, 131.9, 130.9, 130.1, 129.8, 129.4, 129.1, 127.6, 127.6, 127.4, 126.3, 124.2, 123.8, 123.6, 123.5, 123.0. **IR** (ATR): ν_{max} (cm^{-1}) = 3366, 1708, 1662, 1625, 1581, 1524, 1462, 1422, 1349, 1234, 1190, 1146, 1106, 1084, 1026, 978, 896, 845, 781, 739, 708, 627, 604, 574, 497, 413. **HRMS** (ESI+) *m/z* calcd for $C_{24}H_{12}N_4O_4$ $[M + Na]^+$ 443.0756, found 443.0755 (-0.23 ppm).

6-bromo-2-(1,10-phenanthroline-5-yl)-1*H*-benzo[*de*]isoquinoline-1,3(2*H*)-dione (2.27)

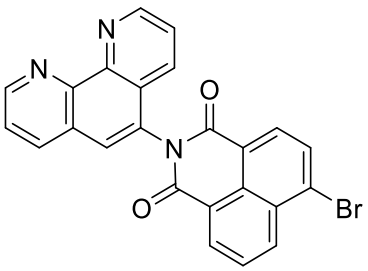

1,10-Phenanthroline-5-amine (0.4 g, 2.049 mmol) and 4-bromo-1,8-naphthalic anhydride (0.568 g, 2.049 mmol) was dissolved in acetic acid (10 mL) in a boiling tube and heated to 140℃ for 6 hours. The reaction mixture was poured into deionised water (150 mL) and a pale brown precipitate was formed. The precipitate was filtered and washed with saturated sodium bicarbonate solution and water to afford a brown solid. (0.382 g, 41 % yield). **^{1}H NMR** (500 MHz, DMSO-d_6) δ 9.20 (dd, J = 4.3, 1.5 Hz, 1H), 9.15 (dd, J = 4.1, 1.4 Hz, 1H), 8.69 (d, J = 8.6 Hz, 1H), 8.64 (d, J = 6.9 Hz, 1H), 8.58 – 8.50 (m, 2H), 8.40 (d, J = 7.8 Hz, 1H), 8.32 (d, J = 7.8 Hz, 1H), 8.21 (s, 1H), 8.13 – 8.05 (m, 1H), 7.85 (dd, J = 8.0, 4.3 Hz, 1H), 7.70 (dd, J = 8.3, 4.2 Hz, 1H). **^{13}C NMR** (126 MHz, DMSO-d_6) δ 163.7, 163.7, 151.0, 150.3, 145.9, 145.5, 136.6, 133.2, 132.2, 131.9, 131.5, 131.3, 131.2, 130.2, 129.6, 129.5, 129.0, 127.7, 127.6, 126.4, 123.8, 123.7, 123.6, 122.8. **IR** (ATR): ν_{max} (cm^{-1}) = 3358, 3067, 1706, 1664, 1585, 1507, 1459, 1420, 1398, 1362, 1235, 1187, 1133, 1107, 1083,1046, 1025, 953, 918, 883, 851, 820, 778, 743, 706, 627, 602, 559, 513, 475. **HRMS** (ESI+) *m/z* calcd for $C_{24}H_{12}BrN_3O_2$ $[M + Na]^+$ 476.0011, found 477.9983 (-1.00 ppm).

6-azido-2-(1,10-phenanthrolin-5-yl)-1*H*-benzo[*de*]isoquinoline-1,3(2*H*)-dione (2.28)

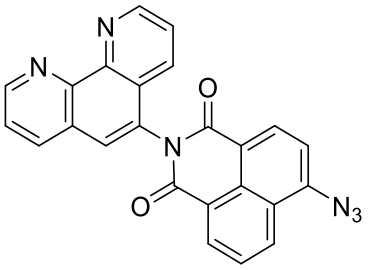

Compound **2.27** (0.708 g, 1.559 mmol) and sodium azide (0.507 g, 7.795 mmol) was dissolved in DMF (30 mL) and stirred for 24 hours at 80 ℃. The reaction mixture was poured into deionised water (150 mL) and a pale brown precipitate was formed. The

precipitate was filtered and washed with water and diethyl ether to afford a brown solid. (0.220 g, 34 % yield). **^{1}H NMR** (500 MHz, DMSO-d_6) δ 9.20 (dd, J = 4.3, 1.7 Hz, 1H), 9.15 (dd, J = 4.2, 1.6 Hz, 1H), 8.63 – 8.50 (m, 4H), 8.48 (dd, J = 8.3, 1.6 Hz, 1H), 8.20 (s, 1H), 7.96 (dd, J = 8.5, 7.3 Hz, 1H), 7.88 – 7.82 (m, 2H), 7.70 (dd, J = 8.3, 4.2 Hz, 1H). **^{13}C NMR** (126 MHz, DMSO-d_6) δ 164.0, 163.5, 150.9, 150.3, 145.9, 145.5, 143.4, 136.5, 132.0, 131.9, 131.9, 131.4, 129.4, 128.9, 127.7, 127.6, 127.5, 126.4, 123.9, 123.8, 123.7, 122.8, 118.7, 116.0. **IR** (ATR): ν_{max} (cm^{-1}) = 3071, 2115, 1708, 1659, 1584, 1509, 1464, 1421, 1359, 1295, 1235, 1187, 1139, 1104, 1053, 1027, 984, 951, 890, 835, 812, 782, 739, 708, 652, 625, 567, 515, 492, 457. **HRMS** (ESI+) *m/z* calcd for $C_{24}H_{12}N_6O_2$ $[M + H]^+$ 417.1100, found 417.1091 (-0.33 ppm).

6-amino-2-(1,10-phenanthrolin-5-yl)-1*H*-benzo[*de*]isoquinoline-1,3(2*H*)-dione (2.26)

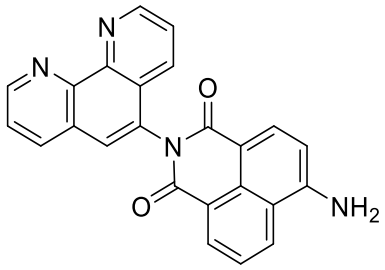

Compound **2.28** (0.220 g, 0.288 mmol) was dissolved in 20 mL DMF with Pd/C (0.023 g, 0.212 mmol) under H_2 gas and stirred for 24 hours. Pd/C was removed from the reaction mixture via filtration with celite and the filtrate was removed *in vacuo* to afford a pure yellow solid. (0.160 g, 78 % yield). **^{1}H NMR** (500 MHz, DMSO-d_6) δ 9.19 (d, J = 3.4 Hz, 1H), 9.14 (d, J = 3.4 Hz, 1H), 8.74 (d, J = 8.4 Hz, 1H), 8.56 – 8.45 (m, 2H), 8.24 (dd, J = 8.3, 2.7 Hz, 2H), 8.12 (s, 1H), 7.84 (dd, J = 8.0, 4.4 Hz, 1H), 7.77 – 7.67 (m, 2H), 7.64 (s, 2H), 6.93 (d, J = 8.4 Hz, 1H). **^{13}C NMR** (126 MHz, DMSO-d_6) δ 164.4, 163.4, 162.3, 153.4, 150.7, 150.1, 146.0, 145.4, 136.4, 134.4, 132.0, 131.8, 131.5, 130.8, 130.0, 127.9, 127.5, 126.5, 124.2, 123.7, 122.1, 119.7, 108.4, 107.5. **IR** (ATR): ν_{max} (cm^{-1}) = 3411, 3310, 3202, 1681, 1645, 1574, 1527, 1482, 1420, 1362, 1302, 1247, 1190, 1143, 1103, 1025, 995, 947, 897, 843, 814, 769, 738, 709, 673, 625, 600, 565, 493, 463, 406. **HRMS** (ESI+) *m/z* calcd for $C_{24}H_{14}N_4O_2$ $[M + H]^+$ 391.1195, found 391.1185 (-0.86 ppm).

ethyl 2-amino-1-methyl-1H-imidazole-5-carboxylate (2.22)

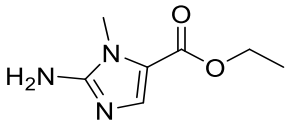

Sarcosine ethyl ester hydrochloride (2 g, 13 mmol) was added to a stirring solution of ethyl formate (45 mL). Sodium hydride (1.09 g, 27.2 mmol) was added slowly to the reaction mixture at 0°C and stirred for 3 hours. Solvent was removed *in vacuo* to afford a beige solid that was triturated with petroleum ether. Ethanol (40 mL) and HCl (8 mL) was then added to the solid and the reaction mixture was refluxed for 90 mintues. The white precipitate formed was filtered out of the solution and the yellow filtrate was concentrated *in vacuo* to afford a yellow oil. The oil was diluted with 10% AcOH (30 mL) and adjusted to pH 3 using NaOAc. Cyanamide (0.9g, 21.2 mmol) was added to the reaction mixture and refluxed for 90 minutes. The mixture was cooled to room temperature and adjusted to pH 9 with K_2CO_3 to afford a precipitate. The precipitate was collected via filtration to yield the product as a pale yellow solid. (0.879 g, 44 % yield). **^{1}H NMR** (500 MHz, DMSO-*d*$_6$) δ 7.27 (s, 1H), 6.16 (s, 2H), 4.15 (q, *J* = 7.1 Hz, 2H), 3.52 (s, 3H), 1.23 (t, *J* = 7.1 Hz, 3H). **^{13}C NMR** (126 MHz, DMSO-*d*$_6$) δ 159.7, 154.3, 136.1, 116.9, 58.9, 30.2, 14.4.

ethyl 1-methyl-2-nitro-1H-imidazole-5-carboxylate (2.23)

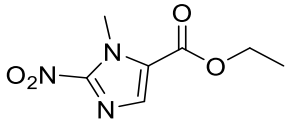

Sodium nitrite (2.71g, 39.4 mmol) was dissolved in 10 mL of water in a 100 mL round bottom flask. Compound **2.22** (0.67 g, 3.94 mmol) was dissolved in 6 mL of acetic acid and was added dropwise at 0°C. The reaction mixture was stirred for 4 hours at room temperature. The reaction mixture was extracted with DCM and washed with water 50 mL, saturated sodium bicarbonate (100 mL), brine (50 mL), and dried with $MgSO_4$. Solvent was removed *in vacuo* to yield a yellow oil that was purified by column chromatography (SiO_2, DCM) to afford an off white crystalline product. (0.427 g, 54 % yield). **^{1}H NMR** (500 MHz, DMSO-*d*$_6$) δ 7.78 (s, 1H), 4.34 (q, *J* = 7.1 Hz, 2H), 4.18 (s, 3H), 1.32 (t, *J* = 7.1 Hz, 3H). **^{13}C NMR** (126 MHz, DMSO-*d*$_6$) δ 158.8, 147.7, 133.8, 126.1, 61.4, 35.2, 14.0.

1-methyl-2-nitro-1H-imidazole-5-carboxylic acid (2.24)

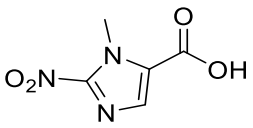

Compound **2.23** (0.840 g, 4.218 mmol) was added to a 1 N aqueous solution of NaOH and stirred for 18 hours. The reaction was then acidified to pH 1 using concentrated HCl, resulting the formation of white precipitate. The organic compound was extracted with EtOAc (3 x 50 mL), and dried with MgSO4. The filtrate was concentrated *in vacuo* to afford a white solid (0.599 g, 82 % yield). **^{1}H NMR** (500 MHz, DMSO-d_6) δ 7.73 (s, 1H), 4.19 (s, 3H). **^{13}C NMR** (126 MHz, DMSO-d_6) δ 160.4, 133.7, 127.0, 35.0.

(1-methyl-2-nitro-1H-imidazol-5-yl)methanol (2.18)

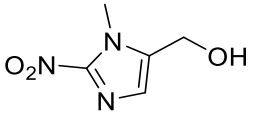

Compound **2.24** (0.36 g, 2.123 mmol) was added to a 100 mL round bottom flask with THF (30 ml) at -15℃ and trimethylamine (0.504 ml, 3.609 mmol). Isobutyl Chloroformate (0.44 ml, 3.396 mmol) was added dropwise to the reaction mixture. The reaction was stirred for 1 hr at -15℃. Sodium borohydride (401.53 mg, 10.614 mmol) was added and stirred for 5 minutes, then water (15 mL) was added slowly and the reaction was stirred as 0℃ for 1 hour. The reaction was filtered to remove the precipitate which was washed with THF. The organic layers were combined, separated from the aqueous layer, and dried with MgSO4. The solvent was removed *in vacuo* to afford a yellow solid which was triturated with diethyl ether to yield the product as a pure yellow solid. (0.176 g, 56 % yield). **^{1}H NMR** (500 MHz, DMSO-d_6) δ 7.11 (s, 1H), 5.48 (t, J = 5.4 Hz, 1H), 4.54 (d, J = 5.2 Hz, 2H), 3.92 (s, 3H). **^{13}C NMR** (126 MHz, DMSO-d_6) δ 145.7, 138.6, 126.6, 53.0, 34.1. **IR** (ATR): ν_{max} (cm^{-1}) = 3224, 1538, 1491, 1395, 1358, 1329, 1275, 1239, 1186, 1123, 1036, 965, 832, 769, 687, 648, 553, 466. This is in agreement with previously published NMR data in the literature.[221]

Bis(1,10-phenanthroline)-(4-nitrobenzyl (1,10-phenanthrolin-5-yl)carbamate)ruthenium(II) Bis(hexafluorophosphate) (2.11)

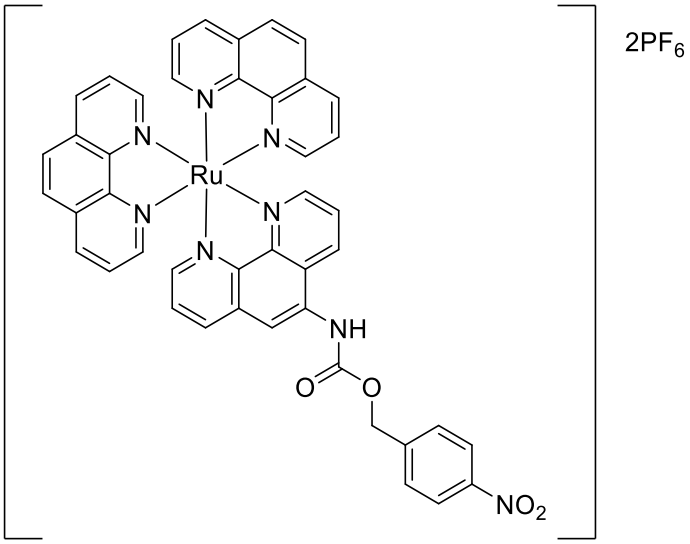

Dichlorobis(1,10-phenathroline)ruthenium(II) (0.1 g, 0.188 mmol) and **2.14** (0.079 g, 0.188 mmol) were added to a 1:1 EtOH:H_2O solution in a microwave tube and bubbled with nitrogen for 15 minutes. The reaction mixture was heated to 110°C in the microwave for 45 minutes. The reaction mixture was then filtered and ammonium hexafluorophosphate was added to the filtrate to form an orange precipitate. The precipitate was isolated via centrifugation and washed with water (2 x 20 mL). The precipitate was dissolved in a 40:4:1 acetonitrile: water: sodium nitrate solution and purified by column chromatography (SiO_2, 40:4:1 acetonitrile: water: sodium nitrate). The product was precipitated with ammonium hexafluorophosphate to afford the product as a red solid. (0.045 g, 42 % yield). **^{1}H NMR** (500 MHz, DMSO-*d*$_6$) δ 10.56 (s, 1H), 8.93 (dd, *J* = 8.4 Hz, 1H), 8.81 – 8.69 (m, 5H), 8.56 (s, 1H), 8.38 (s, 4H), 8.29 (d, *J* = 8.7 Hz, 2H), 8.14 – 8.03 (m, 5H), 7.96 (dd, *J* = 4.7 Hz, 1H), 7.81 – 7.66 (m, 8H), 5.45 (s, 2H). **^{13}C NMR** (126 MHz, DMSO-*d*$_6$) δ 154.2, 152.8, 152.7, 151.5, 147.6, 147.2, 144.7, 144.2, 136.8, 136.1, 134.0, 132.4, 130.4, 130.2, 128.6, 128.0, 126.4, 126.3, 126.1, 125.7, 123.7, 118.0, 65.4. **IR** (ATR): ν_{max} (cm^{-1}) = 3083, 1978, 1728, 1631, 1581, 1517, 1427, 1344, 1212, 1143, 1096, 1025, 951, 823, 719, 590, 554, 424. **HRMS** (ESI+) *m/z* calcd for $C_{44}H_{30}F_{12}N_8O_4P_2Ru$ $[M]^{2+}$ 418.0711, found 418.0724 (+3.11 ppm).

Bis(1,10-phenanthroline)-(1,10-phenanthrolin-5-amine)ruthenium(II) Bis(hexafluorophosphate) (2.17)

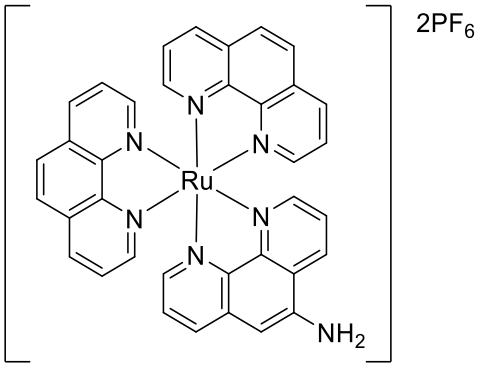

Dichlorobis(1,10-phenathroline)ruthenium(II) (0.03 g, 0.0056 mmol) and **2.15** (0.011g, 0.0056 mmol) was added to a 1:1 EtOH:H_2O solution in a microwave tube and bubbled with nitrogen for 15 minutes. The reaction mixture was heated to 110°C in the microwave for 45 minutes. The reaction mixture was then filtered and ammonium hexafluorophosphate was added to the filtrate to form an orange precipitate. The precipitate was isolated via centrifugation and washed with water (2 x 20 mL). The precipitate was dissolved in a 40:4:1 acetonitrile: water: sodium nitrate solution and purified by column chromatography (SiO_2, 40:4:1 acetonitrile: water: sodium nitrate). The product was precipitated with ammonium hexafluorophosphate to afford the product as a red solid. (0.022 g, 40% yield). **^{1}H NMR** (500 MHz, DMSO-d_6) δ 8.88 (dd, J = 8.5 Hz, 1H), 8.81 – 8.70 (m, 4H), 8.38 (s, 4H), 8.28 (dd, J = 8.4 Hz, 1H), 8.13 – 8.03 (m, 4H), 8.01 (dd, J = 5.2 Hz, 1H), 7.84 – 7.72 (m, 4H), 7.69 (dd, J = 8.5, 5.3 Hz, 1H), 7.56 (dd, J = 5.1 Hz, 1H), 7.46 (dd, J = 8.3, 5.1 Hz, 1H), 7.09 (s, 1H), 6.91 (s, 2H). **^{13}C NMR** (126 MHz, DMSO-d_6) δ 152.7, 152.7, 152.6, 152.5, 152.3, 148.1, 147.3, 147.3, 147.2, 147.2, 146.8, 145.3, 140.9, 136.7, 133.3, 132.6, 131.9, 130.5, 130.4, 130.4, 130.4, 128.1, 126.4, 126.3, 126.3, 125.9, 124.7, 123.3, 101.5. **IR** (ATR): ν_{max} (cm^{-1}) = 3389, 1635, 1593, 1512, 1492, 1460, 1425, 1340, 822, 719, 662, 554, 470. This is in agreement with previously published NMR data in the literature.[222]

Bis(1,10-phenanthroline)-(1-methyl-2-nitro-1*H*-imidazol-5-yl)methyl (1,10-phenathroline-5-yl)carbamate)ruthenium(II) Bis(hexafluorophosphate) (2.12)

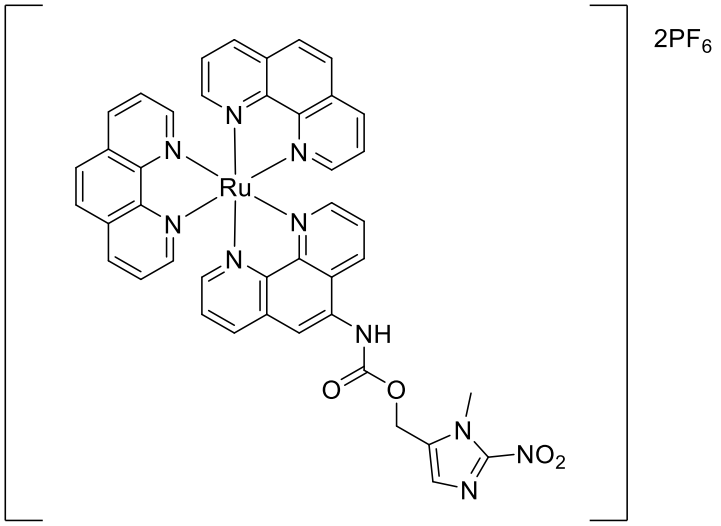

Compound **2.17** (0.1 g, 0.188 mmol) was dissolved in anhydrous MeCN (25 mL) in a round bottom flask. Triethylamine (0.065 mL, 0.47 mmol) was then added and stirred. This mixture was then added dropwise to a MeCN solution of triphosgene (0.056 g, 0.188 mmol) at 0°C in a round bottom flask. After 4 hours the solvent is removed by bubbling nitrogen through the reaction mixture. When dried (1-methyl-2-nitro-1H-imidazol-5-yl)methanol (0.059g, 0.376 mmol) and triethylamine (0.065 mL, 0.47 mmol) dissolved in MeCN (25 mL) was added and the reaction was stirred for 24 hours. The solvent was removed *in vacuo*. The red solid was dissolved in a 40:4:1 acetonitrile: water: sodium nitrate solution and purified by column chromatography (SiO_2, 40:4:1 acetonitrile: water: sodium nitrate). The product was precipitated with ammonium hexafluorophosphate to afford the product as a red solid. (0.031 g, 15 % yield). **^{1}H NMR** (500 MHz, DMSO-*d*$_6$) δ 10.50 (s, 1H), 8.87 (dd, *J* = 8.6 Hz, 1H), 8.81 – 8.69 (m, 6H), 8.53 (s, 1H), 8.39 (s, 5H), 8.15 – 8.02 (m, 6H), 7.96 (dd, *J* = 5 Hz, 1H), 7.81 – 7.66 (m, 7H), 7.36 (s, 1H), 5.43 (s, 2H), 4.00 (s, 3H). **^{13}C NMR** (126 MHz, DMSO-*d*$_6$) δ 153.9, 153.0, 152.8, 151.7, 147.7, 147.3, 146.2, 144.9, 136.9, 136.2, 133.9, 133.1, 132.5, 130.5, 130.2, 129.1, 128.1, 126.5, 126.4, 126.2, 125.7, 118.4, 56.1, 34.4. **IR** (ATR): ν_{max} (cm^{-1}) = 3391, 3093, 2923, 1735, 1658, 1632, 1579, 1536, 1488, 1428, 1351, 1295, 1210, 1152, 1106, 1060, 1025, 947, 838, 776, 722, 652, 626, 557, 528, 472, 408. **HRMS** (ESI+) *m/z* calcd for $C_{44}H_{30}F_{12}N_8O_4P_2Ru$ $[M]^{2+}$ 420.0742, found 420.0710 (-7.61 ppm).

Bis(1,10-phenanthroline)-(6-nitro-2-(1,10-phenanthrolin-5-yl)-1*H*-benzo[*de*]isoquinoline-1,3(2*H*)-dione)ruthenium(II) Bis(hexafluorophosphate) (2.13)

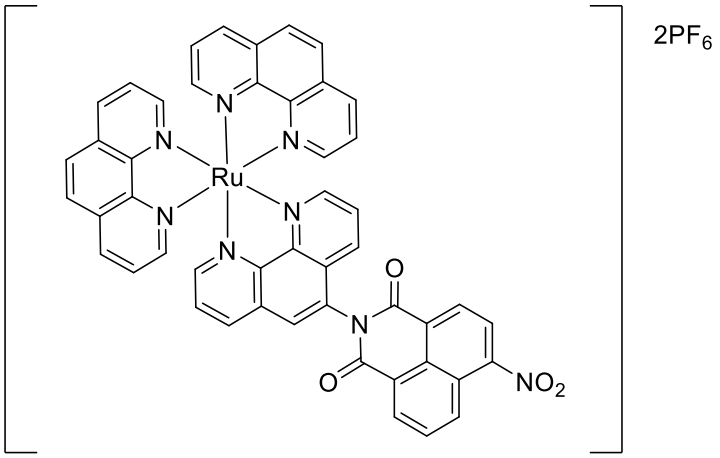

Dichlorobis(1,10-phenathroline)ruthenium(II) (0.1 g, 0.188 mmol) and **2.25** (0.079 g, 0.188 mmol) was added to a 1:1 EtOH:H_2O solution in a microwave tube and bubbled with nitrogen for 15 minutes. The reaction mixture was heated to 110°C in the microwave for 45 minutes. The reaction mixture was then filtered and ammonium hexafluorophosphate was added to the filtrate to form an orange precipitate. The precipitate was isolated via centrifugation and washed with water (2 x 20 mL). The precipitate was then diluted with acetonitrile in a 100 mL RBF and placed in a jar with diethyl ether to afford the pure product as a red crystalline solid. (0.134 g, 61 % yield) **^{1}H NMR** (500 MHz, DMSO-d_6) δ 8.95 (dd, J = 8.5 Hz, 1H), 8.87 – 8.75 (m, 6H), 8.74 – 8.62 (m, 4H), 8.45 – 8.37 (m, 4H), 8.24 – 8.14 (m, 5H), 8.12 (dd, J = 5.2 Hz, 2H), 7.93 – 7.77 (m, 5H), 7.70 (dd, J = 8.5, 5.2 Hz, 1H). **^{13}C NMR** (126 MHz, DMSO-d_6) δ 163.8, 163.7, 163.0, 162.9, 153.9, 153.5, 152.8, 152.6, 149.7, 147.5, 147.3, 147.3, 147.3, 147.2, 137.2, 137.1, 137.0, 136.9, 133.2, 132.6, 131.9, 130.6, 130.5, 130.5, 130.2, 129.7, 129.4, 129.3, 129.2, 128.6, 128.1, 127.4, 127.3, 126.8, 126.6, 126.5, 126.4, 124.2, 123.5, 123.5, 123.0. **IR** (ATR): ν_{max} (cm^{-1}) = 3649, 3087, 1716, 1674, 1628, 1583, 1527, 1463, 1425, 1347, 1236, 1192, 1146, 1095, 1046, 823, 719, 621, 554, 488, 426, 400. **HRMS** (ESI+) *m/z* calcd for $C_{48}H_{28}F_{12}N_8O_4P_2Ru$ $[M]^+$ 441.0633, found 441.0647 (+3.17 ppm).

Bis(1,10-phenanthroline)-(6-amino-2-(1,10-phenanthrolin-5-yl)-1*H*-benzo[*de*]isoquinoline-1,3(2*H*)-dione)ruthenium(II) Bis(hexafluorophosphate) (2.29)

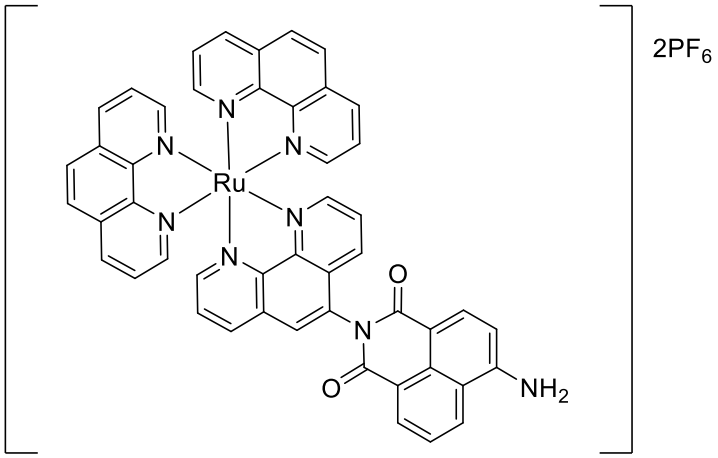

Dichlorobis(1,10-phenathroline)ruthenium(II) (0.096 g, 0.180 mmol) and **2.26** (0.070 g, 0.179 mmol) was added to a 1:1 EtOH:H_2O solution in a microwave tube and bubbled with nitrogen for 15 minutes. The reaction mixture was heated to 110°C in the microwave for 45 minutes. The reaction mixture was then filtered and ammonium hexafluorophosphate was added to the filtrate to form an orange precipitate. The precipitate was isolated via centrifugation and washed with water (2 x 20 mL). The precipitate was dissolved in a 40:4:1 acetonitrile: water: sodium nitrate solution and purified by column chromatography (SiO_2, 40:4:1 acetonitrile: water: sodium nitrate). The product was precipitated with ammonium hexafluorophosphate to afford the product as a red solid. (0.091 g, 44 % yield). **^{1}H NMR** (500 MHz, DMSO-*d*$_6$) δ 8.85 – 8.74 (m, 12H), 8.61 – 8.55 (m, 4H), 8.51 (dd, *J* = 7.3, 0.9 Hz, 1H), 8.45 – 8.38 (m, 9H), 8.27 (d, *J* = 8.4 Hz, 1H), 8.21 – 8.13 (m, 9H), 8.11 (m, 4H), 7.93 – 7.63 (m, 18H), 6.95 (d, *J* = 8.5 Hz, 1H), 6.92 (d, *J* = 8.5 Hz, 1H). **^{13}C NMR** (126 MHz, DMSO-*d*$_6$) δ 164.5, 164.4, 163.3, 163.3, 153.6, 153.3, 152.8, 152.8, 152.5, 147.4, 147.3, 147.3, 147.2, 147.0, 137.0, 137.0, 136.9, 134.5, 133.8, 133.8, 133.1, 131.5, 130.9, 130.6, 130.5, 130.5, 130.1, 129.6, 129.0, 128.8, 128.80, 128.1, 126.7, 126.5, 126.4, 124.2, 124.2, 122.1, 122.00, 119.7, 108.4, 108.4, 107.3, 107.2. **IR** (ATR): ν_{max} (cm^{-1}) = 3338, 3193, 3056, 1634, 1574, 1426, 1366, 1238, 1148, 1097, 1023, 847, 773, 721, 471, 409. **HRMS** (ESI+) *m/z* calcd for $C_{48}H_{28}F_{12}N_8O_4P_2Ru$ $[M]^+$ 852.1535, found 852.1529 (-0.73 ppm).

6.3 Synthetic Procedures for Chapter 3

(5-methyl-2-((4-nitrobenzyl)oxy)-1,3-phenylene)dimethanol (3.10)

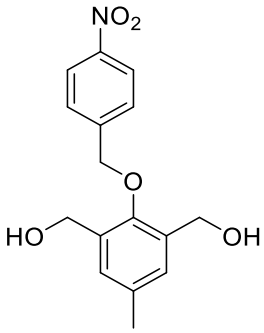

2,6-bis-hydroxymethyl-p-cresol (0.5 g, 2.973 mmol) and 4-nitrobenzyl bromide (0.706 g, 3.270 mmol) were dissolved in MeCN (200 mL) and K_2CO_3 (1.23 g, 8.919 mmol) was added. The reaction was stirred for 24 hours at room temperature. Solvent was removed *in vacuo* and the remaining solid was extracted with EtOAC with the use of a separatory funnel. The organic layers were combined and EtOAC was removed *in vacuo* to afford a crude product which was purified by column chromatography (SiO_2, 5:1 $CHCl_3$: EtOAC) to afford the product as a crystalline white solid. (0.52 g, 58 % yield). **^{1}H NMR** (500 MHz, DMSO-d_6) δ 8.28 (d, J = 8.8 Hz, 2H), 7.76 (d, J = 8.9 Hz, 2H), 7.16 (s, 2H), 5.10 (t, J = 5.5 Hz, 2H), 5.00 (s, 2H), 4.52 (d, J = 5.5 Hz, 4H), 2.29 (s, 3H). **^{13}C NMR** (126 MHz, DMSO-d_6) δ 151,0, 147.0, 145.6, 134.7, 132.9, 128.3, 127.9, 123.6, 74.1, 58.1, 20.8. **IR** (ATR): ν_{max} (cm^{-1}) = 3300, 2914, 2864, 1607, 1522, 1456, 1419, 1343, 1293, 1201, 1140, 1108, 1073, 1027, 867, 826, 731, 684, 608, 576, 521, 457.3. **HRMS** (ESI-) *m/z* calcd for $C_{16}H_{17}NO_5$ $[M - H]^-$ 302.1034, found 302.1036 (-0.8 ppm).

2-butyl-6-nitro-1*H*-benzo[*de*]isoquinoline-1,3(2*H*)-dione (3.13)

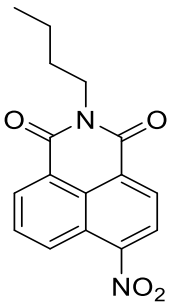

4-nitro-1,8-naphthalic anhydride (1 g, 4.115 mmol) and butyl amine (0.406 mL, 4.115 mmol) were dissolved in EtOH (10 mL) in a microwave tube and heated at 110°C for 50 minutes in the microwave. EtOH was then removed in vacuo and the resulting residue

was purified by column chromatography eluting with DCM to afford the product as a white solid (0.811 g, 66% yield). **^{1}H NMR** (500 MHz, DMSO-d_6) δ 8.69 (dd, J = 8.7, 0.9 Hz, 1H), 8.62 (dd, J = 7.3, 0.9 Hz, 1H), 8.59 (d, J = 8.0 Hz, 1H), 8.54 (d, J = 8.0 Hz, 1H), 8.08 (dd, J = 8.6, 7.4 Hz, 1H), 4.08 – 3.99 (m, 2H), 1.69 – 1.57 (m, 2H), 1.42 – 1.31 (m, 2H), 0.93 (t, J = 7.4 Hz, 3H). This is in agreement with literature precedent.[99]

6-amino-2-butyl-1*H*-benzo[*de*]isoquinoline-1,3(2*H*)-dione (3.11)

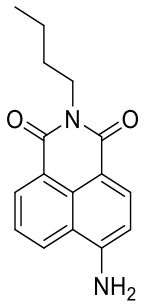

Compound **3.13** (0.5 g, 1.693 mmol) was dissolved in 20 mL MeOH with Pd/C (0.1 g, 0.940 mmol) under H_2 gas and stirred for 24 hours. Pd/C was removed from the reaction mixture via filtration with celite and the filtrate was removed *in vacuo* to afford a pure yellow solid. (0.411 g, 91 % yield). **^{1}H NMR** (500 MHz, DMSO-d_6) δ 8.60 (dd, J = 8.4, 1.1 Hz, 1H), 8.42 (dd, J = 7.3, 1.1 Hz, 1H), 8.18 (d, J = 8.4 Hz, 1H), 7.64 (dd, J = 8.4, 7.3 Hz, 1H), 7.42 (s, 2H), 6.84 (d, J = 8.4 Hz, 1H), 4.05 – 3.94 (m, 2H), 1.64 – 1.49 (m, 2H), 1.37 – 1.27 (m, 2H), 0.91 (t, J = 7.4 Hz, 3H). This is in agreement with literature precedent.[99]

(5-methyl-2-((4-nitrobenzyl)oxy)-1,3-phenylene)bis(methylene) bis((2-butyl-1,3-dioxo-2,3-dihydro-1*H*-benzo[*de*]isoquinolin-6-yl)carbamate) (3.6)

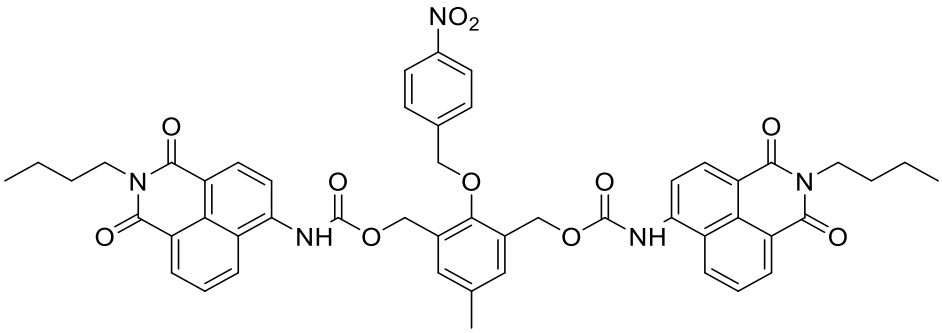

Compound **3.11** (0.2 g, 0.745 mmol) was dissolved in anhydrous $CHCl_3$ (50 mL) in a round bottom flask. Triethylamine (0.415 mL, 2.982 mmol) was then added and stirred. This mixture was then added dropwise to a $CHCl_3$ solution of triphosgene (0.221 g, 0.745 mmol) at 0°C in a round bottom flask. After 4 hours the solvent is removed by bubbling nitrogen through the reaction mixture. When dried **3.10** (0.068 g, 0.224 mmol) and triethylamine (0.415 mL, 0.745 mmol) dissolved in $CHCl_3$ (50 mL) was added and the reaction was stirred for 24 hours. The solvent was removed *in vacuo* and MeCN (20 mL) was added to the crude solid. The precipitate formed was collected via centrifugation to afford the product as an off white solid. (0.082 g, 41 % yield). **^{1}H NMR** (500 MHz, DMSO-d_6) δ 10.29 (s, 2H), 8.61 (d, J = 8.5 Hz, 2H), 8.46 (d, J = 7.1 Hz, 2H), 8.40 (d, J = 8.2 Hz, 2H), 8.08 (d, J = 8.3 Hz, 4H), 7.79 (t, J = 7.9 Hz, 2H), 7.71 (d, J = 8.4 Hz, 2H), 7.43 (s, 2H), 5.32 (s, 4H), 5.21 (s, 2H), 4.01 (t, J = 7.3 Hz, 4H), 2.36 (s, 3H), 1.67 – 1.52 (m, 4H), 1.33 (dd, J = 14.8, 7.4 Hz, 4H), 0.91 (t, J = 7.3 Hz, 6H). **^{13}C NMR** (126 MHz, DMSO-d_6) δ 163.4, 162.9, 153.9, 153.3, 146.8, 145.0, 140.7, 134.0, 131.6, 131.5, 130.9, 129.5, 129.2, 128.3, 127.9, 126.3, 123.9, 123.4, 122.2, 118.3, 117.1, 74.9, 62.2, 29.7, 20.5, 19.8, 13.7. **IR** (ATR): ν_{max} (cm^{-1}) = 3267, 2959, 2873, 1691, 1655, 1592, 1635, 1467, 1443, 1389, 1348, 1224, 1155, 1060, 1003, 956, 844, 780, 734, 657, 579, 495, 465, 415. **HRMS** (ESI+) *m/z* calcd for $C_{50}H_{45}N_5O_{11}$ $[M + Na]^+$ 914.3013, found 914.3002 (-0.36 ppm).

2-(2-(2-hydroxyethoxy)ethyl)-6-nitro-1*H*-benzo[*de*]isoquinoline-1,3(2*H*)-dione (3.14)

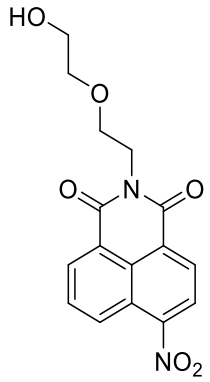

4-nitro-1,8-naphthalic anhydride (0.5 g, 2.056 mmol) was dissolved in THF (150 mL) and 2-(2-aminoethoxy)ethanol (0.412 mL, 4.112 mmol) was added and refluxed at 70°C for 4 hours. THF was then removed *in vacuo.* The crude solid was purified by column chromatography (SiO_2, ACN) to afford a white solid (0.32 g, 48 % yield) **^{1}H NMR** (500 MHz, DMSO-d_6) δ 8.67 (dd, J = 8.7, 1.0 Hz, 1H), 8.62 – 8.55 (m, 2H), 8.52 (d, J = 8.0 Hz, 1H), 8.06 (dd, J = 8.6, 7.4 Hz, 1H), 4.60 – 4.53 (m, 1H), 4.23 (t, J = 6.5 Hz, 2H), 3.67 (t, J = 6.5 Hz, 2H), 3.49 – 3.43 (m, 4H). **^{13}C NMR** (126 MHz, DMSO-d_6) δ 163.0, 162.2, 149.1, 131.8, 130.1, 129.70, 128.8, 128.3, 126.5, 124.3, 122.7, 122.6, 72.1, 66.7, 60.2. **IR** (ATR): ν_{max} (cm^{-1}) = 3481, 1698, 1656, 1623, 1593, 1520, 1463, 1438, 1406, 1333, 1271, 1229, 1185, 1151, 1118, 1051, 946. 891, 861, 842, 785. 760, 730, 666, 632, 579, 538, 519, 485, 456, 410. **HRMS** (ESI+) *m/z* calcd for $C_{16}H_{14}N_2O_6$ $[M + Na]^+$ 353.0750, found 353.0741 (-0.72 ppm).

2-(2-(6-nitro-1,3-dioxo-1*H*-benzo[*de*]isoquinolin-2(3*H*)-yl)ethoxy)ethyl acetate (3.15)

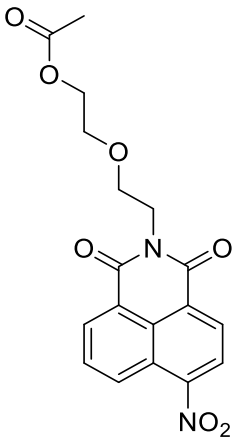

Compound **3.14** (0.56 g, 1.698 mmol) was dissolved in neat pyridine (15 mL) and acetic anhydride (0.24 mL, 2.547 mmol) was added. The reaction was stirred at RT for 24 hours. Pyridine was removed *in vacuo* to result in a yellow oil which was purified by column chromatography (SiO_2, 19 : 1 DCM : MeOH) to afford a white solid (0.317 g, 50 % yield). **^{1}H NMR** (500 MHz, DMSO-d_6) δ 8.91 – 8.29 (m, 4H), 8.09 (s, 1H), 4.25 (t, J = 6.3 Hz, 2H), 4.10 – 4.02 (m, 2H), 3.70 (t, J = 6.3 Hz, 2H), 3.66 – 3.61 (m, 2H), 1.87 (s, 3H). **^{13}C NMR** (126 MHz, DMSO-d_6) δ 170.2, 163.0, 149.2, 131.8, 130.1, 129.7, 128.9, 124.3, 122.8, 68.0, 66.7, 63.0, 20.5. **IR** (ATR): ν_{max} (cm^{-1}) = 3073, 2922, 2877, 1736, 1700, 1662, 1621, 1592, 1525, 1462, 1432, 1407, 1378, 1345, 1326, 1230, 1177, 1152, 1125, 1101, 1060, 976, 922, 880, 831, 791, 762, 732, 647, 608, 581, 509, 458. **HRMS** (ESI+) *m/z* calcd for $C_{18}H_{16}N_2O_7$ $[M + H]^+$ 373.1036, found 373.1027 (-0.72).

2-(2-(6-amino-1,3-dioxo-1*H*-benzo[*de*]isoquinolin-2(3*H*)-yl)ethoxy)ethyl acetate (3.12)

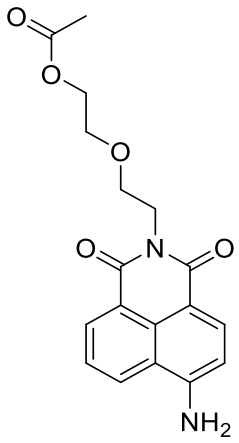

Compound **3.15** (0.3 g, 0.8 mmol) was dissolved in DMF (20 mL) with Pd/C (0.4 g, 3.759 mmol) under H_2 gas and stirred for 24 hours. Pd/C was removed from the reaction mixture via filtration with celite and the filtrate was removed *in vacuo* to afford a pure yellow solid. (0.229g, 84 % yield). **^{1}H NMR** (500 MHz, DMSO-d_6) δ 8.61 (dd, J = 8.4, 1.1 Hz, 1H), 8.42 (dd, J = 7.3, 1.1 Hz, 1H), 8.19 (d, J = 8.4 Hz, 1H), 7.65 (dd, J = 8.4, 7.3 Hz, 1H), 7.44 (s, 2H), 6.84 (d, J = 8.4 Hz, 1H), 4.20 (t, J = 6.5 Hz, 2H), 4.09 – 4.03 (m, 2H), 3.68 – 3.58 (m, 4H), 1.91 (s, 3H). **^{13}C NMR** (126 MHz, DMSO-d_6) δ 170.3, 163.8, 162.9, 152.8, 134.0, 131.1, 129.7, 129.4, 124.0, 121.7, 119.4, 108.2, 107.4, 67.9, 67.0, 63.1, 38.2, 20.5. **IR** (ATR): ν_{max} (cm^{-1}) = 3434, 3353, 3254, 1719, 1688, 1630, 1570, 1522, 1474, 1426, 1374, 1342, 1290, 1245, 1190, 1134, 1094, 1050, 958, 886, 850, 826, 768, 641, 589, 525, 467, 430. **HRMS** (ESI+) *m/z* calcd for $C_{18}H_{18}N_2O_5$ $[M + Na]^+$ 365.1113, found 365.1105 (-0.68).

(((((((((5-methyl-2-((4-nitrobenzyl)oxy)-1,3-phenylene)bis(methylene))bis(oxy))bis(carbonyl))bis(azanediyl))bis(1,3-dioxo-1*H*-benzo[de]isoquinoline-6,2(3*H*)-diyl))bis(ethane-2,1-diyl))bis(oxy))bis(ethane-2,1-diyl) diacetate (3.7)

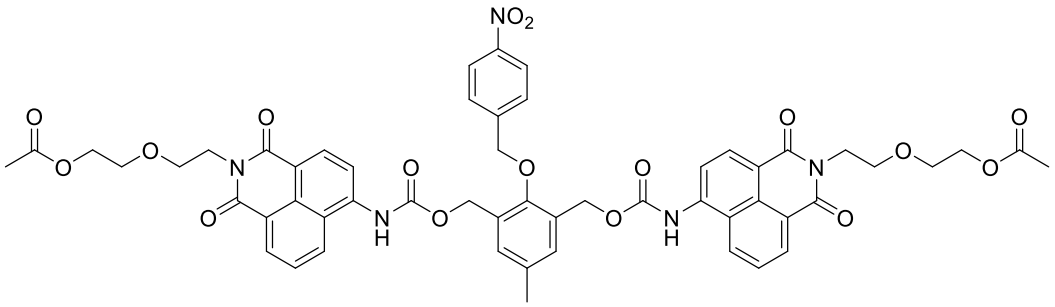

Compound **3.12** (0.15 g, 0.438 mmol) was dissolved in anhydrous DCM (50 mL) in a round bottom flask. Triethylamine (0.244 mL, 1.752 mmol) was then added and stirred. This mixture was then added dropwise to a DCM solution of triphosgene (0.130 g, 0.438 mmol) at 0°C in a round bottom flask. After 4 hours the solvent is removed by bubbling nitrogen through the reaction mixture. When dried **3.10** (0.022 g, 0.073 mmol) and triethylamine (0.244 mL, 1.752 mmol) dissolved in DCM (50 mL) was added and the reaction was stirred for 24 hours. DCM was removed *in vacuo* to result in a yellow oil which was purified by column chromatography (SiO_2, EtOAC) to afford a yellow solid (0.02 g, 26 % yield). **^{1}H NMR** (500 MHz, $CDCl_3$) δ 8.61 (d, *J* = 7.2 Hz, 2H), 8.56 (d, *J* = 8.3 Hz, 2H), 8.31 (d, *J* = 8.3 Hz, 2H), 8.20 (d, *J* = 8.7 Hz, 2H), 8.13 (d, *J* = 8.5 Hz, 2H), 7.74 (dd, *J* = 8.4, 7.4 Hz, 2H), 7.66 (d, *J* = 8.5 Hz, 2H), 7.54 (s, 2H), 7.37 (s, 2H), 5.37 (s, 4H), 5.13 (s, 2H), 4.42 (t, *J* = 6.0 Hz, 4H), 4.20 – 4.14 (m, 4H), 3.83 (t, *J* = 6.0 Hz, 4H), 3.76 – 3.72 (m, 4H), 2.41 (s, 3H), 1.97 (s, 6H). **^{13}C NMR** (126 MHz, $CDCl_3$) δ 171.2, 164.2, 163.7, 153.5, 153.1, 144.0, 138.8, 135.4, 132.6, 132.3, 131.6, 129.2, 129.1, 127.9, 126.9, 126.0, 124.0, 123.5, 68.6, 68.0, 63.8, 63.0, 41.1, 39.1, 21.0. **IR** (ATR): ν_{max} (cm^{-1}) = 3360, 1735, 1696, 1656, 1592, 1544, 1467, 1375, 1345, 1239, 1203, 1104, 1047, 1010, 953, 855, 828, 778, 755, 638, 605, 578, 542, 516, 487, 456, 404. **HRMS** (ESI+) *m/z* calcd for $C_{54}H_{49}N_5O_{17}$ $[M + H]^+$ 1040.3202, found 1040.3179 (0.32 ppm).

2-(2-(6-((((3-(hydroxymethyl)-5-methyl-2-((4-nitrobenzyl)oxy)benzyl)oxy)carbonyl)amino)-1,3-dioxo-1*H*-benzo[*de*]isoquinolin-2(3*H*)-yl)ethoxy)ethyl acetate (3.17)

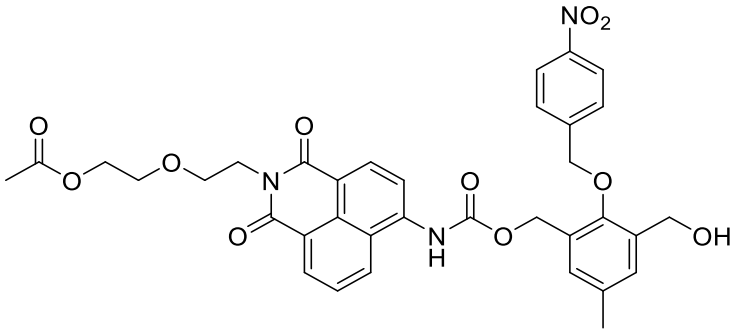

Compound **3.12** (0.05 g, 0.146 mmol) was dissolved in anhydrous DCM (50 mL) in a round bottom flask. Triethylamine (0.061 mL, 0.438 mmol) was then added and stirred. This mixture was then added dropwise to a DCM solution of triphosgene (0.043 g, 0.146 mmol) at 0°C in a round bottom flask. After 4 hours the solvent is removed by bubbling nitrogen through the reaction mixture. When dried **3.10** (0.089 g, 0.292 mmol) and triethylamine (0.061 mL, 0.438 mmol) dissolved in DCM (50 mL) was added and the reaction was stirred for 24 hours. DCM was removed *in vacuo* to result in a yellow oil which was purified by column chromatography (SiO_2, 10:3 Petroleum Ether: Ethyl Acetate) to afford a yellow solid (0.058 g, 59 % yield). **^{1}H NMR** (500 MHz, $CDCl_3$) δ 8.61 (dd, *J* = 7.3, 1.0 Hz, 1H), 8.57 (d, *J* = 8.3 Hz, 1H), 8.32 (d, *J* = 8.2 Hz, 1H), 8.25 – 8.19 (m, 2H), 8.11 (dd, *J* = 8.6, 0.9 Hz, 1H), 7.74 (dd, *J* = 8.5, 7.3 Hz, 1H), 7.65 (d, *J* = 8.8 Hz, 2H), 7.42 (s, 1H), 7.29 (d, *J* = 4.1 Hz, 2H), 5.34 (s, 2H), 5.11 (s, 2H), 4.73 (d, *J* = 5.5 Hz, 2H), 4.42 (t, *J* = 6.0 Hz, 2H), 4.17 (dd, *J* = 5.4, 4.1 Hz, 2H), 3.83 (t, *J* = 6.1 Hz, 2H), 3.76 – 3.72 (m, 2H), 2.38 (s, 3H), 1.98 (s, 3H), 1.88 (t, *J* = 5.7 Hz, 1H). **^{13}C NMR** (126 MHz, $CDCl_3$) δ 171.2, 164.3, 163.7, 153.2, 153.0, 147.8, 144.3, 138.9, 135.3, 134.1, 132.7, 131.5, 131.5, 131.2, 129.1, 128.7, 128.0, 126.8, 125.9, 124.0, 123.6, 123.0, 118.1, 117.0, 75.8, 68.6, 68.0, 63.8, 63.2, 61.0, 39.1, 21.0. **IR** (ATR): ν_{max} (cm^{-1}) = 3222, 2158, 1977, 1735, 1686, 1594, 1542, 1466, 1347, 1229, 1130, 1055, 991, 853, 782, 669, 580, 466. **HRMS** (ESI+) *m/z* calcd for $C_{35}H_{33}N_3O_{11}$ $[M + Na]^+$ 694.2013, found 694.2008 (0.10 ppm).

5-amino-2-(2-(dimethylamino)ethyl)-1*H*-benzo[*de*]isoquinoline-1,3(2*H*)-dione (3.18)

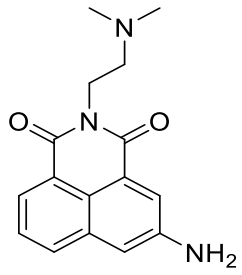

3-nitro-1,8-naphthalic anhydride (0.66 g, 2.714 mmol, 1 eq) was dissolved in EtOH (150 mL) in a RBF and refluxed at 80°C with N,N-dimethylethylenediamine (0.598 mL, 5.428 mmol, 2 eq) for 24 hours. The reaction mixture was cooled on ice and resulted in a brown precipitate that was filtered off and dissolved in a 1:1 mixture of EtOH and MeOH. Pd/C (0.067 g, 6.268 mmol, 0.4 eq) was added and the reaction mixture was placed under H_2 gas and stirred for 24 hours. Pd/C was removed from the reaction mixture via filtration with celite and the filtrate was removed *in vacuo* to afford an orange solid (0.391 g, 51 % yield). **^{1}H NMR** (500 MHz, DMSO-*d*$_6$) δ 8.06 (dd, *J* = 7.2, 1.1 Hz, 1H), 8.03 (dd, *J* = 8.4, 0.8 Hz, 1H), 7.95 (d, *J* = 2.3 Hz, 1H), 7.61 (dd, *J* = 8.2, 7.2 Hz, 1H), 7.27 (d, *J* = 2.3 Hz, 1H), 6.01 (s, 2H), 4.12 (t, *J* = 6.9 Hz, 2H), 2.19 (s, 6H). **^{13}C NMR** (126 MHz, DMSO-*d*$_6$) δ 163.9, 163.7, 148.0, 133.6, 131.6, 127.1, 125.6, 122.6, 121.8, 121.8, 120.6, 111.8, 56.6, 45.5, 37.6. **IR** (ATR): ν_{max} (cm^{-1}) = 3410, 2818, 2770, 1692, 1656, 1617, 1578, 1516, 1444, 1377, 1304, 1236, 1171, 1149, 1104, 1018, 931, 874, 850, 815, 779, 746, 633, 548, 501, 422.

2-(2-(6-((((3-((((2-(2-(dimethylamino)ethyl)-1,3-dioxo-2,3-dihydro-1*H*-benzo[*de*]isoquinolin-5-yl)carbamoyl)oxy)methyl)-5-methyl-2-((4-nitrobenzyl)oxy)benzyl)oxy)carbonyl)amino)-1,3-dioxo-1*H*-benzo[*de*]isoquinolin-2(3*H*)-yl)ethoxy)ethyl acetate (3.8)

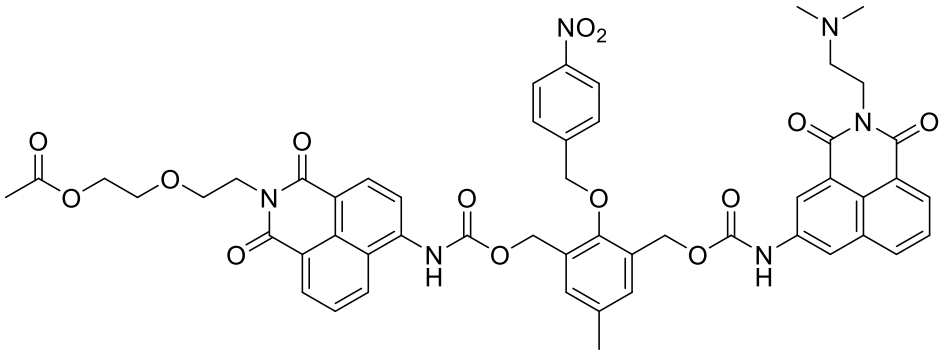

Compound **3.18** (0.05 g, 0.176 mmol) was dissolved in anhydrous DCM (50 mL) in a round bottom flask. Triethylamine (0.074 mL, 0.528 mmol) was then added and stirred. This mixture was then added dropwise to a DCM solution of triphosgene (0.053 g, 0.176 mmol) at 0°C in a round bottom flask. After 4 hours the solvent is removed by bubbling nitrogen through the reaction mixture. When dried **3.17** (0.118 g, 0.176 mmol) and triethylamine (0.074 mL, 0.528 mmol) dissolved in DCM (50 mL) was added and the reaction was stirred for 24 hours. DCM was removed *in vacuo* to result in a yellow oil which was purified by column chromatography (SiO_2, 20:1 DCM: MeOH) to afford a yellow solid (0.0074 g, 4 % yield). **^{1}H NMR** (500 MHz, $CDCl_3$) δ 8.60 (dd, *J* = 7.3, 0.8 Hz, 1H), 8.56 (d, *J* = 8.2 Hz, 1H), 8.37 (s, 1H), 8.31 (dd, *J* = 11.0, 7.9 Hz, 2H), 8.16 (dd, *J* = 18.0, 7.8 Hz, 4H), 7.98 (d, *J* = 8.1 Hz, 2H), 7.75 – 7.59 (m, 5H), 7.41 (d, *J* = 1.9 Hz, 1H), 7.36 (d, *J* = 1.9 Hz, 1H), 5.37 (s, 2H), 5.32 (s, 2H), 5.15 (s, 2H), 4.43 (t, *J* = 6.0 Hz, 2H), 4.29 (t, *J* = 6.4 Hz, 2H), 4.20 – 4.15 (m, 2H), 3.83 (t, *J* = 6.0 Hz, 2H), 3.74 (dd, *J* = 5.4, 4.1 Hz, 2H), 2.70 (t, *J* = 6.2 Hz, 2H), 2.42 (s, 3H), 2.36 (s, 6H), 1.97 (s, 3H). **^{13}C NMR** (126 MHz, $CDCl_3$) δ 171.2, 164.4, 164.3, 164.0, 163.7, 153.7, 153.3, 153.2, 147.8, 144.2, 139.0, 136.9, 135.4, 133.7, 132.6, 132.5, 132.4, 131.5, 129.8, 129.5, 129.1, 129.1, 127.9, 127.7, 126.8, 126.2, 124.6, 124.0, 123.5, 123.4, 123.2, 122.4, 118.2, 75.9, 68.6, 68.1, 63.8, 63.1, 62.6, 57.5, 45.9, 39.1, 38.1, 21.0. **IR** (ATR): ν_{max} (cm^{-1}) = 3309, 2955, 2921, 2859, 1732, 1697, 1655, 1591, 1544, 1520, 1466, 1433, 1376, 1343, 1297, 1234, 1204, 1173, 1146, 1108, 1048, 985. **HRMS** (ESI+) *m/z* calcd for $C_{52}H_{48}N_6O_{14}$ $[M + H]^+$ 981.3307, found 981.3304 (0.33 ppm).

2-(2-(6-((((3-((((4-(*N*-(3,4-dimethylisoxazol-5-yl)sulfamoyl)phenyl)carbamoyl)oxy)methyl)-5-methyl-2-((4-nitrobenzyl)oxy)benzyl)oxy)carbonyl)amino)-1,3-dioxo-1*H*-benzo[*de*]isoquinolin-2(3*H*)-yl)ethoxy)ethyl acetate (3.9)

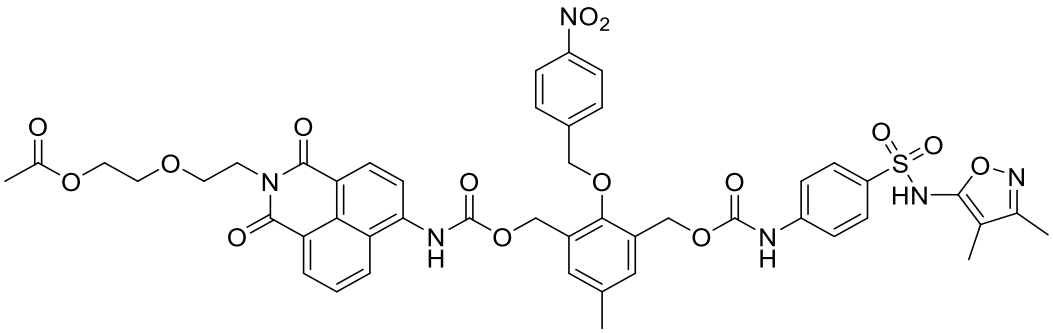

Sulfisoxazole **3.19** (0.05g, 0.187 mmol) was dissolved in anhydrous MeCN (50 mL) in a round bottom flask. Triethylamine (0.078 mL, 0.561 mmol) was then added and stirred. This mixture was then added dropwise to a DCM solution of triphosgene (0.056 g, 0.187 mmol) at 0°C in a round bottom flask. After 4 hours the solvent is removed by bubbling nitrogen through the reaction mixture. When dried **3.17** (0.118 g, 0.176 mmol) and triethylamine (0.078 mL, 0.561 mmol) dissolved in MeCN (50 mL) was added and the reaction was stirred for 24 hours. MeCN was removed *in vacuo* to result in a yellow oil which was purified by column chromatography (SiO_2, 5:1 DCM: ACN) to afford a off white solid (0.0052 g, 3 % yield). **^{1}H NMR** (500 MHz, $CDCl_3$) δ 8.59 (d, *J* = 6.6 Hz, 1H), 8.54 (d, *J* = 8.2 Hz, 1H), 8.26 (d, *J* = 8.0 Hz, 1H), 8.20 – 8.10 (m, 3H), 7.71 (dd, *J* = 8.4, 7.4 Hz, 1H), 7.66 (d, *J* = 8.8 Hz, 2H), 7.60 (d, *J* = 8.5 Hz, 2H), 7.57 (s, 1H), 7.44 (d, *J* = 8.7 Hz, 2H), 7.33 (s, 1H), 7.31 (s, 1H), 7.21 (s, 1H), 5.34 (s, 2H), 5.27 (s, 2H), 5.08 (s, 2H), 4.42 (t, *J* = 6.0 Hz, 2H), 4.20 – 4.13 (m, 2H), 3.83 (t, *J* = 6.0 Hz, 2H), 3.73 (dd, *J* = 5.4, 4.1 Hz, 2H), 2.38 (s, 3H), 2.16 (s, 3H), 1.96 (s, 3H), 1.92 (s, 3H). **^{13}C NMR** (126 MHz, $CDCl_3$) δ 171.3, 164.3, 163.8, 162.3, 154.7, 153.6, 153.2, 152.7, 147.8, 144.1, 144.0, 142.8, 138.9, 135.3, 133.5, 132.6, 132.4, 132.3, 131.6, 129.3, 129.1, 128.9, 127.8, 126.9, 126.2, 124.0, 123.5, 118.2, 108.2, 75.9, 68.6, 68.0, 63.8, 63.1, 62.7, 41.1, 39.1, 21.0, 11.0, 6.8. **IR** (ATR): ν_{max} (cm^{-1}) = 2920, 1734, 1697, 1651, 1592, 1539, 1465, 1380, 1344, 1207, 1162, 1095, 1051, 915, 840, 779, 736, 709, 642, 588, 554, 507, 467. **HRMS** (ESI+) *m/z* calcd for $C_{47}H_{44}N_6O_{15}S$ $[M + H]^+$ 965.2664, found 965.2651 (-0.18 ppm).

(2-(benzyloxy)-5-methyl-1,3-phenylene)dimethanol (3.22)

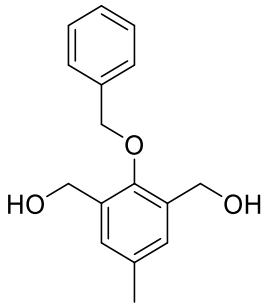

2,6-bis-hydroxymethyl-p-cresol (0.5 g, 2.973 mmol) and benzyl bromide (0.388 mL, 3.270 mmol) were dissolved in MeCN (200 mL) and K_2CO_3 (1.23 g, 8.919 mmol) was added. The reaction was stirred for 24 hours at room temperature. Solvent was removed *in vacuo* and the remaining solid was extracted with EtOAC with the use of a separatory funnel. The organic layers were combined and EtOAC was removed *in vacuo* to afford a crude product which was purified by column chromatography (SiO_2, 5:1 $CHCl_3$: EtOAC) to afford the product as a white solid. (0.3 g, 39 % yield). **^{1}H NMR** (500 MHz, DMSO-d_6) δ 7.48 – 7.44 (m, 2H), 7.44 – 7.38 (m, 2H), 7.38 – 7.33 (m, 1H), 7.15 (d, J = 0.5 Hz, 2H), 5.10 (t, J = 5.6 Hz, 2H), 4.81 (s, 2H), 4.52 (d, J = 5.5 Hz, 4H), 2.28 (s, 3H). **^{13}C NMR** (126 MHz, DMSO-d_6) δ 151.0, 137.7, 134.8, 132.6, 128.5, 128.0, 127.7, 75.6, 58.0, 20.9. **IR** (ATR): ν_{max} (cm^{-1}) = 3315, 2917, 2881, 1455, 1364, 1291, 1201, 1142, 1048, 1023, 976, 917, 868, 790, 766, 737, 697, 588, 566, 494, 469, 411.

(((((((((2-(benzyloxy)-5-methyl-1,3-phenylene)bis(methylene))bis(oxy))bis(carbonyl))bis(azanediyl))bis(1,3-dioxo-1*H*-benzo[*de*]isoquinoline-6,2(3*H*)-diyl))bis(ethane-2,1-diyl))bis(oxy))bis(ethane-2,1-diyl) diacetate (3.21)

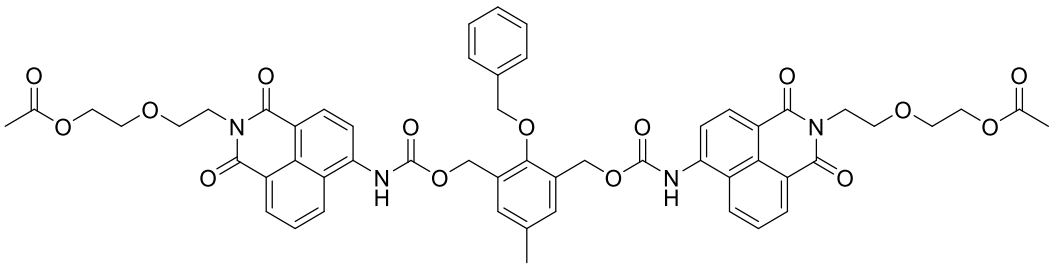

Compound **3.12** (0.15 g, 0.438 mmol) was dissolved in anhydrous DCM (50 mL) in a round bottom flask. Triethylamine (0.244 mL, 1.752 mmol) was then added and stirred. This mixture was then added dropwise to a DCM solution of triphosgene (0.130 g, 0.438 mmol) at 0°C in a round bottom flask. After 4 hours the solvent is removed by bubbling

nitrogen through the reaction mixture. Compound **3.22** (0.019 g, 0.073 mmol) and triethylamine (0.244 mL, 1.752 mmol) dissolved in DCM (50 mL) was added and the reaction was stirred for 24 hours. DCM was removed *in vacuo* to result in a yellow oil which was purified by column chromatography (SiO_2, EtOAC) to afford a yellow solid (0.018 g, 25 % yield). **^{1}H NMR** (500 MHz, $CDCl_3$) δ 8.60 – 8.53 (m, 4H), 8.34 (d, *J* = 8.2 Hz, 2H), 8.12 (dd, *J* = 8.7, 0.9 Hz, 2H), 7.70 (dd, *J* = 8.5, 7.3 Hz, 2H), 7.58 (s, 2H), 7.49 (d, *J* = 7.0 Hz, 2H), 7.41 – 7.33 (m, 5H), 5.36 (s, 4H), 5.01 (s, 2H), 4.41 (t, *J* = 6.0 Hz, 4H), 4.19 – 4.13 (m, 4H), 3.83 (t, *J* = 6.0 Hz, 4H), 3.76 – 3.71 (m, 4H), 2.38 (s, 3H), 1.96 (s, 6H). **^{13}C NMR** (126 MHz, $CDCl_3$) δ 171.2, 164.3, 163.8, 154.1, 153.1, 139.1, 136.6, 134.9, 132.7, 132.4, 131.5, 129.3, 129.1, 128.9, 128.9, 128.7, 128.2, 126.7, 126.2, 123.4, 117.9, 117.0, 68.6, 68.0, 63.8, 63.3, 39.0, 21.0. **IR** (ATR): ν_{max} (cm^{-1}) = 3269, 2907, 2882, 1740, 1721, 1691, 1654, 1592, 1541, 1509, 1447, 1373, 1345, 1236, 1197, 1127, 1051, 989, 957, 891, 854, 778, 753, 696, 647, 607, 578, 526, 487, 455, 406. **HRMS** (ESI+) *m/z* calcd for $C_{54}H_{50}N_4O_{15}$ $[M + Na]^+$ 1017.3170, found 1017.3159 (-0.53 ppm).

6.4 Synthetic Procedures for Chapter 4

11-(6-nitro-1,3-dioxo-1*H*-benzo[*de*]isoquinolin-2(3*H*)-yl)-5,6-dihydropyrazino[1,2,3,4-*lmn*][1,10]phenanthroline-4,7-diium hexafluorophosphate(V) (4.7)

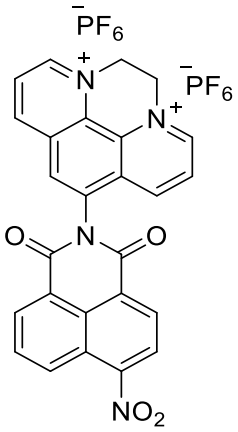

Compound **2.25** (0.3 g, 0.714 mmol) was suspended in a solution of neat dibromoethane (20 mL) and refluxed at 120°C for 72 hours. A brown precipitate was formed and isolated by Buchner filtration to afford a brown solid. The brown solid was washed with water and the filtrate was collected. NH_4PF_6 was added to the filtrate to result in a precipitate

which was isolated via centrifugation. The resulting precipitated was dried and purified by diethyl ether diffusion to afford compound **4.7** as a brown solid (0.112 g, 21 % yield). **^{1}H NMR** (400 MHz, DMSO-d_6) δ 9.93 – 9.83 (m, 3H), 9.68 (d, J = 7.6 Hz, 1H), 9.05 (s, 1H), 8.87 (dd, J = 8.7, 0.9 Hz, 1H), 8.78 (dd, J = 8.4, 5.8 Hz, 1H), 8.75 – 8.62 (m, 4H), 8.21 (dd, J = 8.7, 7.4 Hz, 1H), 5.68 (s, 4H). **^{13}C NMR** (101 MHz, DMSO-d_6) δ 163.12, 162.91, 149.80, 148.58, 133.44, 132.06, 131.97, 131.41, 130.68, 130.44, 130.21, 130.04, 129.85, 129.30, 129.19, 128.74, 127.26, 126.00, 124.22, 123.59, 123.45, 52.55. **IR** (ATR): ν_{max} (cm^{-1}) = 1716, 1676, 1596, 1530, 1502, 1401, 1340, 1236, 829, 782, 757, 705, 645, 556, 497, 473, 425, 405. **HRMS** (ESI+) *m/z* calcd for $C_{26}H_{16}N_4O_4$ $[M]^+$ 448.1172, found 448.1166 (1.42 ppm).

(*E*)-11-(6-(4-nitrostyryl)-1,3-dioxo-1*H*-benzo[*de*]isoquinolin-2(3*H*)-yl)-5,6-dihydropyrazino[1,2,3,4-*lmn*][1,10]phenanthroline-4,7-diium hexafluorophosphate(V) (4.8)

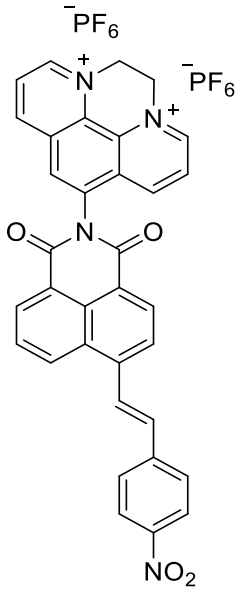

Compound **4.9** (0.1 g, 0.290 mmol) and 5-amine-1,10-phenanthroline (0.056 g, 0.290 mmol) were dissolved in DMF (10 mL) in a microwave tube. TEA (0.242 mL, 1.74 mmol) and $Zn(OAc)_2$ (0.013 g, 0.058 mmol) were added to the reaction mixture and and bubbled with nitrogen for 15 minutes. The reaction mixture was heated to 210°C in the microwave for 90 minutes. DMF was removed *in vacuo* and neat dibromoethane (20 mL) was added and refluxed at 120°C for 72 hours. A brown precipitate was formed and isolated by Buchner filtration to afford a brown solid. The brown solid was washed with water and the filtrate was collected. NH_4PF_6 was added to the filtrate to result in a precipitate which

was isolated via centrifugation. The resulting precipitated was dried and purified by diethyl ether diffusion to afford compound **4.8** as a brown solid (0.026 g, 11 % yield). **^{1}H NMR** (600 MHz, DMSO-d_6) δ 9.84 (dd, J = 12.0, 6.9 Hz, 3H), 9.64 (d, J = 8.2 Hz, 1H), 9.22 (d, J = 8.6 Hz, 1H), 9.06 (s, 1H), 8.76 (dd, J = 8.3, 5.8 Hz, 1H), 8.68 – 8.56 (m, 4H), 8.44 (d, J = 7.8 Hz, 1H), 8.34 (d, J = 8.7 Hz, 2H), 8.19 (d, J = 8.7 Hz, 2H), 8.09 – 8.04 (m, 1H), 7.85 (d, J = 16.1 Hz, 1H), 5.68 (s, 3H). **^{13}C NMR** (151 MHz, DMSO-d_6) δ 164.43, 164.11, 149.96, 149.82, 147.55, 147.14, 143.61, 143.24, 141.05, 134.11, 133.46, 131.81, 131.42, 130.92, 130.75, 130.44, 129.96, 129.71, 129.43, 129.40, 129.36, 128.68, 128.03, 127.90, 127.84, 127.56, 124.45, 124.17, 123.12, 122.18, 52.62, 52.28. **IR** (ATR): ν_{max} (cm^{-1}) = 1708, 1667, 1585, 1515, 1474, 1433, 1401, 1366, 1340, 1238, 1190, 834, 780, 742, 714, 644, 557, 498, 456, 434, 405. **HRMS** (ESI+) *m/z* calcd for $C_{34}H_{22}N_4O_4$ $[M]^+$ 550.1641, found 550.1631 (-0.94 ppm).

6.5 NTR Experiments

6.5.1 Fluorescence Titrations

NTR fluorescence titrations were carried out using an Agilent Spectrofluorometer equipped with a 450 W xenon lamp for excitation. A stock solution of compound 3 mM was prepared in either DMSO or PBS (if water soluble) before being diluted to a final volume of 2.5 mL in a fluorescence cuvette to result in a final concentration of 10 µM in 10 mM PBS where in general the total amount of DMSO present was < 1 %. A stock solution of 30 mM NADH was prepared in PBS and was diluted to a concentration of 500 µM in the final volume of 2.5 mL in a fluorescence cuvette. 1 mg of NTR ≥90% recombinant, expressed in E. coli was purchased from Sigma Aldrich and was diluted to 1 mL with Millipore grade water to give a concentration of 1 µg/µL and was typically added to the fluorescence cuvette in a manner so that the final concentration would be measured in µg mL^{-1} in a range of 0 to 8 µg mL^{-1}. Upon addition of NTR to a final volume of 2.5 mL an excitation wavelength was selected, and emission slit widths were adjusted. The emission spectra were generated from a selected emission wavelength range varying from 400 nm to 800 nm over a certain time period with intermittent cycles running every 2, 5, or 10 minutes.

6.5.2 Dicoumarol Study

NTR dicoumarol inhibitor studies were carried out using an Agilent Spectrofluorometer equipped with a 450 W xenon lamp for excitation. A stock solution of 3 mM of dicoumarol was prepared in DMSO before being diluted to a final volume of 2.5 mL in a fluorescence cuvette to result in a final concentration of 10-100 µM in 10 mM PBS where in general the total amount of DMSO present was < 1 %. A stock solution of 30 mM NADH was prepared in PBS and was diluted to a concentration of 500 µM in the final volume of 2.5 mL in a fluorescence cuvette. A stock solution of NTR 1 µg $µL^{-1}$ was added to the 2.5 mL volume so that the final concentration would be 2.5 µg mL^{-1} this was done prior to the addition of compound. A stock solution of compound 3 mM was prepared in either DMSO or PBS (if water soluble) before being diluted to a final volume of 2.5 mL in a fluorescence cuvette to result in a final concentration of 10 µM in 10 mM PBS where in general the total amount of DMSO present was < 1 %. An excitation wavelength was chosen, and the emission spectra would be generated from a selected emission wavelength

range varying from 400 nm to 800 nm over a certain time period with intermittent cycles running every 2, 5, or 10 minutes.

6.5.3 Selectivity Studies

NTR selectivity studies were carried out using an Agilent Spectrofluorometer equipped with a 450 W xenon lamp for excitation. 13 samples were prepared. A stock solution of compound 3 mM was prepared in either DMSO or PBS (if water soluble) before being diluted to a final volume of 2.5 mL in each glass vial to result in a final concentration of 10 µM in 10 mM PBS where in general the total amount of DMSO present was < 1 %. A stock solution of 30 mM NADH was prepared in PBS and was diluted to a concentration of 500 µM in the final volume of 2.5 mL in each glass vial. Stock solutions were made up for the following biologically relevant species in PBS and a glass vial was assigned for each species to result in a final concentration of NaCl 50 mM, Glucose 1 mM, Cysteine 1 mM, Glutathione 1 mM, DT-Diaphorase 1 µg mL^{-1}, Vitamin C 1 mM, Cytochrome C 1 µg mL^{-1}, Bovine serum albumin (10 mg mL^{-1}), Homocysteine (1mM), H_2O_2 1mM, 1-8 µg mL^{-1} NTR. Two blanks NADH 500 µM, and PBS with no NADH 500 µM were also included in the study. After a set time period the contents of each vial were placed into a fluorescence cuvette and an emission spectrum was recorded for each species at a constant wavelength of excitation.

6.5.4 LCMS Studies

LCMS studies were conducted on an Agilent Technologies 1200 series setup, utilising an Agilent Eclipse XDB-C18 (5µm, 4.6 x 150mm) column at 40°C. A flow rate of 0.2 ml min^{-1} and gradient of 0.1% of formic acid in CH_3CN (solvent A) in 0.1% of formic acid in H_2O (solvent B) was used as mobile phase. Electrospray in positive mode was used for ionisation. Samples were prepared in PBS to a final concentration of either 300 µM (if soluble in PBS) or 40 µM (if the stock was to be redissolved in DMSO) with NADH 500 µM in 10 mM PBS where the total amount of DMSO present was < 1%. In general, the final concentration of NTR in each study was 8-15 µg mL^{-1}. Before each LCMS was ran sufficient incubation time was given for reduction of the compound to occur. Solutions where the final volume of the compound was 300 µM were injected straight from the PBS solution onto the LCMS. Whereas, the compounds where the final volume of the

compound was 40 µM were subject to lyophilisation followed by dilution in 250 µL DMSO and were then injected onto the LCMS.

6.6 Sodium Dithionite Studies

Soidum dithionite studies were carried out using an Agilent Spectrofluorometer equipped with a 450 W xenon lamp for excitation. A stock solution of 3 mM of sodium dithiontite was prepared in 10mM PBS. A stock solution of compound 3 mM was prepared in DMSO before being diluted to a final volume of 2.5 mL in a fluorescence cuvette to result in a final concentration of 10 µM in either 10 mM PBS or 10mM Tris HCl of varying percentages of DMSO. Sodium dithionite was then diluted to a final volume of 2.5 mL in a fluorescence cuvette to result in a final concentration of 1 mM. An excitation wavelength was chosen, and the emission spectra would be generated from a selected emission wavelength range varying from 400 nm to 800 nm with intermittent cycles running every 5 minutes.

6.7 Quantum Yield Calculations

Quantum yield calculations were estimated with the use of the following formula.

$$\emptyset_x = \emptyset_{st} \cdot \left(\frac{A_{st}}{A_x}\right) \cdot \left(\frac{F_x}{F_{st}}\right) \cdot \left(\frac{{n_x}^2}{{n_{st}}^2}\right) \cdot \left(\frac{D_x}{D_{st}}\right)$$

Where Φ_{st} is the reference quantum yield value for $[Ru(bpy)_3]^{2+}$ which was 0.028.[223, 224] A_{st} and A_x are the absorbance values of the standard and the unknown sample respectively, at the excitation wavelength chosen which was kept constant for both samples. F is the area under the emission curve. n is the refractive index values. D is the dilution ratio.

6.8 DNA Titrations

A stock solution of stDNA was prepared in H_2O. Generally, 14 mg of stDNA was stirred in 10 mL of H_2O until it appeared to be fully dissolved. The concentration of 10 µL of the stock solution in 2.5 mL of PBS was determined from UV/Vis spectroscopy recording the absorbance at 260 nm and using beer lamberts law equation $A = \varepsilon Cl$ where $\varepsilon = 6600\ M^{-1}cm^{-1}$. The known concentration was then added in 10 µL aliquots for all titrations UV/Vis and fluorescence titrations.

6.9 Cytotoxicity Assay

Carried out by Dr. Catherine Grillon, CNRS, Orleans, France. Cells were plated in 96-well plates and incubated in either a standard normoxic incubator or a hypoxia workstation (1% O_2). Cells were then treated for 24h with **2.11**, **2.12** or **2.13** at various concentrations (in triplicate) in the culture medium containing 0.5% DMSO. Cytotoxicity was determined using the Alamar Blue Cell Viability Reagent. Fluorescence was measured using the CLARIOstar Microplate Reader (Ex 545 +/- 20, Em 600 +/- 40). Results are expressed as the percentage of cell viability compared to the control (0.5% DMSO in the medium).

6.10 HeLa Cell Imaging

Carried out by Dr. Martina Shroeder. Compound **2.29** was dissolved in DMSO result in a stock solution of 20 mM. HeLa cells were grown on coverslips. The final concentration of compound 18 was 20 µM diluted directly into the cell culture supernatants. The cells were then incubated for 30 minutes at 37 °C. After incubation the cells were washed with PBS and then mounted onto slides with Sigma Fluoromount and were imaged immediately on an Olympus Fluoview FV1000 Confocal microscope and the proprietary software for it. A 488nm laser for excitation of the compound **2.29** was used and a 405nm laser for the DAPI. Scanning with both lasers was sequential. Emission window for **2.29** was set to 585-685nm. Emission window for DAPI was 416-452nm.

6.11 Bacteria Cell Imaging

Carried out by Luke Brennan within the Elmes group. *S. aureus* were grown to stationary phase overnight before being isolated (1 mL – OD600 – 1.0) washed twice with PBS, and resuspended in 100 µL PBS, where they were treated with compound **2.13** at 3 µM or dicoumarol at 10 µM for 30 minutes in the absence of light. Thereafter, cells were once again isolated, washed twice with PBS and resuspended in 100 µL PBS (4% paraformaldehyde, pH 8) and fixed for 30 minutes before being isolated, washed as previous and resuspended in 20 µL prolong golf anti fade mountant. 10µL aliquots of cell suspensions were placed atop slides which catered for both super resolution, STimulated Emission Depletion Nanoscopy (STED), and diffraction limited Confocal Scanning Microscopy (*d*-LSCM) and covered with a similarly compatible coverslip before being sealed with varnish, and stored in the dark until they were used for imaging. Using a Leica Stellaris 8 STED falcon microscope. Utilising both LSCM White Light (WL) laser (EL $\lambda_{455/465/495\ nm}$) and STED Depletion Laser (DL) (EL $\lambda_{455/465/495\ nm}$, DL $\lambda_{775\ nm}$, 30% power) alterations to the fluorescence lifetime of Compound **2.13** was analysed, when excited by WL, and when emission is depleted (DL), using Fluorescence Lifetime Imaging Microscopy (FLIM). Obtaining both fluorescence lifetime phasor plots and lifetime histograms from both *d*-LSCM and STED depleted images, the STED compatibility of compound **2.13** was demonstrated. Given the STED compatibility of compound **2.13** cells were imaged using LSCM (EL $l_{455/465/495\ nm}$) and STED (EL $l_{455/465/495\ nm}$, DL $l_{775\ nm}$, 30% power, time gating; 0.5 – 11 ns).

Bibliography

(1) *World Health Organisation*. 2020. https://www.who.int/en/news-room/fact-sheets/detail/cancer (accessed 2022.

(2) *National Cancer Registry Ireland*. 2023. https://www.ncri.ie/publications/statistical-reports/cancer-ireland-1994-2014-annual-report-national-cancer-registry (accessed 2023.

(3) Hanahan, D.; Weinberg, R. A. The Hallmarks of Cancer. *Cell* **2000**, *100* (1), 57-70. DOI: https://doi.org/10.1016/S0092-8674(00)81683-9.

(4) Hanahan, D.; Weinberg, Robert A. Hallmarks of Cancer: The Next Generation. *Cell* **2011**, *144* (5), 646-674. DOI: https://doi.org/10.1016/j.cell.2011.02.013.

(5) Hanahan, D. Hallmarks of Cancer: New Dimensions. *Cancer Discovery* **2022**, *12* (1), 31-46. DOI: 10.1158/2159-8290.CD-21-1059 (acccessed 6/7/2023).

(6) Burrell, R. A.; McGranahan, N.; Bartek, J.; Swanton, C. The causes and consequences of genetic heterogeneity in cancer evolution. *Nature* **2013**, *501* (7467), 338-345. DOI: 10.1038/nature12625.

(7) Debela, D. T.; Muzazu, S. G.; Heraro, K. D.; Ndalama, M. T.; Mesele, B. W.; Haile, D. C.; Kitui, S. K.; Manyazewal, T. New approaches and procedures for cancer treatment: Current perspectives. *SAGE Open Med* **2021**, *9*, 20503121211034366. DOI: 10.1177/20503121211034366 From NLM.

(8) Jin, M.-Z.; Jin, W.-L. The updated landscape of tumor microenvironment and drug repurposing. *Signal Transduction and Targeted Therapy* **2020**, *5* (1), 166. DOI: 10.1038/s41392-020-00280-x.

(9) Bożyk, A.; Wojas-Krawczyk, K.; Krawczyk, P.; Milanowski, J. Tumor Microenvironment-A Short Review of Cellular and Interaction Diversity. *Biology (Basel)* **2022**, *11* (6). DOI: 10.3390/biology11060929 From NLM.

(10) Xiao, Y.; Yu, D. Tumor microenvironment as a therapeutic target in cancer. *Pharmacol Ther* **2021**, *221*, 107753. DOI: 10.1016/j.pharmthera.2020.107753 From NLM.

(11) Bejarano, L.; Jordão, M. J. C.; Joyce, J. A. Therapeutic Targeting of the Tumor Microenvironment. *Cancer Discovery* **2021**, *11* (4), 933-959. DOI: 10.1158/2159-8290.CD-20-1808 (acccessed 6/19/2023).

(12) Qiu, G. Z.; Jin, M. Z.; Dai, J. X.; Sun, W.; Feng, J. H.; Jin, W. L. Reprogramming of the Tumor in the Hypoxic Niche: The Emerging Concept and Associated Therapeutic Strategies. *Trends Pharmacol Sci* **2017**, *38* (8), 669-686. DOI: 10.1016/j.tips.2017.05.002 From NLM.

(13) Thorsson, V.; Gibbs, D. L.; Brown, S. D.; Wolf, D.; Bortone, D. S.; Ou Yang, T. H.; Porta-Pardo, E.; Gao, G. F.; Plaisier, C. L.; Eddy, J. A.; et al. The Immune Landscape of Cancer. *Immunity* **2018**, *48* (4), 812-830.e814. DOI: 10.1016/j.immuni.2018.03.023 From NLM.

(14) Thomlinson, R. H.; Gray, L. H. The Histological Structure of Some Human Lung Cancers and the Possible Implications for Radiotherapy. *British Journal of Cancer* **1955**, *9* (4), 539-549. DOI: 10.1038/bjc.1955.55.

(15) Chen, Z.; Han, F.; Du, Y.; Shi, H.; Zhou, W. Hypoxic microenvironment in cancer: molecular mechanisms and therapeutic interventions. *Signal Transduction and Targeted Therapy* **2023**, *8* (1), 70. DOI: 10.1038/s41392-023-01332-8.

(16) Popel, A. S. Theory of oxygen transport to tissue. *Crit Rev Biomed Eng* **1989**, *17* (3), 257-321. From NLM.

(17) Denny, W. A. The role of hypoxia-activated prodrugs in cancer therapy. *The Lancet Oncology* **2000**, *1* (1), 25-29. DOI: https://doi.org/10.1016/S1470-2045(00)00006-1.

(18) Husain, A.; Chiu, Y. T.; Sze, K. M.; Ho, D. W.; Tsui, Y. M.; Suarez, E. M. S.; Zhang, V. X.; Chan, L. K.; Lee, E.; Lee, J. M.; et al. Ephrin-A3/EphA2 axis regulates cellular metabolic plasticity to enhance cancer stemness in hypoxic hepatocellular carcinoma. *J Hepatol* **2022**, *77* (2), 383-396. DOI: 10.1016/j.jhep.2022.02.018 From NLM.

(19) Dewhirst, M. W.; Ong, E. T.; Braun, R. D.; Smith, B.; Klitzman, B.; Evans, S. M.; Wilson, D. Quantification of longitudinal tissue pO2 gradients in window chamber tumours: impact on tumour hypoxia. *Br J Cancer* **1999**, *79* (11-12), 1717-1722. DOI: 10.1038/sj.bjc.6690273 From NLM.

(20) Dachs, G. U.; Dougherty, G. J.; Stratford, I. J.; Chaplin, D. J. Targeting gene therapy to cancer: a review. *Oncol Res* **1997**, *9* (6-7), 313-325. From NLM.

(21) Krock, B. L.; Skuli, N.; Simon, M. C. Hypoxia-induced angiogenesis: good and evil. *Genes Cancer* **2011**, *2* (12), 1117-1133. DOI: 10.1177/1947601911423654 From NLM.

(22) Li, Y.; Zhao, L.; Li, X. F. Hypoxia and the Tumor Microenvironment. *Technol Cancer Res Treat* **2021**, *20*, 15330338211036304. DOI: 10.1177/15330338211036304 From NLM.

(23) Düvel, K.; Yecies, J. L.; Menon, S.; Raman, P.; Lipovsky, A. I.; Souza, A. L.; Triantafellow, E.; Ma, Q.; Gorski, R.; Cleaver, S.; et al. Activation of a metabolic gene regulatory network downstream of mTOR complex 1. *Mol Cell* **2010**, *39* (2), 171-183. DOI: 10.1016/j.molcel.2010.06.022 From NLM.

(24) van Uden, P.; Kenneth, N. S.; Webster, R.; Müller, H. A.; Mudie, S.; Rocha, S. Evolutionary conserved regulation of HIF-1β by NF-κB. *PLoS Genet* **2011**, *7* (1), e1001285. DOI: 10.1371/journal.pgen.1001285 From NLM.

(25) Wan, J.; Wu, W. Hyperthermia induced HIF-1a expression of lung cancer through AKT and ERK signaling pathways. *Journal of Experimental & Clinical Cancer Research* **2016**, *35* (1), 119. DOI: 10.1186/s13046-016-0399-7.

(26) Li, Y.; Xu, Y.; Wang, R.; Li, W.; He, W.; Luo, X.; Ye, Y. Expression of Notch–Hif-1α signaling pathway in liver regeneration of rats. *Journal of International Medical Research* **2020**, *48* (9), 0300060520943790. DOI: 10.1177/0300060520943790 (acccessed 2023/07/24).

(27) Gordan, J. D.; Thompson, C. B.; Simon, M. C. HIF and c-Myc: Sibling Rivals for Control of Cancer Cell Metabolism and Proliferation. *Cancer Cell* **2007**, *12* (2), 108-113. DOI: https://doi.org/10.1016/j.ccr.2007.07.006.

(28) Akakura, N.; Kobayashi, M.; Horiuchi, I.; Suzuki, A.; Wang, J.; Chen, J.; Niizeki, H.; Kawamura, K.; Hosokawa, M.; Asaka, M. Constitutive expression of hypoxia-inducible factor-1alpha renders pancreatic cancer cells resistant to apoptosis induced by hypoxia and nutrient deprivation. *Cancer Res* **2001**, *61* (17), 6548-6554. From NLM.

(29) Brahimi-Horn, C.; Berra, E.; Pouysségur, J. Hypoxia: the tumor's gateway to progression along the angiogenic pathway. *Trends in Cell Biology* **2001**, *11* (11), S32-S36. DOI: https://doi.org/10.1016/S0962-8924(01)02126-2.

(30) Jaakkola, P.; Mole, D. R.; Tian, Y.-M.; Wilson, M. I.; Gielbert, J.; Gaskell, S. J.; Kriegsheim, A. v.; Hebestreit, H. F.; Mukherji, M.; Schofield, C. J.; et al. Targeting of HIF-α to the von Hippel-Lindau Ubiquitylation Complex by O2-Regulated Prolyl Hydroxylation. *Science* **2001**, *292* (5516), 468-472. DOI: 10.1126/science.1059796 (acccessed 2023/07/24).

(31) Evinger, M. J.; Cikos, S.; Nwafor-Anene, V.; Powers, J. F.; Tischler, A. S. Hypoxia Activates Multiple Transcriptional Pathways in Mouse Pheochromocytoma Cells. *Annals of the New York Academy of Sciences* **2002**, *971* (1), 61-65, https://doi.org/10.1111/j.1749-6632.2002.tb04434.x. DOI: https://doi.org/10.1111/j.1749-6632.2002.tb04434.x (acccessed 2023/07/24).

(32) Wu, D.; Potluri, N.; Lu, J.; Kim, Y.; Rastinejad, F. Structural integration in hypoxia-inducible factors. *Nature* **2015**, *524* (7565), 303-308. DOI: 10.1038/nature14883.

(33) Kizaka-Kondoh, S.; Konse-Nagasawa, H. Significance of nitroimidazole compounds and hypoxia-inducible factor-1 for imaging tumor hypoxia. *Cancer Science* **2009**, *100* (8), 1366-1373. DOI: 10.1111/j.1349-7006.2009.01195.x (acccessed 2019/02/12).

(34) Lal, A.; Peters, H.; St. Croix, B.; Haroon, Z. A.; Dewhirst, M. W.; Strausberg, R. L.; Kaanders, J. H. A. M.; van der Kogel, A. J.; Riggins, G. J. Transcriptional Response to Hypoxia in Human Tumors. *JNCI: Journal of the National Cancer Institute* **2001**, *93* (17), 1337-1343. DOI: 10.1093/jnci/93.17.1337 (acccessed 7/24/2023).

(35) Hoefflin, R.; Harlander, S.; Schäfer, S.; Metzger, P.; Kuo, F.; Schönenberger, D.; Adlesic, M.; Peighambari, A.; Seidel, P.; Chen, C.-y.; et al. HIF-1α and HIF-2α differently regulate tumour development and inflammation of clear cell renal cell carcinoma in mice. *Nature Communications* **2020**, *11* (1), 4111. DOI: 10.1038/s41467-020-17873-3.

(36) Vander Heiden, M. G.; Cantley, L. C.; Thompson, C. B. Understanding the Warburg Effect: The Metabolic Requirements of Cell Proliferation. *Science* **2009**, *324* (5930), 1029-1033. DOI: 10.1126/science.1160809 (acccessed 2023/07/25).

(37) Richard, D. E.; Berra, E.; Pouysségur, J. Nonhypoxic Pathway Mediates the Induction of Hypoxia-inducible Factor 1α in Vascular Smooth Muscle Cells*. *Journal of Biological Chemistry* **2000**, *275* (35), 26765-26771. DOI: https://doi.org/10.1016/S0021-9258(19)61441-9.

(38) Hlatky, L.; Tsionou, C.; Hahnfeldt, P.; Coleman, C. N. Mammary fibroblasts may influence breast tumor angiogenesis via hypoxia-induced vascular endothelial growth factor up-regulation and protein expression. *Cancer Res* **1994**, *54* (23), 6083-6086. From NLM.

(39) Ramakrishnan, S.; Anand, V.; Roy, S. Vascular endothelial growth factor signaling in hypoxia and inflammation. *J Neuroimmune Pharmacol* **2014**, *9* (2), 142-160. DOI: 10.1007/s11481-014-9531-7 From NLM.

(40) Semenza, Gregg L. Hypoxia-Inducible Factors in Physiology and Medicine. *Cell* **2012**, *148* (3), 399-408. DOI: https://doi.org/10.1016/j.cell.2012.01.021.

(41) Greijer, A. E.; van der Wall, E. The role of hypoxia inducible factor 1 (HIF-1) in hypoxia induced apoptosis. *J Clin Pathol* **2004**, *57* (10), 1009-1014. DOI: 10.1136/jcp.2003.015032 From NLM.

(42) Jing, X.; Yang, F.; Shao, C.; Wei, K.; Xie, M.; Shen, H.; Shu, Y. Role of hypoxia in cancer therapy by regulating the tumor microenvironment. *Molecular Cancer* **2019**, *18* (1), 157. DOI: 10.1186/s12943-019-1089-9.

(43) Skarsgard, L. D.; Vinczan, A.; Skwarchuk, M. W.; Chaplin, D. J. The effect of low ph and hypoxia on the cytotoxic effects of SR4233 and mitomycin C in vitro. *International Journal of Radiation Oncology*Biology*Physics* **1994**, *29* (2), 363-367. DOI: https://doi.org/10.1016/0360-3016(94)90290-9.

(44) Yokoi, K.; Fidler, I. J. Hypoxia Increases Resistance of Human Pancreatic Cancer Cells to Apoptosis Induced by Gemcitabine. *Clinical Cancer Research* **2004**, *10* (7), 2299-2306. DOI: 10.1158/1078-0432.CCR-03-0488 (acccessed 7/25/2023).

(45) Sakata, K.; Kwok, T. T.; Murphy, B. J.; Laderoute, K. R.; Gordon, G. R.; Sutherland, R. M. Hypoxia-induced drug resistance: comparison to P-glycoprotein-associated drug resistance. *British Journal of Cancer* **1991**, *64* (5), 809-814. DOI: 10.1038/bjc.1991.405.

(46) Telarovic, I.; Wenger, R. H.; Pruschy, M. Interfering with Tumor Hypoxia for Radiotherapy Optimization. *Journal of Experimental & Clinical Cancer Research* **2021**, *40* (1), 197. DOI: 10.1186/s13046-021-02000-x.

(47) Bristow, R. G.; Hill, R. P. Hypoxia, DNA repair and genetic instability. *Nature Reviews Cancer* **2008**, *8* (3), 180-192. DOI: 10.1038/nrc2344.

(48) Mukherjee, B.; McEllin, B.; Camacho, C. V.; Tomimatsu, N.; Sirasanagandala, S.; Nannepaga, S.; Hatanpaa, K. J.; Mickey, B.; Madden, C.; Maher, E.; et al. EGFRvIII and DNA Double-Strand Break Repair: A Molecular Mechanism for Radioresistance in Glioblastoma. *Cancer Research* **2009**, *69* (10), 4252-4259. DOI: 10.1158/0008-5472.CAN-08-4853 (acccessed 7/25/2023).

(49) Harris, B.; Saleem, S.; Cook, N.; Searle, E. Targeting hypoxia in solid and haematological malignancies. *Journal of Experimental & Clinical Cancer Research* **2022**, *41* (1), 318. DOI: 10.1186/s13046-022-02522-y.

(50) Le, Q. T.; Courter, D. Clinical biomarkers for hypoxia targeting. *Cancer Metastasis Rev* **2008**, *27* (3), 351-362. DOI: 10.1007/s10555-008-9144-9 From NLM.

(51) Vordermark, D.; Horsman, M. R. Hypoxia as a Biomarker and for Personalized Radiation Oncology. *Recent Results Cancer Res* **2016**, *198*, 123-142. DOI: 10.1007/978-3-662-49651-0_6 From NLM.

(52) Godet, I.; Doctorman, S.; Wu, F.; Gilkes, D. M. Detection of Hypoxia in Cancer Models: Significance, Challenges, and Advances. *Cells* **2022**, *11* (4). DOI: 10.3390/cells11040686 From NLM.

(53) Gaertner, F. C.; Souvatzoglou, M.; Brix, G.; Beer, A. J. Imaging of hypoxia using PET and MRI. *Curr Pharm Biotechnol* **2012**, *13* (4), 552-570. DOI: 10.2174/138920112799436267 From NLM.

(54) Walsh, J. C.; Lebedev, A.; Aten, E.; Madsen, K.; Marciano, L.; Kolb, H. C. The clinical importance of assessing tumor hypoxia: relationship of tumor hypoxia to prognosis and therapeutic opportunities. *Antioxid Redox Signal* **2014**, *21* (10), 1516-1554. DOI: 10.1089/ars.2013.5378 From NLM.

(55) Qlark Jr, L. C. Monitor and control of blood and tissue oxygen tensions. *Asaio Journal* **1956**, *2* (1), 41-48.

(56) Gatenby, R. A.; Kessler, H. B.; Rosenblum, J. S.; Coia, L. R.; Moldofsky, P. J.; Hartz, W. H.; Broder, G. J. Oxygen distribution in squamous cell carcinoma metastases and its relationship to outcome of radiation therapy. *Int J Radiat Oncol Biol Phys* **1988**, *14* (5), 831-838. DOI: 10.1016/0360-3016(88)90002-8 From NLM.

(57) Daponte, A.; Ioannou, M.; Mylonis, I.; Simos, G.; Minas, M.; Messinis, I. E.; Koukoulis, G. Prognostic significance of Hypoxia-Inducible Factor 1 alpha(HIF-1 alpha) expression in serous ovarian cancer: an immunohistochemical study. *BMC Cancer* **2008**, *8*, 335. DOI: 10.1186/1471-2407-8-335 From NLM.

(58) Nordsmark, M.; Loncaster, J.; Aquino-Parsons, C.; Chou, S. C.; Gebski, V.; West, C.; Lindegaard, J. C.; Havsteen, H.; Davidson, S. E.; Hunter, R.; et al. The prognostic value of pimonidazole and tumour pO2 in human cervix carcinomas after radiation therapy: a prospective international multi-center study. *Radiother Oncol* **2006**, *80* (2), 123-131. DOI: 10.1016/j.radonc.2006.07.010 From NLM.

(59) O'Connor, J. P. B.; Robinson, S. P.; Waterton, J. C. Imaging tumour hypoxia with oxygen-enhanced MRI and BOLD MRI. *Br J Radiol* **2019**, *92* (1095), 20180642. DOI: 10.1259/bjr.20180642 From NLM.

(60) Gertsenshteyn, I.; Giurcanu, M.; Vaupel, P.; Halpern, H. Biological validation of electron paramagnetic resonance (EPR) image oxygen thresholds in tissue. *J Physiol* **2021**, *599* (6), 1759-1767. DOI: 10.1113/jp278816 From NLM.

(61) Krishna, M. C.; Matsumoto, S.; Yasui, H.; Saito, K.; Devasahayam, N.; Subramanian, S.; Mitchell, J. B. Electron paramagnetic resonance imaging of tumor pO_2. *Radiat Res* **2012**, *177* (4), 376-386. DOI: 10.1667/rr2622.1 From NLM.

(62) Lee, C. P.; Payne, G. S.; Oregioni, A.; Ruddle, R.; Tan, S.; Raynaud, F. I.; Eaton, D.; Campbell, M. J.; Cross, K.; Halbert, G.; et al. A phase I study of the nitroimidazole hypoxia marker SR4554 using 19F magnetic resonance spectroscopy. *Br J Cancer* **2009**, *101* (11), 1860-1868. DOI: 10.1038/sj.bjc.6605425 From NLM.

(63) Bowen, S. R.; van der Kogel, A. J.; Nordsmark, M.; Bentzen, S. M.; Jeraj, R. Characterization of positron emission tomography hypoxia tracer uptake and tissue oxygenation via electrochemical modeling. *Nucl Med Biol* **2011**, *38* (6), 771-780. DOI: 10.1016/j.nucmedbio.2011.02.002 From NLM.

(64) Lin, X.; Ruan, Q.; Lin, L.; Zhang, X.; Duan, X.; Teng, Y.; Zhang, J. Biological evaluation and SPECT imaging of tumor hypoxia using a novel technetium-99m labeled tracer with 2-nitroimidazole moiety. *Journal of Radioanalytical and Nuclear Chemistry* **2018**, *317* (3), 1463-1468. DOI: 10.1007/s10967-018-6005-z.

(65) Apte, S.; Chin, F. T.; Graves, E. E. Molecular Imaging of Hypoxia: Strategies for Probe Design and Application. *Curr Org Synth* **2011**, *8* (4), 593-603. DOI: 10.2174/157017911796117179 From NLM.

(66) Elmes, R. B. P. Bioreductive fluorescent imaging agents: applications to tumour hypoxia. *Chem. Commun. (Cambridge, U. K.)* **2016**, *52* (58), 8935-8956, 10.1039/C6CC01037G. DOI: 10.1039/C6CC01037G.

(67) Romani, A.; Clementi, C.; Miliani, C.; Favaro, G. Fluorescence Spectroscopy: A Powerful Technique for the Noninvasive Characterization of Artwork. *Accounts of Chemical Research* **2010**, *43* (6), 837-846. DOI: 10.1021/ar900291y.

(68) Kasha, M. Characterization of electronic transitions in complex molecules. *Discussions of the Faraday Society* **1950**, *9* (0), 14-19, 10.1039/DF9500900014. DOI: 10.1039/DF9500900014.

(69) Instruments, E. *What is a Jablonski Diagram (Perrin-Jablonski Diagram)?* 2024. https://www.edinst.com/blog/jablonski-diagram-2/ (accessed 2024.

(70) Godet, I.; Shin, Y. J.; Ju, J. A.; Ye, I. C.; Wang, G.; Gilkes, D. M. Fate-mapping post-hypoxic tumor cells reveals a ROS-resistant phenotype that promotes metastasis. *Nat Commun* **2019**, *10* (1), 4862. DOI: 10.1038/s41467-019-12412-1 From NLM.

(71) Karlsson, H.; Fryknäs, M.; Larsson, R.; Nygren, P. Loss of cancer drug activity in colon cancer HCT-116 cells during spheroid formation in a new 3-D spheroid cell culture system. *Exp Cell Res* **2012**, *318* (13), 1577-1585. DOI: 10.1016/j.yexcr.2012.03.026 From NLM.

(72) Le, A.; Stine, Z. E.; Nguyen, C.; Afzal, J.; Sun, P.; Hamaker, M.; Siegel, N. M.; Gouw, A. M.; Kang, B. H.; Yu, S. H.; et al. Tumorigenicity of hypoxic respiring cancer cells revealed by a hypoxia-cell cycle dual reporter. *Proc Natl Acad Sci U S A* **2014**, *111* (34), 12486-12491. DOI: 10.1073/pnas.1402012111 From NLM.

(73) Wang, Y.; Wang, H.; Li, J.; Entenberg, D.; Xue, A.; Wang, W.; Condeelis, J. Direct visualization of the phenotype of hypoxic tumor cells at single cell resolution in vivo using a new hypoxia probe. *Intravital* **2016**, *5* (2). DOI: 10.1080/21659087.2016.1187803 From NLM.

(74) Wu, D.; Sedgwick, A. C.; Gunnlaugsson, T.; Akkaya, E. U.; Yoon, J.; James, T. D. Fluorescent chemosensors: the past, present and future. *Chem. Soc. Rev.* **2017**, *46* (23), 7105-7123, 10.1039/C7CS00240H. DOI: 10.1039/C7CS00240H.

(75) Elmes, R. B. P. Bioreductive fluorescent imaging agents: applications to tumour hypoxia. *Chemical Communications* **2016**, *52* (58), 8935-8956, 10.1039/C6CC01037G. DOI: 10.1039/C6CC01037G.

(76) Yin, J.; Huang, L.; Wu, L.; Li, J.; James, T. D.; Lin, W. Small molecule based fluorescent chemosensors for imaging the microenvironment within specific cellular regions. *Chemical Society Reviews* **2021**, *50* (21), 12098-12150, 10.1039/D1CS00645B. DOI: 10.1039/D1CS00645B.

(77) de Silva, A. P.; Gunaratne, H. Q. N.; Gunnlaugsson, T.; Huxley, A. J. M.; McCoy, C. P.; Rademacher, J. T.; Rice, T. E. Signaling Recognition Events with Fluorescent Sensors and Switches. *Chemical Reviews* **1997**, *97* (5), 1515-1566. DOI: 10.1021/cr960386p.

(78) Czarnik, A. W. Chemical Communication in Water Using Fluorescent Chemosensors. *Accounts of Chemical Research* **1994**, *27* (10), 302-308. DOI: 10.1021/ar00046a003.

(79) He, H.; Mortellaro, M. A.; Leiner, M. J. P.; Fraatz, R. J.; Tusa, J. K. A Fluorescent Sensor with High Selectivity and Sensitivity for Potassium in Water. *Journal of the American Chemical Society* **2003**, *125* (6), 1468-1469. DOI: 10.1021/ja0284761.

(80) Marraccini, C.; Farruggia, G.; Lombardo, M.; Prodi, L.; Sgarzi, M.; Trapani, V.; Trombini, C.; Wolf, F. I.; Zaccheroni, N.; Iotti, S. Diaza-18-crown-6 hydroxyquinoline derivatives as flexible tools for the assessment and imaging of total intracellular magnesium. *Chemical Science* **2012**, *3* (3), 727-734, 10.1039/C1SC00751C. DOI: 10.1039/C1SC00751C.

(81) Carter, K. P.; Young, A. M.; Palmer, A. E. Fluorescent Sensors for Measuring Metal Ions in Living Systems. *Chemical Reviews* **2014**, *114* (8), 4564-4601. DOI: 10.1021/cr400546e.

(82) Rivera-Fuentes, P.; Wrobel, A. T.; Zastrow, M. L.; Khan, M.; Georgiou, J.; Luyben, T. T.; Roder, J. C.; Okamoto, K.; Lippard, S. J. A far-red emitting probe for unambiguous detection of mobile zinc in acidic vesicles and deep tissue. *Chemical Science* **2015**, *6* (3), 1944-1948, 10.1039/C4SC03388D. DOI: 10.1039/C4SC03388D.

(83) Goshisht, M. K.; Tripathi, N. Fluorescence-based sensors as an emerging tool for anion detection: mechanism, sensory materials and applications. *Journal of Materials Chemistry C* **2021**, *9* (31), 9820-9850, 10.1039/D1TC01990B. DOI: 10.1039/D1TC01990B.

(84) Amendola, V.; Bergamaschi, G.; Boiocchi, M.; Fabbrizzi, L.; Mosca, L. The Interaction of Fluoride with Fluorogenic Ureas: An ON1-OFF-ON2 Response. *J. Am. Chem. Soc.* **2013**, *135* (16), 6345-6355, 10.1021/ja4019786. DOI: 10.1021/ja4019786.

(85) Dickinson, B. C.; Huynh, C.; Chang, C. J. A Palette of Fluorescent Probes with Varying Emission Colors for Imaging Hydrogen Peroxide Signaling in Living Cells. *J. Am. Chem. Soc.* **2010**, *132* (16), 5906-5915, 10.1021/ja1014103. DOI: 10.1021/ja1014103.

(86) Jia, X.; Chen, Q.; Yang, Y.; Tang, Y.; Wang, R.; Xu, Y.; Zhu, W.; Qian, X. FRET-Based Mito-Specific Fluorescent Probe for Ratiometric Detection and Imaging of Endogenous Peroxynitrite: Dyad of Cy3 and Cy5. *J Am Chem Soc* **2016**, *138* (34), 10778-10781. DOI: 10.1021/jacs.6b06398 From NLM.

(87) Li, X.; Qian, S.; He, Q.; Yang, B.; Li, J.; Hu, Y. Design and synthesis of a highly selective fluorescent turn-on probe for thiol bioimaging in living cells. *Organic & Biomolecular Chemistry* **2010**, *8* (16), 3627-3630, 10.1039/C004344C. DOI: 10.1039/C004344C.

(88) Ji, S.; Guo, H.; Yuan, X.; Li, X.; Ding, H.; Gao, P.; Zhao, C.; Wu, W.; Wu, W.; Zhao, J. A Highly Selective OFF-ON Red-Emitting Phosphorescent Thiol Probe with Large Stokes Shift and Long Luminescent Lifetime. *Organic Letters* **2010**, *12* (12), 2876-2879. DOI: 10.1021/ol100999j.

(89) Ou, Y.; Wilson, R. E.; Weber, S. G. Methods of Measuring Enzyme Activity Ex Vivo and In Vivo. *Annu Rev Anal Chem (Palo Alto Calif)* **2018**, *11* (1), 509-533. DOI: 10.1146/annurev-anchem-061417-125619 From NLM.

(90) Geraghty, C.; Wynne, C.; Elmes, R. B. P. 1,8-Naphthalimide based fluorescent sensors for enzymes. *Coordination Chemistry Reviews* **2021**, *437*, 213713. DOI: https://doi.org/10.1016/j.ccr.2020.213713.

(91) Chyan, W.; Raines, R. T. Enzyme-activated fluorogenic probes for live-cell and in vivo imaging. *ACS chemical biology* **2018**, *13* (7), 1810-1823.

(92) Kobayashi, H.; Ogawa, M.; Alford, R.; Choyke, P. L.; Urano, Y. New strategies for fluorescent probe design in medical diagnostic imaging. *Chemical reviews* **2010**, *110* (5), 2620-2640. DOI: 10.1021/cr900263j PubMed.

(93) Chen, X.; Pradhan, T.; Wang, F.; Kim, J. S.; Yoon, J. Fluorescent chemosensors based on spiroring-opening of xanthenes and related derivatives. *Chemical reviews* **2012**, *112* (3), 1910-1956.

(94) Li, X.; Gao, X.; Shi, W.; Ma, H. Design strategies for water-soluble small molecular chromogenic and fluorogenic probes. *Chemical reviews* **2014**, *114* (1), 590-659.

(95) Yuan, L.; Lin, W.; Zheng, K.; He, L.; Huang, W. Far-red to near infrared analyte-responsive fluorescent probes based on organic fluorophore platforms for fluorescence imaging. *Chemical Society Reviews* **2013**, *42* (2), 622-661.

(96) Asanuma, D.; Sakabe, M.; Kamiya, M.; Yamamoto, K.; Hiratake, J.; Ogawa, M.; Kosaka, N.; Choyke, P. L.; Nagano, T.; Kobayashi, H.; et al. Sensitive β-galactosidase-targeting fluorescence probe for visualizing small peritoneal metastatic tumours in vivo. *Nature Communications* **2015**, *6*, Article. DOI: 10.1038/ncomms7463 Scopus.

(97) Kim, T.-I.; Kim, H.; Choi, Y.; Kim, Y. A fluorescent turn-on probe for the detection of alkaline phosphatase activity in living cells. *Chemical Communications* **2011**, *47* (35), 9825-9827.

(98) Liu, Z.-M.; Feng, L.; Ge, G.-B.; Lv, X.; Hou, J.; Cao, Y.-F.; Cui, J.-N.; Yang, L. A highly selective ratiometric fluorescent probe for in vitro monitoring and cellular imaging of human carboxylesterase 1. *Biosensors and Bioelectronics* **2014**, *57*, 30-35.

(99) Ao, X.; Bright, S. A.; Taylor, N. C.; Elmes, R. B. P. 2-Nitroimidazole based fluorescent probes for nitroreductase; monitoring reductive stress in cellulo. *Org. Biomol. Chem.* **2017**, *15* (29), 6104-6108, 10.1039/C7OB01406F. DOI: 10.1039/C7OB01406F.

(100) Dai, Z.-R.; Ge, G.-B.; Feng, L.; Ning, J.; Hu, L.-H.; Jin, Q.; Wang, D.-D.; Lv, X.; Dou, T.-Y.; Cui, J.-N. A highly selective ratiometric two-photon fluorescent probe for human cytochrome P450 1A. *Journal of the American Chemical Society* **2015**, *137* (45), 14488-14495.

(101) Zhang, L.; Duan, D.; Liu, Y.; Ge, C.; Cui, X.; Sun, J.; Fang, J. Highly Selective Off–On Fluorescent Probe for Imaging Thioredoxin Reductase in Living Cells. *Journal of the American Chemical Society* **2014**, *136* (1), 226-233. DOI: 10.1021/ja408792k.

(102) Blum, G.; Von Degenfeld, G.; Merchant, M. J.; Blau, H. M.; Bogyo, M. Noninvasive optical imaging of cysteine protease activity using fluorescently quenched activity-based probes. *Nature chemical biology* **2007**, *3* (10), 668-677.

(103) Kiyose, K.; Hanaoka, K.; Oushiki, D.; Nakamura, T.; Kajimura, M.; Suematsu, M.; Nishimatsu, H.; Yamane, T.; Terai, T.; Hirata, Y. Hypoxia-sensitive fluorescent probes for in vivo real-time fluorescence imaging of acute ischemia. *Journal of the American Chemical Society* **2010**, *132* (45), 15846-15848.

(104) Mu, J.; Liu, F.; Rajab, M. S.; Shi, M.; Li, S.; Goh, C.; Lu, L.; Xu, Q. H.; Liu, B.; Ng, L. G. A small-molecule FRET reporter for the real-time visualization of cell-surface proteolytic enzyme functions. *Angewandte Chemie* **2014**, *126* (52), 14585-14590.

(105) Podder, A.; Alex, S. M.; Maiti, M.; Maiti, K. K.; Bhuniya, S. Self-calibrated fluorescent probe resembled as an indicator of the lysosomal phosphatase pertaining to the cancer cells. *Journal of Photochemistry and Photobiology B: Biology* **2017**, *177*, 105-111. DOI: https://doi.org/10.1016/j.jphotobiol.2017.10.019.

(106) Zhou, J.; Shi, W.; Li, L. H.; Gong, Q. Y.; Wu, X. F.; Li, X. H.; Ma, H. M. A Lysosome-Targeting Fluorescence Off-On Probe for Imaging of Nitroreductase and Hypoxia in Live Cells. *Chemistry–An Asian Journal* **2016**, *11* (19), 2719-2724.

(107) Silvers, W. C.; Prasai, B.; Burk, D. H.; Brown, M. L.; McCarley, R. L. Profluorogenic reductase substrate for rapid, selective, and sensitive visualization and

detection of human cancer cells that overexpress NQO1. *Journal of the American Chemical Society* **2013**, *135* (1), 309-314. DOI: 10.1021/ja309346f PubMed.

(108) Lee, M. H.; Kim, J. S.; Sessler, J. L. Small molecule-based ratiometric fluorescence probes for cations, anions, and biomolecules. *Chemical Society Reviews* **2015**, *44* (13), 4185-4191, 10.1039/C4CS00280F. DOI: 10.1039/C4CS00280F.

(109) Liu, H.-W.; Chen, L.; Xu, C.; Li, Z.; Zhang, H.; Zhang, X.-B.; Tan, W. Recent progresses in small-molecule enzymatic fluorescent probes for cancer imaging. *Chemical Society Reviews* **2018**, *47* (18), 7140-7180, 10.1039/C7CS00862G. DOI: 10.1039/C7CS00862G.

(110) Weissleder, R. A clearer vision for in vivo imaging. *Nature biotechnology* **2001**, *19* (4), 316-317.

(111) Duan, C.; Won, M.; Verwilst, P.; Xu, J.; Kim, H. S.; Zeng, L.; Kim, J. S. In vivo imaging of endogenously produced HClO in zebrafish and mice using a bright, photostable ratiometric fluorescent probe. *Analytical chemistry* **2019**, *91* (6), 4172-4178.

(112) Espinar-Barranco, L.; Luque-Navarro, P.; Strnad, M. A.; Herrero-Foncubierta, P.; Crovetto, L.; Miguel, D.; Giron, M. D.; Orte, A.; Cuerva, J. M.; Salto, R. A solvatofluorochromic silicon-substituted xanthene dye useful in bioimaging. *Dyes and Pigments* **2019**, *168*, 264-272.

(113) Bao, X.; Wu, X.; Berry, S. N.; Howe, E. N. W.; Chang, Y.-T.; Gale, P. A. Fluorescent squaramides as anion receptors and transmembrane anion transporters. *Chemical Communications* **2018**, *54* (11), 1363-1366.

(114) Kim, H. N.; Lee, M. H.; Kim, H. J.; Kim, J. S.; Yoon, J. A new trend in rhodamine-based chemosensors: application of spirolactam ring-opening to sensing ions. *Chemical Society Reviews* **2008**, *37* (8), 1465-1472.

(115) Loudet, A.; Burgess, K. BODIPY dyes and their derivatives: syntheses and spectroscopic properties. *Chemical reviews* **2007**, *107* (11), 4891-4932.

(116) Sedgwick, A. C.; Hayden, A.; Hill, B.; Bull, S. D.; Elmes, R. B. P.; James, T. D. A simple umbelliferone based fluorescent probe for the detection of nitroreductase. *Frontiers of Chemical Science and Engineering* **2018**, *12* (2), 311-314. DOI: 10.1007/s11705-017-1697-0.

(117) Wang, S.; Wu, X.; Zhang, Y.; Zhang, D.; Xie, B.; Pan, Z.; Ouyang, K.; Peng, T. Discovery of a highly efficient nitroaryl group for detection of nitroreductase and imaging of hypoxic tumor cells. *Organic & Biomolecular Chemistry* **2021**, *19* (15), 3469-3478, 10.1039/D1OB00356A. DOI: 10.1039/D1OB00356A.

(118) Park, S.; Lim, S.-Y.; Bae, S. M.; Kim, S.-Y.; Myung, S.-J.; Kim, H.-J. Indocyanine-Based Activatable Fluorescence Turn-On Probe for γ-Glutamyltranspeptidase and Its Application to the Mouse Model of Colon Cancer. *ACS Sensors* **2016**, *1* (5), 579-583. DOI: 10.1021/acssensors.5b00249.

(119) Iwatate, R. J.; Kamiya, M.; Umezawa, K.; Kashima, H.; Nakadate, M.; Kojima, R.; Urano, Y. Silicon Rhodamine-Based Near-Infrared Fluorescent Probe for γ-Glutamyltransferase. *Bioconjugate Chemistry* **2018**, *29* (2), 241-244. DOI: 10.1021/acs.bioconjchem.7b00776.

(120) Redy-Keisar, O.; Kisin-Finfer, E.; Ferber, S.; Satchi-Fainaro, R.; Shabat, D. Synthesis and use of QCy7-derived modular probes for the detection and imaging of biologically relevant analytes. *Nature Protocols* **2014**, *9* (1), 27-36. DOI: 10.1038/nprot.2013.166.

(121) Shi, L.; Yan, C.; Ma, Y.; Wang, T.; Guo, Z.; Zhu, W.-H. In vivo ratiometric tracking of endogenous β-galactosidase activity using an activatable near-infrared fluorescent probe. *Chemical Communications* **2019**, *55* (82), 12308-12311, 10.1039/C9CC06869D. DOI: 10.1039/C9CC06869D.

(122) Janczy-Cempa, E.; Mazuryk, O.; Kania, A.; Brindell, M. Significance of Specific Oxidoreductases in the Design of Hypoxia-Activated Prodrugs and Fluorescent Turn off-on Probes for Hypoxia Imaging. *Cancers (Basel)* **2022**, *14* (11). DOI: 10.3390/cancers14112686 From NLM.

(123) Lugrin, J.; Rosenblatt-Velin, N.; Parapanov, R.; Liaudet, L. The role of oxidative stress during inflammatory processes. **2014**, *395* (2), 203-230. DOI: doi:10.1515/hsz-2013-0241 (acccessed 2023-08-03).

(124) Xiao, W.; Loscalzo, J. Metabolic Responses to Reductive Stress. *Antioxid Redox Signal* **2020**, *32* (18), 1330-1347. DOI: 10.1089/ars.2019.7803 From NLM.

(125) Eales, K. L.; Hollinshead, K. E. R.; Tennant, D. A. Hypoxia and metabolic adaptation of cancer cells. *Oncogenesis* **2016**, *5* (1), e190-e190. DOI: 10.1038/oncsis.2015.50.

(126) Wilson, W. R.; Hay, M. P. Targeting hypoxia in cancer therapy. *Nat Rev Cancer* **2011**, *11* (6), 393-410. DOI: 10.1038/nrc3064 From NLM.

(127) Fitzsimmons, S. A.; Workman, P.; Grever, M.; Paull, K.; Camalier, R.; Lewis, A. D. Reductase enzyme expression across the National Cancer Institute Tumor cell line panel: correlation with sensitivity to mitomycin C and EO9. *J Natl Cancer Inst* **1996**, *88* (5), 259-269. DOI: 10.1093/jnci/88.5.259 From NLM.

(128) Kling, J. Hypoxia-activated prodrugs forge ahead in cancer. *Nature Biotechnology* **2012**, *30*, 381. DOI: 10.1038/nbt0512-381.

(129) Brezden, C. B.; Horn, L.; McClelland, R. A.; Rauth, A. M. Oxidative Stress and 1-Methyl-2-nitroimidazole Cytotoxicity. *Biochemical Pharmacology* **1998**, *56* (3), 335-344. DOI: https://doi.org/10.1016/S0006-2952(98)00158-0.

(130) Takasawa, M.; Moustafa Ramez, R.; Baron, J.-C. Applications of Nitroimidazole In Vivo Hypoxia Imaging in Ischemic Stroke. *Stroke* **2008**, *39* (5), 1629-1637. DOI: 10.1161/STROKEAHA.107.485938 (acccessed 2019/02/12).

(131) Okuda, K.; Okabe, Y.; Kadonosono, T.; Ueno, T.; Youssif, B. G. M.; Kizaka-Kondoh, S.; Nagasawa, H. 2-Nitroimidazole-Tricarbocyanine Conjugate as a Near-Infrared Fluorescent Probe for in Vivo Imaging of Tumor Hypoxia. *Bioconjugate Chemistry* **2012**, *23* (3), 324-329. DOI: 10.1021/bc2004704.

(132) Varghese, A. J.; Gulyas, S.; Mohindra, J. K. Hypoxia-dependent Reduction of 1-(2-Nitro-1-imidazolyl)-3-methoxy-2-propanol by Chinese Hamster Ovary Cells and KHT Tumor Cells in Vitro and in Vivo1. *Cancer Research* **1976**, *36* (10), 3761-3765. (acccessed 8/9/2023).

(133) Li, Y.; Zhao, L.; Li, X.-F. The Hypoxia-Activated Prodrug TH-302: Exploiting Hypoxia in Cancer Therapy. *Frontiers in Pharmacology* **2021**, *12*, Review.

(134) Middleton, R. W.; Parrick, J.; Clarke, E. D.; Wardman, P. Synthesis and fluorescence of N-substituted-1, 8-naphthalimides. *Journal of heterocyclic chemistry* **1986**, *23* (3), 849-855.

(135) Fu, Y.; Finney, N. S. Small-molecule fluorescent probes and their design. *RSC advances* **2018**, *8* (51), 29051-29061.

(136) Duke, R. M.; Veale, E. B.; Pfeffer, F. M.; Kruger, P. E.; Gunnlaugsson, T. Colorimetric and fluorescent anion sensors: an overview of recent developments in the use of 1, 8-naphthalimide-based chemosensors. *Chemical society reviews* **2010**, *39* (10), 3936-3953.

(137) Fleming, C. L.; Nalder, T. D.; Doeven, E. H.; Barrow, C. J.; Pfeffer, F. M.; Ashton, T. D. Synthesis of N-substituted 4-hydroxynaphthalimides using palladium-catalysed hydroxylation. *Dyes and Pigments* **2016**, *126*, 118-120.

(138) Liu, T.; Xu, Z.; Spring, D. R.; Cui, J. A lysosome-targetable fluorescent probe for imaging hydrogen sulfide in living cells. *Organic letters* **2013**, *15* (9), 2310-2313.

(139) Chen, S.; Hou, P.; Foley, J. W.; Song, X. A colorimetric and ratiometric fluorescent probe for Cu 2+ with a large red shift and its imaging in living cells. *RSC advances* **2013**, *3* (16), 5591-5596.

(140) Panchenko, P. A.; Fedorov, Y. V.; Perevalov, V. P.; Jonusauskas, G.; Fedorova, O. A. Cation-dependent fluorescent properties of naphthalimide derivatives with N-benzocrown ether fragment. *The Journal of Physical Chemistry A* **2010**, *114* (12), 4118-4122.

(141) Yu, H.; Guo, Y.; Zhu, W.; Havener, K.; Zheng, X. Recent advances in 1,8-naphthalimide-based small-molecule fluorescent probes for organelles imaging and tracking in living cells. *Coordination Chemistry Reviews* **2021**, *444*, 214019. DOI: https://doi.org/10.1016/j.ccr.2021.214019.

(142) Tamanini, E.; Flavin, K.; Motevalli, M.; Piperno, S.; Gheber, L. A.; Todd, M. H.; Watkinson, M. Cyclam-Based "Clickates": Homogeneous and Heterogeneous Fluorescent Sensors for Zn(II). *Inorganic Chemistry* **2010**, *49* (8), 3789-3800. DOI: 10.1021/ic901939x.

(143) Xu, Z.; Qian, X.; Cui, J. Colorimetric and Ratiometric Fluorescent Chemosensor with a Large Red-Shift in Emission: Cu(II)-Only Sensing by Deprotonation of Secondary Amines as Receptor Conjugated to Naphthalimide Fluorophore. *Organic Letters* **2005**, *7* (14), 3029-3032. DOI: 10.1021/ol051131d.

(144) Duke, R. M.; Gunnlaugsson, T. Selective fluorescent PET sensing of fluoride (F−) using naphthalimide–thiourea and –urea conjugates. *Tetrahedron Letters* **2007**, *48* (45), 8043-8047. DOI: https://doi.org/10.1016/j.tetlet.2007.09.026.

(145) Esteban-Gómez, D.; Fabbrizzi, L.; Licchelli, M. Why, on Interaction of Urea-Based Receptors with Fluoride, Beautiful Colors Develop. *The Journal of Organic Chemistry* **2005**, *70* (14), 5717-5720. DOI: 10.1021/jo050528s.

(146) Liu, S.-Z.; Xu, J.-H.; Ma, Q.-J.; Wang, B.-Y.; Li, L.-K.; Zhu, N.-N.; Liu, S.-Y.; Wang, G.-G. A naphthalimide-based and Golgi-targetable fluorescence probe for quantifying hypochlorous acid. *Spectrochimica Acta Part A: Molecular and Biomolecular Spectroscopy* **2023**, *286*, 121986. DOI: https://doi.org/10.1016/j.saa.2022.121986.

(147) Kim, D.; Kim, G.; Nam, S.-J.; Yin, J.; Yoon, J. Visualization of Endogenous and Exogenous Hydrogen Peroxide Using A Lysosome-Targetable Fluorescent Probe. *Scientific Reports* **2015**, *5* (1), 8488. DOI: 10.1038/srep08488.

(148) Williams, E. M.; Little, R. F.; Mowday, A. M.; Rich, M. H.; Chan-Hyams, J. V. E.; Copp, J. N.; Smaill, J. B.; Patterson, A. V.; Ackerley, D. F. Nitroreductase gene-directed enzyme prodrug therapy: insights and advances toward clinical utility. *Biochemical journal* **2015**, *471* (2), 131-153.

(149) White, S. A.; Christofferson, A. J.; Grainger, A. I.; Day, M. A.; Jarrom, D.; Graziano, A. E.; Searle, P. F.; Hyde, E. I. The 3D-structure, kinetics and dynamics of the E. coli nitroreductase NfsA with NADP+ provide glimpses of its catalytic mechanism. *FEBS Letters* **2022**, *596* (18), 2425-2440. DOI: https://doi.org/10.1002/1873-3468.14413 (acccessed 2024/05/06).

(150) Kobori, T.; Sasaki, H.; Lee, W. C.; Zenno, S.; Saigo, K.; Murphy, M. E. P.; Tanokura, M. Structure and Site-directed Mutagenesis of a Flavoprotein fromEscherichia coli That Reduces Nitrocompounds: ALTERATION OF PYRIDINE NUCLEOTIDE BINDING BY A SINGLE AMINO ACID SUBSTITUTION*. *Journal of Biological Chemistry* **2001**, *276* (4), 2816-2823. DOI: https://doi.org/10.1074/jbc.M002617200.

(151) Race, P. R.; Lovering, A. L.; White, S. A.; Grove, J. I.; Searle, P. F.; Wrighton, C. W.; Hyde, E. Kinetic and Structural Characterisation of Escherichia coli Nitroreductase Mutants Showing Improved Efficacy for the Prodrug Substrate CB1954. *Journal of*

Molecular Biology **2007**, *368* (2), 481-492. DOI: https://doi.org/10.1016/j.jmb.2007.02.012.

(152) Liu, Y.; Xu, Y.; Qian, X.; Liu, J.; Shen, L.; Li, J.; Zhang, Y. Novel fluorescent markers for hypoxic cells of naphthalimides with two heterocyclic side chains for bioreductive binding. *Bioorganic & Medicinal Chemistry* **2006**, *14* (9), 2935-2941. DOI: https://doi.org/10.1016/j.bmc.2005.12.012.

(153) Dai, M.; Zhu, W.; Xu, Y.; Qian, X.; Liu, Y.; Xiao, Y.; You, Y. Versatile nitro-fluorophore as highly effective sensor for hypoxic tumor cells: design, imaging and evaluation. *Journal of Fluorescence* **2008**, *18*, 591-597.

(154) Yin, H.; Zhu, W.; Xu, Y.; Dai, M.; Qian, X.; Li, Y.; Liu, J. Novel aliphatic N-oxide of naphthalimides as fluorescent markers for hypoxic cells in solid tumor. *European journal of medicinal chemistry* **2011**, *46* (7), 3030-3037.

(155) Cui, L.; Zhong, Y.; Zhu, W.; Xu, Y.; Du, Q.; Wang, X.; Qian, X.; Xiao, Y. A new prodrug-derived ratiometric fluorescent probe for hypoxia: high selectivity of nitroreductase and imaging in tumor cell. *Organic letters* **2011**, *13* (5), 928-931.

(156) He, Z.; Chou, Y.; Zhou, H.; Zhang, H.; Cheng, T.; Liu, G. A nitroreductase and acidity detecting dual functional ratiometric fluorescent probe for selectively imaging tumor cells. *Organic & biomolecular chemistry* **2018**, *16* (17), 3266-3272.

(157) Fang, Y.; Shi, W.; Hu, Y.; Li, X.; Ma, H. A dual-function fluorescent probe for monitoring the degrees of hypoxia in living cells via the imaging of nitroreductase and adenosine triphosphate. *Chemical Communications* **2018**, *54* (43), 5454-5457.

(158) Zhang, Z.; Lv, T.; Tao, B.; Wen, Z.; Xu, Y.; Li, H.; Liu, F.; Sun, S. A novel fluorescent probe based on naphthalimide for imaging nitroreductase (NTR) in bacteria and cells. *Bioorganic & Medicinal Chemistry* **2020**, *28* (3), 115280. DOI: https://doi.org/10.1016/j.bmc.2019.115280.

(159) Wei, C.; Shen, Y.; Xu, Z.; Peng, S.; Yuan, Z.; He, Y.; Yin, J.; Chen, H. A novel off-on fluorescent probe for imaging of hypoxia in tumor cell. *Journal of Photochemistry and Photobiology A: Chemistry* **2018**, *353*, 292-298.

(160) Xu, A.; Tang, Y.; Lin, W. Endoplasmic reticulum-targeted two-photon turn-on fluorescent probe for nitroreductase in tumor cells and tissues. *Spectrochimica Acta Part*

A: Molecular and Biomolecular Spectroscopy **2018**, *204*, 770-776. DOI: https://doi.org/10.1016/j.saa.2018.05.092.

(161) Leslie, K. G.; Jacquemin, D.; New, E. J.; Jolliffe, K. A. Expanding the Breadth of 4-Amino-1, 8-naphthalimide Photophysical Properties through Substitution of the Naphthalimide Core. *Chemistry–A European Journal* **2018**, *24* (21), 5569-5573.

(162) Yang, K.; Leslie, K. G.; Kim, S. Y.; Kalionis, B.; Chrzanowski, W.; Jolliffe, K. A.; New, E. J. Tailoring the properties of a hypoxia-responsive 1, 8-naphthalimide for imaging applications. *Organic & Biomolecular Chemistry* **2018**, *16* (4), 619-624.

(163) Adair, L. D.; Trinh, N.; Verite, P. M.; Jacquemin, D.; Jolliffe, K. A.; New, E. J. Synthesis of Nitro-Aryl functionalised 4-Amino-1, 8-Naphthalimides and their evaluation as fluorescent hypoxia sensors. *Chemistry–A European Journal* **2020**, *26* (44), 10064-10071.

(164) Zhang, Z.; Feng, Q.; Yang, M.; Tang, Y. A ratiometric fluorescent biosensor based on conjugated polymers for sensitive detection of nitroreductase and hypoxia diagnosis in tumor cells. *Sensors and Actuators B: Chemical* **2020**, *318*, 128257. DOI: https://doi.org/10.1016/j.snb.2020.128257.

(165) Wu, M.; Zhang, Z.; Yong, J.; Schenk, P. M.; Tian, D.; Xu, Z. P.; Zhang, R. Determination and Imaging of Small Biomolecules and Ions Using Ruthenium(II) Complex-Based Chemosensors. *Top Curr Chem (Cham)* **2022**, *380* (5), 29. DOI: 10.1007/s41061-022-00392-8 From NLM.

(166) Shum, J.; Leung, P. K.-K.; Lo, K. K.-W. Luminescent Ruthenium(II) Polypyridine Complexes for a Wide Variety of Biomolecular and Cellular Applications. *Inorganic Chemistry* **2019**, *58* (4), 2231-2247. DOI: 10.1021/acs.inorgchem.8b02979.

(167) Rashid, A.; Mondal, S.; Ghosh, P. Development and Application of Ruthenium(II) and Iridium(III) Based Complexes for Anion Sensing. In *Molecules*, 2023; Vol. 28.

(168) Poynton, F. E.; Bright, S. A.; Blasco, S.; Williams, D. C.; Kelly, J. M.; Gunnlaugsson, T. The development of ruthenium(ii) polypyridyl complexes and conjugates for in vitro cellular and in vivo applications. *Chemical Society Reviews* **2017**, *46* (24), 7706-7756, 10.1039/C7CS00680B. DOI: 10.1039/C7CS00680B.

(169) Zhang, R.; Ye, Z.; Song, B.; Dai, Z.; An, X.; Yuan, J. Development of a Ruthenium(II) Complex-Based Luminescent Probe for Hypochlorous Acid in Living Cells. *Inorganic Chemistry* **2013**, *52* (18), 10325-10331. DOI: 10.1021/ic400767u.

(170) Zhang, R.; Ye, Z.; Yin, Y.; Wang, G.; Jin, D.; Yuan, J.; Piper, J. A. Developing Red-Emissive Ruthenium(II) Complex-Based Luminescent Probes for Cellular Imaging. *Bioconjugate Chemistry* **2012**, *23* (4), 725-733. DOI: 10.1021/bc200506w.

(171) Friedman, A. E.; Chambron, J. C.; Sauvage, J. P.; Turro, N. J.; Barton, J. K. A molecular light switch for DNA: Ru(bpy)2(dppz)2+. *Journal of the American Chemical Society* **1990**, *112* (12), 4960-4962. DOI: 10.1021/ja00168a052.

(172) Boynton, A. N.; Marcélis, L.; Barton, J. K. [Ru (Me4phen) 2dppz] 2+, a light switch for DNA mismatches. *Journal of the American Chemical Society* **2016**, *138* (15), 5020-5023.

(173) Walker, M. G.; Ramu, V.; Meijer, A. J. H. M.; Das, A.; Thomas, J. A. A ratiometric sensor for DNA based on a dual emission Ru(dppz) light-switch complex. *Dalton Transactions* **2017**, *46* (18), 6079-6086, 10.1039/C7DT00801E. DOI: 10.1039/C7DT00801E.

(174) Ryan, G. J.; Quinn, S.; Gunnlaugsson, T. Highly Effective DNA Photocleavage by Novel “Rigid” Ru(bpy)3-4-nitro- and -4-amino-1,8-naphthalimide Conjugates. *Inorganic Chemistry* **2008**, *47* (2), 401-403. DOI: 10.1021/ic700967y.

(175) Ryan, G. J.; Gunnlaugsson, T.; Quinn, S. J. Hook, Line, and Sinker! Spectroscopic Studies of Bi-Modular Mono- and Bis-1,8-naphthalimide-Ru(bpy)3-conjugates as DNA “Light Switches”. *Inorganic Chemistry* **2022**, *61* (31), 12073-12086. DOI: 10.1021/acs.inorgchem.2c00064.

(176) Elmes, R. B. P.; Ryan, G. J.; Erby, M. L.; Frimannsson, D. O.; Kitchen, J. A.; Lawler, M.; Williams, D. C.; Quinn, S. J.; Gunnlaugsson, T. Synthesis, Characterization, and Biological Profiling of Ruthenium(II)-Based 4-Nitro- and 4-Amino-1,8-naphthalimide Conjugates. *Inorganic Chemistry* **2020**, *59* (15), 10874-10893. DOI: 10.1021/acs.inorgchem.0c01395.

(177) Burke, C. S.; Byrne, A.; Keyes, T. E. Highly Selective Mitochondrial Targeting by a Ruthenium(II) Peptide Conjugate: Imaging and Photoinduced Damage of

Mitochondrial DNA. *Angewandte Chemie International Edition* **2018**, *57* (38), 12420-12424. DOI: https://doi.org/10.1002/anie.201806002 (acccessed 2023/12/11).

(178) Tyson, D. S.; Luman, C. R.; Zhou, X.; Castellano, F. N. New Ru(II) Chromophores with Extended Excited-State Lifetimes. *Inorganic Chemistry* **2001**, *40* (16), 4063-4071. DOI: 10.1021/ic010287g.

(179) Hara, D.; Komatsu, H.; Son, A.; Nishimoto, S.-i.; Tanabe, K. Water-Soluble Phosphorescent Ruthenium Complex with a Fluorescent Coumarin Unit for Ratiometric Sensing of Oxygen Levels in Living Cells. *Bioconjugate Chemistry* **2015**, *26* (4), 645-649. DOI: 10.1021/acs.bioconjchem.5b00093.

(180) Zhang, P.; Huang, H.; Chen, Y.; Wang, J.; Ji, L.; Chao, H. Ruthenium(II) anthraquinone complexes as two-photon luminescent probes for cycling hypoxia imaging in vivo. *Biomaterials* **2015**, *53*, 522-531. DOI: https://doi.org/10.1016/j.biomaterials.2015.02.126.

(181) Mazuryk, O.; Maciuszek, M.; Stochel, G.; Suzenet, F.; Brindell, M. 2-Nitroimidazole-ruthenium polypyridyl complex as a new conjugate for cancer treatment and visualization. *Journal of Inorganic Biochemistry* **2014**, *134*, 83-91. DOI: https://doi.org/10.1016/j.jinorgbio.2014.02.001.

(182) Wachter, E.; Heidary, D. K.; Howerton, B. S.; Parkin, S.; Glazer, E. C. Light-activated ruthenium complexes photobind DNA and are cytotoxic in the photodynamic therapy window. *Chemical Communications* **2012**, *48* (77), 9649-9651, 10.1039/C2CC33359G. DOI: 10.1039/C2CC33359G.

(183) Keyes, T. E.; Vos, J. G.; Kolnaar, J. A.; Haasnoot, J. G.; Reedijk, J.; Hage, R. Tuning of the photostability of bis(2,2′-biquinoline)ruthenium(II) complexes containing pyridyltriazole ligands by variation of pH. *Inorganica Chimica Acta* **1996**, *245* (2), 237-242. DOI: https://doi.org/10.1016/0020-1693(95)04817-0.

(184) Kappe, C. O. Controlled microwave heating in modern organic synthesis. *Angew Chem Int Ed Engl* **2004**, *43* (46), 6250-6284. DOI: 10.1002/anie.200400655 From NLM.

(185) O'Connor, L. J.; Cazares-Körner, C.; Saha, J.; Evans, C. N. G.; Stratford, M. R. L.; Hammond, E. M.; Conway, S. J. Efficient synthesis of 2-nitroimidazole derivatives and

the bioreductive clinical candidate Evofosfamide (TH-302). *Organic Chemistry Frontiers* **2015**, *2* (9), 1026-1029, 10.1039/C5QO00211G. DOI: 10.1039/C5QO00211G.

(186) Elmes, R. B. P.; Gunnlaugsson, T. Luminescence anion sensing via modulation of MLCT emission from a naphthalimide–Ru(II)–polypyridyl complex. *Tetrahedron Letters* **2010**, *51* (31), 4082-4087. DOI: https://doi.org/10.1016/j.tetlet.2010.05.127.

(187) Čėnas, N.; Nemeikaitė-Čėnienė, A.; Kosychova, L. Single- and Two-Electron Reduction of Nitroaromatic Compounds by Flavoenzymes: Mechanisms and Implications for Cytotoxicity. In *International Journal of Molecular Sciences*, 2021; Vol. 22.

(188) Kumari, R.; R, V.; Sunil, D.; Ningthoujam, R. S.; Pandey, B. N.; Kulkarni, S. D.; Varadavenkatesan, T.; Venkatachalam, G.; V, A. K. N. A Nitronaphthalimide Probe for Fluorescence Imaging of Hypoxia in Cancer Cells. *Journal of Fluorescence* **2021**, *31* (6), 1665-1673. DOI: 10.1007/s10895-021-02800-6.

(189) Johansson, E.; Parkinson, G. N.; Denny, W. A.; Neidle, S. Studies on the Nitroreductase Prodrug-Activating System. Crystal Structures of Complexes with the Inhibitor Dicoumarol and Dinitrobenzamide Prodrugs and of the Enzyme Active Form. *Journal of Medicinal Chemistry* **2003**, *46* (19), 4009-4020. DOI: 10.1021/jm030843b.

(190) Babu, E.; Muthu Mareeswaran, P.; Singaravadivel, S.; Bhuvaneswari, J.; Rajagopal, S. A selective, long-lived deep-red emissive ruthenium(II) polypyridine complexes for the detection of BSA. *Spectrochimica Acta Part A: Molecular and Biomolecular Spectroscopy* **2014**, *130*, 553-560. DOI: https://doi.org/10.1016/j.saa.2014.04.060.

(191) Tomczyk, M. D.; Walczak, K. Z. l,8-Naphthalimide based DNA intercalators and anticancer agents. A systematic review from 2007 to 2017. *European Journal of Medicinal Chemistry* **2018**, *159*, 393-422. DOI: https://doi.org/10.1016/j.ejmech.2018.09.055.

(192) Yang, D.; Tian, H. Y.; Zang, T. N.; Li, M.; Zhou, Y.; Zhang, J. F. Hypoxia imaging in cells and tumor tissues using a highly selective fluorescent nitroreductase probe. *Scientific Reports* **2017**, *7* (1), 9174. DOI: 10.1038/s41598-017-09525-2.

(193) Amir, R. J.; Pessah, N.; Shamis, M.; Shabat, D. Self-Immolative Dendrimers. *Angewandte Chemie International Edition* **2003**, *42* (37), 4494-4499. DOI: https://doi.org/10.1002/anie.200351962 (acccessed 2023/10/16).

(194) de Groot, F. M. H.; Albrecht, C.; Koekkoek, R.; Beusker, P. H.; Scheeren, H. W. "Cascade-Release Dendrimers" Liberate All End Groups upon a Single Triggering Event in the Dendritic Core. *Angewandte Chemie International Edition* **2003**, *42* (37), 4490-4494. DOI: https://doi.org/10.1002/anie.200351942 (acccessed 2023/10/16).

(195) Szalai, M. L.; Kevwitch, R. M.; McGrath, D. V. Geometric Disassembly of Dendrimers: Dendritic Amplification. *Journal of the American Chemical Society* **2003**, *125* (51), 15688-15689. DOI: 10.1021/ja0386694.

(196) Avital-Shmilovici, M.; Shabat, D. Self-immolative dendrimers: A distinctive approach to molecular amplification. *Soft Matter* **2010**, *6* (6), 1073-1080, 10.1039/B922341J. DOI: 10.1039/B922341J.

(197) Shamis, M.; Lode, H. N.; Shabat, D. Bioactivation of Self-Immolative Dendritic Prodrugs by Catalytic Antibody 38C2. *Journal of the American Chemical Society* **2004**, *126* (6), 1726-1731. DOI: 10.1021/ja039052p.

(198) Danieli, E.; Shabat, D. Molecular probe for enzymatic activity with dual output. *Bioorganic & Medicinal Chemistry* **2007**, *15* (23), 7318-7324. DOI: https://doi.org/10.1016/j.bmc.2007.08.046.

(199) Redy-Keisar, O.; Ferber, S.; Satchi-Fainaro, R.; Shabat, D. NIR Fluorogenic Dye as a Modular Platform for Prodrug Assembly: Real-Time in vivo Monitoring of Drug Release. *ChemMedChem* **2015**, *10* (6), 999-1007. DOI: https://doi.org/10.1002/cmdc.201500060 (acccessed 2023/10/16).

(200) Meng, X.; Zhang, J.; Sun, Z.; Zhou, L.; Deng, G.; Li, S.; Li, W.; Gong, P.; Cai, L. Hypoxia-triggered single molecule probe for high-contrast NIR II/PA tumor imaging and robust photothermal therapy. *Theranostics* **2018**, *8* (21), 6025-6034, Research Paper. DOI: 10.7150/thno.26607.

(201) Liu, Z.; Song, F.; Shi, W.; Gurzadyan, G.; Yin, H.; Song, B.; Liang, R.; Peng, X. Nitroreductase-Activatable Theranostic Molecules with High PDT Efficiency under Mild

Hypoxia Based on a TADF Fluorescein Derivative. *ACS Applied Materials & Interfaces* **2019**, *11* (17), 15426-15435. DOI: 10.1021/acsami.9b04488.

(202) Calatrava-Pérez, E.; Marchetti, L. A.; McManus, G. J.; Lynch, D. M.; Elmes, R. B. P.; Williams, D. C.; Gunnlaugsson, T.; Scanlan, E. M. Real-Time Multi-Photon Tracking and Bioimaging of Glycosylated Theranostic Prodrugs upon Specific Enzyme Triggered Release. *Chemistry – A European Journal* **2022**, *28* (3), e202103858. DOI: https://doi.org/10.1002/chem.202103858 (acccessed 2023/10/17).

(203) Walunj, D.; Thankarajan, E.; Prasad, C.; Tuchinsky, H.; Baldan, S.; Sherman, M. Y.; Patsenker, L.; Gellerman, G. Targeted methylation facilitates DNA double strand breaks and enhances cancer suppression: A DNA intercalating/methylating dual-action chimera Amonafidazene. *European Journal of Medicinal Chemistry* **2021**, *225*, 113811. DOI: https://doi.org/10.1016/j.ejmech.2021.113811.

(204) Sharrock, A. V.; McManaway, S. P.; Rich, M. H.; Mumm, J. S.; Hermans, I. F.; Tercel, M.; Pruijn, F. B.; Ackerley, D. F. Engineering the Escherichia coli Nitroreductase NfsA to Create a Flexible Enzyme-Prodrug Activation System. *Front Pharmacol* **2021**, *12*, 701456. DOI: 10.3389/fphar.2021.701456 From NLM.

(205) Rudy, B. C.; Senkowski, B. Z. Sulfisoxazole. In *Analytical Profiles of Drug Substances*, Florey, K. Ed.; Vol. 2; Academic Press, 1973; pp 487-506.

(206) Shah, K.; Gupta, J. K.; Chauhan, N. S.; Upmanyu, N.; Shrivastava, S. K.; Mishra, P. Prodrugs of NSAIDs: A Review. *Open Med Chem J* **2017**, *11*, 146-195. DOI: 10.2174/1874104501711010146 From NLM.

(207) Kim, S. J.; Park, S. Y.; Yoon, S. A.; Kim, C.; Kang, C.; Lee, M. H. Naphthalimide-4-(4-nitrophenyl)thiosemicarbazide: A Fluorescent Probe for Simultaneous Monitoring of Viscosity and Nitric Oxide in Living Cells. *Analytical Chemistry* **2021**, *93* (10), 4391-4397. DOI: 10.1021/acs.analchem.0c04019.

(208) Sella, E.; Shabat, D. Self-immolative dendritic probe for direct detection of triacetone triperoxide. *Chemical Communications* **2008**, (44), 5701-5703, 10.1039/B814855D. DOI: 10.1039/B814855D.

(209) Chen, X.; Ma, X.; Zhang, Y.; Gao, G.; Liu, J.; Zhang, X.; Wang, M.; Hou, S. Ratiometric fluorescent probes with a self-immolative spacer for real-time detection of β-

galactosidase and imaging in living cells. *Analytica Chimica Acta* **2018**, *1033*, 193-198. DOI: https://doi.org/10.1016/j.aca.2018.05.071.

(210) Gavriel, A. G.; Sambrook, M. R.; Russell, A. T.; Hayes, W. Recent advances in self-immolative linkers and their applications in polymeric reporting systems. *Polymer Chemistry* **2022**, *13* (22), 3188-3269, 10.1039/D2PY00414C. DOI: 10.1039/D2PY00414C.

(211) Gorbatov, S. A.; Uvarov, D. Y.; Scherbakov, A. M.; Zavarzin, I. V.; Volkova, Y. A.; Romieu, A. A novel water-soluble BODIPY dye as red fluorescent probe for imaging hypoxic status of human cancer cells. *Mendeleev Communications* **2020**, *30* (6), 750-752. DOI: https://doi.org/10.1016/j.mencom.2020.11.020.

(212) Na, S.-Y.; Park, S.; Kim, S.-Y.; Kim, H.-J. A benzothiazole-based water soluble and pH-independent probe for nitroreductase with a dramatic change of chromogenic and fluorogenic properties. *Dyes and Pigments* **2019**, *161*, 247-251. DOI: https://doi.org/10.1016/j.dyepig.2018.09.053.

(213) Xue, C.; Lei, Y.; Zhang, S.; Sha, Y. A cyanine-derived "turn-on" fluorescent probe for imaging nitroreductase in hypoxic tumor cells. *Analytical Methods* **2015**, *7* (24), 10125-10128, 10.1039/C5AY02312B. DOI: 10.1039/C5AY02312B.

(214) Phillips, T.; Haq, I.; Meijer, A. J. H. M.; Adams, H.; Soutar, I.; Swanson, L.; Sykes, M. J.; Thomas, J. A. DNA Binding of an Organic dppz-Based Intercalator. *Biochemistry* **2004**, *43* (43), 13657-13665. DOI: 10.1021/bi049146r.

(215) Phillips, T.; Rajput, C.; Twyman, L.; Haq, I.; Thomas, J. A. Water-soluble organic dppz analogues—tuning DNA binding affinities, luminescence, and photo-redox properties. *Chemical Communications* **2005**, (34), 4327-4329, 10.1039/B506946G. DOI: 10.1039/B506946G.

(216) Ryan, G. J.; Elmes, R. B. P.; Quinn, S. J.; Gunnlaugsson, T. Synthesis and photophysical evaluations of fluorescent quaternary bipyridyl-1,8-naphthalimide conjugates as nucleic acid targeting agents. *Supramolecular Chemistry* **2012**, *24* (3), 175-188. DOI: 10.1080/10610278.2011.638381.

(217) Elmes, R. B. P.; Erby, M.; Cloonan, S. M.; Quinn, S. J.; Williams, D. C.; Gunnlaugsson, T. Quaternarized pdppz: synthesis, DNA-binding and biological studies

of a novel dppz derivative that causes cellular death upon light irradiation. *Chemical Communications* **2011**, *47* (2), 686-688, 10.1039/C0CC04303F. DOI: 10.1039/C0CC04303F.

(218) Lee, J.; Yoon, S. A.; Chun, J.; Kang, C.; Lee, M. H. A red-emitting styrylnaphthalimide-based fluorescent probe providing a ratiometric signal change for the precise and quantitative detection of H2O2. *Analytica Chimica Acta* **2019**, *1080*, 153-161. DOI: https://doi.org/10.1016/j.aca.2019.07.008.

(219) Wynne, C. Responsive Synthetic Peptide Conjugates - From Sensors to Peptidomimetics. Maynooth University, 2024.

(220) Yi, Y.; Han, J.; Park, M. H.; Park, N.; Nam, E.; Jin, H. K.; Bae, J.-s.; Lim, M. H. Tunable regulatory activities of 1,10-phenanthroline derivatives towards acid sphingomyelinase and Zn(ii)–amyloid-β. *Chemical Communications* **2019**, *55* (42), 5847-5850, 10.1039/C9CC01005J. DOI: 10.1039/C9CC01005J.

(221) Herrlinger, E.-M.; Hau, M.; Redhaber, D. M.; Greve, G.; Willmann, D.; Steimle, S.; Müller, M.; Lübbert, M.; Miething, C. C.; Schüle, R.; et al. Nitroreductase-Mediated Release of Inhibitors of Lysine-Specific Demethylase 1 (LSD1) from Prodrugs in Transfected Acute Myeloid Leukaemia Cells. *ChemBioChem* **2020**, *21* (16), 2329-2347. DOI: https://doi.org/10.1002/cbic.202000138 (acccessed 2023/10/18).

(222) Wang, Y.; Hu, Y.-T.; Zhang, H.-L.; Chen, Y.-Y.; Shi, H.-D.; Liu, J.-G.; Zhang, Q.-L. Cellular membrane-targeting ruthenium complexes as efficient photosensitizers for broad-spectrum antibacterial activity. *Dalton Transactions* **2023**, *52* (23), 8051-8057, 10.1039/D3DT01001E. DOI: 10.1039/D3DT01001E.

(223) Nakamaru, K. Solvent Effect on the Nonradiative Deactivation of the Excited State of Tris(2,2′-bipyridyl)ruthenium(II) Ion. *Bulletin of the Chemical Society of Japan* **1982**, *55* (5), 1639-1640. DOI: 10.1246/bcsj.55.1639 (acccessed 1/25/2024).

(224) Van Houten, J.; Watts, R. J. Temperature dependence of the photophysical and photochemical properties of the tris(2,2'-bipyridyl)ruthenium(II) ion in aqueous solution. *Journal of the American Chemical Society* **1976**, *98* (16), 4853-4858. DOI: 10.1021/ja00432a028.

Appendix

Chapter 2 Appendix Data

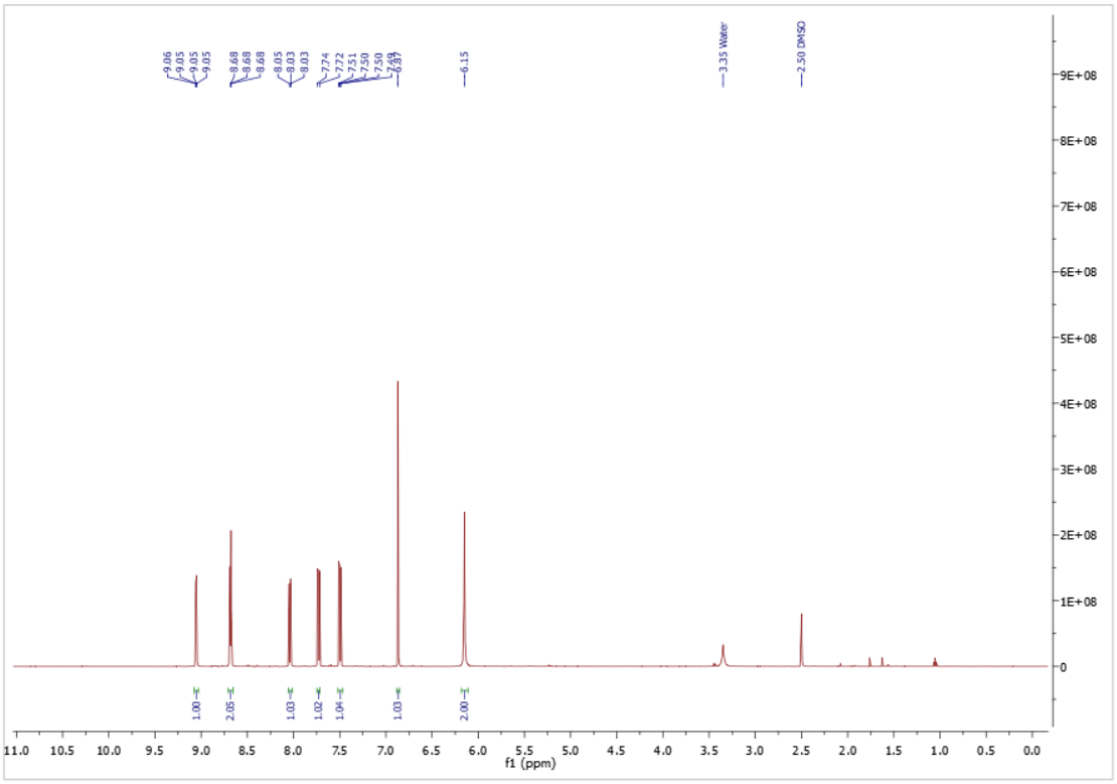

Figure A1: *[1]H NMR spectrum of* ***2.15***

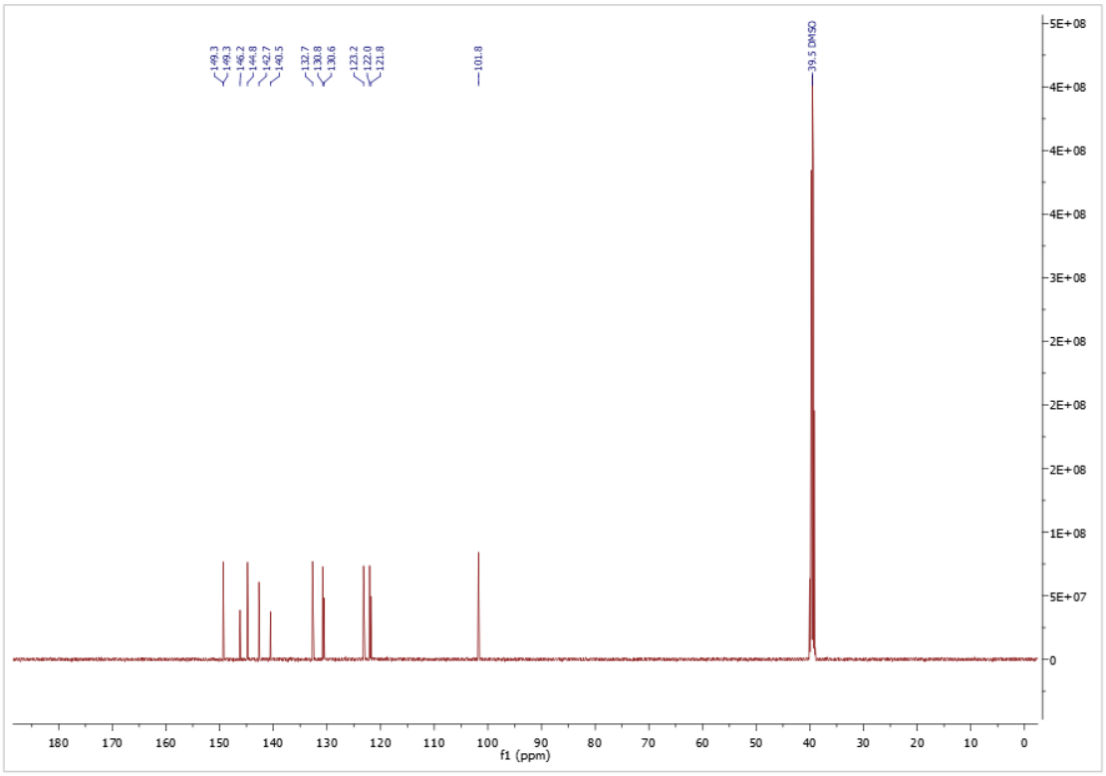

Figure A2: *[13]C NMR spectrum of* ***2.15***

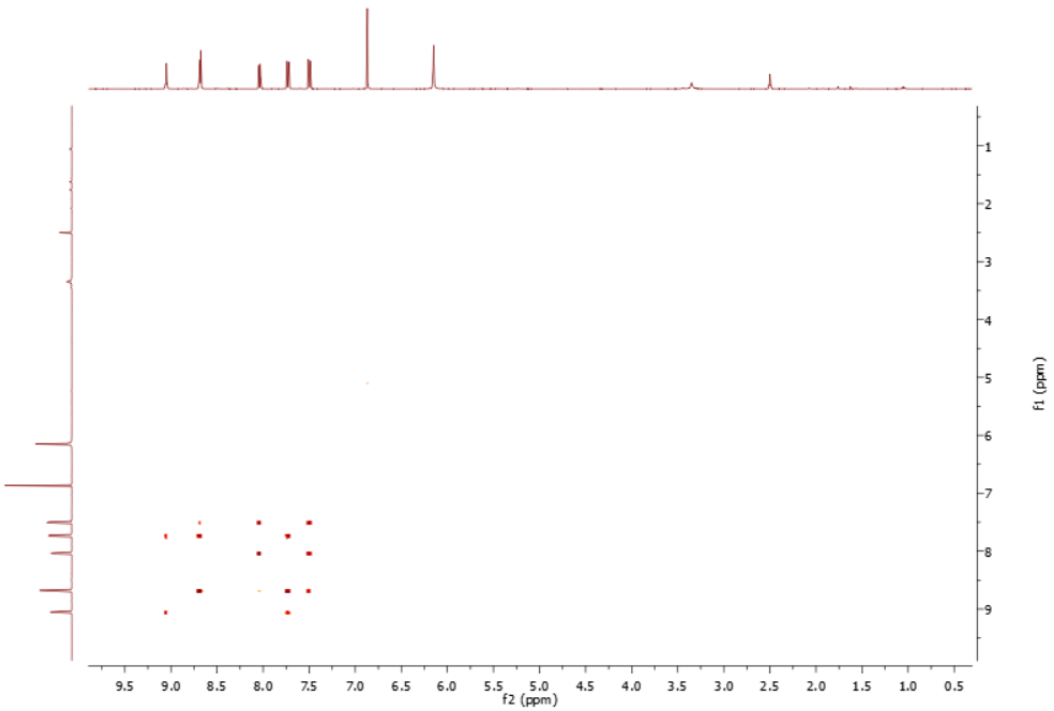

Figure A3: *^{1}H–^{1}H COSY spectrum of* ***2.15***

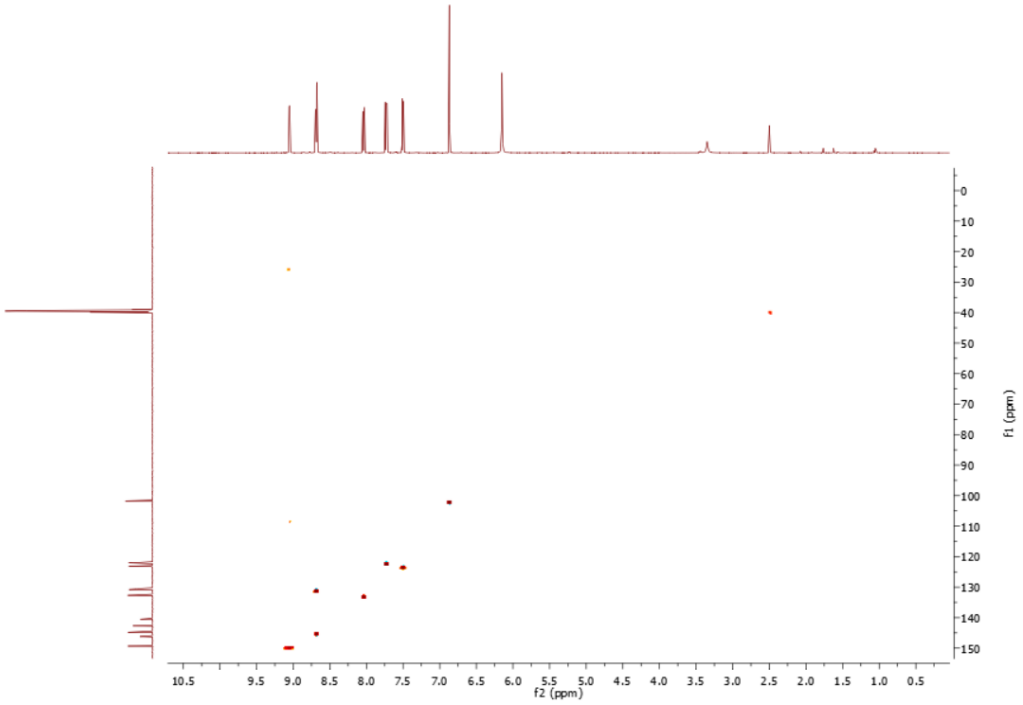

Figure A4: *HSQC spectrum of* ***2.15***

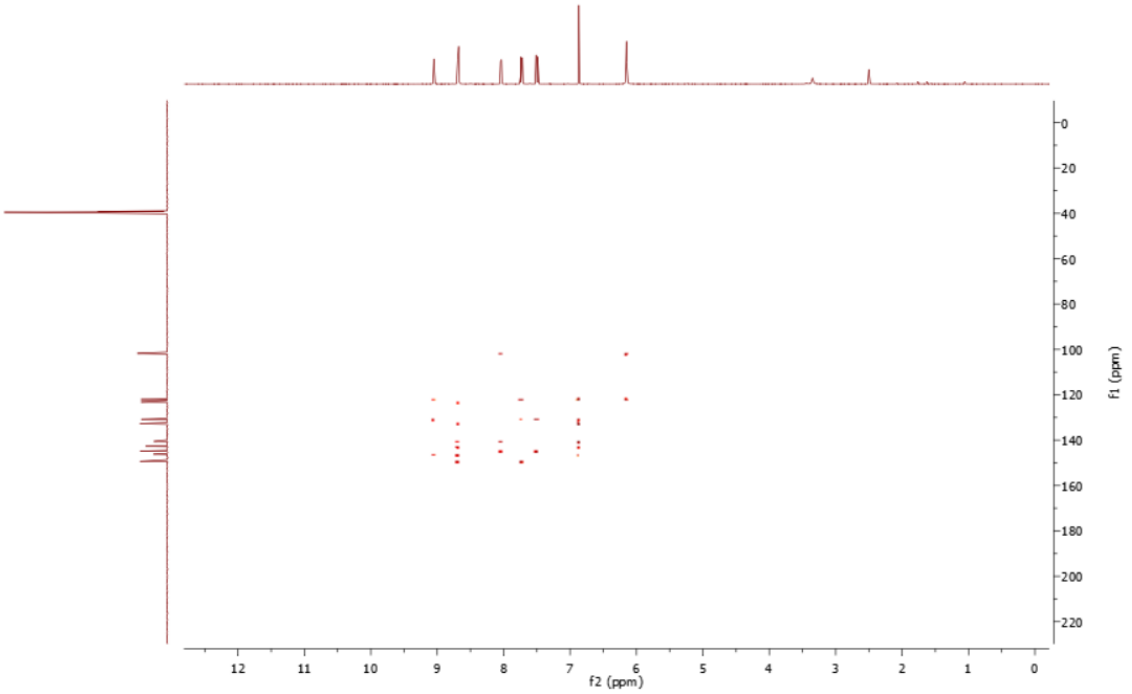

Figure A5: *HMBC spectrum of* ***2.15***

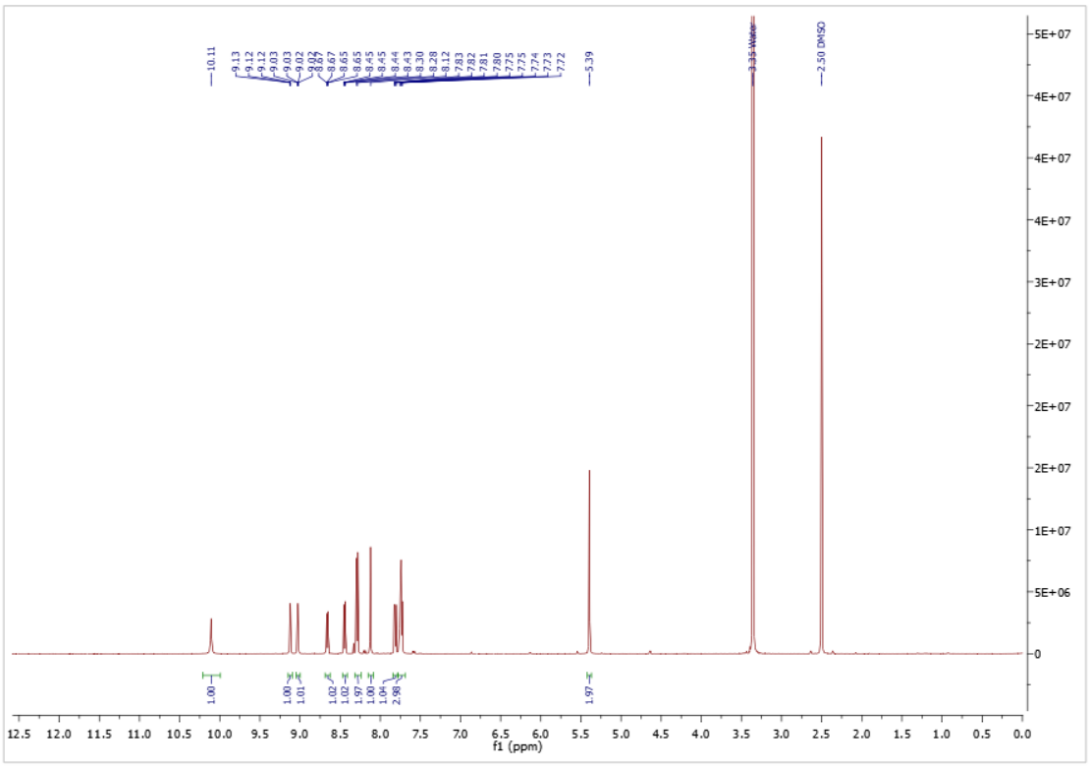

Figure A6: *^{1}H NMR spectrum of* ***2.14***

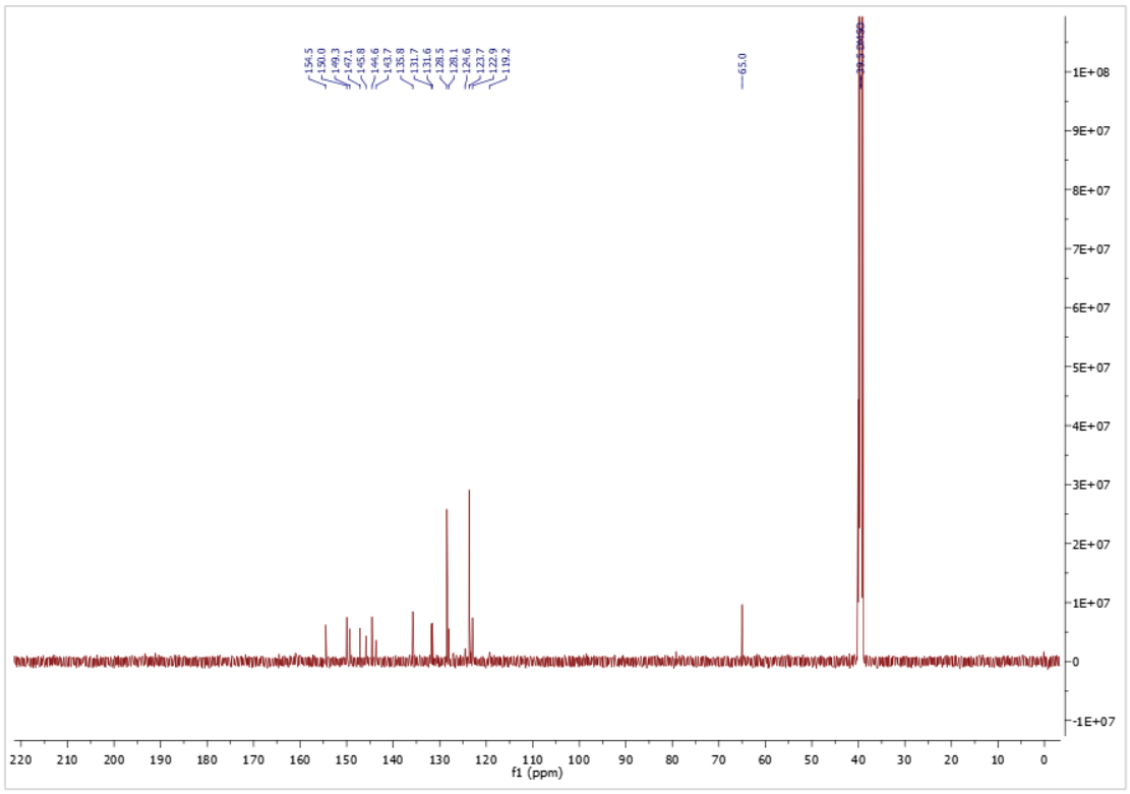

Figure A7: *^{13}C NMR spectrum of **2.14***

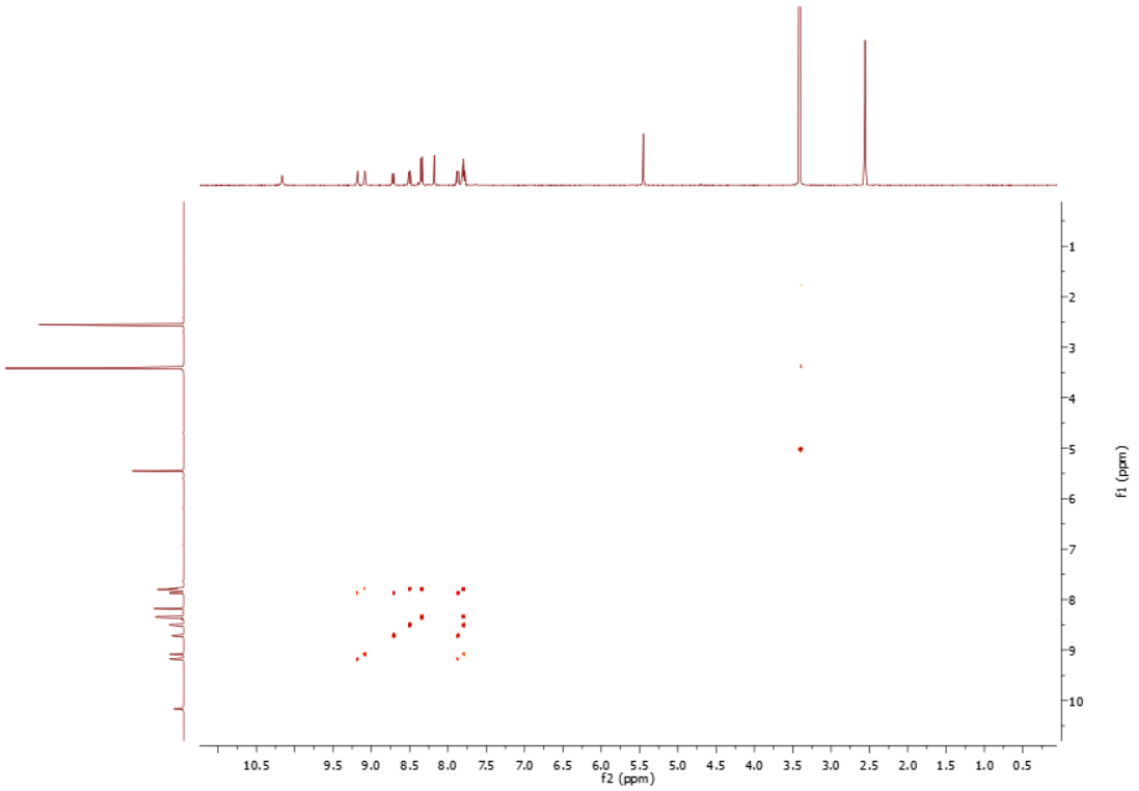

Figure A8: *^{1}H–^{1}H COSY spectrum of **2.14***

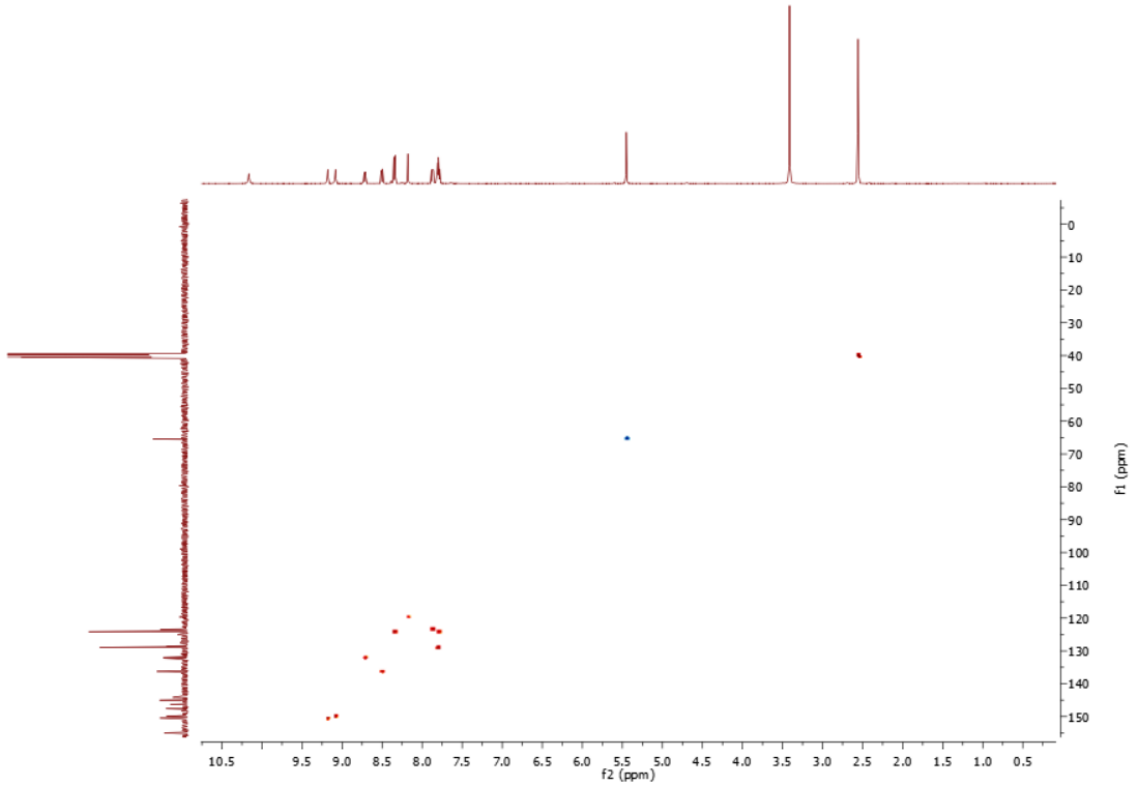

Figure A9: *HSQC spectrum of* ***2.14***

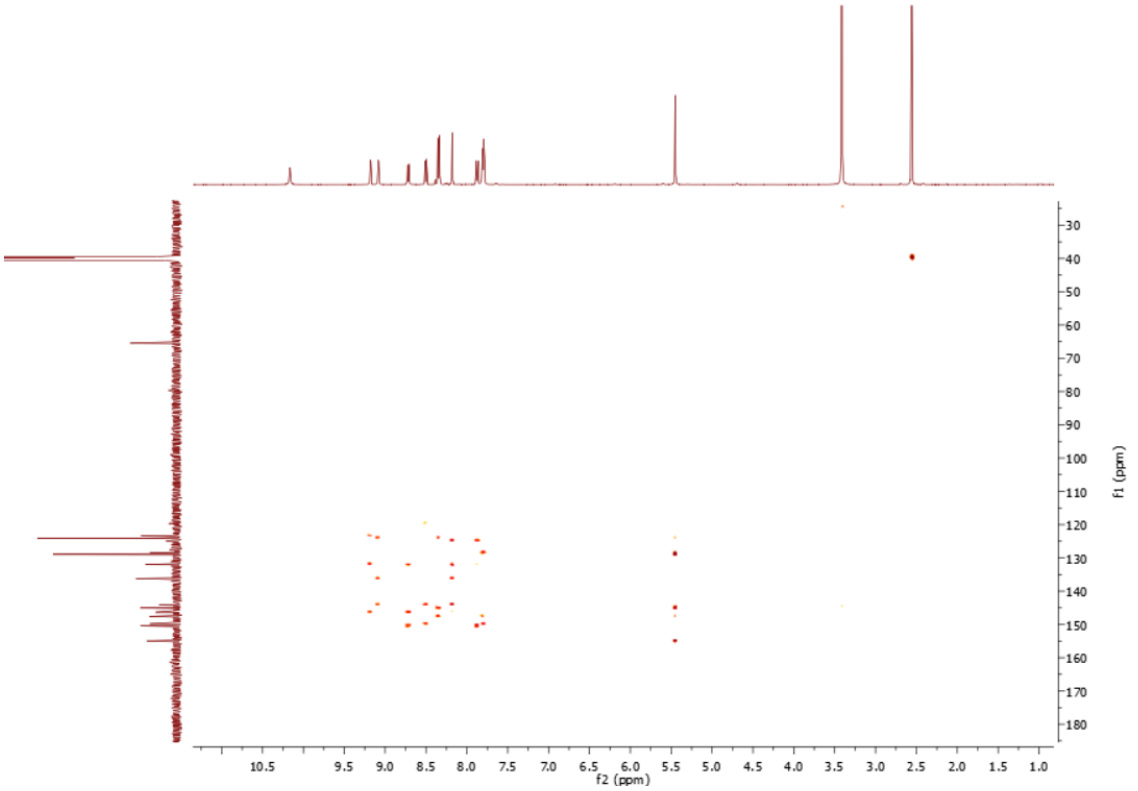

Figure A10: *HMBC spectrum of* ***2.14***

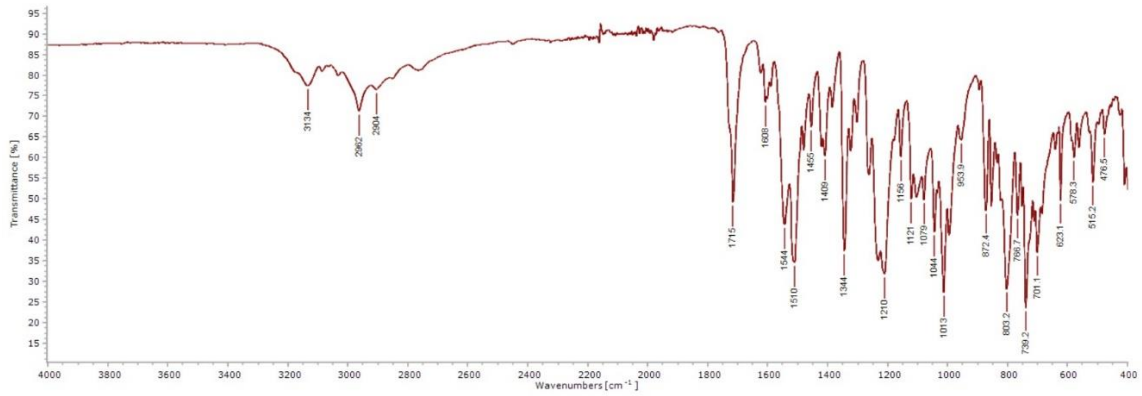

Figure A11: *IR spectrum of* ***2.14***

Compound specific information

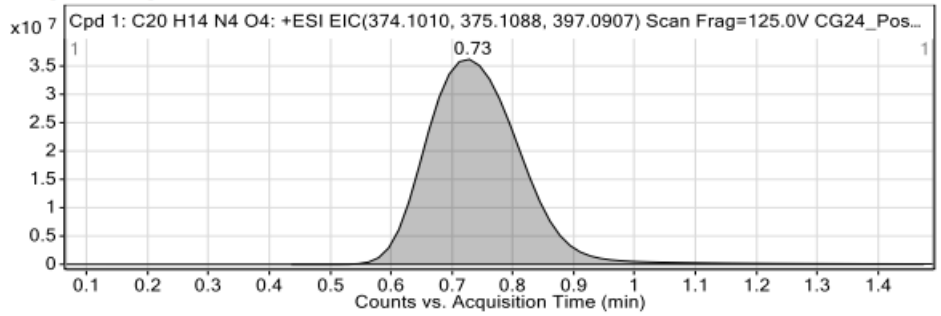

Figure: Extracted ion chromatogram (EIC) of compound.

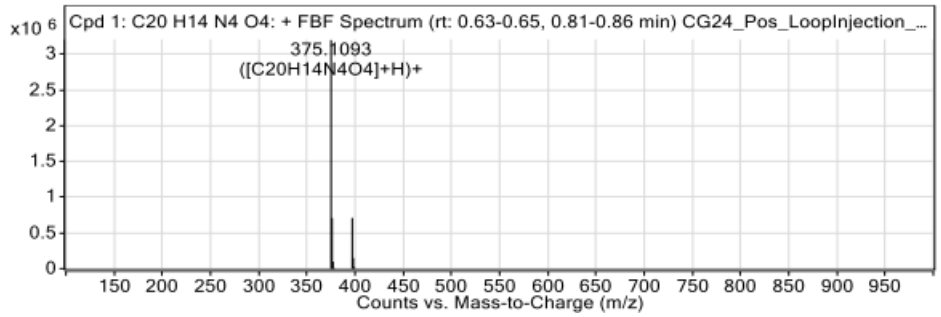

Compound Table

Compound Label	RT (min)	Observed mass (m/z)	Neutral observed mass (Da)	Theoretical mass (Da)	Mass error (ppm)	Isotope match score (%)
Cpd 1: C20 H14 N4 O4	0.73	375.1093	374.1020	374.1015	1.31	99.33

Mass errors of between -5.00 and 5.00 ppm with isotope match scores above 60% are considered confirmation of molecular formulae

Figure A12: *HRMS of* ***2.14***

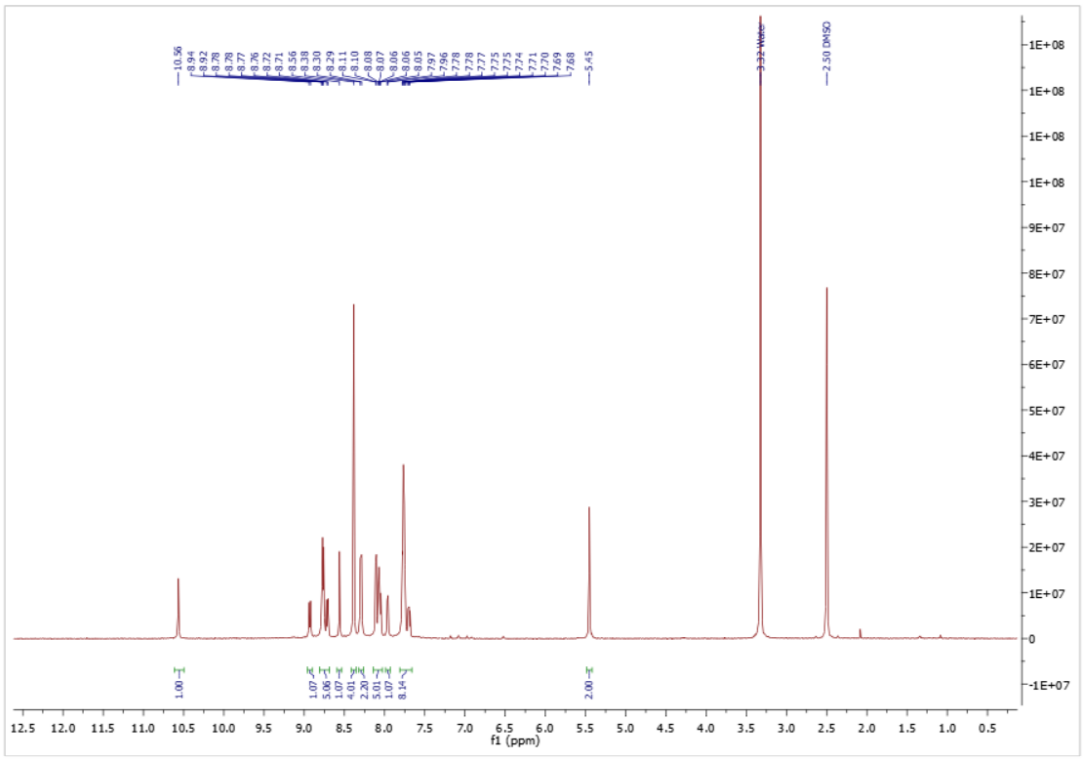

Figure A13: *[1]H NMR spectrum of* ***2.11***

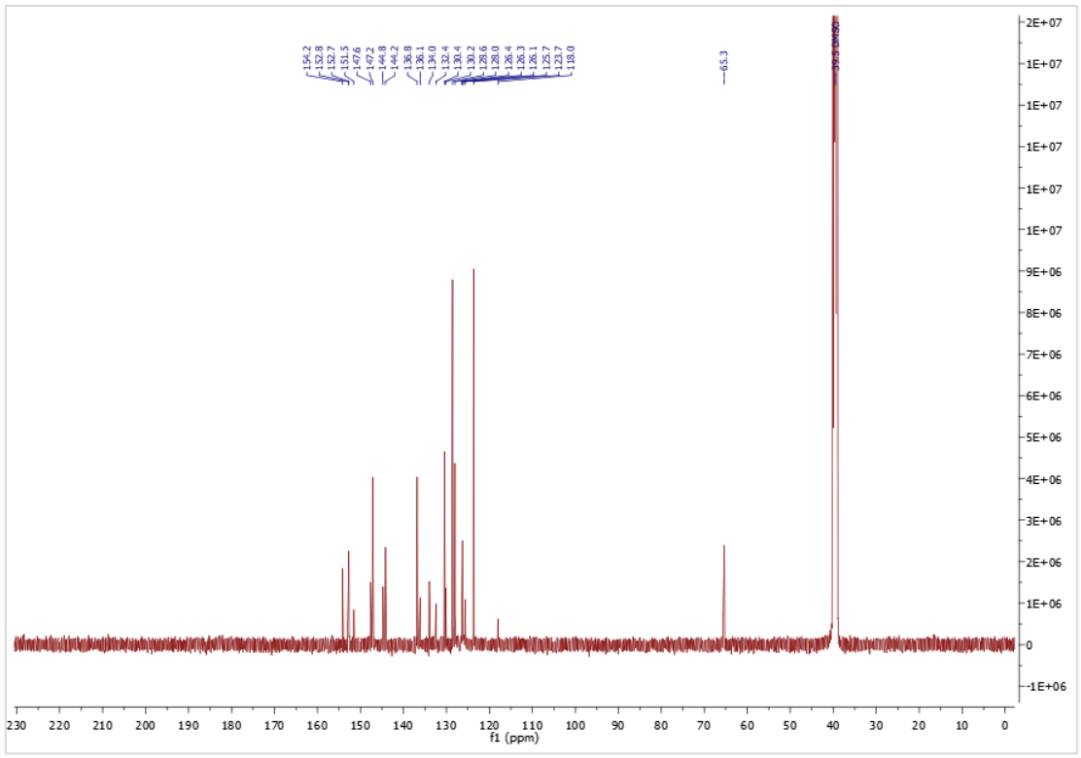

Figure A14: *[13]C NMR spectrum of* ***2.11***

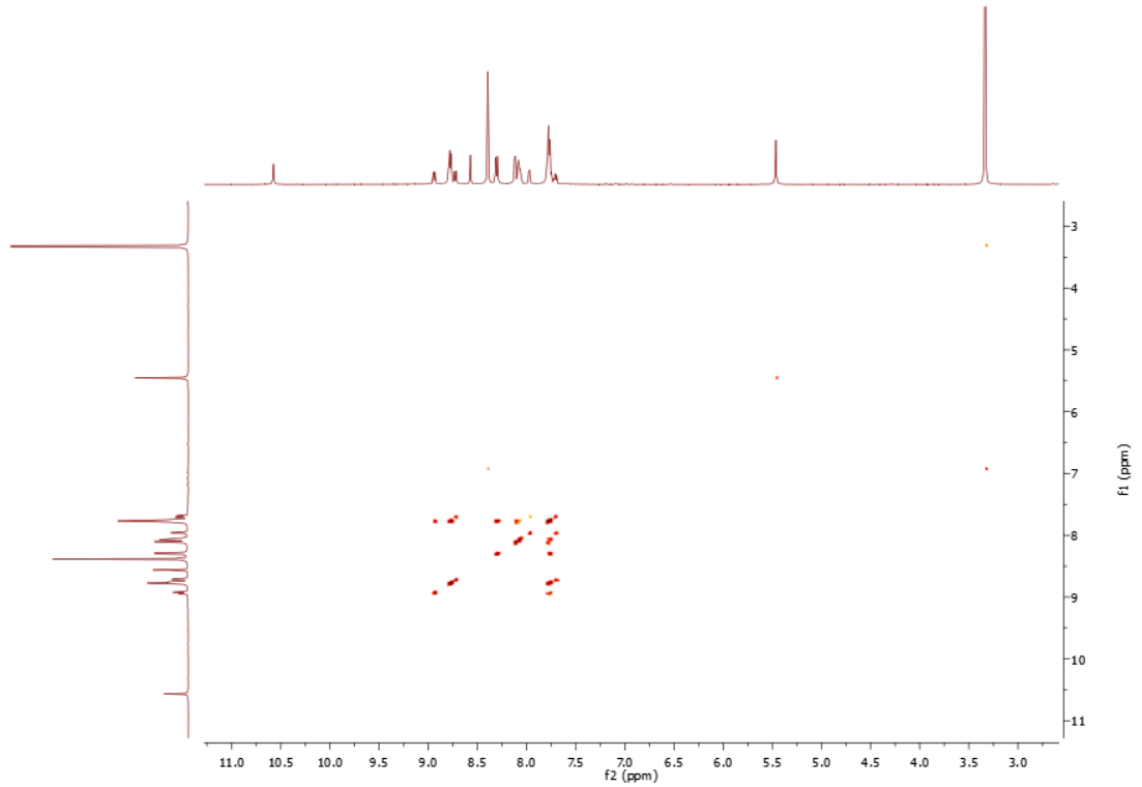

Figure A15: *^{1}H-^{1}H COSY spectrum of **2.11***

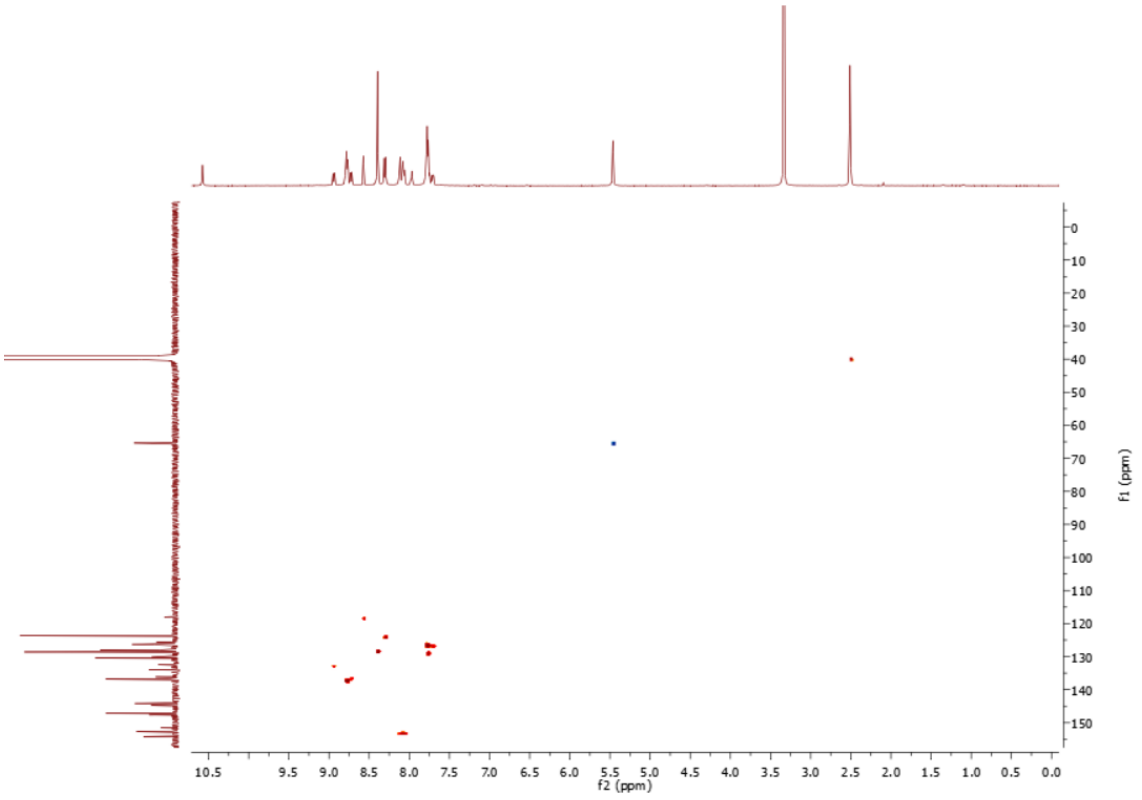

Figure A16: *HSQC spectrum of **2.11***

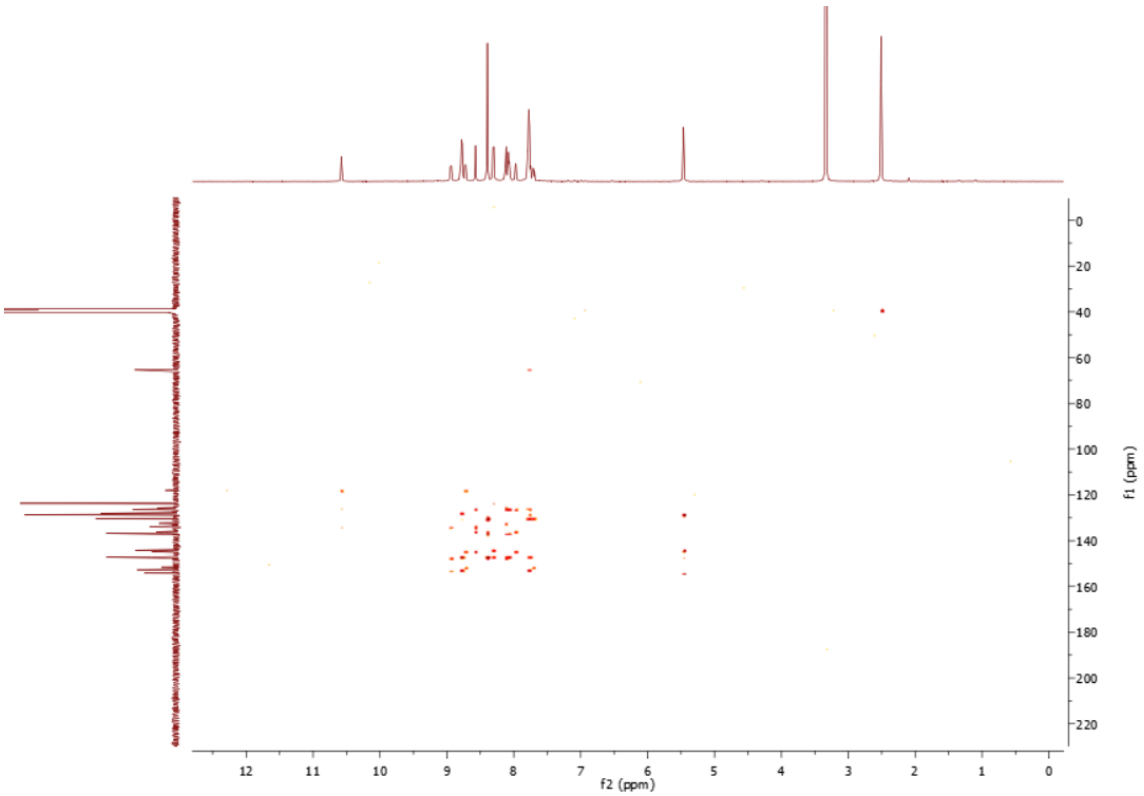

Figure A17: *HMBC spectrum of* ***2.11***

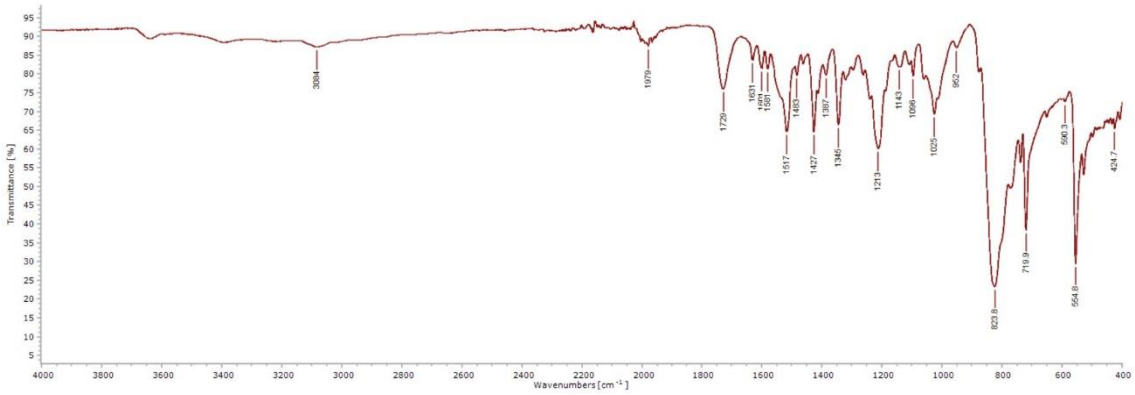

Figure A18: *IR spectrum of* ***2.11***

Compound specific information

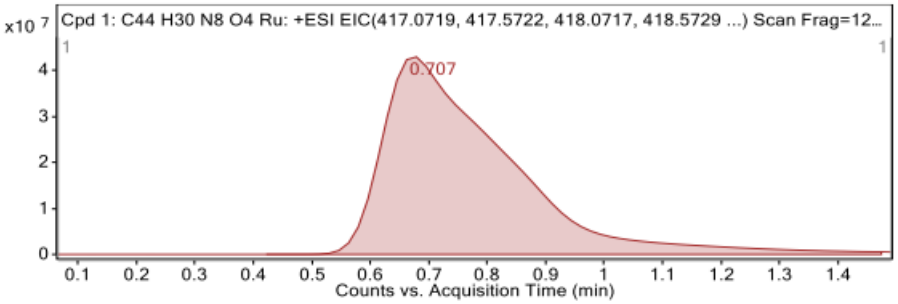

Figure: Extracted ion chromatogram (EIC) of compound.

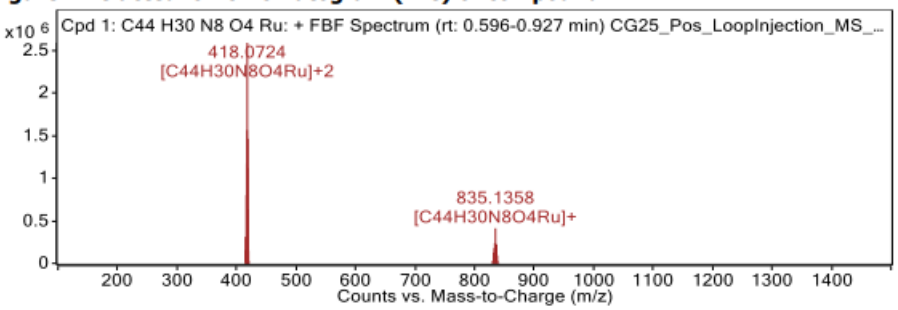

Compound Table

Compound Label	RT (min)	Observed mass (m/z)	Neutral observed mass (Da)	Theoretical mass (Da)	Mass error (ppm)	Isotope match score (%)
Cpd 1: C44 H30 N8 O4 Ru	0.71	418.0724	830.1466	830.1466	0.03	99.38
Cpd 2: C44 H30 F6 N8 O4 P Ru	0.73	981.1077	975.1102	975.1108	-0.59	99.56
Cpd 3: C44 H30 F12 N8 O4 P2 Ru				1120.0750		

Mass errors of between -5.00 and 5.00 ppm with isotope match scores above 60% are considered confirmation of molecular formulae

Figure A19: *HRMS of* ***2.11***

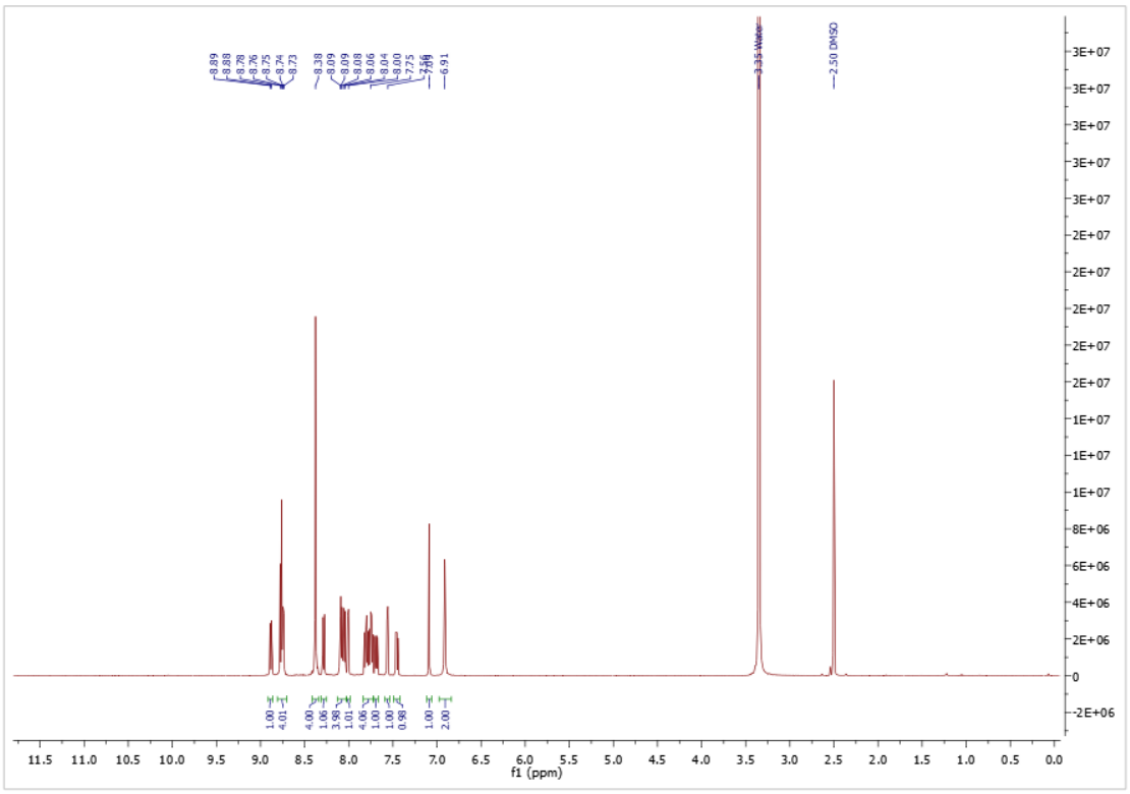

Figure A20: *[1]H NMR spectrum of* ***2.17***

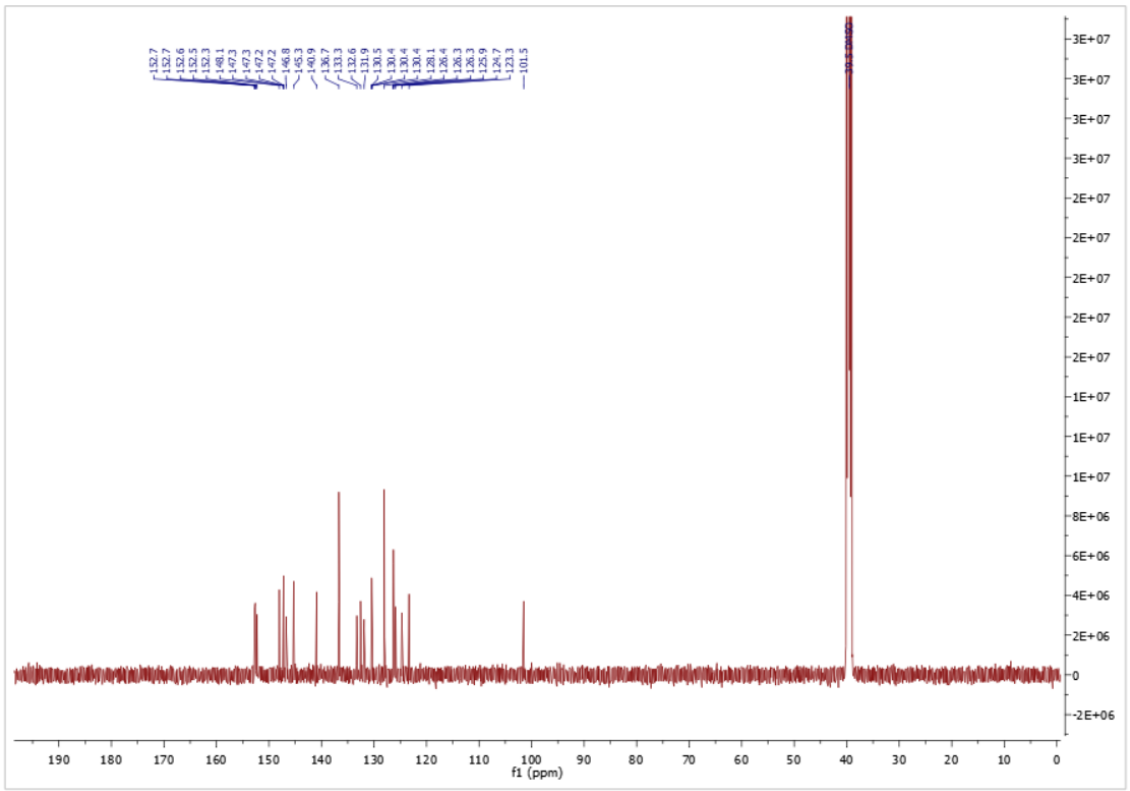

Figure A21: *[13]C NMR spectrum of* ***2.17***

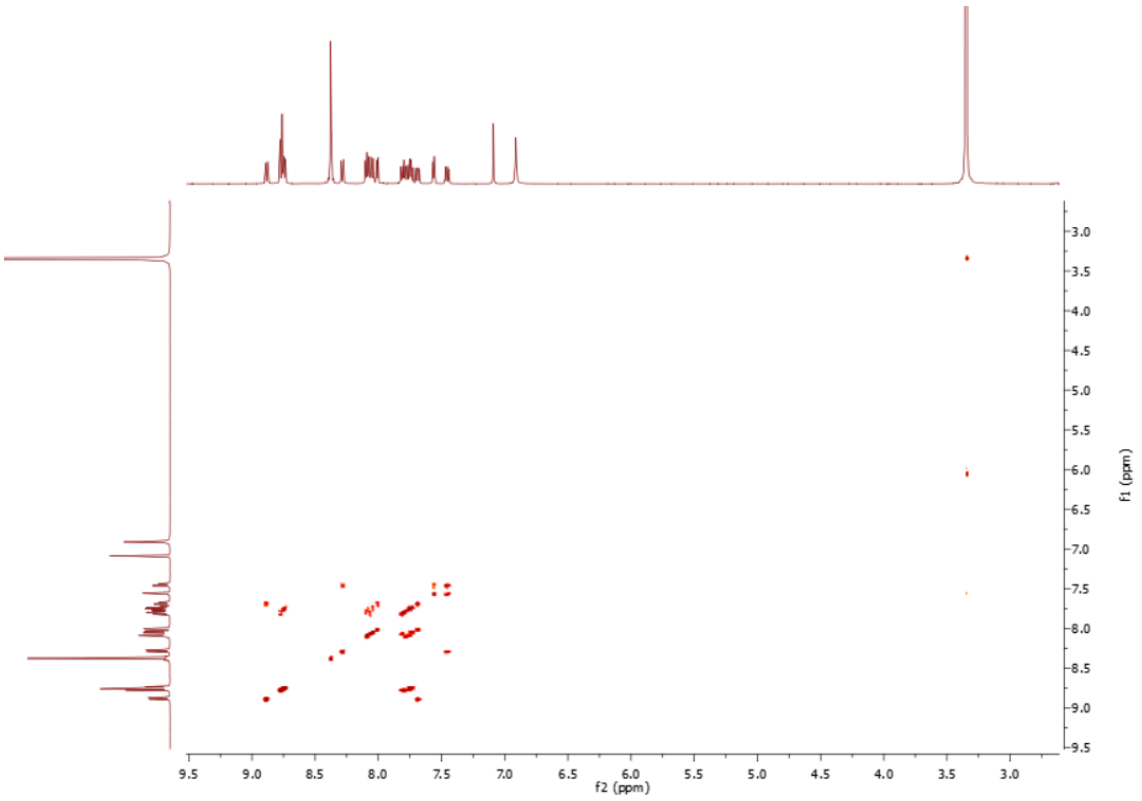

Figure A22: *^{1}H-^{1}H COSY spectrum of **2.17***

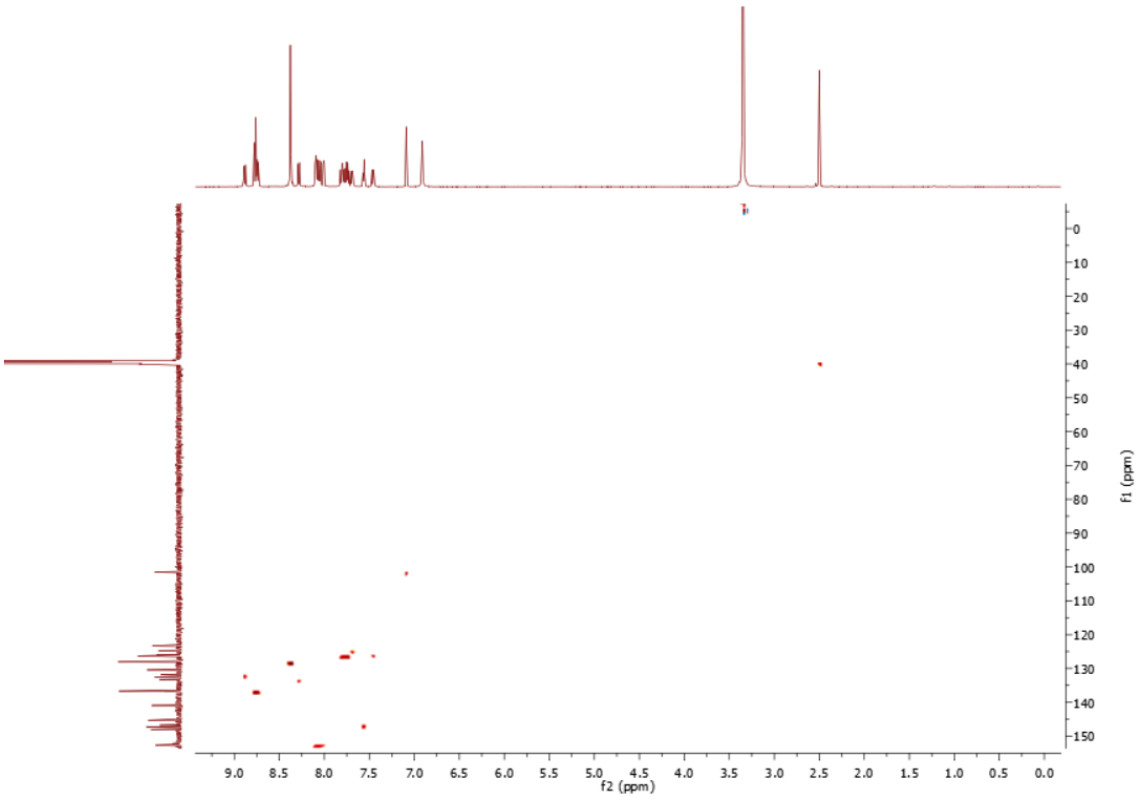

Figure A23: *HSQC spectrum of **2.17***

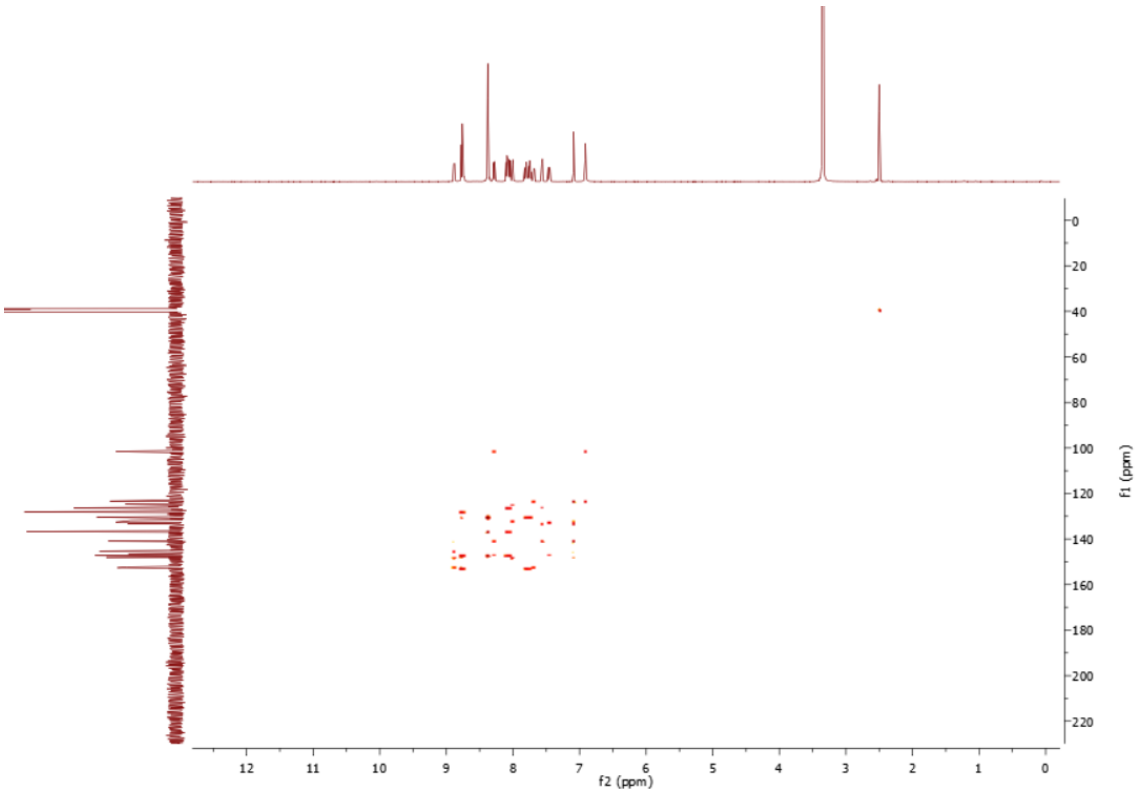

Figure A24: *HMBC spectrum of* ***2.17***

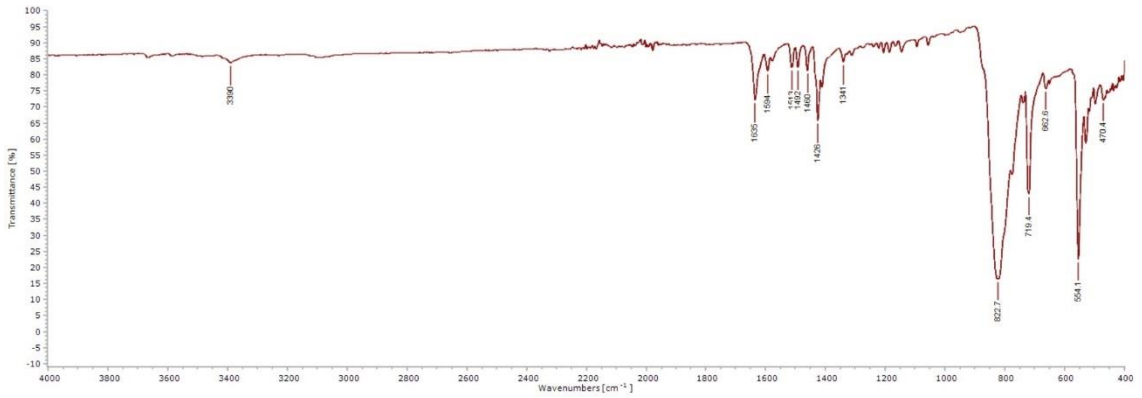

Figure A25: *IR spectrum of* ***2.17***

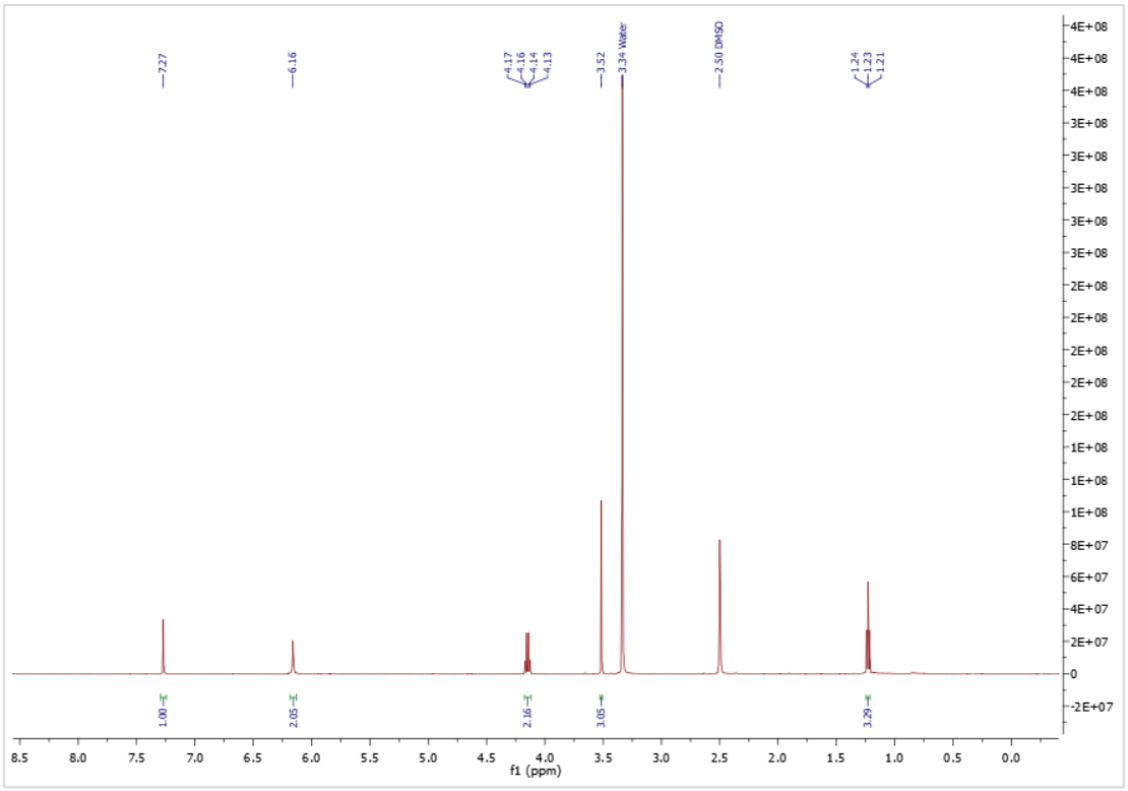

Figure A26: *[1]H NMR spectrum of* ***2.22***

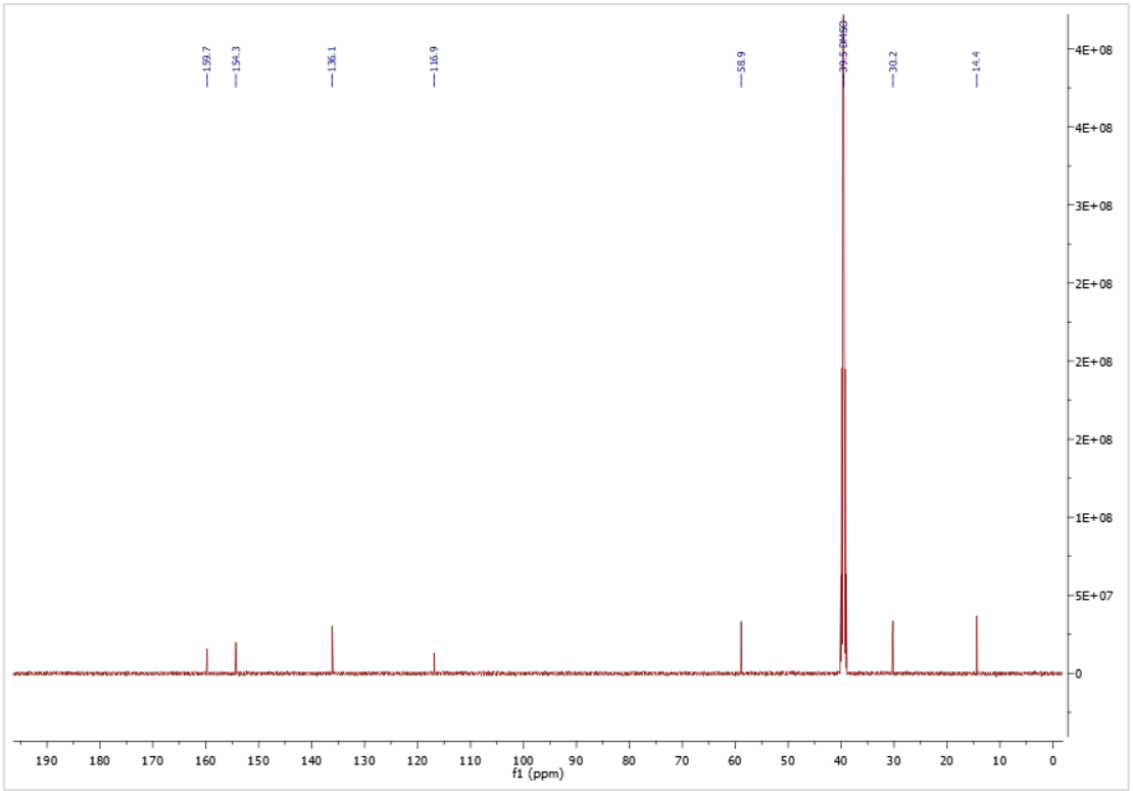

Figure A27: *[13]C NMR spectrum of* ***2.22***

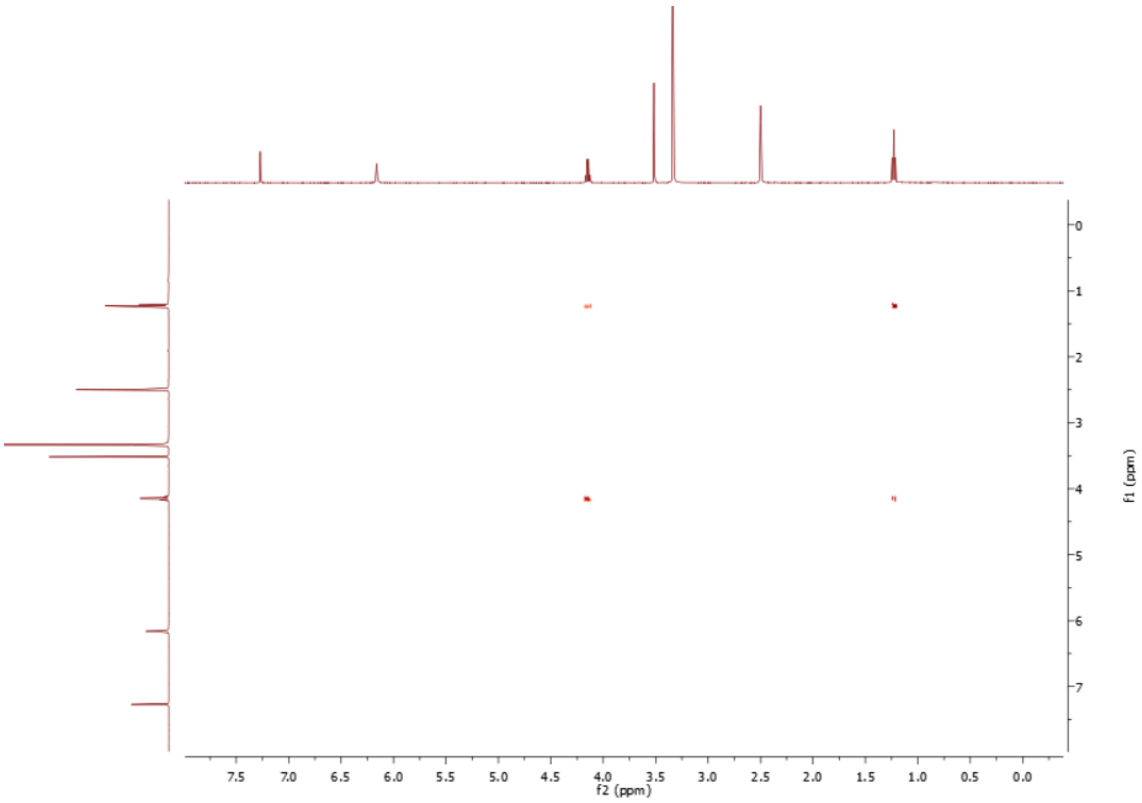

Figure A28: *^{1}H-^{1}H COSY spectrum of* ***2.22***

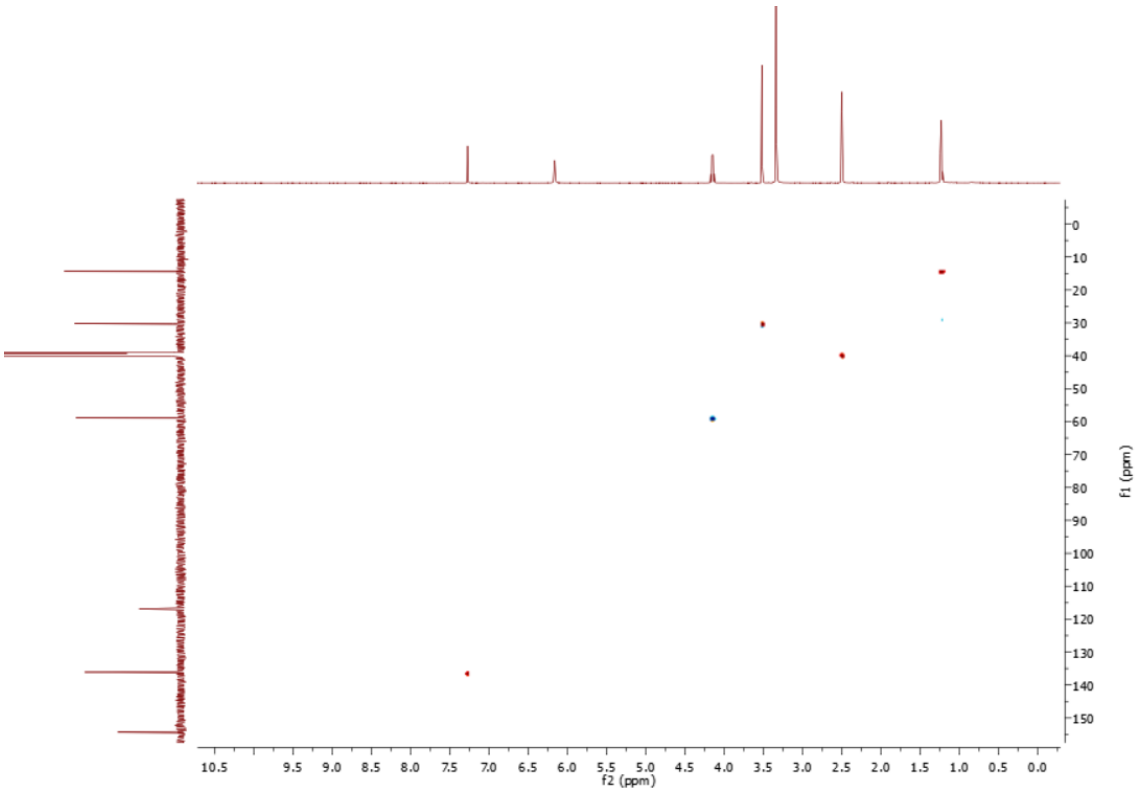

Figure A29: *HSQC spectrum of* ***2.22***

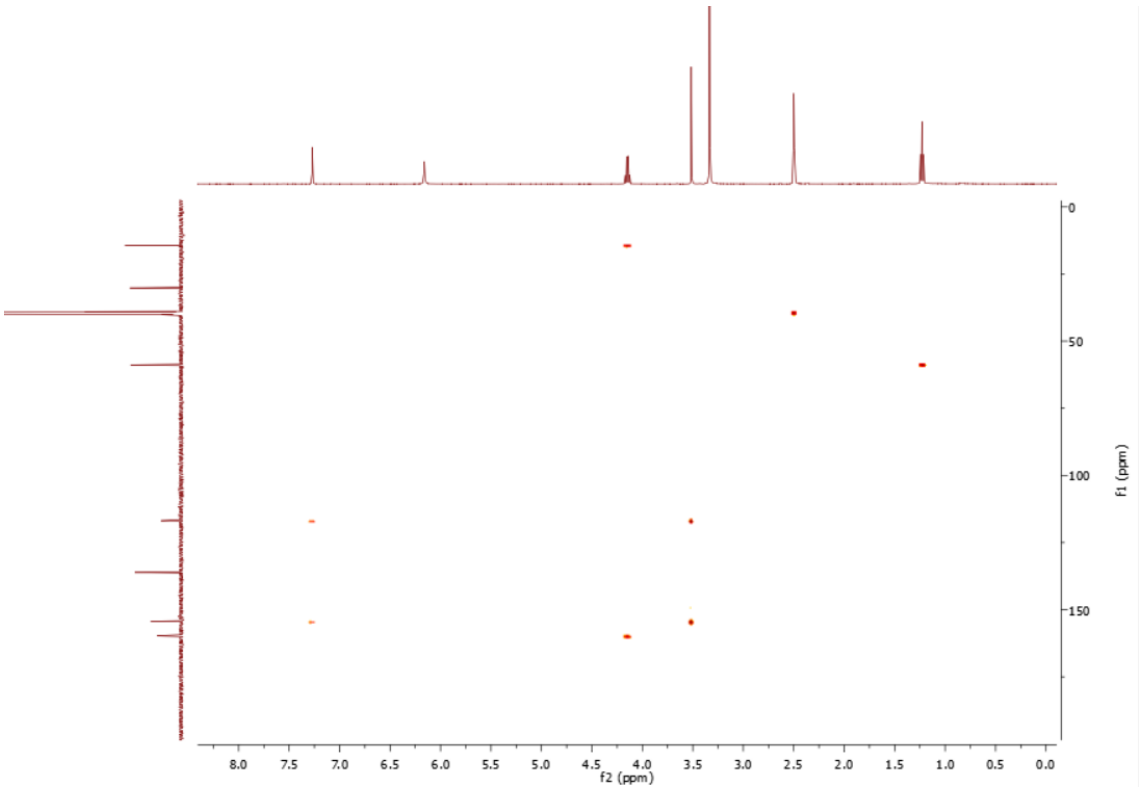

Figure A30: *HMBC spectrum of* ***2.22***

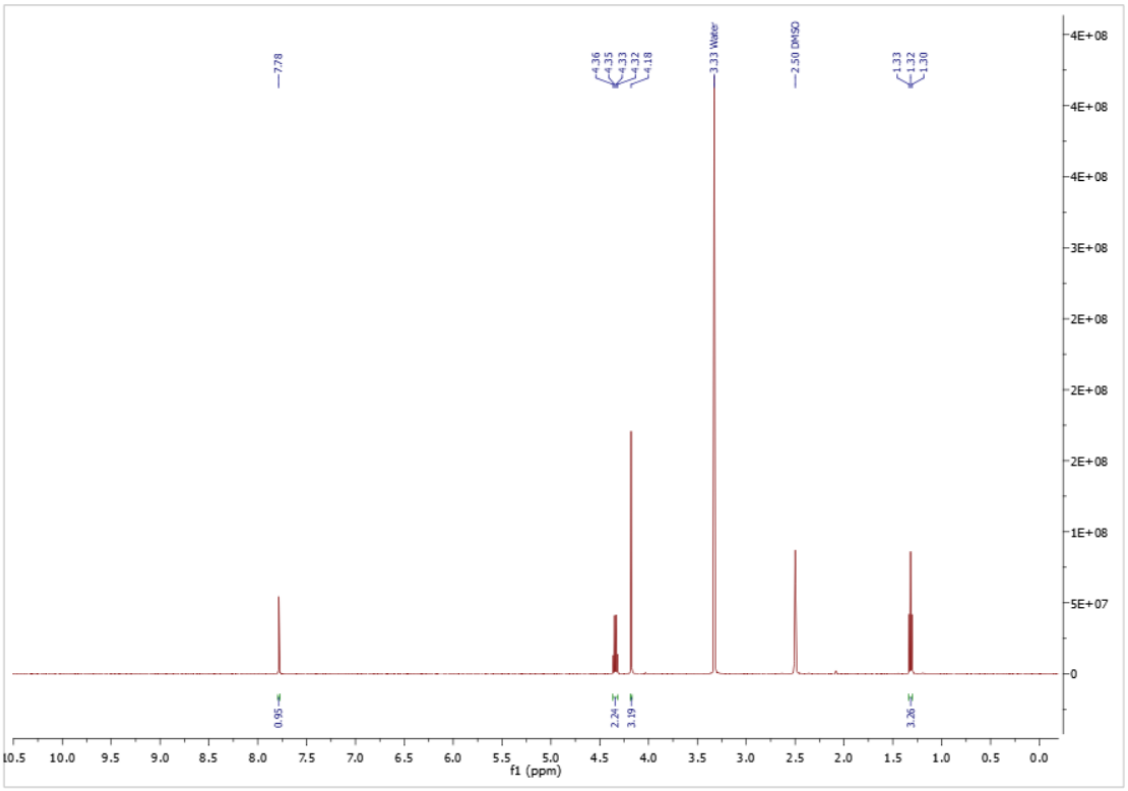

Figure A31: *^{1}H NMR spectrum of* ***2.23***

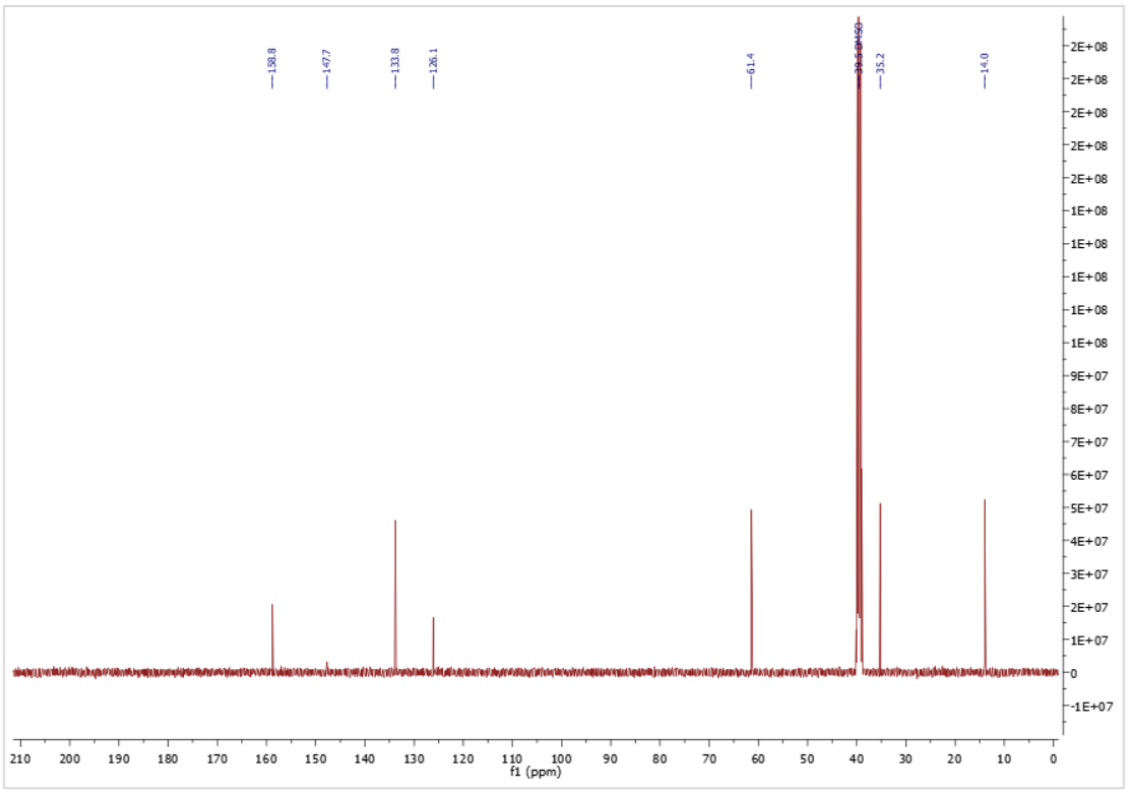

Figure A32: *^{13}C NMR spectrum of **2.23***

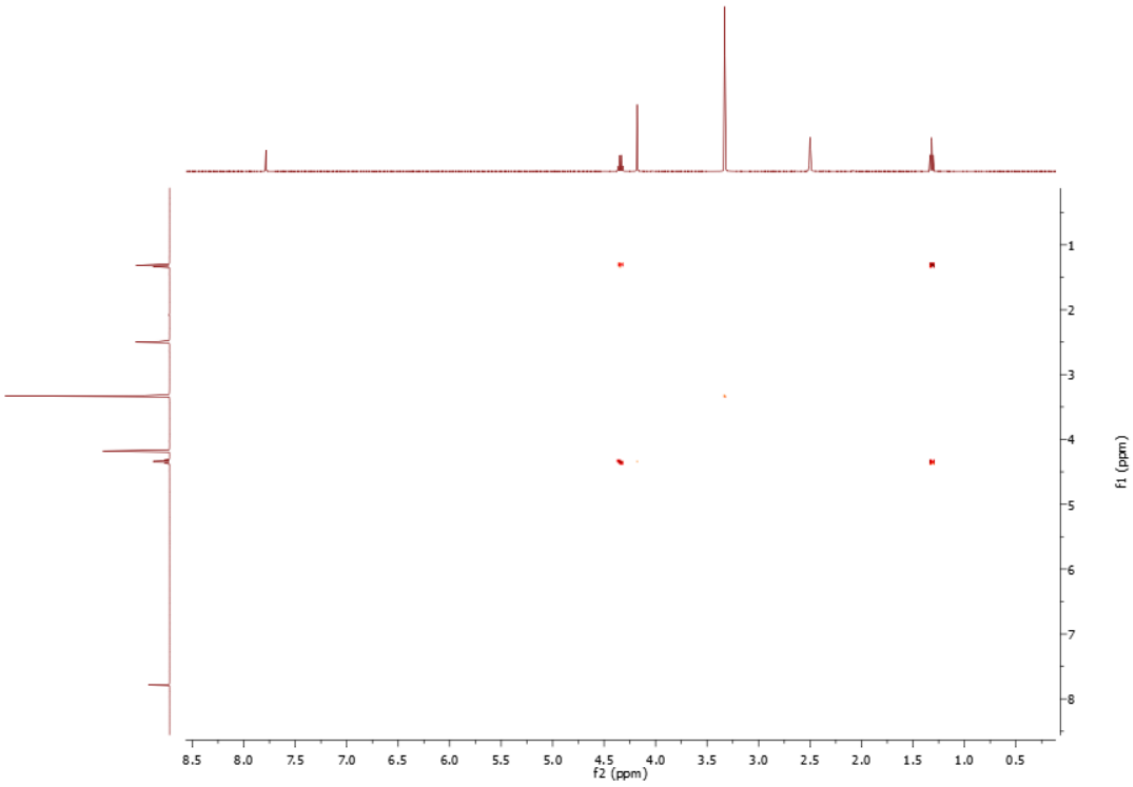

Figure A33: *^{1}H-^{1}H COSY spectrum of **2.23***

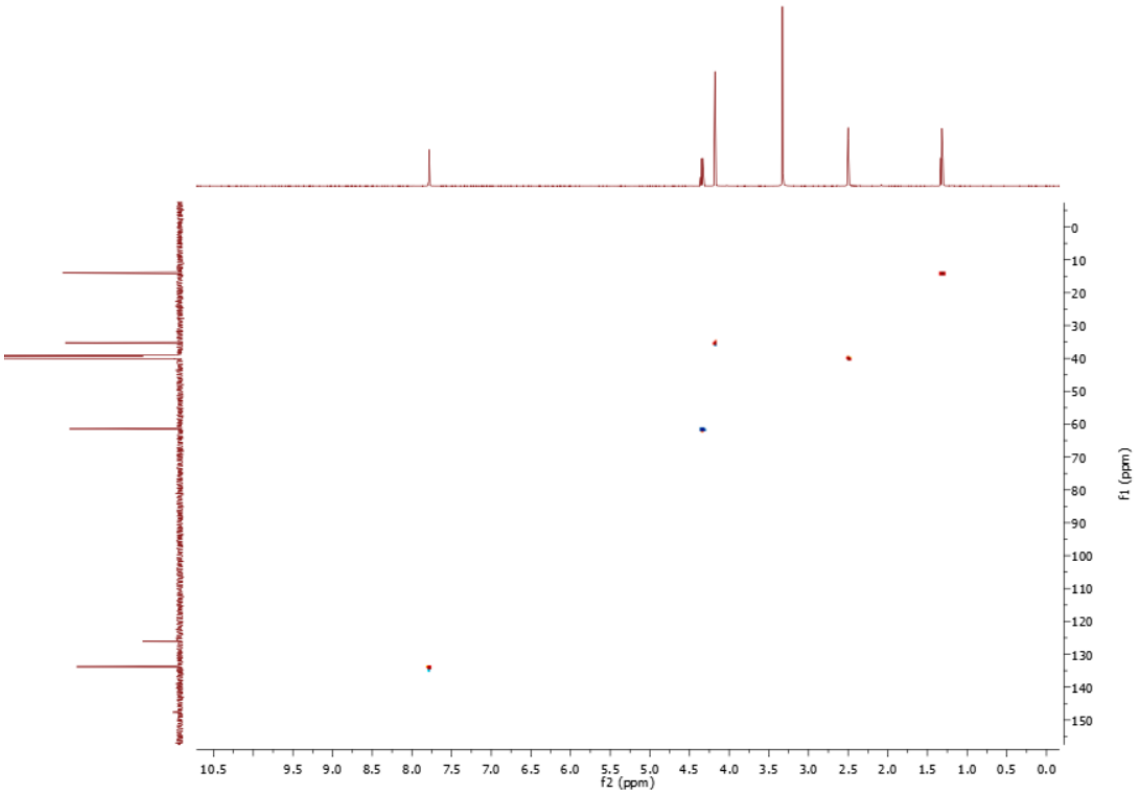

Figure A34: *HSQC spectrum of* ***2.23***

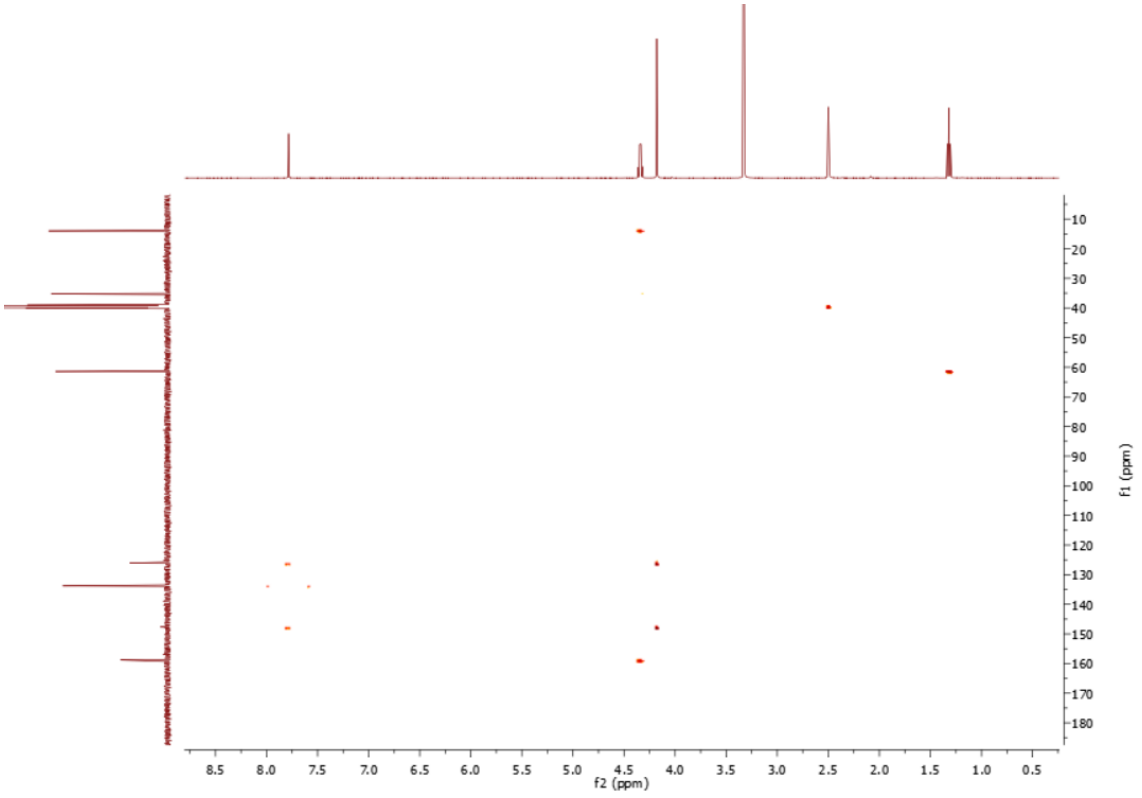

Figure A35: *HMBC spectrum of* ***2.23***

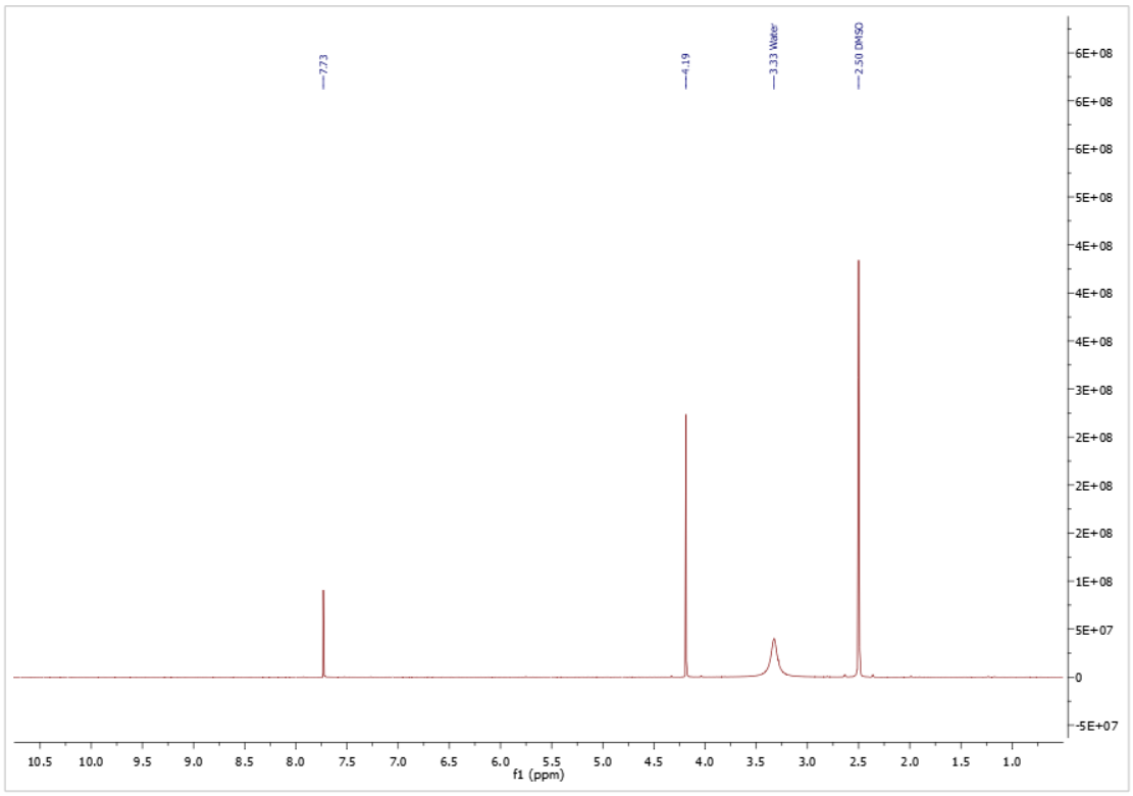

Figure A36: *[1]H NMR spectrum of* ***2.24***

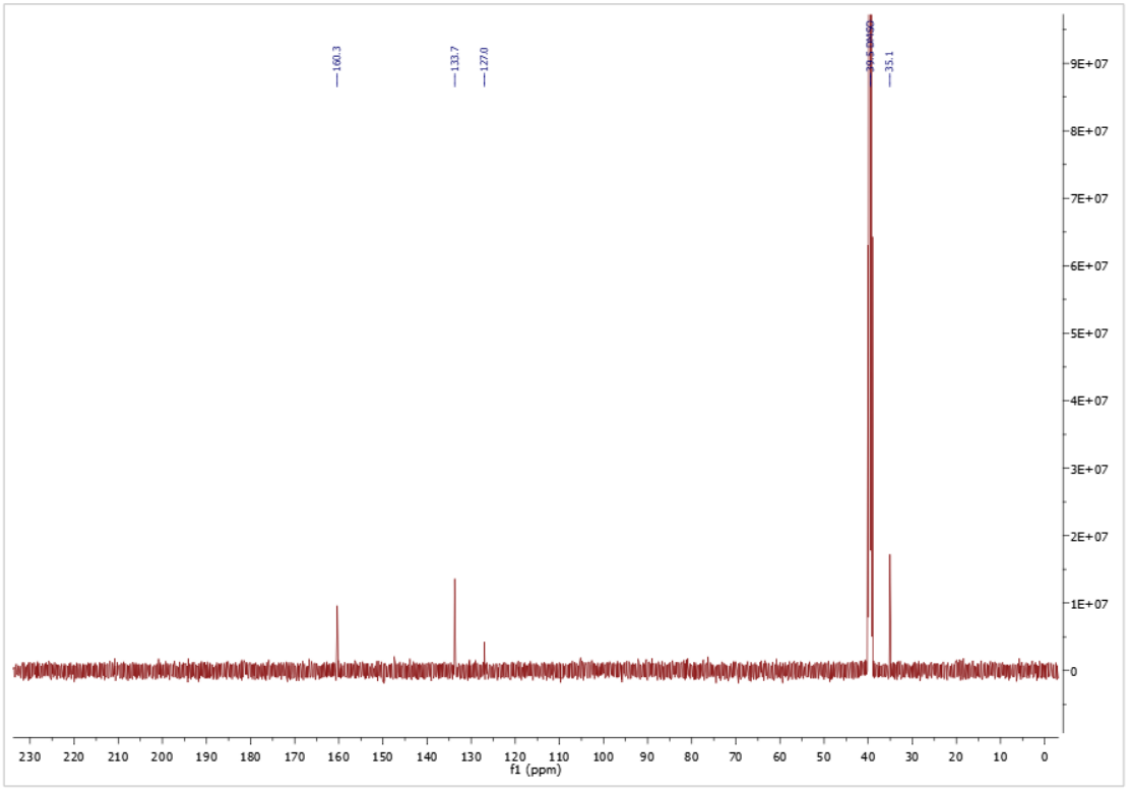

Figure A37: *[13]C NMR spectrum of* ***2.24***

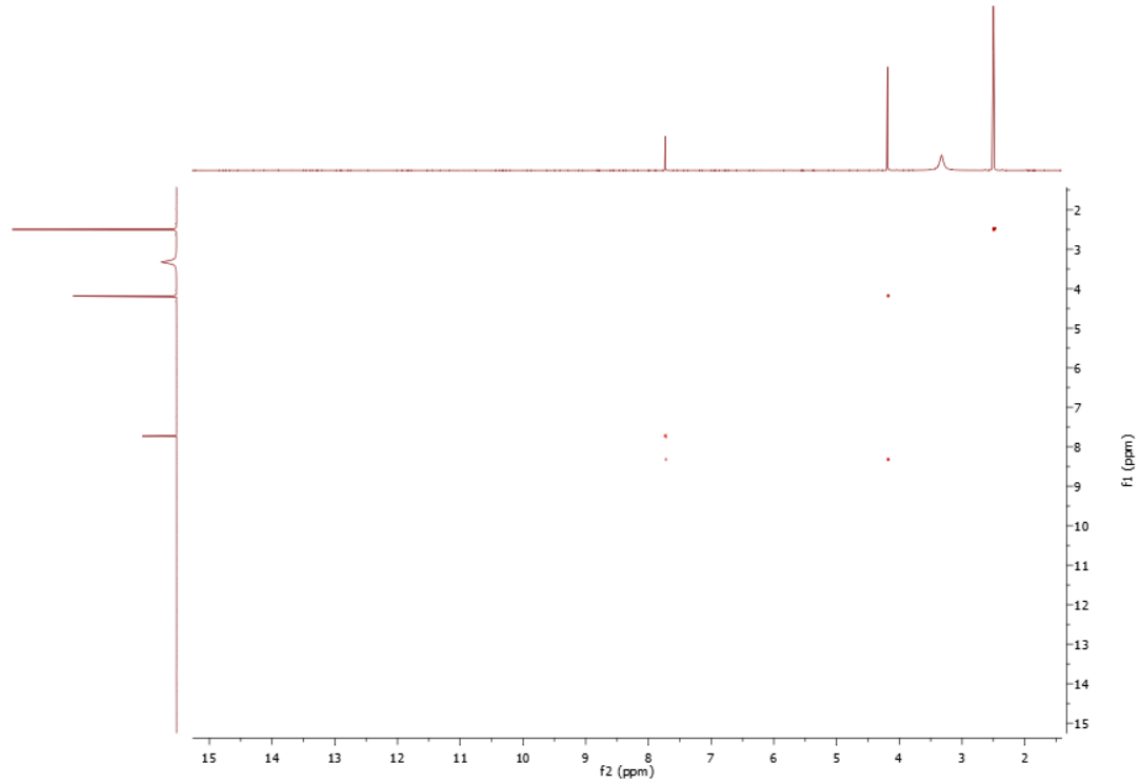

Figure A38: *^{1}H-^{1}H COSY spectrum of **2.24***

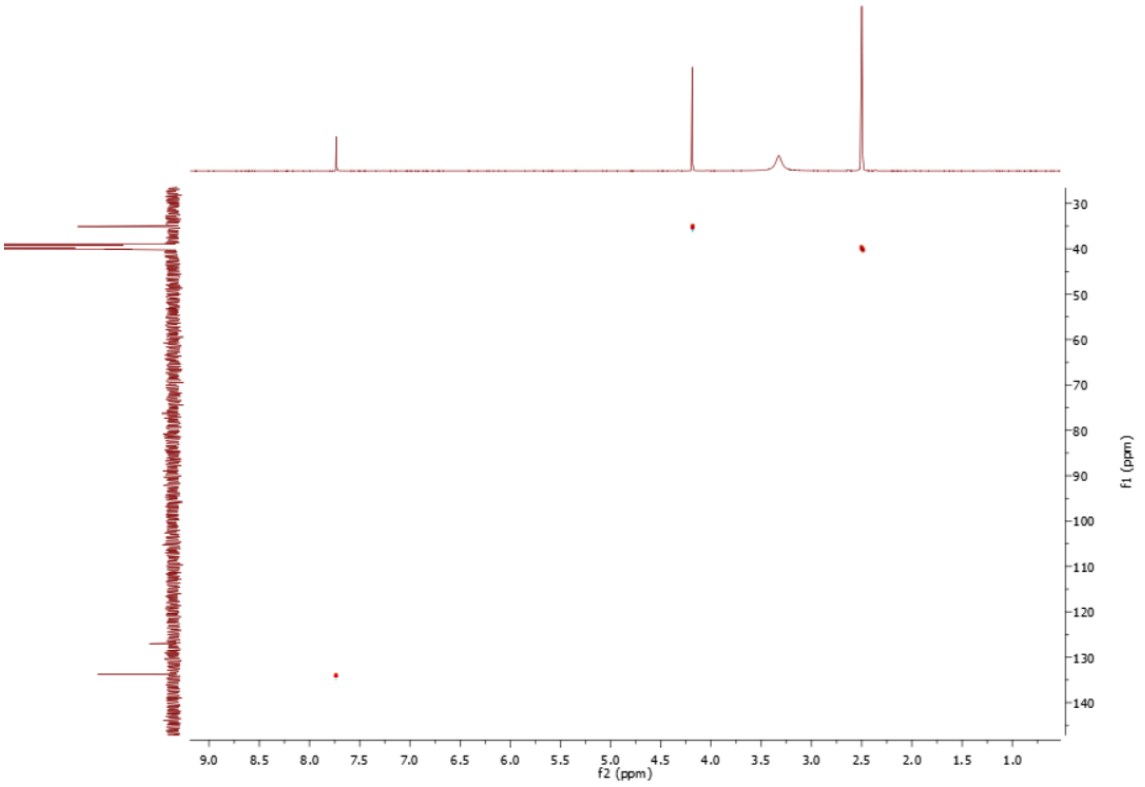

Figure A39: *HSQC spectrum of **2.24***

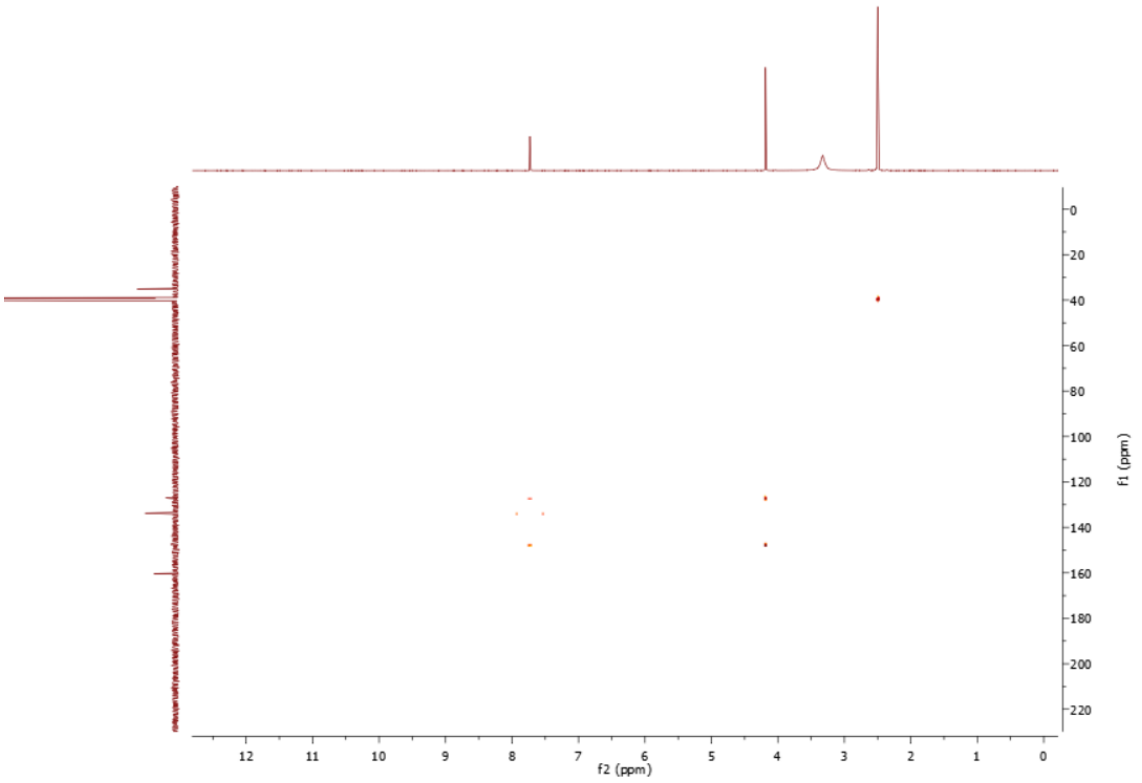

Figure A40: *HMBC spectrum of* ***2.24***

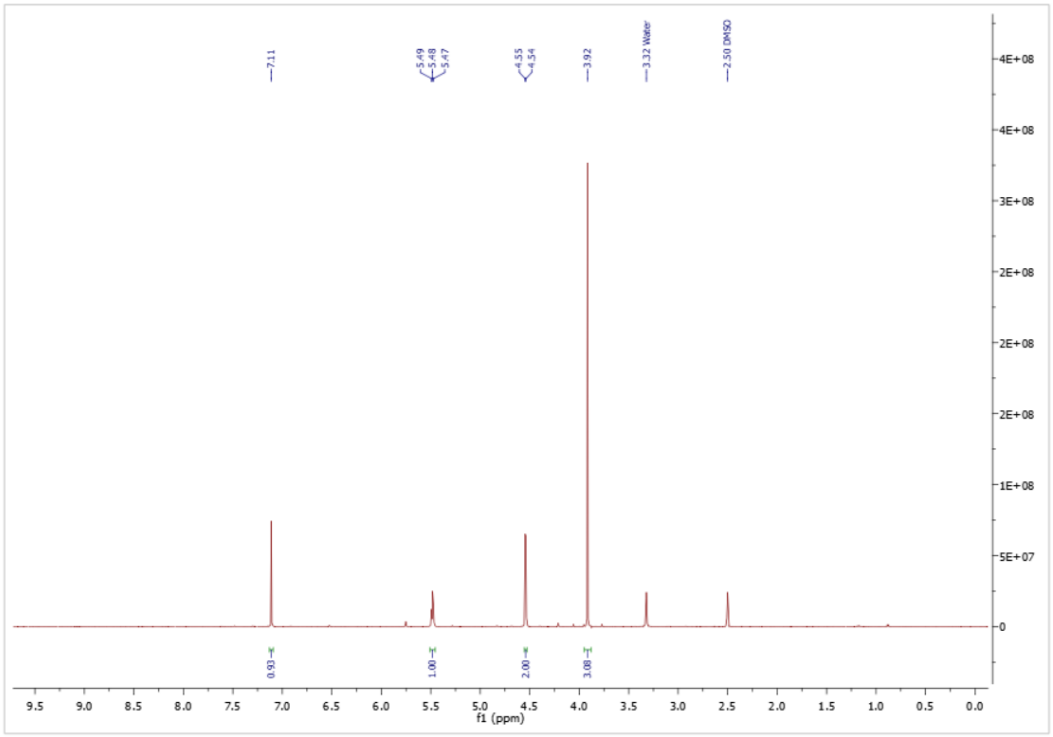

Figure A41: *^{1}H NMR spectrum of* ***2.18***

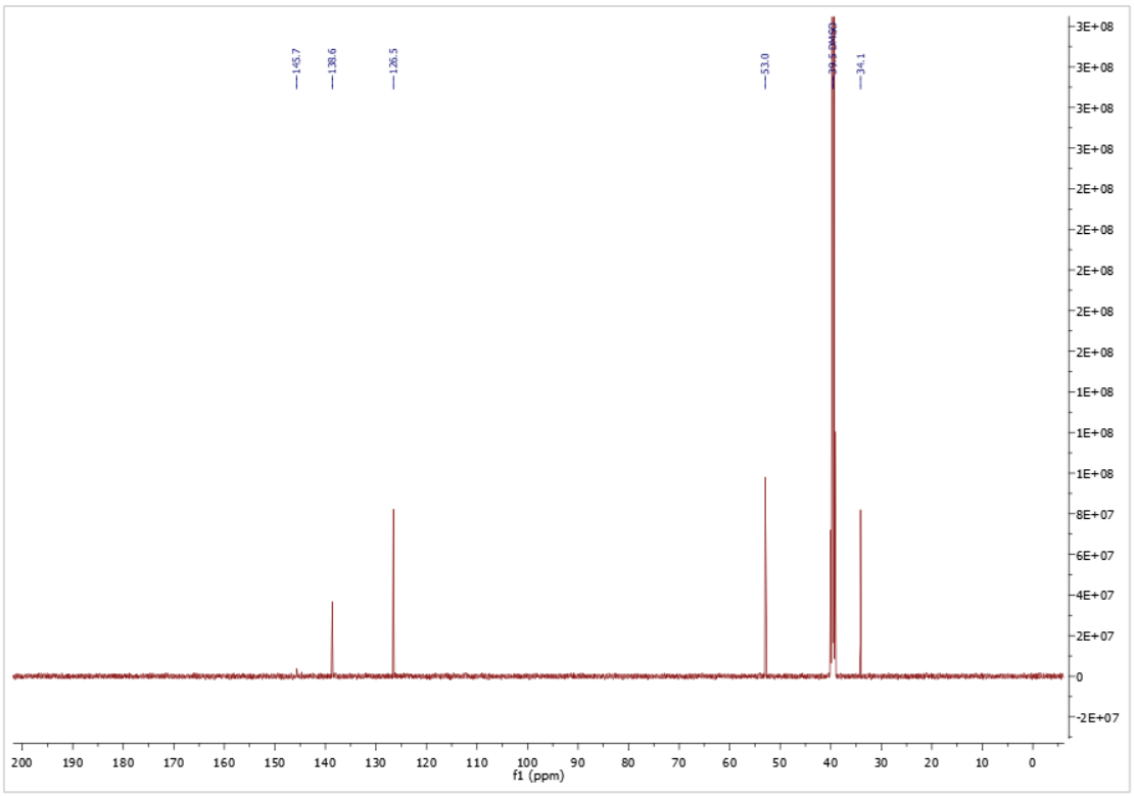

Figure A42: *^{13}C NMR spectrum of* ***2.18***

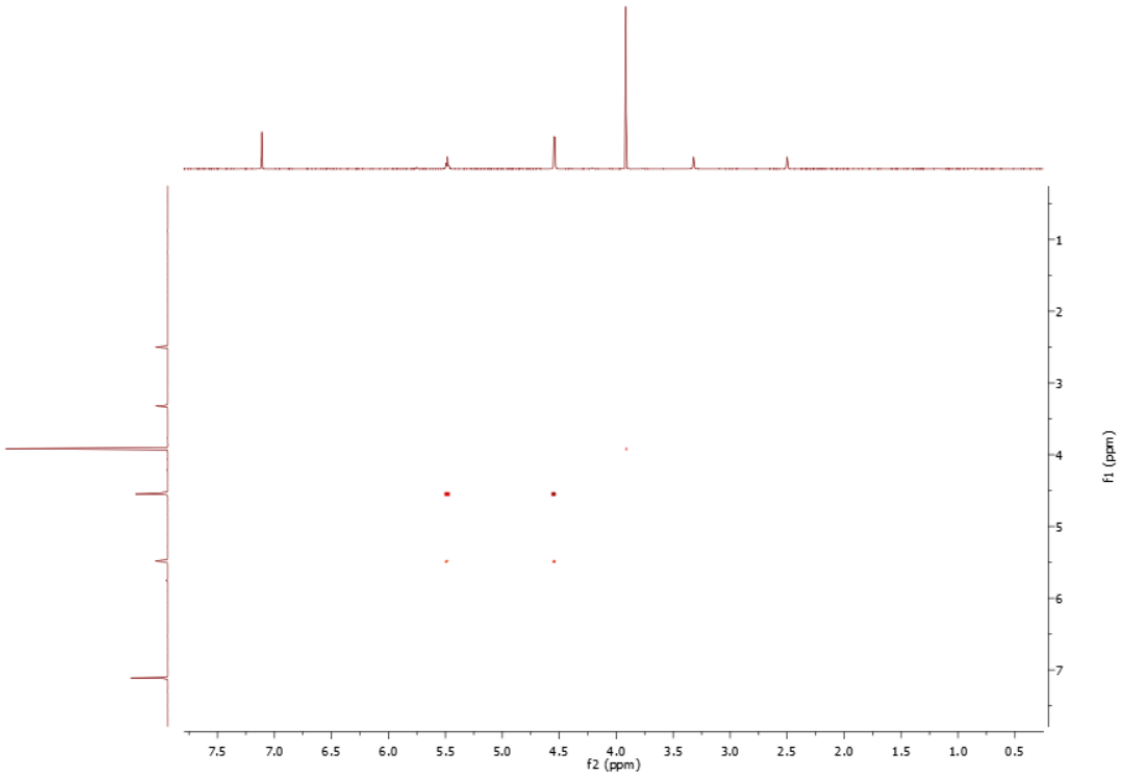

Figure A43: *^{1}H-^{1}H COSY spectrum of* ***2.18***

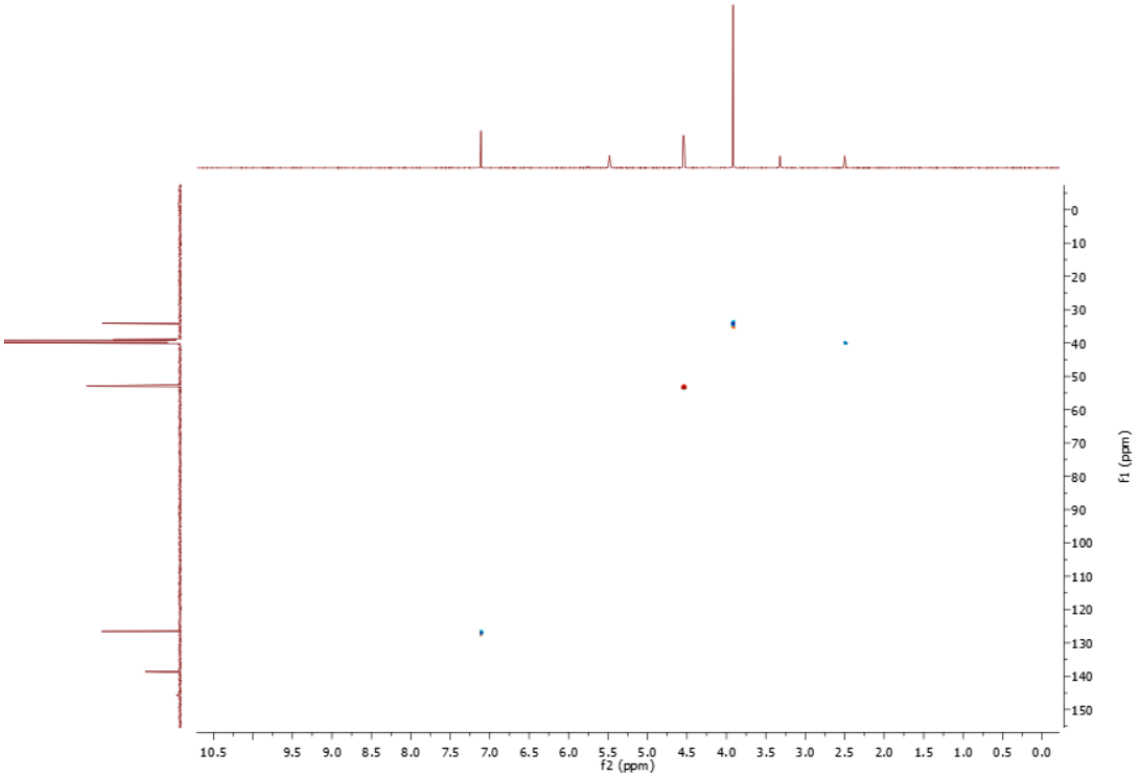

Figure A44: *HSQC spectrum of **2.18***

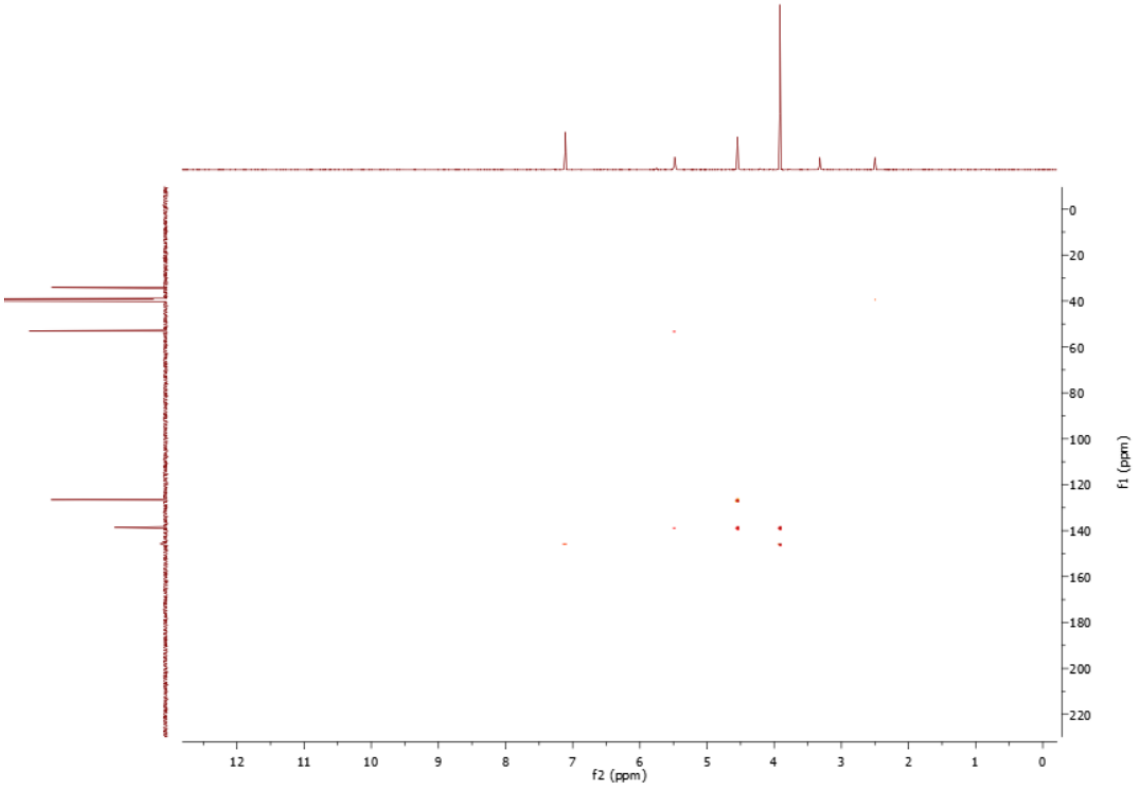

Figure A45: *HMBC spectrum of **2.18***

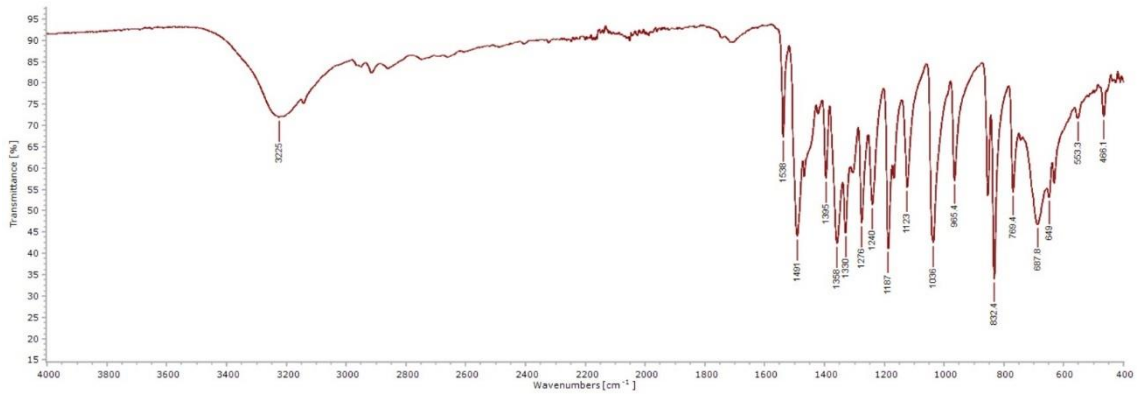

Figure A46: *IR spectrum of **2.18***

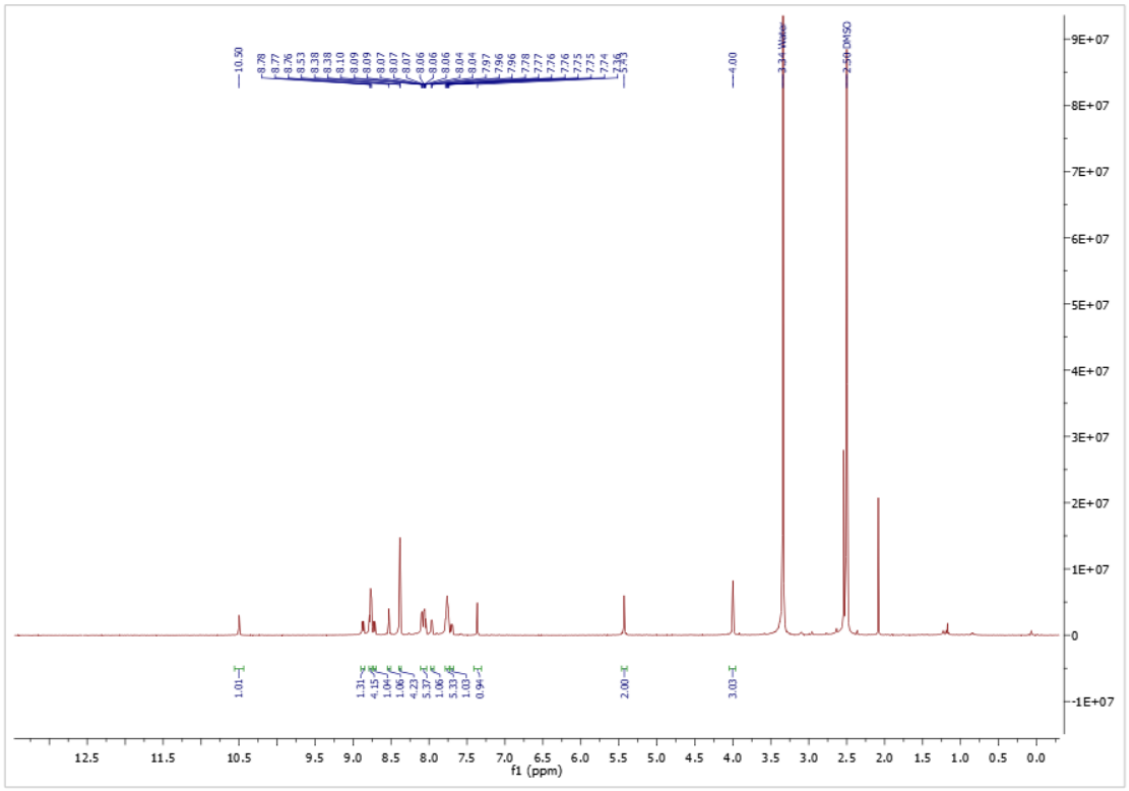

Figure A47: *^{1}H NMR spectrum of **2.12***

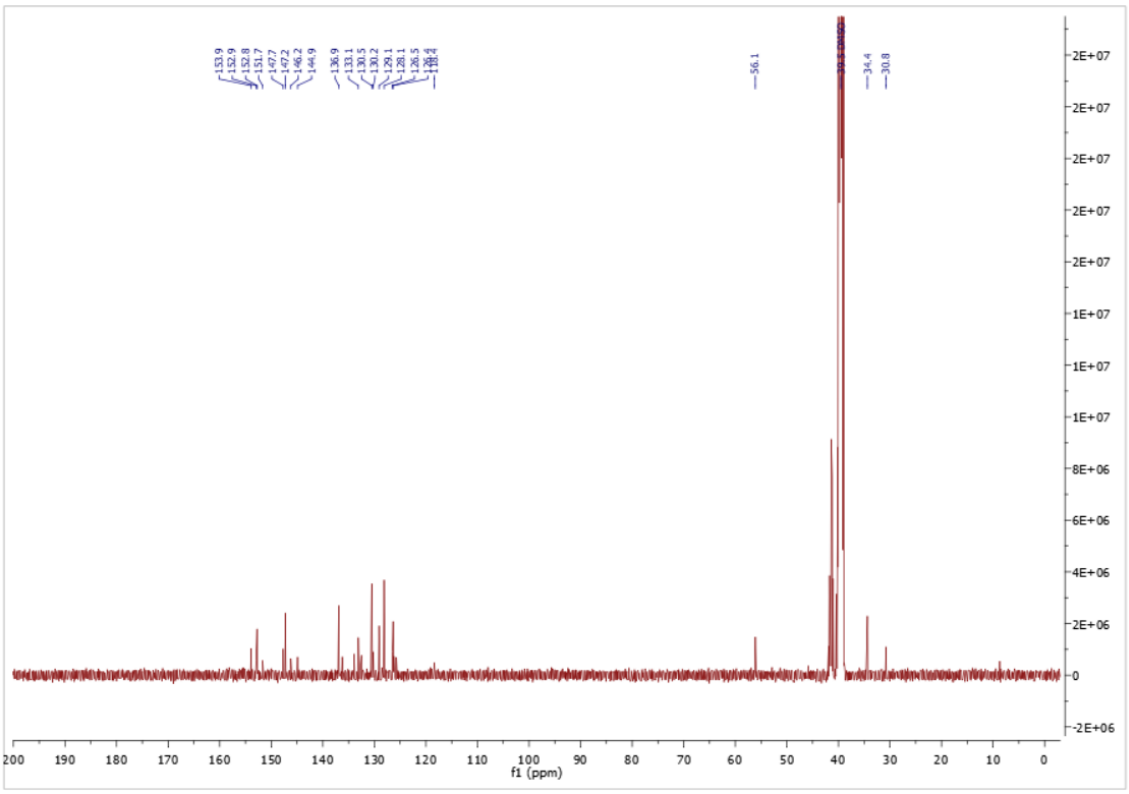

Figure A48: *^{13}C NMR spectrum of **2.12***

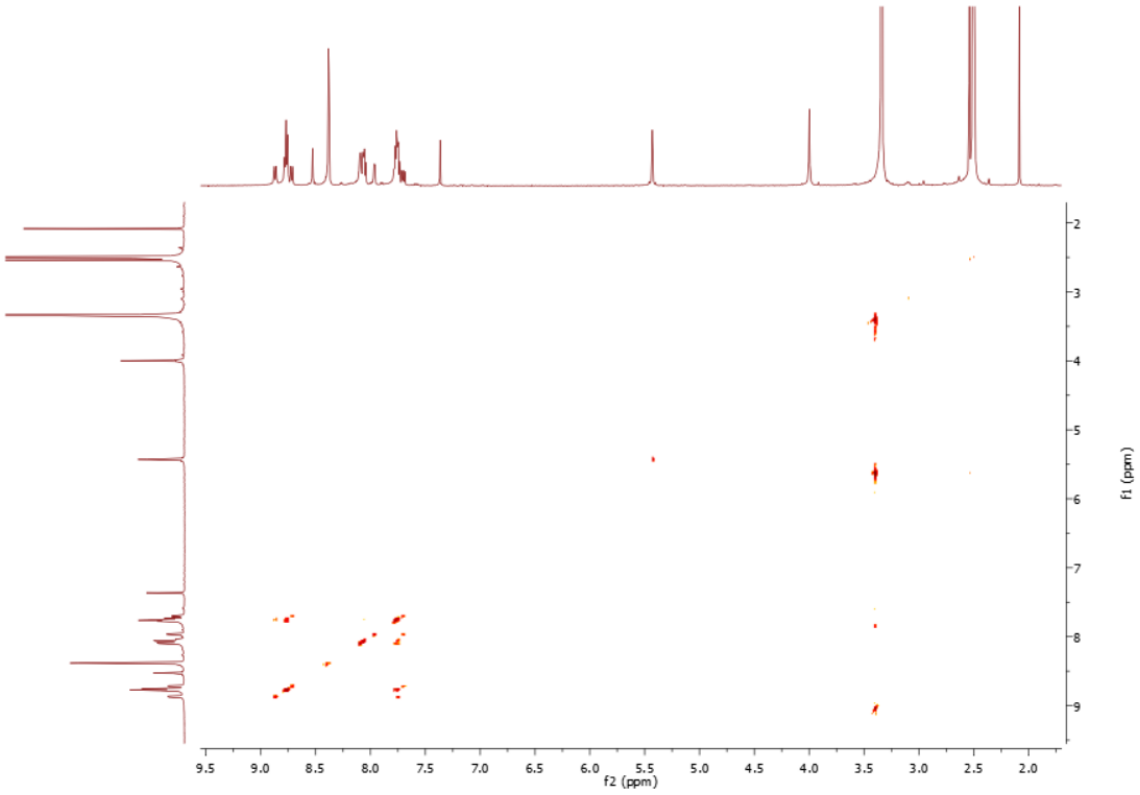

Figure A49: *^{1}H-^{1}H NMR spectrum of **2.12***

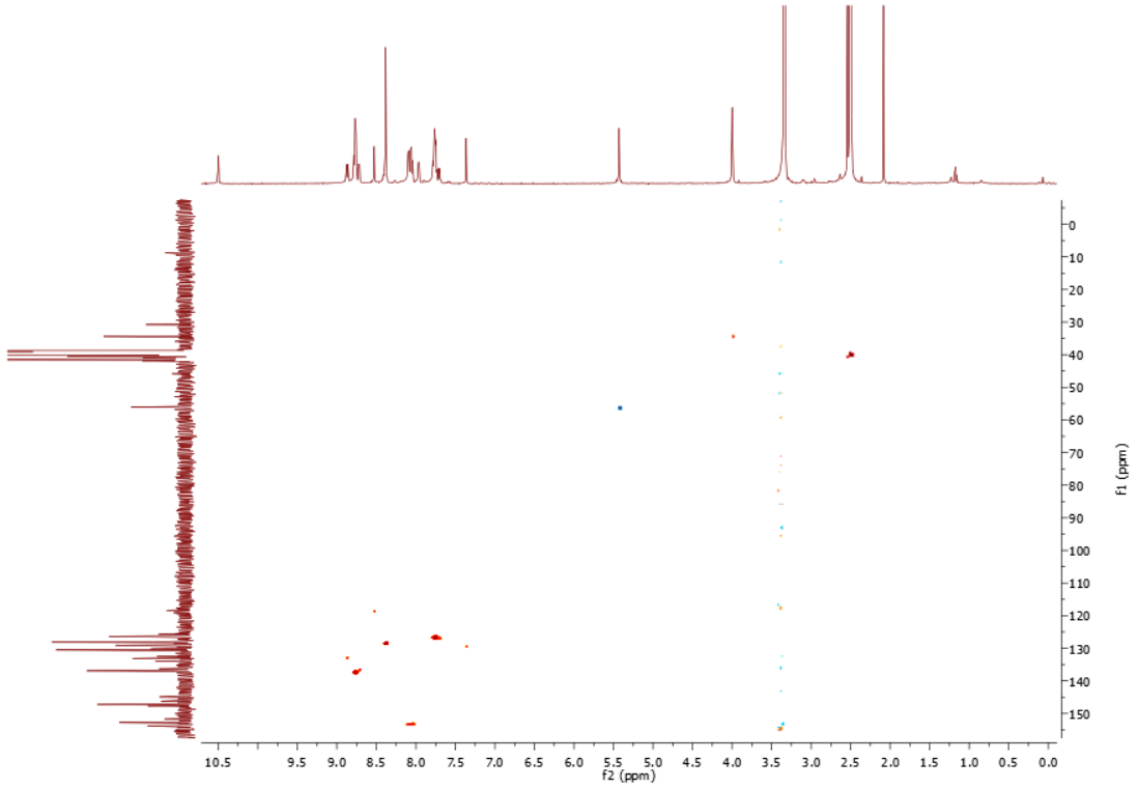

Figure A50: *HSQC spectrum of* ***2.12***

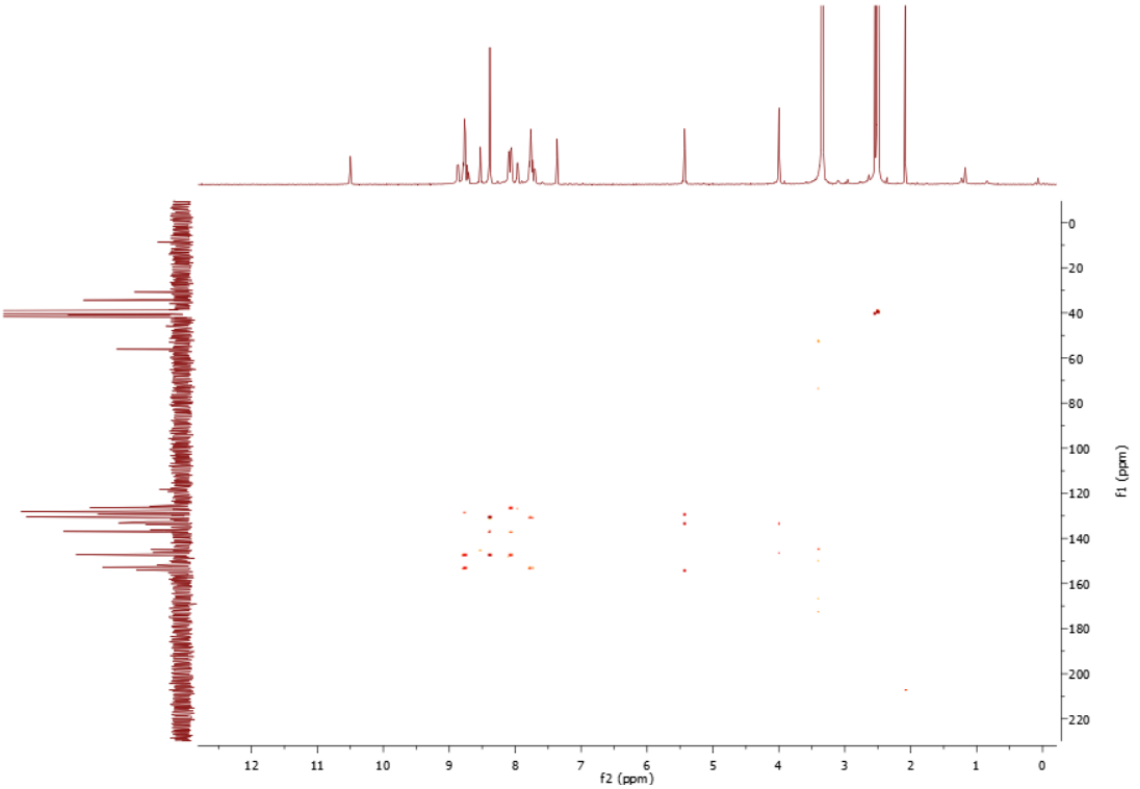

Figure A51: *HMBC spectrum of* ***2.12***

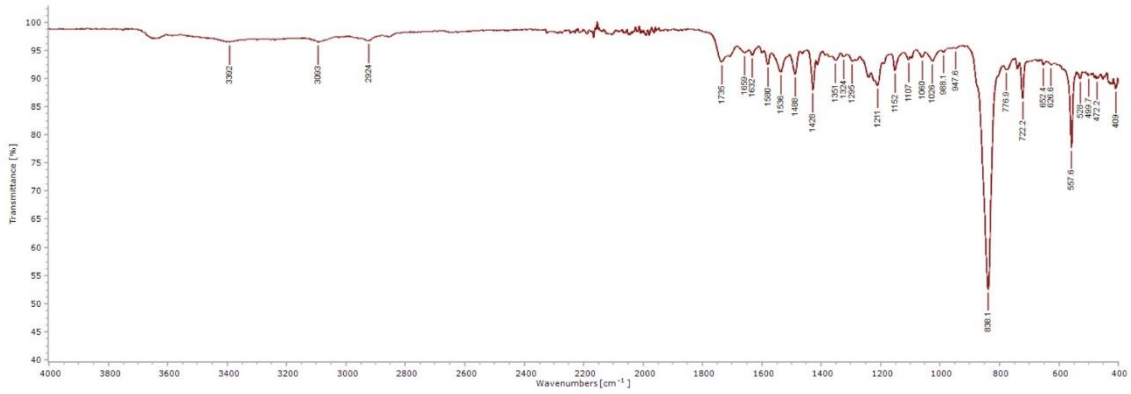

Figure A52: *IR spectrum of* ***2.12***

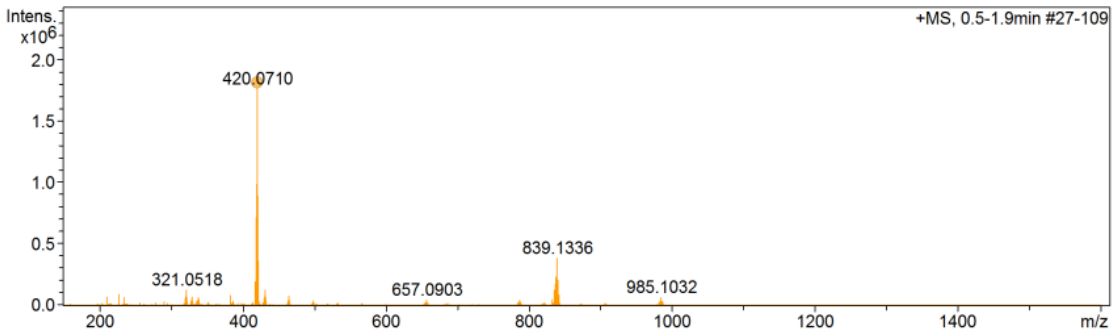

Figure A53: *HRMS of* ***2.12***

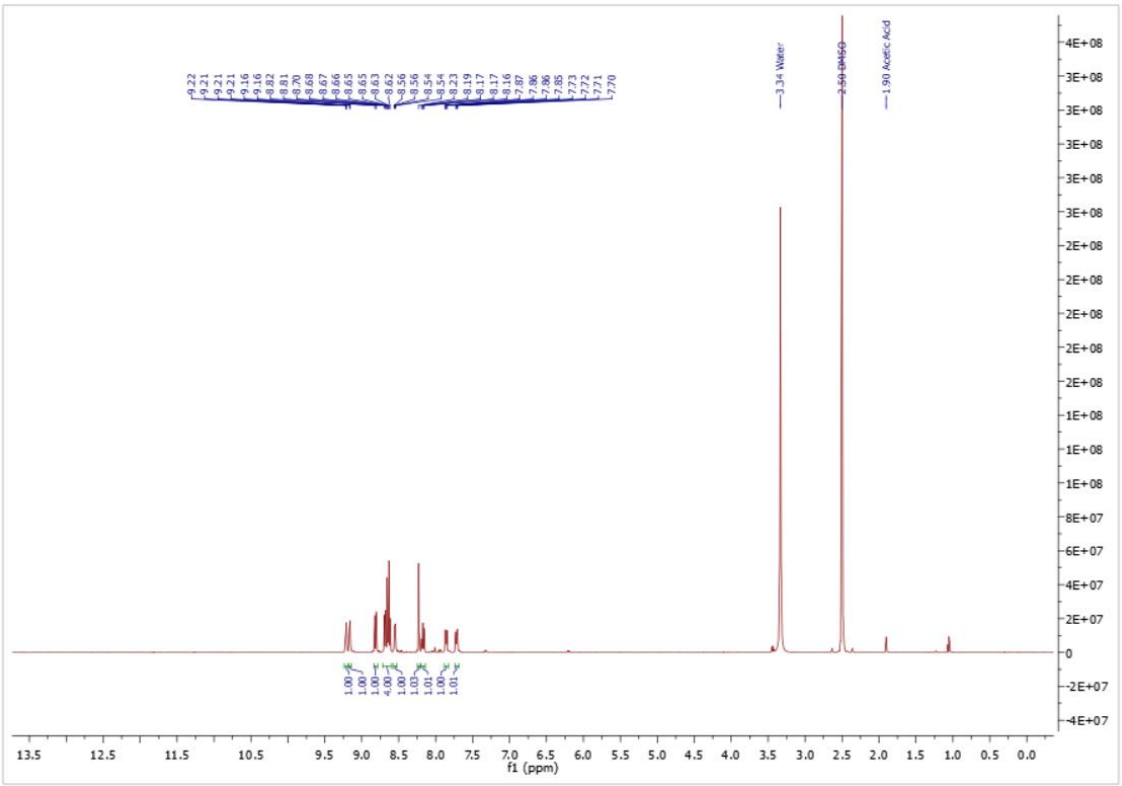

Figure A54: *^{1}H NMR spectrum of* ***2.25***

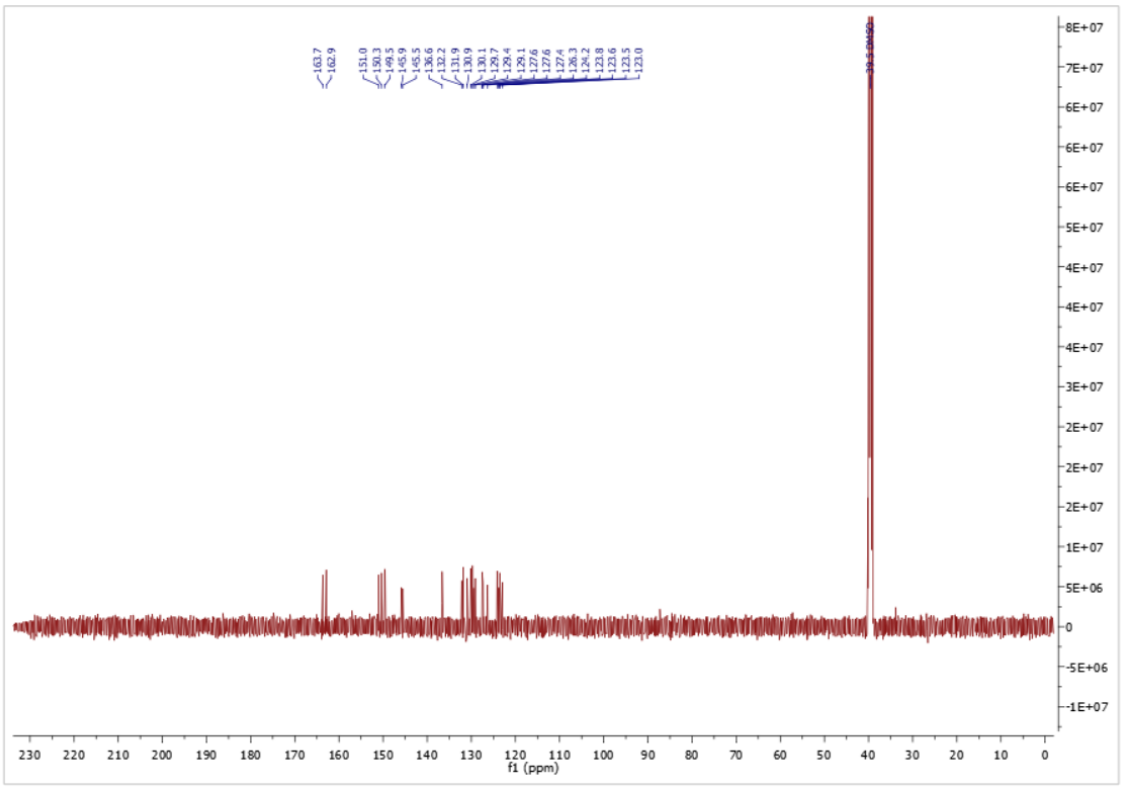

Figure A55: *^{13}C NMR spectrum of **2.25***

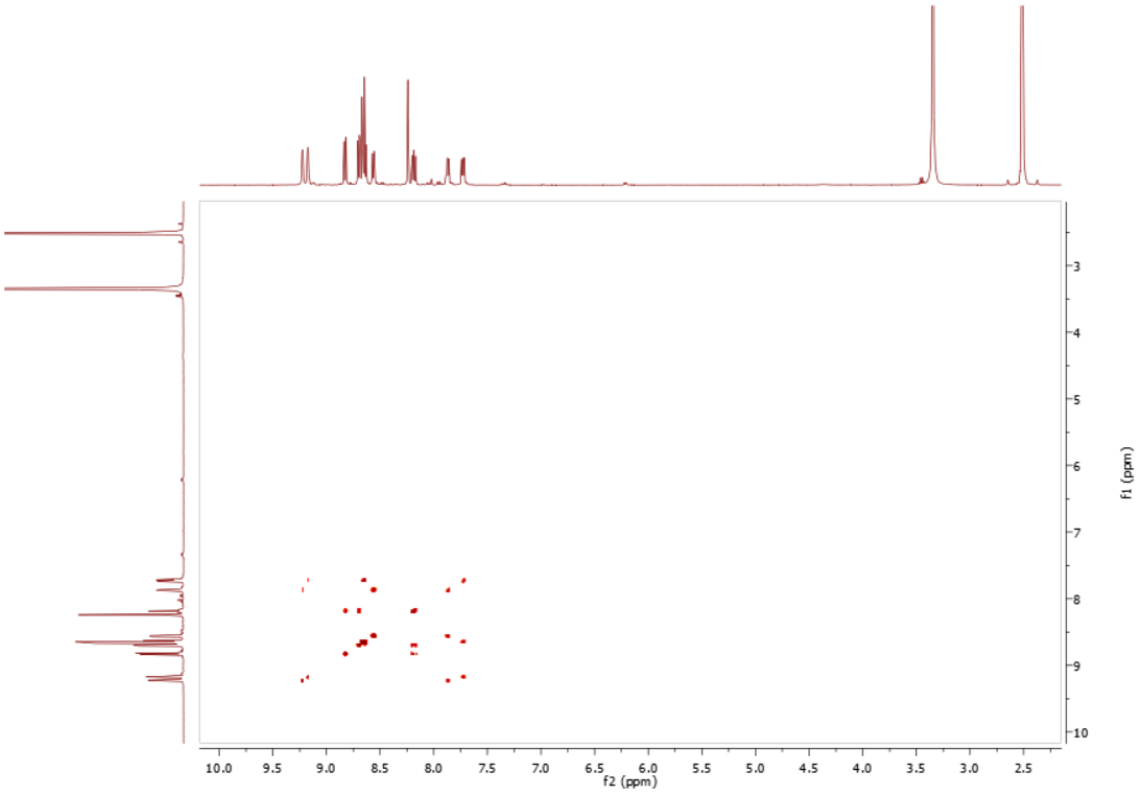

Figure A56: *^{1}H-^{1}H COSY spectrum of **2.25***

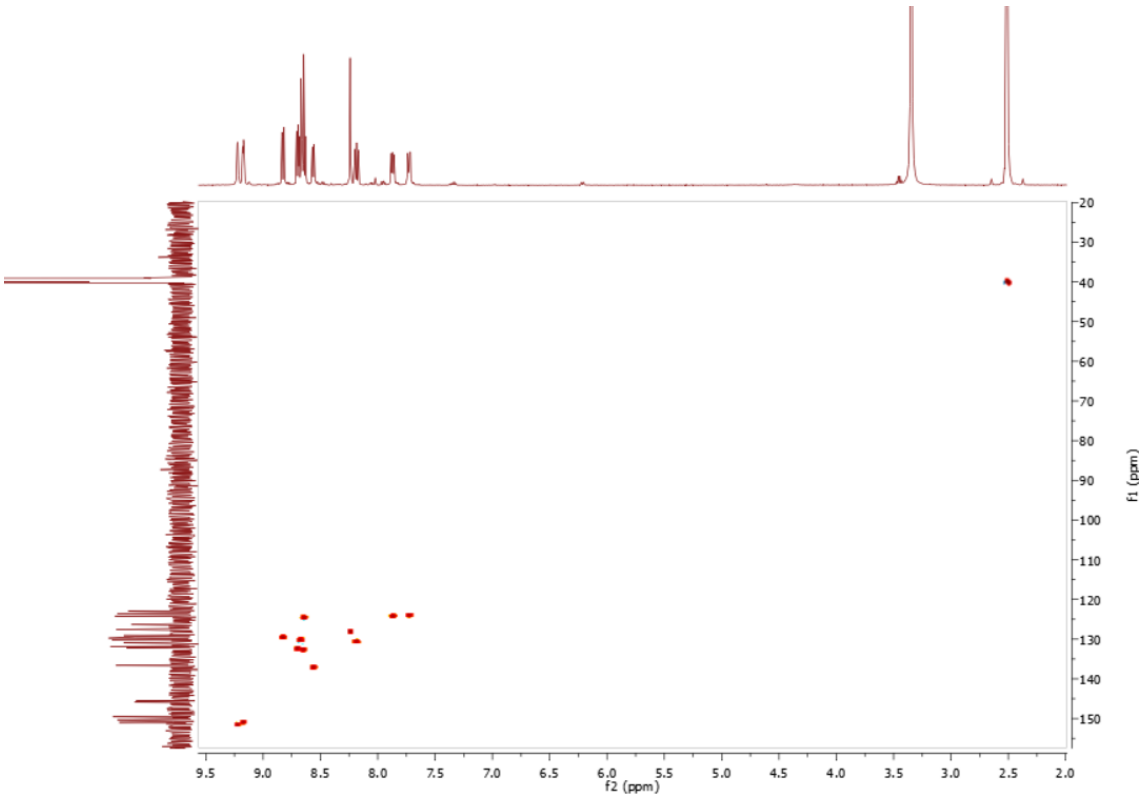

Figure A57: *HSQC spectrum of* ***2.25***

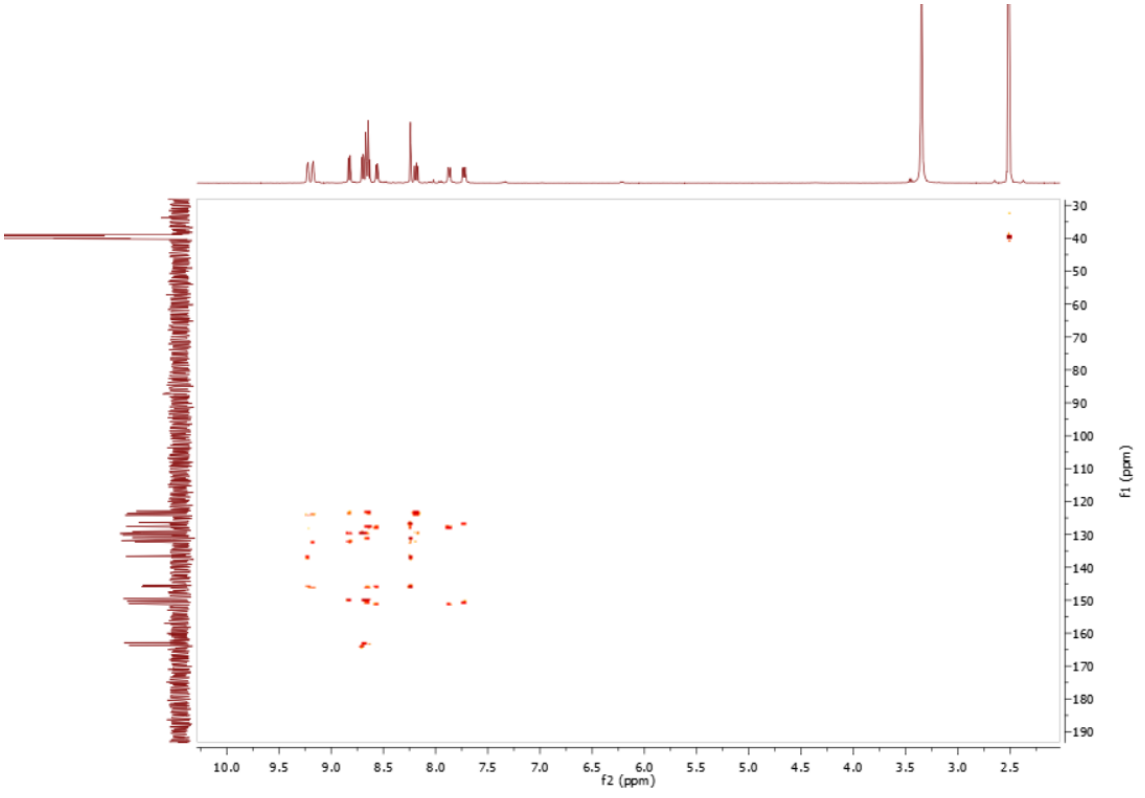

Figure A58: *HMBC spectrum of* ***2.25***

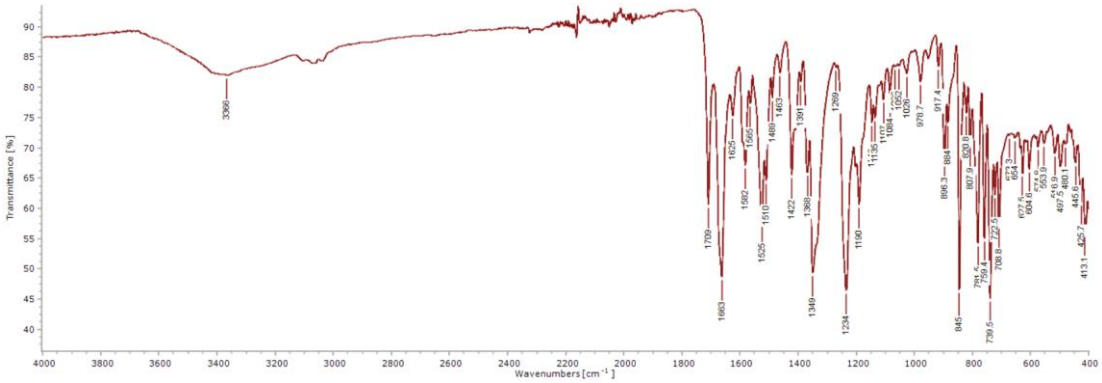

Figure A59: *IR spectrum of* ***2.25***

Compound specific information

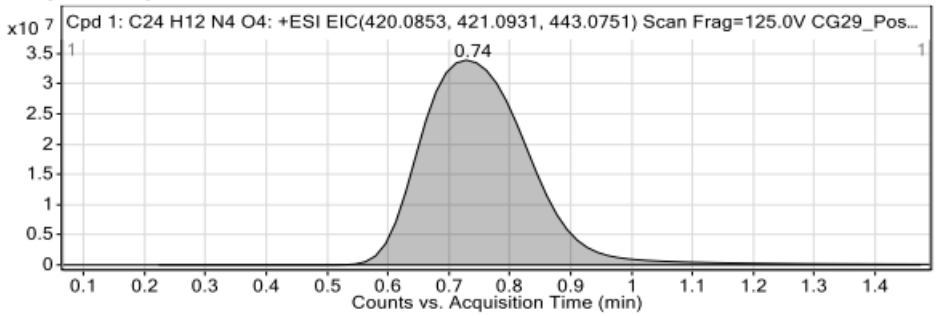

Figure: Extracted ion chromatogram (EIC) of compound.

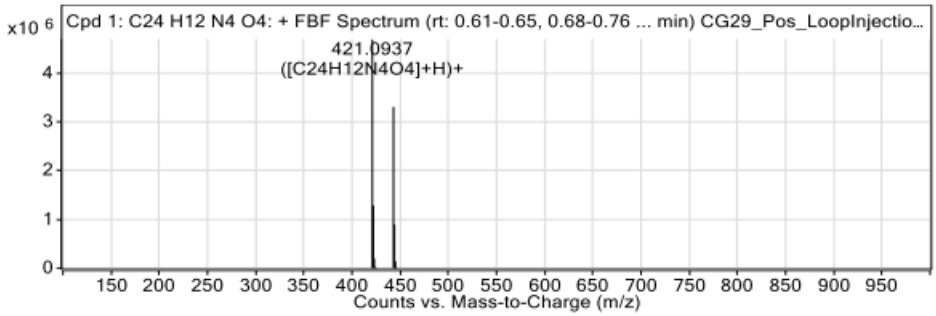

Compound Table

Compound Label	RT (min)	Observed mass (m/z)	Neutral observed mass (Da)	Theoretical mass (Da)	Mass error (ppm)	Isotope match score (%)
Cpd 1: C24 H12 N4 O4	0.74	443.0755	420.0864	420.0859	1.23	99.83

Mass errors of between -5.00 and 5.00 ppm with isotope match scores above 60% are considered confirmation of molecular formulae

Figure A60: *HRMS of* ***2.25***

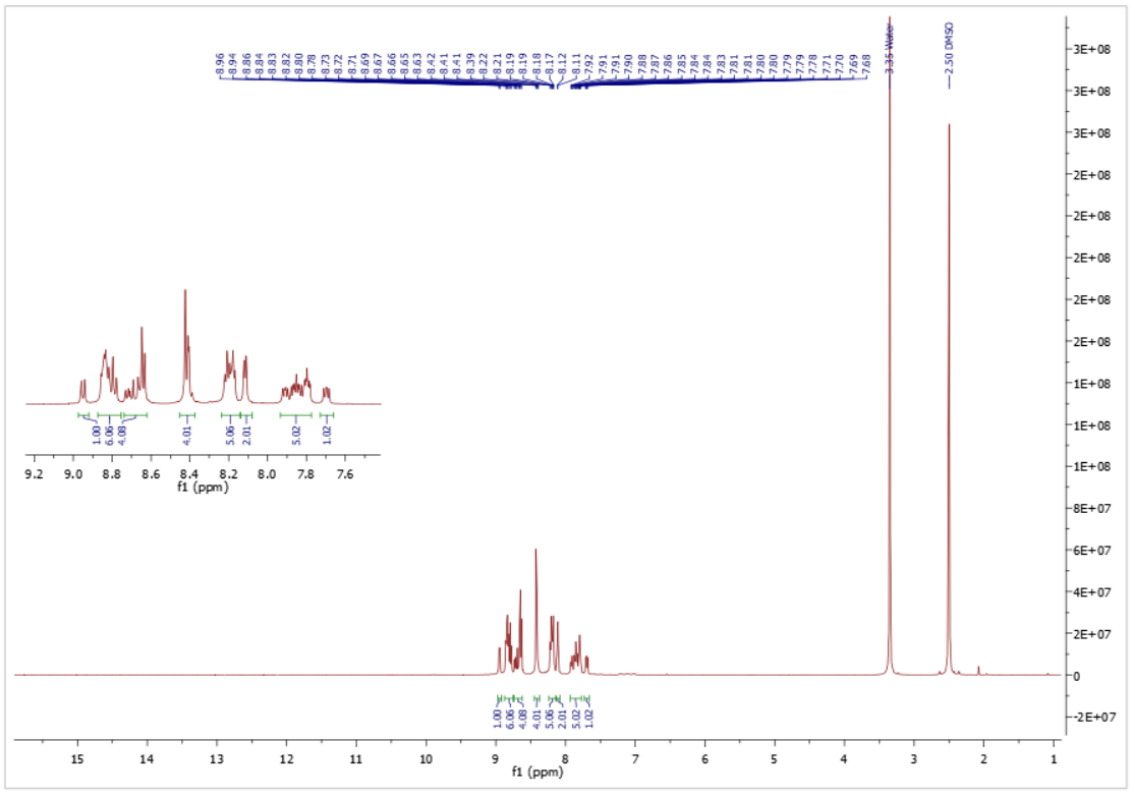

Figure A61: *^{1}H NMR spectrum of* ***2.13***

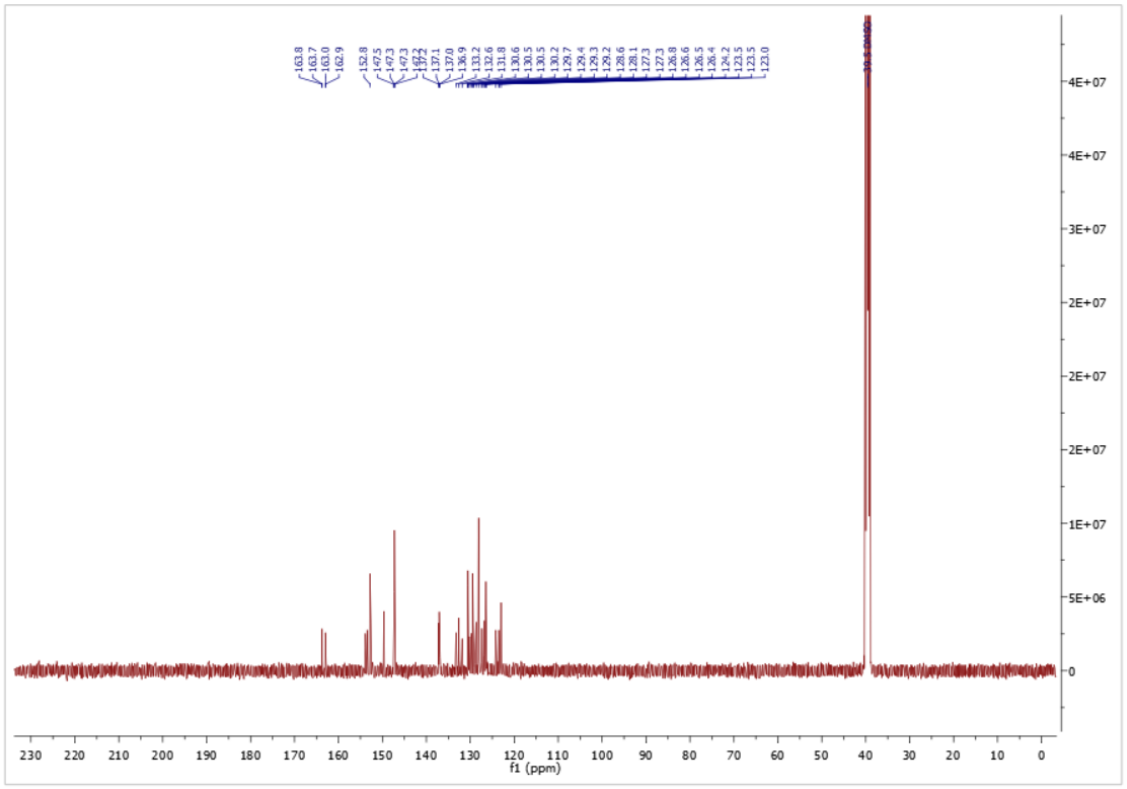

Figure A62: *^{13}C NMR spectrum of* ***2.13***

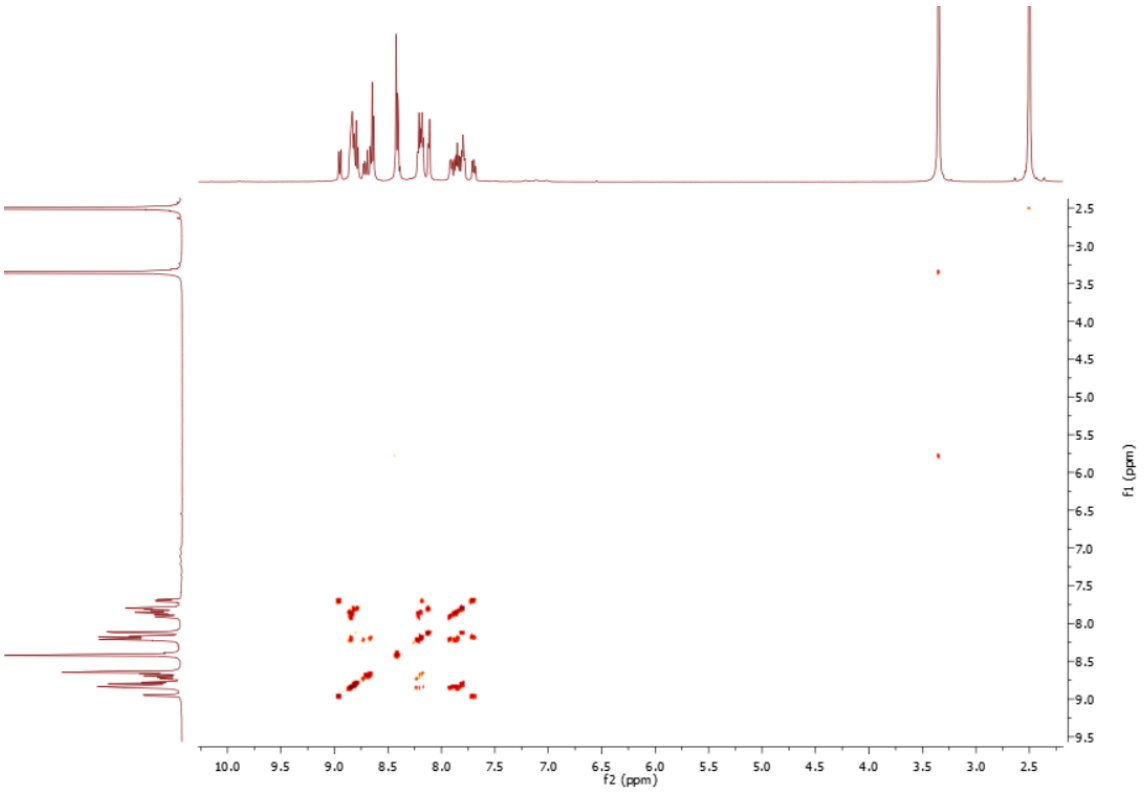

Figure A63: *^{1}H-^{1}H COSY spectrum of* ***2.13***

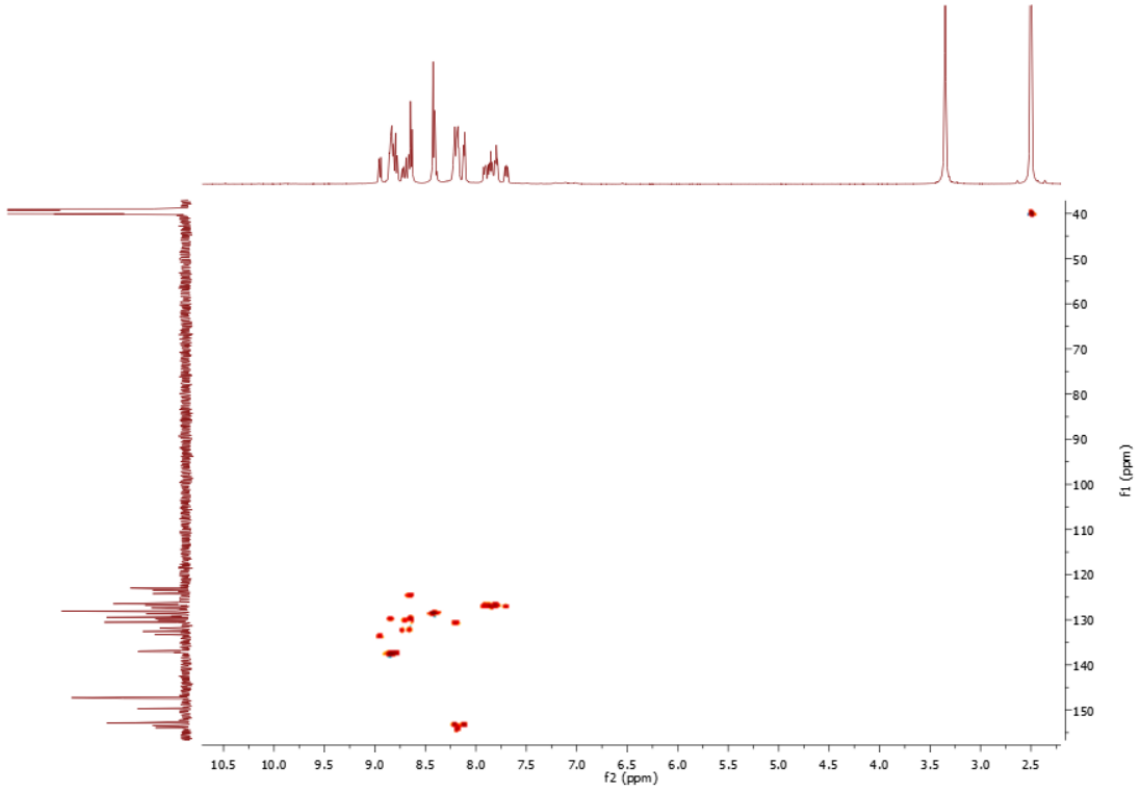

Figure A64: *HSQC spectrum of* ***2.13***

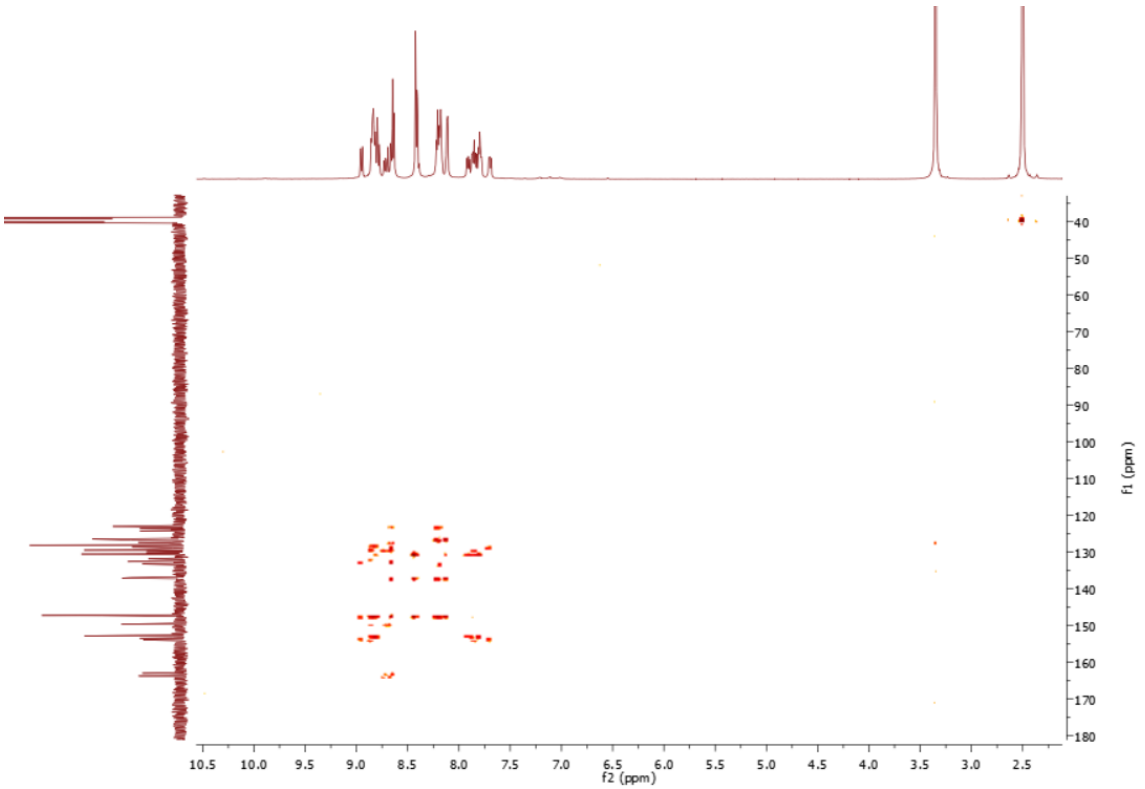

Figure A65: *HMBC spectrum of* ***2.13***

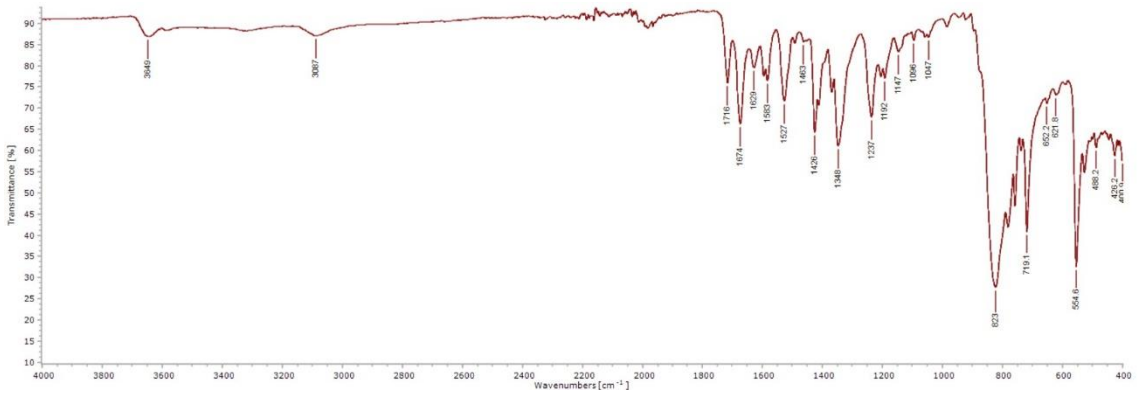

Figure A66: *IR spectrum of* ***2.13***

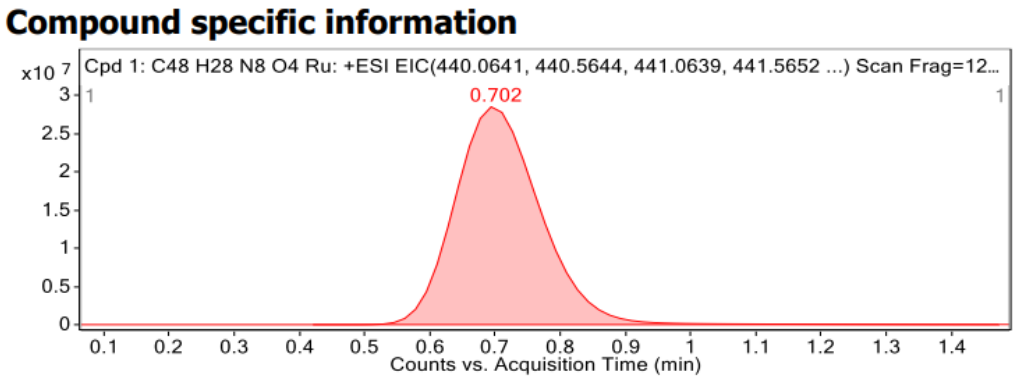

Figure: Extracted ion chromatogram (EIC) of compound.

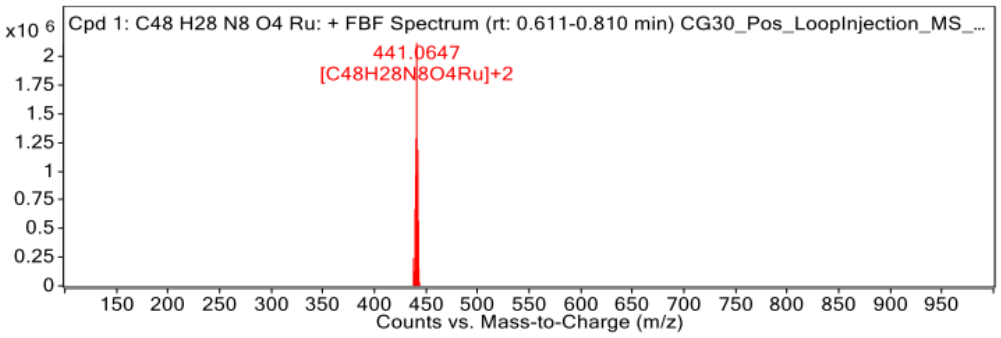

Figure A67: *HRMS of* ***2.13***

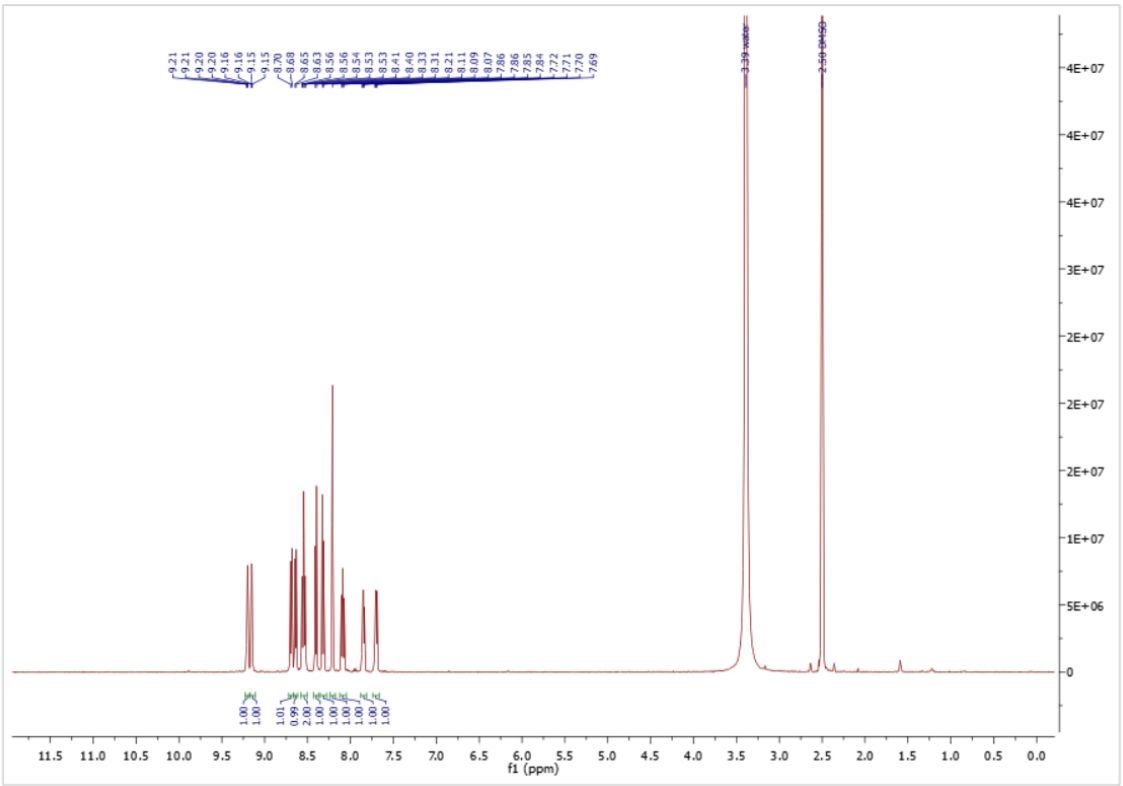

Figure A68: *^{1}H NMR spectrum of* ***2.27***

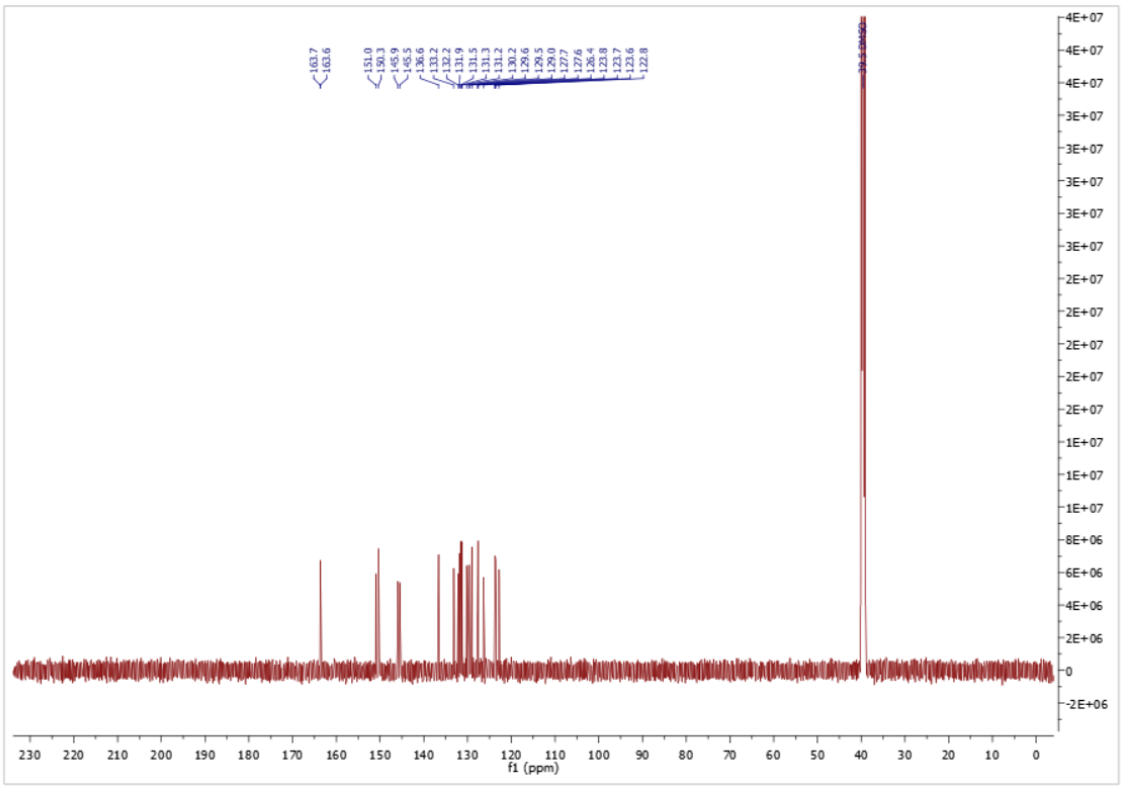

Figure A69: *^{13}C NMR spectrum of* ***2.27***

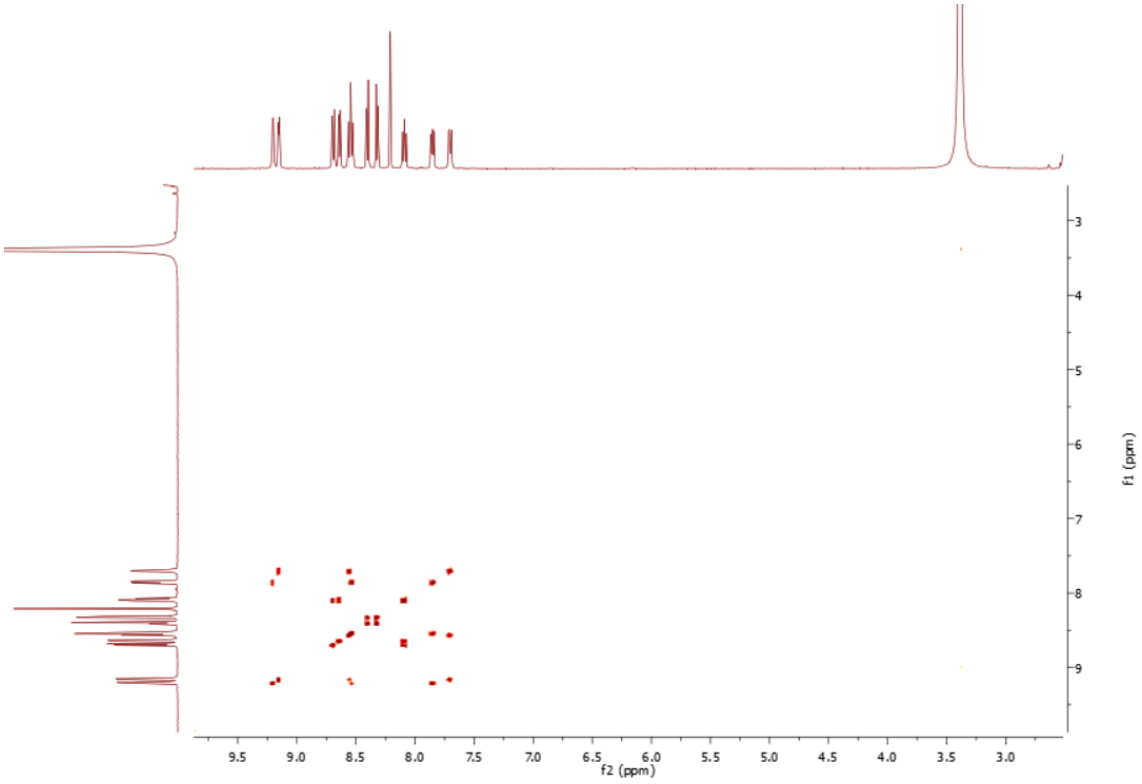

Figure A70: *^{1}H-^{1}H COSY spectrum of* ***2.27***

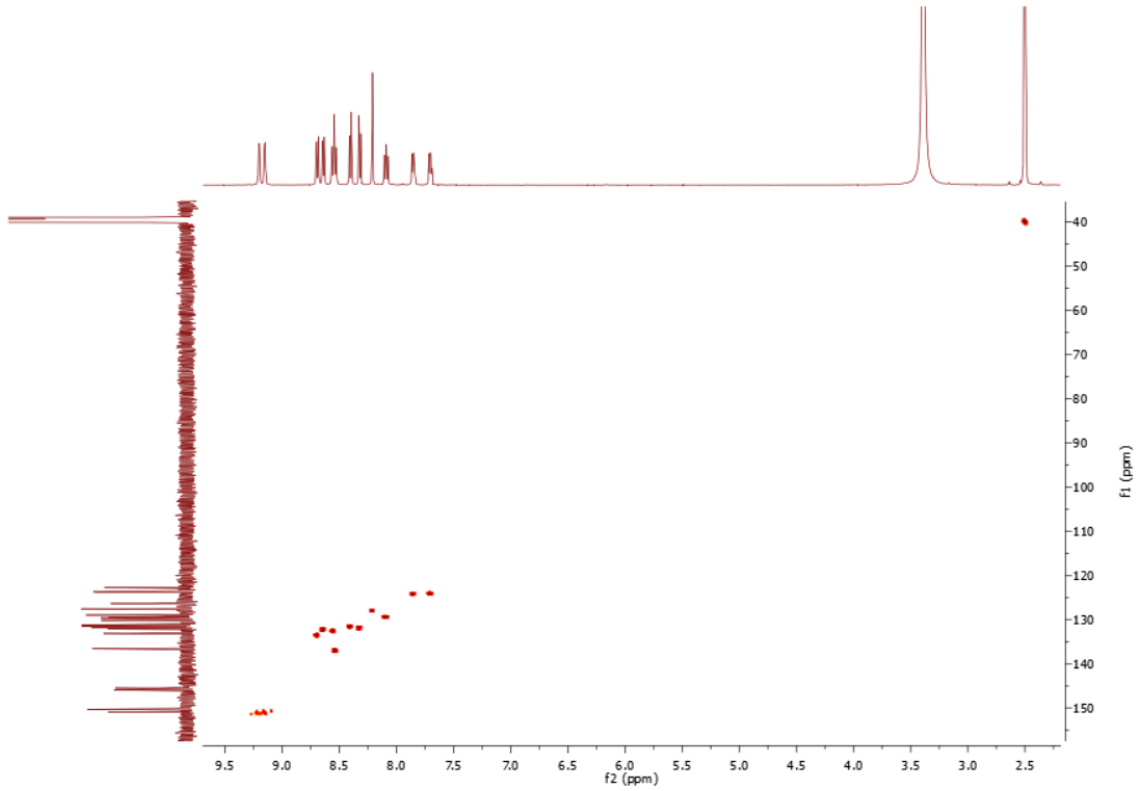

Figure A71: *HSQC spectrum of* ***2.27***

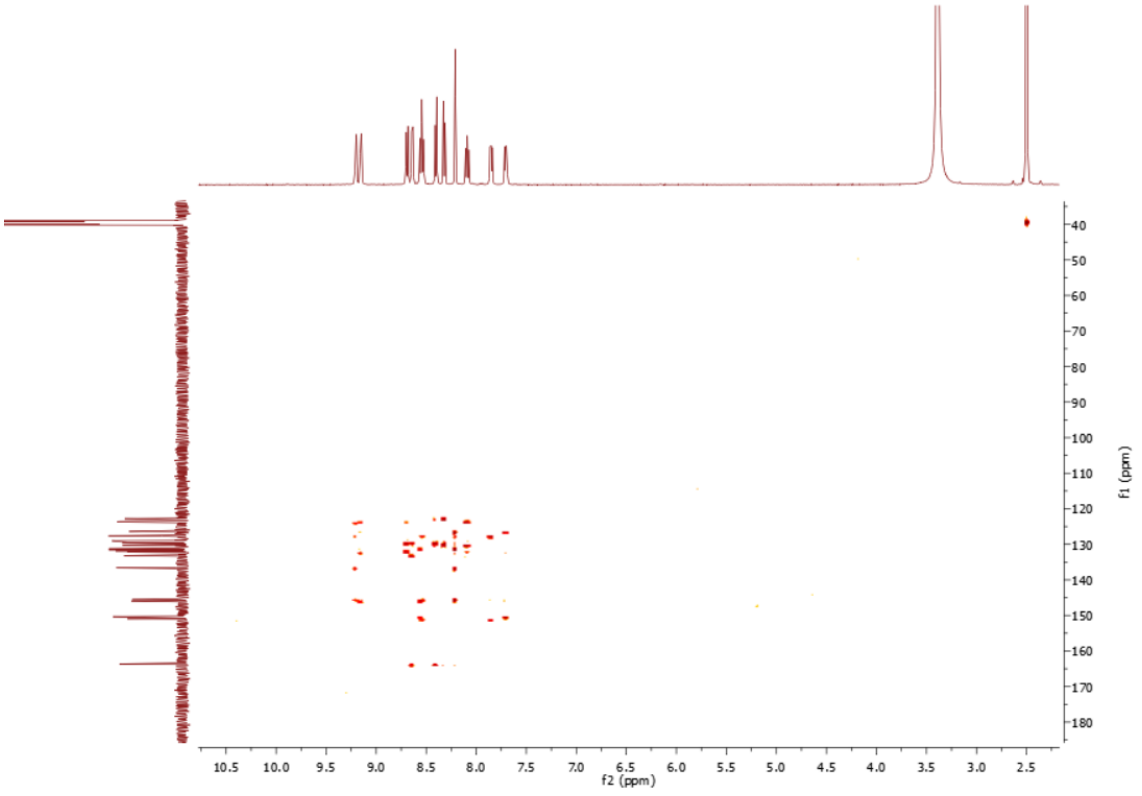

Figure A72: *HMBC spectrum of* ***2.27***

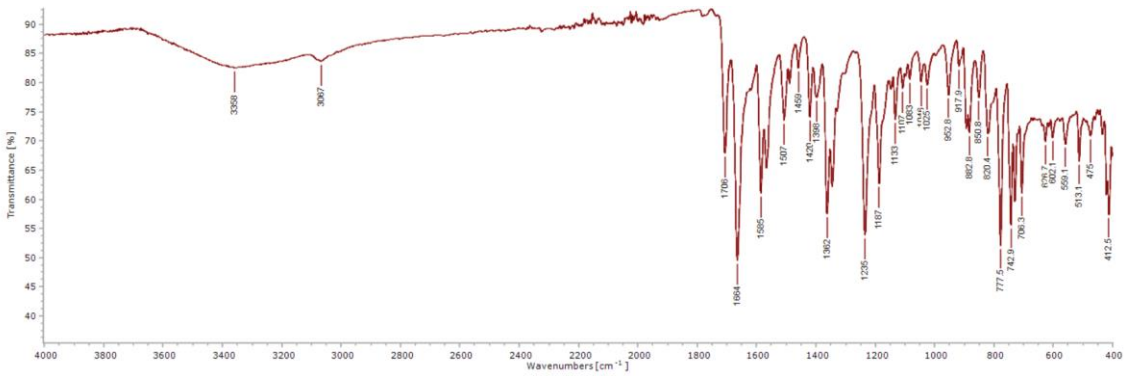

Figure A73: *IR spectrum of* ***2.27***

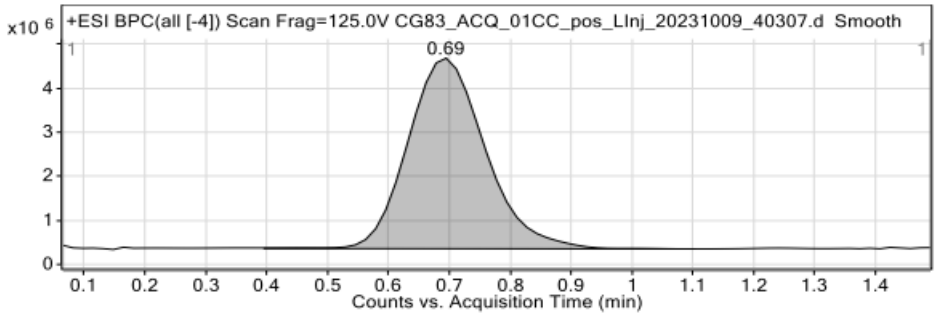

Figure 1: Base peak chromatogram

User Chromatogram Peak List

RT (min)	Area	Area %	Area Sum (%)	Base Peak (m/z)	Width (min)
0.69	38306474	100.00	100.00	101.0057	0.170

Compound Table

Compound Label	RT (min)	Observed mass (m/z)	Neutral observed mass (Da)	Theoretical mass (Da)	Mass error (ppm)	Isotope match score (%)
Cpd 1: C24 H12 Br N3 O2	0.69	477.9983	453.0108	453.0113	-1.00	99.76

Mass errors of between -5.00 and 5.00 ppm with isotope match scores above 60% are considered confirmation of molecular formulae

Figure: Extracted ion chromatogram (EIC) of compound.

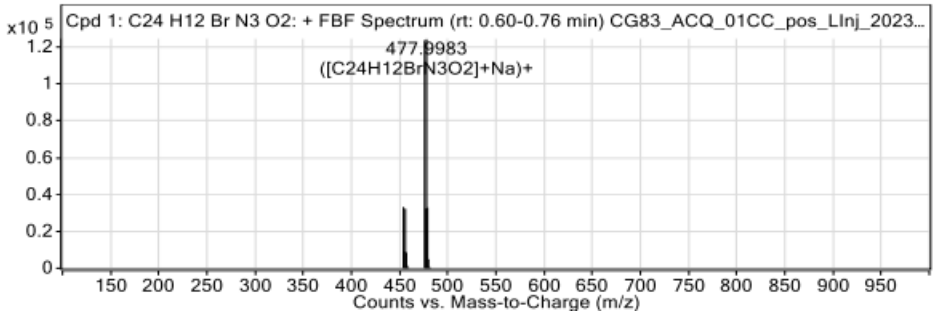

Figure A74: *HRMS of* ***2.27***

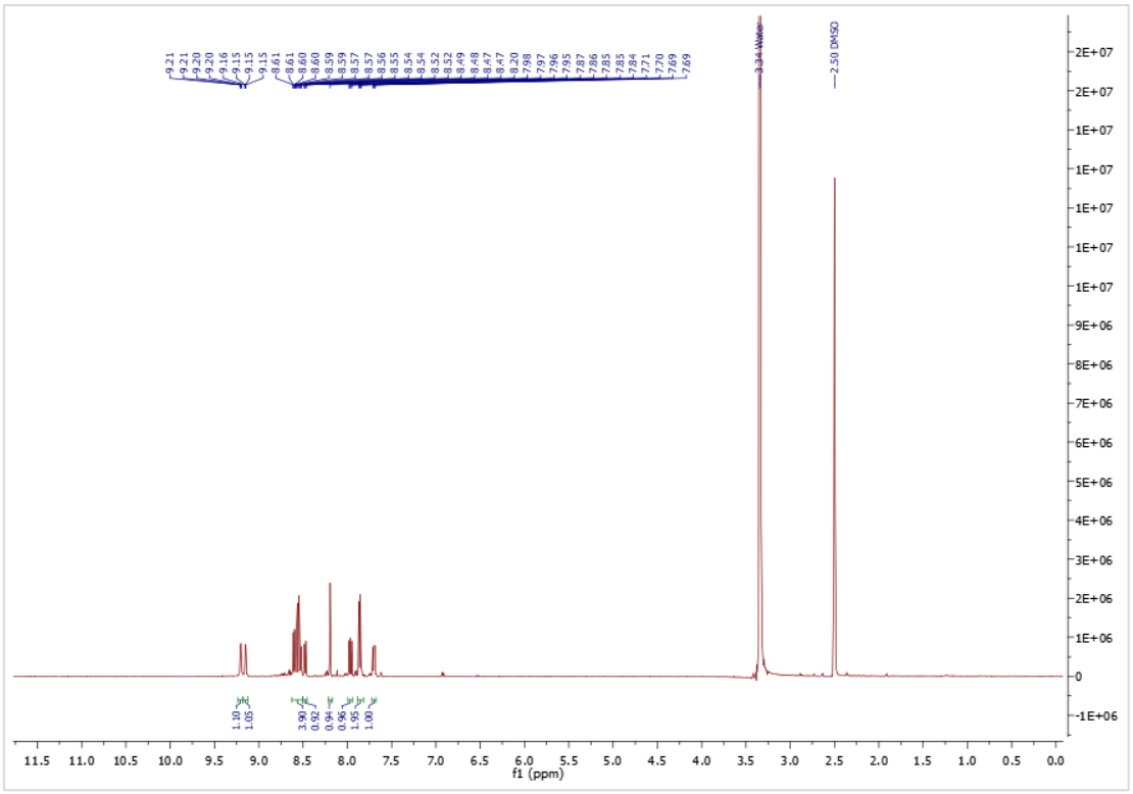

Figure A75: *[1]H NMR spectrum of* ***2.28***

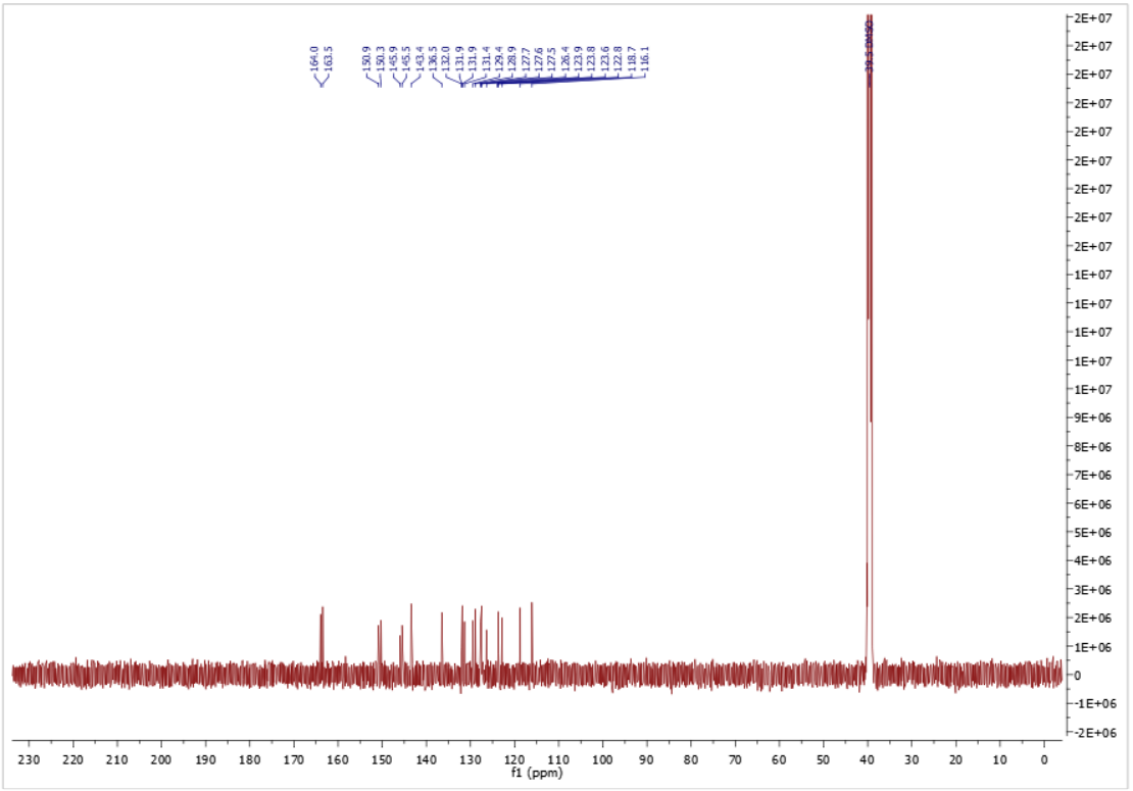

Figure A76: *[13]C NMR spectrum of* ***2.28***

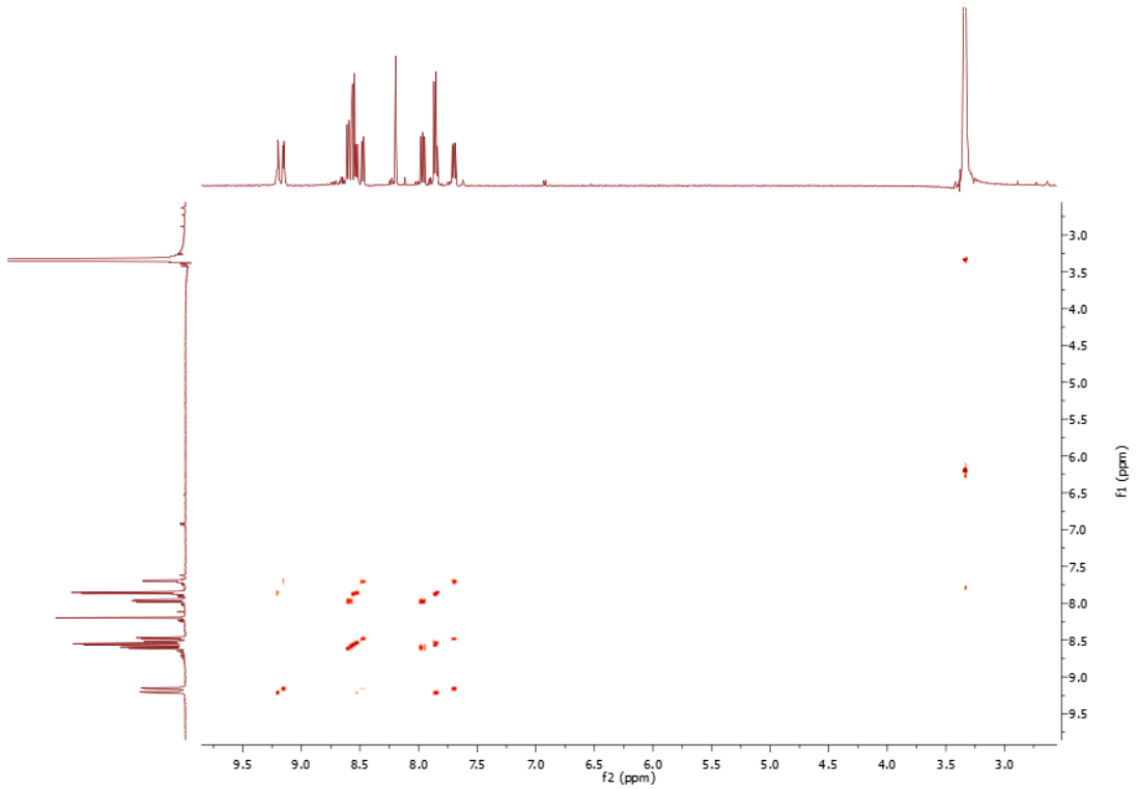

Figure A77: *^{1}H-^{1}H COSY of* ***2.28***

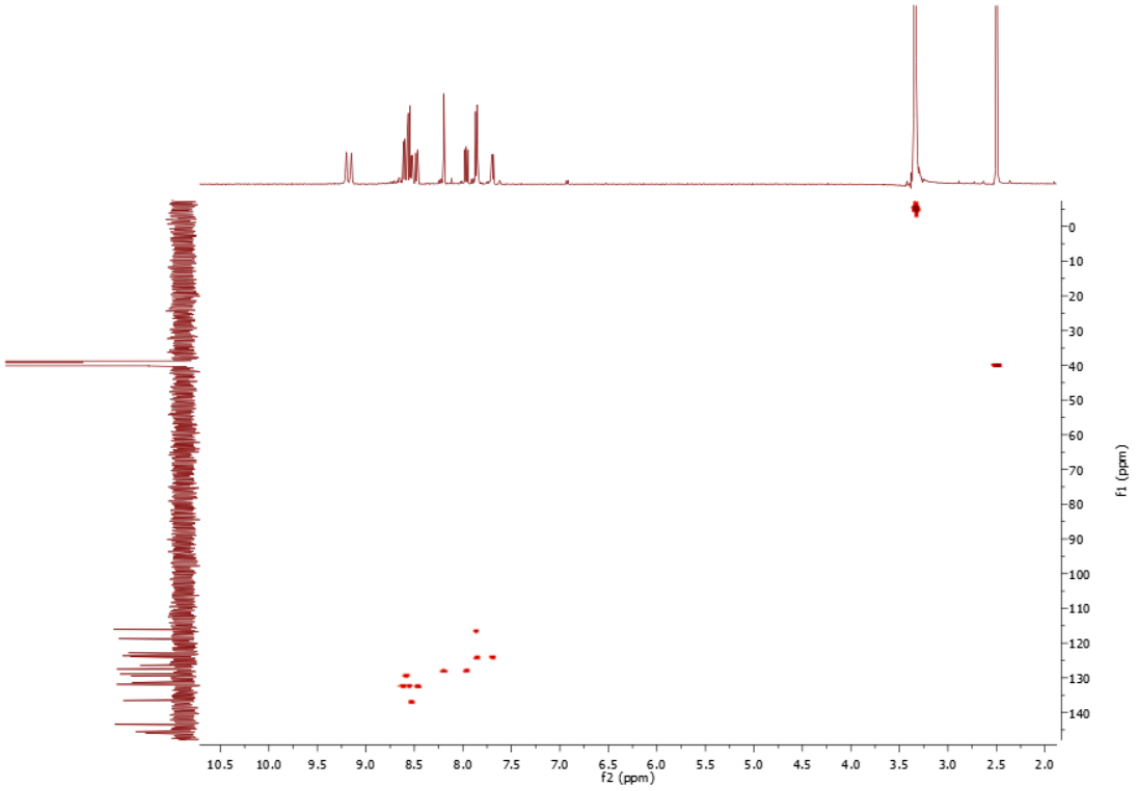

Figure A78: *HSQC of* ***2.28***

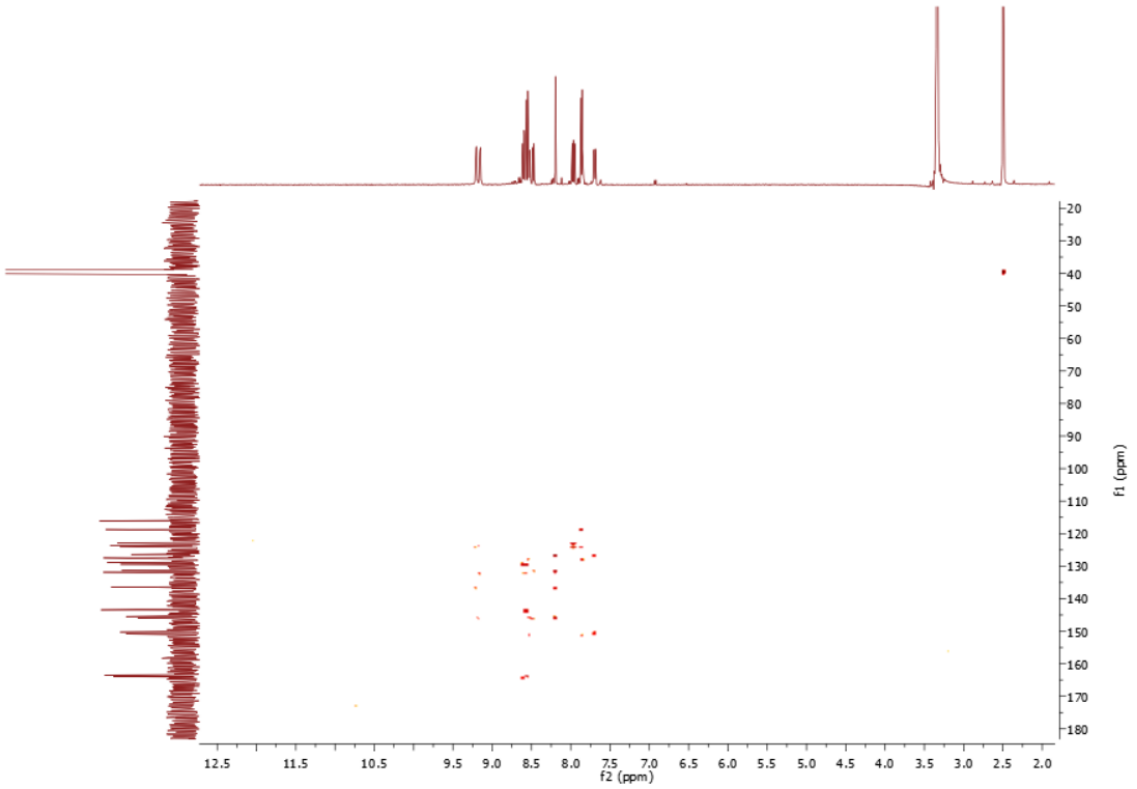

Figure A79: *HMBC of **2.28***

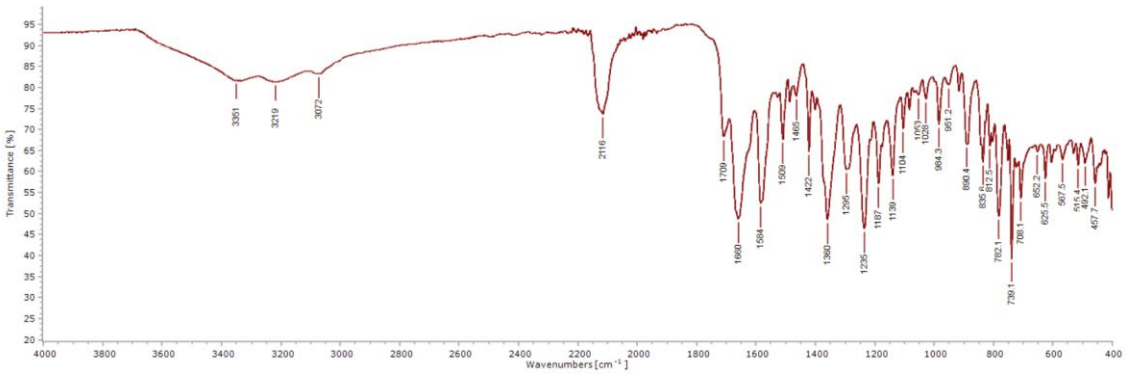

Figure A80: *IR of **2.28***

Compound specific information

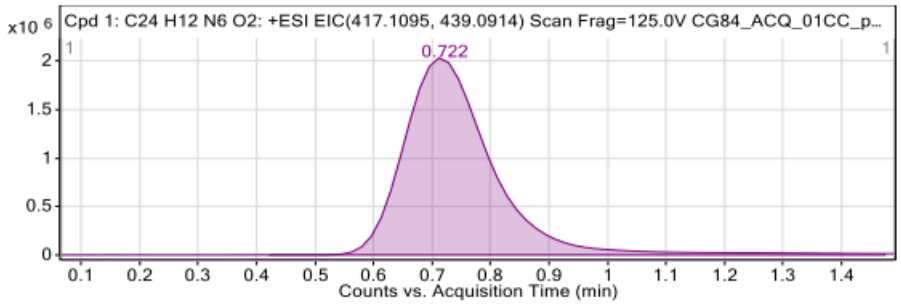

Figure: Extracted ion chromatogram (EIC) of compound.

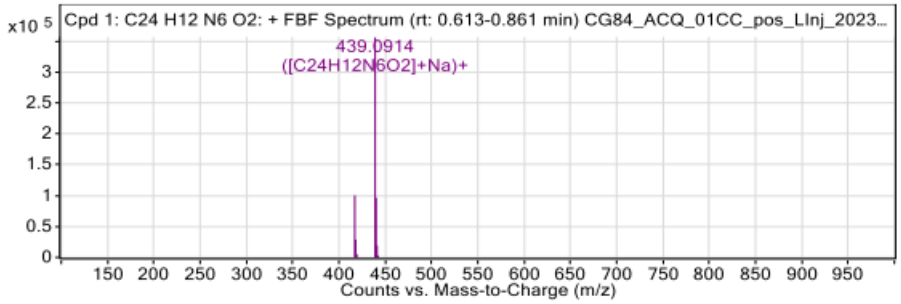

Figure: Full range view of Compound spectra and potential adducts.

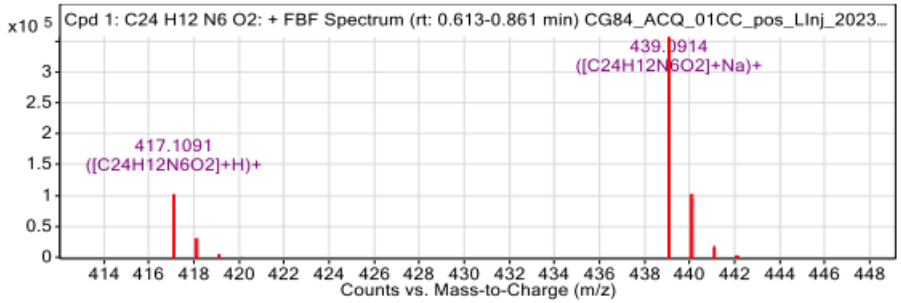

Compound Table

Compound Label	RT (min)	Observed mass (m/z)	Neutral observed mass (Da)	Theoretical mass (Da)	Mass error (ppm)	Isotope match score (%)
Cpd 1: C24 H12 N6 O2	0.72	417.1091	416.1020	416.1022	-0.33	99.15

Mass errors of between -5.00 and 5.00 ppm with isotope match scores above 60% are considered confirmation of molecular formulae

Figure A81: *HRMS of* ***2.28***

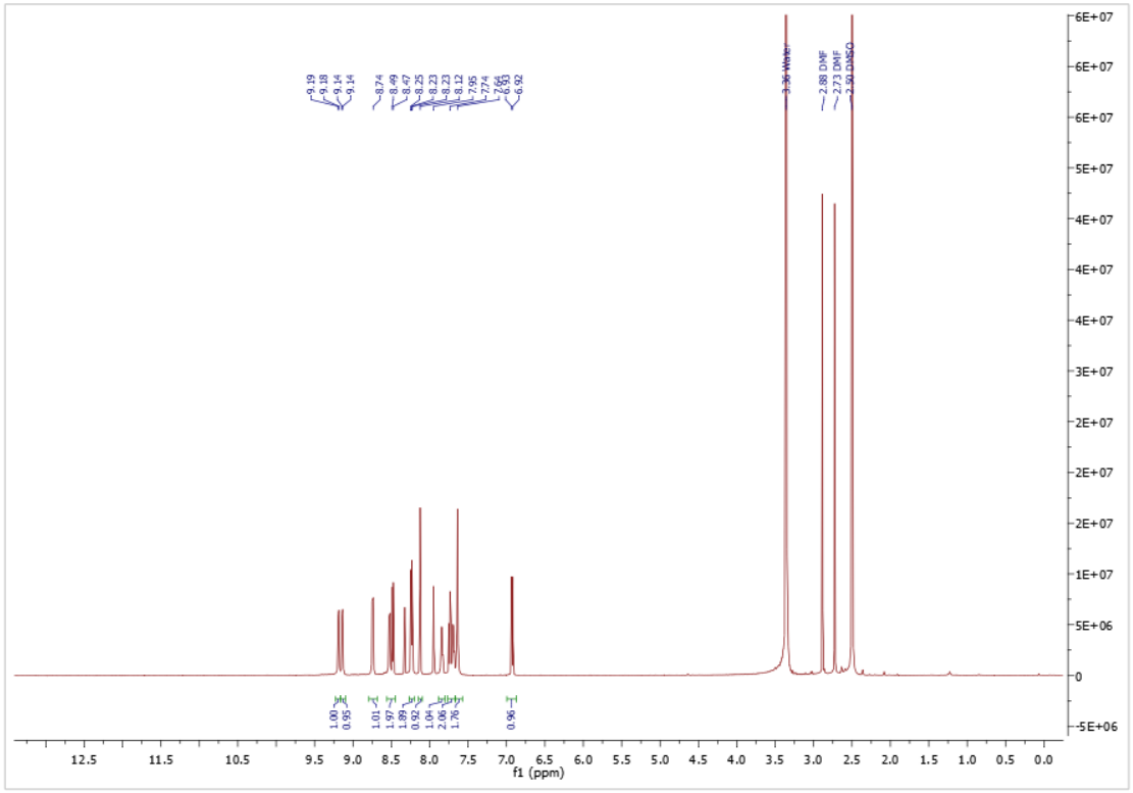

Figure A82: *[1]H NMR spectrum of* ***2.26***

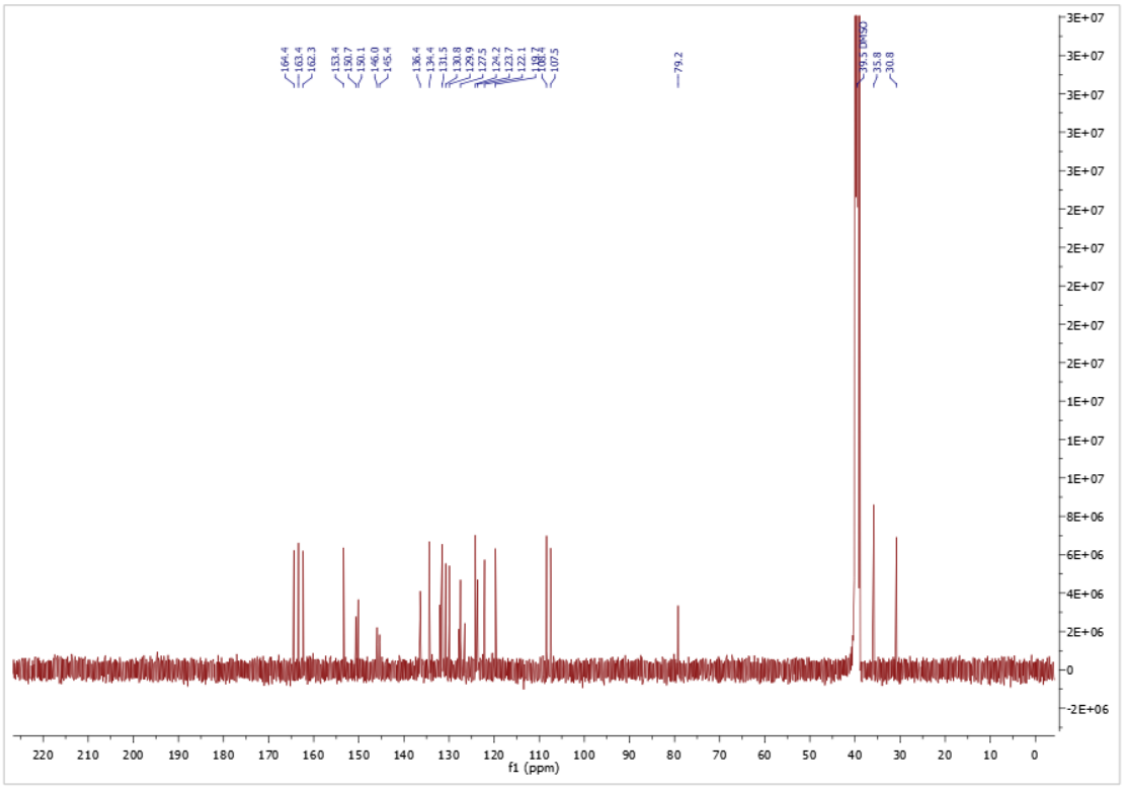

Figure A83: *[13]C NMR spectrum of* ***2.26***

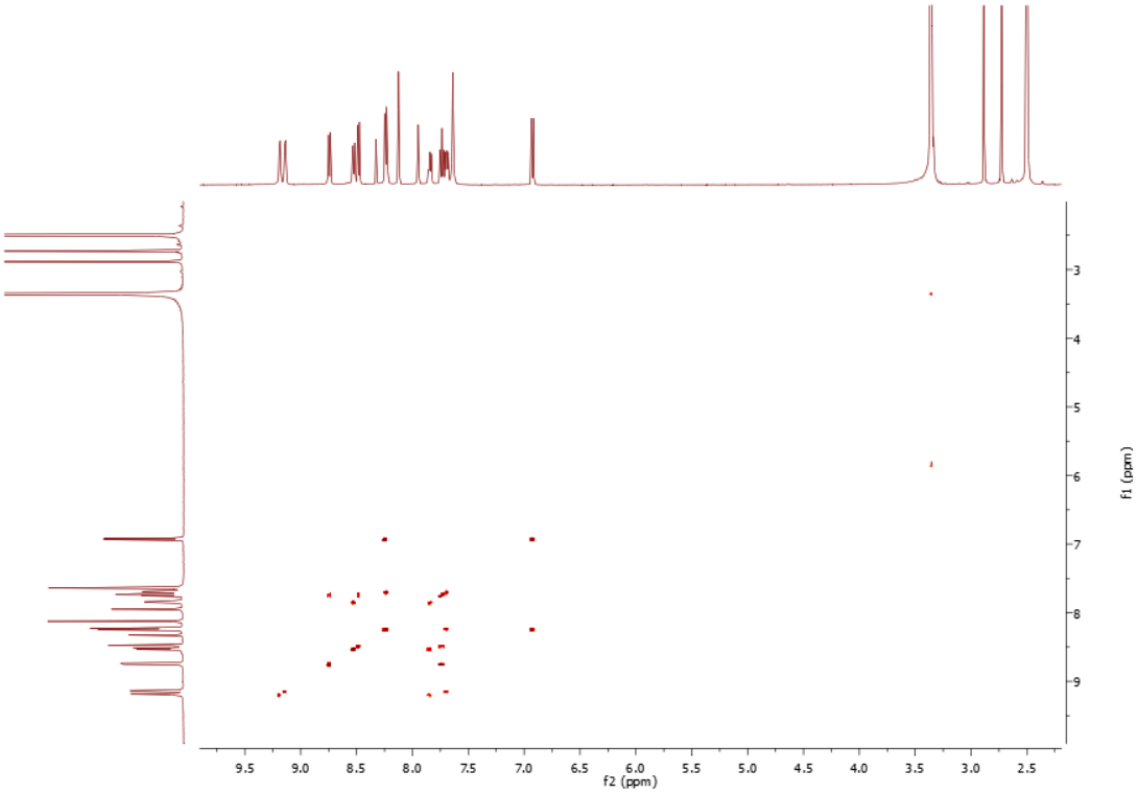

Figure A84: *^{1}H-^{1}H COSY of* ***2.26***

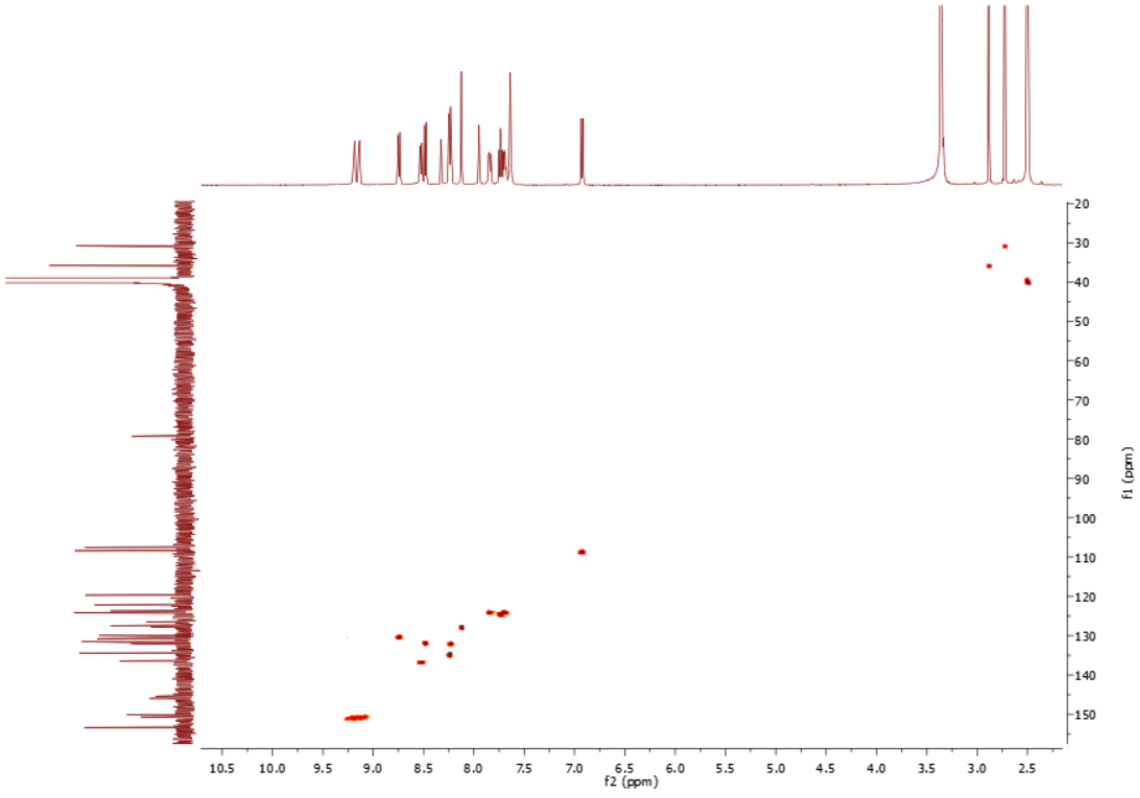

Figure A85: *HSQC of* ***2.26***

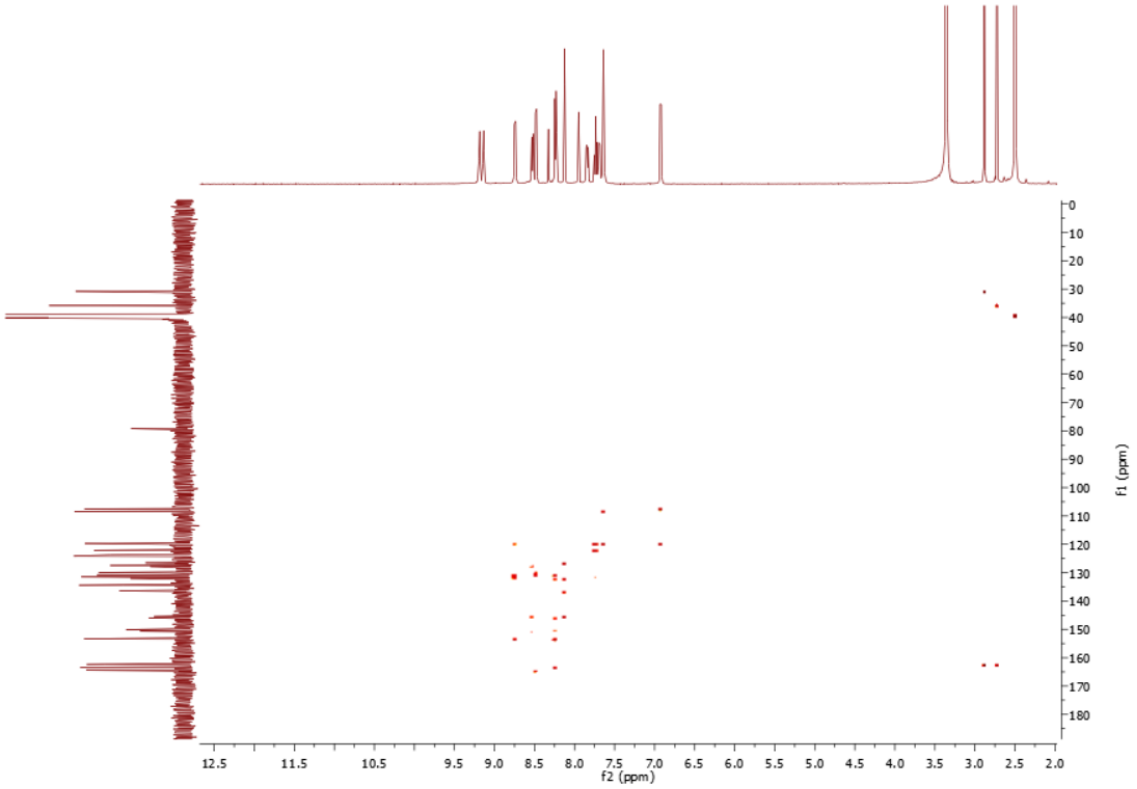

Figure A86: *HMBC of **2.26***

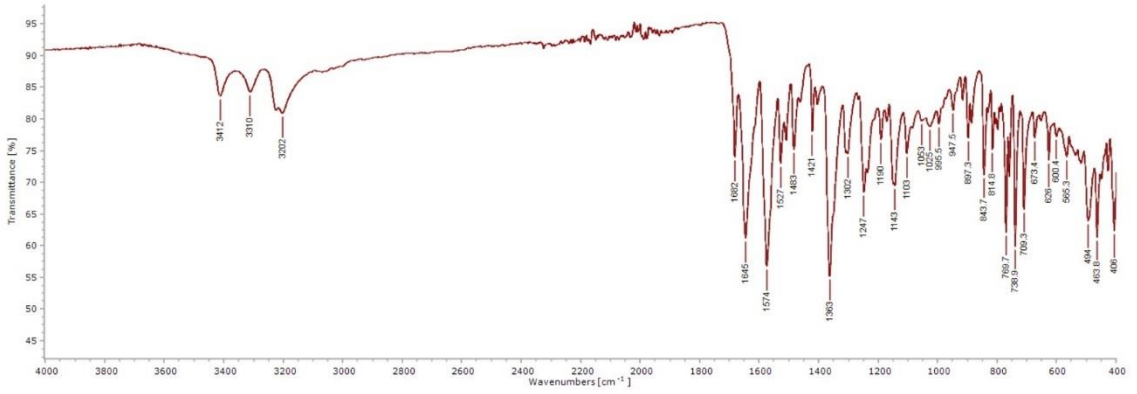

Figure A87: *IR of **2.26***

Compound specific information

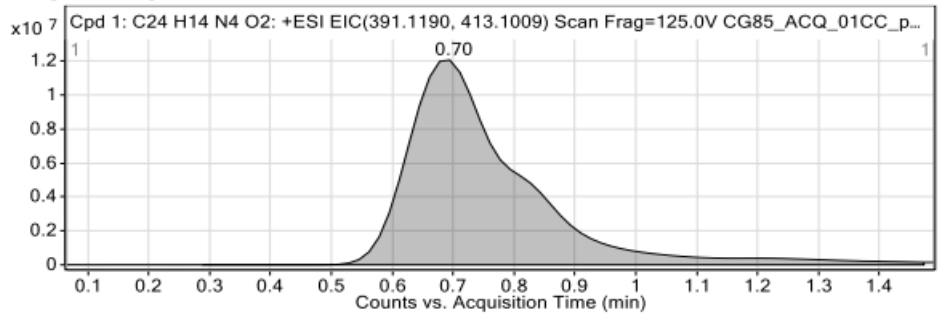

Figure: Extracted ion chromatogram (EIC) of compound.

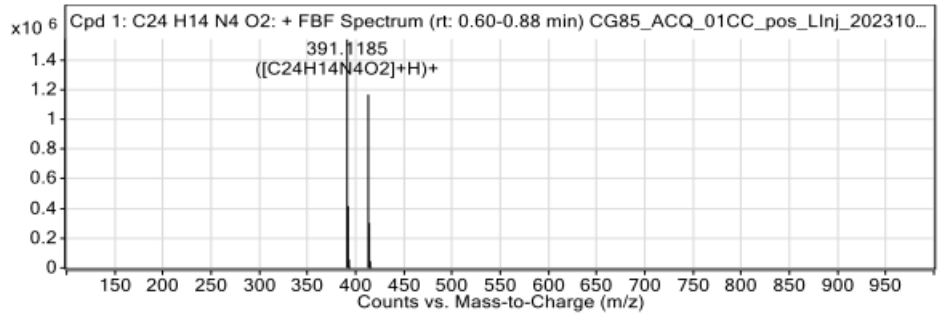

Compound Table

Compound Label	RT (min)	Observed mass (m/z)	Neutral observed mass (Da)	Theoretical mass (Da)	Mass error (ppm)	Isotope match score (%)
Cpd 1: C24 H14 N4 O2	0.70	391.1185	390.1113	390.1117	-0.86	99.69

Mass errors of between -5.00 and 5.00 ppm with isotope match scores above 60% are considered confirmation of molecular formulae

Figure A88: *HRMS of* ***2.26***

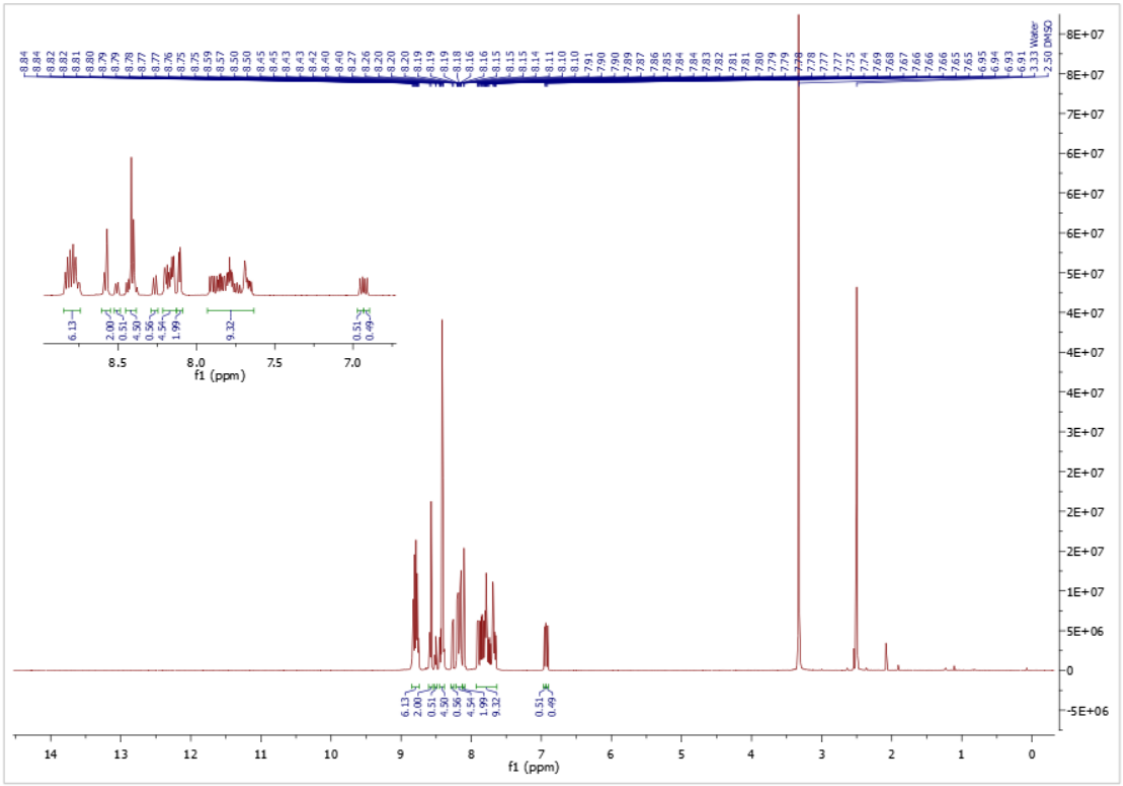

Figure A89: *^{1}H NMR spectrum of* ***2.29***

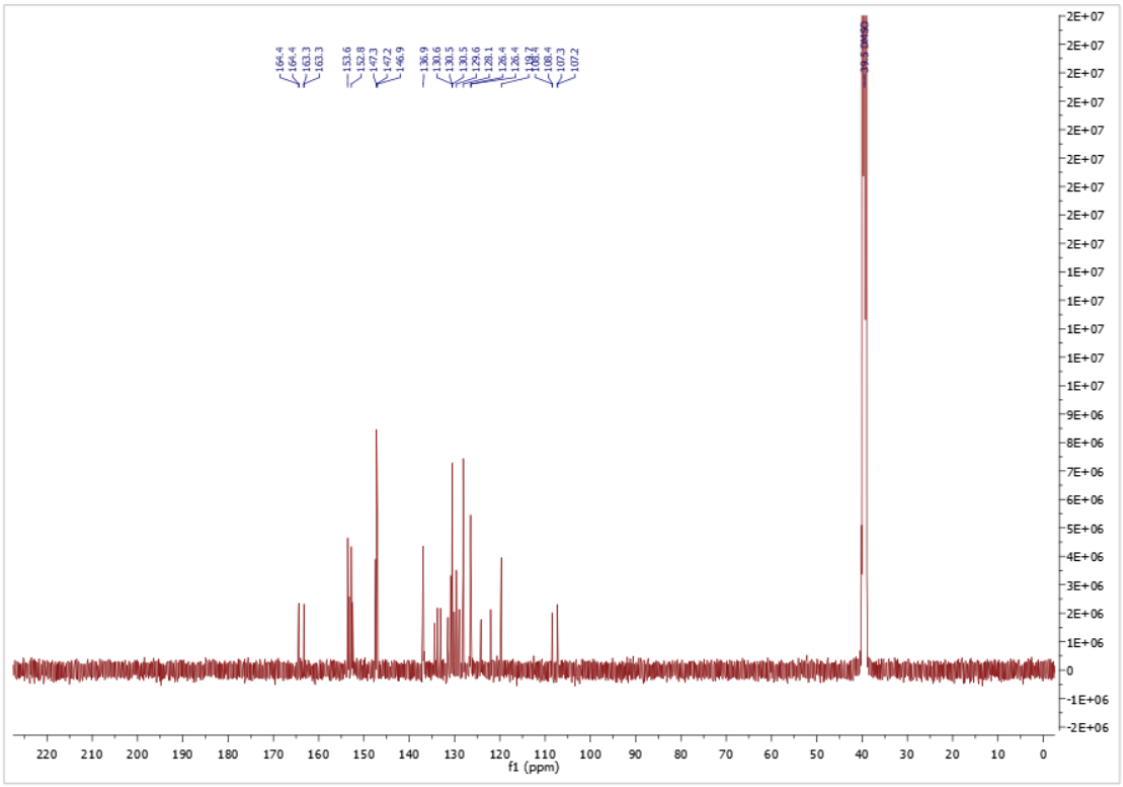

Figure A90: *^{13}C NMR spectrum of* ***2.29***

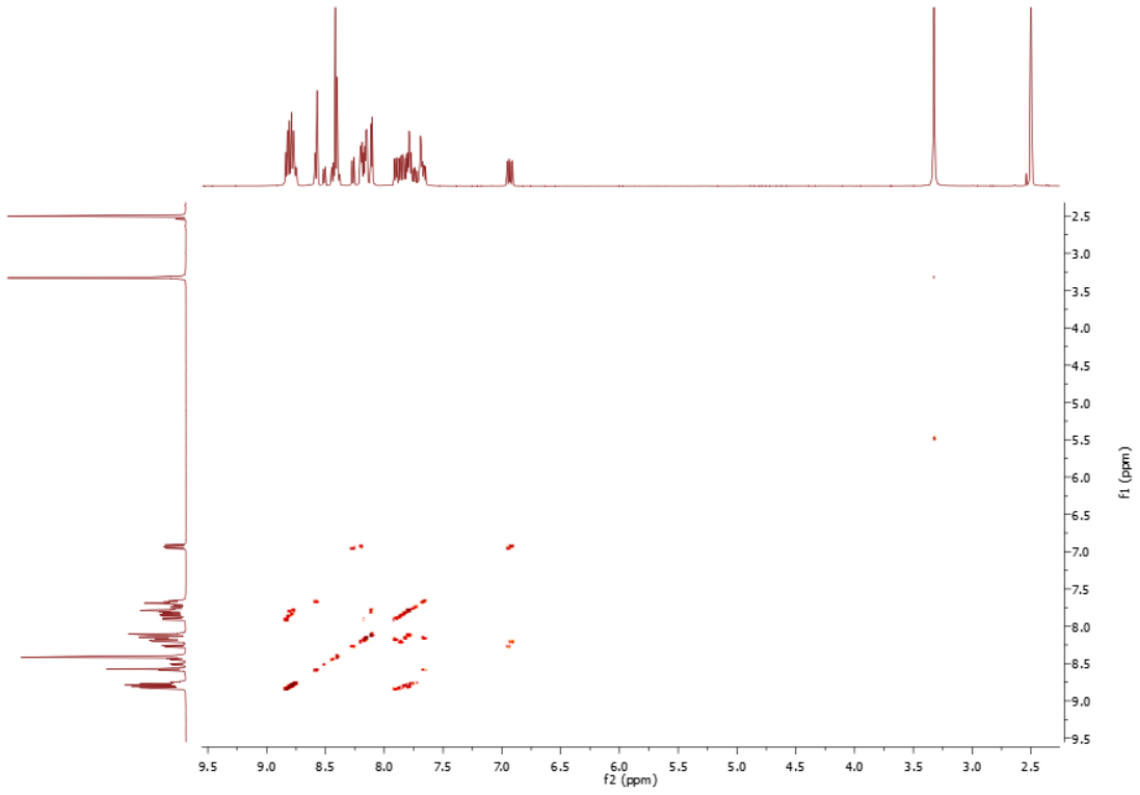

Figure A91: *^{1}H-^{1}H COSY of* ***2.29***

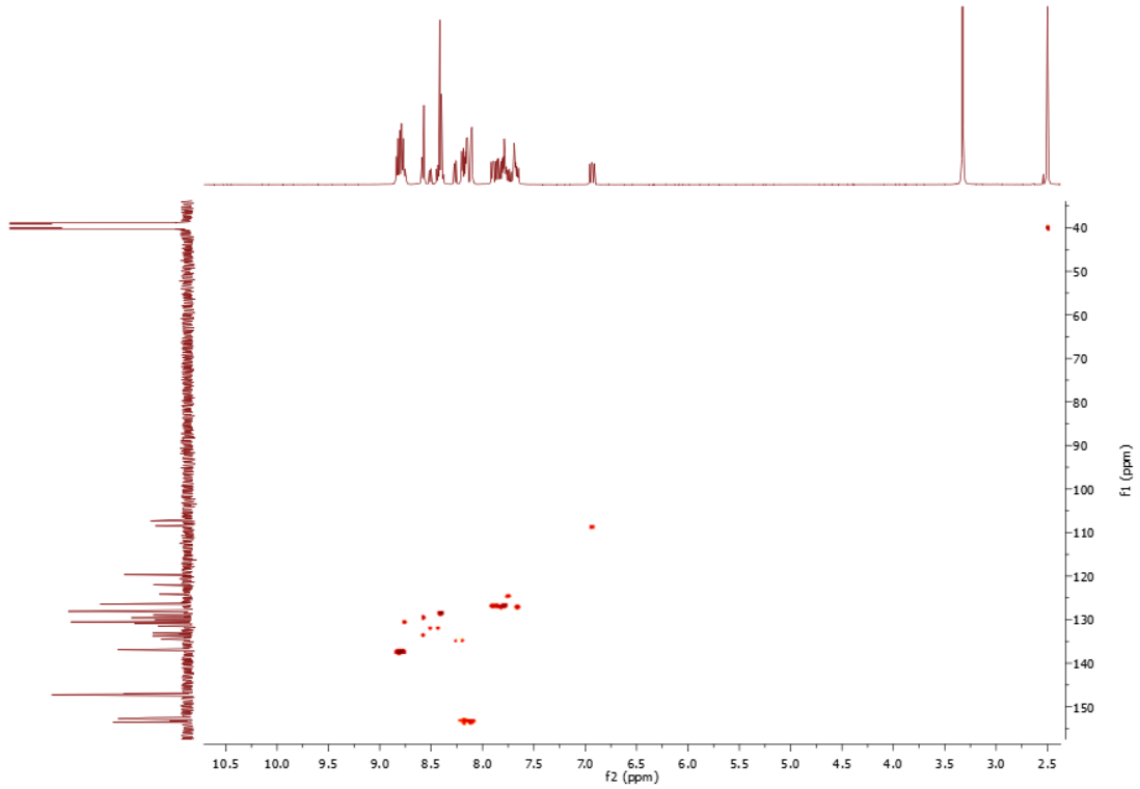

Figure A92: *HSQC of* ***2.29***

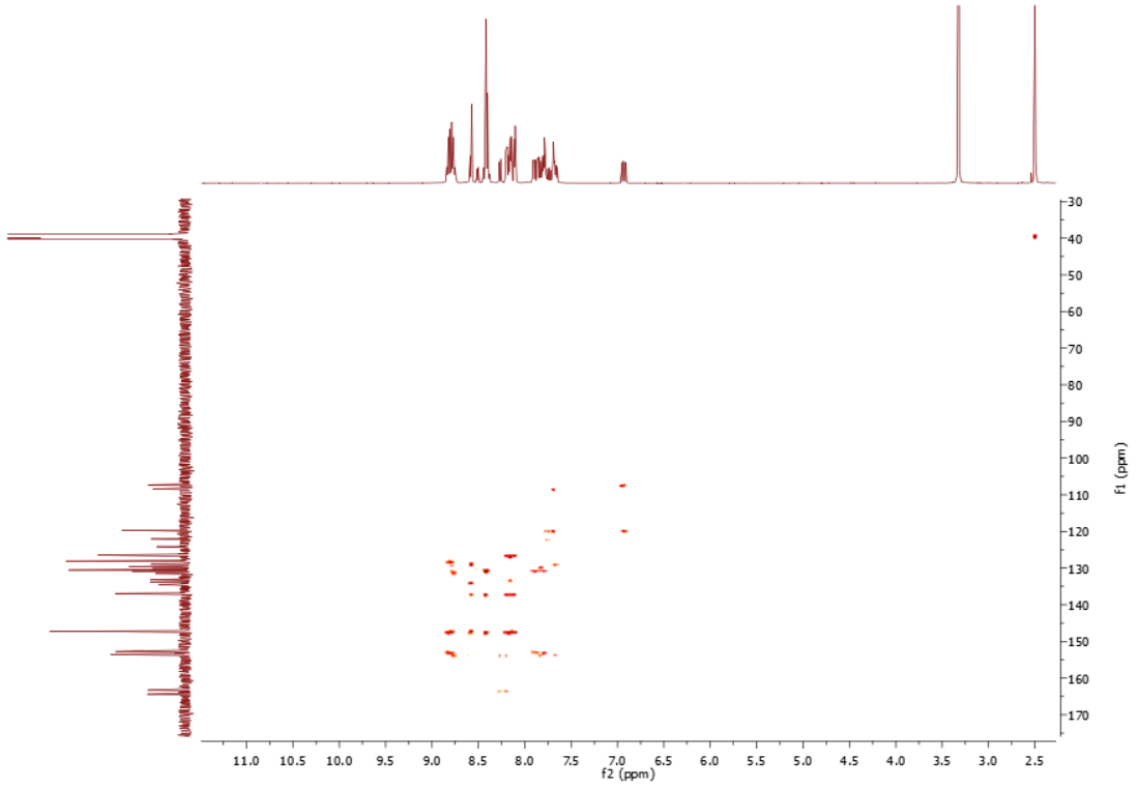

Figure A93: *HMBC of* ***2.29***

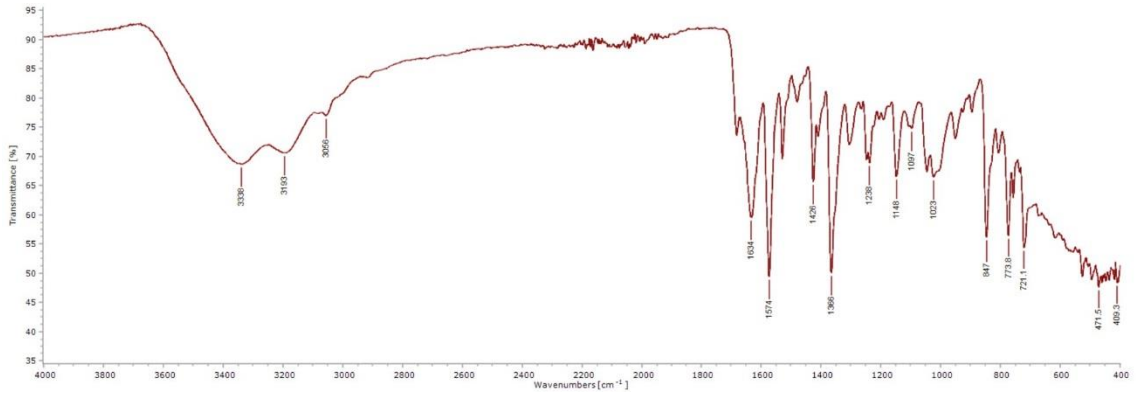

Figure A94: *IR of* ***2.29***

Compound specific information

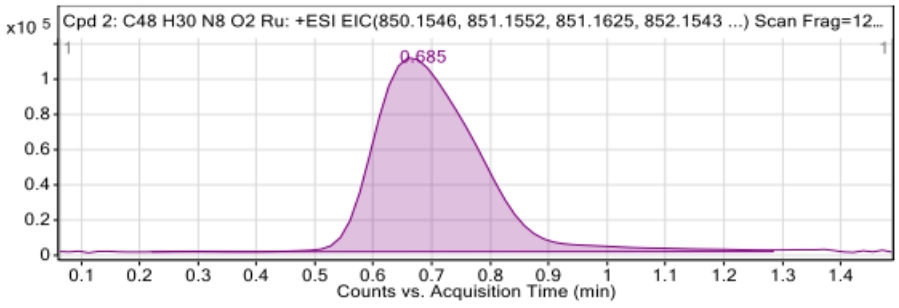

Figure: Extracted ion chromatogram (EIC) of compound.

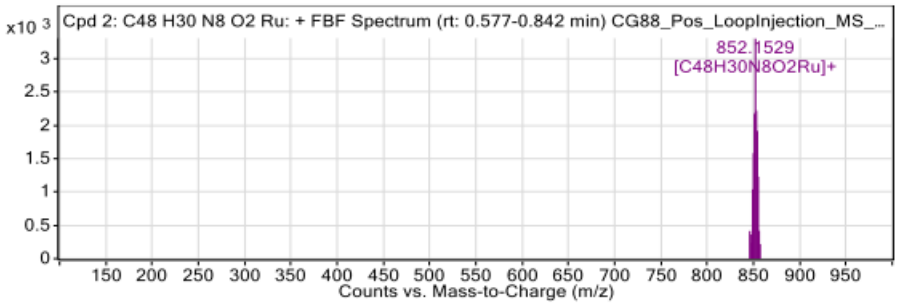

Compound Table

Compound Label	RT (min)	Observed mass (m/z)	Neutral observed mass (Da)	Theoretical mass (Da)	Mass error (ppm)	Isotope match score (%)
Cpd 1: C48 H30 F12 N8 O2 P2 Ru	0.69	1165.0720	1136.0855	1136.0851	0.28	55.07
Cpd 2: C48 H30 N8 O2 Ru	0.69	852.1529	846.1562	846.1568	-0.73	80.76
Cpd 3: C48 H30 F6 N8 O2 P Ru	0.68	997.1191	991.1136	991.1210	-7.43	32.30

Mass errors of between -5.00 and 5.00 ppm with isotope match scores above 60% are considered confirmation of molecular formulae

Figure A95: *HRMS of* ***2.29***

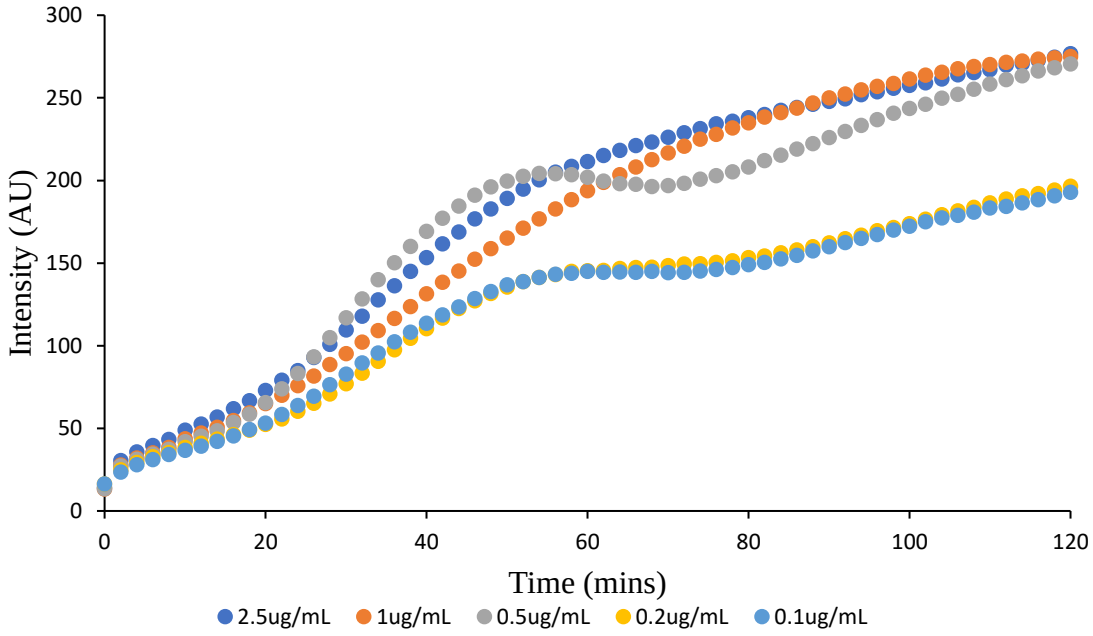

Figure A96: *Compound 2.13 (10 µM) and NADH (500 µM) in the presence of varying concentrations of NTR over 120 minutes.*

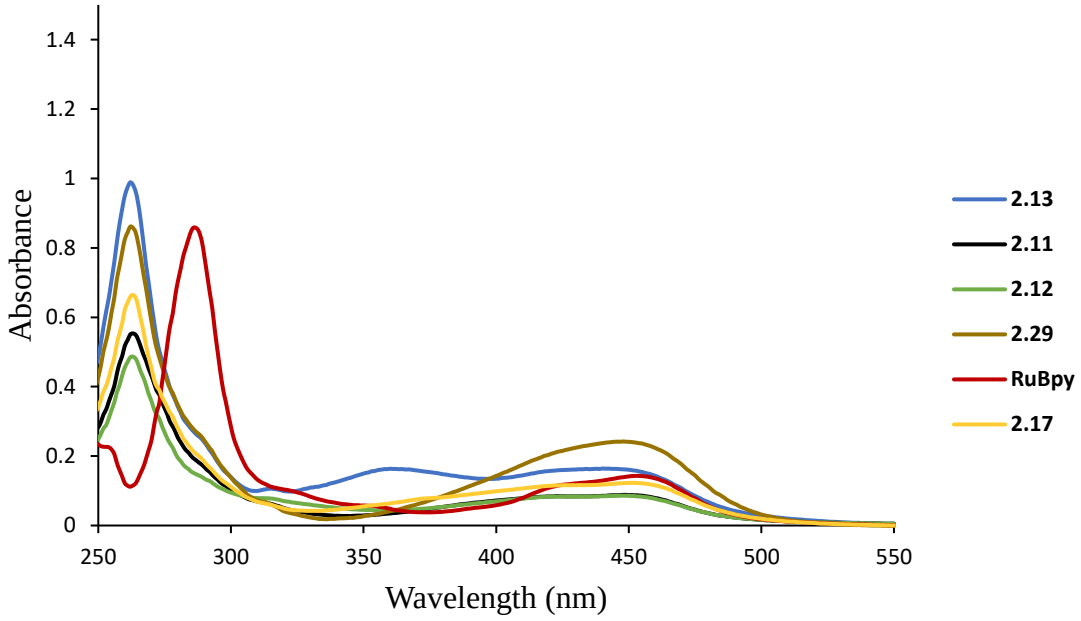

Figure A97: *UV/Vis spectra used for determination of quantum yield. Compound (10 µM).*

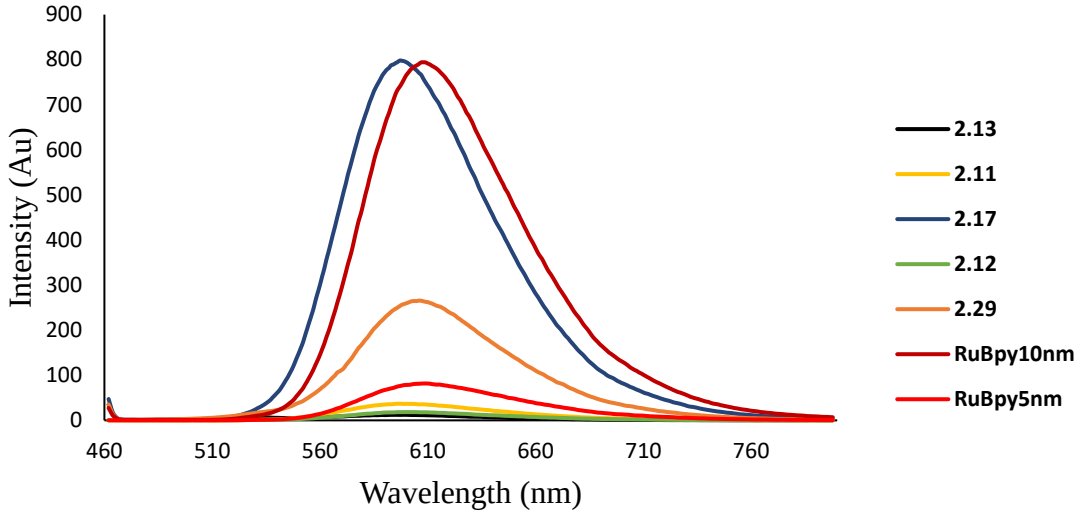

Figure A98: *Emission spectra used for determination of quantum yield. Compound (10 µM).*

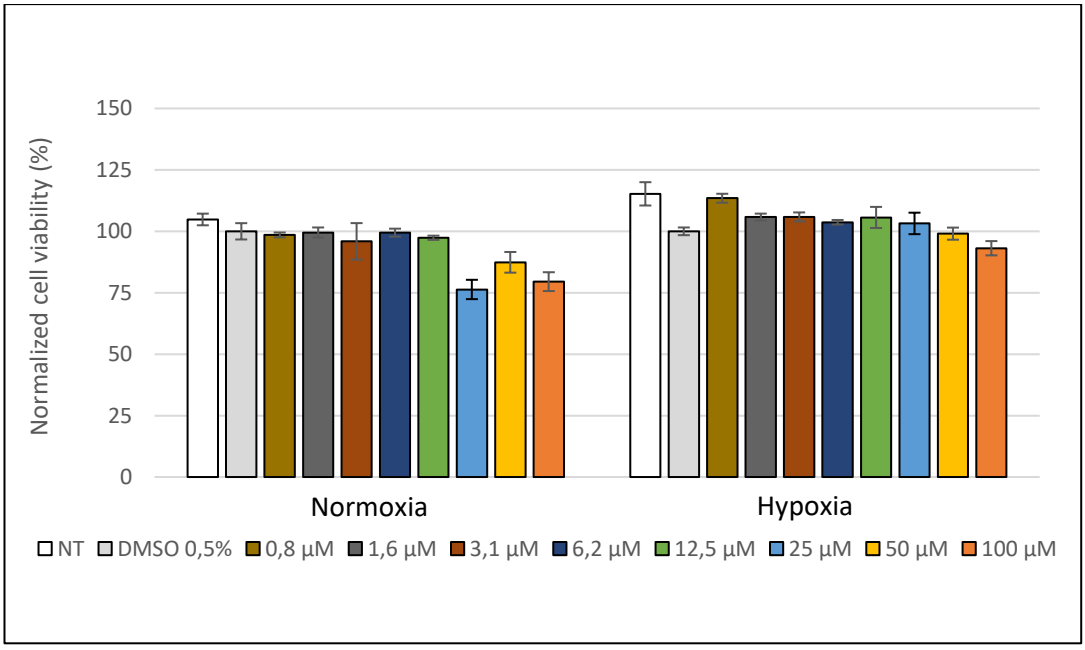

Figure A99: *Cell viability of dermal fibroblasts incubated with varying concentrations of compound **2.11** under normoxia and hypoxia.*

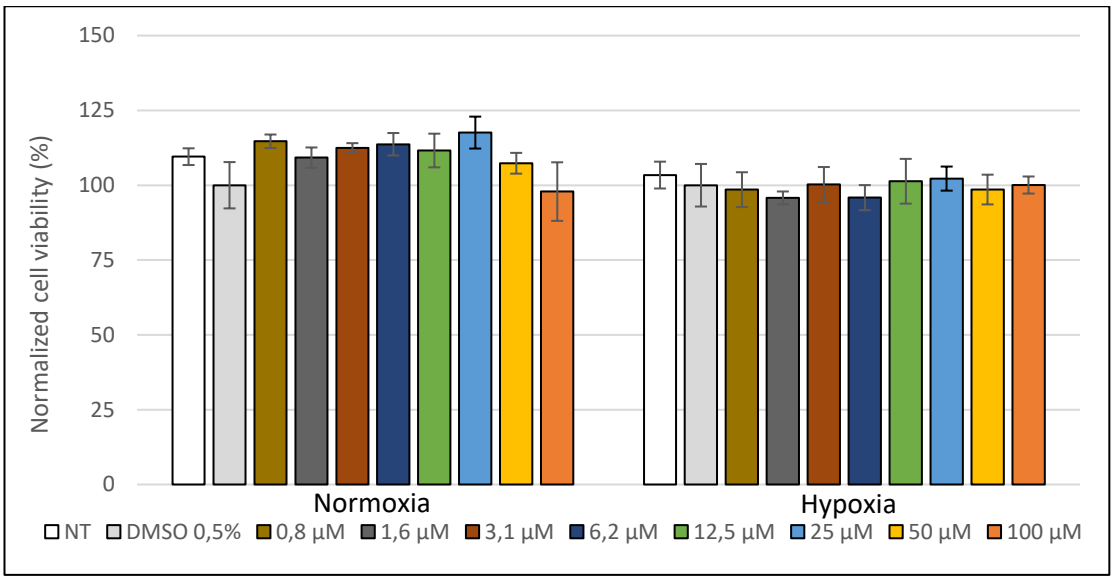

Figure A100: *Cell viability of dermal fibroblasts incubated with varying concentrations of compound **2.12** under normoxia and hypoxia.*

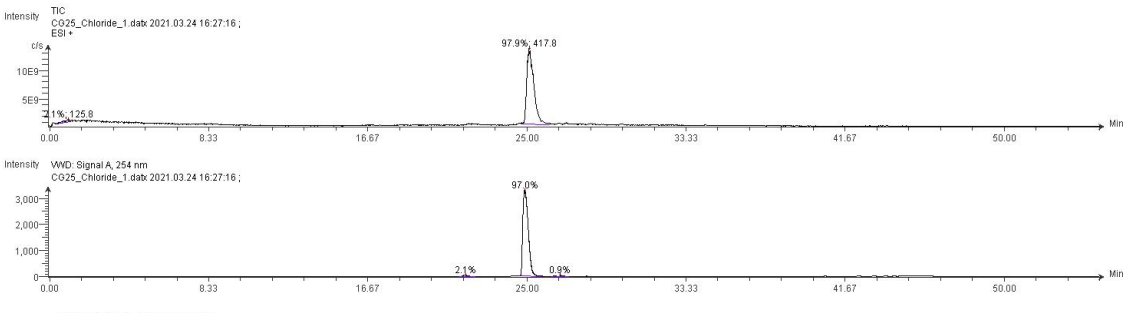

Figure A101: *LCMS of **2.11***

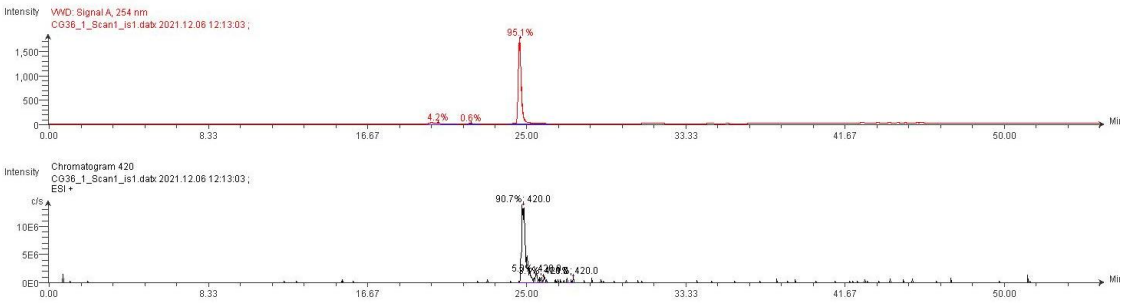

Figure A102: *LCMS of **2.12***

Chapter 3 Appendix Data

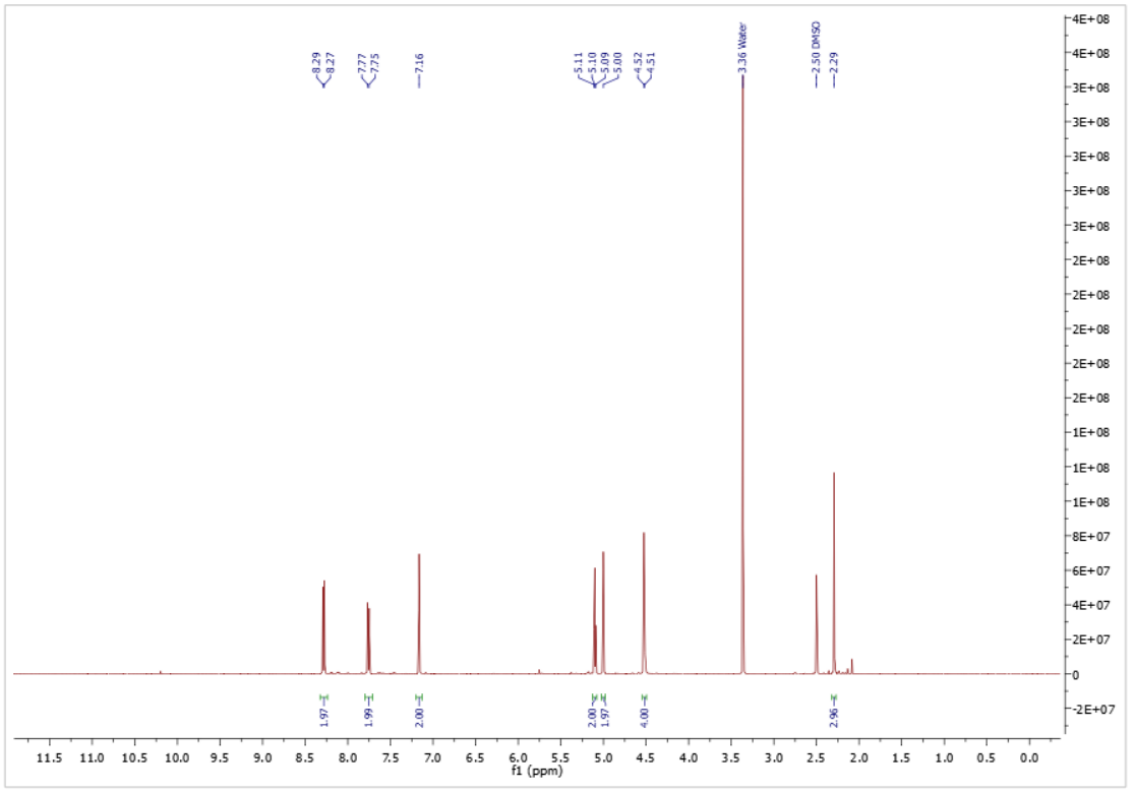

Figure B1: *[1]H NMR spectrum of* ***3.10***

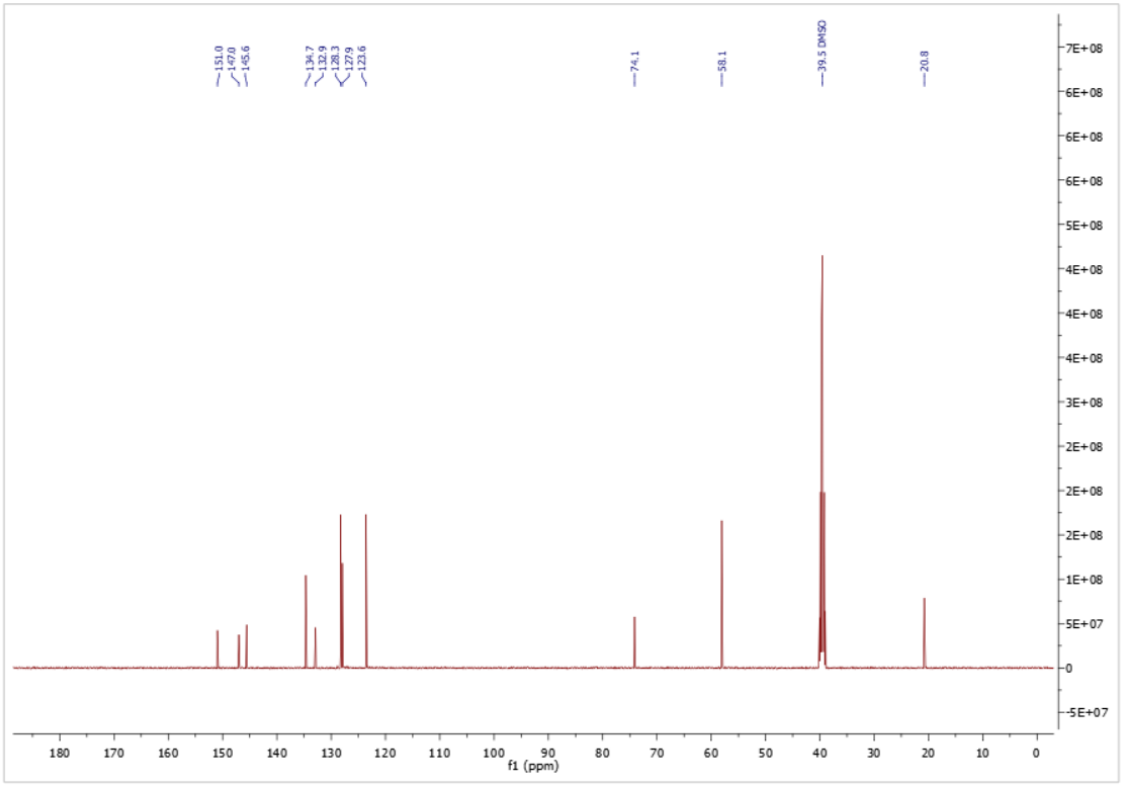

Figure B2: *[13]C NMR spectrum of* ***3.10***

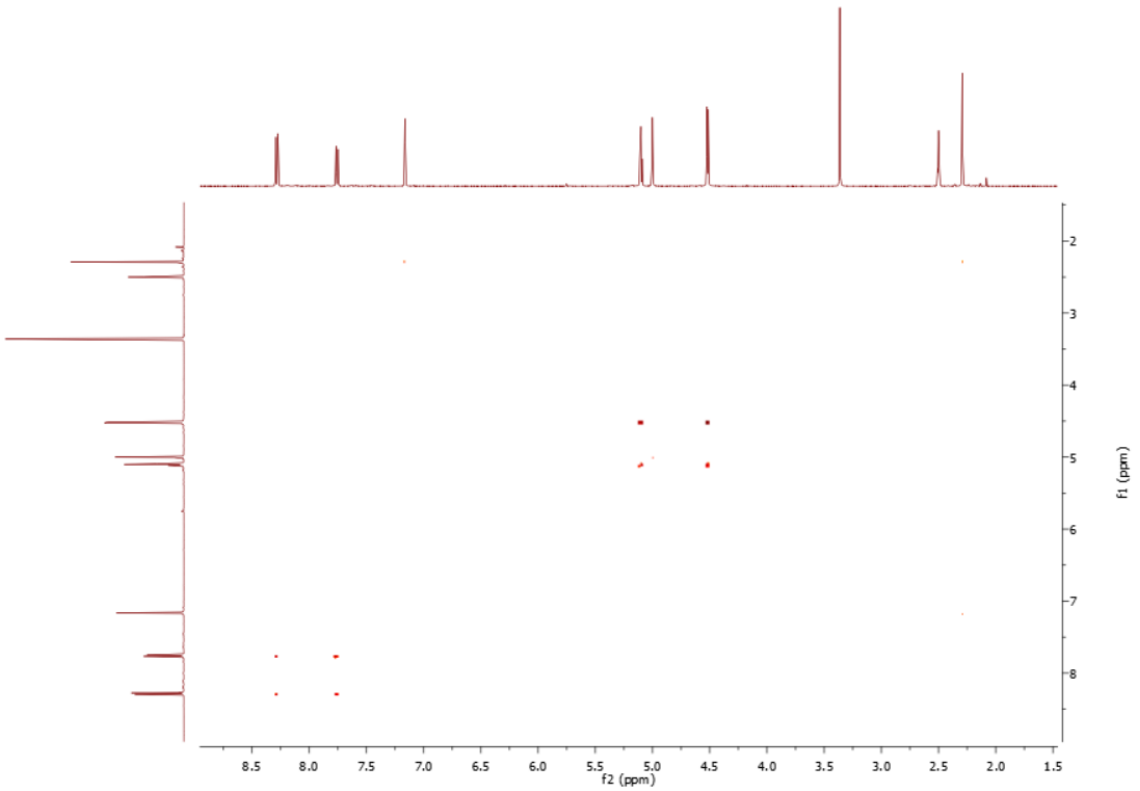

Figure B3: *^{1}H-^{1}H COSY of **3.10***

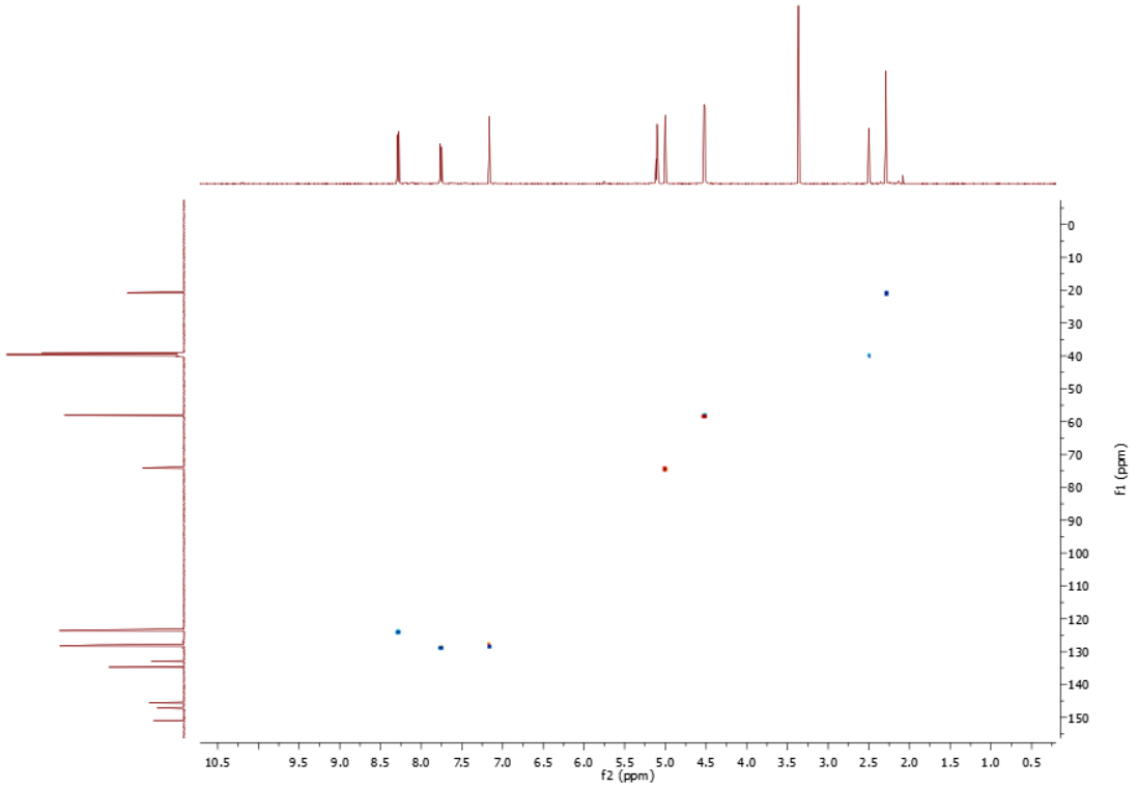

Figure B4: *HSQC of **3.10***

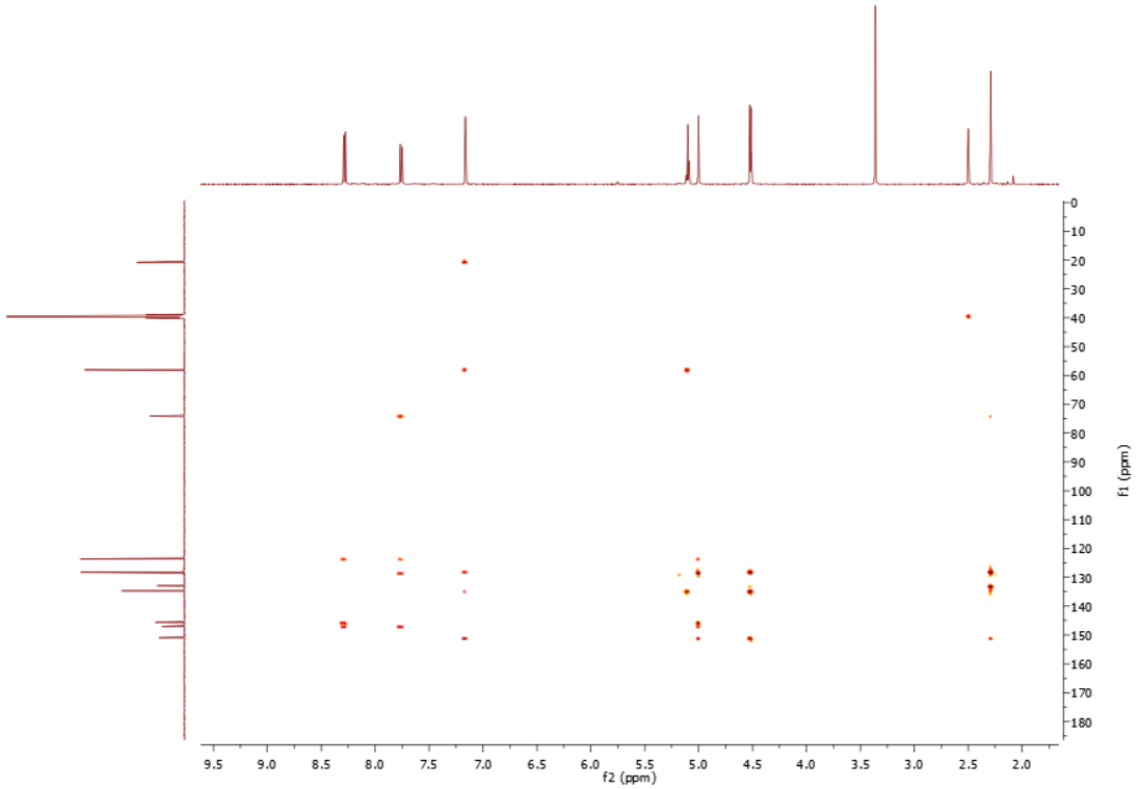

Figure B5: *HMBC of **3.10***

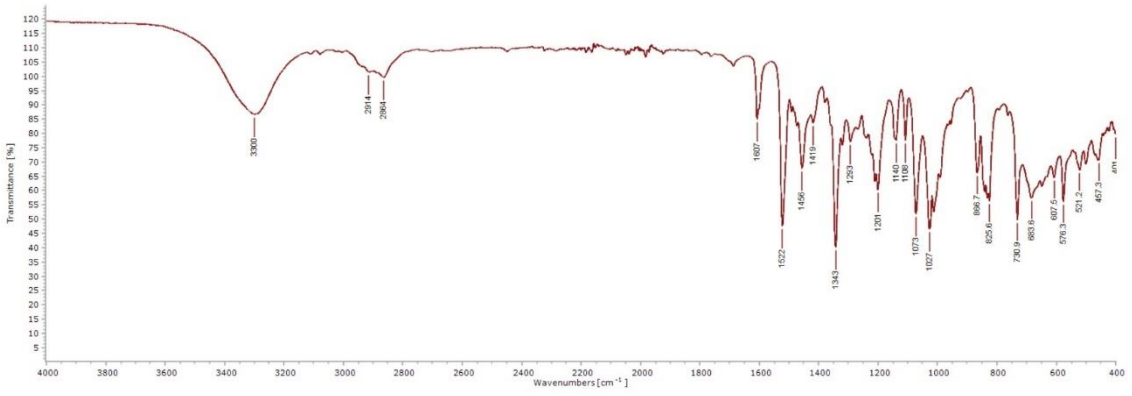

Figure B6: *IR of **3.10***

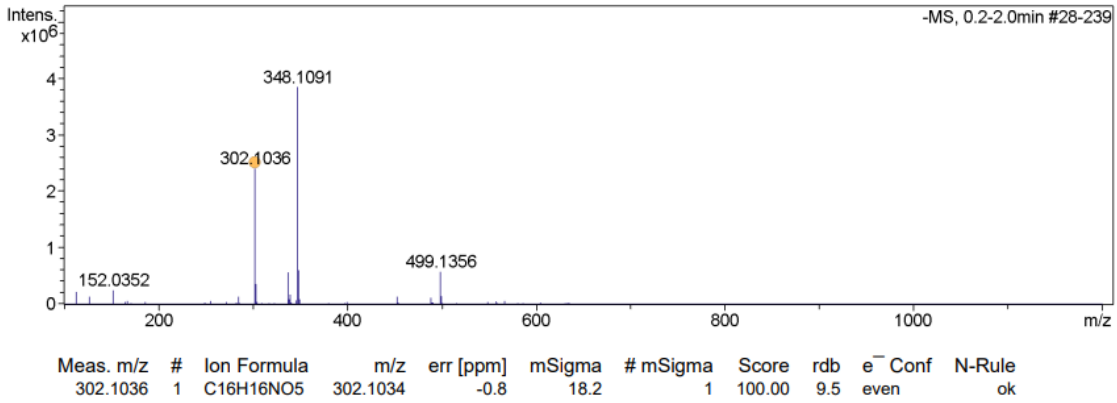

Meas. m/z	#	Ion Formula	m/z	err [ppm]	mSigma	# mSigma	Score	rdb	e¯ Conf	N-Rule
302.1036	1	C16H16NO5	302.1034	-0.8	18.2	1	100.00	9.5	even	ok

Figure B7: *HRMS of* ***3.10***

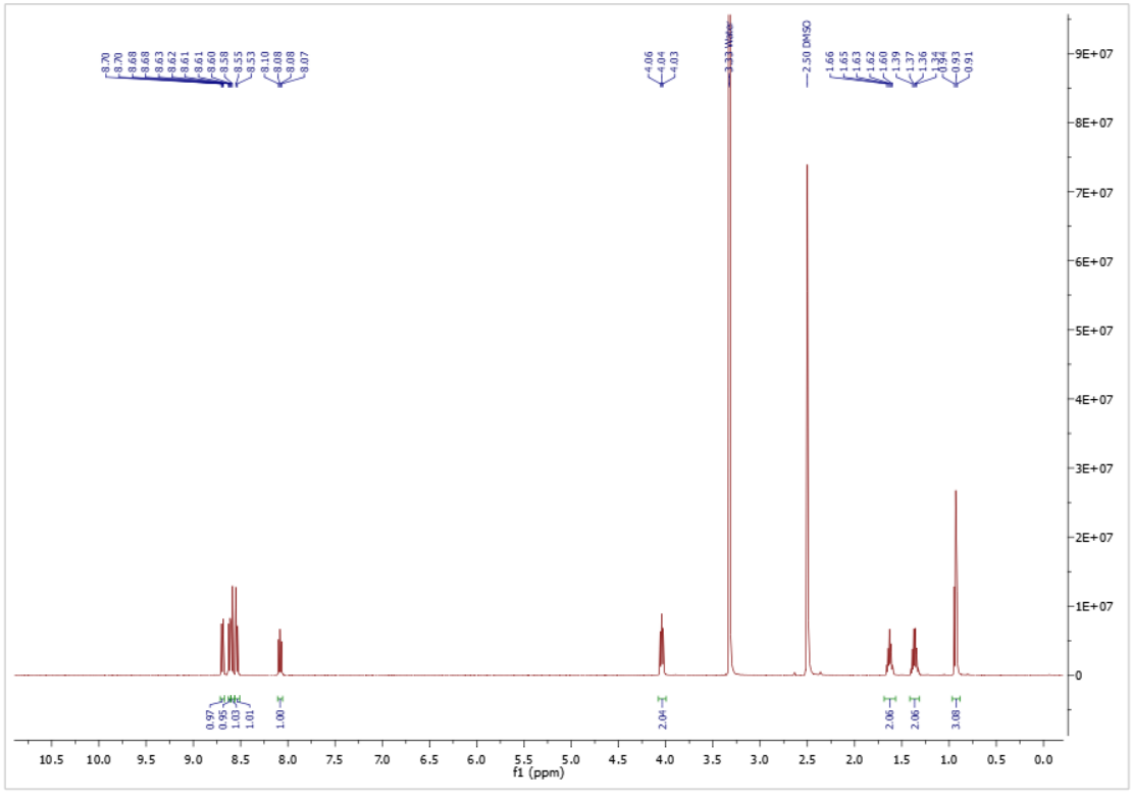

Figure B8: *^{1}H NMR spectrum of* ***3.13***

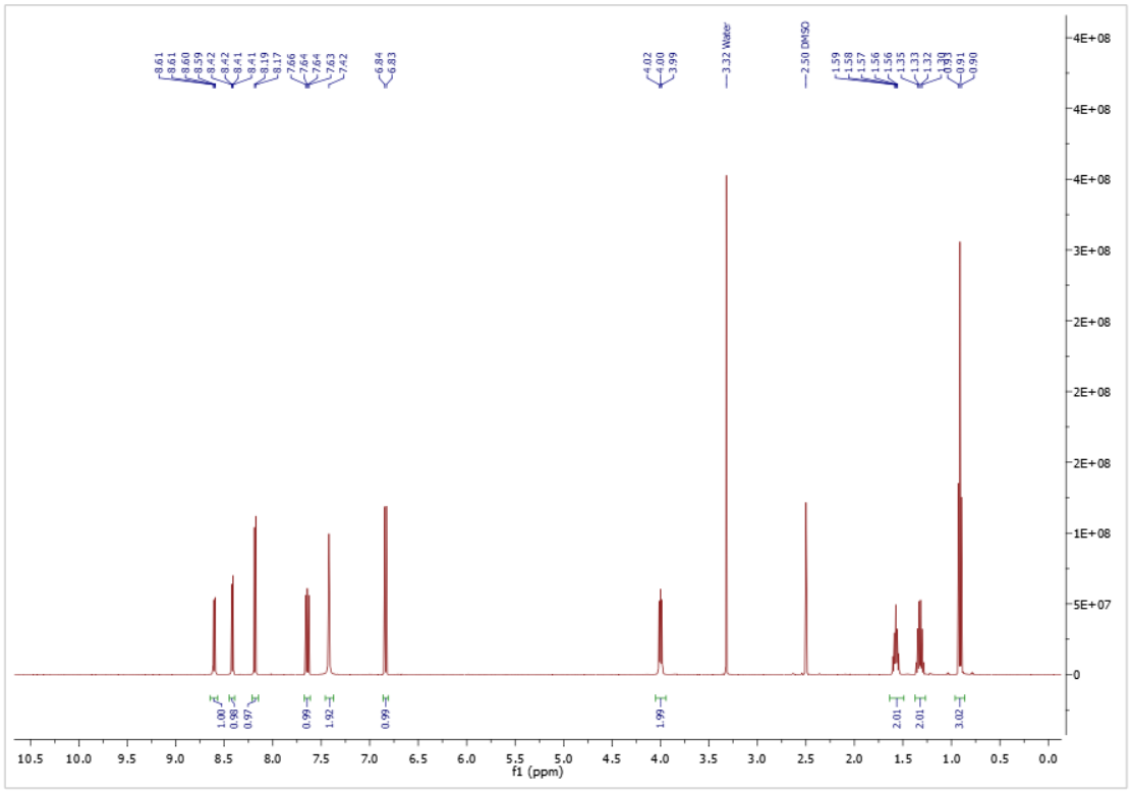

Figure B9: *[1]H NMR spectrum of* ***3.11***

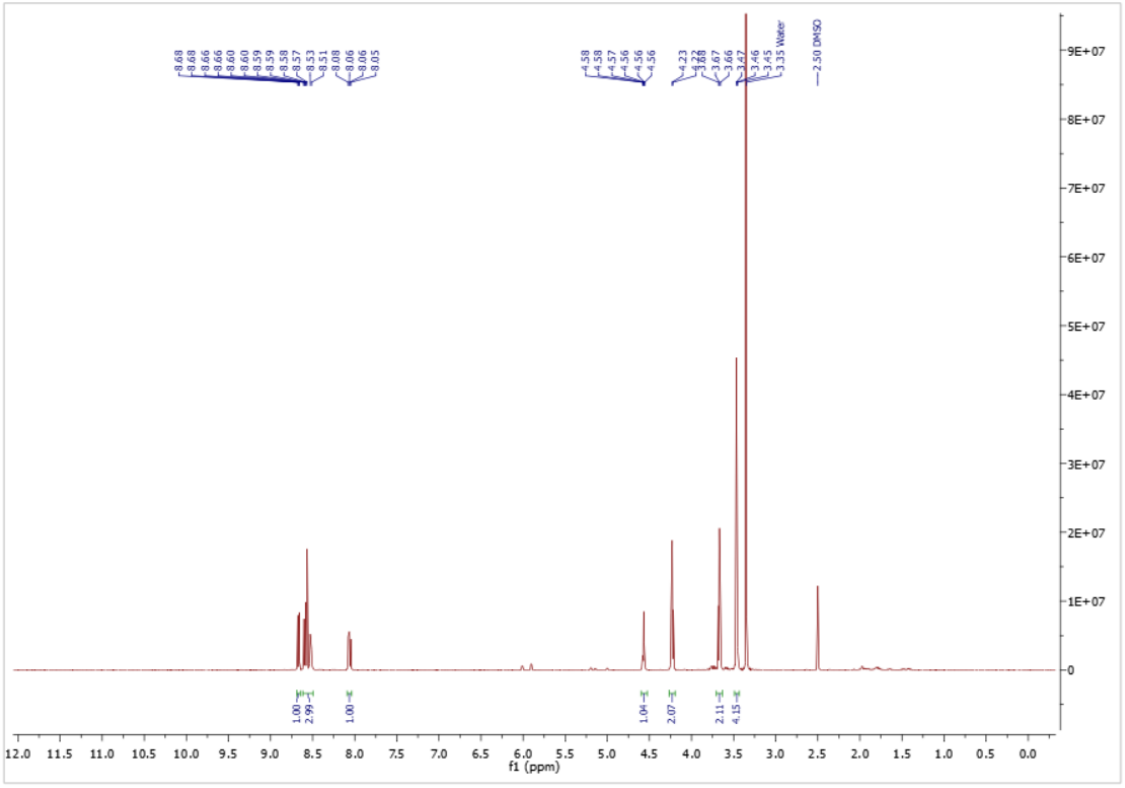

Figure B10: *[1]H NMR spectrum of* ***3.14***

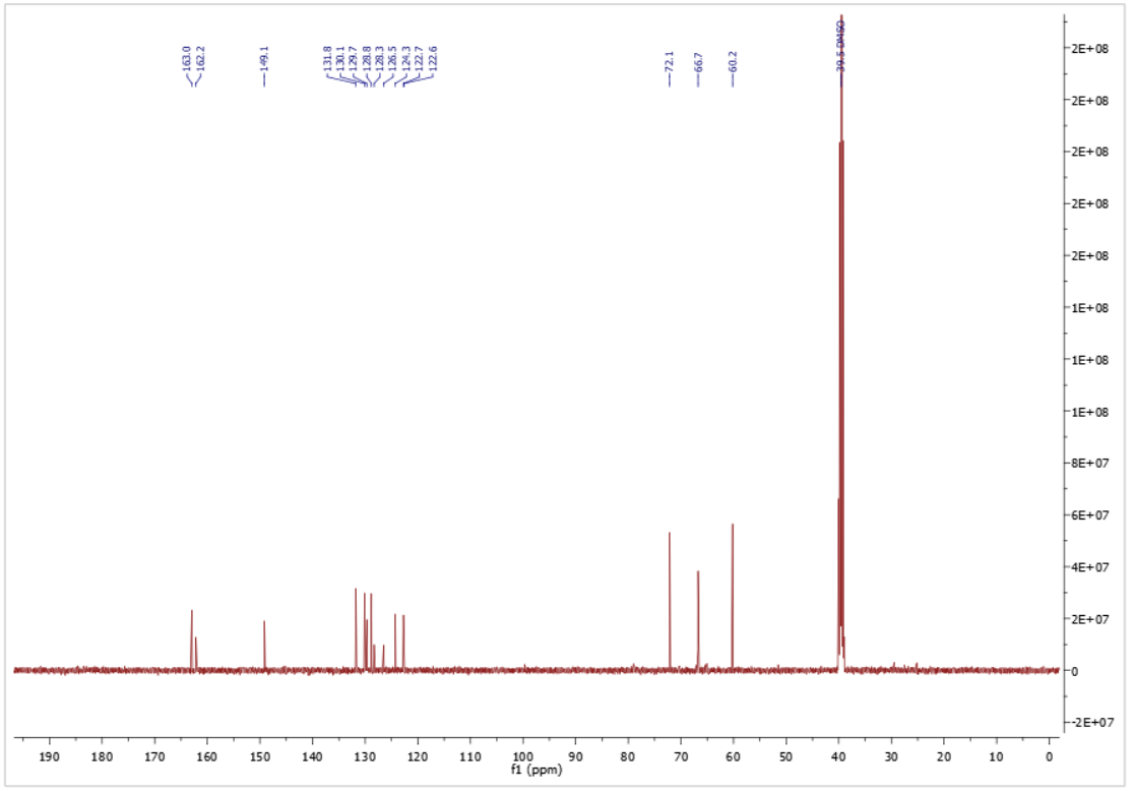

Figure B11: *^{13}C NMR spectrum of **3.14***

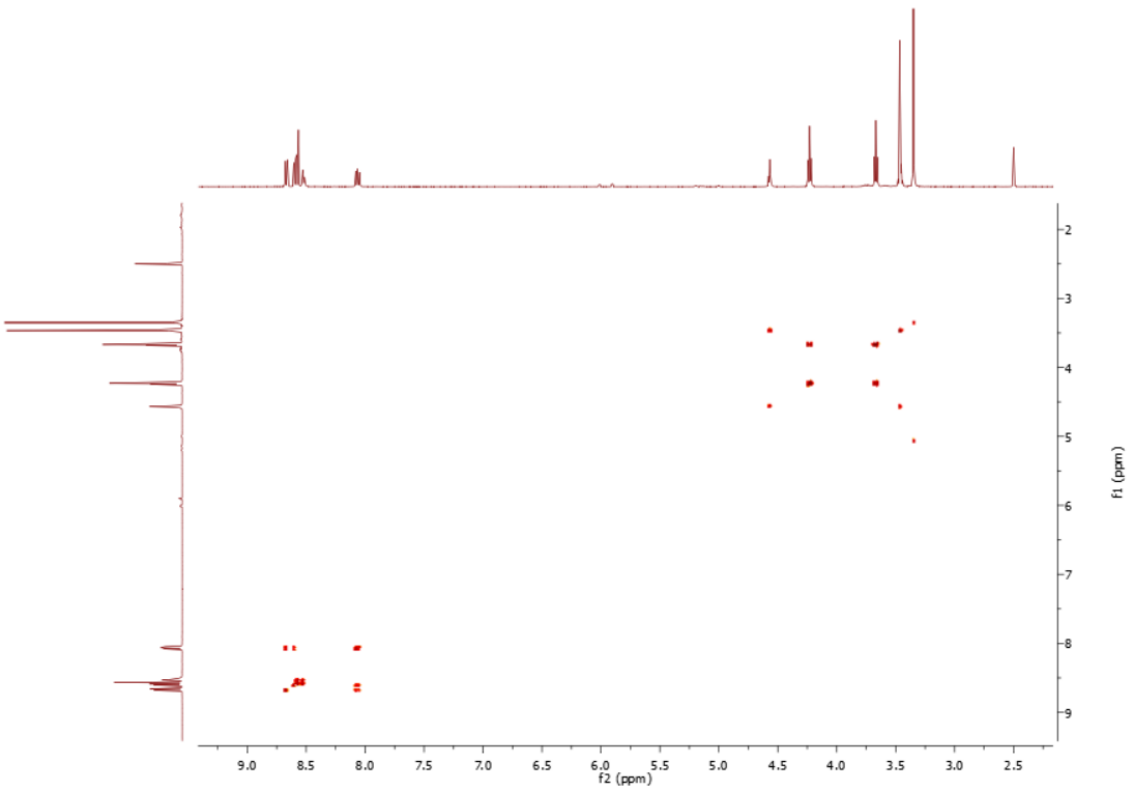

Figure B12: *^{1}H-^{1}H COSY of **3.14***

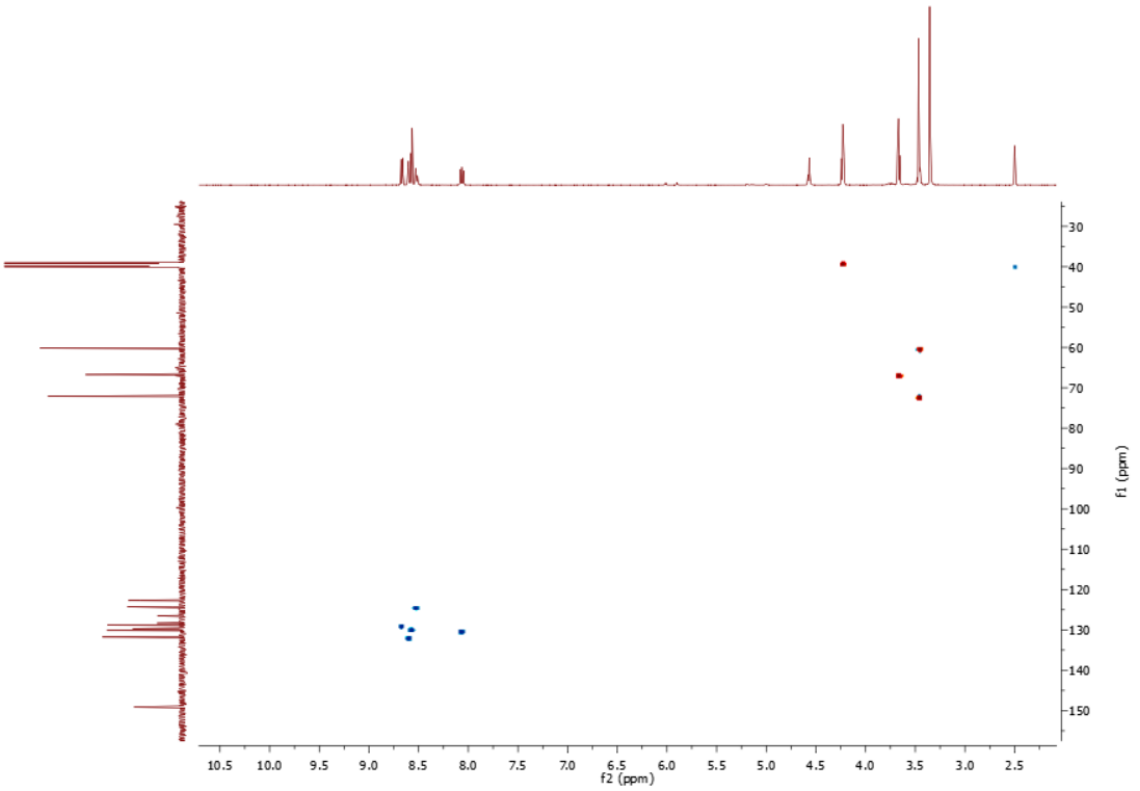

Figure B12: *HSQC of **3.14***

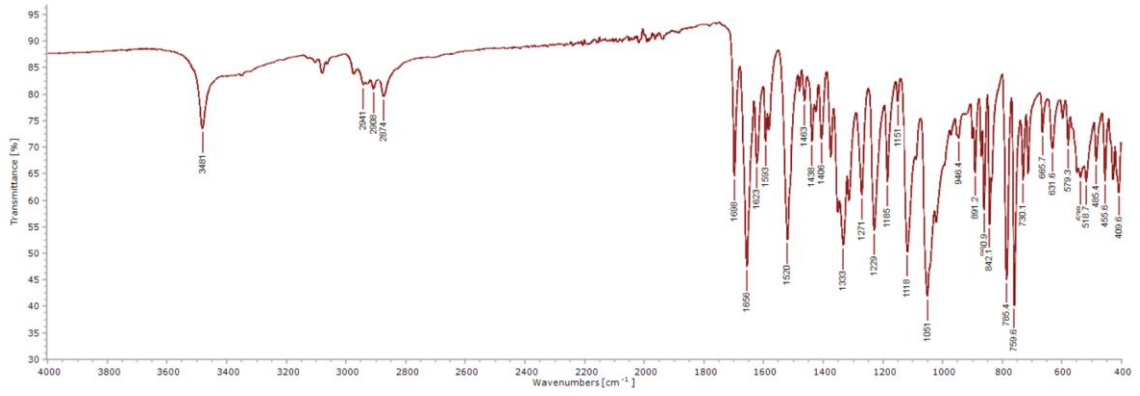

Figure B13: *IR of **3.14***

Compound specific information

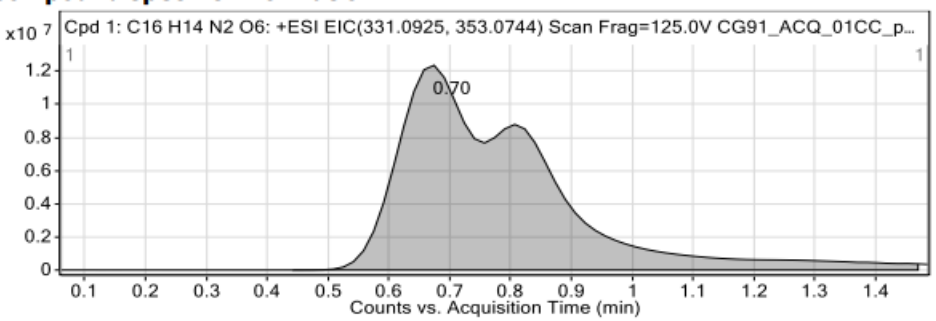

Figure: Extracted ion chromatogram (EIC) of compound.

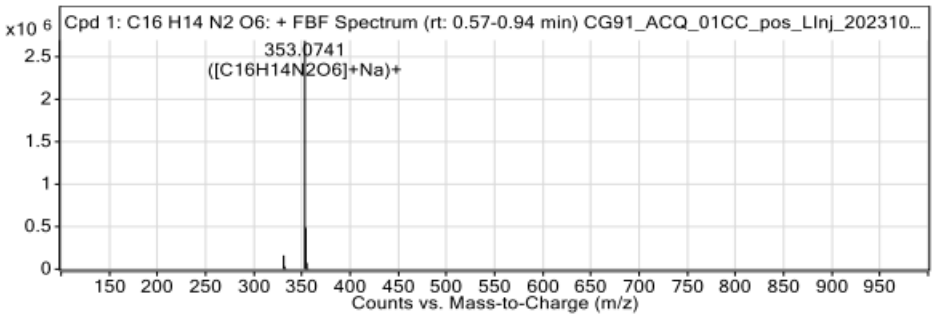

Compound Table

Compound Label	RT (min)	Observed mass (m/z)	Neutral observed mass (Da)	Theoretical mass (Da)	Mass error (ppm)	Isotope match score (%)
Cpd 1: C16 H14 N2 O6	0.70	353.0741	330.0849	330.0852	-0.72	99.48

Mass errors of between -5.00 and 5.00 ppm with isotope match scores above 60% are considered confirmation of molecular formulae

Figure B14: *HRMS of* ***3.14***

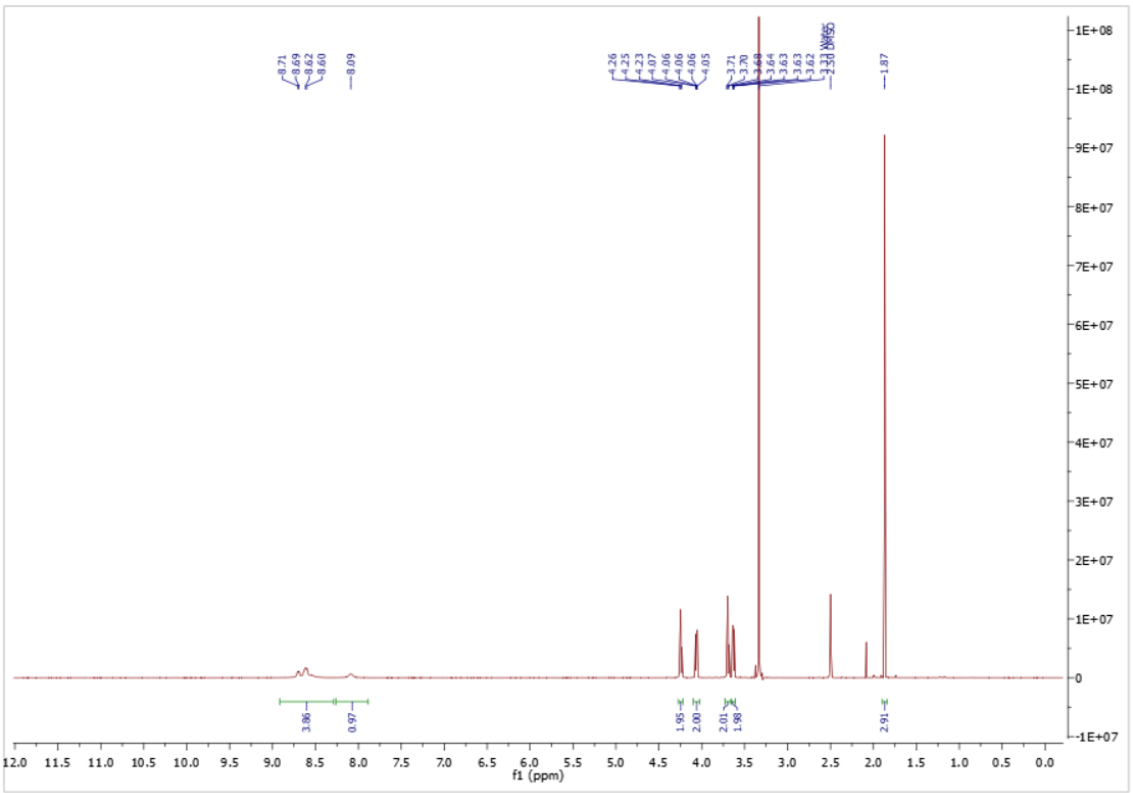

Figure B15: *^{1}H NMR spectrum of* ***3.15***

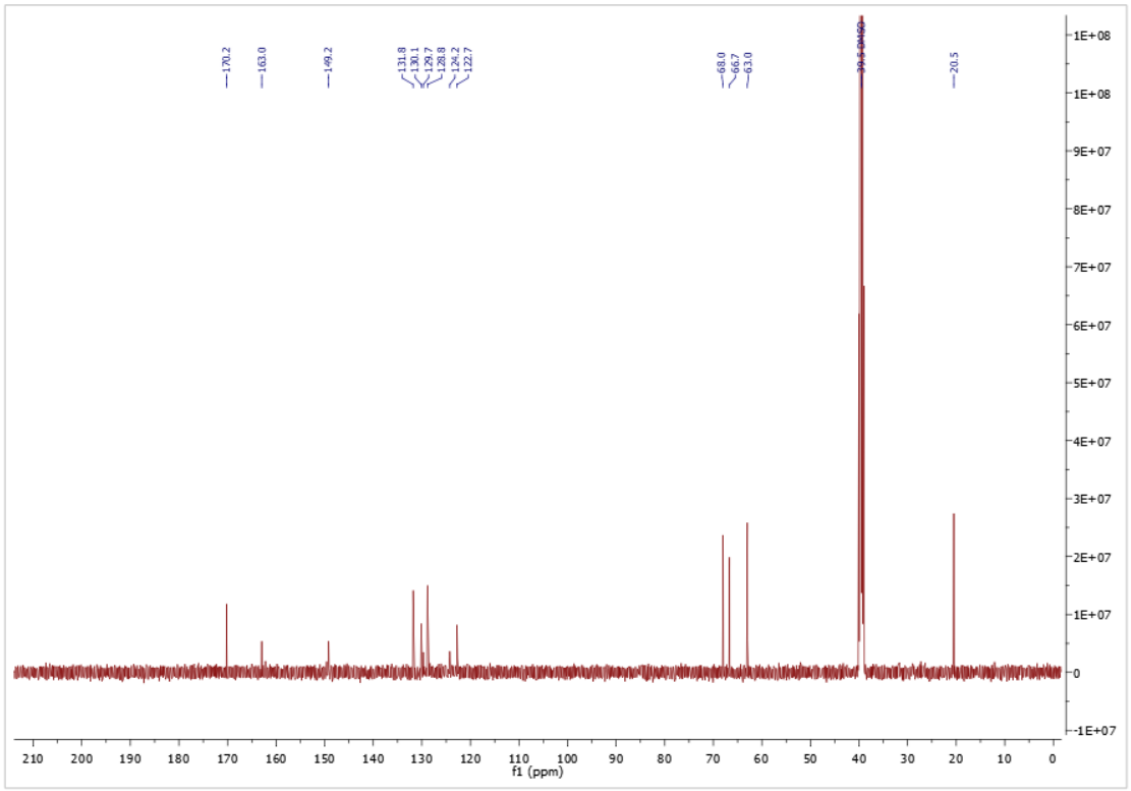

Figure B16: *^{13}C NMR spectrum of* ***3.15***

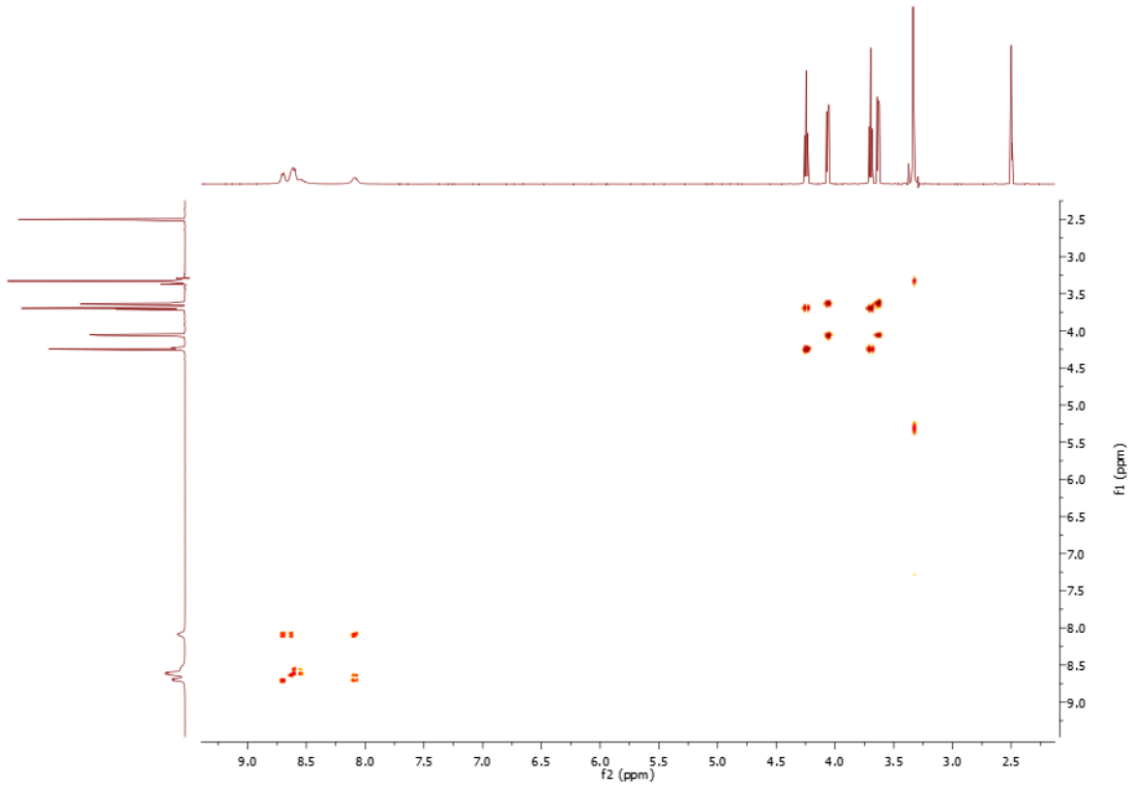

Figure B17: *^{1}H-^{1}H COSY of* ***3.15***

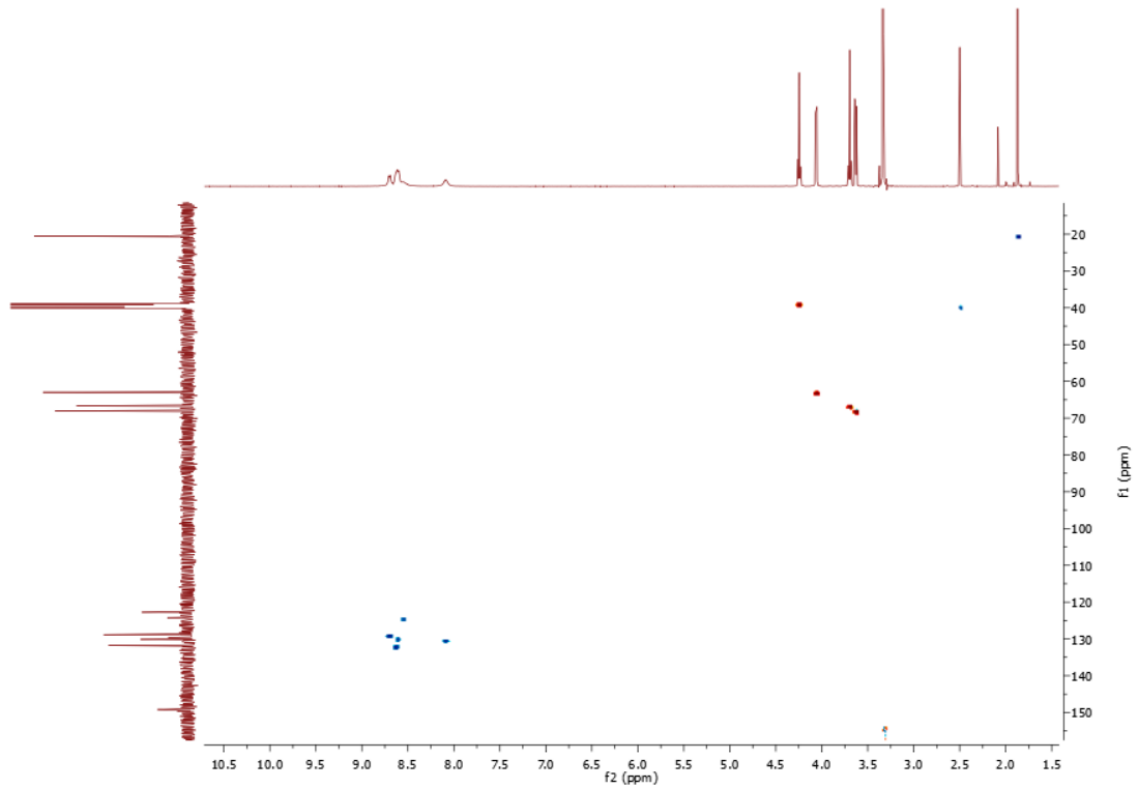

Figure B18: *HSQC of **3.15***

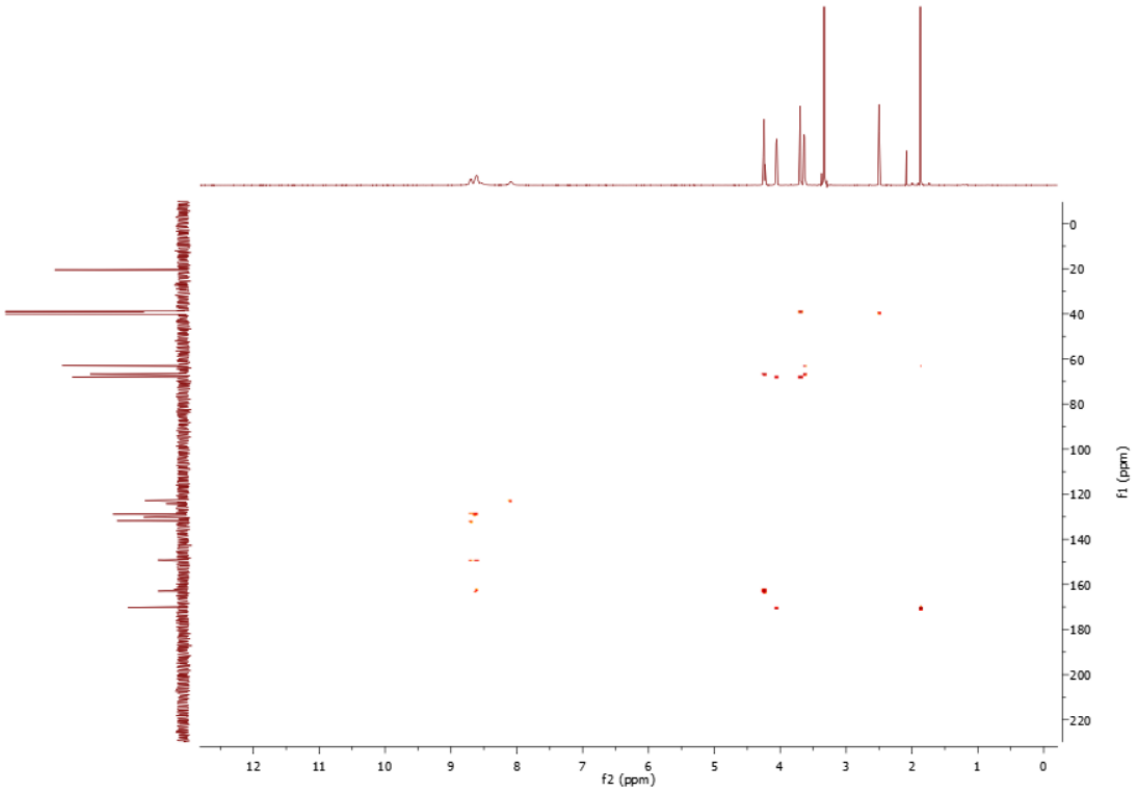

Figure B19: *HMBC of **3.15***

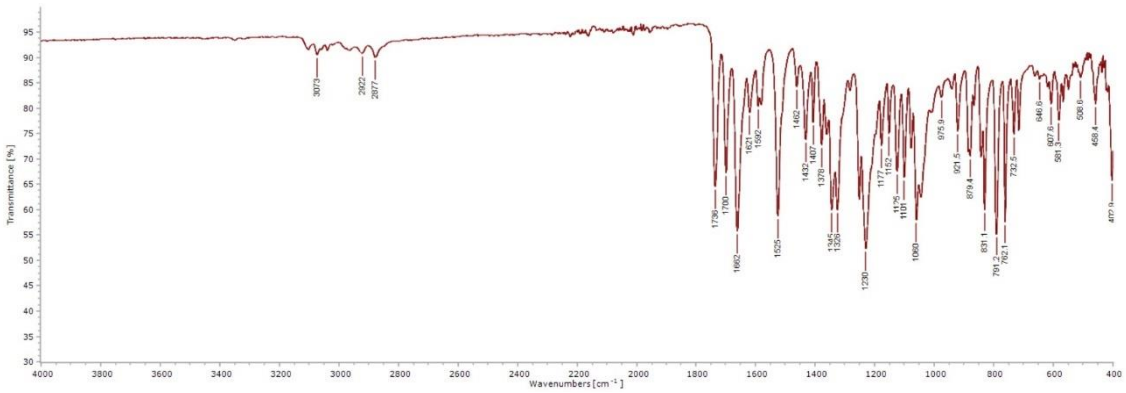

Figure B20: *IR of* ***3.15***

Compound specific information

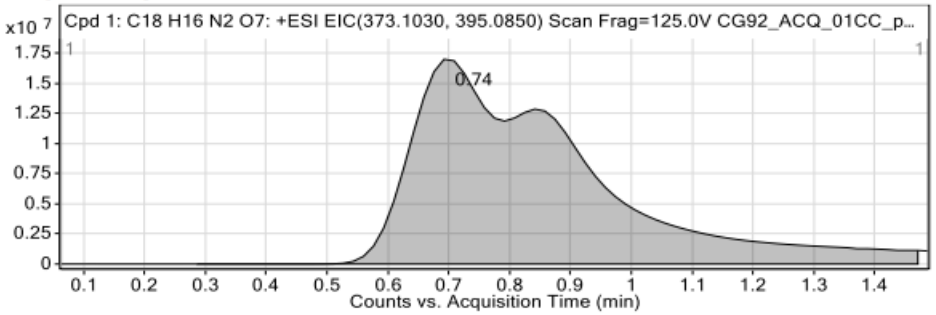

Figure: Extracted ion chromatogram (EIC) of compound.

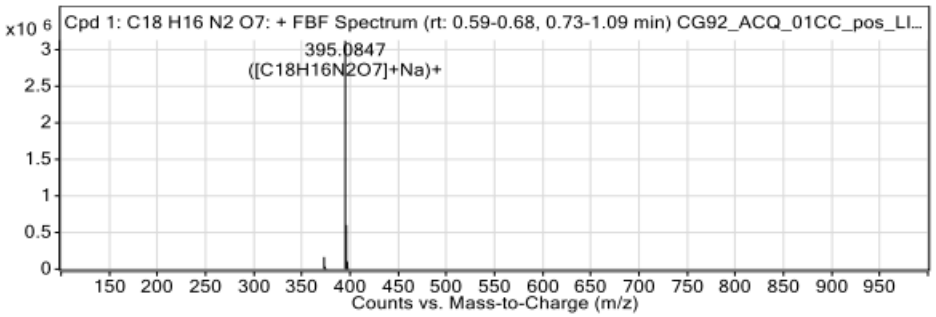

Compound Table

Compound Label	RT (min)	Observed mass (m/z)	Neutral observed mass (Da)	Theoretical mass (Da)	Mass error (ppm)	Isotope match score (%)
Cpd 1: C18 H16 N2 O7	0.74	373.1027	372.0955	372.0958	-0.72	99.96

Mass errors of between -5.00 and 5.00 ppm with isotope match scores above 60% are considered confirmation of molecular formulae

Figure B21: *HRMS of* ***3.15***

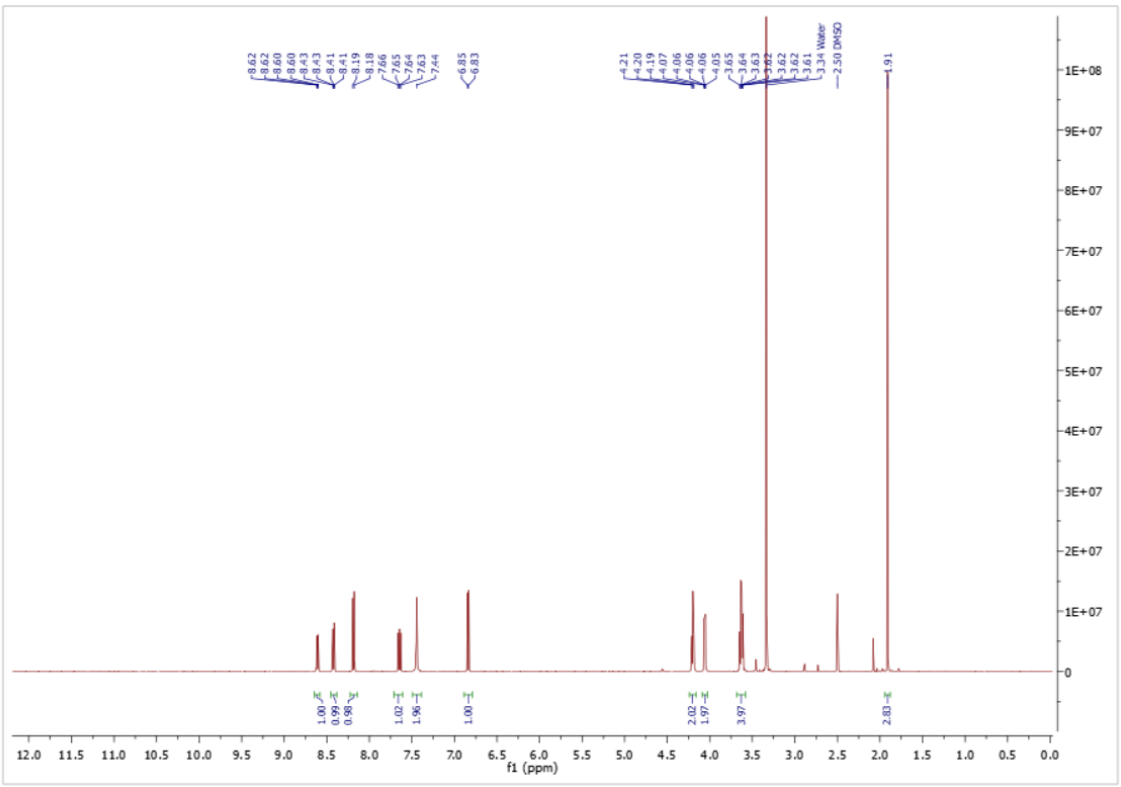

Figure B22: *[1]H NMR spectrum of* ***3.12***

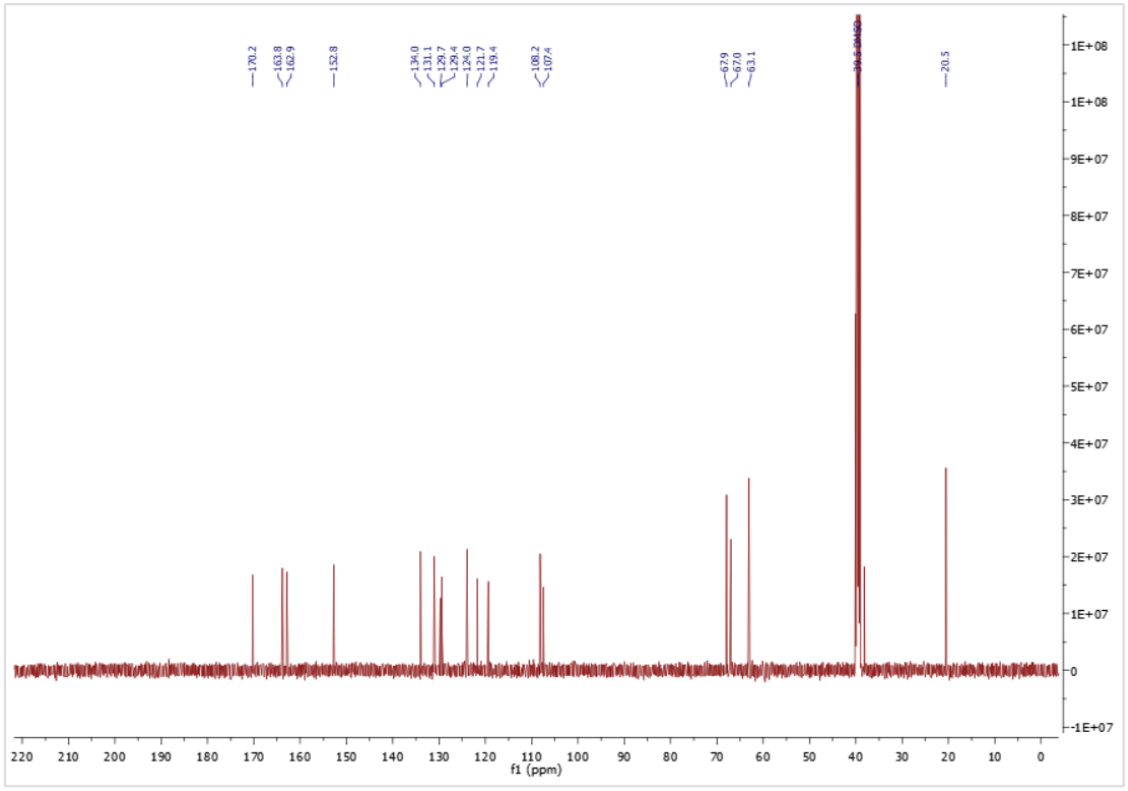

Figure B23: *[13]C NMR spectrum of* ***3.12***

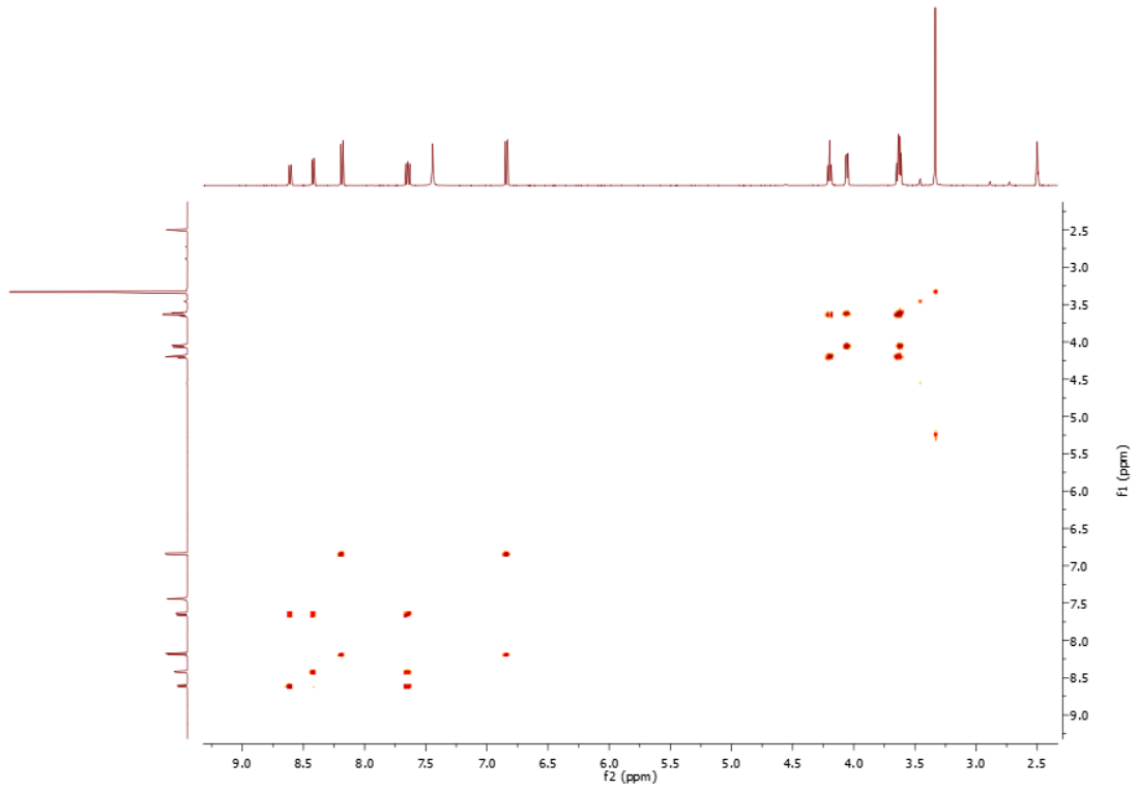

Figure B24: *^{1}H-^{1}H COSY of **3.12***

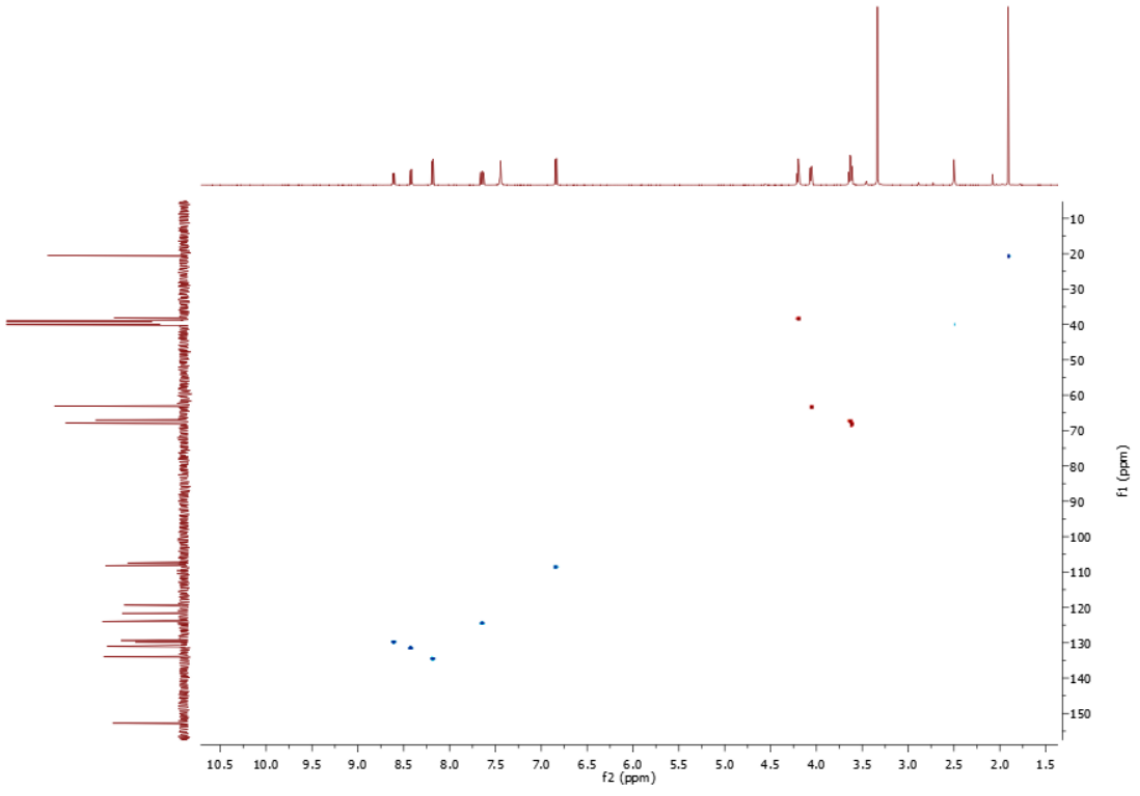

Figure B25: *HSQC of **3.12***

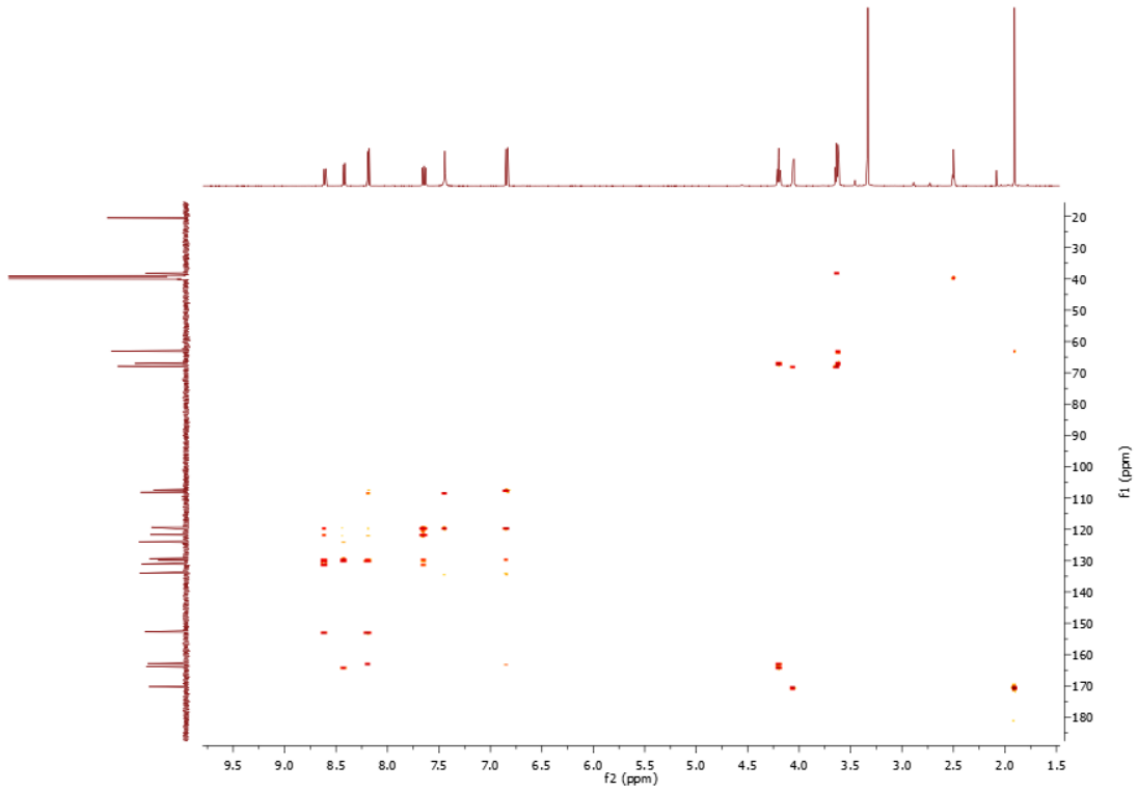

Figure B26: *HMBC of **3.12***

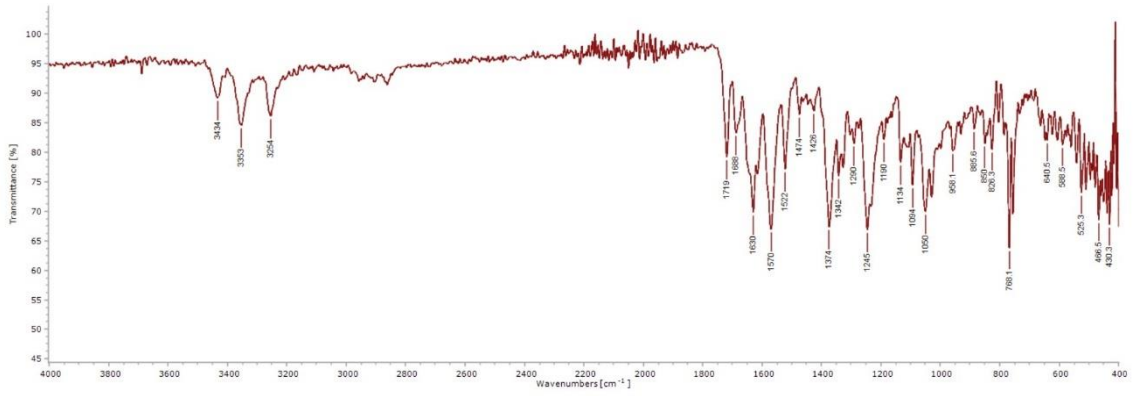

Figure B27: *IR of **3.12***

Compound specific information

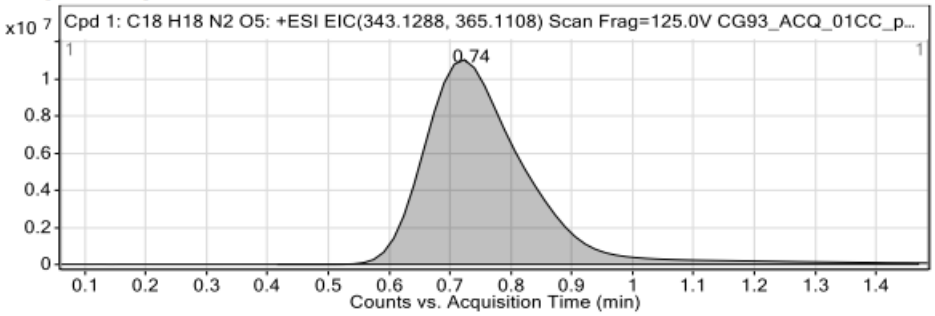

Figure: Extracted ion chromatogram (EIC) of compound.

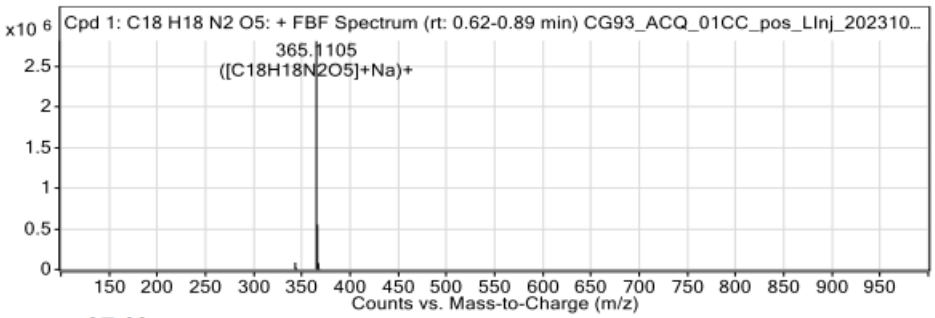

Compound Table

Compound Label	RT (min)	Observed mass (m/z)	Neutral observed mass (Da)	Theoretical mass (Da)	Mass error (ppm)	Isotope match score (%)
Cpd 1: C18 H18 N2 O5	0.74	365.1105	342.1213	342.1216	-0.68	99.61

Mass errors of between -5.00 and 5.00 ppm with isotope match scores above 60% are considered confirmation of molecular formulae

Figure B28: *HRMS of* ***3.12***

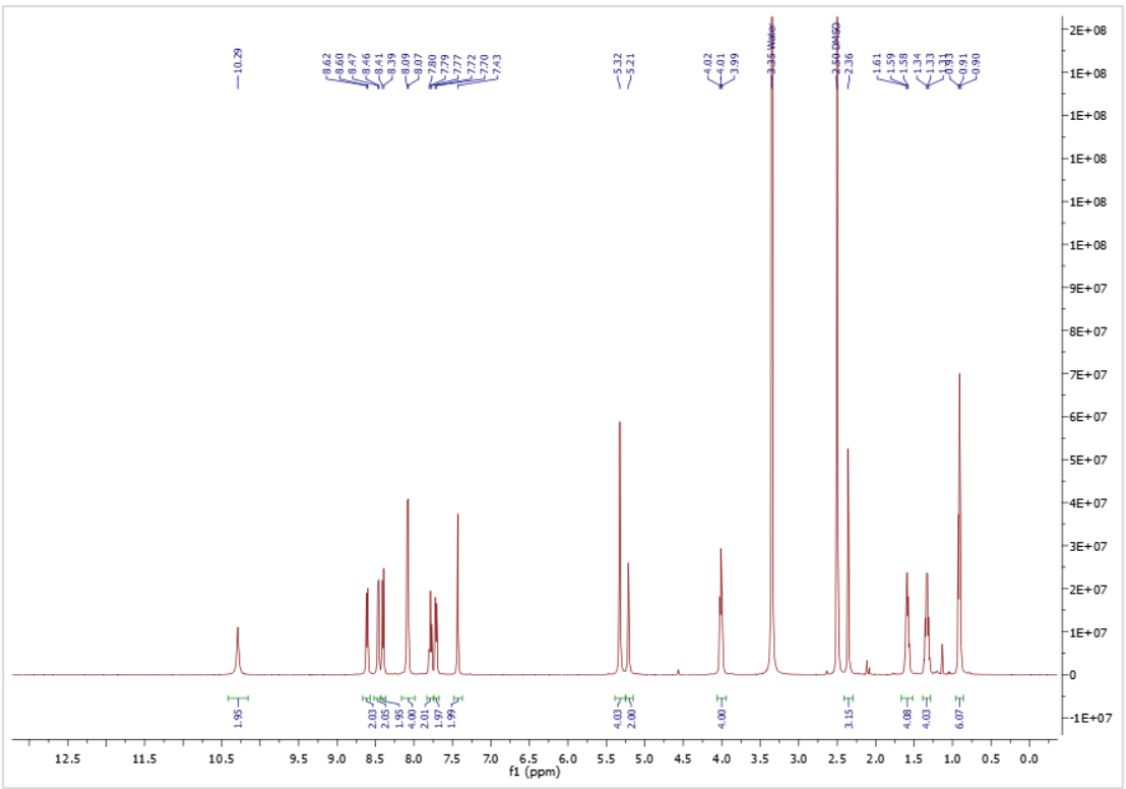

Figure B29: *^{1}H NMR spectrum of* ***3.6***

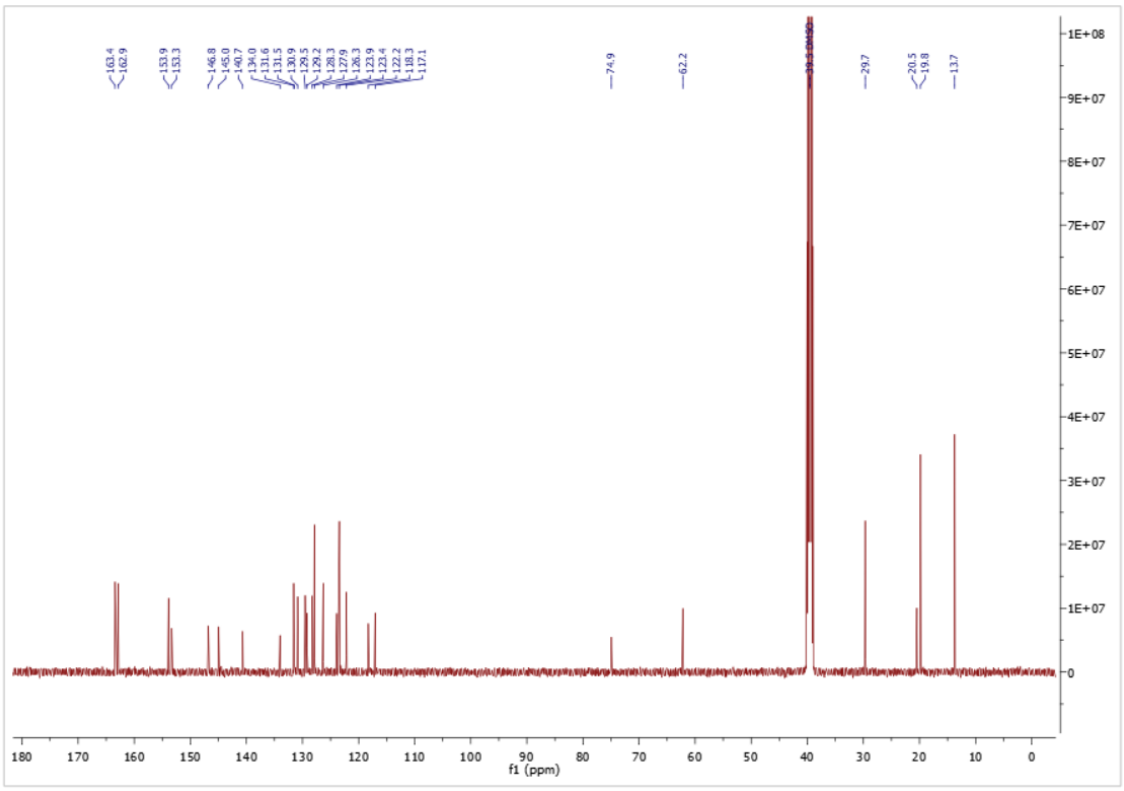

Figure B30: *^{13}C NMR spectrum of* ***3.6***

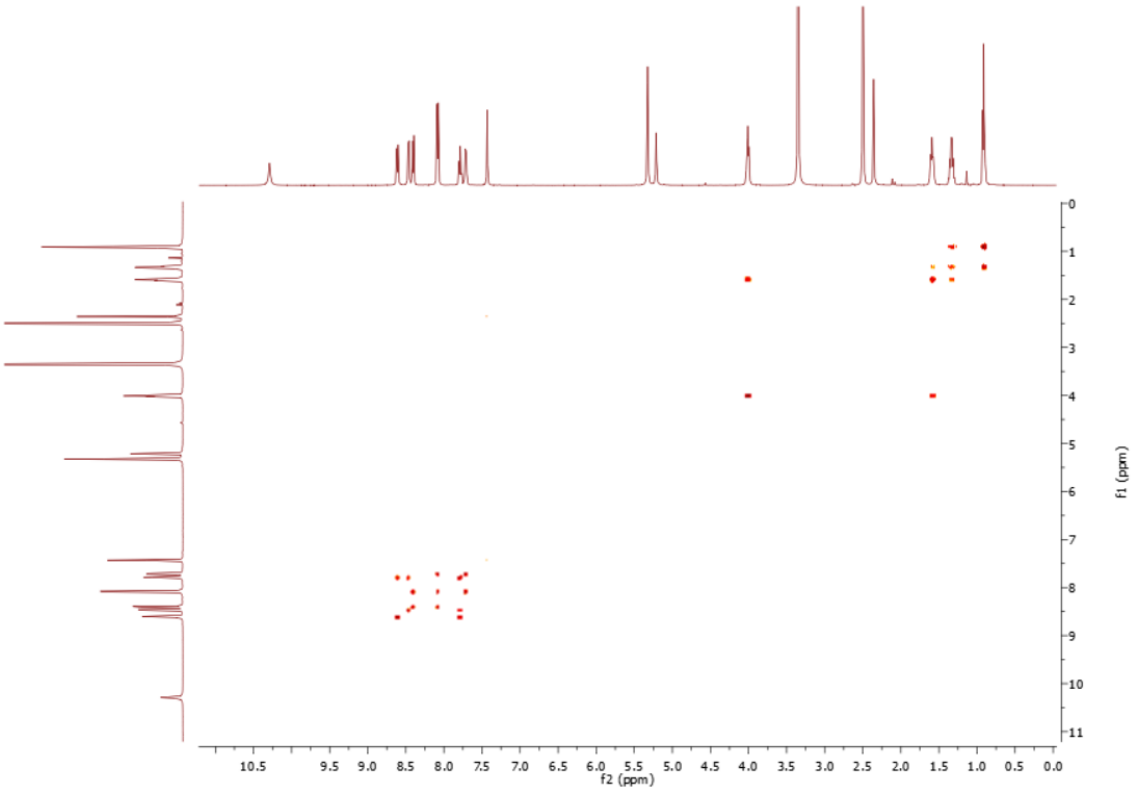

Figure B31: *^{1}H-^{1}H COSY of* ***3.6***

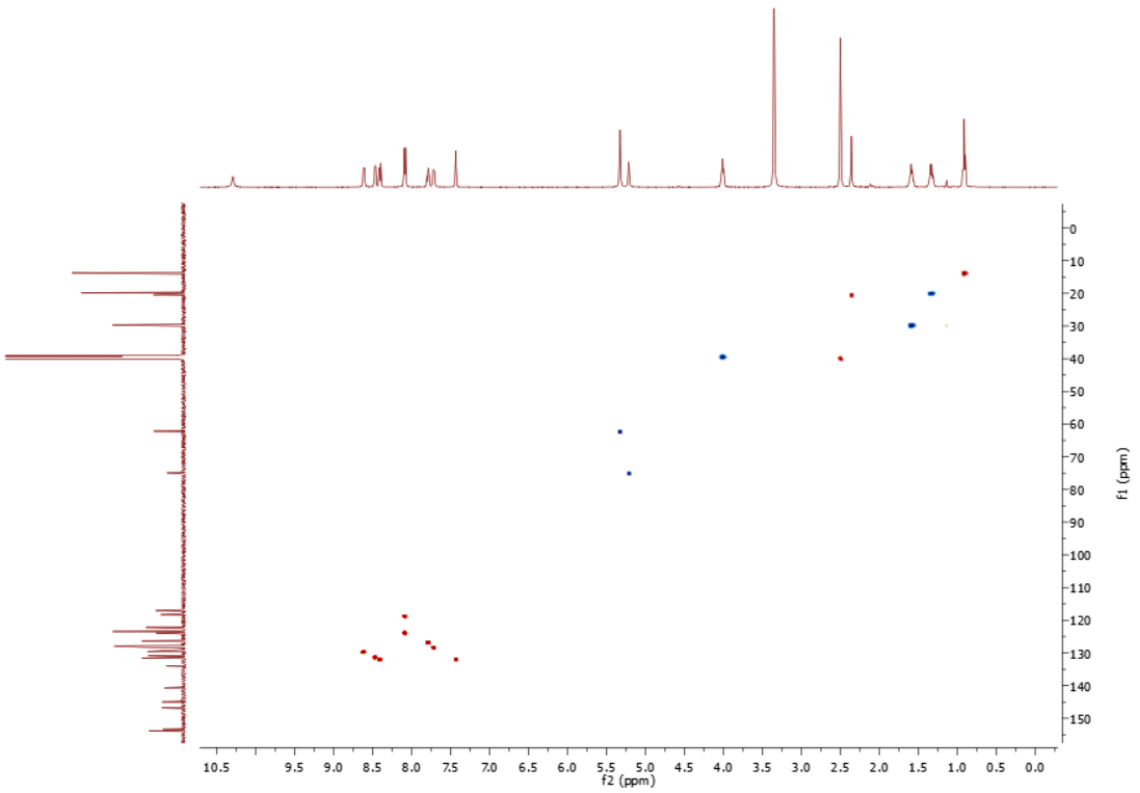

Figure B32: *HSQC of* ***3.6***

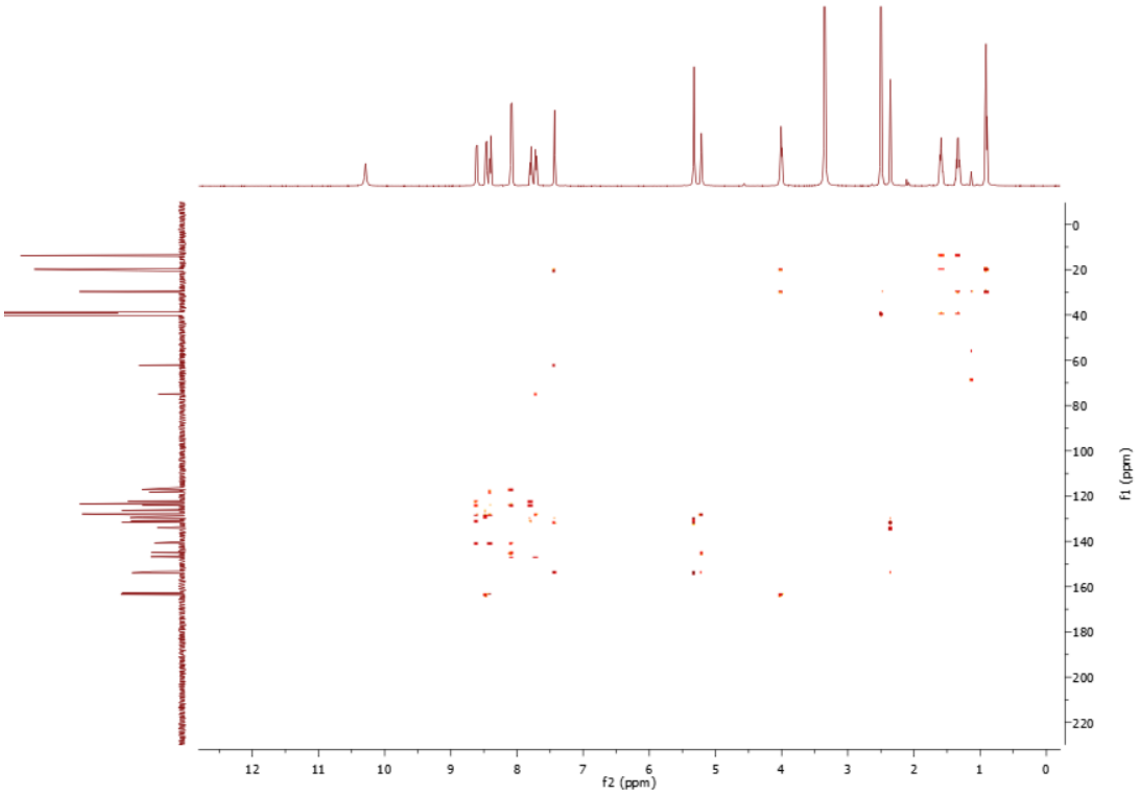

Figure B33: *HMBC of* ***3.6***

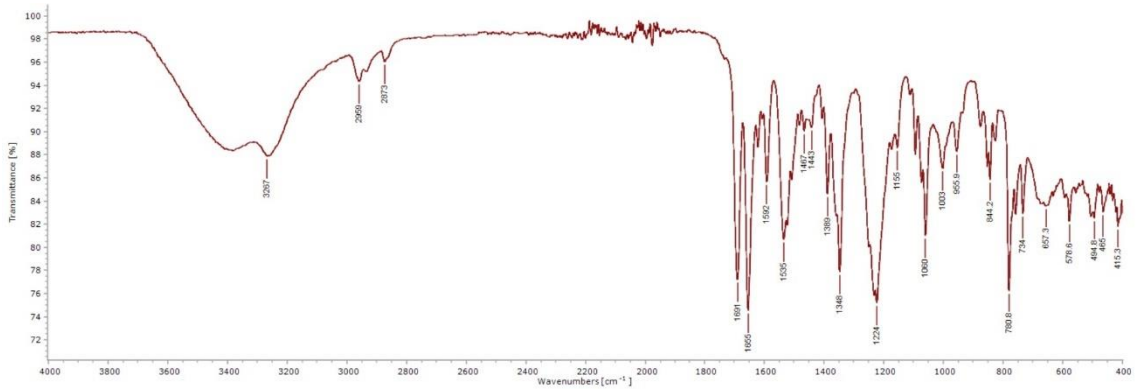

Figure B34: *IR of* ***3.6***

Compound specific information

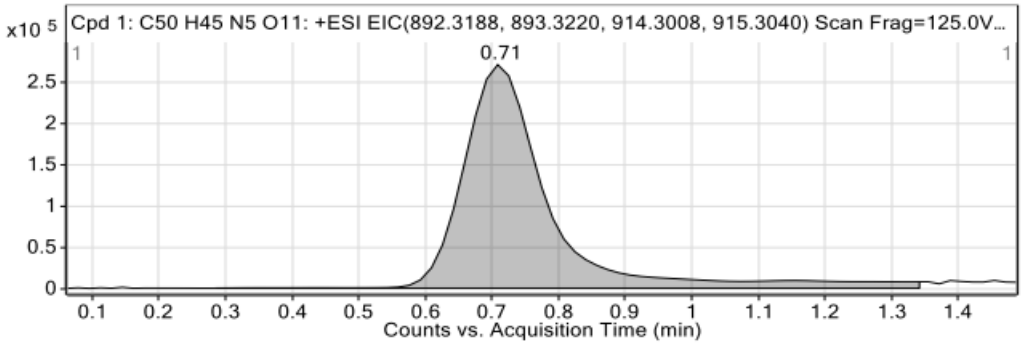

Figure: Extracted ion chromatogram (EIC) of compound.

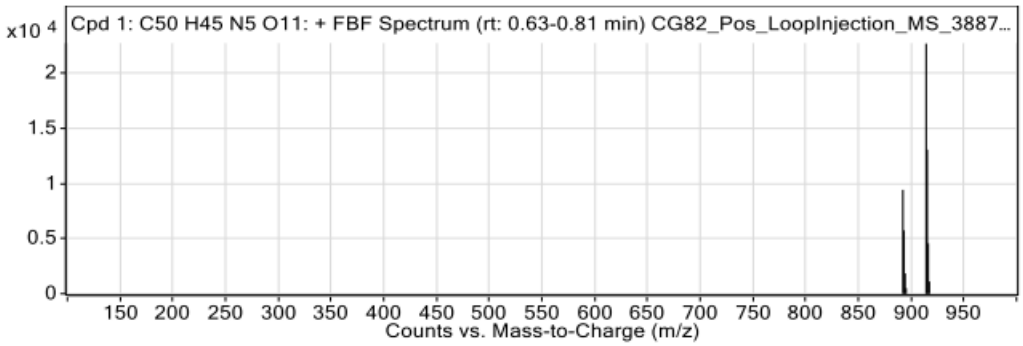

Figure: Full range view of Compound spectra and potential adducts.

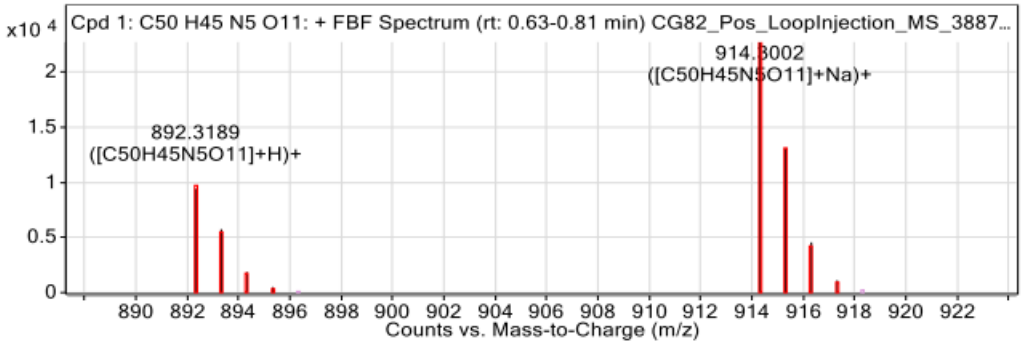

Compound Table

Compound Label	RT (min)	Observed mass (m/z)	Neutral observed mass (Da)	Theoretical mass (Da)	Mass error (ppm)	Isotope match score (%)
Cpd 1: C50 H45 N5 O11	0.71	914.3002	891.3112	891.3116	-0.36	98.41

Mass errors of between -5.00 and 5.00 ppm with isotope match scores above 60% are considered confirmation of molecular formulae

Figure B35: *HRMS of* ***3.6***

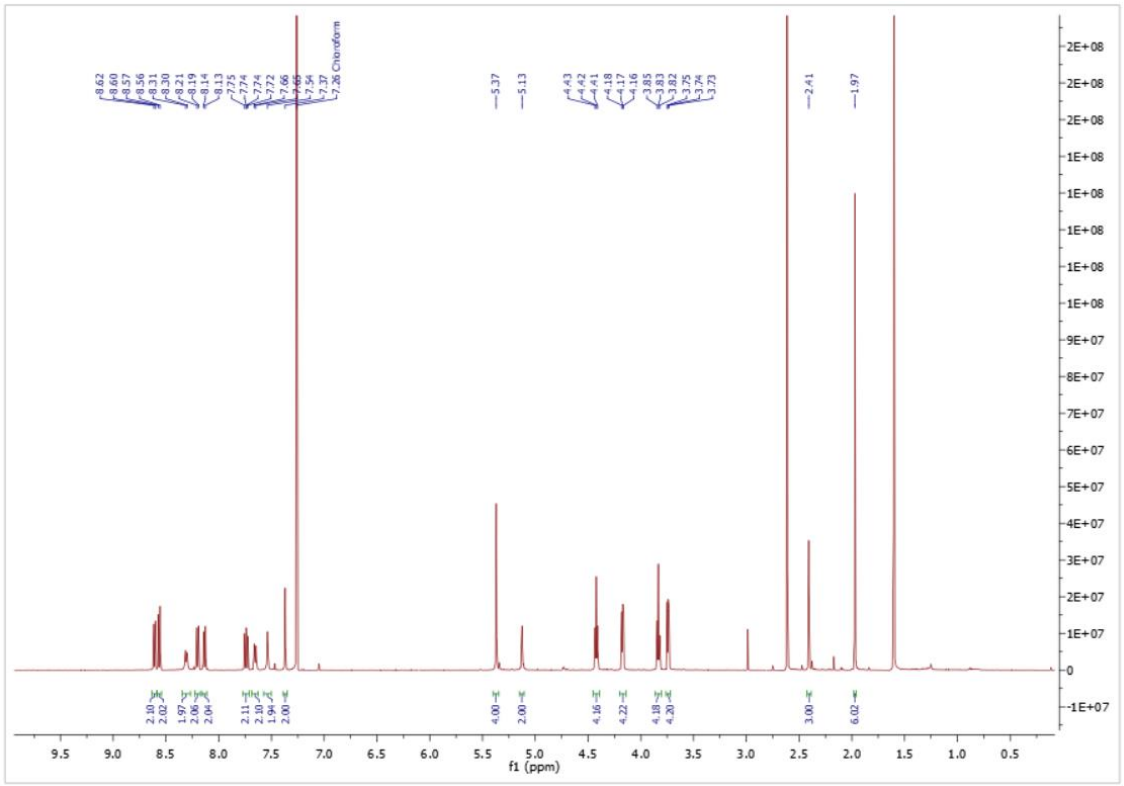

Figure B36: *[1]H NMR spectrum of **3.7***

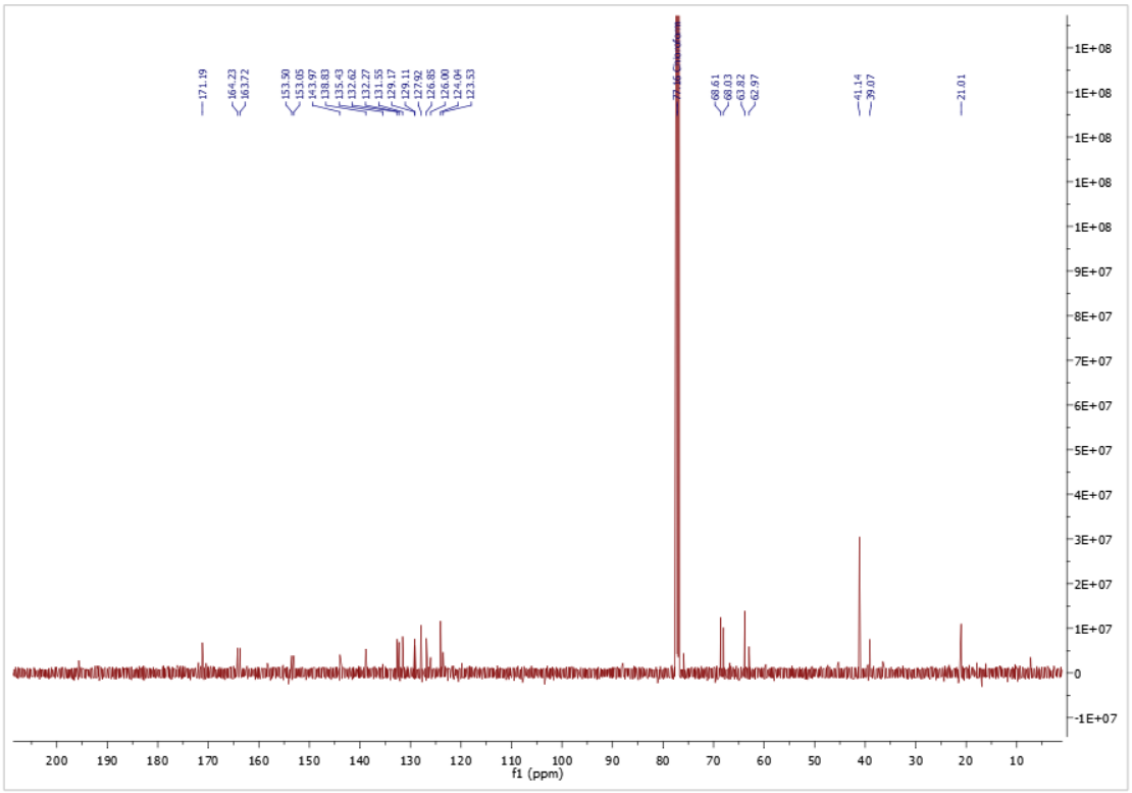

Figure B37: *[13]C NMR spectrum of **3.7***

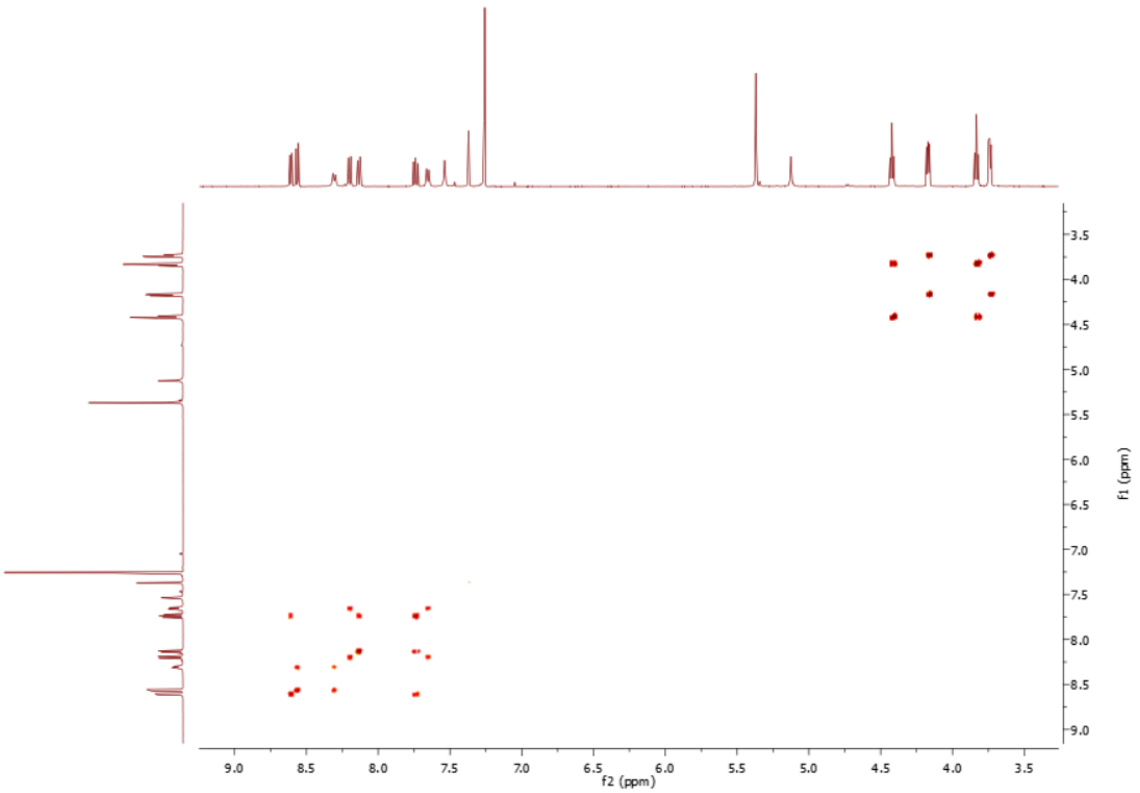

Figure B38: *^{1}H-^{1}H COSY of **3.7***

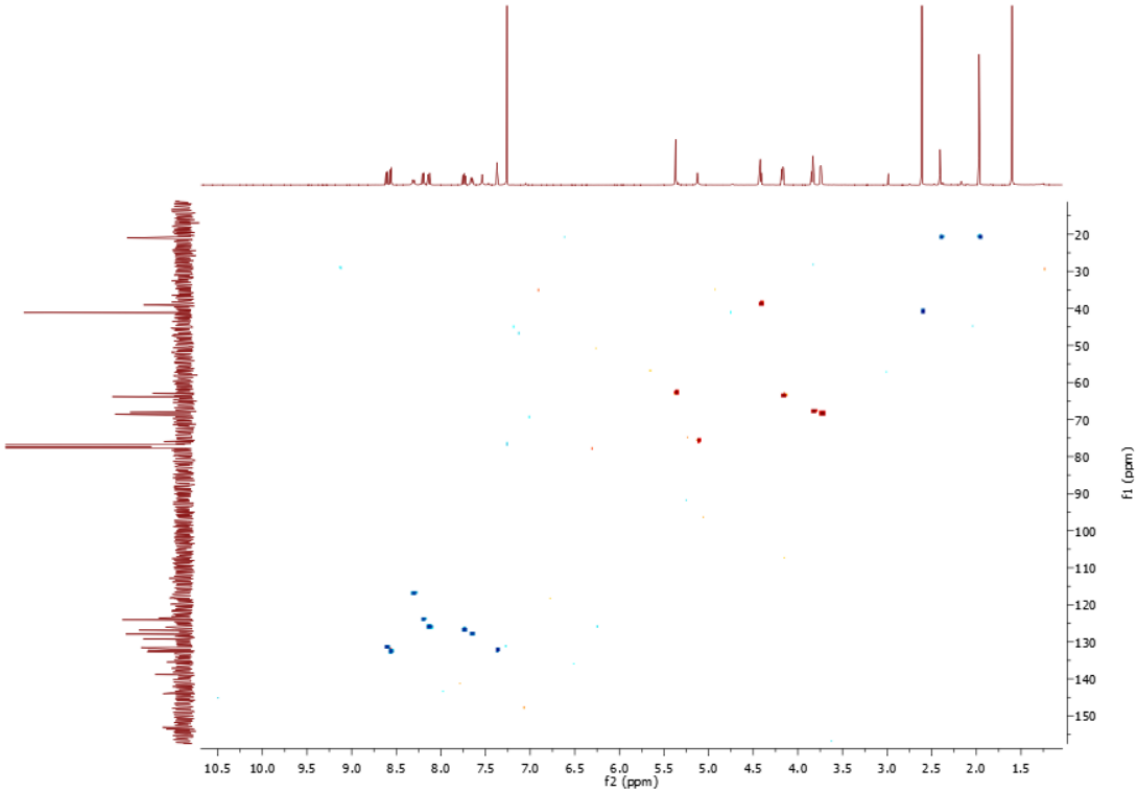

Figure B39: *HSQC of **3.7***

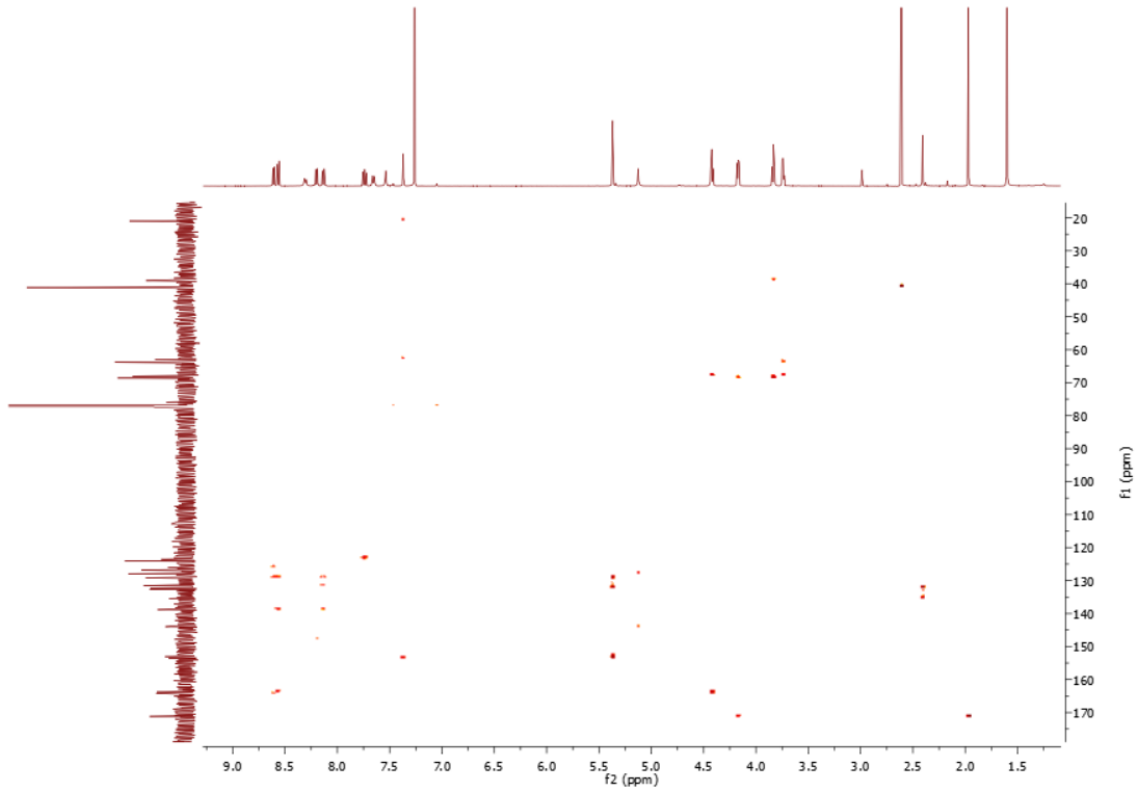

Figure B40: *HMBC of **3.7***

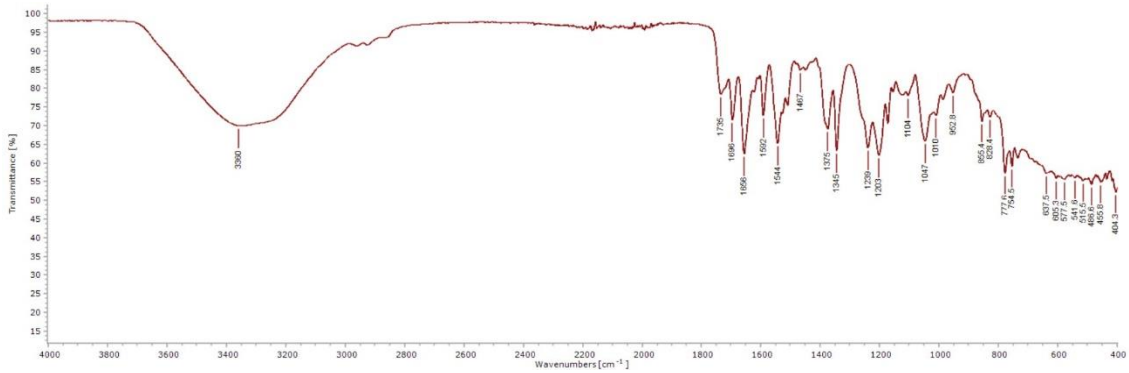

Figure B41: *IR of **3.7***

Compound specific information

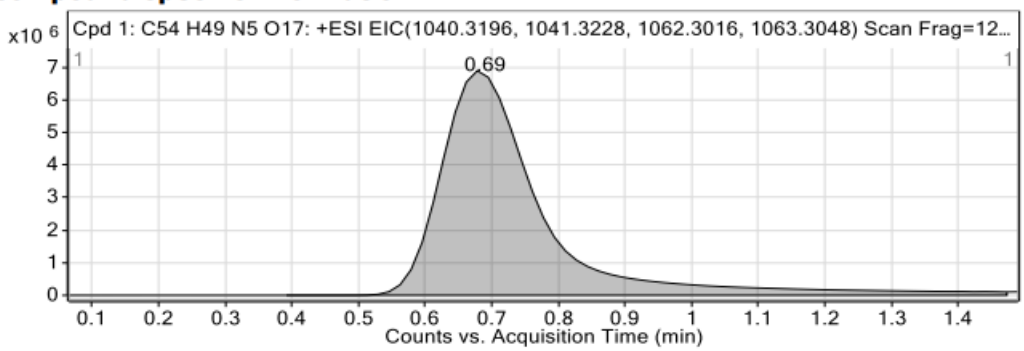

Figure: Full range view of Compound spectra and potential adducts.

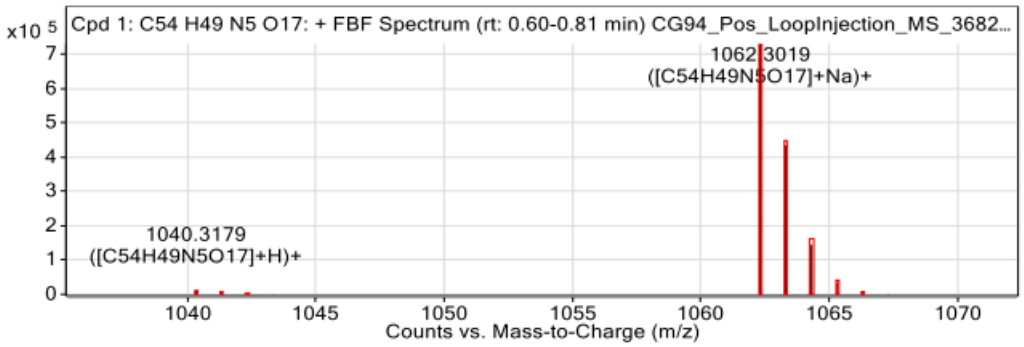

Compound Table

Compound Label	RT (min)	Observed mass (m/z)	Neutral observed mass (Da)	Theoretical mass (Da)	Mass error (ppm)	Isotope match score (%)
Cpd 1: C54 H49 N5 O17	0.69	1040.3179	1039.3127	1039.3123	0.32	99.62

Mass errors of between -5.00 and 5.00 ppm with isotope match scores above 60% are considered confirmation of molecular formulae

Figure B42: *HRMS of* ***3.7***

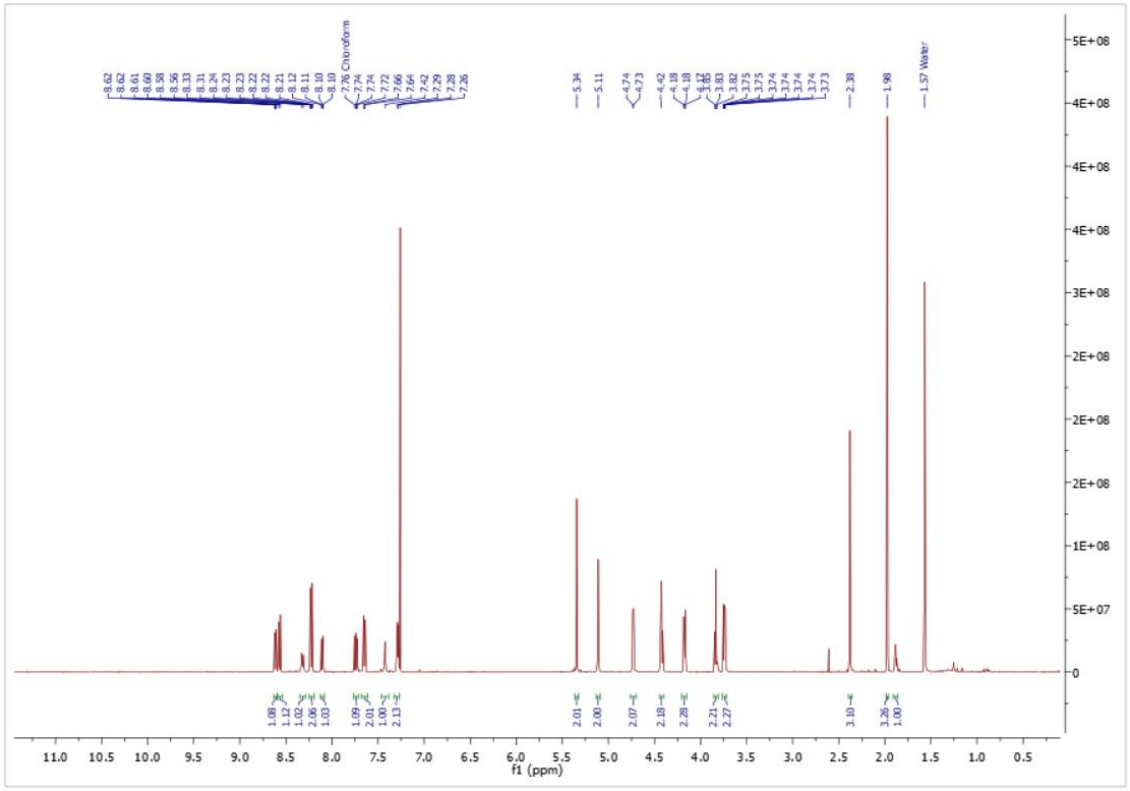

Figure B43: *^{1}H NMR spectrum of **3.17***

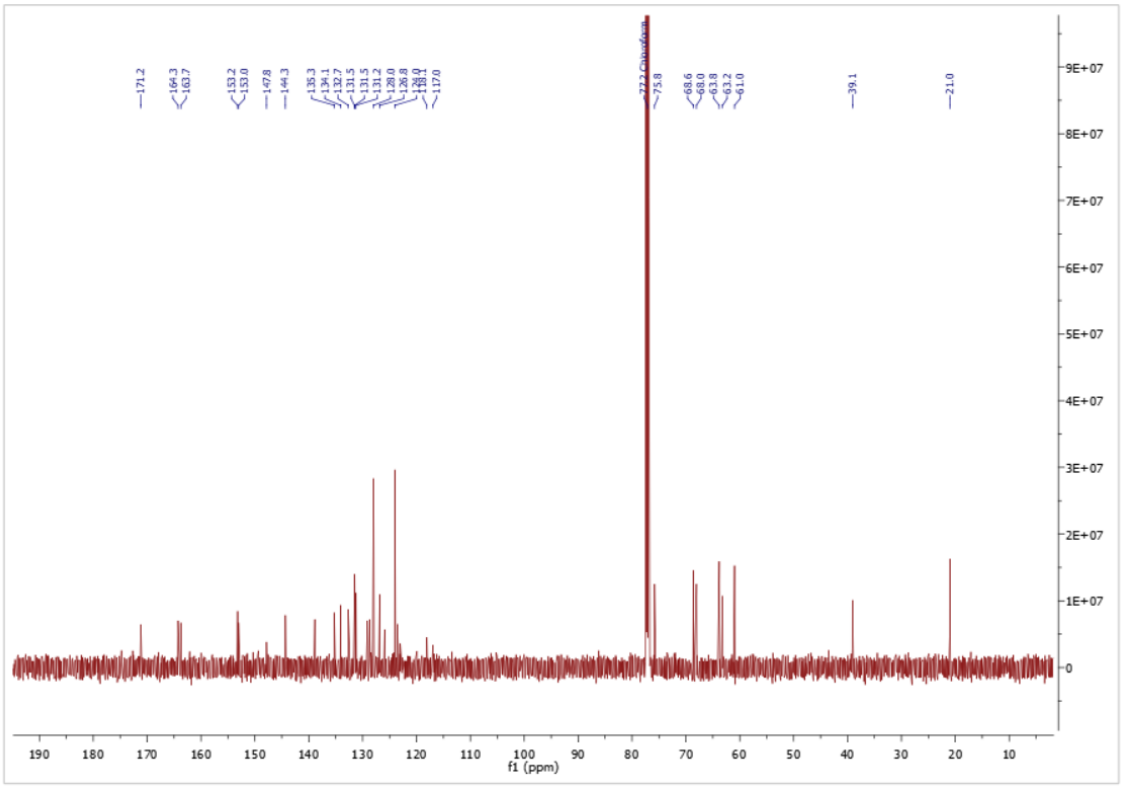

Figure B44: *^{13}C NMR spectrum of **3.17***

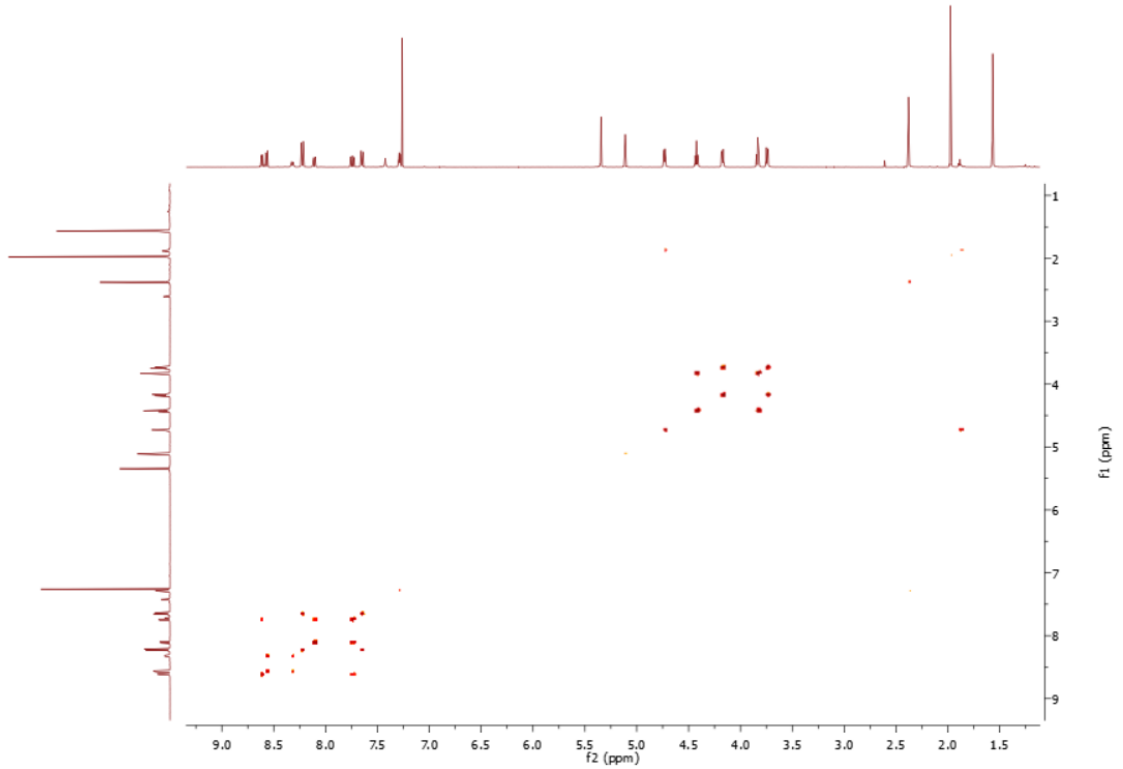

Figure B45: *^{1}H-^{1}H COSY of **3.17***

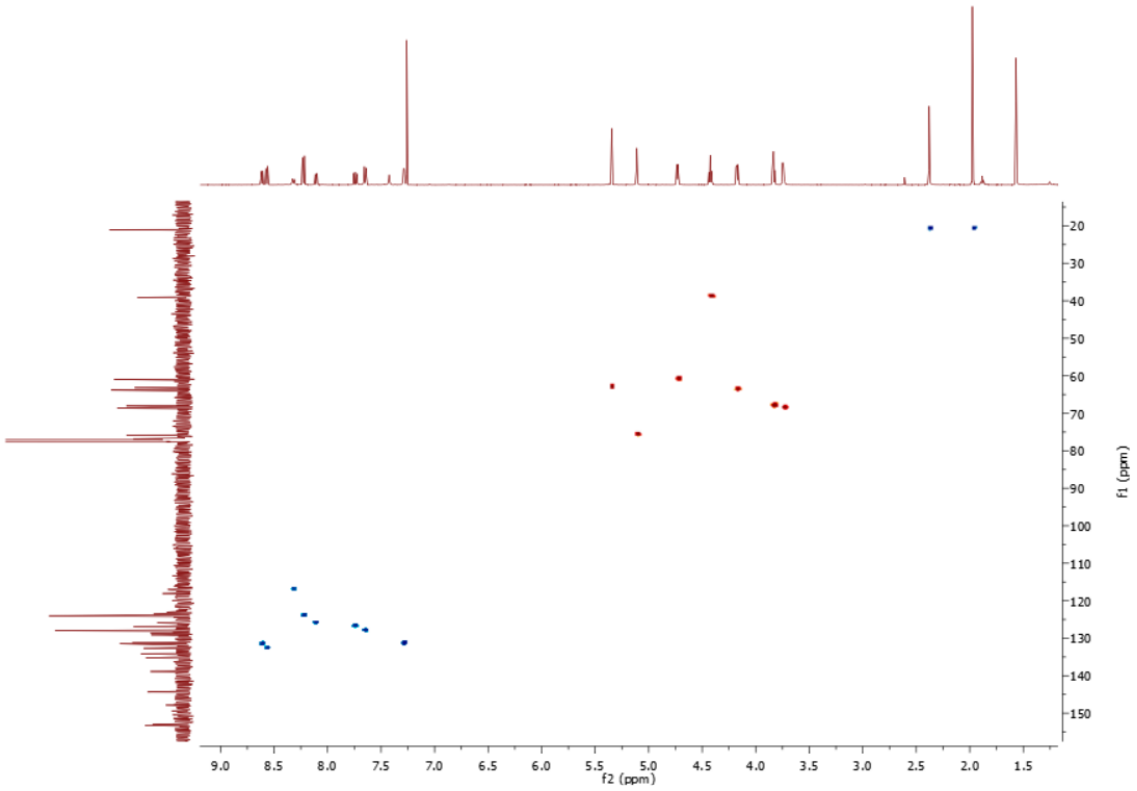

Figure B46: *HSQC of **3.17***

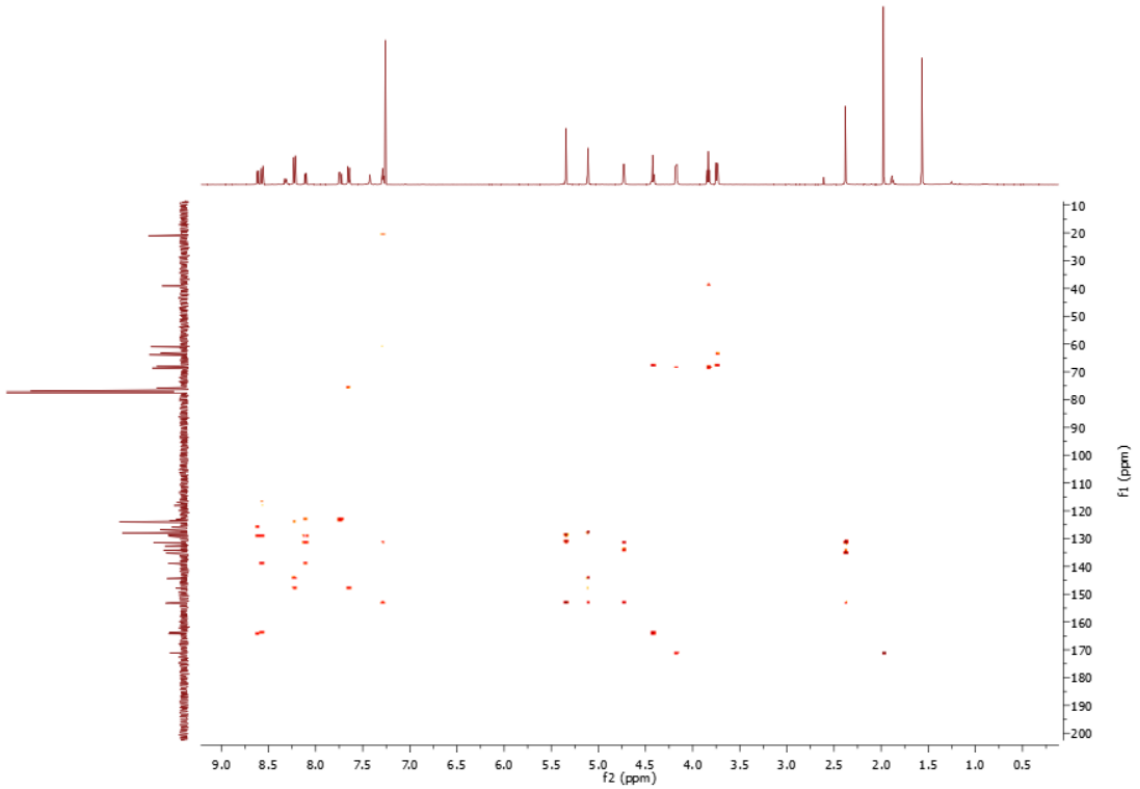

Figure B47: *HMBC of **3.17***

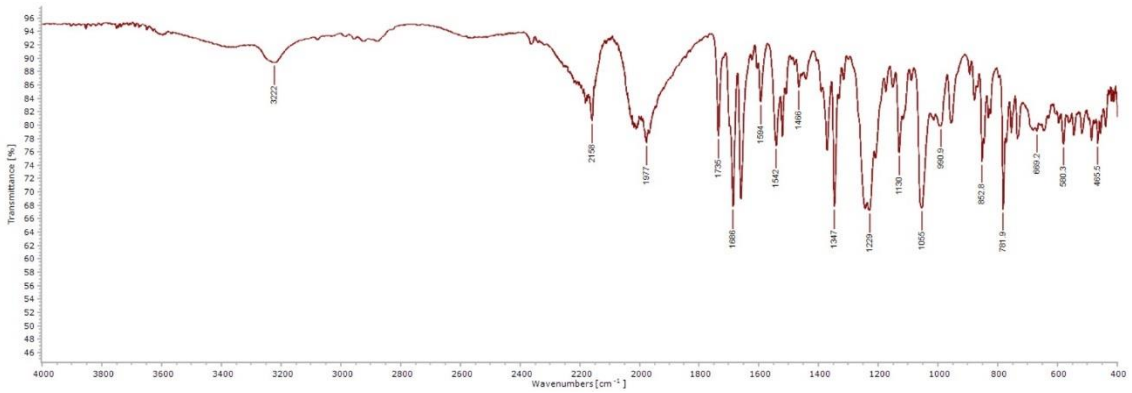

Figure B48: *IR of **3.17***

Compound specific information

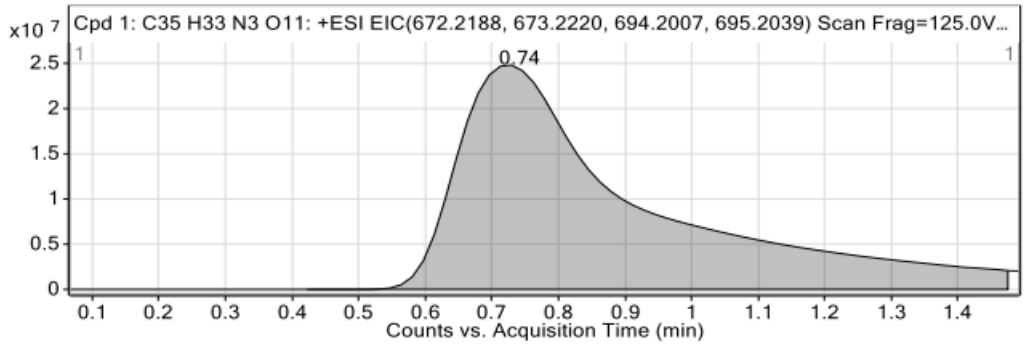

Figure: Extracted ion chromatogram (EIC) of compound.

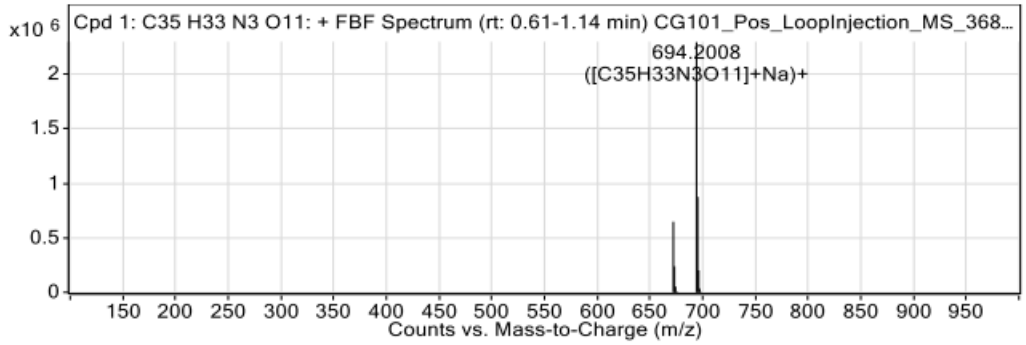

Compound Table

Compound Label	RT (min)	Observed mass (m/z)	Neutral observed mass (Da)	Theoretical mass (Da)	Mass error (ppm)	Isotope match score (%)
Cpd 1: C35 H33 N3 O11	0.74	694.2008	671.2116	671.2115	0.10	99.33

Mass errors of between -5.00 and 5.00 ppm with isotope match scores above 60% are considered confirmation of molecular formulae

Figure B49: *HRMS of* ***3.17***

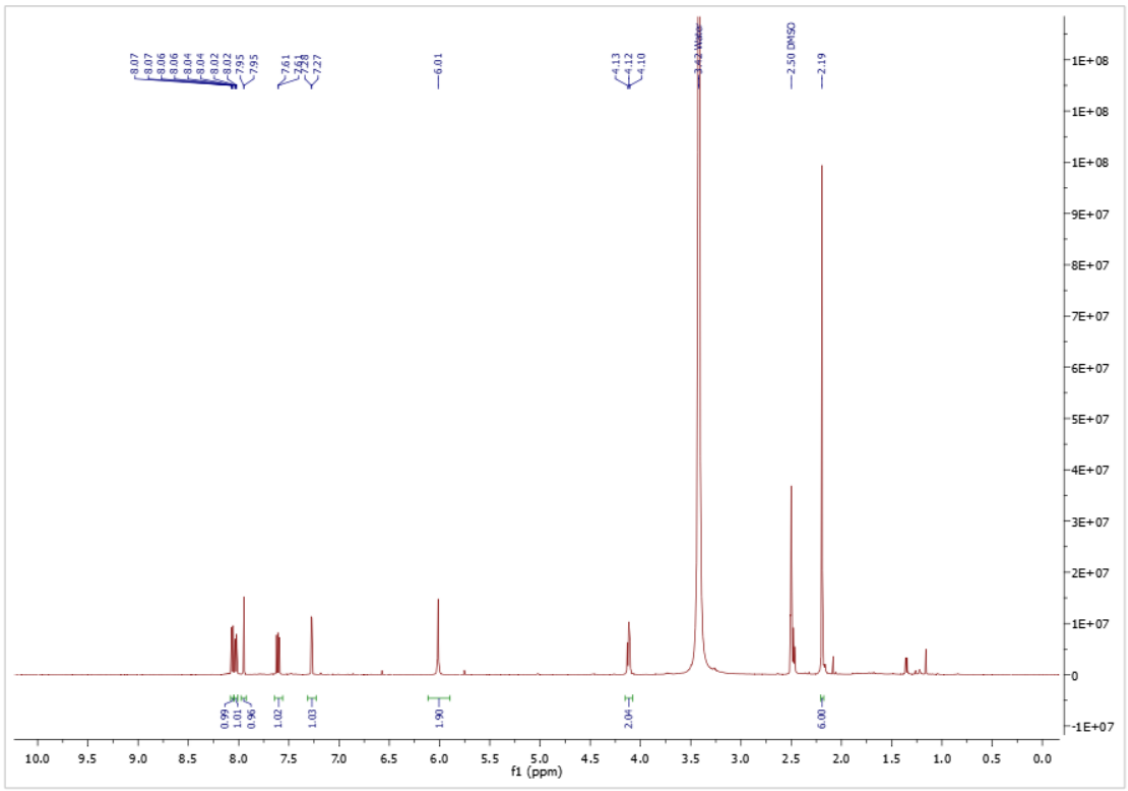

Figure B50: *[1]H NMR spectrum of **3.18***

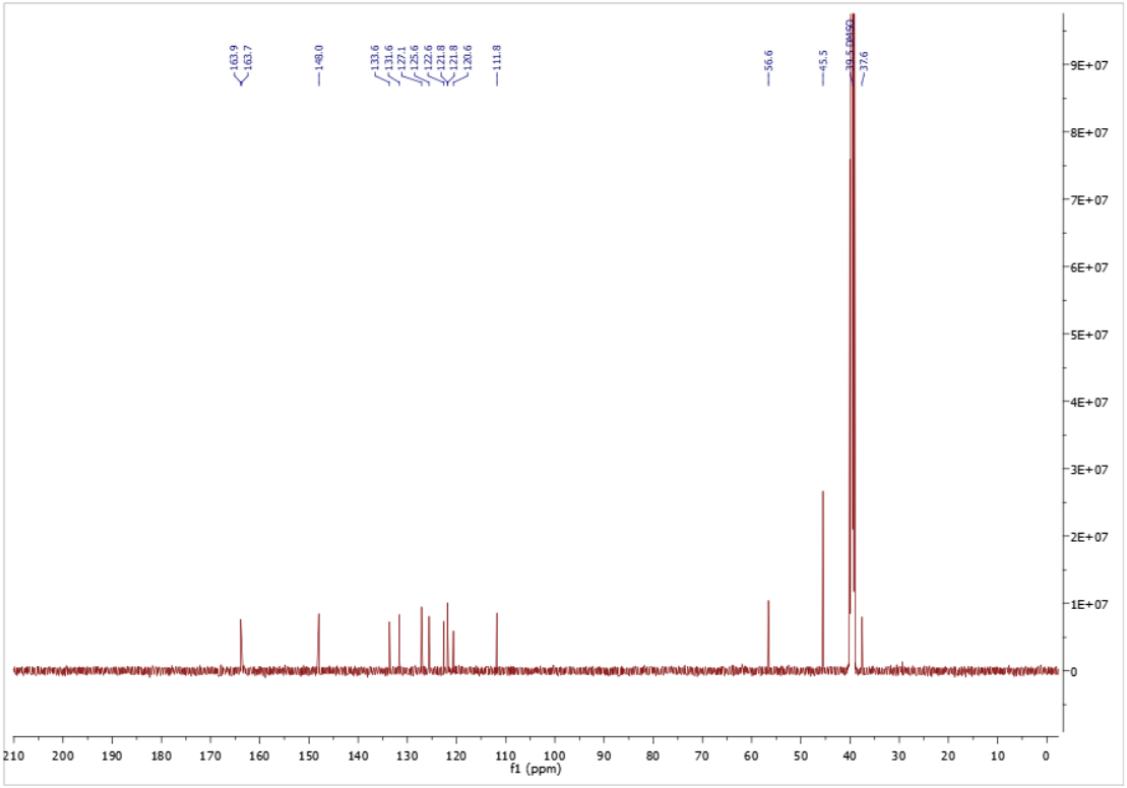

Figure B51: *[13]C NMR spectrum of **3.18***

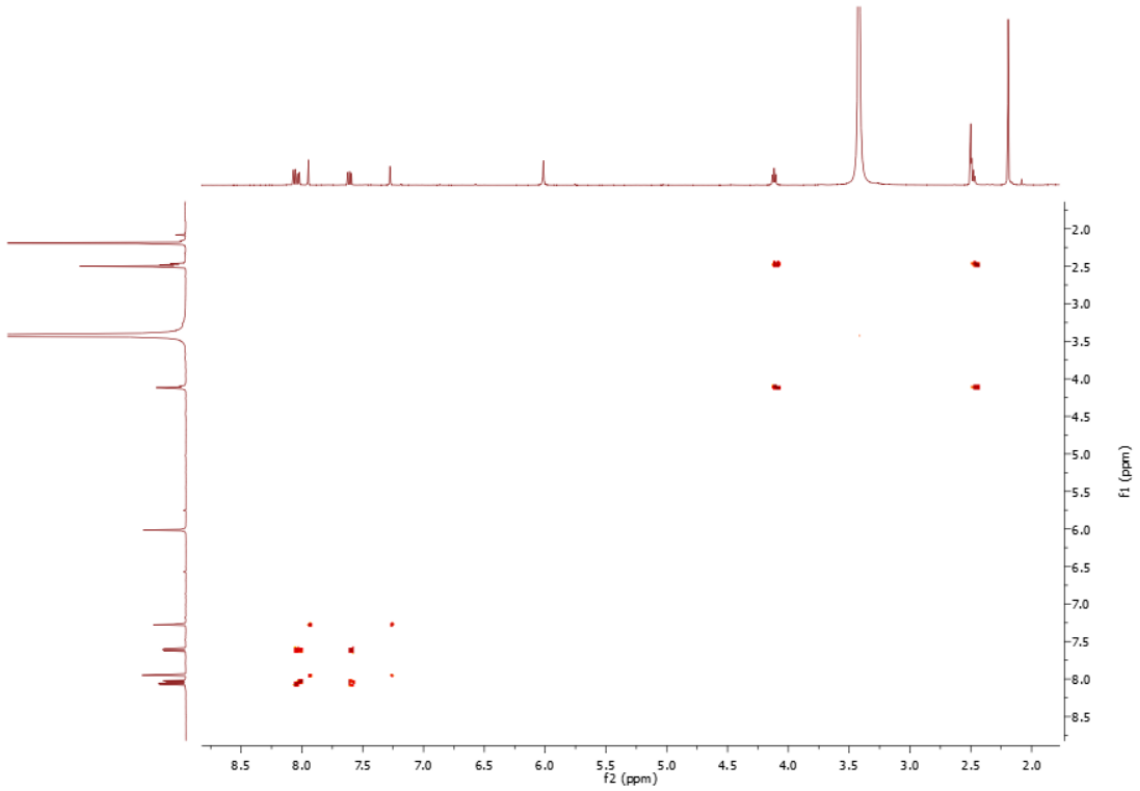

Figure B52: *^{1}H-^{1}H COSY of* ***3.18***

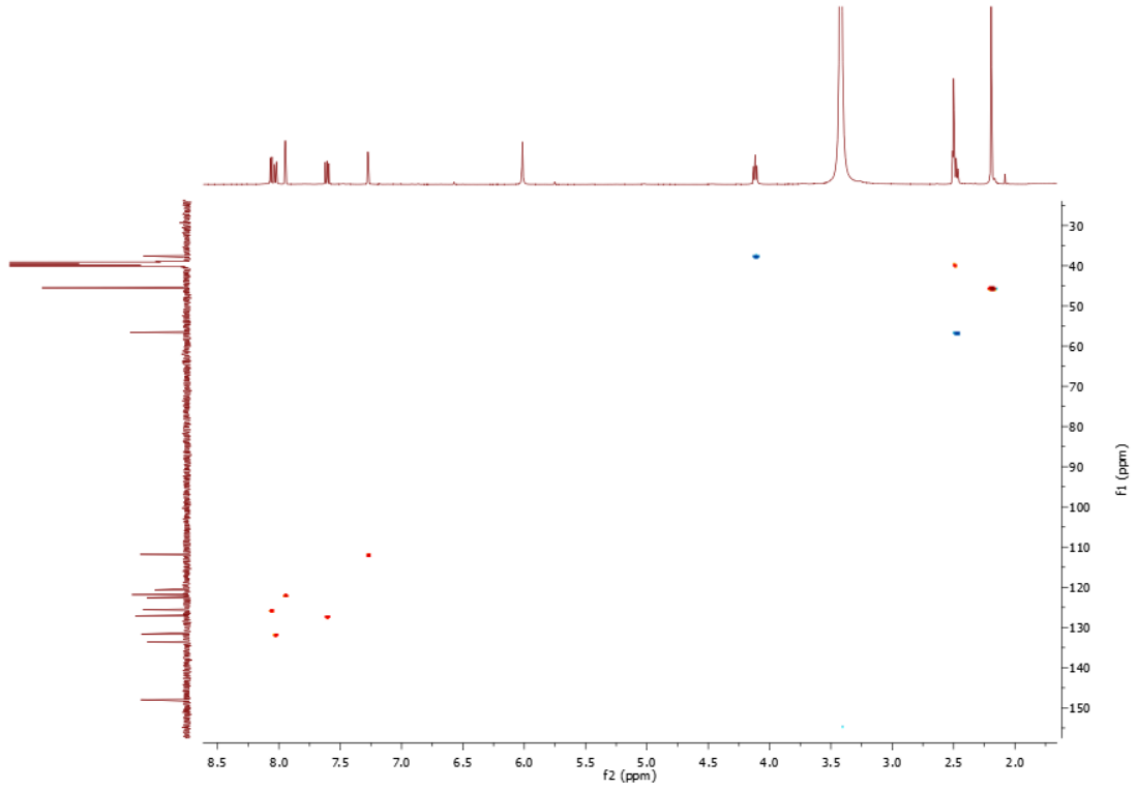

Figure B53: *HSQC of* ***3.18***

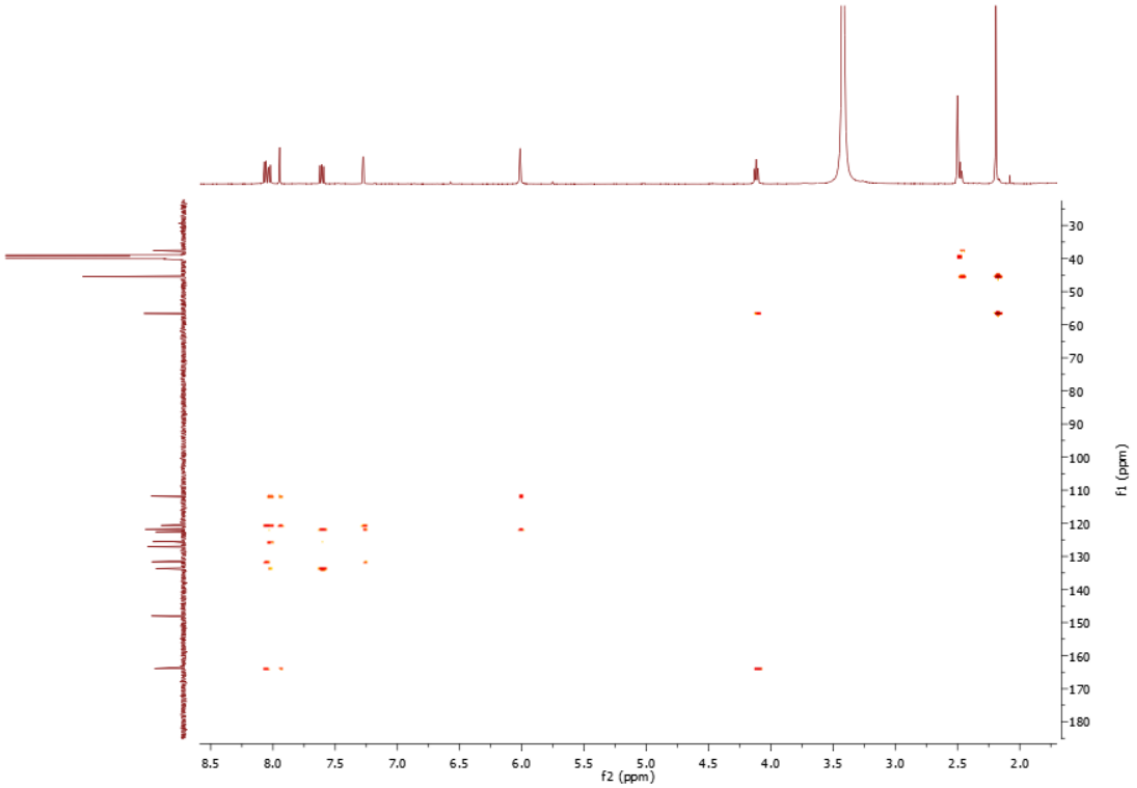

Figure B54: *HMBC of **3.18***

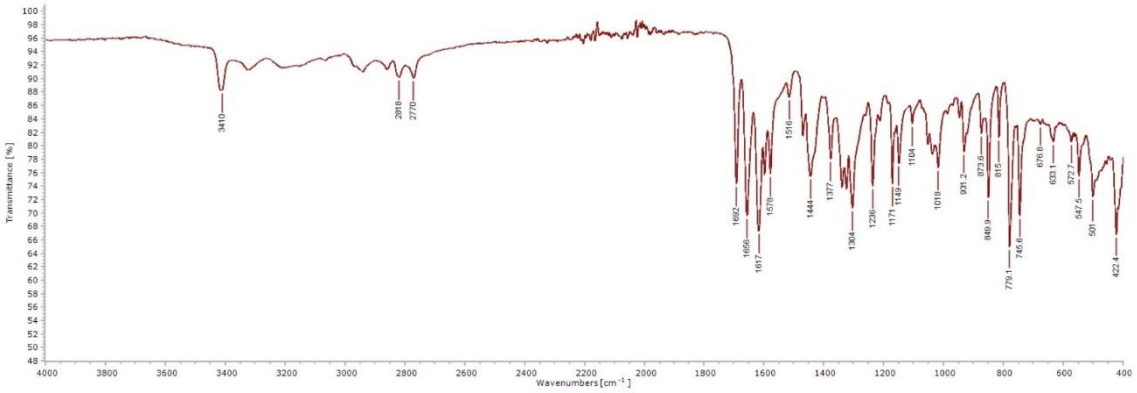

Figure B55: *IR of **3.18***

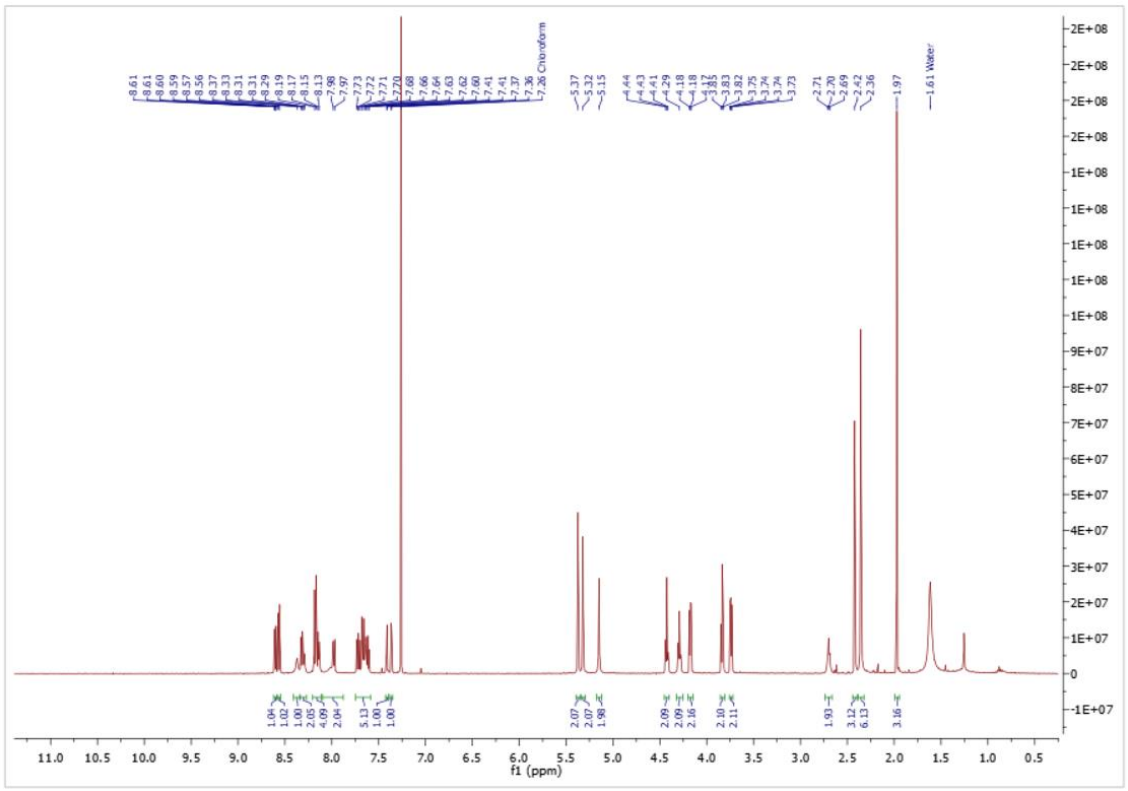

Figure B56: *[1]H NMR spectrum of **3.8***

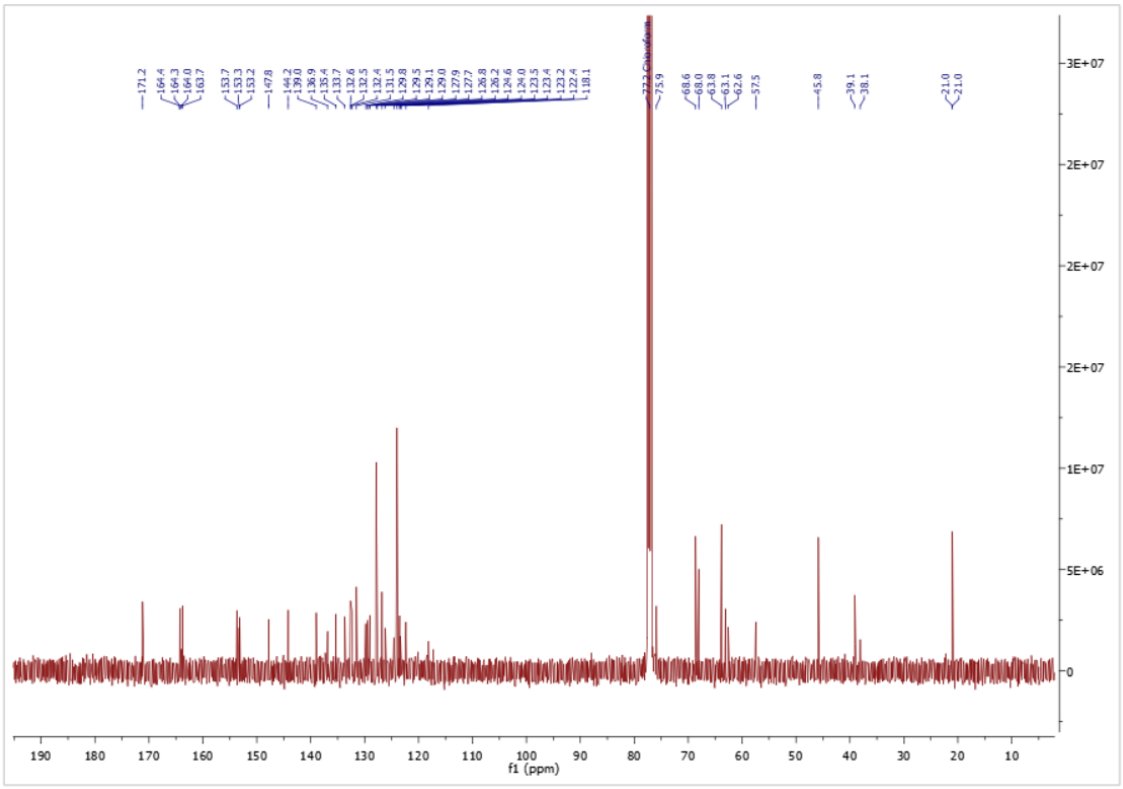

Figure B57: *[13]C NMR spectrum of **3.8***

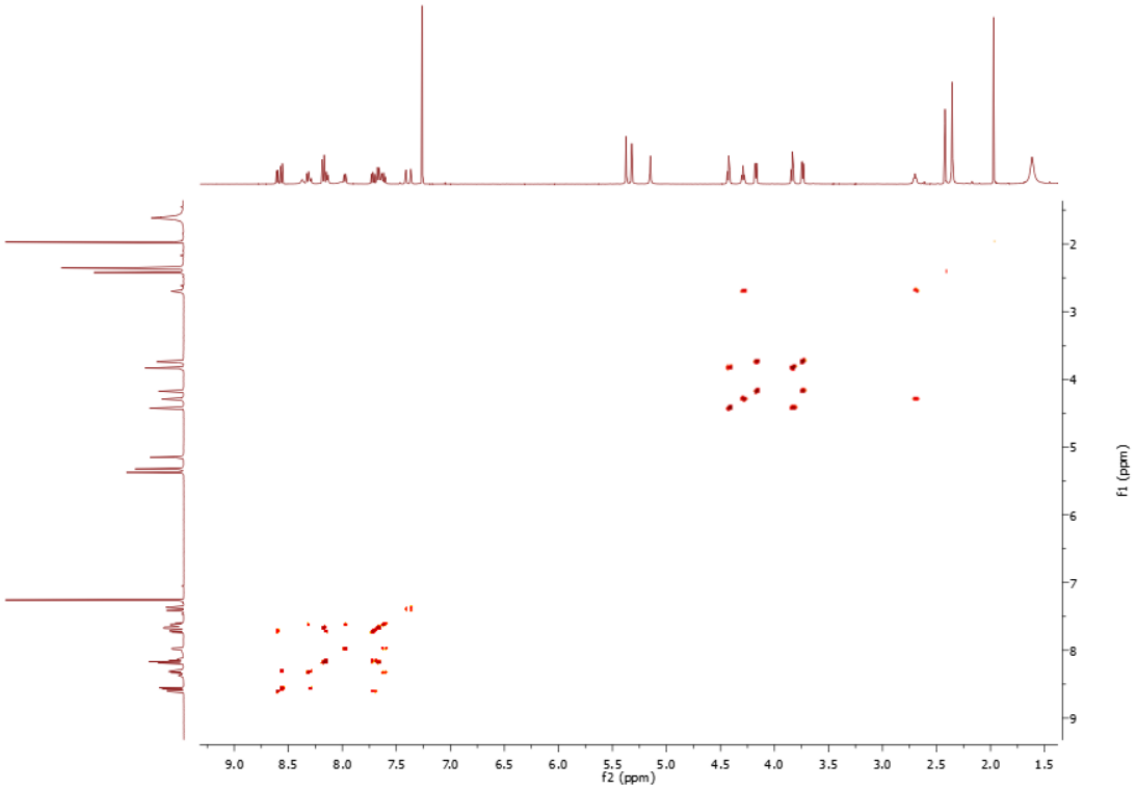

Figure B58: *^{1}H-^{1}H COSY of **3.8***

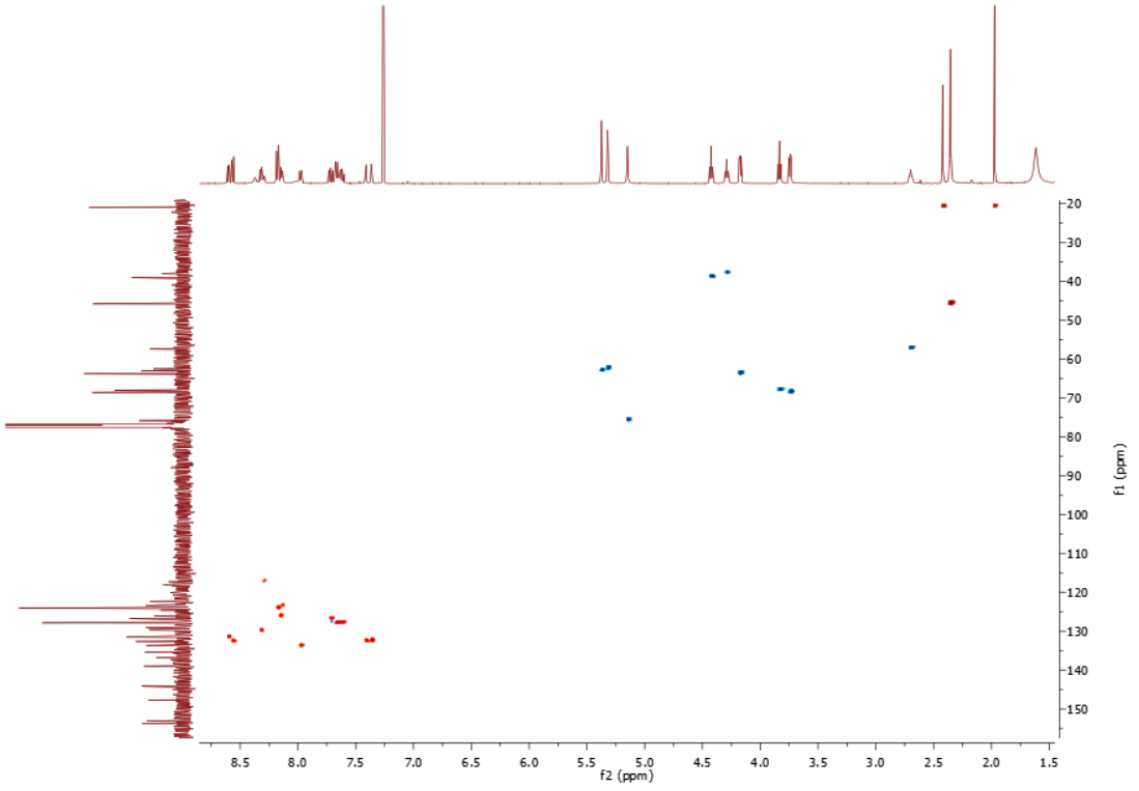

Figure B59: *HSQC of **3.8***

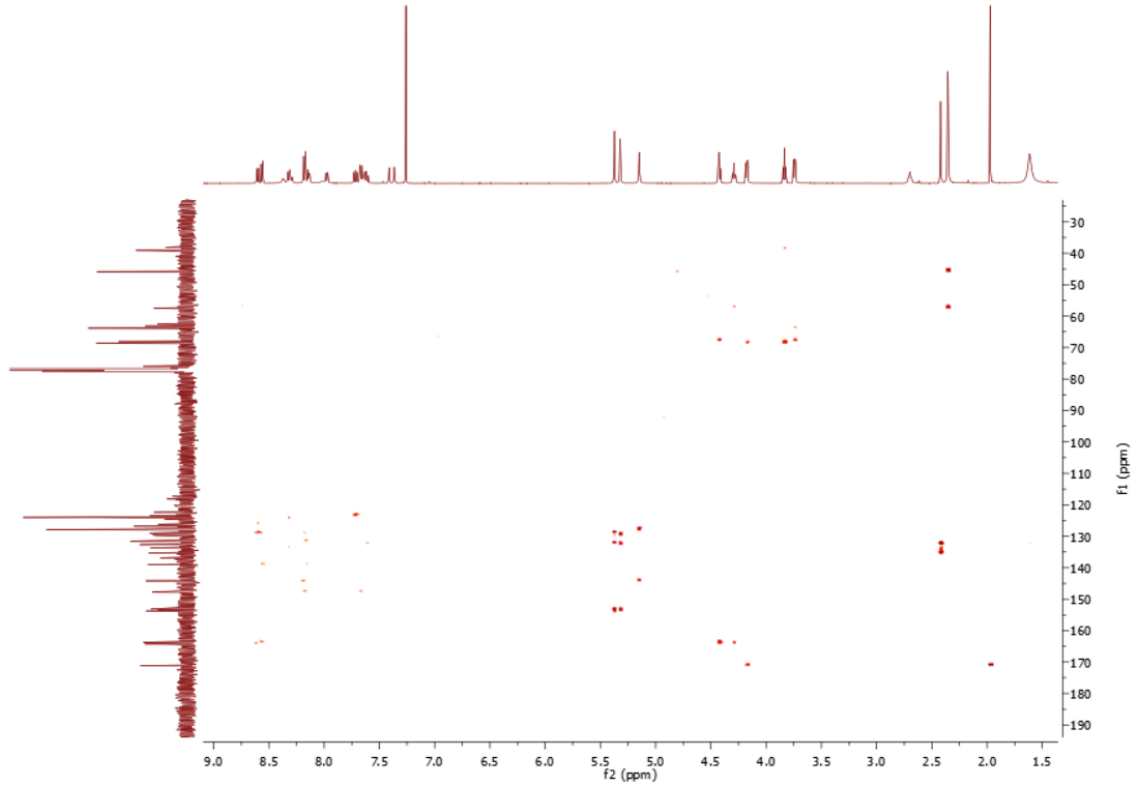

Figure B60: *HMBC of **3.8***

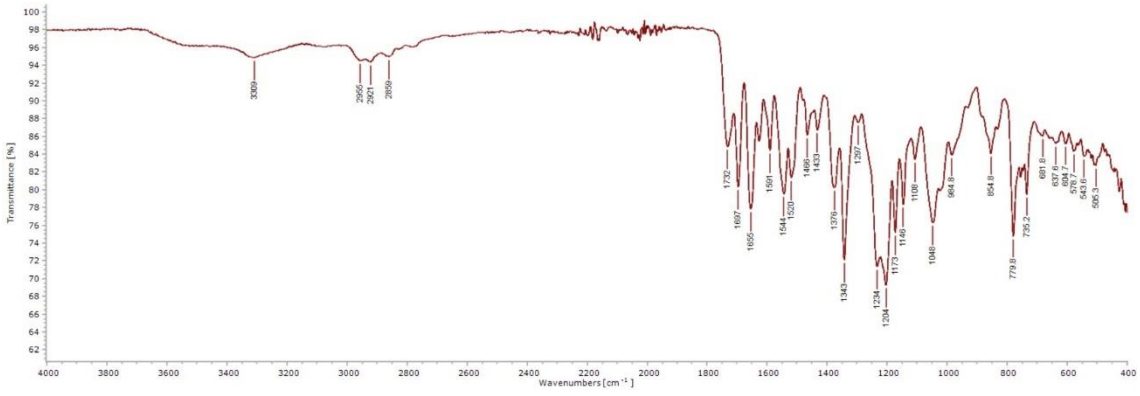

Figure B61: *IR of **3.8***

Compound specific information

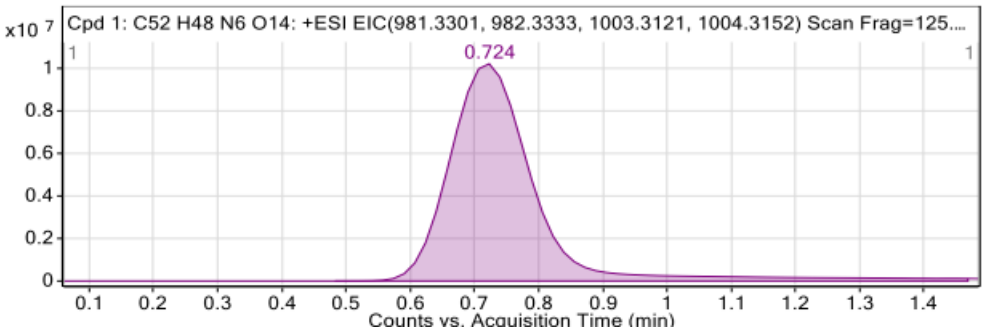

Figure: Full range view of Compound spectra and potential adducts.

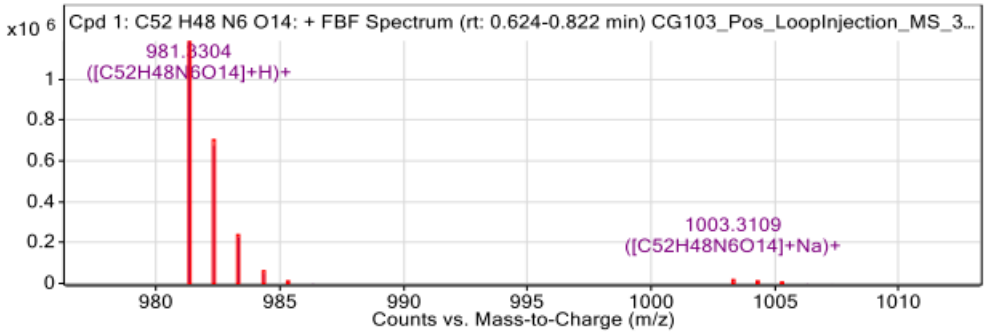

Compound Table

Compound Label	RT (min)	Observed mass (m/z)	Neutral observed mass (Da)	Theoretical mass (Da)	Mass error (ppm)	Isotope match score (%)
Cpd 1: C52 H48 N6 O14	0.72	981.3304	980.3232	980.3229	0.33	99.35

Mass errors of between -5.00 and 5.00 ppm with isotope match scores above 60% are considered confirmation of molecular formulae

Figure B62: *HRMS of* ***3.8***

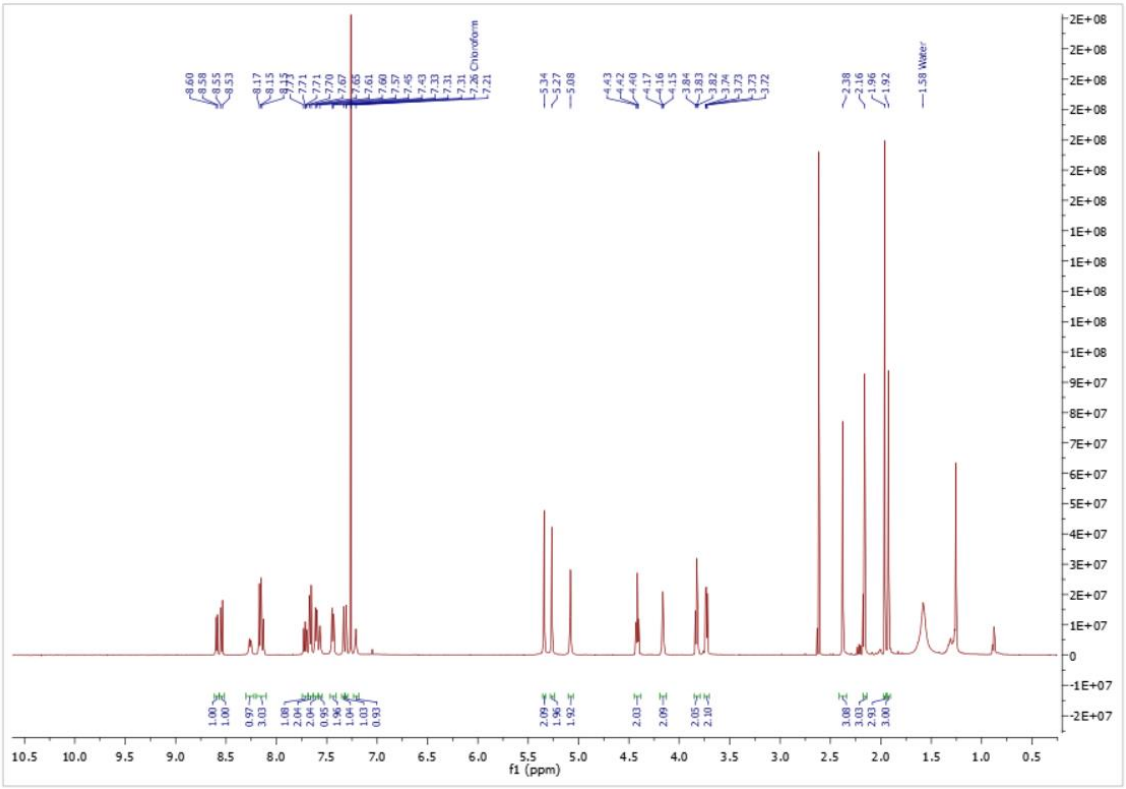

Figure B63: *^{1}H NMR spectrum of* ***3.9***

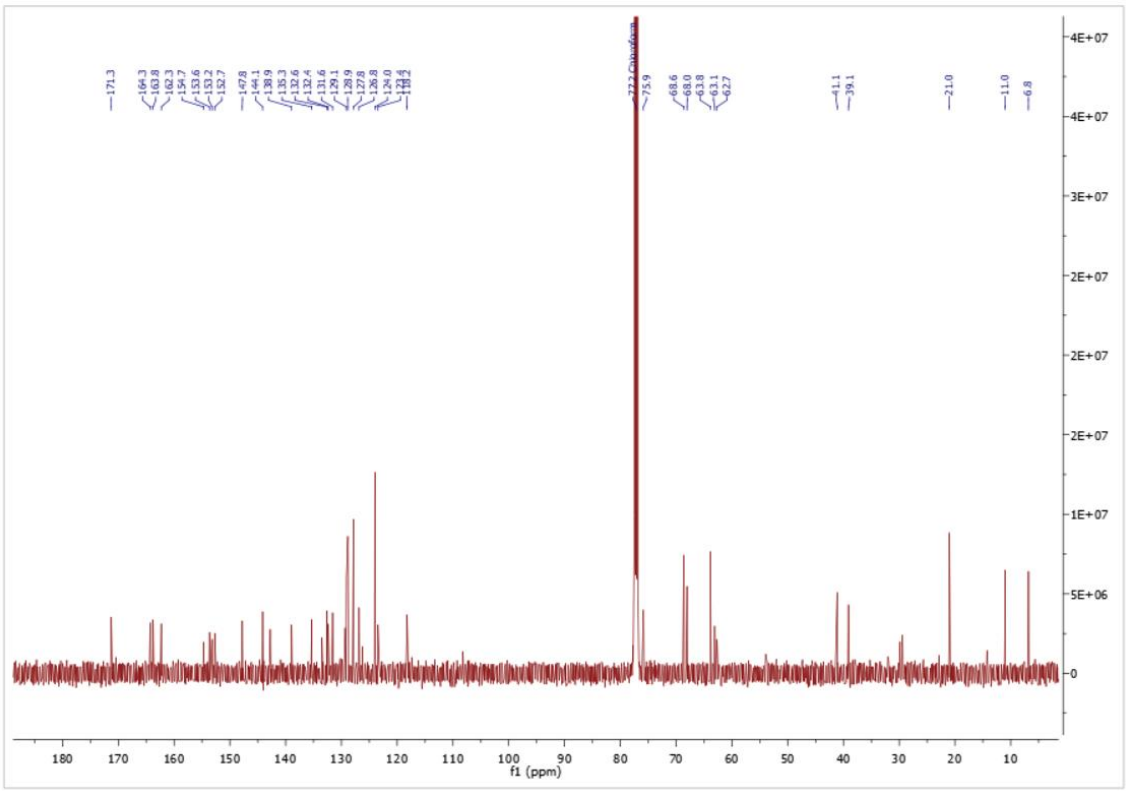

Figure B64: *^{13}C NMR spectrum of **3.9***

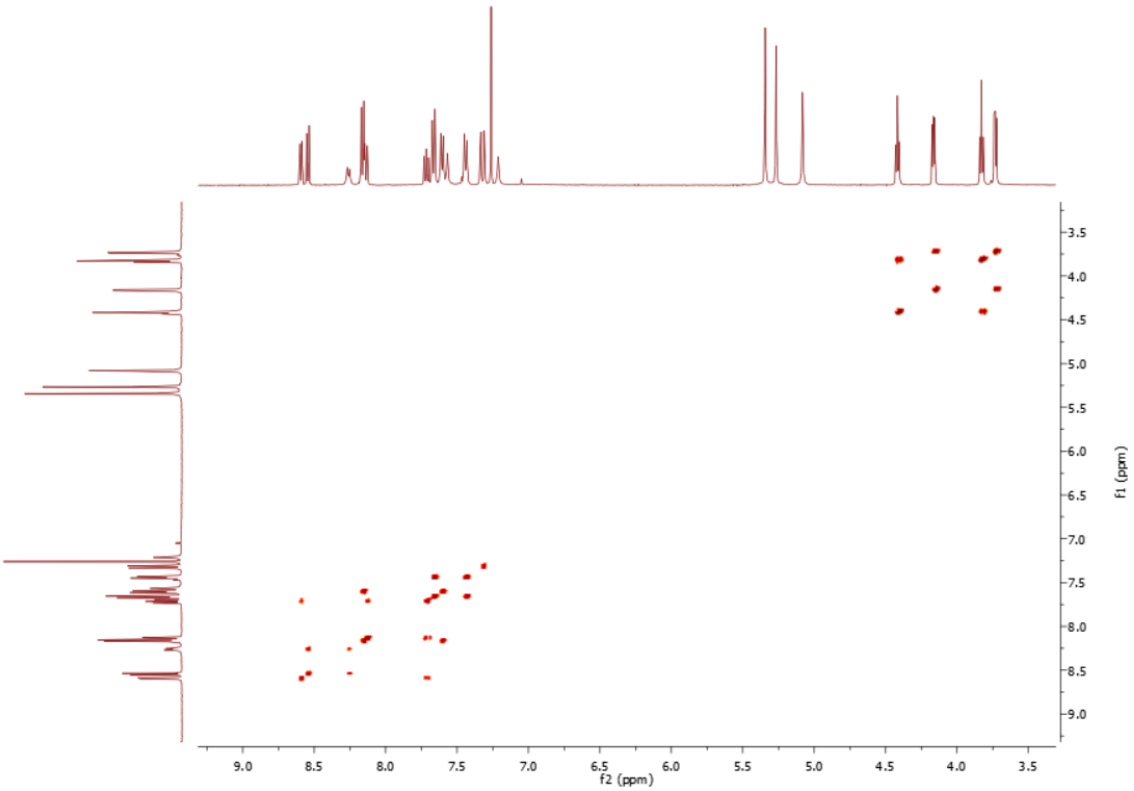

Figure B65: *^{1}H-^{1}H COSY of **3.9***

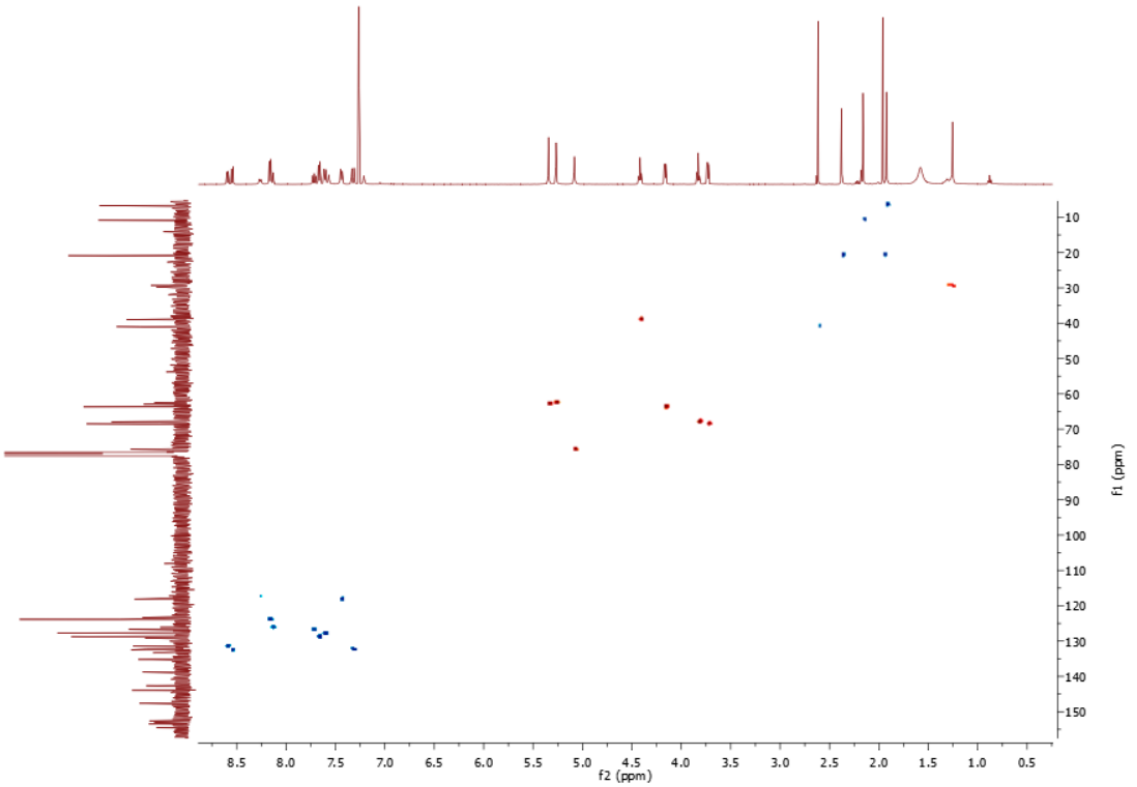

Figure B66: *HSQC of **3.9***

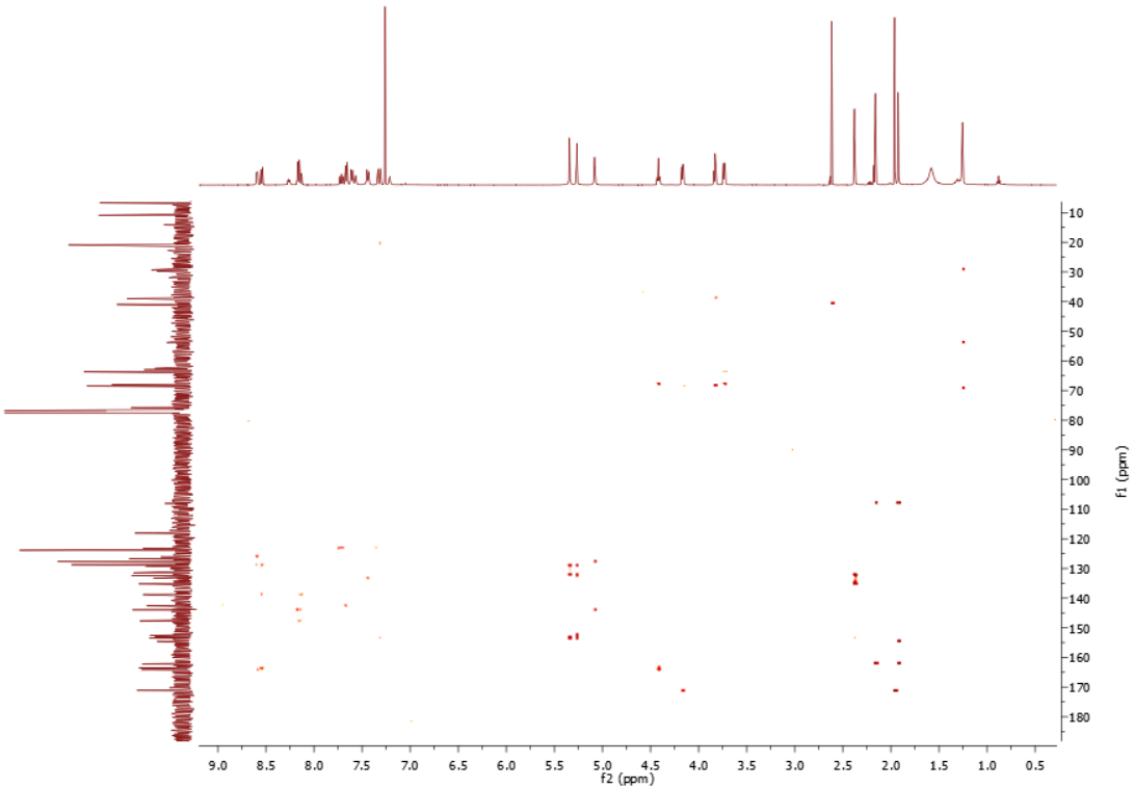

Figure B67: *HMBC of **3.9***

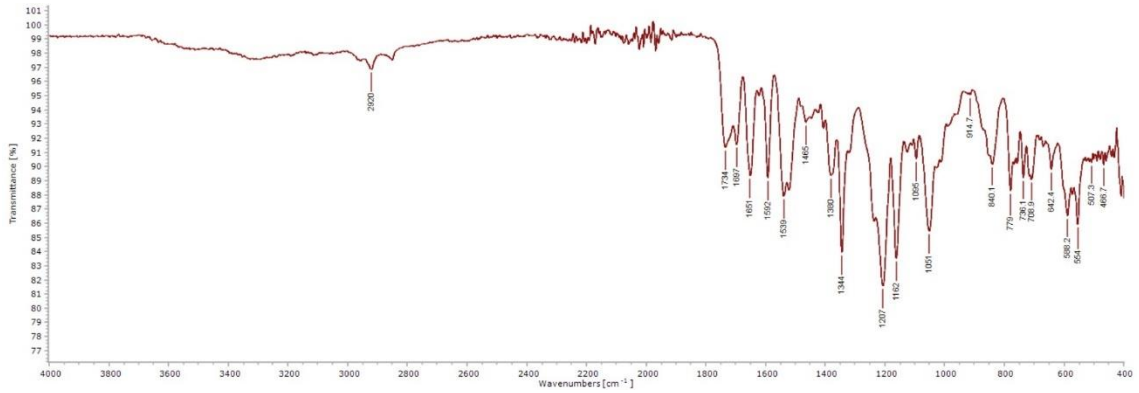

Figure B68: *IR of* ***3.9***

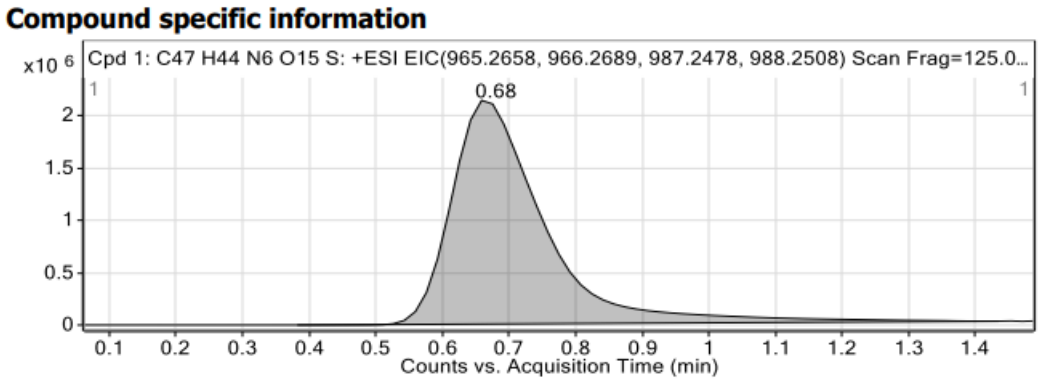

Figure: Full range view of Compound spectra and potential adducts.

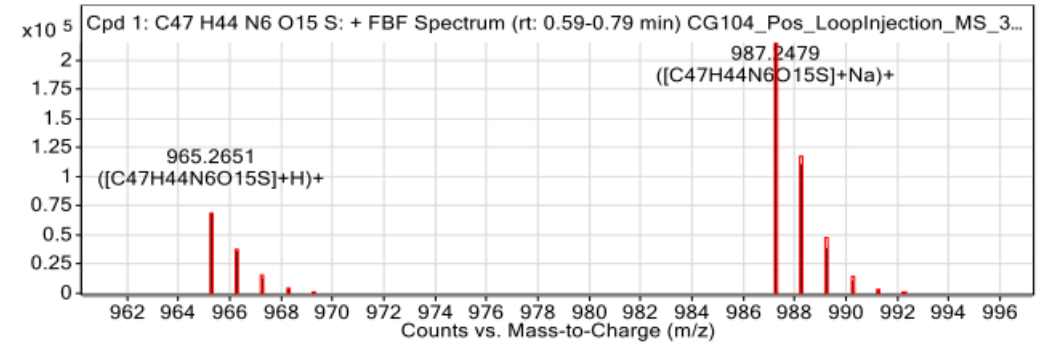

Compound Table

Compound Label	RT (min)	Observed mass (m/z)	Neutral observed mass (Da)	Theoretical mass (Da)	Mass error (ppm)	Isotope match score (%)
Cpd 1: C47 H44 N6 O15 S	0.68	965.2651	964.2584	964.2585	-0.18	98.21

Mass errors of between -5.00 and 5.00 ppm with isotope match scores above 60% are considered confirmation of molecular formulae

Figure B69: *HRMS of* ***3.9***

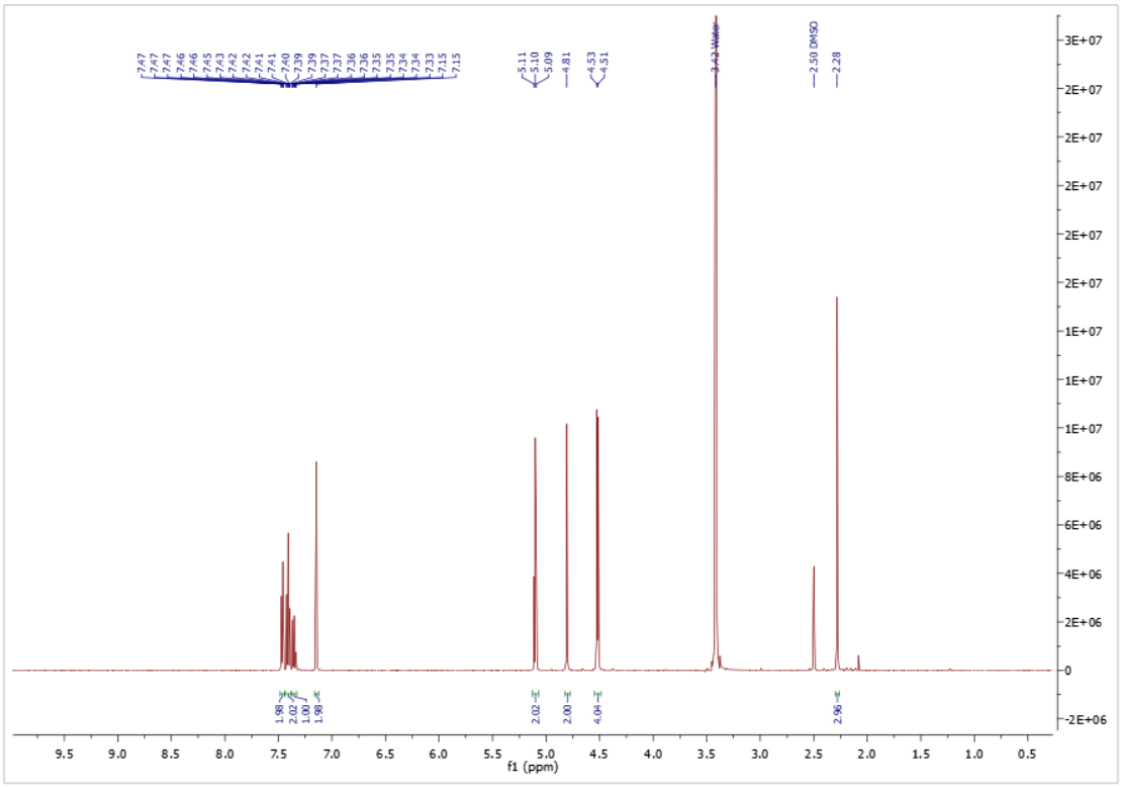

Figure B70: *[1]H NMR spectrum of **3.22***

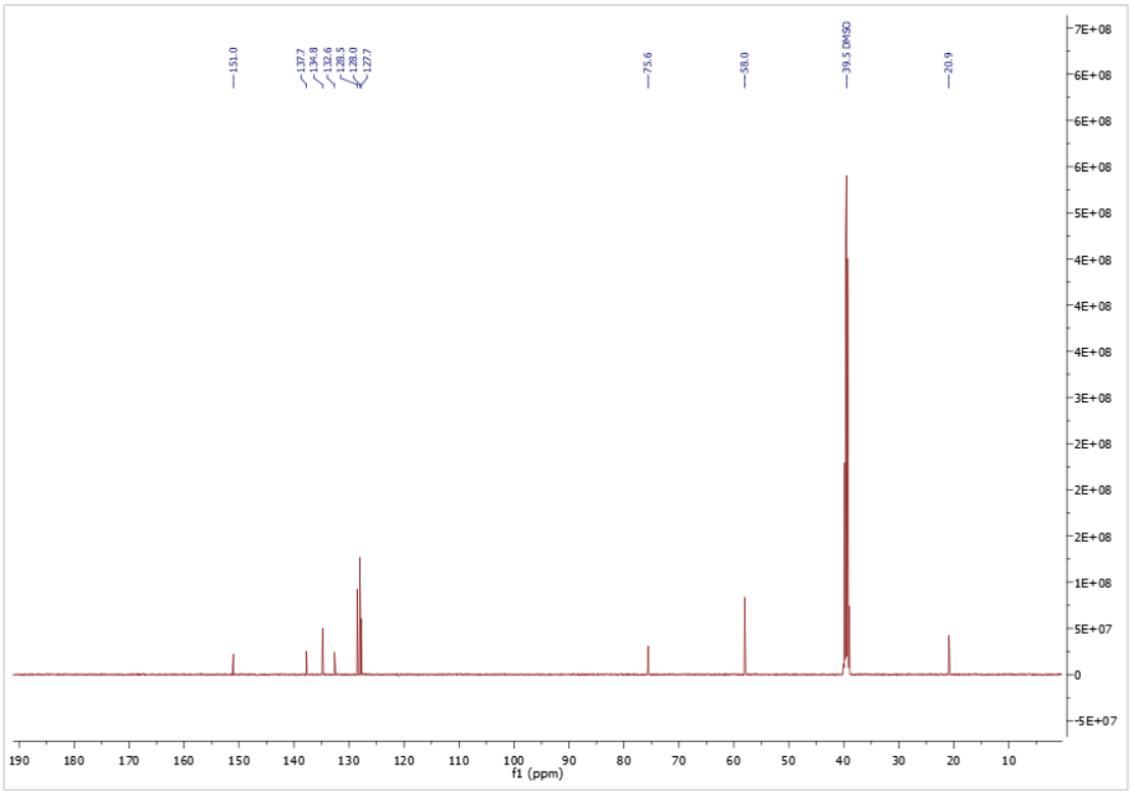

Figure B71: *[13]C NMR spectrum of **3.22***

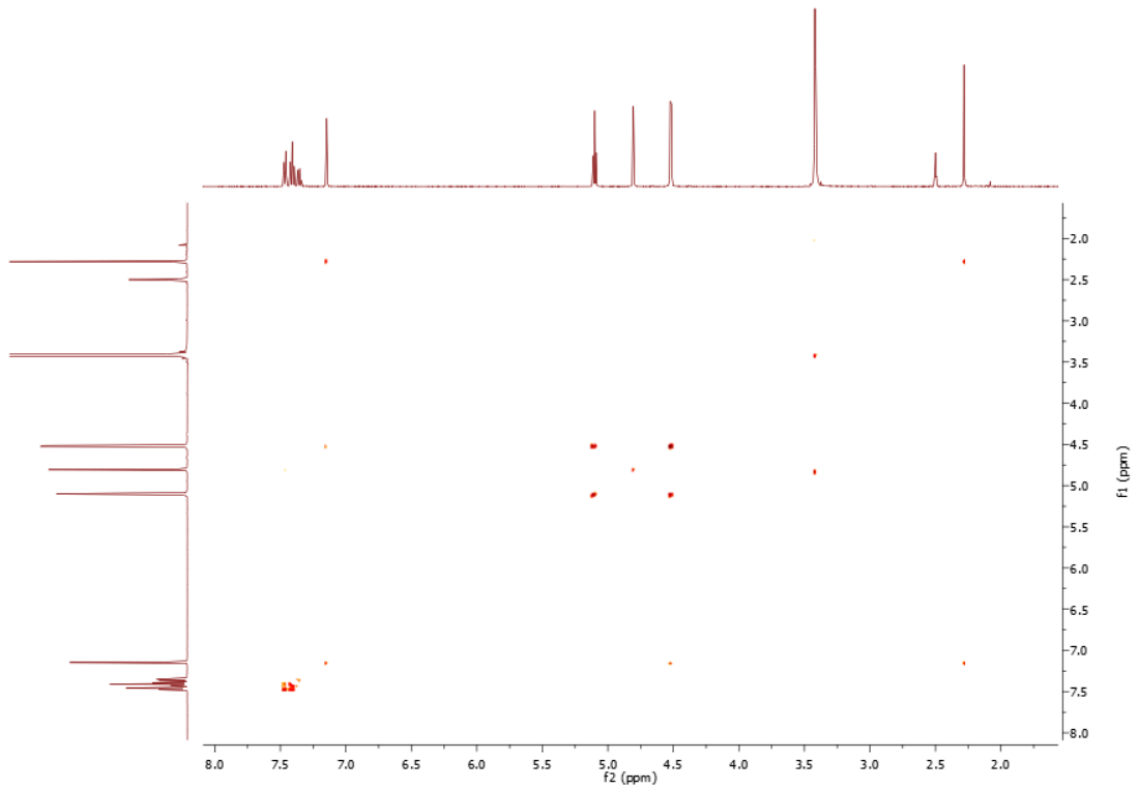

Figure B72: *^{1}H-^{1}H COSY of* ***3.22***

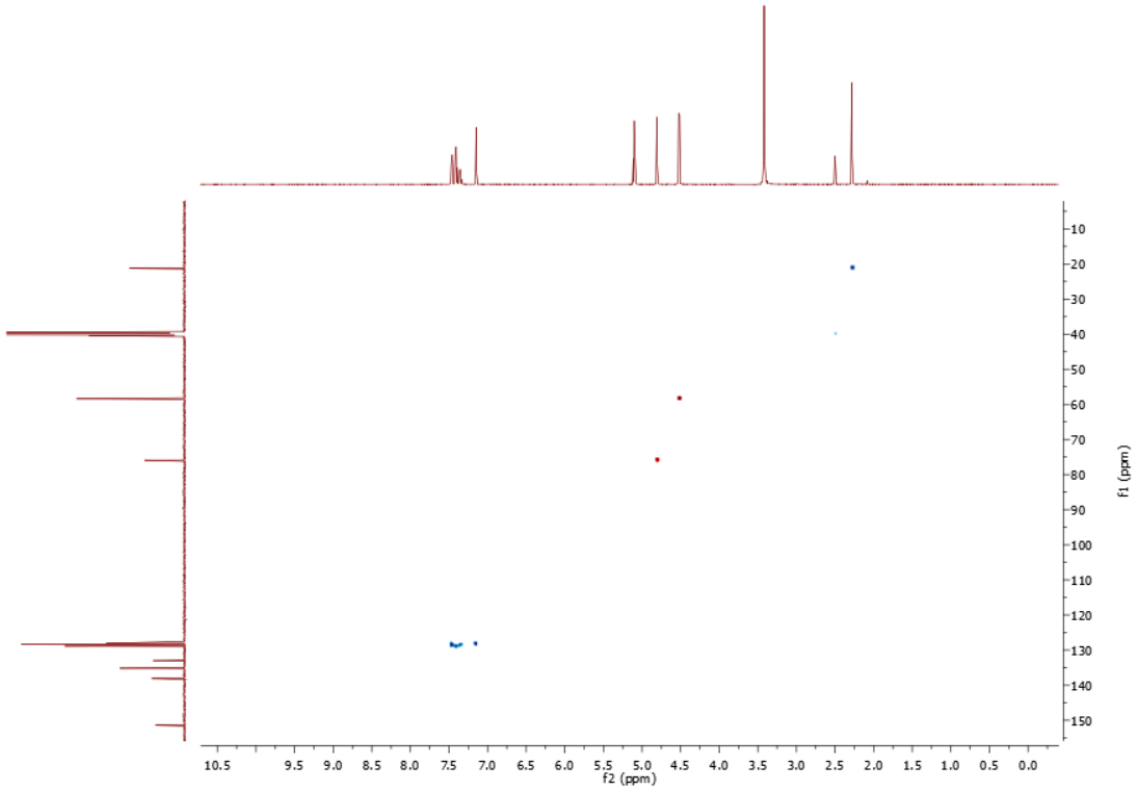

Figure B73: *HSQC of* ***3.22***

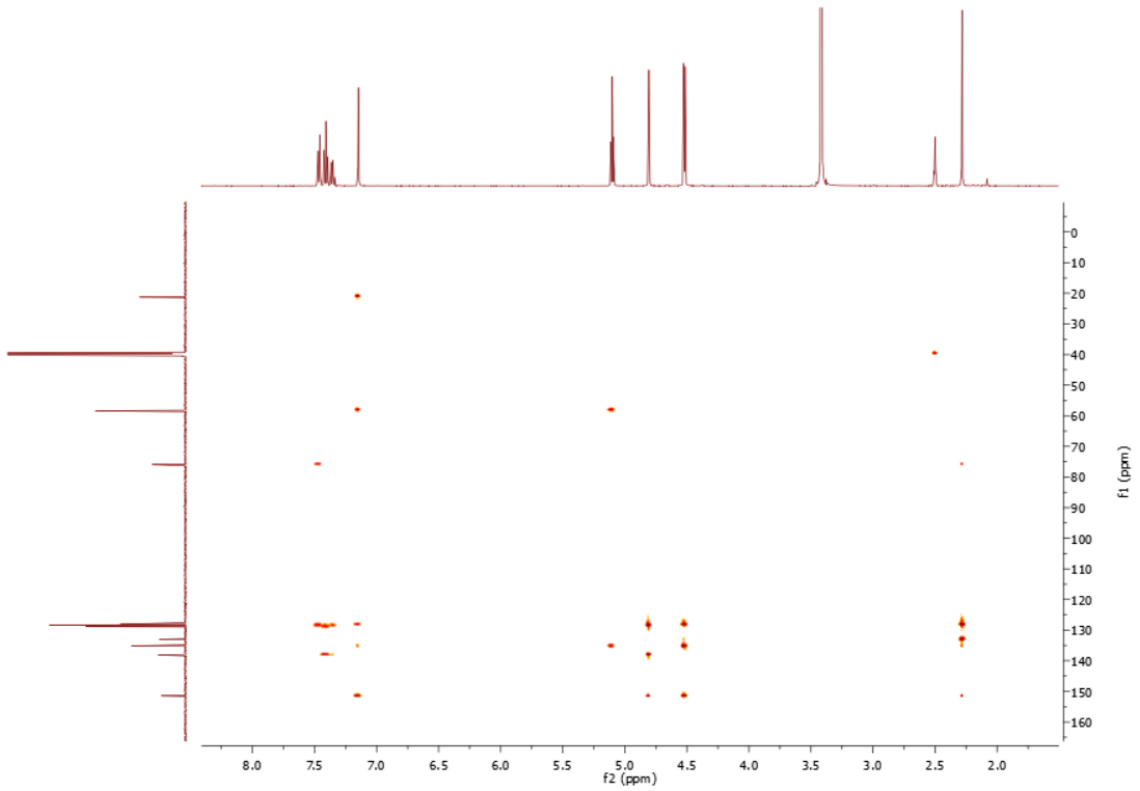

Figure B74: *HMBC of **3.22***

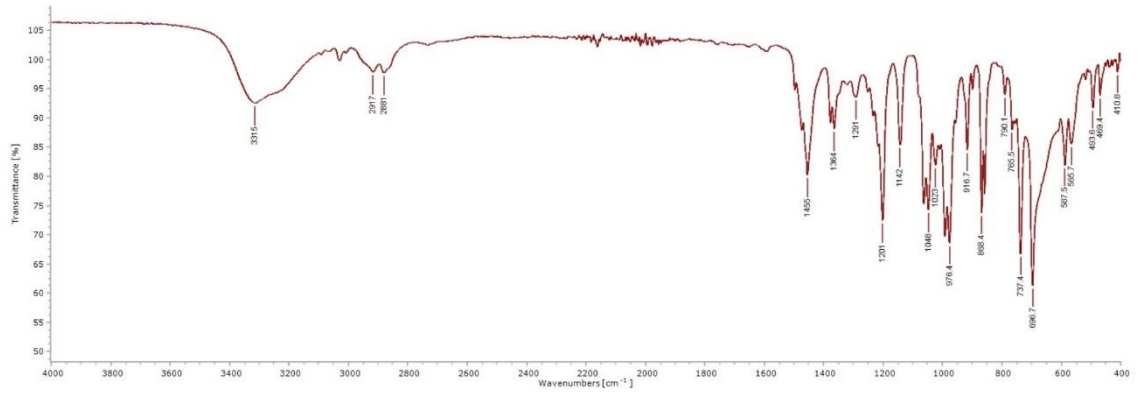

Figure B75: *IR of **3.22***

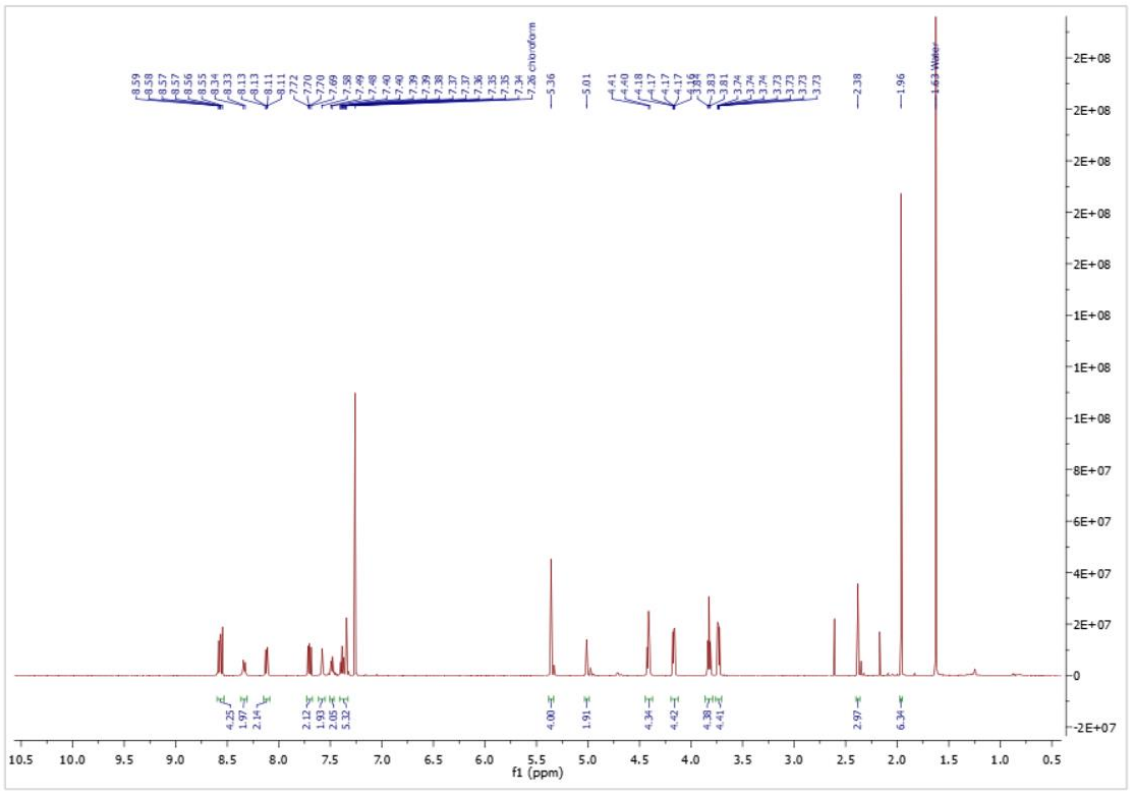

Figure B76: *[1]H NMR spectrum of* ***3.21***

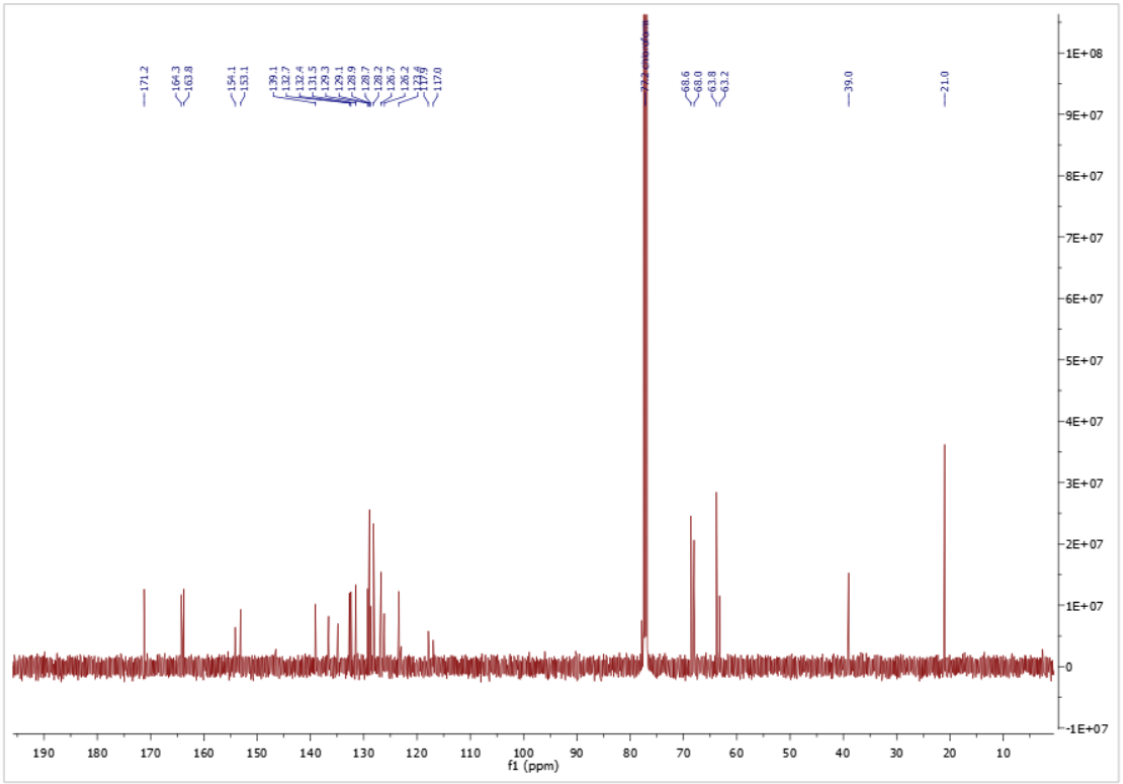

Figure B77: *[13]C NMR spectrum of* ***3.21***

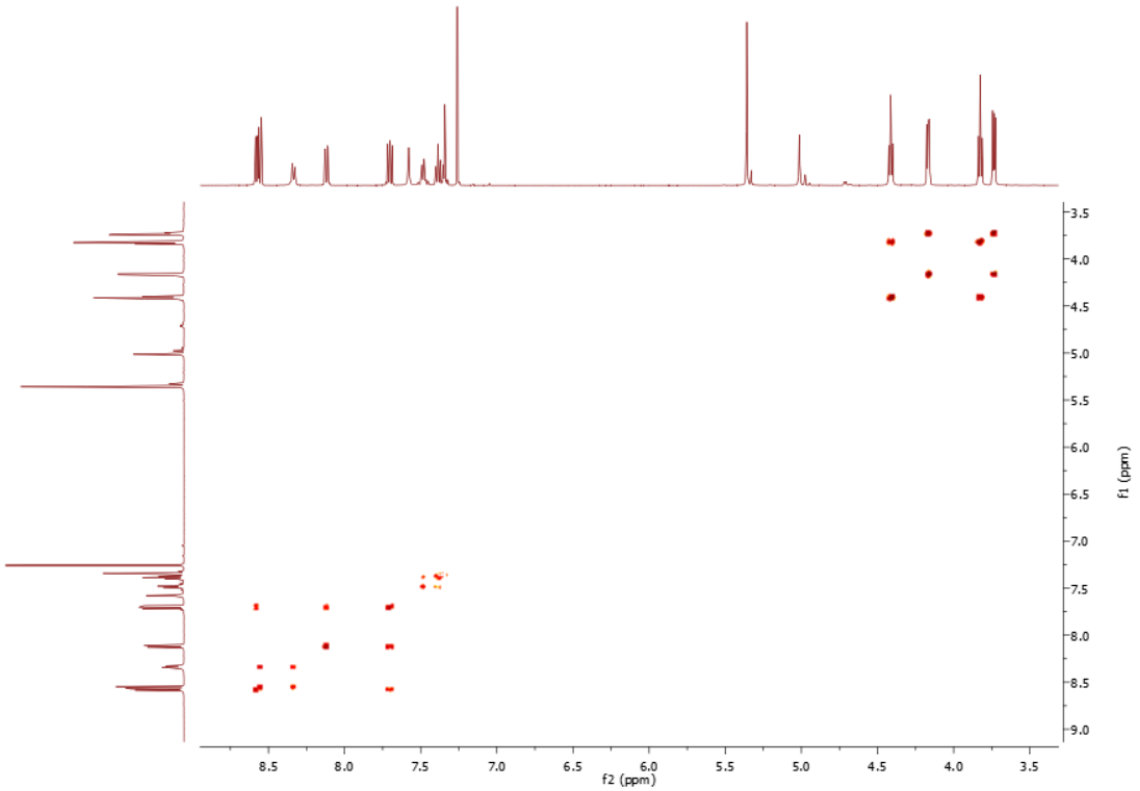

Figure B78: *^{1}H-^{1}H COSY of* ***3.21***

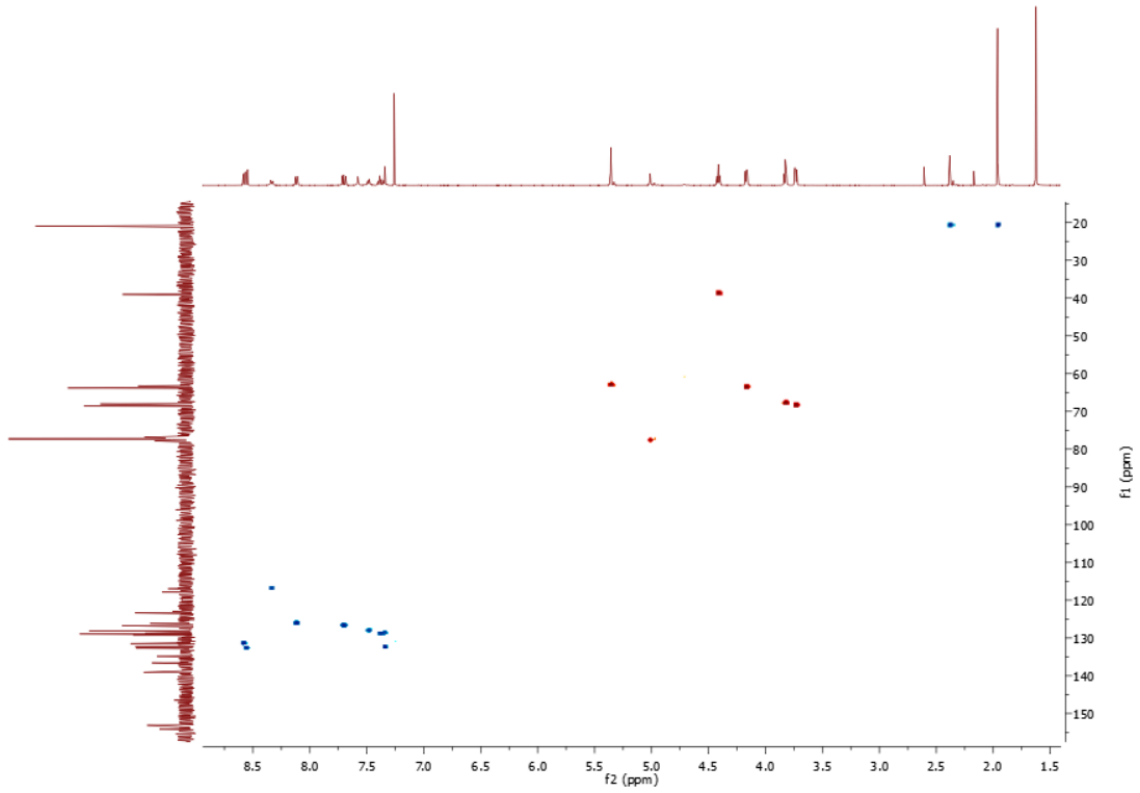

Figure B79: *HSQC of* ***3.21***

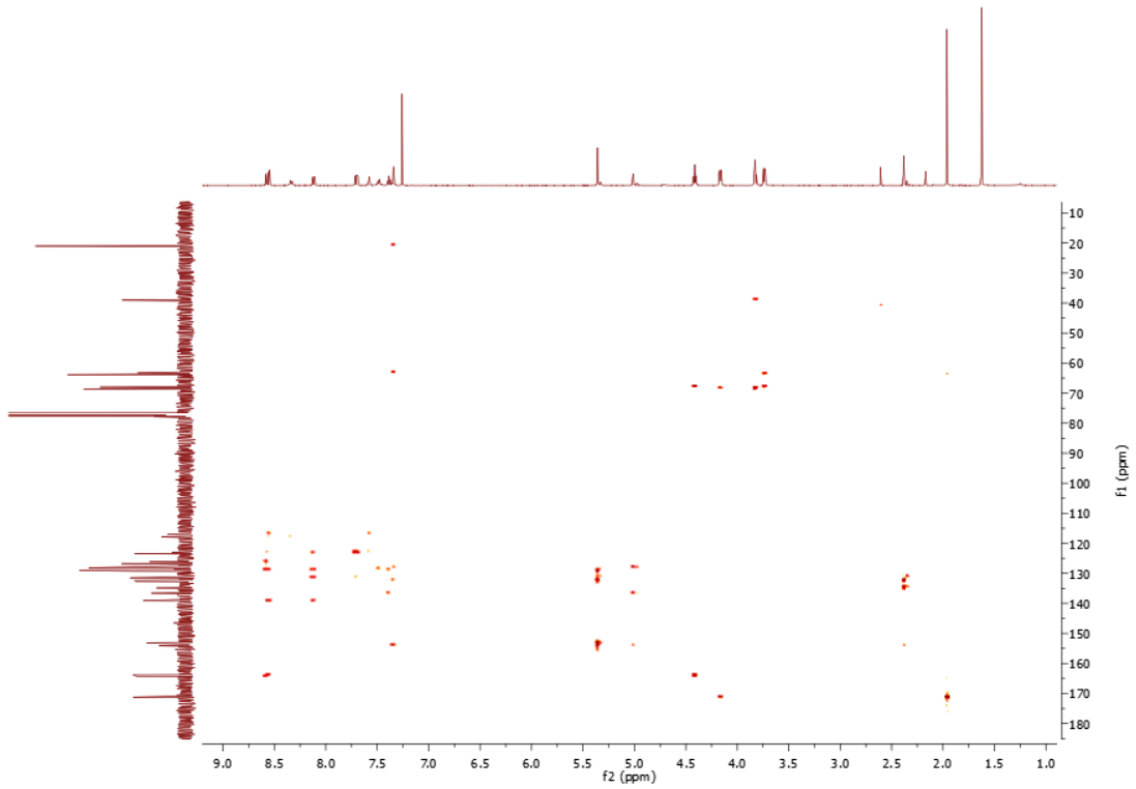

Figure B80: *HMBC of **3.21***

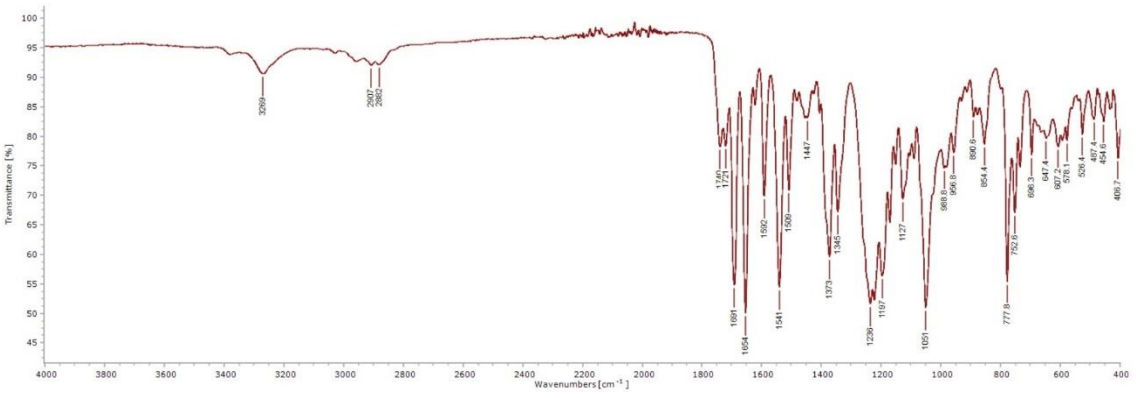

Figure B81: *IR of **3.21***

Compound specific information

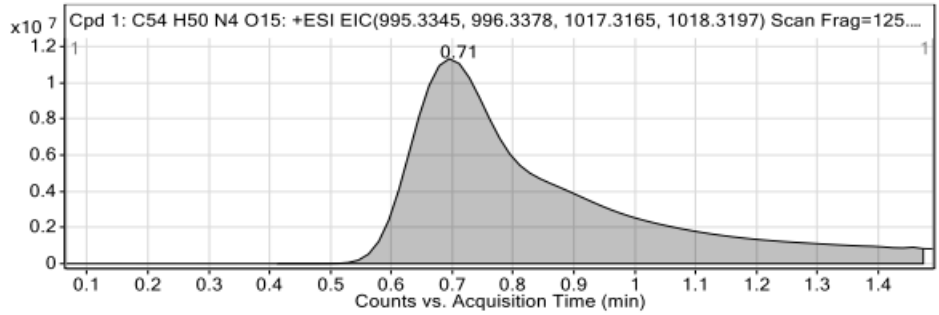

Figure: Full range view of Compound spectra and potential adducts.

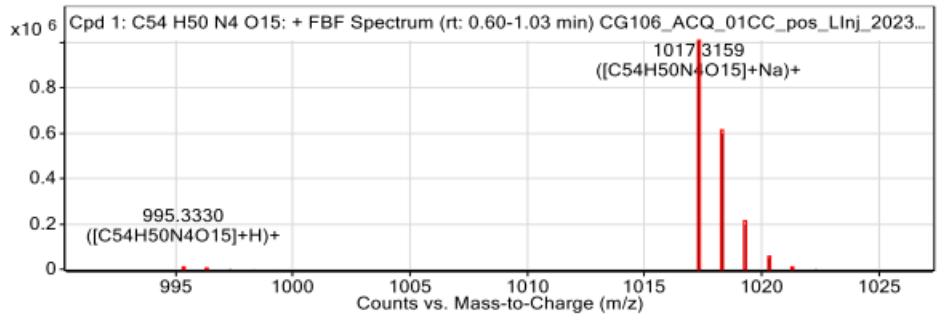

Compound Table

Compound Label	RT (min)	Observed mass (m/z)	Neutral observed mass (Da)	Theoretical mass (Da)	Mass error (ppm)	Isotope match score (%)
Cpd 1: C54 H50 N4 O15	0.71	1017.3159	994.3267	994.3273	-0.53	99.40

Mass errors of between -5.00 and 5.00 ppm with isotope match scores above 60% are considered confirmation of molecular formulae

Figure B82: *HRMS of* ***3.21***

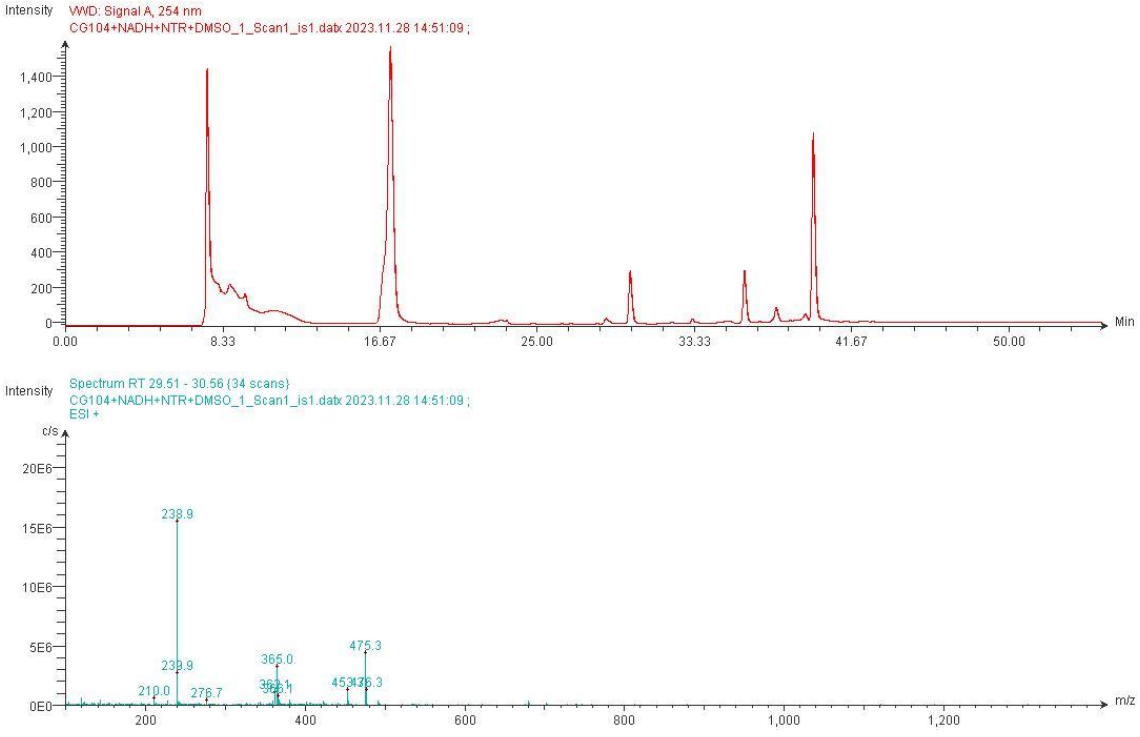

Figure B83: *ESI + spectrum corresponding to the peak at Rt = 29.90 minutes*

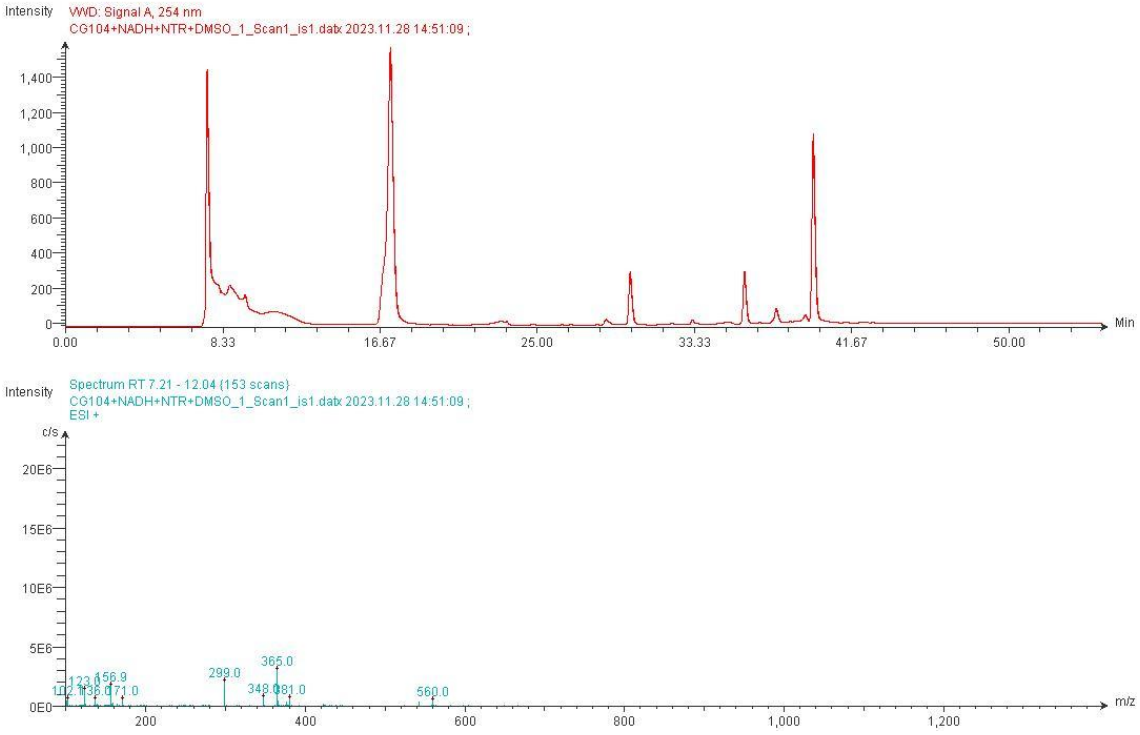

Figure B83: *ESI + spectrum corresponding to the peak at Rt = 7.47 minutes*

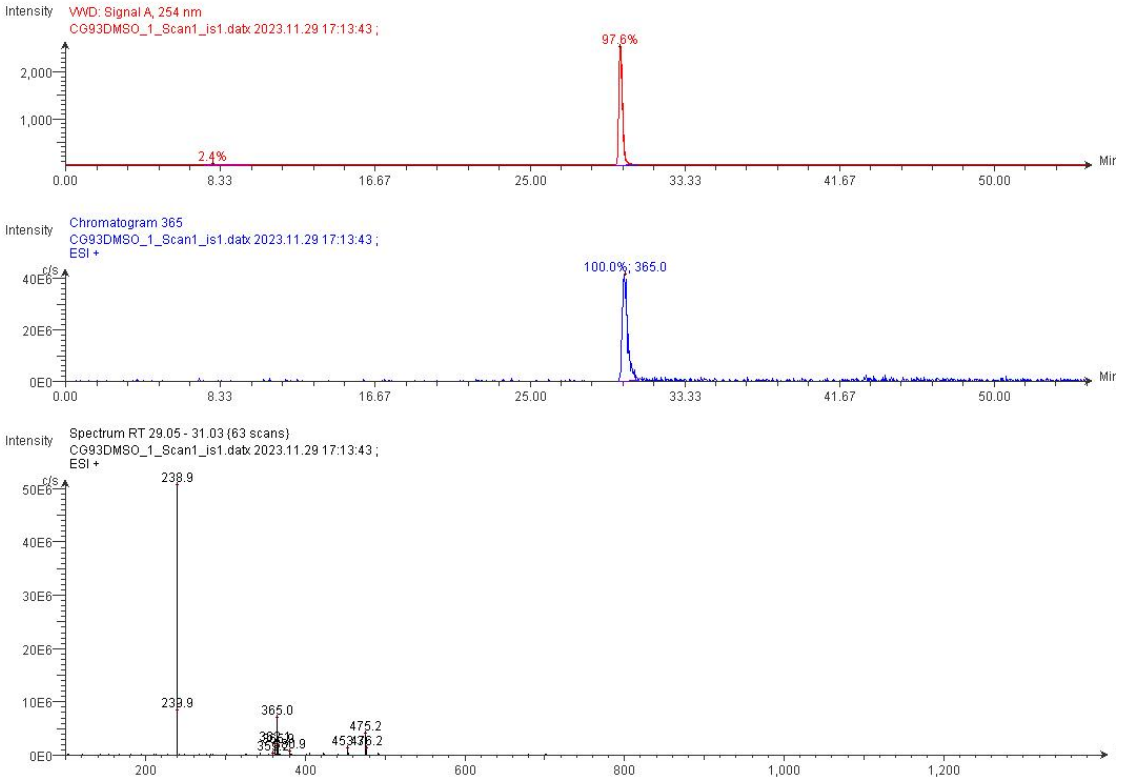

Figure B83: *LCMS of **3.12**.*

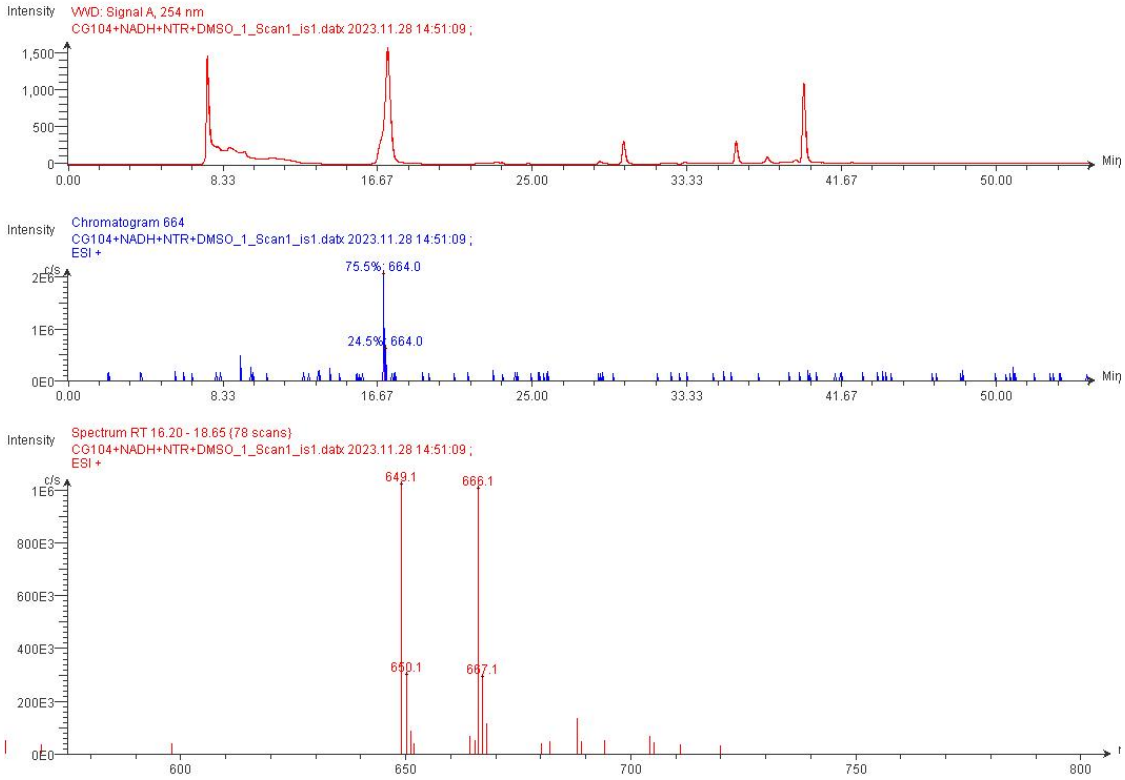

Figure B83: *ESI + spectrum corresponding to the peak at Rt = 17.19 minutes*

Chapter 4 Appendix Data

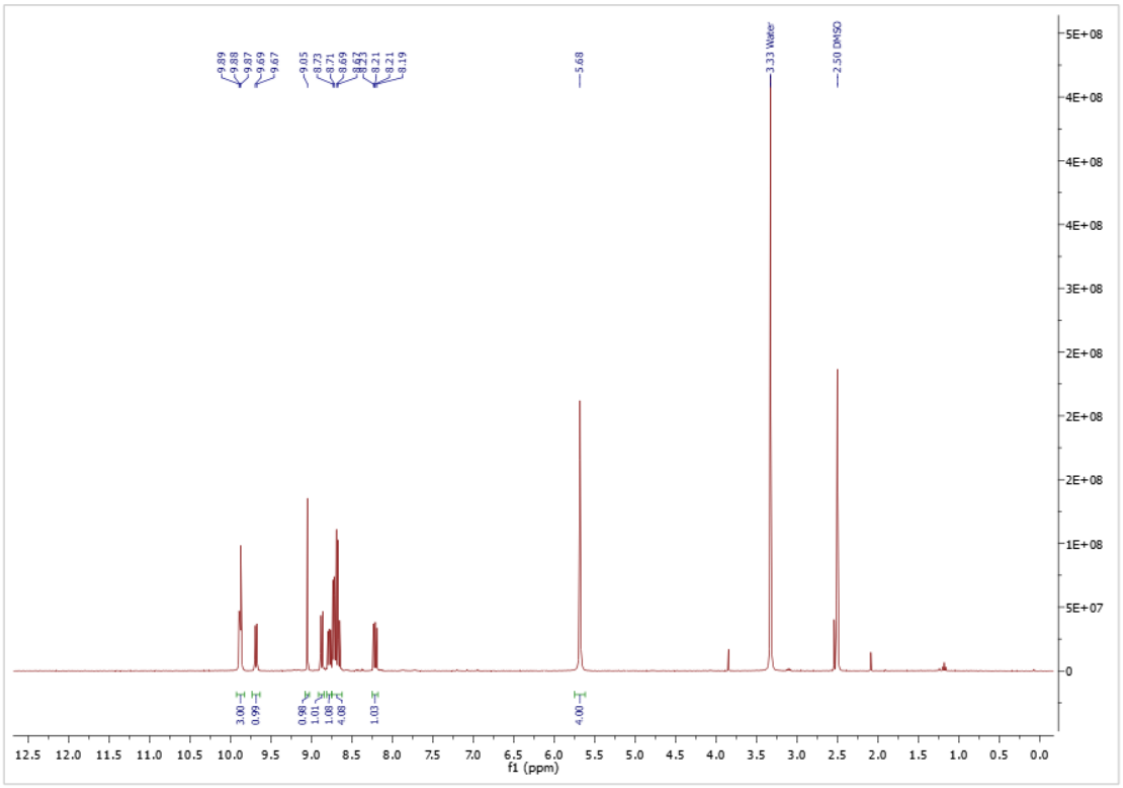

Figure C1: *[1]H NMR spectrum of **4.7***

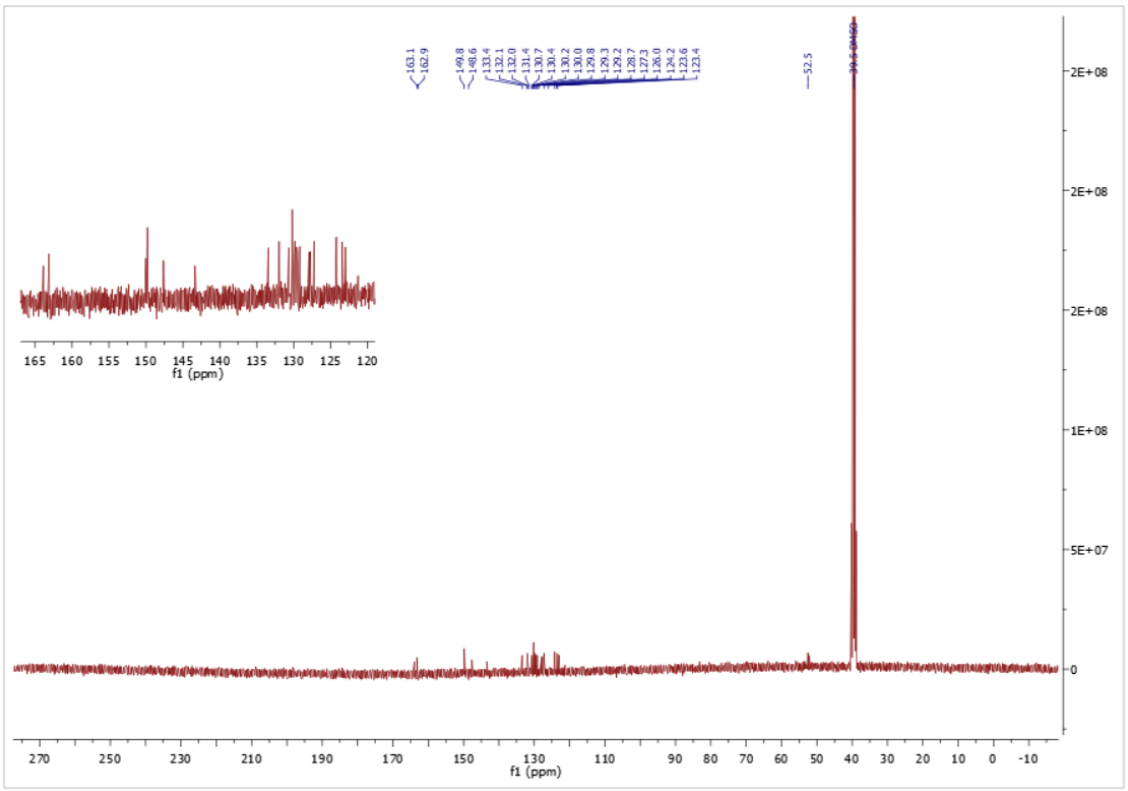

Figure C2: *[13]C NMR spectrum of **4.7***

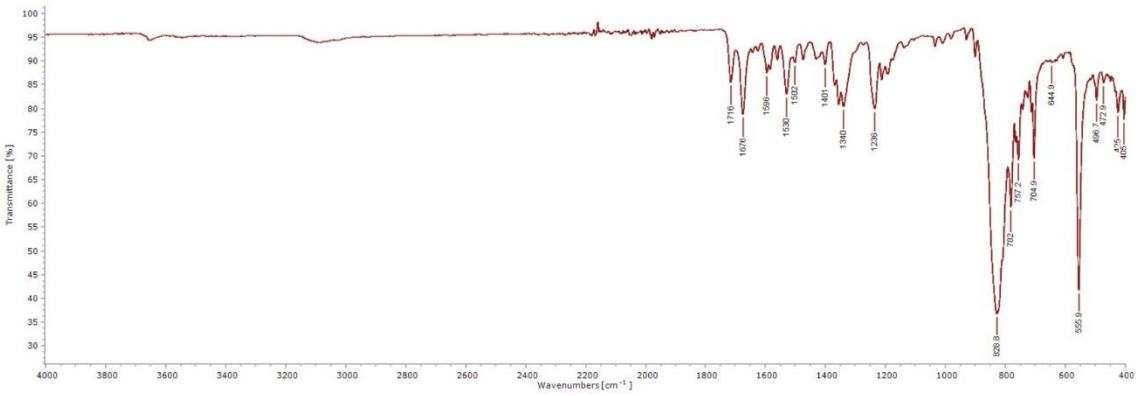

Figure C3: *IR of **4.7***

Compound specific information

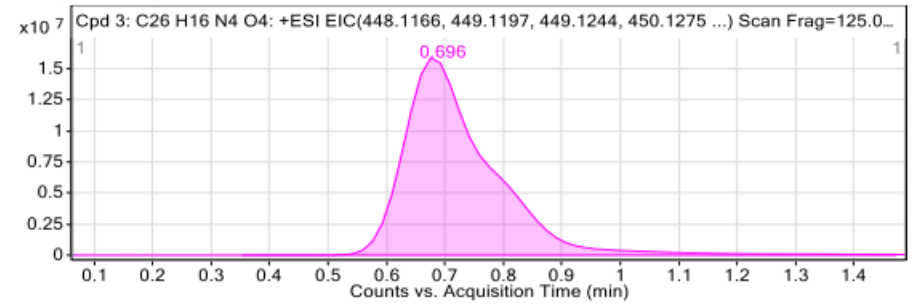

Figure: Extracted ion chromatogram (EIC) of compound.

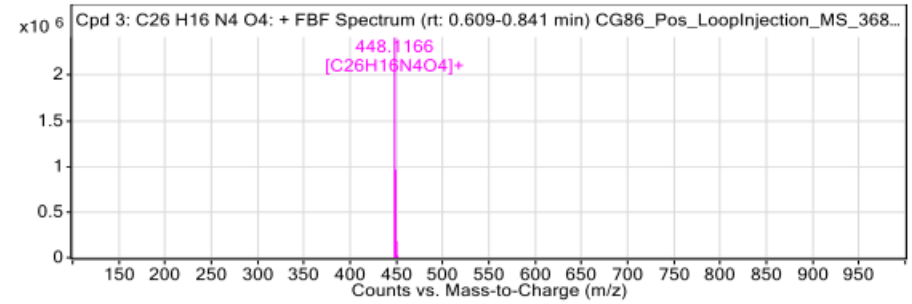

Figure: Full range view of Compound spectra and potential adducts.

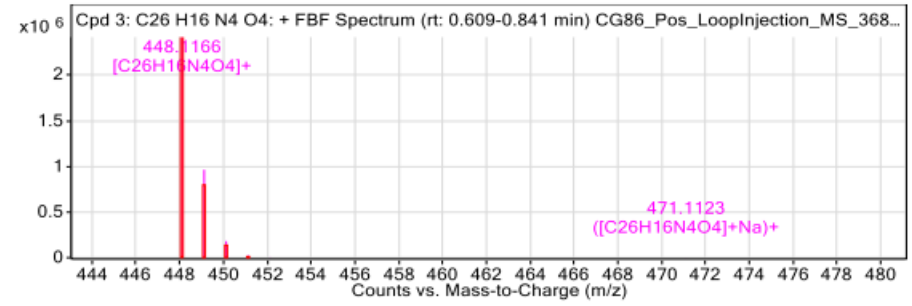

Compound Table

Compound Label	RT (min)	Observed mass (m/z)	Neutral observed mass (Da)	Theoretical mass (Da)	Mass error (ppm)	Isotope match score (%)
Cpd 1: C26 H16 Cl2 N4 O4				518.0549		
Cpd 2: C26 H16 Cl N4 O4	0.71	483.0842	483.0858	483.0860	-0.37	83.29
Cpd 3: C26 H16 N4 O4	0.70	448.1166	448.1178	448.1172	1.42	72.47

Mass errors of between -5.00 and 5.00 ppm with isotope match scores above 60% are considered confirmation of molecular formulae

Figure C4: *HRMS of **4.7***

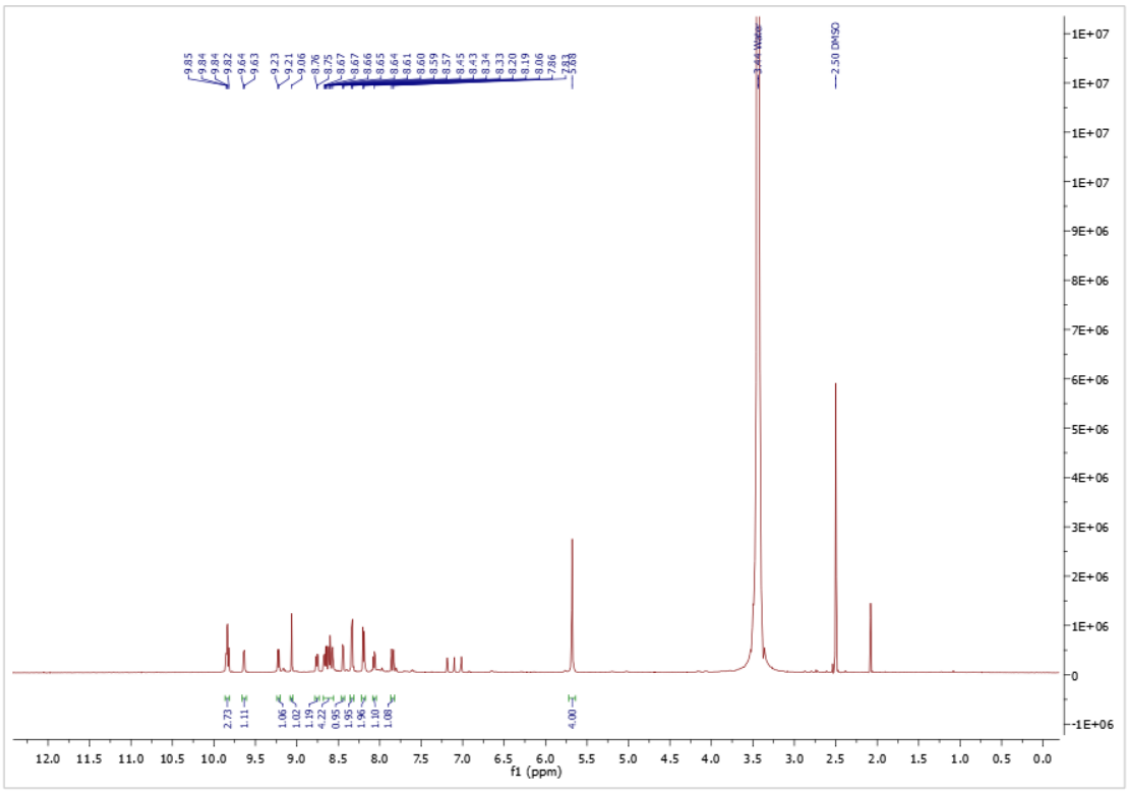

Figure C5: *^{1}H NMR spectrum of* ***4.8***

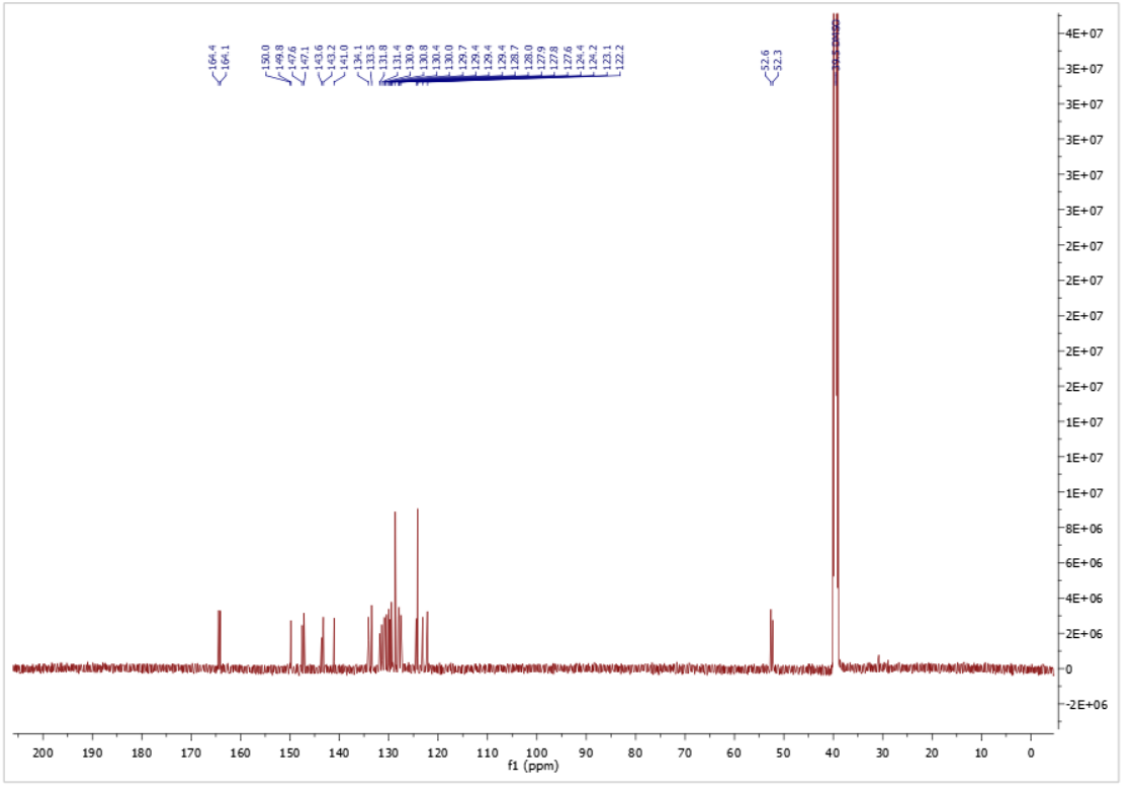

Figure C6: *^{13}C NMR spectrum of* ***4.8***

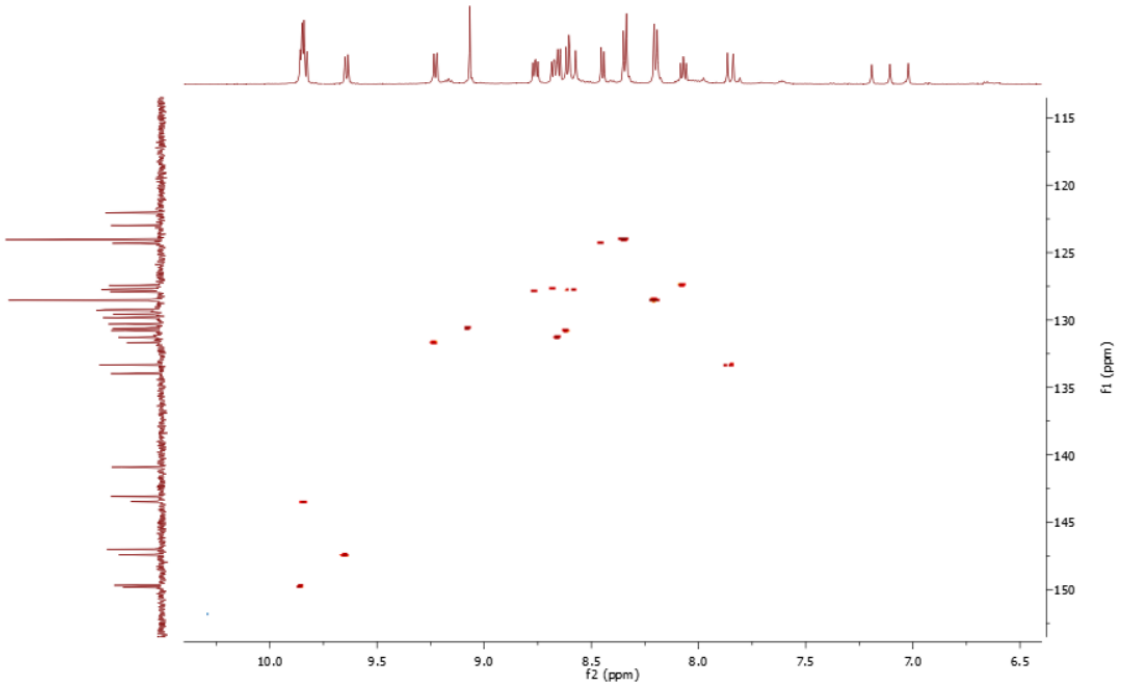

Figure C7: *HSQC of* ***4.8***

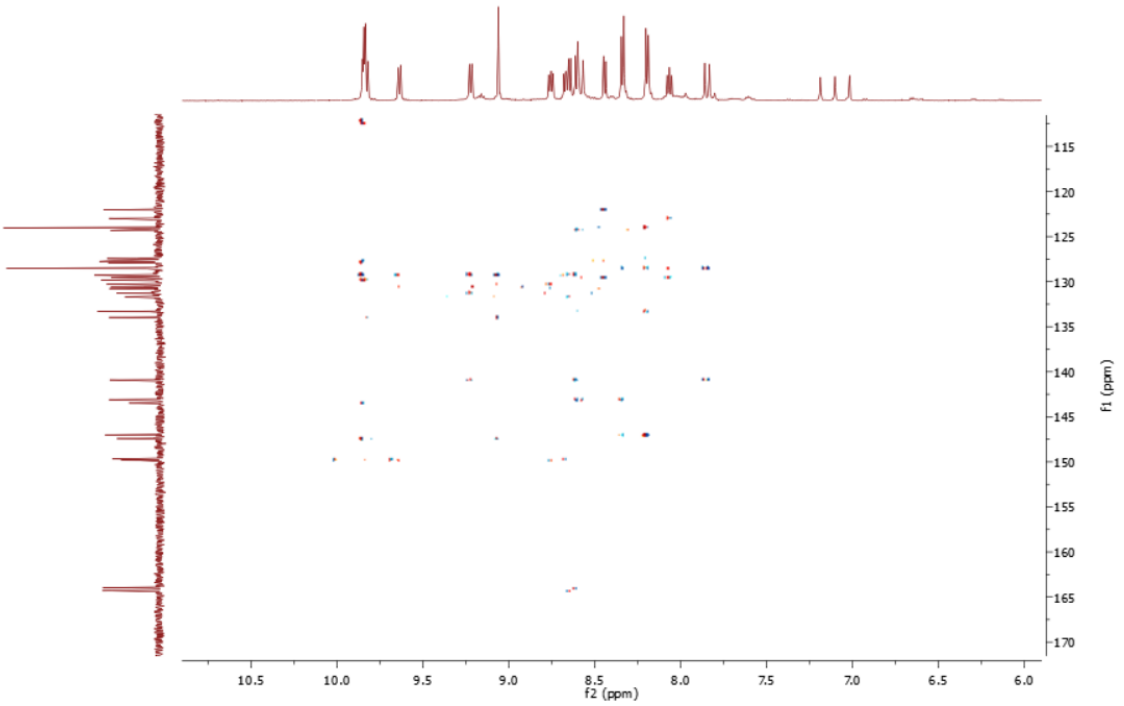

Figure C8: *HMBC of* ***4.8***

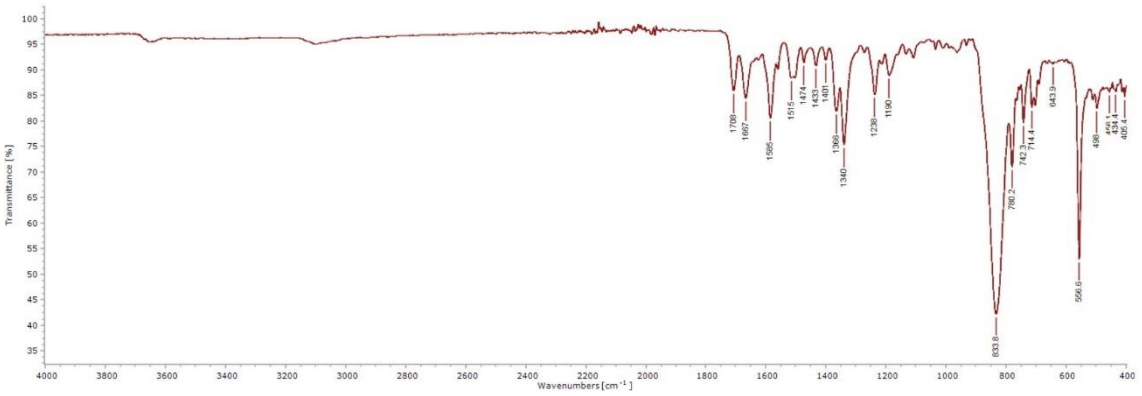

Figure C9: *IR of* ***4.8***

Compound specific information

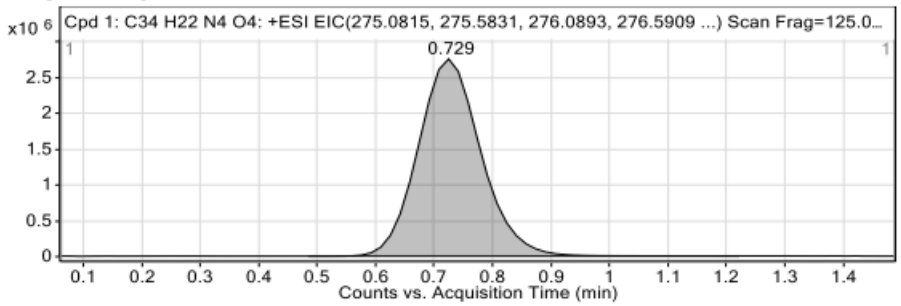

Figure: Extracted ion chromatogram (EIC) of compound.

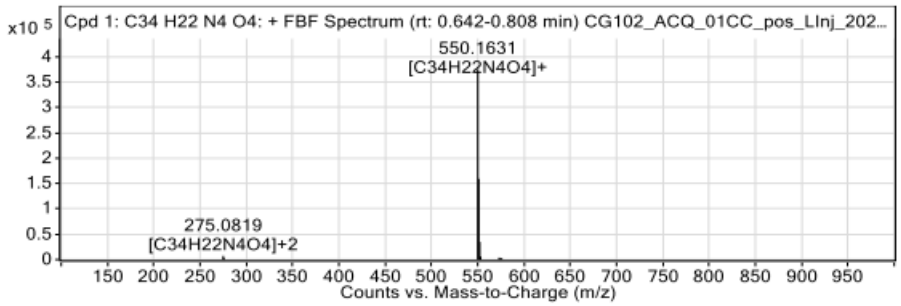

Compound Table

Compound Label	RT (min)	Observed mass (m/z)	Neutral observed mass (Da)	Theoretical mass (Da)	Mass error (ppm)	Isotope match score (%)
Cpd 1: C34 H22 N4 O4	0.73	550.1631	550.1636	550.1641	-0.94	96.17

Mass errors of between -5.00 and 5.00 ppm with isotope match scores above 60% are considered confirmation of molecular formulae

Figure C10: *HRMS of* ***4.8***